EXPERIMENT INVESTIGATION OF LATENT HEAT ENERGY STORAGE SYSTEM (LHTESS) FOR ENHANCING PERFORMANCE OF DRY-COOLING POWERPLANT

A Dissertation

by

NAVIN KUMAR

Submitted to the Office of Graduate and Professional Studies of
Texas A&M University
in partial fulfillment of the requirements for the degree of

DOCTOR OF PHILOSOPHY

Chair of Committee,	Debjyoti Banerjee
Co-Chair of Committee	Sai Lau
Committee Members,	Yassin A. Hassan
	Matt Pharr
Head of Department,	Andreas A. Ploycarpou

December 2018

Major Subject: Mechanical Engineering

ABSTRACT

Conventional electric power production primarily relies on water as a coolant - to remove low grade heat from the steam exiting from the turbines in thermal power-plants. It is anticipated that in the near future - these conventional techniques for water cooling of thermal power-plants will become unsustainable in various geographical regions that have scarcity of water resources. This is expected to arise from a combination of environmental concerns, increased water demand due to population growth, and the impact of climate change. Therefore, air-cooled platforms (dry cooling systems) are the obvious option for the replacement of water-cooled platforms. However, dry-cooling systems suffer from several performance limitations that compromise their reliability. Supplemental cooling systems can enhance the operational reliability and thermal performance of dry cooling systems. Hence, a latent heat thermal energy storage system (LHTESS) was developed and validated in this study as a proof of concept for a supplemental cooling system. The goal of this study to is to demonstrate the viability of LHTESS as a supplemental cooling platform with the aim of improving the energy efficiency and thermal performance ratings of air-cooled systems.

To improve the operational reliability of the LHTESS explored in this study, different phase change materials (PCMs) were explored (with and without additives). Both organic (e.g., paraffin) and inorganic (e.g., salt hydrates) materials were explored as candidate PCMs.

Material stability of the candidate PCM samples and additives were analyzed by subjecting them to thermocycling: consisting of repeated cycles of melting and freezing. Corrosion experiments were performed for evaluating the material compatibility of the chosen list of PCMs with candidate materials used in construction of LHTESS.

The incorporation of candidate PCMs in various heat exchanger configurations and validating their thermal performance was performed to meet the deliverables specified by the

sponsor of this research study, as part of the ARID program (Advanced Research in Dry-Cooling) of ARPA-E (Advanced Research Programs Agency – Energy). The different heat exchanger configurations explored in this study are: shell-and-tube heat exchanger (using Additive Manufacturing techniques, i.e., 3-D Printing), chevron-plate heat exchangers and a compact heat exchanger. Thermal conductivity enhancement techniques were explored by incorporating aluminum mesh as a metal foam in the compact heat exchanger.

DEDICATION

My Father (Subramaniam) and Mother (Malathi)

Whose love for me knew no bounds and who taught me the value of hard work. Thank you for always believing in me.

My Uncle (Selvarajan)

For being my role model throughout my life.

My Aunts (Usha and Jagdip Kaur)

Thank you for believing in me and supporting me throughout my PhD program.

My Sister and Brother (Prima, Manoj, and Arvin)

ACKNOWLEDGEMENTS

I would like to thank my Committee Chair: Dr. Debjyoti Banerjee, and Co-Chair: Dr. Sai Lau, as well as my committee members: Dr. Yassin Hassan and Dr. Matt Pharr for their guidance and support throughout the course of this research.

Thanks also go to my friends and colleagues and the department faculty and staff for making my time at Texas A&M University a great learning experience. Finally, thanks to my Mother and Father for their encouragement and love.

I would like to thank the Department of Energy (DOE) and Advance Research Project Agency – Energy (ARAP-E) for my Ph.D. dissertation through the ARID Program ("Advanced Research in Dry-Cooling").

I would like to thank our collaborators in our research team for the ARID Program:

(1) led by the University of Cincinnati (Principal Investigator: Dr. Raj Manglik, Dr. Milind Jog);

(2) University of California, Los Angeles (Dr. Vijay K. Dhir);

(3) University of California, Berkeley (Dr. Van P. Carey);

(4) Boeing (Dr. Arun Muley, Dr. Mike Stoia);

(5) Evapco Inc. (Dr. Jean-Pierre "JP" Libert); and

(6) Maulbetsch Consulting Inc. (Dr. John Maulbetsch).

My special thanks to Dr. Yordanos Bisrat at the Materials Characterization Facility (MCF) at Texas A&M University for her help and support, especially for helping us with the use of the Hot-Disk apparatus and Scanning Electron Microscopy (SEM) platforms. I am grateful to everyone who have helped me throughout this entire duration of my graduate studies.

CONTRIBUTORS AND FUNDING SOURCES

This work was supervised by a dissertation committee consisting of Professor Debjyoti Banerjee (Advisor) and Professor Sai Lau (Co-Advisor) and Professor Matt Pharr of the Department of Mechanical Engineering and Professor Hassan Yassin of the Department of Nuclear Engineering.

The experimental work for Chapter 12 was conducted by Reynaldo Chavez Jr of Texas A&M Department of Mechanical Engineering.

The experimental work for Chapter 14 was conducted by Ryan Von Ness of Texas A&M Department of Mechanical Engineering.

All other work conducted for the dissertation was completed by the student independently.

Funding Sources

Graduate study was supported by funding from Department of Energy ARPA-E ARID Program under the Grant Number [DE-FOA-00001002]

(and)

this work was also made possible in part by funding from the Department of Mechanical Engineering (e.g., for my Teaching Assistantships) at Texas A&M university.

Its contents are solely the responsibility of the authors and do not necessarily represent the official views of the Department of Energy.

TABLE OF CONTENTS

LIST OF FIGURES

Page

LIST OF TABLES

Page

CHAPTER I

INTRODUCTION AND LITERATURE REVIEW

Chapter 1 is divided into three sections. The first section provides a brief review of phase change materials (PCM) and their implementation in thermal energy storage (TES), particularly latent heat thermal energy storage systems (LHTESS).

The second part (or section) of chapter 1 provides a brief review of power-plant cooling systems, with a focus on supplementary cooling platforms, particularly, the various aspects of LHTESS that could be leveraged to enhance the efficacy, reliability and thermal performance of dry-cooling platforms in power-plants. Hence, LHTESS can be used to mitigate s an acute problem for power plants during high temperature excursions (i.e., in arid climates during hot days in summer when the ambient temperature exceeds a critical threshold, power plants exclusively relying on dry cooling have to shut down). Integrating LHTESS in these power plants (to serve as a supplementary cooling platform) can enable the power plants to be operational - even after the ambient temperature has exceeded the threshold value. Additional discussions on the nuances of this problem and mitigation techniques are provided in this section.

The third section of this chapter is devoted to the identification and delineation of the motivation, objectives, and significance of this study. At the end of this chapter (and all the remaining chapters in this dissertation), a synopsis of the contents of the chapter are also provided.

1.1 Introduction

In contemporary literature, multiple authors have argued the need for change in public policy goals regarding energy consumption (e.g., on incorporation of renewable energy in tandem with the utilization of fossil fuels). There is a desire to reduce the dependency on fossil fuels for meeting the energy consumption needs in the society. Potential strategies for developing sustainable options for power production include: increasing the capacity of power production from renewable energy sources and enhancing the energy efficiency of these power plants. Also, "Moore's" law predicts that device energy density (and therefore processing power of computing chips and electronics) doubles every 2 years. The shrinking form factors in electronic devices have resulted in techno-economic demand cycles for the invention of novel technologies to improve the cooling capabilities (e.g., for cooling of data centers, for the drive electronics in transportation sector – such as in electric vehicles, ships and autonomous transportation, including drones and self-driving cars).

In these applications, thermal energy storage (TES) can play an important role in improving the energy efficiency at the system level (i.e., depending on the duty cycle for each application). Phase change materials (PCMs) have gained popularity in contemporary literature as a potential option for TES platforms. PCMs primarily leverage latent heat during phase transformation processes to minimize material usage for thermal energy storage (TES) or for thermal management applications (TMA). PCMs effectively serve as thermal capacitors that help to mitigate the imbalance between energy demand and supply, to address the inherently transient nature of applications that require TES or TMA. The wide range of phase transition temperatures available for different types of PCMs – enable their incorporation in a diverse range of applications.

However, there is a need for improving the power rating (i.e., the thermal conductivity), reliability, and the energy storage capacity of PCMs. As novel PCMs continue to be introduced into the market, further research is needed to guarantee the reliability as well as the physical and chemical stability of these novel PCMs. Hence, one of the goals of this study is to explore strategies for improving the thermo-physical properties of these PCMs (e.g., salt hydrates). It is envisioned that improvement of the thermo-physical properties of these PCMs (e.g., salt hydrates) will augment their efficacy for applications requiring the enhancement of the thermal performance of dry-cooling platforms in power-plants.

1.2 Phase Change Materials

A material with significantly large value of phase change enthalpy (e.g., latent heat of fusion for melting and solidification) enable their capability to store large amounts of thermal energy in small form factors (i.e., while occupying smaller volume or requiring smaller quantities of material for a required duty cycle). As the material changes phase, from liquid state to solid state or vice versa, it can release or absorb large quantities of heat, respectively. These materials are classified as phase change materials (PCMs) or latent heat storage (LHS) units. Depending on the application, a PCM is chosen to undergo a solid-liquid, solid-gas, liquid-gas, and solid-solid phase transformation. In thermal engineering applications, typically the term "PCM" refers to solid-liquid phase transformation commonly known as melting-solidification cycle. PCMs are classified into several categories, as shown in Figure 1.

When a PCM undergoes phase transformation from liquid to solid, it releases thermal energy to the surrounding, which often requires substantial sub-cooling for initiating the freezing process. Referring to PCM, "subcooling" is the temperature drop below the freezing point attained by a pool of liquid during the initiation of the freezing process. During the melting process (i.e., during phase transformation from solid to liquid) PCM absorbs energy from the surroundings. The thermal energy absorbed by the PCM increases the internal energy of the atoms or molecules. This causes the intermolecular bonds (e.g., through hydrogen or chemical hydration bonding) to be broken. Thus, the ordered crystalline and semi crystalline structures are disrupted causing the molecules to be randomly distributed and structurally disoriented as the material changes from solid to liquid phase as illustrated in Figure 2. During the solidification process, the reverse of melting occurs, during which the PCM loses energy to the surrounding, and the atomic or

molecules renew their chemical association (i.e. chemical bonds) thus reforming the ordered phase resulting in solidification – as shown in . However, as mentioned before, to initiate the solidification process, a substantial degree of sub-cooling is often required to drive the nucleation process. Also, significant volume changes are encountered during phase change due to variation in solid and liquid density.

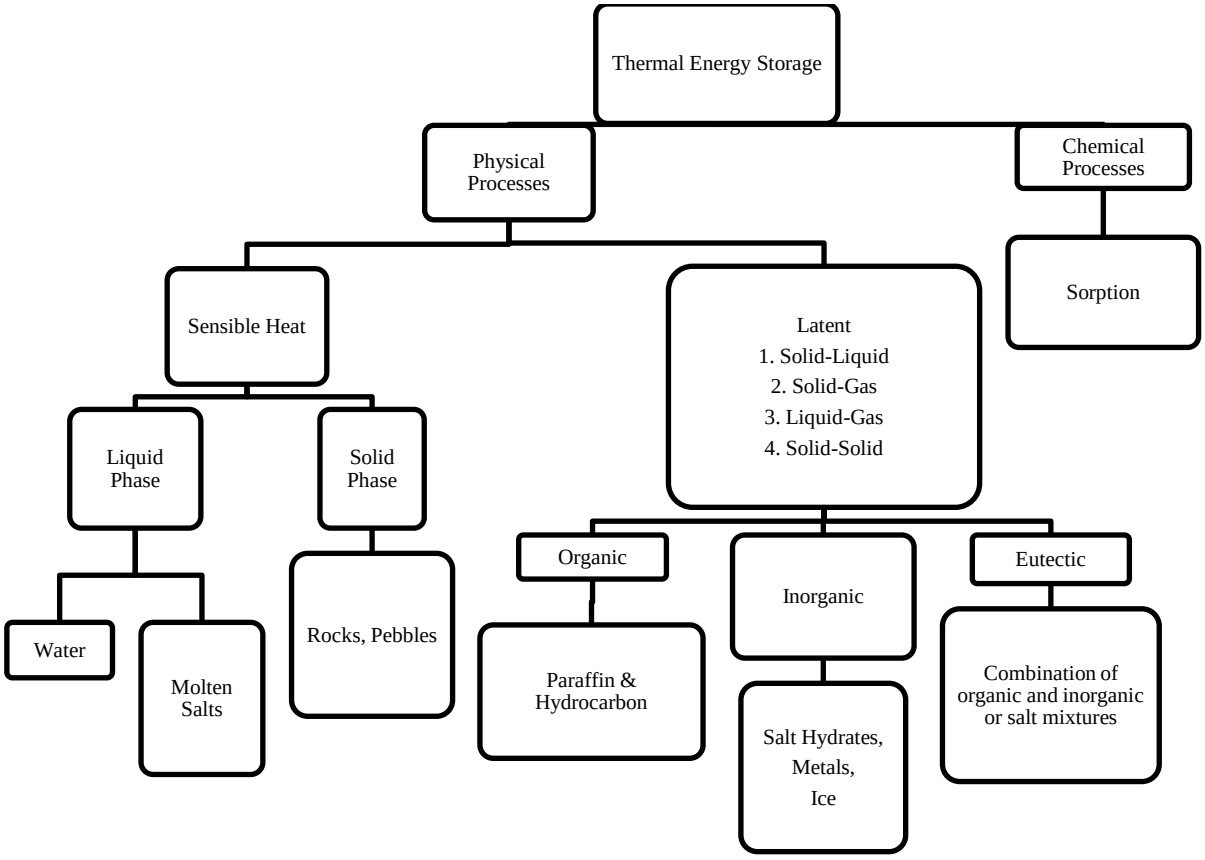

Figure 1: Classification of thermal energy storage materials.

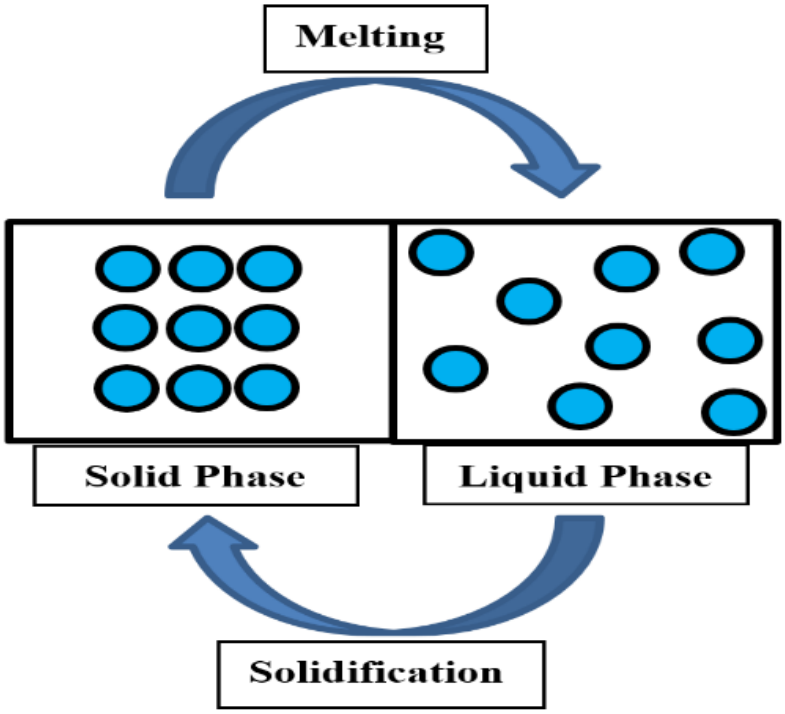

Figure 2: Representation of melting and solidification process at the molecular level.

As PCM undergoes melting or solidification, it has the capability to store energy in the form of sensible heat and latent heat as shown in Figure 3. A typical discharging cycle for PCM begins in subcooled solid state, which is then heated up to the phase transition point through sensible heating. As the energy input continues, the phase transformation is initiated for a portion of the PCM which is at a constant temperature. The energy absorbed by the PCM aids in phase transformation to progress throughout the volume of the PCM. After the phase transformation proceeds to completion, the PCM is in liquid phase, and any further energy input causes temperature increase which enables sensible heat to be stored in the system. The energy storage in the form of sensible heat is a function of the temperature change (ΔT) of the system and the specific heat capacity of the PCM, whereas the energy storage in the form of latent heat is determined solely by the enthalpy (i.e., the heat of fusion) of the PCM. Thermodynamic considerations require

phase change of pure and homogeneous substances to be isothermal. Due to heterogeneous features associated with typical engineering systems, often superheating or subcooling may be required, to initiate melting and freezing.

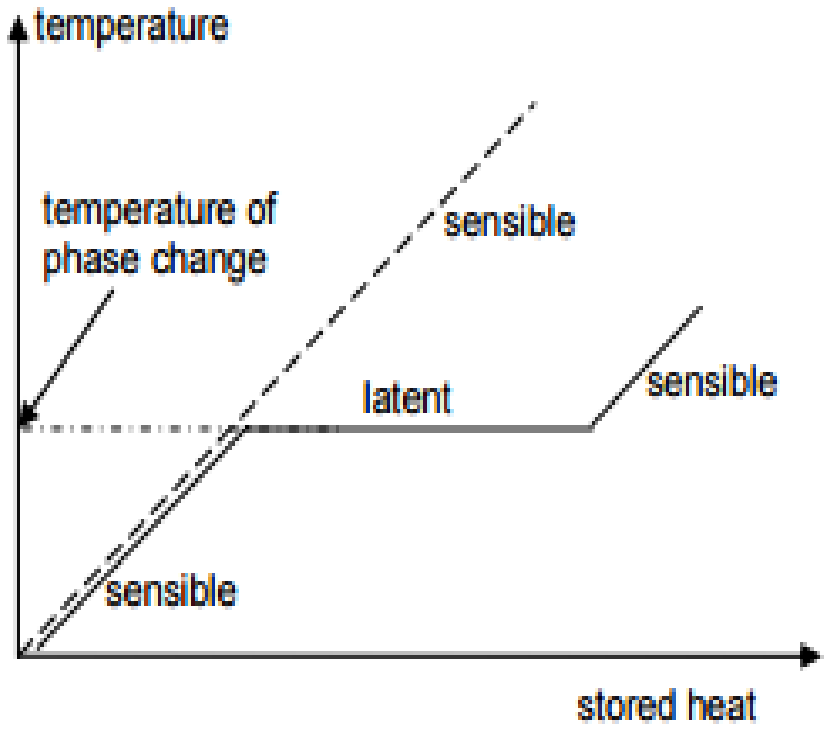

Figure 3: Schematic representation of energy storage capacity of phase change materials during phase transition. "Reprinted from [1]"

1.2.1 A Brief History of PCM Research

Rapid strides in PCM research were achieved during the 1970s and 1980s, when occupant comfort in buildings was explored by several research groups with the aim of minimizing energy usage footprint by leveraging thermal energy storage. In the 1980s, the concept of embedding PCMs in construction materials was utilized to reduce the heating and cooling loads of buildings [2]. Simultaneously in the 1980s, PCMs were considered for usage in thermal energy storage systems for both large solar plants and domestic hot water systems [3]. Rapid advances in the development and study of phase change materials occurred during the late 1970s, when research activities at the National Aeronautics and Space Administration (NASA) spurred the use of PCMs for thermal management of devices and systems in the space shuttle program [4] . In 1977, research at NASA resulted in the publication of a seminal reference on PCM titled "A Design Handbook for Phase Change Thermal Control and Energy Storage Devices" [5]. This reference is still of contemporary relevance, as evidenced by the wide use of this handbook in engineering design and professional practice. In the early 1990s, PCMs were explored for thermal management applications for electronic cooling, especially for cooling of high-performance computational platforms and high-heat flux optoelectronic devices. From the early 2000s, studies on PCMs have been focused on both high-temperature and low-temperature applications. These studies have branched off from conventional topics into the realm of waste heat energy recovery and storage, as well as thermal management in space program and applications involving cooling of optoelectronic devices, such as the directed energy weapon (DEW) systems.

1.2.2 Material Classifications

Material properties can be exploited for TES and TMA through physical mechanisms (e.g., TES) or chemical reactions (i.e., thermochemical energy storage, or "TCES"). Physical mechanisms are further classified into sensible heat and latent heat as shown in Figure 1. Thermal energy storage achieved by modulating the system temperature is termed as sensible heat storage. Therefore, the effectiveness of sensible heat storage platforms depends on the specific heat capacity of the energy storage material. Sensible storage systems typically use rocks, ground (i.e., soil), or molten salt as the storage medium. The energy storage in latent heat thermal energy storage system (LHTESS) is achieved by realizing phase transformation from solid to liquid or liquid to vapor, which typically occurs at quasi-isothermal conditions. The storage medium in LHTESS are also classified as phase change materials (PCMs), where the major proportion of the total stored thermal energy is in the form of latent heat. In addition, PCMs can be classified as organic and inorganic. Often, inorganic PCMs are realized in the form of eutectic mixtures that enable quasi-isothermal operation. These classifications are summarized in Figure 1. The different types of PCMs that are available commercially are typically classified as organic, inorganic, and eutectic [6, 7, 8].

Table 2 provides a comparison of the relative advantages and disadvantages conferred by the different categories of latent heat energy storage medium. This literature review is primarily focused on solid-liquid PCMs due to their relative ease of implementation in TES and TMA. In the realm of solid-liquid PCMs, provides a summary of the relative advantages and disadvantages of the different classes of PCMs.

A) Organic PCMs

Covalent bonding is typically encountered in organic PCMs. Organic PCMs are sourced from agricultural/food processing and hydrocarbon processing industries (e.g., oil, wax, fatty acids, etc.). Therefore, these materials are inexpensive, provide ease of implementation in thermal applications, usually have low environmental footprint in the applications, and are available abundantly from natural sources (e.g. from oil and gas explorations worldwide as well as beeswax harvesting, alcohol derivatives, and fatty acids). Hence historically speaking, they are one of the most widely used among commercially available PCMs. Having a long history of applications in thermal devices that have been tested thoroughly over the years and owing to their better material stability when subjected to repeated thermo-cycling (i.e., repeated melting and solidification).

The common traits of organic PCMS are congruent melting (i.e., minimal complications due to phase separation that arise from repeated thermo-cycling), self-nucleation properties (i.e., they do not need additives for promoting nucleation), and non-corrosive nature. This is because organic PCMs typically comprise of a mixture of long-chain hydrocarbons (such as paraffin and natural waxes). Hence the melting point of organic PCMs varies over a wider band of temperatures depending on the chemical composition. Organic PCMs typically melt or solidify slowly over a range of temperatures, as shown in Figure 4. Therefore, organic PCMs are categorized by melting

temperature range rather than a single melting temperature. Organic PCMs are typically classified based on their latent heat and melting temperature [6, 9].

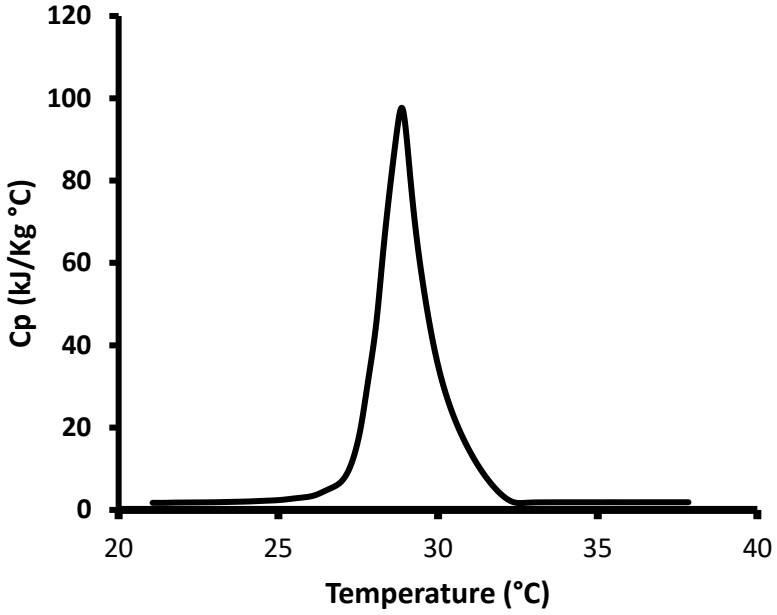

Figure 4: Typical melting curve of organic PCMs (paraffin) obtained from differential scanning calorimetry (DSC) experiments.

The chemical composition of organic PCMs includes paraffin and fatty acids are of the form: [CH3(CH2)2n(COOH)], where *n* is an integer. The most commonly used paraffin-based PCMs are typically straight chain n-alkanes [9] . The melting temperature range and the latent heat capacity of this material class depend on the length of the polymer chain. Non-paraffin PCMs consist of esters, fatty acids, alcohols, and glycols. The primary distinguishing feature between paraffin and fatty acids is their melting temperatures. Typically, fatty acids have lower range of melting temperatures than paraffin and are therefore more suitable for building and textile applications. The main disadvantage of organic PCMs is their low thermal conductivity. This impedes the power rating of devices involving organic PCMs and decreases their effectiveness for

TMA applications. The low melting temperature ranges also make them unsuitable for TES applications. However, the primary advantages conferred by organic PCMs are their ease of availability and cost. Figure 5 illustrates the images of different organic PCMs.

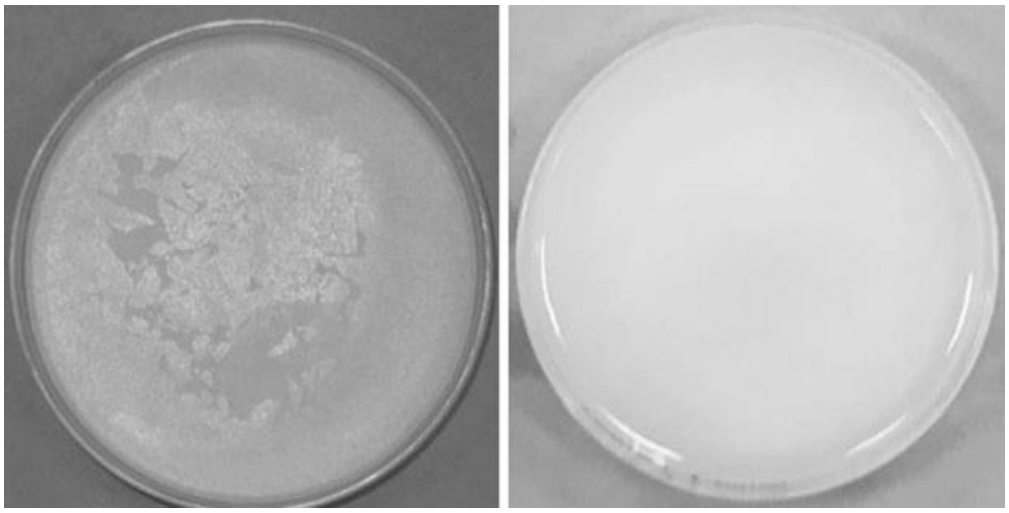

Figure 5: Photographs of organic PCMs: (left) poly- ethylene-glycol (PEG 600); and (right) paraffin wax.

The properties of several common organic PCMs are listed in Table 1. Several research reports in contemporary literature have been focused on exploring the properties of blended PCMs with the objective of manipulating the phase transition temperatures and latent heat storage capacities - that are often tailored for specific applications [1].

Table 1: Representative examples of organic PCMs. Adapted from [1] .

Material	Type	Melting temperature [° C]	Melting enthalpy [kJ/kg]	Thermal conductivity [W/ (m . K)]
Heptadecane	Paraffin	19	240	0.21 (solid)
Octadecane	Paraffin	28	245	0.358 (solid)
				0.148 (liquid)
Polyethylene	Paraffin	35	200	–
Caprylic acid	Fatty	16	149	0.149 (liquid)
Lauric acid	Fatty	42	178	0.147 (liquid)
Palmitic acid	Fatty	61	185	–

B) Inorganic PCMs

Ionic bonding is typically encountered in inorganic PCMs. Typical examples of inorganic PCMs include various types of metals, salts, and salt hydrates. The thermo-physical properties of several inorganic PCMs are listed in Table 2. Both pure salts and salt hydrates have similar thermo-physical properties and chemical characteristics.

Typically, alkali metal salts are used as commercial inorganic PCMs. The anions in these salts and salt hydrates consist of oxides, hydroxides, chlorides, chlorates, citrates, carbonates, sulfates, and nitrates. Inorganic PCMs confer applicability over a wider range of temperatures and higher values of volumetric energy storage capacity, as well as higher values of thermal conductivity compared to that of organic PCMs. Figure 6 shows images of inorganic PCMs.

Table 2: Thermo-physical properties of inorganic PCMs. Adapted from [1]

Material	Type	Transition Temperature [°C]	Melting Enthalpy [kJ/kg]	Thermal Conductivity [W/ (m. K)]
$LiNO_3$	Salt	245	360	0.58 (liquid)
				1.37 (solid)
KNO_3	Salt	333	266	0.5 (liquid)
$MgCl_2$	Salt	714	266	–
KF	Salt	857	452	–
$KF{\cdot}(3H_2O)$	Salt	18.5	231	–
	Hydrate			
$CaCl_2{\cdot}(6H_2O)$	Salt	30	190	0.54 (liquid)
	Hydrate			1.088 (solid)
$Na_2HPO_4{\cdot}(12H_2O)$	Salt	35	280	0.476 (liquid)
	Hydrate			0.514 (solid)
$MgCl_2{\cdot}(6H_2O)$	Salt	117	169	0.57 (liquid)
	Hydrate			0.704 (solid)

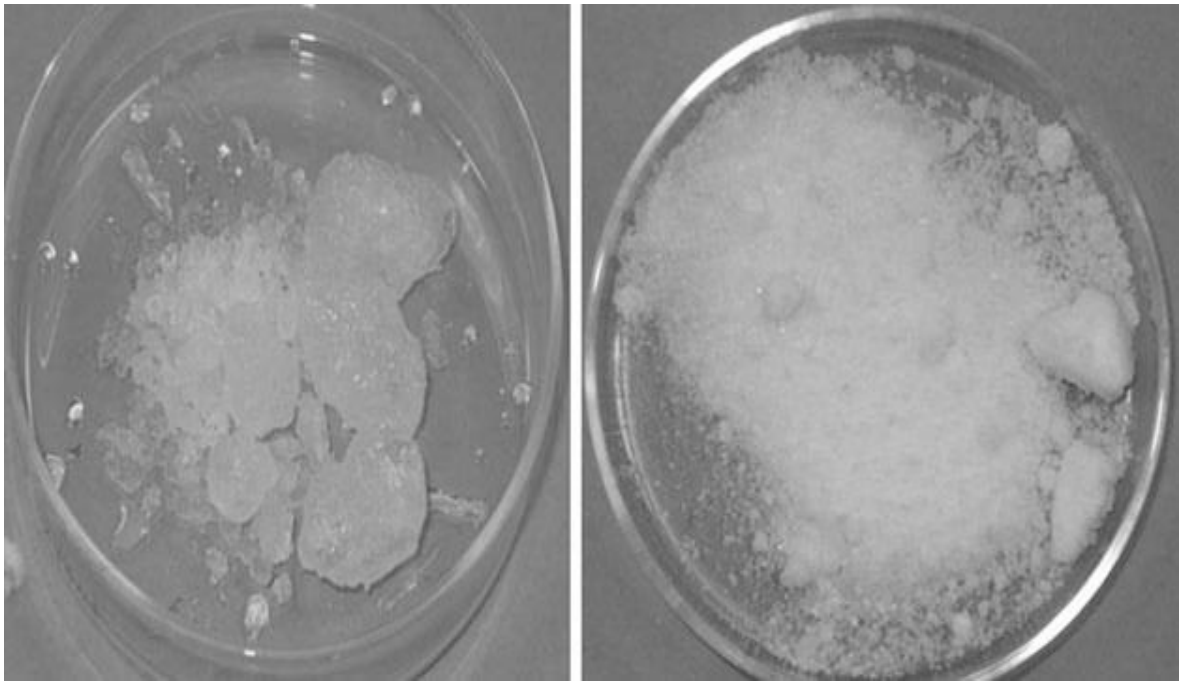

Figure 6: Photographs of salt hydrates and anhydrous salts: (left) calcium chloride hexahydrate: [$CaCl_2{\cdot}(6H_2O)$]; and (right) lithium nitrate [$LiNO_3$].

When certain anhydrous salts are combined with water molecules in a specific stoichiometric ratio, crystalline structure of hydrated salts is sometimes obtained from this hydration process (depending on the level of hydration). Hence the salt hydrate composition consists of the salt molecules and water molecules in a specific mixing ratio (in the process, forming discrete crystal structures depending on the level of hydration). The chemical bonding within the crystal structure enables the incorporation of the water molecules at specific locations in well-defined orientation within the unit cell. Salt hydrates usually form an ion-dipole bond or hydrogen bond.

In salt hydrates, the solid-liquid phase transformation typically occurs reversibly by hydration and dehydration process, respectively. The transition temperature of salt hydrates varies from 5 °C to 130 °C. Above an operating point of 150°C, different types of anhydrous salts (i.e. molten salts) can be used as PCMs rather than salt hydrates. The most significant issues that impede the use of salt and salt hydrates in engineering applications are their: (1) reliability (due to phase segregation which causes significant variation in material composition and creep in the measured values of latent heat capacity as well as in transition temperature); and (2) varying degree of sub-cooling required to initiate nucleation (especially, when subjected to repeated thermo-cycling). Also, inorganic PCMs are often corrosive with metals and therefore require additional consideration for material compatibility during engineering design. These issues often give rise to the need for incorporating additives for: (1) enhancing their reliability during operation (i.e., for impeding or preventing phase segregation); (2) minimizing the degree of sub-cooling required to initiate nucleation; and (3) mitigating or reducing corrosion.

When a salt hydrate is heated above the chemical dehydration temperature for prolonged period of time, the chemically hydrated water molecules are liberated resulting in the formation of

pure anhydrous salt. Therefore, the chemical dehydration temperature should also be considered during the engineering design process.

Other categories of inorganic PCMs include metals and metal eutectics that have low melting points. Eutectic PCMs are composed of two or more constituent materials in a specific ratio that confer the unique property of melting and freezing congruently thus providing the appearance of a single melting point. Often, eutectic compositions of mixtures have similar crystal structures as of their constituents. The classification of inorganic PCMs is shown in Figure 7. In this schematic plot, the inorganic PCMs are classified based on their energy storage capacity values and phase transition temperatures.

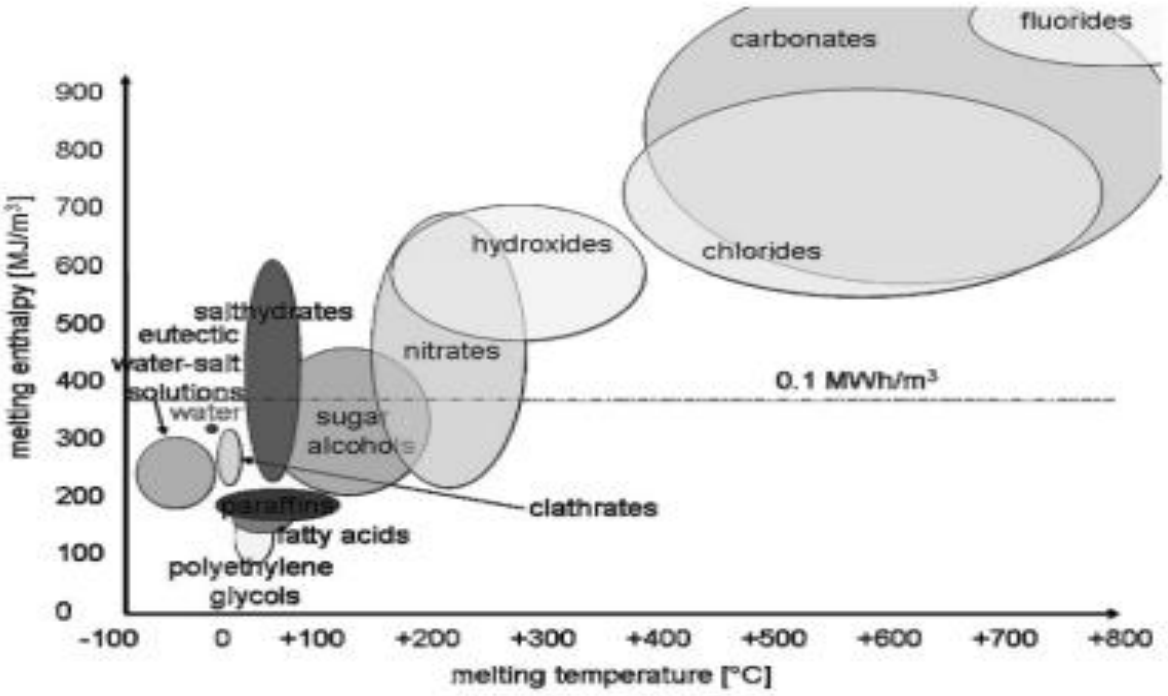

Figure 7: Various types of PCMs classified according to their latent heat capacity for fusion – plotted as a function of their range of phase transition temperatures. "Reprinted from [1]"

1.2.3 Thermo-Physical Properties

Selection of PCMs for various thermal engineering applications are based on their desirable thermodynamic properties, chemical kinetics, chemical compatibility, techno-economic feasibility, low environmental impact, and easy availability (for sourcing or procurement) [10]. The discussions in the following sections further elaborate on these requirements.

A) Thermal Properties

The desired thermal properties of PCMs include the ability to transmit high rates of heat (i.e. high thermal conductivity), stable single-point phase-transition temperature, and high phase change enthalpy [11]. The most important parameter guiding the selection of a PCM is phase transition temperature. The phase transition temperature should match the range of heating and cooling temperatures for charging and discharging of a thermal energy storage system. High latent heat values for a given phase transition temperature helps minimize the weight and form factor of the storage system. High heat transfer capability allows rapid charging and discharging of the storage system (i.e., enables higher power rating).

B) Chemical Kinetics

Fast, stable, reversible, and reliable chemical kinetics are essential to minimizing the need for sub-cooling [1]. The need for high sub-cooling and the variability in the degree of sub-cooling between successive thermo-cycles has typically encumbered the application of salt hydrates in engineering applications. Even minor level of sub-cooling could significantly impact the energy extraction during solidification, thereby compromising the performance and the reliability of the system (compared to the design specifications). Typically, any PCM requiring sub-cooling that exceed 10°C could completely prevent energy extraction during solidification, since heat

exchangers typically operate on small temperature margins (especially for power production applications). Additional discussions on sub-cooling requirements are provided in later sections.

C) Chemical Properties

The desired chemical properties of PCMs include: material stability [12] (i.e. minimal phase segregation with thermo-cycling), material compatibility (with containment structures), non-toxicity, and non-flammability. Commonly salt hydrates are known to suffer from chemical decomposition and degradation (i.e. often due to parasitic hydration from ambient humidity). More detailed discussion on phase segregation in salt hydrates, due to repeated thermo-cycling are provided in later sections. The material compatibility (i.e., corrosiveness and chemical reactivity) between PCM and containment structures - is an important factor in the selection process. Depending on the application, the toxicity and flammability of PCMs are also important issues in the selection process. Commonly, paraffin waxes are considered as flammable substances and often constitute a fire hazard.

1.3 General Background in Thermal Power - Plant Cooling

The societal impact of water usage on power production is commonly termed as the "water-energy nexus" or sometimes as the "food-energy-water" (FEW) nexus. Conventional electric power production primarily relies on water as a coolant for removing low grade heat from the condensing steam (at turbine exit) in thermal power plants. These water-cooling platforms rely on cooling towers and spray ponds, resulting in loss of significant amounts of fresh water resources by evaporation and the discharge of water at elevated temperatures in the local ecosystems, such as, into lakes/ ponds and rivers (which, in turn, can impact the flora and fauna of the local ecosystems). The waste heat (e.g., evaporation losses) from power plants can also affect the micro-climates as well as pollution levels in the vicinity.

It is anticipated that in the next two to three decades - these conventional techniques that depend on water cooling of thermal power plants will be unsustainable in various geographical regions that have scarcity of water resources. This is expected to arise from a combination of environmental concerns, increased water demand due to population growth, and the impact of climate change. Hence, these factors are expected to significantly constrain the available water supply that can be allocated to power plant cooling. It is also anticipated that distributed electric power generation will continue to penetrate the markets, including in regions where water cooling for low-grade heat removal is not economically feasible [13].

Thermoelectric power generation in the U.S. requires approximately 139 billion gallons of water per day (BGD) for wet cooling, making it the largest single use of fresh water resources in the U.S. [14]. Of the fresh water withdrawn for the power generation, 4.3 BGD are dissipated to

the atmosphere by cooling towers and spray ponds [14]. Consumption and loss of water resources in power plant cooling therefore renders them unavailable for other societal uses.

The typical energy conversion efficiency of power plants (that rely on water cooling) ranges from 35-55% [15]. Power plants that produce hundreds of megawatts of electricity must also dissipate hundreds of megawatts of low-grade waste heat. The temperature at which this heat is rejected to the environment directly impacts thermodynamic efficiency. Heat rejection to a lower temperature increases the net power production and augments the thermodynamic energy efficiency. A lower cooling water temperature allows for a lower steam condensation pressure in a steam Rankine cycle, reducing the backpressure on the turbine outlet and allowing for more power to be extracted by the turbine. For every 3 °C rise in the steam condensation temperature, it is estimated that the power production from the turbines are reduced by 1%. To adequately reject megawatts of low-grade heat from low pressure condensing steam, the thermal capacity of the cold sink is concomitantly required to be of substantially higher magnitude.

The heat sinks historically used for heat rejection from commercial power plants are: (a) large water bodies, and (b) ambient air (atmosphere). Water is favored because rivers, lakes, and oceans tend to be cooler than ambient air (resulting in higher energy conversion efficiency). Water cooling enables the achievement of more uniform temperature and enables higher rates of heat transfer for heat exchanging surfaces. Water cooled condensers are smaller in size than air-cooled units owing to the high rate of convective heat transfer (i.e., higher power ratings per unit volume of the heat exchanger envelope). Therefore, water cooled condensers are considerably less expensive (both for capital investment and for operating costs). This is fundamentally due to the fact that the thermal conductivity of water is approximately twenty-fold higher than that of air

while the specific heat capacity of water is ~4 times that of air. The techno-economic superiority and higher energy conversion efficiency afforded by water cooling confers various advantages and therefore have led to the current industrial paradigm for base-load operation for power generation - where 99% of commercial thermal power plants are water cooled, while only 1% of commercial power plants are air cooled.

Uncertainty in the availability of fresh water resources in the near future and the quality of water supply due to climate change - add further complexity in the viability and sustainability of water cooling of thermal power plants in many regions within U.S. Hence, the development of cost competitive and energy efficient power plant cooling systems (that do not rely on fresh water resources) will significantly enhance the viability of power production infrastructure. This will also help to reduce the dependence on precious fresh water resources that can be utilized for other societal purposes (e.g., meeting the demands for increased human consumption due to population growth, agriculture and food production, etc.). Moreover, deployment of distributed power generation can be enhanced further (since large bodies of water would not be required for cooling).

1.3.1 Dry Cooling in Thermal Power-Plants

Dry cooling platforms can help obviate the use of cooling water that is primarily used for steam condensation. In most cases (involving wet cooling), the remaining water use, totaling perhaps 5% of the amount used in recirculating systems, is required for: (a) boiler make-up, (b) other cooling applications, and (c) the so-called “hotel load” (i.e., for other uses that are not directly associated with power production). In dry cooling systems, the ultimate heat rejection to the environment is achieved with air-cooled heat exchangers and equipment that discharges heat directly to the ambient by heating the surrounding air. Dry systems are of two types: direct and

indirect. Direct systems duct the steam to air-cooled condensers (ACCs) that can be either mechanical (forced flow) or natural draft units. Indirect systems condense the steam in water cooled surface condensers, from which the heated water is pumped to air-cooled heat exchangers where it is cooled and then re-circulated to the steam condenser, as shown in Figure 8.

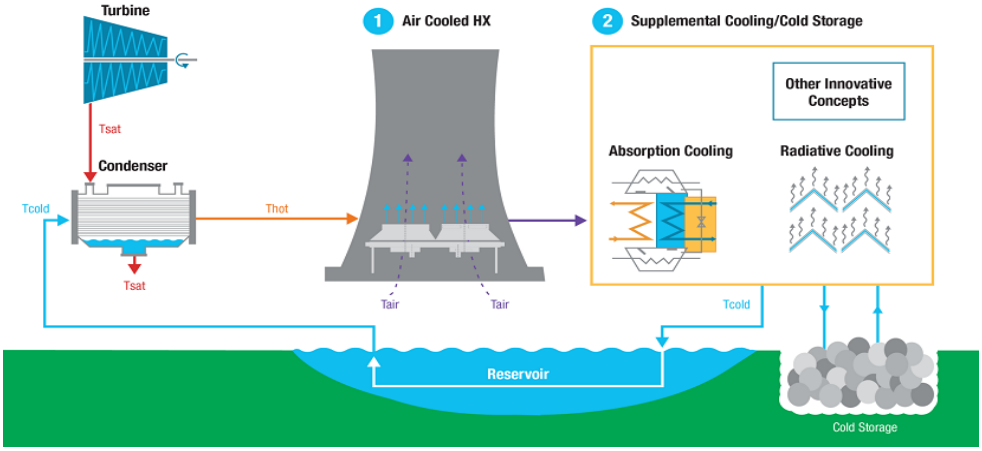

Figure 8: Indirect Dry Cooling Systems . The prosed idea consists of supplemental cooling system to enhance the overall efficiency of the power-plant during peak hours. "Reprinted from [16]"

In direct systems, the steam exiting the turbine exhaust is delivered directly to an air-cooled condenser (ACC), as shown in Figure 9. Heat rejection to the environment takes place in a single step, where steam is condensed inside finned tubes, which are typically arranged in an A-frame configuration and is then cooled by air blown across the finned surfaces.

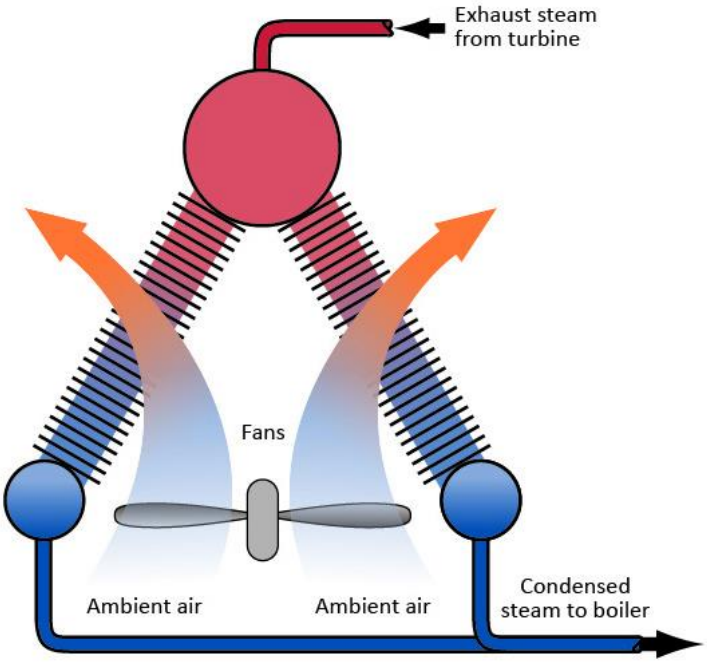

Figure 9: Direct dry air cooling systems for power-plant cooling applications "Reprinted from [16]".

Approximately 1% of total number of thermal power plants in the U.S. utilize air-cooled condensers [15]. Indirect dry cooling combines a water-cooled condenser with a convective air-cooled heat exchanger and water is continuously recirculated between the two in a closed loop. In regions of the U.S. where water scarcity and environmental concerns make permitting for wet-cooled systems difficult - there has been a recent trend toward dry-cooling systems [18]. With current technology, power producers are reluctant to use dry-cooling systems for two principle reasons: (1) the low air-side heat transfer coefficient necessitates massive heat exchangers that are costly and require a large footprint (with concomitant land usage and real-estate issues); and (2) air cooling imposes a performance penalty when ambient temperatures are high, and therefore imposes several challenges, which are discussed next.

A) Air-Side Heat Transfer Coefficient

The air-side convective heat transfer coefficient (10–100 W/m^2 K) is roughly two orders of magnitude lower than that for water (1,000–10,000 W/m^2 K), depending on the operating regime (laminar or turbulent). Therefore, an air-cooled system requires significantly more surface area and higher fan power compared to a wet-cooled system with the same heat rejection requirements. Both the capital and operating costs for an air-cooled condenser can each be 3.5 times of a comparable wet-cooled system (with the same heat load) [18].

B) Ambient dry bulb temperature and second law limitation

The dry bulb ambient air temperature (and the second law of thermodynamics) sets the lower limit for steam condensation temperature within an air-cooled condenser. In contrast, evaporative water cooling within a cooling tower utilizes latent heat transport (due to evaporation) enables the operating temperature to be lower than the ambient air-dry bulb temperature. The lower limit for evaporative cooling is the wet bulb temperature (only in exceptional circumstances this is the same as the dry bulb temperature – i.e., only at 100% relative humidity which occurs when the ambient air is fully saturated). Under all other conditions, water can evaporate into the ambient air and the wet bulb temperature is lower than the dry bulb temperature, typically by a margin of 3 – 5 °C [15]. As a result of these fundamental thermodynamic limitations, the use of air-cooled condensers results in loss of power output from the steam turbine compared to that of water-cooled operation, by a typical margin of ~2%. Periodically, there are ambient temperature excursions that result in large differences between the wet and dry bulb temperatures. For such temperature excursions, there can be upwards of 10% [15] reduction in power production when using dry cooling. In addition to the two principle challenges associated with dry cooling cited above, there

are other considerations such as wind loading, fan failure, fan noise, and fluid leakage that can impede adoption of dry-cooling systems.

1.3.2 Need for Supplemental Cooling

A major drawback associated with managing the entire power plant heat rejection load solely with air cooling is that temperature excursions can compromise the operational reliability. Temperature excursions, particularly on hot days, can lead to dramatic increase in the turbine back pressure, as shown in Figure 10. Increasing turbine back pressure causes less power extraction by the turbine, thus dramatically reducing the energy conversion efficiency.

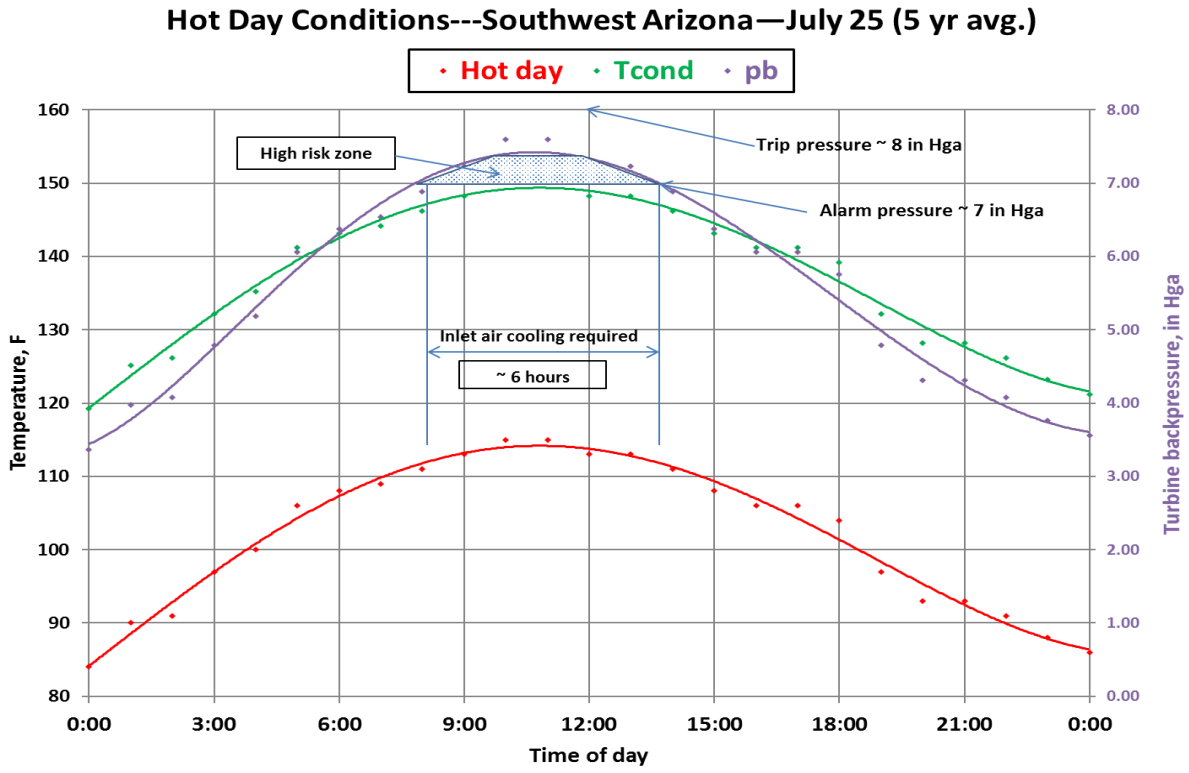

Figure 10: Variation in turbine backpressure ("p_b") during different times on a hot day as a function of increasing ambient air temperature (and temperature of air- cooled condenser, "T_{cond}") for an aspirational target air cooled heat exchanger. (Data was provided by Dr. John Maulbetsch, Maulbetsch Consulting Inc.).

The plots in Figure 10 also show that during the hottest periods of the day the back pressure can increase dramatically causing the system alarms to be activated. Associated with this alarm are severe systemic risks as the power plant may need to be shut down since the turbine back pressure is close to the trip pressure (thus exposing various components to risk of severe damage). If a power plant is subjected to unscheduled shut down (particularly during the hottest parts of the day, which are also typically periods of high electricity demand in the electric grid), the electric grid can be at risk of going unstable as the demand and supply are unbalanced – thus leading to wider scale power outage in a geographical region and across multiple utility providers. To overcome these limitations and reducing the risks (as well as improving performance and reliability), supplemental cooling is often desirable. The need for supplemental cooling and the associated system sizing requirements varies regionally, seasonally, and daily (i.e., depending on the duty cycles).

An attractive embodiment of a supplemental cooling system is realized using Latent Heat Thermal Energy Storage System (LHTESS). LHTESS can be tailored to store and release large amounts of thermal energy, thus offering a cost-effective way to mitigate disadvantages of air-cooled systems that require frequent load balancing. During the day, when the air temperature becomes too hot for the air-cooled heat exchanger to be effective, the LHTESS can be used to cool the air inlet temperature down to acceptable temperature values (or directly cool the condensing steam). The LHTESS removes heat from the incoming hot air at certain times during the day and cooled air is then supplied to the steam condenser (as shown in Figure 10). During periods when the ambient air is cooler, the LHTESS could release the stored heat to ambient and become ready for reuse in the power cycle during the next period of peak demand. Phase Change Materials (PCMs) are considered to be attractive for LHTESS applications for their ability to store and

release heat over a wide range of temperatures. LHTESS that utilize PCM can potentially be customized to provide supplemental dry cooling for different climates, including regions with high ambient temperatures, such as the southwestern United States.

The PCM candidates are selected primarily based on phase transition temperatures. The primary selection criteria can typically be based on the historic data for climate patterns for a chosen location (i.e., for a chosen thermal power plant). Secondary considerations include: (a) the system size and power rating requirements for the heat exchangers used in the LHTESS, which are based on thermo-physical considerations (such as latent heat storage density, thermal conductivity, density, specific heat capacity, rheology, diffusivity, etc.); (b) thermo-chemical considerations are based on material compatibility considerations (such as corrosion, fouling, material/ chemical stability for repeated melt-freeze cycles, etc.); and (c) reliability.

A brief review of PCM was presented in the earlier sections. The review enables the exploration and selection of appropriate candidate PCMs for applications in LHTESS that are suitable for dry-cooling configurations in conventional power generation.

1.4 Objective, Motivation, Goals and Scope of Study

The objective of this comprehensive study is to generate a rank order of PCMs (which is currently lacking in the literature) for LHTESS. The aim of this study is to identify PCM candidates for potential application in Latent Heat Thermal Energy Storage System (LHTESS) for supplemental cooling of thermal power-plants. The prototype LHTESS platform developed as a part of this study is motivated by application of similar platforms in dry cooling of power plants that meet the goals of the ARPA-E ARID program [16]**.** The goals and tasks of this study, include:

(1) Perform experiments to determine the material properties of a chosen list of PCMs (with and without additives) as well as the material compatibility of these PCMs for heat exchangers. The performance of these chosen PCMs were characterized for evaluating the total thermal energy storage capacity, power rating and long-term reliability.

(2) Perform experiments incorporating a selected list of PCMs in various types of heat exchangers to realize different LHTESS configurations (e.g., shell and tube heat exchangers as well as plate heat exchangers and compact heat exchangers). The performance of these heat exchangers were evaluated under transient operating conditions (e.g., for different profiles of duty cycles). The performance of these chosen PCMs in combination with the various LHTESS configurations were characterized for evaluating the total thermal energy storage capacity, power rating and long-term reliability.

(3) Perform experiments involving “Cold Finger” technique to prove feasibility of this approach for obviating sub-cooling of PCM (to improve the performance and reliability).

(4) Complement the experimental studies with predictions for thermal performance (based on numerical and analytical models). The objective of this task is to perform experimental validation of the predictions obtained from the analytical and numerical models.

The scope of this study is limited to PCM candidates that can address thermal energy storage needs and range of phase transition temperatures required for supplemental cooling of air-cooled thermal power plants involving Rankine cycle (i.e., steam-water cycle). Based on the diurnal variation of ambient temperatures in typical arid regions the range of operating temperatures is restricted to 20 ~ 40 °C. As a result, PCM with phase transition temperatures in the vicinity of 29 ~ 33 °C is desired. Secondary requirements include high latent heat, material stability and material compatibility. Hence, the scope of the proposed study was restricted to:

(a) Inorganic PCMs: Calcium Chloride Hexahydrate and Sodium Sulfate Decahydrate (Glauber's Salt), Lithium nitrate Trihydrate, Zinc Nitrate Hexahydrate, and S32 (procured from Rubitherm);

The choice of PCMs was based on the scope of this study (i.e., to address the needs of and deliverables for - the ARID program). The list of additives as nucleation promoters (or nucleators) (to obviate sub cooling) was limited to: zinc nitrate hydroxyl, zinc oxide, strontium chloride, sodium chloride, and borax. The list of additives to mitigate phase segregation (i.e., as agents for promoting water retention by thickening or gelling) was restricted to: gelatin, appaligate clay, and guar gum. The mass fraction of the additives used in this study was in the range of 1 ~ 9% for nucleators and 1 ~ 20% for gelling agents. It is expected that the additives will enhance a few of the desired characteristics of the chosen list of PCMs (which are of higher priority) and at the expense of degradation in the performance as well as other characteristics of the PCM.

1.5 Significance of Current Study

This study has contributed to advancing the field of thermal-fluids sciences and engineering in the following ways:

- Generated results from quantitative measurements and comprehensive analysis of a list of PCMs (with and without additives) for their: (a) thermo-physical properties (e.g., specific heat capacity, latent heat, melting point, thermal conductivity, etc.), (b) chemical/ material stability, (c) materials compatibility and performance characteristics (subcooling, phase segregation, etc.).
- Test results were generated for novel additives and helped develop new techniques for obviating sub-cooling and phase segregation in PCMs.
- Material compatibility between the target PCM samples and the heat exchanger materials were explored by performing corrosion testing.
- Rank order of PCMs were established based on tests performed in this study which involved incorporating a chosen list of PCMs in a variety of LHTESS platforms. These results can be used to validate the design and analysis for candidate LHTESS platforms (for design and scale-up of LHTESS in conventional power plant applications involving dry cooling in arid climates).
- Helped address societal needs for mitigating the issues associated with the food-energy-water (FEW) nexus.

1.6 ARPA-E Arid Program Targets

The targets of the ARID program are shown in Table 3. As mentioned before, based on the ARID Requirements the selected list of phase change materials (PCMs) explored in this study are:

(a) Inorganic PCMs: Calcium Chloride Hexahydrate and Sodium Sulfate Decahydrate (Glauber's Salt), Lithium nitrate Trihydrate, Zinc Nitrate Hexahydrate, and S32 (procured from Rubitherm).

(b) Organic PCMS: PureTemp29 (procured from Entropy Solutions)

The selected list of PCMs were tested for evaluating their applicability and reliability based on the measured values of their thermo-physical properties (i.e., based on material degradation rates obtained after subjecting the samples of candidate PCMs to repeated thermal cycling.

Table 3: ARID PCM target specification.

Requirement Properties	
Transition Temperature (°C)	30-35
Latent Heat (KJ/Kg)	>150
Thermal Stability	>1000 Cycles

The target for specifications in the ARID Program for the desired LHTESS were summarized in Table 4. Based on the ARID program requirements this study focused on development and testing of three different configurations on heat exchangers as LHTESS: (1) shell and tube heat exchanger (using Additive Manufacturing, i.e. 3D printed); (2) Chevron Plate Heat Exchanger; and (3) Compact heat exchanger. Some of these heat exchanger configurations

incorporated metallic foam for improving the effective thermal conductivity with aim of thermal performance enhancement (i.e., for improving the power rating of the heat exchangers).

Table 4: ARID storage system target specification.

Requirement Properties	
Prototype Storage Capacity P_{cool}	200 - 500 kWh
Time to fully charge t_{charge}	<10 Hours
$T_{condenser}$	<140 °F
Capital cost of system	<$150/$kW_{th}$

1.7 Summary and Report Structure

In order to ascertain the reliability in dry cooling applications using a variety of LHTESS configurations, the thermo-physical properties, thermal stability (chemical/ material stability) and material compatibility of a chosen list of PCMs (with and without additives) were measured experimentally in this study. The motivation for studying the effect of additives and experimental techniques is to obviate subcooling and phase segregation effects that often compromise device performance and reliability of PCMs that are incorporated in LHTESS platforms. The additives include nucleators (nucleation promoters) and hydration accelerators (gelling agents and thickening agents). The additives were tested for mass fractions ranging up to 1.5% for nucleators and up to 20% for hydration accelerators. Experimental techniques involved both DSC and T-History methods. "*Cold Finger"* technique was also experimentally analyzed and studied to obviate sub-cooling completely with partial melting. The thermal performance of LHTESS was experimentally validated in shell and tube heat exchanger, chevron-plate heat exchanger and offset-fin compact heat exchanger for dry cooling applications.

The results obtained from this study and the information derived from these results are categorized as follows:

- Chapter 2 provides an insight into salt hydrates (Inorganic PCMs) properties and their inherent complications. This chapter also provides an insight into nucleation theory and concepts to obviate sub cooling and phase segregation. In-depth review on salt hydrates PCMs.
- Chapter 3 provides an insight into different LHTESS systems and provides a summary on current literature and requirements.

- Chapter 4 provides detail description about experimental procedure (i.e. apparatus, data reduction, and techniques) and characterization techniques for ascertaining the relevant thermo-physical property values.
- Chapter 5 provides detailed descriptions about the synthesis techniques of PCMs involving the chosen salt hydrates, nucleating additives, and gelling agent.
- Chapter 6 describes the results obtained from the initial characterization and thermal-cycling of lithium nitrate trihydrate with and without nucleating additives. The results summarize the effects of nucleating additives and *"cold finger"* technique on suppressing sub-cooling and their effectiveness in accelerated aging tests involving over 1000 thermal-cycles (i.e. for operational lifetime of 3.5 years, corresponding to a single thermo-cycle each day involving incomplete melting and complete solidification).
- Chapter 7 describes the results obtained from the initial characterization and thermal-cycling of calcium chloride hexahydrates with and without nucleating additives. The results summarize the effects of nucleating additives on suppressing sub-cooling and their effectiveness over 1000 thermal-cycles (i.e. 3.5 years).
- Chapter 8 describes the results obtained from the initial characterization and thermo-cycling of zinc nitrate hexahydrate with and without nucleating additives. The results summarize the effects of nucleating additives on suppressing sub-cooling and their effectiveness over 1000 thermal-cycles (i.e. 3.5 years).
- Chapter 9 describes the results obtained from the initial characterization and thermal-cycling of sodium sulfate decahydrate with and without nucleating additives. The results summarize the effects of nucleating additives and gelling in suppressing sub-cooling and phase segregation over 300 thermal-cycles (i.e. 10 Months).

- Chapter 10 describes the results obtained from the initial characterization and thermal-cycling of PureTemp 29 (PT 29) [1]– biodegradable organic PCMs. The results summarize the effectiveness of latent heat energy storage capacity of PT 29 over 300 thermal-cycles (i.e. 10 months).
- Chapter 11 summarizes the corrosion effects of salt hydrates on stainless steel (SS 317) and aluminum (Al 1100H) metals over 18-week period.
- Chapter 12 describes the thermal performance results of chevron - plate heat exchanger encapsulated with PureTemp 29 and lithium nitrate trihydrate
- Chapter 13 describes the melt/freeze wave front propagation of PCM in a shell- tube heat exchanger for the outward melting case (i.e. single tube) and thermal performance of multi tube 3D printed shell-tube heat exchanger encapsulated with PureTemp 29 and lithium nitrate trihydrate.
- Chapter 14 describes the thermal performance of compact heat exchanger (CHX) encapsulated with lithium nitrate trihydrate and provides a brief initial characterization of the CHX system with water. This chapter also summarize the system level thermal stability of lithium nitrate trihydrate.
- Chapter 15 provides the overall summary of the work done and path for future work.

[1] PureTemp 29 is trademark product of Entropy Solution (Plymouth, MN).

CHAPTER II

LOW AND MID TEMPERATURE SALT HYDRATE

This chapter provides an overview review on salt hydrates, the challenges facing salt hydrate utilization in latent heat thermal energy storage system, and essential future works. Despite the advantages of salt hydrates (i.e. high volumetric energy storage density, thermal conductivity) in comparison to organic PCMs, there are still some reliability challenges and technical issues with salt hydrates. Disadvantages of salt hydrates as a latent heat energy storage material include:

- High sub-cooling required to initiate freezing ($\Delta T_{sub\text{-}cooling} > 20°C$)
- Phase segregation due to incongruent melting
- Low reliability for thermos-cycling (especially for complete melting)
- Highly hygroscopic (even small amounts of water absorption can lead to significant alteration in thermal properties)
- Corrosive (limited options for materials selection)

---

*Part of this chapter is reprinted with permission from *Phase Change Materials in Handbook of Thermal Science and Engineering* by N. Kumar and D. Banerjee, 2018, Springer Nature, USA. Copyright 2018 by Rightslink License.

2.1 Introduction

Ionic bonding is typically encountered in the chemical composition analyses of inorganic PCMs. Typical examples of inorganic PCMs include various types of metals, salts, and salt hydrates. The thermo-physical properties of several inorganic PCMs are listed in and . Both pure salts and salt hydrates have similar thermo-physical properties and chemical characteristics. Typically, alkali metal salts are used as commercial inorganic PCMs. The anions in these salts and salt hydrates consist of oxides, hydroxides, chlorides, chlorates, citrates, carbonates, sulfates, and nitrates. Although inorganic PCM's inherit high volumetric storage capacity density, but often give rise to:

1. Performance is degraded, and reliability is often compromised due to considerable amount of sub-cooling needed to initiate freezing with each succeeding cycle of complete melting and solidification.
2. A degradation of the material properties of the PCM resulting from different rates crystallization (as well as heterogeneity in the sample mass) arising from water loss, chemical decomposition and phase segregation.

The composition of salt hydrates consists of an anhydrous salt combined with a specific stoichiometric ratio of water molecules that are incorporated into the crystal. Hence the salt hydrate composition consists of salt and water in a discrete and specific mixing ratio. Salt hydrates form stable 3-dimensional crystal structures. The chemical bonding within the crystal structure incorporates the water molecules at specific locations in a well-defined orientation.

Typically, the solid-liquid phase transformation in salt hydrates (i.e. melting and solidification) occurs reversibly by dehydration and hydration process, respectively. The phase transition temperature of salt hydrates may vary from 5°C to 130°C. Above an operating point of 150 °C different types of anhydrous salts can be used as PCMs rather than salt hydrates. The most significant issues that impede the use of salt and salt hydrates in engineering applications are:

1. Reliability (due to phase segregation which causes significant variation in material composition and creep in the measured values of latent heat capacity as well as the melting/solidification temperature)
2. Varying degree of sub-cooling required to initiate nucleation (freezing) when subjected to repeated thermal cycling.

Furthermore, inorganic PCMs are often corrosive with metals and therefore require additional consideration for material compatibility during the design phase. These issues often give rise to the need for incorporating additives for enhancing their reliability during operation (i.e. impeding or preventing phase segregation), minimizing the degree of sub-cooling required to initiate solidification, and reducing/mitigating corrosion.

Other categories of inorganic PCMs include metals and metal eutectics that have low melting points. Eutectic PCMs are composed of two or more micro-constituents in a specific ratio that confer to the unique property of melting and freezing congruently thus providing the appearance of a single transition point. Often, eutectic compositions of mixtures and their constituents have similar crystal structures.

2.2 Sub-Cooling

During the solidification process, PCMs remain in the liquid phase when cooled to their phase transition temperature. This phenomenon is known as subcooling or supercooling. Subcooling is a naturally occurring phenomenon but often neglected by investigators pursuing fundamental research. Phase change materials exhibiting a subcooling require additional energy for the onset of nucleation (i.e. for commencement of crystallization). Hence, PCMs requiring a considerable amount of subcooling for initiation of solidification are usually avoided for applications that are time-constrained since a higher percentage of total cycle time is lost to simply starting (or initiating) the phase transformation. Nonetheless, subcooling effects could be beneficial in applications where the liquid and ambient temperatures are kept in thermal equilibrium for long periods of time. Hence, during subcooling the latent heat is not released immediately even after the PCM sample reaches phase transition temperature. In such a situation, the latent heat is released at a time when the PCM sample is well below the phase transition temperature (therefore reducing the net storage capacity for a specified phase transition temperature, since enough time may not be available to complete the solidification as the power rating of the heat exchanger apparatus is also significantly affected due to this complication). As shown in Figure 11, if the subcooling temperature is within the envelope of operating temperature of the system, nucleation could occur, but the energy storage density is severely compromised. Likewise, if the required subcooling is beyond the envelope of the system's operating temperature range, then the PCM will not solidify and will always be in liquid state - thereby degrading the designed capability to store latent heat (as a consequence the net capacity rating and the power rating of the thermal energy storage platform is severely compromised, which in turn can be classified as a catastrophic system failure for thermal energy storage). Hence, due to subcooling

the power rating and net storage capacity of the designed thermal system are significantly compromised.

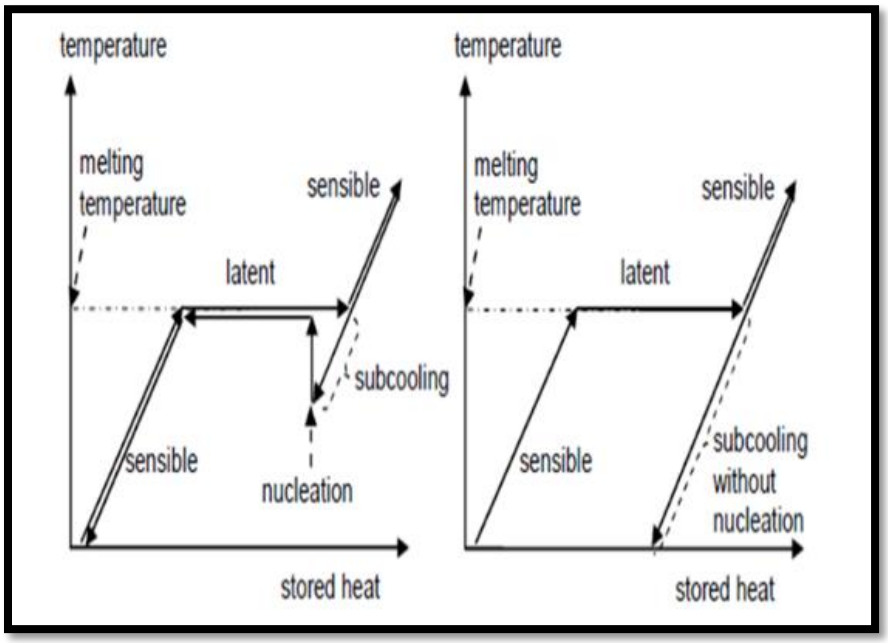

Figure 11: Effect of sub-cooling on latent heat energy storage. "Reprinted from [1]"

Subcooling is not an intrinsic material property, other factors, both inherent and extraneous to the thermal system, may affect nucleation rates, such as, experimental parameters (e.g. cooling rates, sample volume, container material, vibration, and purity). Figure 12 shows subcooling curves of salt hydrates due to the effects of nucleation or crystallization. Figure 12a and Figure 12b shows subcooling due to poor nucleation, where the temperature immediately rises and stabilizes at the phase transition temperature. The difference between Figure 12a and Figure 12b is the time required to achieve the isothermal phase transition temperature (T_m). Figure 12b reaches T_m quickly indicating a higher thermal diffusivity. Figure 12c shows that at high rates of cooling (or power transfer) the crystallizing (or nucleation) process is initiated at T_m but the bulk of the

liquid phase is supercooled as the system temperature attains the minimum value in the cycle (during thermo-cycling) and the minimal amount of solid phase formed in the process is also cooled to the minimum temperature of the system. Such a situation can arise when the PCM samples are subjected to very high rate of heat removal. Although several researchers have studied subcooling behavior in salt hydrates, the prediction of thermo-physical properties, and reliably controlling the solidification behavior of salt-hydrates (that require subcooling to initiate solidification) - still remain to be resolved for thermal engineering applications.

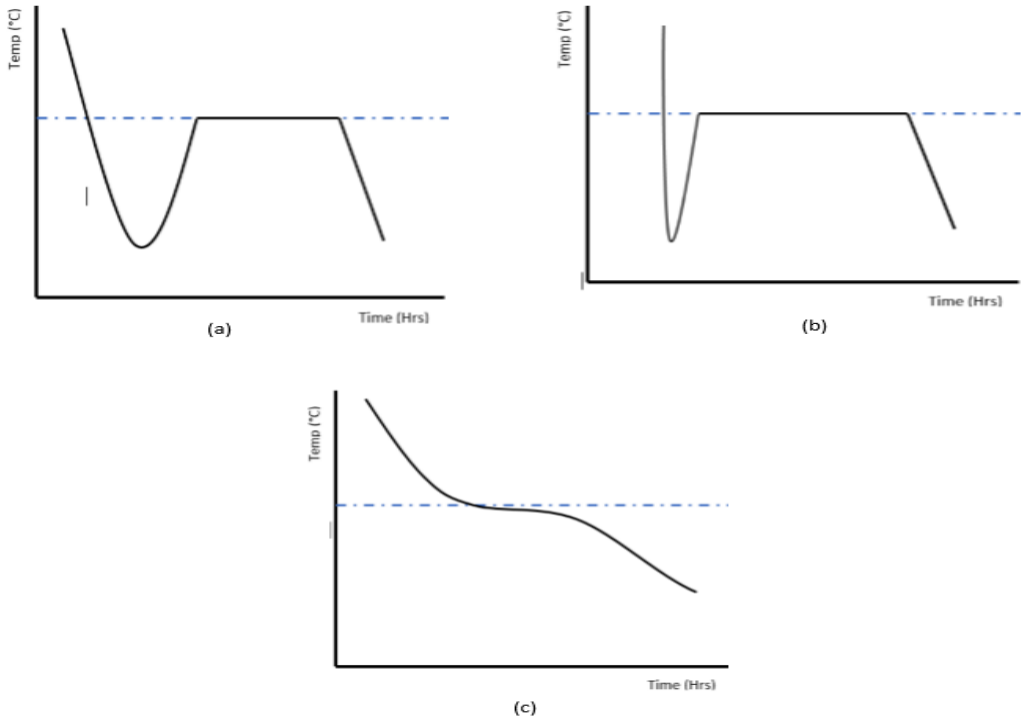

Figure 12: Examples of sub-cooling curves of salt hydrates used as PCM. (a) Poor nucleation rates and low thermal diffusivity. (b) Poor nucleation rates and higher thermal diffusivity, than in (a). (c) Nucleation is suppressed as the subcooling required to initiate solidification is below the nucleation temperature (as well as the minimum temperature of the system).

2.2.1 Energy Storage Potential in Subcooled Phase Change Materials

In theory, the total capacity for thermal energy storage (i.e., the net amount of heat transfer) in a given storage module during the melting process can be expressed as:

$$\boldsymbol{E_{theoretical,melting} = m_{PCM}\left[(T_{transition} - T_{initial})C_{ps} + H_f + (T_{final} - T_{transtion})\,C_{pl}\right] + m_{Storage\ Module}C_{p_{Heat\ Storage\ Module}}\,(T_{final} - T_{initial})} \quad (2.1)$$

where, $T_{ransition}$ is the phase transition temperature of the PCM, $T_{initial}$ and T_{final} are the average temperature of the PCM at the start until the end of the melting process as well as superheating process, C_{ps} and C_{pl} are the specific heat capacity [J/(g·K)] values in the solid and liquid phase respectively, while $C_{p,\ Heat\ Storage\ Module}$ is the heat capacity [J/(g·K)] of the storage medium, and m_{PCM} is the mass of PCM sample.

When the storage medium is cooled from a liquid state of $T_{superheat}$ to a temperature of T_{min} (i.e., without any inception of nucleation, where the temperature T_{min} can be less than or greater than the subcooling required to initiate nucleation), only the sensible heat of the phase change material and the heat capacity of the storage medium is released by the PCM sample. The theoretical value of heat discharged (i.e., the net amount of heat transfer) for a subcooled PCM combined with other components in the storage module, in such a scenario, can be expressed as:

$$\boldsymbol{E_{theoretical,solid} = \left[(m_{pcm}C_{pl}) + \left(m_{Storage\ Module}C_{p_{Heat\ Storage\ Module}}\right)\right](T_{superheat} - T_{min})} \quad (2.2)$$

However, the PCM sample can undergo complete solidification followed by reduction in temperature to the minimum temperature setting for the thermo-cycling protocol (T_{min}). The thermal energy stored in such a situation can be estimated theoretically as:

$$\boldsymbol{E_{thermal,solidi} = m[(T_{transition} - T_{subcooling})C_{pl} + H_{fs} + (T_{transtion} - T_{subcooling})C_{ps}]} \quad (2.3)$$

2.2.2 Degree of Subcooling

The degree of subcooling is the temperature difference between the onset of solidification and the phase transition temperature as shown in Equation 6 [1]:

$$(\Delta \boldsymbol{T})_{\boldsymbol{sub}} = \boldsymbol{T}_{\boldsymbol{melting}} - \boldsymbol{T}_{\boldsymbol{onset}} \tag{2.4}$$

where, $(\Delta T)_{sub}$ denotes the degree of subcooling, $T_{melting}$ is the phase transition temperature, and T_{onset} is the onset temperature for inception of nucleation (i.e., the start of the crystal formation in the bulk liquid phase of the PCM samples). Table 5 shows the degree of subcooling in different salt hydrates as well as the corresponding materials that serve as nucleation promoters or nucleation agent.

2.2.3 Measurement of Subcooling

There are various methods for measuring the degree of subcooling in salt hydrates with acceptable accuracy. One of the common measurement techniques is the "T-History" method [19]. Typically, in the "T-History" method the experimental apparatus consists of a data acquisition system (or a data logger or some form of data recording system) that is typically controlled by a computer, a reference material (e.g. Water), a thermocouple, and an environmental chamber (for accurate temperature control of the ambient temperature that in turn causes the temperature of the PCM samples and the reference material to change with time). The photograph of a typical experimental configuration housed in an environmental chamber is shown in Figure 13. Salt hydrate samples and the reference material are enclosed in individual containers with the same orientation (e.g., contained in long glass tubes) and placed inside an environmental control chamber (that has the capability to accurately control and impose a uniform value of the heating rate for the contents placed inside the chamber, particularly the reference material). In this method,

the temperature of the salt hydrates is measured by placing a thermocouple in the center of each tube (or container) enclosing the PCM samples as well as the reference material. For the photograph shown in Figure 13 the thermocouples were calibrated to an accuracy of (±0.3°C). The temperature data recorded in these experiments are then used to plot the transient profile of temperature data for each sample (reference material and PCM samples). These temperature-time diagrams are useful in identifying the effect of variation of the heating rates on the subcooling required to initiate solidification. Such an exercise helps to ascertain the efficacy of the salt-hydrates for energy storage applications (i.e., as a PCM) for the range of operating temperatures used in these studies.

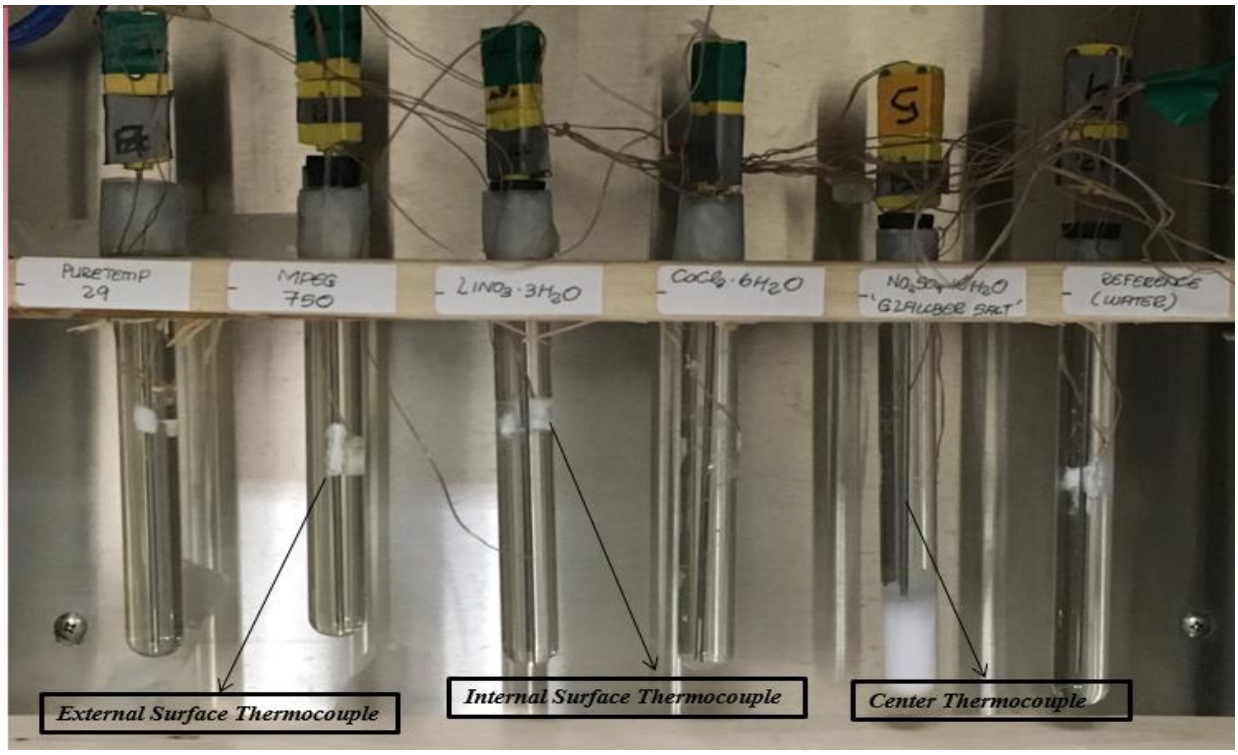

Figure 13: Image of PCM samples in multiple test tubes placed in an environmental control chamber. Measurement of transient temperature profiles of each PCM samples (in each test tube) is utilized for the analyses of thermal-physical properties using the "T-History" method.

2.2.4 Factors Influencing Degree of Subcooling

Nucleation kinetics and subcooling are not intrinsic material properties, since these values are affected by experimental parameters (e.g., cooling rates, sample volume, container material, vibration and sample purity). There are no standard procedures or recommendations for decreasing subcooling or controlling the degree of subcooling (or for ensuring that the variation in subcooling is minimized) for each individual cycle during thermo-cycling in practical applications (involving repeated melting and solidification). Hence, the significant factors influencing the degree of subcooling are also explored in this review.

2.2.5 Homogeneous Nucleation

Homogenous nucleation is solely initiated by the liquid molecules in the bulk phase of the PCM samples. During homogenous nucleation, solid nuclei form (without the incorporation of any additives or nucleation promoters). During homogenous nucleation, crystal nuclei of the solid phase are formed spontaneously and are distributed throughout the bulk of the liquid pool of the PCM. This is predicted to occur, according to thermodynamic models, when the nuclei grow to the critical size that is stable (i.e., crystal nuclei that are spontaneously formed in the liquid pool are inherently unstable and can dissolve back into the liquid phase, when the size of these nuclei are smaller than a critical size). The critical size required for obtaining stable nuclei can be predicted by various thermodynamic models. Study of homogenous nucleation is important, as it determines the ability of the material to nucleate spontaneously and is an indicator for the free energy distribution (or thermodynamic availability) of the molecules in the bulk phases. [1].

2.2.6 Heterogeneous Nucleation

In heterogeneous nucleation, additives, and impurities (e.g., suspended particles or colloids) can initiate nucleation and the spontaneous formation of the solid phase, typically in the form of tiny nuclei of crystals of the solid phase. Currently, heterogeneous nucleation is one of the most effective strategy that is used to reduce/ control the degree of subcooling in salt hydrates [20].

2.2.7 Surface Finish

The surface finish of the container walls can also have an impact on the degree of subcooling. Faucheus, et al., studied the effects of surface finish on the degree of subcooling when freezing an aqueous solution of ethanol [21]. The authors reported that roughness is an important parameter since the degree of subcooling required to initiate solidification is very sensitive to the surface roughness of the container. The authors reported that surface roughness aids in promoting nucleation of the solid phase, and therefore reduces the degree of subcooling required for initiating solidification. Hence, enhancing surface roughness can be an effective way to reduce subcooling.

2.2.8 Influence of Experimental Conditions

Studies have shown that different thermal characterization techniques employed for measuring the same property values (e.g., specific heat capacity or enthalpy of phase change) can yield contradictory measurements. In other words, the property values measured using different techniques could yield different results. The variability in measurements can be traced back to the amount of sample mass employed for each measurement technique as the diffusion kinetics during phase change (e.g., due to phase segregation) could significantly affect the nucleation process and the level of subcooling required for solidification. This in turn could affect the property values measured by each measurement technique and therefore has been a controversial topic (as different

research groups have reported contradictory results). For example, Taylor, et al., studied the influence of the rate of cooling on the thermo-physical properties and the thermal performance of certain proprietary salt hydrates (i.e. PC25 and PC29) [22]. The authors reported that the degree of subcooling increases with cooling rate (i.e., solidification is initiated at higher degrees of subcooling at higher cooling rates). Also, the authors reported that as the cooling rate decreases, there is a delay in nucleation, as the time required to reach the requisite subcooling (for initiating solidification) is also delayed. Hence, the total duration of the experiments performed for measuring the thermo-physical parameters could also affect the results obtained. In contrast, Diarce, et al. [23], studied the influence of experimental conditions on the thermal response of samples of Glauber's salt, with a potential application for thermal energy storage. The authors reported the effects of mass, superheat temperature, time, and cooling rate. The authors concluded that the measurements are not sensitive to the variation of the cooling rate. However, the authors reported that the nucleation process is significantly affected by the sample size (mass), superheat temperature (i.e., the temperature at which the melted PCM samples are held for extended periods of time under superheated condition), and the holding time under superheated condition. The authors reported that the superheated (holding) temperature and holding time significantly influenced the amount of subcooling required to initiate nucleation. The authors reported that higher superheat temperatures and longer holding times increased the amount of subcooling.

2.2.9 Theory of Nucleation

In an ideal scenario, as predicted by equilibrium conditions assumed in thermodynamic models, a liquid phase would spontaneously solidify when the said liquid is cooled slightly below its phase transition temperature (T_m). However, this not always the case, as the liquid phase

survives and often exists in a meta-stable equilibrium state as a supercooled liquid. When a liquid is cooled below its phase transition temperature (T_m), there exists a driving potential for solidification to occur (which is often modeled to be governed by Gibbs free energy [24]). Consider a homogenous nucleation scenario when the system is completely in liquid phase and the liquid phase is just below the phase transition temperature (T_m) with total availability (or Gibbs energy) value of G_1. In this state, the liquid phase is in meta-stable equilibrium as a subcooled liquid. As the liquid pool is being cooled down progressively with time - the liquid reaches a critical degree of subcooling $(\Delta T)_{sub}$ – causing some of the molecules in the liquid phase with lower kinetic energy to coalesce and form a small solid nucleus as shown in Figure 14.

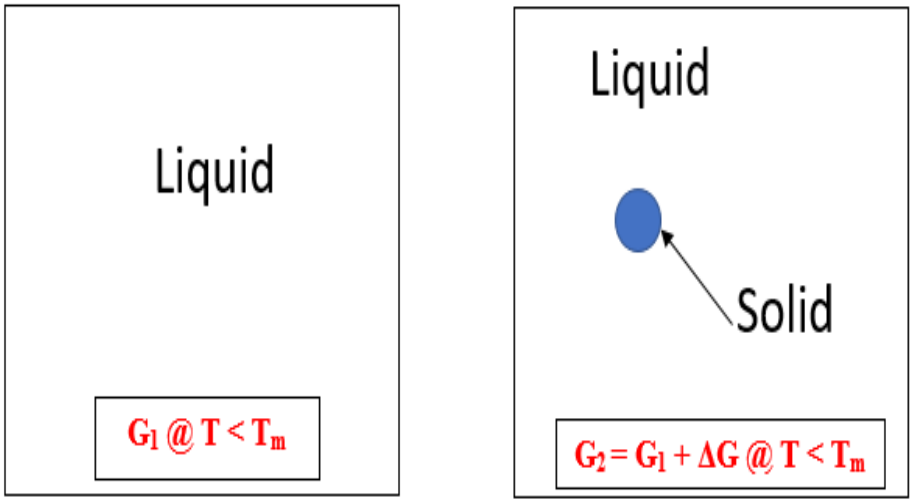

Figure 14: Numerical model formulation for transition from subcooled liquid to nucleation of the first solid nucleus (modeled as a sphere).

As a result, the total availability of the system (i.e., the Gibbs free energy of the system) is changed to a value of G_2, as shown in Equation 2.5. In this equation, V_s and V_L are the volume of the nucleated solid sphere and liquid phase, G_{VS} and G_{VL} are the free energies per unit volume of the solid and liquid phases, while A_{SL} and Y_{SL} are the surface area of the interface (between the solid

and liquid phase) and the interfacial free energy, respectively. For a pure liquid case, Gibbs free energy, G_1, can be expressed as shown in Equation 2.6.

$$\boldsymbol{G_2 = V_s G_{V_s} + V_L G_{V_L} + A_{SL}\gamma_{SL}} \tag{2.5}$$

$$\boldsymbol{G_1 = (V_s + V_L) G_{V_L}} \tag{2.6}$$

Therefore, the formation of the solid phase results in a change in free energy (ΔG) as shown in Equation 2.7 (i.e., the difference between G_1 and G_2), where ΔG_V is change in G_{VL} and $G_{VG.}$ The change in G_{VL} and $G_{VG\ \text{can}}$ be defined in terms of the latent heat of fusion and the degree of subcooling (using Clausius-Clapeyron relationship [25]), as shown in Equation 2.8, where H_{sf} is the latent heat of fusion per unit volume and $(\Delta T)_{sub}$ is the degree of subcooling [26, 27] :

$$\boldsymbol{\Delta G = -V_s\, \Delta G_V + A_{SL}\gamma_{SL}} \tag{2.7}$$

$$\boldsymbol{\Delta G_V = \frac{H_{sf}(\Delta T)_{sub}}{T_m}} \tag{2.8}$$

$$\boldsymbol{\Delta G_r = -\frac{4}{3}\pi r^3 \Delta G_V + 4\pi r^2 \gamma_{SL}} \tag{2.9}$$

As seen in Equation 2.9, the surface energy and the heat dissipation rates from each particle are proportional to the surface area ($\sim r^2$). However, the total energy released during phase change is proportional to the volume ($\sim r^3$). Therefore, the creation of small particles of solid always changes the free energy. Before the formation of the stable solid nuclei in the subcooled (or supercooled) liquid - the liquid phase is in a metastable state. Therefore, for a given degree of subcooling, there exists a critical radius, r^*, where the change in free energy is maximized. For the nucleated solid particles to be stable (and not dissolve back into the liquid pool), the free energy of the system needs to decrease. This could be achieved when the size of the nucleated particles, $r > r^*$. This

condition implies that the free energy of the system decreases with growth in the size of the nucleus (and therefore prevents spontaneous dissolution of these particles in the bulk liquid pool). Then the critical radius (r^*), can be defined by Gibbs-Thomson relationship and critical free energy as shown in Equation 2.10 and 2.11. It shows that r^* and ΔG_{r*} decreases with increasing degree of subcooling. At some temperature, sufficiently below T_m, then $_{\Delta}G_{r*}$ will be small enough to form the nuclei with $r > r^*$, above which further growth of the nuclei is energetically favorable, as shown below:

$$\boldsymbol{r^* = \frac{2\gamma_{SL}T_m}{H_{sf}}\frac{1}{[T_m - T]}} \tag{2.10}$$

$$\boldsymbol{\Delta G_r{}^* = \frac{16\pi\gamma_{SL}{}^3T_m^2}{3H_{sf}}\frac{1}{[T_m - T]^2}} \tag{2.11}$$

Homogenous nucleation, the liquid needs be subcooled to sufficiently low temperatures for achieving the onset of solidification. In contrast, heterogeneous nucleation can be achieved for only a small degree of subcooling. Hence, a simple and effective way to reduce the interfacial energy is through heterogeneous nucleation. The critical free energy change for heterogeneous nucleation is shown in Equations 2.11 and 2.12. [20]

$$\boldsymbol{\Delta G_{Het}{}^* = \frac{16\pi\gamma_{SL}{}^3T_m^2}{3L_v}\left[\frac{1}{(T_m - T)^2}\right]f(\theta)} \tag{2.11}$$

$$\boldsymbol{f(\theta) = \left[\frac{1}{4}\right][2 + \cos(\theta)\,[1 - \cos(\theta)]^2} \tag{2.12}$$

where, $f(\theta)$ is the shape factor with a numerical value less than unity depending only on the wetting angle (θ). Therefore, this function, $f(\theta)$, depends on the shape of the nucleated solid particle and the contact angle (or surface energy balance between the solidified nucleus and the liquid pool).

2.2.10 Methods for Nucleating Subcooled Salt Hydrates

Development of methods for controlling and inducing crystallization of subcooled salt hydrates at a desired temperature can help to improve the reliability of operations using PCMs. The strategies for promoting nucleation can be classified into seeding and dynamic nucleation. In seeding, crystallization occurs through heterogeneous nucleation. Seeding is one of the most effective ways to induce crystallization. Dynamic Nucleation on other hand, uses external methods to induce crystallization. Dynamic nucleation can be agitation, stirring, cold finger, and ultrasonic vibration. Dynamic nucleation requires additional equipment and design considerations. Hence, dynamic techniques are often not the most cost-effective way to induce nucleation in salt hydrates. Different mechanisms for inducing nucleation of salt hydrates are reported in the literature, which will be discussed next.

A) Nucleating Agents (Seeding)

An effective strategy for reducing subcooling is to mix the PCM samples with special additives, which are essentially nucleating agents for the PCM to promote heterogeneous nucleation. However, the design specific nucleation agents for a specified PCM remains a non-trivial task. Currently, heterogeneous nucleation is believed to occur when the additives have the similar atomic arrangements (i.e., crystal lattice structures). When the lattice structures of the solid PCM and the additive (nucleation promoters) are the same, it promotes the solidification of the solid nuclei for smaller values of subcooling (i.e., the solidification is achieved at a higher

temperature) as the energy barrier for the phase change process is reduced. A list of additives used for promoting nucleation in salt hydrate PCMs is provided in Table 5.

The disadvantage of this strategy is that similar crystal structures usually have similar melting temperature ranges, therefore the choice of additives (as nucleation promoters) are fairly limited as they are typically not stable above the melting temperature [1]. A random (or trial-and error) approach in the selection of nucleating agents can be a laborious strategy, while it can also hinder the complete cognition of the transport mechanisms responsible for the promotion of nucleation (and therefore process optimization becomes a challenging endeavor in such cases). In 1983, Lane gave an in-depth description on nucleation, crystallization, and nucleators (i.e. nucleation promoting agents or additives) [7].

In 2014, Shamberger and O'Malley demonstrated that heterogeneous nucleation can be promoted by matching close-packed atomic rows at the interface with the chosen additive. The authors demonstrated a close correlation of the subcooling temperature with the polyhedral lattice mismatch for various candidate additives for promoting nucleation [28]. This approach saves a significant amount of time over the experimental trial-and-error method for the discovery of nucleation promoters for various types of PCM samples (i.e., simple to complex structures).

Table 5: Degree of sub-cooling of different phase change materials.

PCM	T_m (°C)	H_{fs} (J/g)	Analytical Parameters		Additives (Size)	Reference
			$\Delta T_{sub\text{-}cooling}$ (°C)	$\Delta T_{sub\text{-}cooling}$ With Additives (°C)		
Lithium Nitrate Trihydrate [$LiNO_3$•$3H_2O$]	30	296	40	8	Zinc Hydroxyl Nitrate [$Zn_3(OH)_4(NO_3)_2$] Mass Percentage: 5%	Hoover et.al [29] Shamberger and Malley [28]
				10.1	Zirconium (IV) Silicate [$ZrSiO_4$]	Shamberger and Malley [28]
				2.5	Likasite Copper Hydroxyl Nitrate Hydrate [$Cu_3(OH)_5(NO_3)_2.2(H_2O)$] Mass Percentage: 1%	Shamberger and Malley [28]
Glauber Salt [Na_2SO_4•$10H_2O$]	32.5	254	15-18	3-4	Borax [$Na_2B_4O_7 \cdot 10H_2O$] Mass Percentage: 2%	Shin Et.al [30]
Calcium Chloride Hexahydrate [$CaCl_2$•$6H_2O$]	29.5	185	>20	2-4	Barium Carbonate [$BaCO_3$] Mass Percentage: 3%	Schroder and Gawron [31]
				5-7	Strontium Carbonate [$SrCO_3$] Mass Percentage :3%	
				5-7	Barium Fluoride [BaF_2] Mass Percentage: 0.15%	
				8-10	Strontium Fluoride [SrF_2] Mass Percentage: 3%	
				2.8-3.9	Sodium Chloride [NaCl] Mass Percentage: 1%	Kimuara and Kai [32]
				1.6-2.1	strontium Chloride ($SrCl_2$) Mass Percentage: 3%	Lane [33]
Sodium Phosphate Dodecahydrate [Na_2HPO_4•$12H_2O$]	35-44	280	>20	6-9	Borax [$Na_2B_4O_7 \cdot 10H_2O$] (20 µm ×500µm ~ 200 µm ×250µm)	Ryu Et.al [34]
				0-1	Carbon (1.5 µm ~ 6.7 µm) Mass Percentage: 3.7%	
				0-1	Titanium DioxideTiO_2 (2 µm ~200 µm) Mass Percentage: 3.7%	
				0.5-1	Copper (1.5 µm ~2.5 µm)	

Table 5 Continued

PCM	T_m (°C)	H_{fs} (J/g)	Analytical Parameters		Additives (Size)	Reference
			$\Delta T_{sub\text{-}cooling}$ (°C)	$\Delta T_{sub\text{-}cooling}$ With Additives (°C)		
Sodium Thiosulfate Pentahydrate ($Na_2S_2O_3$•$5H_2O$)	48-55	189	30	0-3	K_2SO_4	Farid Et.al [35]
				0-2	$Na_2P_2O_4.10H_2O$	
				3-4	$SrSO_4$ Mass Percentage: 5%	Ryu Et.al [34]
Sodium Acetate Trihydrate [CH_3COON_a•$3H_2O$]	58	226	20	0-2	$SrSO_4$	Farid Et.al [35]
				4-7	$Na_2HPO_4.7H_2O$	Cabeza Et.al [36]
				0-2	K_2SO_4	Ryu et.al [34]
				3.5-4.69	Silver Nanoparticles Mass Percentage: 0.92% - 0.8%	Ramirez Et.al [37]
Zinc Nitrate Hexahydrate [Zn $(NO_3)_2$•$6H_2O$]	35.6	146	15	3-5	Zinc Hydroxyl Nitrate	
				1-6	Zinc Oxide [ZnO]	Abhat Et.al [38]
Potassium Fluride Dihydrate [KF•$2H_2O$]	41	203	>25	5-8	Al_2O_3	Schroder [39]
Lithium Chlorate Trihydrate [$LiClO_3$•$3H_2O$]	8	155	2-8	0.5	$KClO_4$	
Potassium Fluoride Tetrahydrate [KF•$4H_2O$]	19	246	15-24	9.5	Pumice	
Manganese Nitrate Hexahydrate [Mn $(NO_3)_2$•$6H_2O$]	26	127	25	5	Zinc Nitrate Hexahydrate	Danilin et al [40]
Magnesium Nitrate Hexahydrate [Mg $(NO_3)_2$•$6H_2O$]	90	150	11	3	Copper Sulphate Trihydrate	Lane et al [41]
				1	Magnesium Oxide	

Controversies exist in the literature on the effect of impurities in a contaminated PCM and the possibility that this could potentially influence the solidification process by reducing degree of subcooling. Shamberger and O'Malley also studied the effects of purity and impurities on the degree of subcooling on lithium nitrate trihydrate. The authors reported that this is not an effective or reliable strategy for reducing subcooling (i.e., by introducing impurities or by utilizing lower purity materials [28]). In contrast, Garg, et al., reported significant sensitivity of the solidification temperature to the level of sample purity, as shown in Figure 15 [42].

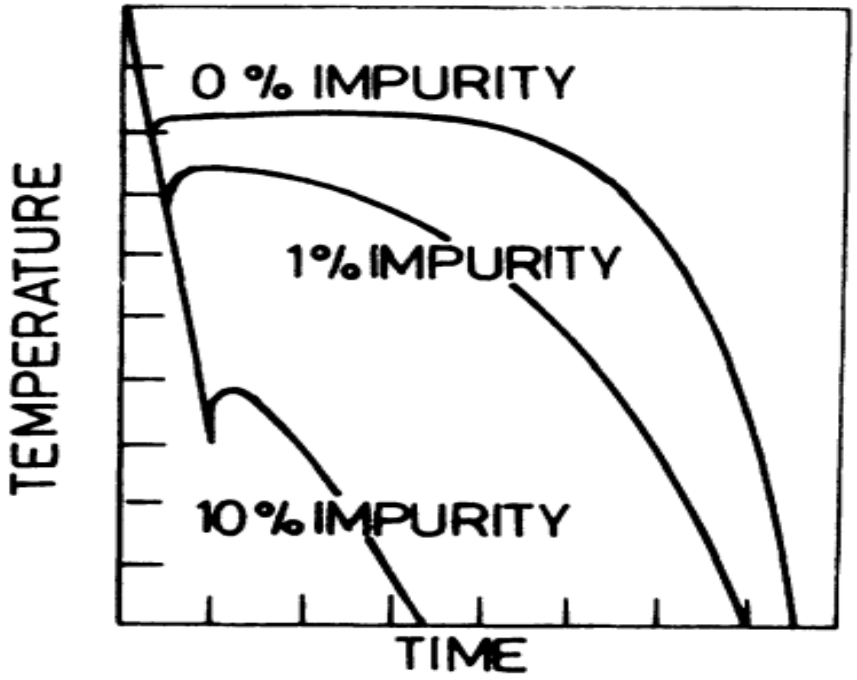

Figure 15: Effects of impurity on solidification curves. The plots illustrate the effects of varying percentage of impurities on sub-cooling. The mass concentration of impurities was varied from 0% to 10%. "Reprinted from [6]"

B) Dynamic Nucleation Techniques.

The "*Cold Finger"* technique is a localized cooling technique where a cold spot is created intentionally in the vicinity of the PCM sample such that a portion of the sample is always maintained in solid state. This technique is only useful when the phase transition temperature of the PCM is higher than the ambient temperature [43].

A recent set of strategies is based on the concept that *shock waves* and *high pressures* could be utilized to promote inception of solidification. This is a relatively new concept and is in the early stages of development. In 2017, Gunther, et al. [44], released a study showing the feasibility of nucleating salt hydrates by imposing high pressures. In these experiments, the authors used pressure up to 800 MPa. However, such strategies involving high static pressures can be cost-prohibitive and cumbersome for typical engineering applications. In contrast, strategies involving dynamic pressures (i.e., by imposing pressure waves) can be less cumbersome and have the potential for providing a more cost-effective approach [44].

2.3 Current Issues with Salt Hydrates as Phase Change Materials

Salt hydrates provide an attractive option as PCMs but also suffer from several disadvantages that compromise their reliability in engineering applications. The disadvantages include: effects arising from phase segregation, long-term stability when subjected to repeated thermal cycling that causes variation in performance parameters (or their response to thermal loads), and the variation in thermal performance of these PCM samples depending on the variation of the thermal cycling protocols (i.e., the effect of the experimental setup). Awareness of these issues can help to design remediation measures as well as improve the system reliability that leverage these types of PCMs.

Phase segregation is a common phenomenon that typically occurs during the melting of salt hydrates (and occasionally for organic PCM composed of small chain and long chain hydrocarbon mixtures, such as for paraffins). The melting and freezing of salt hydrates arise from a reversible thermo-chemical reaction involving dehydration-hydration process involving water molecules that are chemisorbed into the crystal lattice of the salt hydrate (hydrated or anhydrous state). During melting, salt hydrates undergo different levels of hydration loss. In some cases, the process of melting involves the partial loss of water molecules that are chemisorbed into the crystal lattice of the salt hydrate. In other cases, this involves the complete loss of all the hydrated water molecules, thus leading to the formation of an anhydrous salt in the solid phase. Hence, often times the salt hydrates melt incongruently (i.e., a portion of the sample suffers from partial loss of hydration while the other portions of the PCM sample can be in a completely anhydrous state).

The formation of salt hydrates with fewer number of water molecules (i.e., mixture of stoichiometric and non-stoichiometric compositions) and the pure salt in the liquid solution causes

significantly large density difference as well as density gradients in the system during melting. If the melting process occurs slowly enough the denser component segregates and often sinks to the bottom due to gravity, thereby forming a non-homogenous mixture in the body of the PCM. The different levels of phase separation could progressively accumulate with each cycle during repeated thermo-cycling resulting in loss of energy storage capacity due to degradation in the net latent heat of the PCM.

A typical example of these complexities is demonstrated by Glauber's salt, also known as sodium sulfate decahydrate ($Na_2SO_4 \cdot 10H_2O$). As shown in Figure 16, when Glauber's salt is heated, the composition follows the vertical line corresponding to the mass fraction of 43% of Na_2SO_4. When the transition temperature of 32°C is reached, two different phases are formed consisting of anhydrous Na_2SO_4 in solid state and a liquid suspension which contains approximately a mass fraction of 32% Na_2SO_4. These two phases have two very different densities. The pure Na_2SO_4 has higher density than the solution, therefore the solid phase of the PCM sample of Na_2SO_4 sinks to the bottom of the container. This effect is further amplified for PCM samples that are placed in slender vertical enclosures. When the temperature is raised further, the concentration of Na_2SO_4 decreases as the solubility of Na_2SO_4 decreases with increasing temperature. When cooled below 32.4°C, it can undergo the reverse process where the anhydrous sodium sulfate is hydrated while the kinetics of the chemical reaction is modulated by the diffusion of the water molecules through the solid phase of the sodium sulfate decahydrate and in to the anhydrous sodium sulfate particles (which are coated with the decahydrate particles). Repeated thermo-cycles cause more of these anhydrous salt samples to sink, hence causing further reduction in the energy storage capacity (as well as increase in the time required to rehydrate the PCM

samples during the solidification process, which in turn can exacerbate the requirements for subcooling to initiate the solidification process).

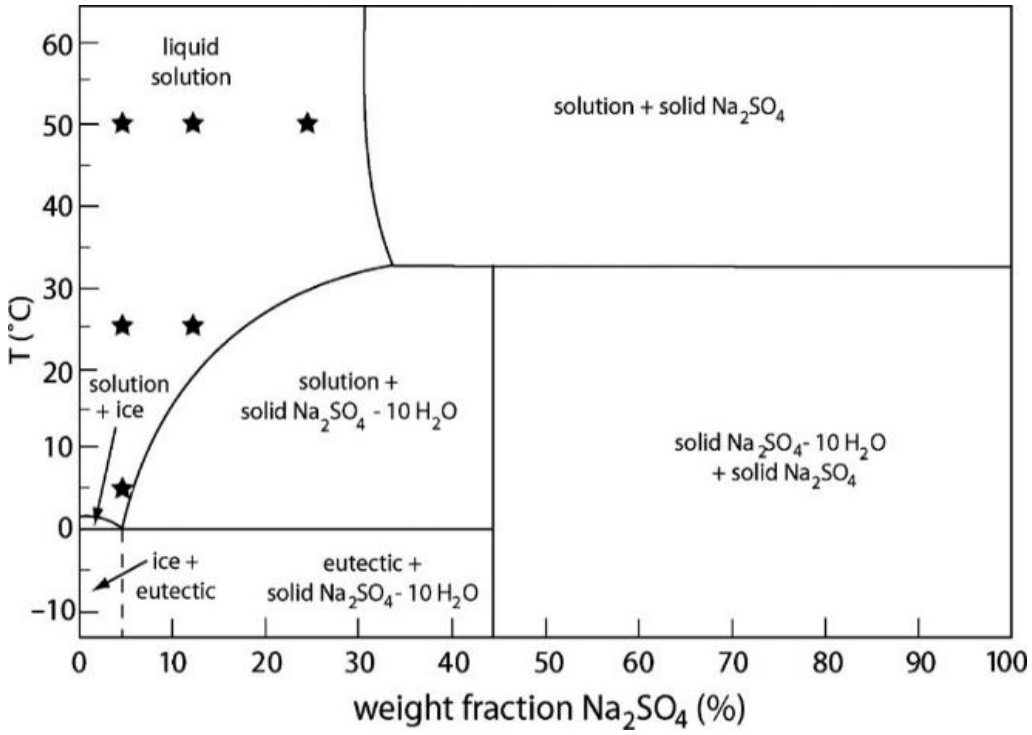

Figure 16: Sample phase diagram of Na_2SO_4· (10 H_2O) (Glauber Salt), which shows incongruent melting at 30 to 32 °C due to formulation of other phases. "Reprinted from [45]".

Studies in the literatures have demonstrated that severity of phase segregation in salt hydrates could be reduced or prevented by addition of excess water and through controlled diffusion [1]. The simplest approach is to add excess amounts of water to the salt hydrate - i.e., in excess of stoichiometric ratio. The excess water can enable rapid homogenization of the liquid phase by faster diffusion into the salt hydrate. The disadvantage of this method is that the overall storage density or chemical compatibility can be compromised in addition to the larger range of phase transition temperatures that can arise from such complications. The second strategy to reduce phase segregation is through the implementation of a controlled diffusion method.

Diffusion is faster for smaller quantities of materials since the speed of diffusion is inversely proportional to the square of the container size or radius (or the square of an appropriate length scale). Therefore, controlled diffusion is only effective for smaller quantities of PCM. Hence partitioning the PCM samples into smaller compartments (i.e. microencapsulation) can obviate the difficulties associated with mass and thermal diffusion resistances.

Other strategies to prevent phase segregation that have been explored in the literature include the addition of materials that promote thickening (or "gelling") of the PCM. In gelling, the distance between the phases (i.e., hydrous and anhydrous phases) are reduced to micron-scale dimension, thus enabling faster diffusion of the water molecules in to the crystal lattice of the salt hydrate particles embedded in the gel network. The bulk phase of the PCM particles are embedded in the three-dimensional network of the gel. This three-dimensional network confines the different phases of the PCM in close vicinity (thus reducing the diffusion resistance). The gel can be formed by a polymer, water-gelled cellulose, gelatin, and gums.

The strategy for "thickening" the PCM samples is typically implemented by mixing the PCM samples with specific additives that increases its viscosity. As the viscosity increases, different phases are impeded from flowing. The alternate strategy is to add materials that promote thickening such that the *phase diagram* is modified resulting in congruent melting of the segregated phases. Hence, this strategy involves a trial and error approach. Thickening agents are usually solutions with high viscosity compared to that of the chosen PCM. Examples of thickening agents include: starch, cellulose and bentonite (clay). The thickening process usually consists of melting the salt hydrate and mixing vigorously with the thickening agent. Cabeza, et al., studied the thermal performance of sodium acetate trihydrate mixed with different thickening agents. The

authors observed that the thickening agent prevented phase segregation and showed similar thermal behavior, but the effective value of the latent heat (i.e., the storage capacity) was reduced by 20% to 35% depending on the final concentration of the thickening agent [36]. Marks studied the effect of crystal size on the thermal energy storage capacity of a thickened Glauber salt (i.e., sodium nitrate decahydrate). The authors controlled the crystal size through the addition of crystal modifiers (acrylamides, i.e., acrylic acid polymers) and used polymeric polycarboxylic acid as thickener. The author reported that 67% to 82% of the initial thermal storage capacity was retained even after 1600 thermal cycles (i.e., repeated melting and solidification) [46]. Hee, et al., studied stabilization of various salt hydrates such as Glauber salt ($Na_2SO_4 \bullet 10H_2O$), sodium phosphate dodecahydrate ($Na_2HPO_4 \bullet 12H_2O$), and sodium acetate trihydrate ($CH_3COONa \bullet 3H_2O$) with super-absorbent polymers (SAP), carboxy-methyl-cellulose (CMC), and polyvinyl alcohol (PVA). The authors reported that Glauber's salt and sodium phosphate dodecahydrate thickened when mixed with a mass fraction of 3% and 3.5% of SAP respectively. The authors observed that sodium acetate trihydrate mixed with CMC at a mass concentration of 3% produced the most desirable results [34].

Based on this overview of methods to reduce subcooling and phase segregation, it is clear that the appropriate choice of additives can help reduce and minimize phase segregation. However, this is achieved at the expense of thermal energy storage capacity and degradation in the thermal performance (i.e., power rating) of the salt hydrate PCM based energy storage platform. In addition, this can also lead to alterations in the phase transition temperature of the composite mixture, thus compromising the reliability of the thermal response of the energy storage platform. Table 6 summarizes the different additives for thickening and gelling of salt hydrates.

Table 6: Thickening and gelling additives utilized in salt hydrates for stabilization of phase separation.

PCM	Analytical Parameters			Thickening/ Gelling Medium	Reference
	Melting Point after Thickening/Gelling (°C)	Initial Latent Heat Capacity (J/g)	Latent Heat Capacity Thickening (J/g)		
Sodium Acetate Trihydrate ($CH_3COON_a.3H_2O$)	57	237-243	206	carboxymethyl cellulose (CMC) Weight Percentage: (3.0%)	Ryu Et.al [34]
	54.7		180-189	Starch Weight Percentage: (20.0%)	Cabeza Et.al [36]
	56.4		153-161	Bentonite Weight Percentage: (50.0%)	Cabeza Et.al [36]
	55.1		165	Methyl hydroxyethyl-Cellulose Weight Percentage: (30.0%)	Cabeza Et.al [36]
	-	254	230	Polyvinyl Alcohol, Acetone, Liquid Paraffin Weight Percentage: [1.0%,0.5%, 1.0%]	Meisingset and Gronvold [47]
	52.5	238	227.5	carboxymethyl cellulose (CMC) Weight Percentage: (4.0%)	Hu et.al [48]
	-	-	-	Xanthan Rubber Weight Percentage: (0.5-1.0%)	Meisingset and Gronvold [47]
Glauber Salt ($Na_2SO_4.10H_2O$)	32	254 [1]	227	Super-Absorbent Polymers (SAP) Weight Percentage: (3.0%)	Ryu Et.al [34]
	-	238	202	Attapulgite Clay	Marks [49]
	-	254 [1]	182-207	α-type of $CaSO_4.0.5H_2O$ Fine Powder of Silica Weight Percentage: (3% - 6%)	Saita and Fujioka [50]
	-	-	-	Amorphous Silica (Particle Size not >20 nm) Weight Percentage: (3-4%)	Grubmueller and Pritsching [51]
	-	-	-	Astro Gun (Carboxyl-Methyl-Amylose Gel) Weight Percentage: (2-5%)	Chadwick and Sherwood [52]
Sodium Thiosulfate Pentahydrate ($Na_2S_2O_3.5H_2O$)	46	202	186	carboxymethyl cellulose (CMC) Weight Percentage: (3.0%)	Ryu Et.al [53]
Sodium phosphate dodecahydrate ($Na_2HPO_4.12H_2O$)	36	-	104	Super-Absorbent Polymers (SAP) Weight Percentage: (3.0%)	Ryu Et.al [34]
	-	-	-	Acrylamide Polymer Weight Percentage: (10%)	Kent and Page [54]

Another commonly explored method for reducing phase segregation in salt hydrates is the addition of excess water. This method consists of adding water in quantities exceeding the stoichiometric ratio (to the salt hydrate) so that all the anhydrous salt can be dissolved in the water at the melting point. In 1977 Biswas used this principle in sodium sulfate hexahydrate (i.e., Glauber salt) to mitigate phase separation by preventing the formation of the heavy anhydrous salt. The author compared the results with pure Glauber salt and reported that the chemisorption of the melted water into the Glauber salt samples occurred spontaneously, without necessitating the mixing with any nucleating agent [55].

In similar experiments, Furbo [56] reported preliminary results involving different salt hydrates. The author reported that this method makes the system more stable when subjected to repeated thermo-cycling, but this strategy reduces the storage density [56]. Table 7 summarizes the influence of excess water on the thermal performance of salt hydrates as PCM candidates. Micro/Nano-scale encapsulation techniques provide an attractive strategy for reducing phase segregation in the salt hydrates. Micro/Nano-scale encapsulation prevents phase segregation in salt hydrates but cannot always be implemented successfully since it is a labor-intensive process and the reliability is low. As a result, brute force techniques involving trial and error approaches are often used for parametric optimization of these encapsulated PCM samples. Several studies have explored the effect of encapsulation of salt hydrates for inhibiting phase segregation using a silica matrix and graphite composite. The authors reported that, to prevent leakage, the ratio of salt hydrates to silica can be as high as 70:30. Secondly, encapsulation also protects the salt hydrates from the environment, thereby preventing water evaporation and water absorption in hygroscopic salt hydrates which enhances the reliability and thermal-cycling stability [57] [58]. Milian, et al.,

analyzed different synthesis techniques and the advantages/ disadvantages of encapsulating salt hydrates [59].

Table 7: Influence of excess of water in salt hydrate on its thermal properties. Adapted from [60].

Composition, % by weight		Melting Behavior	T_m (°C)	Latent Heat (J/g)
Glauber Salt (Sodium sulphate Decahydrate) *[Na_2SO_4•10H_2O]*				
Na_2SO_4. 10H_2O	H_2O			
94.7	5.3	Incongruent	32	237
90.4	9.6	Incongruent	32	214
84.9	15.1	Incongruent	29	199
79.9	20.1	Incongruent	27	178
75.1	24.9	Incongruent	24	159
Sodium Acetate Trihydrate *[CH_3COONa•3H_2O]*				
$CH_3COONa.3H_2O$	H_2O			
95	5	Congruent	55	220
90	10	Congruent	52	190
80	20	Congruent	50	100
Sodium hydroxide monohydrate [NaOH•H_2O]				
NaOH.H_2O	H_2O			
93	7	Congruent	53	150
89	11	Congruent	44	95
Barium Hydroxide Octahydrate [Ba $(OH)_2$•8H_2O]				
Ba $(OH)_2$.8H_2O	H_2O			
94	6	Congruent	77.5	280
85	15	Congruent	73	230
75	25	Congruent	69	207

2.4 Long Term Stability

Long-term stability of PCMs is often unknown *apriori* and is a problem that has limited their widespread use in latent heat thermal energy storage systems (LHTESS). During the service life of latent heat storage system, the storage capacity should not change significantly as a result of thermal cycling or from interactions between the phase change materials and the container [61] [62]. Long term material stability of phase change materials is affected by thermal-cycling, and corrosion. Therefore, for an application in a LHTESS, the interaction between the PCMs and the containers must be considered.

The required stability (life-cycle) of PCMs depends on the applications, but nevertheless the longest possible duration for material stability is always desired (as reported by Fleischer [11]). In power plant applications, 10-20 years of lifetime of the PCM samples may be required to be cost effective option for energy storage. Studies have shown that typically for PCMs the energy storage capacity degrades when subjected to prolonged thermal cycling.

Shukla examined the thermal cycling of erythritol, paraffin waxes, di-sodium tetraborate, sodium hydroxide, and barium hydroxide [63]. The author reported that none of the inorganic PCMs are useful for latent heat thermal energy storage capacity due to high rates of performance degradation with each thermo- cycle. However, the author confirmed that paraffin waxes and erythritol yielded promising stability since the latent heat for erythritol samples and paraffin wax samples degraded by 10% and 26% after 1000 thermal cycles, which equates to 2.7 years in actual life cycle. Tyagi and Buddhi studied the changes in latent heat of fusion and melting temperature of calcium chloride hexahydrate ($CaCl_2 \cdot 6H_2O$) for 1000 cycles of accelerated thermo-cycling tests using a (DSC). The authors reported no change in the phase transition temperature and the enthalpy

of fusion after these tests [64]. Kimura and Kai examined the effects of thermal cycling of calcium chloride hexahydrate mixed with nitrate hydrates, such as [Ca $(NO_3)_2 \cdot 4H_2O$] and [Mg $(NO_3)_2 \cdot 6H_2O$], as well as with barium fluoride as a nucleating agent. The experiments were performed using either a vertical or a horizontal tube. The latent heat storage property showed no degradation after 1000 thermal cycles [65] in this study. Ting, et al., conducted accelerated cycle tests of a latent heat storage unit containing sodium sulfate decahydrate [$Na_2SO_4 \cdot 10H_2O$]. They studied the effect of 1000 thermal cycles on the container tube but did not analyze the thermo-physical properties of the PCM [66]. Shamberger and O'Malley conducted accelerated 1000 thermal cycling test using a 40-day thermal aging test for lithium nitrate trihydrate [$LiNO_3 \cdot 3H_2O$] with copper hydroxyl nitrate hydrate [$Cu_3(OH)_5(NO)_3 \cdot 2(H_2O)$] and zinc hydroxyl nitrate [$Zn_3(OH)_4 \cdot (NO_3)_2$] as nucleating additives. The activity of lithium nitrate trihydrate with zinc hydroxyl nitrate degraded after 400 cycles. In contrast lithium nitrate trihydrate samples mixed with copper hydroxyl nitrate were reported to be stable over 900 cycles [28]. Wada, et al., studied the latent heat storage capacity of sodium acetate trihydrate [$(CH_3COONa) \cdot (3H_2O)$] with and without thickening agents and reported that the performance improved considerably with thickening agents after 500 cycles [67]. Table 8 summarizes thermal cycling results of various salt hydrates and inorganic eutectics. The stability of the PCM samples subjected to repeated thermo-cycles depend on the configuration of the experimental apparatus, the protocol for the thermo-cycling experiments, and the data analysis method. Moreover, the sample size, sample cycling rate (heating rate), and container configuration could affect the stability of the PCM samples. Therefore, the design of experiments is crucial for ensuring the repeatability and the reliability of the measurements.

Table 8: Thermal cycling of salt hydrates and inorganic eutectics.

PCM	Analytical Parameters			Thermal Equipment/ Thermal Cycles	Reference
	Initial Melting Point (°C)	Initial Latent Heat Capacity (J/g)	Final Latent Heat Capacity (J/g)		
$CaCl_2.6H_2O$ (80 Mol %) + $CaBr_2.6H_2O$ (20 Mol%)	20	117	120	1)Perkin Elmer DSC 2 2)1000 Cycles	Kimuara et.al [65]
$CaCl_2.6H_2O$ (93.3 Wt %) + $(NO_3)_2.4H_2O$ (5 Wt %) + Mg $(NO_3)_2.6H_2O$ (2 Wt %)	24	125	128	1)Perkin Elmer DSC 2 2)1000 Cycles	Kimuara et.al [65]
Mg $(NO_3)_2.6H_2O$ (93 wt. %) + $MgCl_2.6H_2O$ (7 Wt %)	78	152.4	-	1)DSC 2)1000 Cycles	Nagano et.al [[68]
Calcium Chloride Hexahydrate [$CaCl_2.6H_2O$]	29.8	190.8	No Change	1)Perkin Elmer DSC 2 2)1000 Cycles	Kimuara et.al [32]
	28	86	No Change	1)Mettler DSC 2)1000 Cycles	Fellchenfeld et.al [69]
	23.3	125.4	No Change	1)TA Q-100 DSC 2)1000 Cycles	Tyagi et.al [70]
	27	Not Provided	Not Provided	1)Thermostatic Water Bath Chamber 2)5650 Cycles	Porosini [71]
Magnesium Chloride Hexahydrate [$MgCl_2.6H_2O$]	111.5	155.11	85	1)Shimadzu DSC 60 2)500 Cycles	El-Sebaii et.al [72]
Na_2SO_4. ½ NaCl.$10H_2O$	20	Not Provided	Not Provided	1)Thermostatic Water Bath Chamber 2)5650 Cycles	Porosini [71]
Glauber Salt ($Na_2SO_4.10H_2O$)	32.4	238	105	1)Thermostatic Bath Chamber 2)350 Cycles	Marks [49]
NaOH.$3.5H_2O$	15	Not Provided	Not Provided	1)Thermostatic Water Bath Chamber 2)5650 Cycles	Porosini [71]
Trichlorofluoromethane Heptadecahydrate ($CCl_3F.17H_2O$)	8.5	274	-	1)Perkin Elmer DSC 2 2)100 Cycles	Kimuara et.al [73]
Sodium Acetate Trihydrate and Mixtures ($CH_3COON_a.3H_2O$)	57 *After 1000 Cycles* 51.2	Not Provided	Not Provided	1)Thermostatic Water Bath Chamber 2) 1000 Cycles	Kimuara et.al [74]

The protocols used for thermo-cycling measurements can be categorized into two types: (a) the pyramid method [75]: where the samples are heated and cooled without isothermal stages; and (b) the dynamic method. The latter is similar to the pyramid method except that the samples are maintained at an isothermal temperature at the end of each cycle of heating and cooling. The thermal cycling in pyramid and dynamic methods are controlled by two variables: the heating and cooling temperature and the transient rate of change of temperature (°C/min). The temperature range utilized for the measurements typically depends on the applications. In the contemporary literature, there are multiple ranges of heating rates that are used during the thermal cycling of the PCMs. The heating rates reported in the literature ranges from 0.7°C/min to 10°C/min. Therefore, there is no clear pattern (or an optimum value) for choosing the values of heating and cooling rates. The degradation of PCMs could be analyzed by measuring the changes in the values of latent heat, phase transition temperature, degree of subcooling, mass loss, thermal conductivity, and the specific heat capacity [76]. Usually, only the changes in the values of latent heat and phase transition temperatures are used for characterization of material degradation when subjected to thermal cycling. The measured results for calculating the latent heat and phase transition temperature could be analyzed using the pyramid method or dynamic method. Usually the same method type used to cycle the samples are also the ones used by the authors to measure the thermal properties (for ensuring consistency in the results).

The experimental apparatus used for thermal cycling could be grouped into two different groups. The two groups are: differential scanning calorimetry (DSC) and non-DSC (i.e., thermostatic bath or environmental chamber). The experimental set-up should have the capabilities to conduct thermal cycling either through the pyramid method or dynamic method.

The DSC technique can be used for both sample cycling (material degradation tests) and thermal property analysis. In contrast, a non-DSC type experimental apparatus is usually designed for thermo-cycling of PCM only. Another method for thermal cycling testing involves incorporating T-History into a non-DSC experimental set-up (for both thermal cycling tests and thermal property measurement). This method enables the testing of large quantities of samples (unlike DSC techniques where only mg quantities of PCM samples are usually tested). [77]. On closer observation of the thermal cycling data presented in various literature reports, a huge variety of equipment are used for thermal cycling and the analysis of thermal properties obtained from different thermal cycling experiments are therefore often contradictory [32, 72, 64].

2.5 Compatibility of Salt Hydrates and Packaging Materials

Salt hydrates can cause high rates of corrosion for various metals and alloys. It is therefore necessary to study the chemical compatibility (i.e., corrosivity) of the salt hydrates with the container materials. Metal corrosion effects includes localized pitting, erosion, oxidation, fatigue and dealloying, and galvanic corrosion [78]. Pitting is a form of localized corrosion that results in pits in a surface which can grow to form holes in thin sheets. Corrosion of salt hydrates in an energy storage system can be simulated by immersion testing of metal and alloys (i.e., test coupons of representative samples) in contact with seawater (or different types of electrolytes and by parametrically varying the system temperature). Whereas in energy storage system, salt hydrate may behave as an electrolyte while the active metals (e.g. aluminum and copper) will behave as an anode and corrode. Typically, noble metals (e.g. gold and silver) are chosen as materials for cathode and can be free of corrosion mass loss. Porisini [71] examined corrosion in metals containing different types of commercially available salt hydrates – with melting temperatures of 20 °C [(Na_2SO_4) ·(NaCl•) · $(10H_2O)$] and 15 °C [(NaOH)· $(2.5H_2O)$]. These electrolytes were used to determine the corrosion rates for stainless steel, aluminum alloys and copper. Following corrosion testing, the author concluded that stainless steel was the most corrosion resistant of these metals for use with salt hydrates, though copper was shown to have a corrosion period that did not increase after long periods of time, similar results were also reported by other authors [79, 80, 81]. Despite the techno-economic significance of monitoring such corrosion data, the literature on the corrosion studies involving salt-hydrates is very scarce. Table 9 summarizes results in the literature obtained from corrosion tests for different salt hydrates for a variety of packaging materials. These results show that stainless steel is the most reliable choice as a packaging material for salt hydrates.

Additional studies are required for understanding the effects of corrosion caused by salt hydrates on a variety of packaging materials, especially for non-metallic packaging materials.

Table 9: Summary of salt hydrate and corrosion compatibility.

Salt Hydrates	Testing Temperature (°C)	Compatible Material	Incompatible Material	Reference
Lithium Perchlorate Trihydrate [$LiClO_3$•$3H_2O$]	20	Mild steel alloy, Anodized aluminum	Al 99, Zinc coated steel	[82]
Calcium chloride hexahydrate [$CaCl_2$•$6H_2O$]	4-40	SS 330 SS 430 Copper Brass	Al 99.5 (Al 1000 Series), Al AG3 (5000 Series), Aluminum-magnesium alloy	[6] [71]
Sodium sulphate decahydrate ($Na_2SO_4.10H_2O$)	4-55	SS 430 SS 304L Mild steels, copper and anodized aluminum	Al 99.5 (Al 1000 series), Al AG3 (5000 Series) Al Dural (2007) aluminum magnesium alloy	[83] [71]
Zinc nitrate hexahydrate [$Zn(NO_3)_2$•$6H_2O$]	55	SS 430 Mild Steel (1.0330) Tin Plated Stainless Steel	Al 99.5 (Al 1000 series), Al AG3 (5000 Series) Al (2007 alloy) Brass Copper	Heine D ref .by [6] [80]
Sodium orthophosphate Dodecahydrate [$Na_3PO_4.12H_2O$]	55	SS (430), mild steel and copper Brass	Aluminum 99.5, aluminum-magnesium alloy	[83] [79]
	40	Mild, zinc-covered, alloyed steel, F20 cooper	Zinc-coated steel, Al 99, aluminum, aluminum-magnesium alloys	[82]
Sodium thiosulphate pentahydrate [$Na_2S_2O_3.5H_2O$]	70	D16 anodized alloy	St.3 steel, D-16T alloy, L-62 brass	Heine D ref by [6]
Potassium fluoride tetrahydrate [KF•$4H_2O$]	20	Mild, zinc-covered, alloyed steels, A119 aluminum, anodized aluminum-magnesium alloy, F20 cooper		[82]
Barium hydroxide octahydrate $Ba(OH)_2.8H_2O$	85-105	SS	D-16T alloy, L-62 brass	[84]
Sodium acetate trihydrate $NaCH_3COO.3H_2O$	60	Tinned mild steel		[85]

2.6 Summary

Despite the advantages of salt hydrates and their ability to store high thermal energy, there are still some reliability challenges (i.e. subcooling, phase segregation, and long-term stability) compared to organic PCMs (e.g. paraffin waxes, and fatty acids). The technical issues hindering the large-scale deployment of salt hydrates in various thermal engineering applications have been explored in this study. Due to reliability issues pertaining to salt hydrates, organic PCMs are commonly utilized in latent heat thermal energy storage system (LHTESS) and latent heat thermal management systems.

Subcooling and phase segregation pose major problems that hinder the reliability of the salt hydrate samples that are subjected to thermal cycling. While the incorporation of nucleating additives, gelling, or thickening agents can help with increase the storage performance of salt hydrates, additional studies are necessary for ensuring the reliability of the PCM samples when subjected to thermal cycling involving repeated solidification and complete melting.

Contemporary literature on PCM is lacking adequate information on the reliability and performance of modified salt hydrates for different test conditions. Literature reports show that DSC is the most commonly selected equipment by the authors for study of PCM thermal performance during thermal cycling. However, this may not be the most appropriate strategy for characterizing PCM samples. DSC techniques utilize small mass of test samples (~ 10 mg quantities). As a result, significant issues relating to large PCM samples are often not captured in these tests (such as those relating to phase segregation, diffusion, high subcooling, etc.). The studies in the literature also involve a large variety of analysis conditions, temperature ranges, heating/cooling rates, and the total number of cycles involving solidification with complete

melting of the PCM samples. In addition, a small sample size typically used in these studies is not representative of the actual engineering application or systems involving large quantities of PCM, especially for inhomogeneous materials (or due to presence of impurities in commercially procured PCM samples). Therefore, incorporating the T-History method [19] into thermal cycling would allow for sufficiently larger sample mass for the measurements, and allow for reliable measurements of the enthalpies of phase change. This would allow the measurement of phase transition temperatures with sufficient accuracy and precision without the need for expensive instrumentation (in contrast, DSC equipment is prohibitively expensive).

Standard test protocols for thermal cycling and materials characterization is lacking in contemporary literature. Contradictory results have been reported in the literature by different authors performing experiments involving different measurement protocols (e.g. involving different instrumentation, temperature ranges, and ramp rates). These authors also reported their results in different parameter ranges (i.e. melting temperature, latent heat of crystallization, etc.). Hence, a standardized set of test protocols involving instrumentation, test protocols, data analyses methods as well as sample size is necessary to bring a closure to the controversies in the PCM literature.

2.7 Current Challenges and Opportunities

The current challenges involving salt hydrates can be grouped into: reliability (change in material properties) and compatibility of salt hydrates with packaging (containment) materials. Augmenting the reliability of salt hydrates focuses on minimizing subcooling and obviating phase segregation over repeated melt-freeze cycles. The main reliability challenges are maintaining low sub-cooling and negligible phase segregation in salt hydrates (e.g., for over 1000 melt-freeze cycles). The compatibility of salt hydrates with packaging materials can be ascertained using corrosion tests. The contemporary literature is lacking adequate experimental data on corrosion of metals exposed to salt hydrates for long durations while standardized testing protocols that are responsive to the applications involving TES also need to be developed. Long term corrosion tests can provide reliable and statistically significant results that are often needed for the selection of appropriate materials for packaging (or containment of) salt hydrates.

In this regard, opportunities exist for improving the operational reliability of salt hydrates for applications in TES. This can be achieved by selecting and incorporating additives – such as - nucleation promoters and thickening agents (in order to maintain low sub-cooling and negligible phase segregation, say, in excess of 1000 melt-freeze cycles). Conducting long-term corrosion tests (e.g., using salt-hydrates over 18 weeks) for metals such as aluminum and stainless-steel can be beneficial for the engineering design community. Such tests can be implemented using ASTM protocols [88].

CHAPTER III

REVIEW OF LATENT HEAT THERMAL ENERGY STORAGE SYSTEMS

Latent heat thermal energy storage (LHTESS) systems provide the capability to store or absorb excess energy gradually during the off-peak period (usually of longer duration which can be dissipated rapidly during the peak demand period (usually of shorter duration). LHTESS is basically a heat exchanger with integrated phase change materials (PCMs). The PCM provides the latent heat energy storage capacity in LHTESS. The storage capacity and thermal performance of LHTESS depends on heat exchanger configuration (e.g. type, pass arrangement, number of tubes or plates), sizing, and power rating. Currently, research topics on LHTESS are mainly focused on shell and tube heat exchanger configurations and thermal performance enhancement techniques (e.g. increasing effective thermal conductivity of PCM). Literature reports on other heat exchanger configuration are scarce. This section provides a brief literature review on various types of LHTESS and their thermal performance enhancement techniques currently available in the literature.

3.1 Introduction on Latent Heat Thermal Energy Storage System

Latent Heat Thermal Energy Storage System (LHTHESS) are realized using different types of heat exchanger designs which are then with integrated phase change materials (PCMs). Heat exchangers can be classified into indirect-contact and direct-contact type. In direct-contact heat exchangers, the cold and hot streams come in contact and mixes, therefore causing enhancement in heat transfer. However, direct contact heat exchangers are only applicable to systems with two compatible fluids. For the indirect-contact heat exchangers, the hot and cold fluid streams are separated by a solid wall to prevent mixing. In case of LHTESS, only indirect-contact heat exchangers designs are applicable due to the incompatibility between PCM and heat transfer fluid. The function of the indirect-contact heat exchanger is to separate heat source, heat storage materials and heat sink, so that different mediums can be used as heat transfer fluid and phase change materials. Typically, the indirect-contact heat exchangers can be further divided into shell-tube, chevron-plate, and compact heat exchangers. Currently a significant portion of research studies are focused on shell-tube (tubular) heat exchangers because of their ease of manufacturing (compared to chevron-plate and compact heat exchanger configurations). A detailed discussion on the various types of heat exchangers employed in LHTESS applications were summarized by Agyenim, et al. [89].

3.1.1 Literature Review of Current LHTESS System

Agyenim, et al. [89] discussed about the integration of PCMs into heat exchangers and design requirements for LHTESS. The authors only considered LHTESS systems in the temperature range of 0 °C ~ 60 °C. Rathod and Banerjee [91] designed a double-pipe shell heat exchanger to investigate their efficacy as the LHTESS. The authors encapsulated the PCM (i.e., paraffin) on the shell side in a vertical orientation, thus enabling an outward melting configuration. The mass flowrate and the inlet temperature of the HTF were varied from 1–5 kg/ minute and 75–85 °C, respectively. The authors concluded that reduction in melting time can be achieved by increasing the flowrate and inlet temperature. The authors observed that the melting time is more sensitive to the increase in the inlet temperature than increase in the mass flowrate. The authors concluded that the transport phenomena during melting was dominated by convection whereas, solidification was dominated by conduction. Similarly, Kosha, et al. [92] investigated the effects of inclination and orientation of double-pipe heat exchangers on the melting and solidification times. The authors studied the effects of orientation and inclination using both experimental and numerical approaches. The authors concluded that the time required for melting is more sensitive to the variation in inclination than the time required for solidification. Horizontal orientation enables for faster melting, while the vertical orientation allows for a faster solidification. The results obtained from this study are therefore consistent with similar studies by Seddegh [93], and Agarwal and Sarviya [94].

Ibrahim, et al. [95] performed a critical review of geometric parameters and thermal conductivity enhancement techniques being used in heat exchangers. All PCMs exhibit a low thermal conductivity and therefore require techniques for enhancement of thermal conductivity. The authors summarized the common techniques including fins, porous mediums and

nanoparticles on enhancement of thermal conductivity. In similar work Merlin [96] studied the effects of radial fins, graphite powder, and ENG matrix in a vertical orientation shell-and-tube LHTESS. The author studied five different types of materials and surfaces: (a) Copper tube (without fins), (b) Aluminum finned, (c) Copper finned, (d) Graphite powder, and (e) ENG matrix. The authors concluded that the melting time for aluminum fin is about twice as fast (as the base case). The heat exchanger without insulation also enabled faster melting while the heat transfer was further enhanced with copper fin. The best heat transfer performance was achieved by ENG matrix in comparison to that of the tubes with fins and that of the graphite powders. Based on the trends observed in the experimental data, the authors predicted that better fin performance could be achieved with a thinner fin (i.e. enabling lower thermal resistance), compared to that of the thick fins used in the study.

Gasia, et al. [19] investigated the rate of heat storage and the thermal efficiency of an automobile integrated with a thermal storage system. The authors analyzed the performance of the heat exchanger based on two variables: (1) the fluid flow rate and (2) the PCM thickness. The authors concluded that the warm up time for the vehicle could be shortened by 33.7% with the aid of LHTESS.

In contemporary literature, the majority of studies involving LHTESS are focused on shell and tube designs (as well as thermal conductivity enhancement techniques). Currently there is no literature data for LHTESS involving compact heat exchanger configurations. Compact heat exchanger could be a good option for LHTESS (e.g., for maximizing power ratings) due to their high values of net heat transfer area (for a given form factor or footprint). Such a configuration could also enable significant savings in volume, weight and cost of LHTESS.

3.2 Current Challenges and Opportunities

The current issues involving LHTESS are the power rating, storage capacity and long-term reliability. The power rating of LHTESS are often limited by constraints that limit the rates of heat transfer, such as: thermal conductivity of PCM, pressure drop in HTF side (pump penalty) and sizing issues for the heat exchanger itself. For a shell-and-tube heat exchanger, the size considerations depend primarily on the shell configurations (number of passes, type, diameter, and length) and tube (number of passes, diameter, number, layout, surface texturing, and pass arrangement). For plate heat exchangers and compact heat exchangers, the sizing problem depends on the plate configuration (type, size, number, pass arrangement, surface texturing, etc.).

Opportunities exist for making ground-breaking advances in LHTESS system design for maximizing the power ratings while minimizing the pump penalty (for any given application). The desired increase in power rating could be achieved by studying and analyzing different heat exchanger configurations and by varying the net heat transfer area while also minimizing the metal to PCM ratio. The analyses steps involve exploring and predicting the variations in the non-linear power rating (and transient behavior of the LHTESS) during melting and freezing cycles. The future opportunities involving LHTESS are expected to be in the realm of enhancing the net area of compact heat exchangers with embedded porous metal fins (for a given form factor). As compact heat exchangers have the capability to provide high values of net heat transfer area (for a given volume) while minimizing weight and cost. This can be achieved by impregnating the PCM into porous metal fins (which is a technique for enhancing the effective thermal conductivity of the PCM and for enhancing the net heat transfer).

CHAPTER IV

EXPERIMENTAL METHODS

This chapter covers the experimental apparatus, methods and procedures employed for measuring the material properties of phase change materials (e.g. latent heat, phase transition temperature, thermal stability and thermal conductivity) as well as the thermal performance of various configurations of heat exchangers (that were integrated with various phase change materials). Dynamic nucleation techniques (e.g., "Cold finger") and corrosion protocols used in this study are also discussed in this chapter.

The thermal characterization section mainly focuses on the T-History method and transient plane source (TPS) technique (which is used for measuring the thermal conductivity of different samples). These experimental apparatus were used for the thermal characterization of latent heat, phase transition temperature, and thermal conductivity measurement (for both liquid and solid phase). The thermal stability section provides details on experimental set-up and procedures that were used for conducting 1000 cycles of accelerated tests involving repeated melt-freeze cycles and accelerated aging tests (performed at fixed temperatures) spanning over 30 days.

The heat exchanger section provides the experimental techniques and apparatus that were used for validating the thermal performance of shell-and-tube heat exchangers, plate heat exchanger and compact heat exchanger – when employed as LHTESS.

The section on corrosion tests provides details on the experimental apparatus and procedures that were used for conducting corrosion experiments spanning over 18 weeks of continuous exposure of the metal coupons immersed in the chosen PCM samples.

4.1 Measurement of Thermal Properties

Thermal properties of phase change materials were measured experimentally using modulated differential scanning calorimetry technique or “MDSC” (i.e., for obtaining latent heat, and phase transition temperature values). MDSC techniques utilize milligrams quantities of samples for measurement. As an alternate approach - lump capacitance method (i.e., “T-History” method) was also used. T-History involves the use of larger quantities of sample mass (e.g., 30 ~ 50 grams) for the validation of the measured values of latent heat, phase transition temperature, sub-cooling and phase segregation. The solid and liquid thermal conductivity of the samples were measured using the transient plane source (TPS) technique.

4.1.1 Latent Heat, Specific Heat and Melting Temperature

During the initial characterization, modulated differential scanning calorimetry (MDSC) was utilized for measuring the heat of fusion, and transition temperature. Although MDSC methods are well developed, their shortcomings are obvious: the samples tested by MDSC are very small (1-15mg). Hence, thermo-physical properties of samples measured by MDSC generally varies with the bulk materials properties used in practical systems. When salt hydrates PCMs are contained in a small container, the degree of sub-cooling is amplified while the degree of phase segregation is alleviated. Secondly MDSC instruments are complicated, expensive and requires constant calibration. In view of these facts, we developed a new method; the lumped capacitance-temperature history (T-History) technique, of determining the transition temperature, degree of sub-cooling, and heat of fusion of several PCM samples simultaneously. This method is especially useful for the selection of candidate PCMs or for the preparation of new PCMs for use in practical systems.

A) Modulated Differential Scanning Calorimetry (MDSC)

The MDSC tests were performed using DSC Q6000 TA Instrument to measure the latent heat and transition temperature of the phase change materials. The measurements were performed from 0°C to 50°C. The advantage of MDSC is that by applying a sinusoidal modulated heating rate in addition to a constant heating rate, the temperature response of the samples is obtained and recorded by the MDSC instrument; which enables the separation of the total heat flow into reversible part and non-reversible part (based on the temperature response for the varying heating rate). By analyzing the reversible heat flow signals - the specific heat capacity values can then be obtained directly for each cycle as follows:

$$\frac{dH}{dt} = C_p \frac{dT}{dt} + f(T, t) \tag{4.1}$$

$$Total = Reversing + Nonreversing$$

where, H is the total heat flow, T is the instantaneous temperature of the sample, C_p is specific heat capacity of the material, and f is the non-reversible component of heat flow. Zero™ hermetic pans and lids (manufacturer: TA Instruments) were used to store the PCM samples. The MDSC sample pan was prepared by; first heating the target testing sample vial (large quantity) in a convection gravity oven at 40°C for roughly 50 minutes until the PCM sample is completely melted. Then a small amount (~15mg) of sample were suctioned using a syringe for measurement. The empty pan and lid were weighed before and after filling with PCM sample to accurately determine the sample mass.

B) Lumped Capacitance Method (T-History)

The setup of the T-History test is shown in Figure 17. One test-tube is filled with reference: distilled water (sample mass: ~15g) and an identical test tube is filled with PCMs to the similar height as the reference to preserve the heat transfer area between the reference and the PCM sample. The mass and dimensions (i.e. length, inner diameter, and outer diameter) of each test tube is carefully measured and recorded before and after filling using microbalance (sartorius ELT-130, and Ohaus SPX223) and Vernier Caliper (Mitutoyo 500-196). The test-tubes were sealed with rubber stopper with a center hole for thermocouple placement. Both PCM and reference test-tubes were placed in environmental chamber (TPS, Tenney Jr Chamber, PA) and equilibrated at 40°C. The temperature change in the PCM and reference samples were monitored using 0.062" sheathed K-type thermocouples (Omega, KMQXL-02G-12, CT). The ambient temperatures around the test-tubes were monitored at 4 different locations using 36 gage bare wire K-type thermocouples (Omega, TT-K-30, CT). The thermocouples were calibrated in water bath using a NTSI calibrated mercury thermometer from 10°C to 46°C at intervals of 0.5°C. Appendix A provides the calibration curve for every thermocouple utilized in T-History method. For performing the T-History measurements, the chamber temperature was ramped between 24°C and 40°C with a ramp rate of 1.5°C/minute. The temperature change of both PCM and reference samples were recorded at 1HZ frequency.

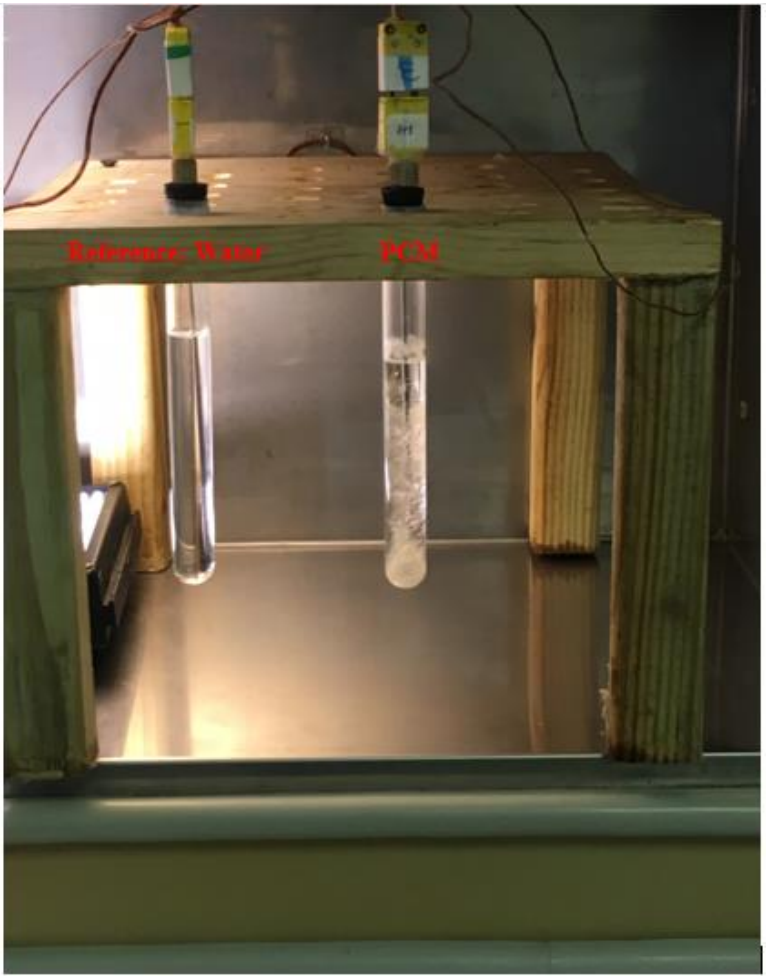

Figure 17: Experimental apparatus for T-History Measurements.

In our setup, 15mm diameter by 200mm test-tube was used to contain the samples (i.e. $L/R_o > 10$), this approximation permits the assumption of one-dimensional conduction in radial direction. It is also essential to validate that the Biot number (Bi) is less than 0.1, for implementation of lumped capacitance technique (e.g. T-History method). The Biot Number of PCM and reference samples in the test-tube can be expressed as:

$$\boldsymbol{Bi} = \frac{\boldsymbol{h_{air} L_c}}{\boldsymbol{k}} = \frac{\boldsymbol{h_{air} R}}{\boldsymbol{2k}} \tag{4.2}$$

Where, h_{air} is the natural convection coefficient of air, k is the thermal conductivity of the sample, L_C is the characteristic length of the sample, R is the outer radius of the test-tube. Assuming the natural convective heat transfer coefficient of air is about 5-6 W m^{-2} K^{-1}, so the condition about Bi < 0.1 can be satisfied when the thermal conductivity is more than 0.2 W m^{-2} K^{-1} (i.e. k of salt hydrates is larger than 0.4 W m^{-2} K^{-1}).

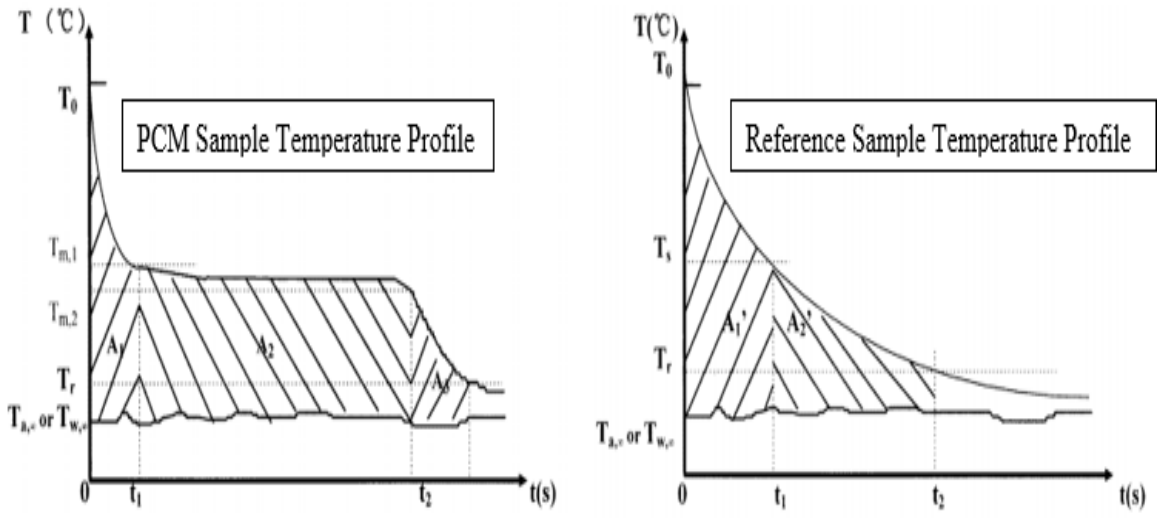

Figure 18: A typical Temperature-History (T-History) curve of PCM (Left) and reference (Right) during cooling process.

If a test-tube containing a liquid PCM whose temperature is uniform and equal to T_0 (T_0 > Tm, (Tm is the melting temperature of the PCM) is suddenly exposed to an ambient air whose temperature is T∞,a (which can be time dependent), the temperature versus time curve of the PCM, (i.e. the T -history curve), is as shown in Figure 18. Based on the lumped capacitance technique, we could show that the sensible heating in liquid phase is:

$$\left(m_t C_{p,t} + m_p C_{p,l}\right)(T_0 - T_s) = hA_c A_1 \qquad (4.3)$$

where m_p and m_t are the masses of the PCM and test-tube respectively, $Cp_{,l}$ and $C_{p,t}$ are the mean specific heats of the liquid PCM and of the test-tube material (i.e. Pyrex) respectively, and A_c is the convective heat transfer area of the PCM sample; $A_1 = \int_0^{t_1}(T - T_{\infty,a})\,dt$. During the period of phase transition we have;

$$(m_p H_m) = hA_cA_2 \tag{4.4}$$

where H_m is the heat of fusion of the PCM and $A_2 = \int_{t_1}^{t_2}(T_m - T_{\infty,a})\,dt$, and t_1 and t_2 is the time during which the phase transition process occurs. After the end of phase transition, we could show that the sensible heating in solid phase is;

$$(m_tC_{p,t} + m_pC_{p,s})(T_s - T_r) = hA_cA_3 \tag{4.5}$$

where $C_{p,s}$ is the mean specific heat of solid PCM and $A_3 = \int_{t_2}^{t_3}(T - T_{\infty,a})\,dt$, and T_r is steady state temperature at the end of the processor. If the reference test-tube is suddenly exposed to the same ambient condition as mentioned above as shown Figure 18. We will similarly have;

$$(m_tC_{p,t} + m_wC_{p,w})(T_0 - T_s) = hA_cA_1' \tag{4.6}$$

$$(m_tC_{p,t} + m_wC_{p,w})(T_s - T_r) = hA_cA_2' \tag{4.7}$$

where m_w and $Cp_{,w}$ is the mass and mean specific heat of water, respectively. $A_1' = \int_0^{t_1'}(T - T_{\infty,a})\,dt$ and $A_2' = \int_{t_1'}^{t_2'}(T - T_{\infty,a})\,dt$. T-history measurement is based on assumption that both reference and PCM samples have the same heating surface area and same heat transfer coefficient at a given temperature. Therefore, from equation (4.3) - (4.7), we could obtain:

$$H_m = \frac{m_w C_{p,w} + m_t C_{p,t}}{m_p} \frac{A_2}{A_1'} \left(T_0 - T_{m,1}\right) - \frac{m_t C_{p,t} \left(T_{m,1} - T_{m,2}\right)}{m_p} \tag{4.8}$$

$$C_{p,s} = \frac{m_w C_{p,w} + m_t C_{p,t}}{m_p} \frac{A_3}{A_2'} - \frac{m_t C_{p,t}}{m_p} \tag{4.9}$$

$$C_{p,l} = \frac{m_w C_{p,w} + m_t C_{p,t}}{m_p} \frac{A_2}{A_1'} - \frac{m_t C_{p,t}}{m_p} \tag{4.10}$$

As salt hydrates are prone to sub-cooling, where the temperature range of the phase-change process is between T_m and T_s as shown in Figure 19. The expression for $Cp_{,l}$ and $Cp_{,s}$ is the same as those above, but the heat of fusion should be rewritten as follows:

$$H_m = \frac{m_w C_{p,w} + m_t C_{p,t}}{m_p} \frac{A_2}{A_1'} \left(T_0 - T_s\right) \tag{4.11}$$

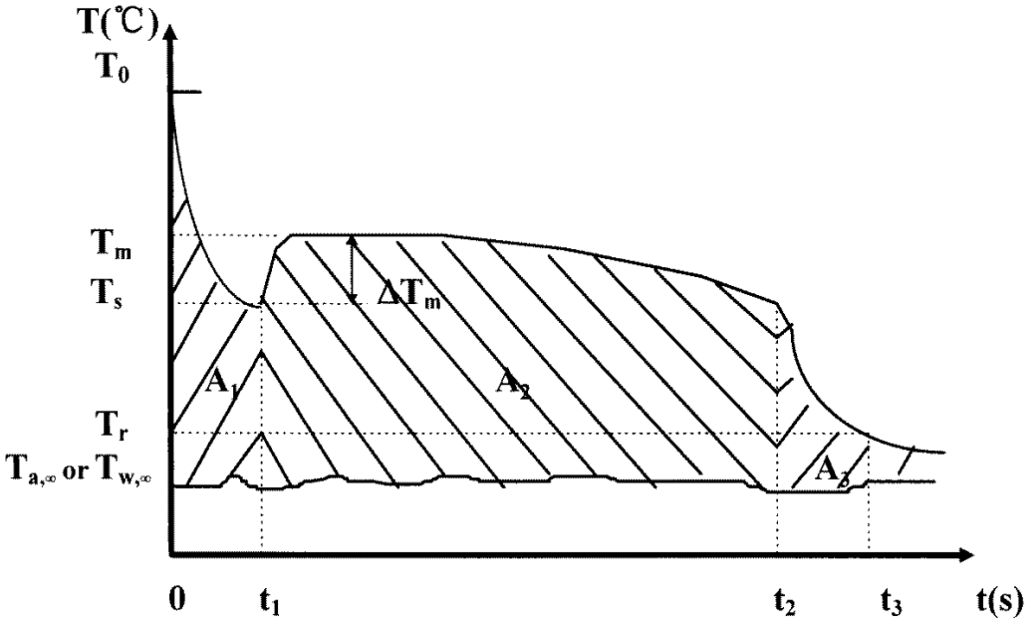

Figure 19: T-history curve of a salt hydrate during cooling process with sub-cooling.

From Equations (4.8) – (4.11), it can be shown that the errors in measurement of $\boldsymbol{H_m}$, $\mathbf{C_P}$, and $\boldsymbol{T_m}$ are mainly due to errors in measurement of temperature. So, its errors in measurement are:

$$\frac{\boldsymbol{U_{H_M}}}{\boldsymbol{H_m}} \approx \frac{\boldsymbol{2U_T}}{\boldsymbol{T_m - T_{\infty,a}}} + \frac{\boldsymbol{2U_T}}{\boldsymbol{T_0 - T_m}} \tag{4.12}$$

$$\frac{\boldsymbol{U_{C_p}}}{\boldsymbol{C_p}} \approx \frac{\boldsymbol{4U_T}}{\boldsymbol{T_m - T_{\infty,a}}} \tag{4.13}$$

$$\frac{\boldsymbol{U_{T_M}}}{\boldsymbol{T_m}} \approx \frac{\boldsymbol{0.1°C}}{\boldsymbol{T_m}} \tag{4.14}$$

The relative errors of the aforementioned parameters for various errors in measurement of the temperature $\boldsymbol{U_T}$ are summarized in Table 10. It can be concluded that, if $\boldsymbol{U_T}$ < **0.1°C**, the measurement uncertainty is less than 10%, which satisfies the precision requirement for thermo-physical properties measurement.

Table 10: Relative errors of measurement for T-History technique. The main contribution of error in T-History is from temperature measurement (i.e. thermocouple).

$\boldsymbol{U_T}$ (°$\boldsymbol{C}$)	***0.5***	***0.1***	***0.01***
$\boldsymbol{U_{C_p}}/\boldsymbol{C_p}$ (%)	20	4	0.4
$\boldsymbol{U_{H_m}}/\boldsymbol{H_m}$ ***(%)***	30	6	0.6

4.1.2 Thermal Conductivity

The thermal conductivity of the liquid and solid phases of PCMs were analyzed by transient plane source technique (Thermites' Hot Disk TPS 2500S thermal constant analyzer). The transient plane source (TPS) thermal characterization technique was preferred due to its robust design, rapid characterization time of complex materials. In order to obtain accurate results using this technique, the sensor power and measurement period must be selected such that the thermal penetration depth into the sample is less than the distance to the opposite edge of the surrounding material. The thermal properties of the materials are determined by measuring the temperature rise of the sensor as a function of time and applying the fundamental semi-infinite transient heat conduction equation to the sensor geometry as follows:

$$\boldsymbol{k\nabla^2 T + \frac{Q}{\rho . C_p} = \frac{\partial T}{\partial t}} \tag{4.15}$$

where k is the thermal conductivity of the material, Q is the heat flux, ρ is the density and C_p is the specific heat capacity. In order to validate the semi-infinite boundary condition, the penetration depth (Δp) is computed as follows:

$$\boldsymbol{\Delta p = 2\sqrt{\alpha . t}} \tag{4.16}$$

where α represents the thermal diffusivity of the sample and t represents the measurement period as specified by the user. The measurement period is defined as the difference between the final and the initial time of the measurement, which are selected by the user. This allows the user to selectively prevent the interfacial resistance between the sensor and the specimen. The hot disk sensor itself serves as both a heat source and a temperature sensor. The sensor is made of a double-spiral nickel foil wire and is coiled into a known number of "n" concentric rings with equal spacing.

The double-spiral nickel foil wire is encapsulated in two 25 μm thick Kapton sheets for electrical insulation of the nickel foil wire as shown in Figure 20.

Figure 20: Example of TPS sensor (Sensor Number: C5501, Radius: 6.403 mm) used.

The sensor must be sandwiched between two solid samples in order to measure thermal conductivity. In principle, when the sensor is powered, its temperature will increase rapidly when sandwiched between insulating materials and slowly for thermally conductive materials. A detailed formulation of solutions for measurement thermal conductivity using TPS can be found in [97].

A) “Solid Phase” Thermal Conductivity Measurement Technique

In this study, TPS is used to determine the thermal conductivity of solid specimens. As shown in Figure 21, the sensor is clamped into the sample holder and the bottom specimen piece is placed on the adjustable plate, which is raised to make contact with the sensor and the top specimen is placed on top of the sensor and a light pressure is applied to ensure good contact between sensor and sample.

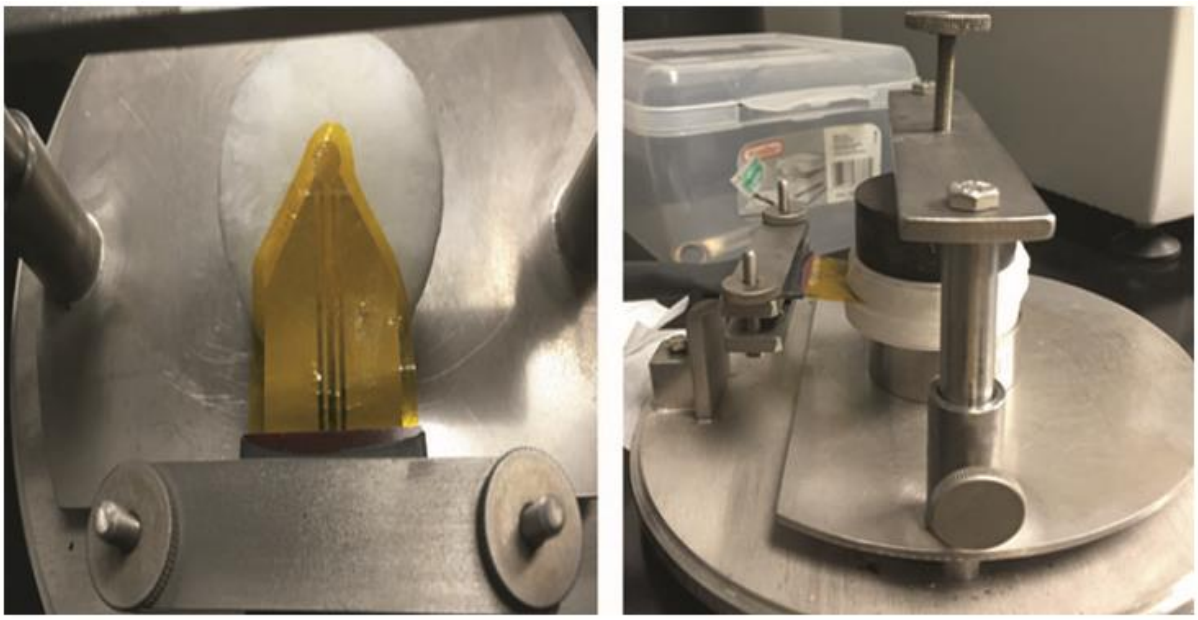

Figure 21: Solid thermal conductivity measurement technique using TPS. (Sensor: 7577; Radius: 2mm).

The molds for solid specimens were synthesized and build in-house. As shown in Figure 22, synthesized salt hydrates were poured into a plastic petri dish (Diameter: 3mm) and immediately placed in a -15°C freezer to stimulate crystallization, so that the quality of salt hydrate can be guaranteed. After 12 hours of sub-zero freezing, the samples were removed from freezer and the molds were detached from the petri dish. Due to the hygroscopic nature of salt hydrates, multiple samples were prepared with varying water concentration (i.e. lower concentration) to

account for water absorption during synthesis and testing. The concentration of water was measured before and after thermal conductivity measurement. The testing procedures and measurement uncertainties are listed in Table 11.

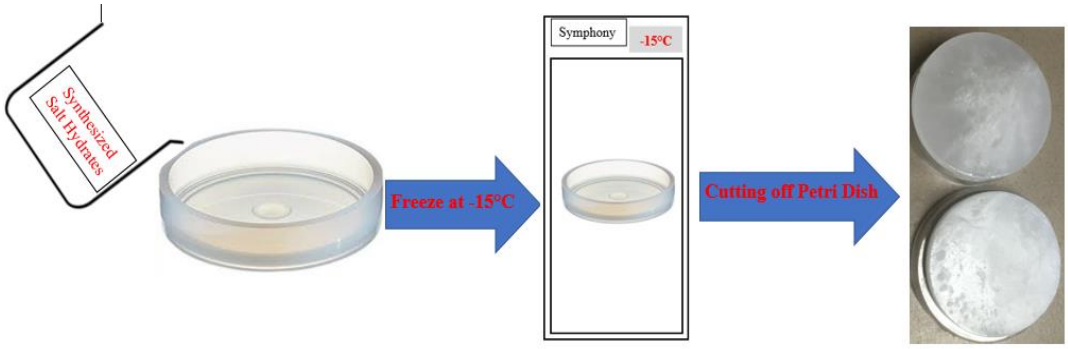

Figure 22: Procedures to manufacture solid molds for measuring thermal conductivity in solid phase.

Table 11: Testing parameters for measuring thermal conductivity in solid phase.

Experimental Parameter	***Condition***
Temperature of Measurement	24°C
Number of Measurements / Sample	5
Cooling period between each measurement	40 minutes
Calibration Uncertainty*	0.2%
Sensor Model	7577
Sensor Radius	2 mm
Penetration Depth	10mm

* Measurement Uncertainty in solid phase was analyzed using a reference Stainless Steel as standard.

B) "Liquid Phase" Thermal Conductivity Measurement Technique

The use of TPS method described here are described for accurate measurement of thermal conductivity in solids. However, when evaluating the thermal conductivity of liquids, TPS method's accuracy is found to be substantially lower than solids due to buoyancy-related fluid movement over the sensor face. The self-heating of TPS sensor can create natural convective currents, when long measurement times are used. Thus, the measurement accuracy is strongly affected by measurement period and heating power. Therefore, to obtain accurate measurements the total measurement time and heating power must be carefully selected in order to avoid natural convection across the sensor face.

Upon test initiation, the sensor produces a constant heat flux and the temperatures of both the sensor and the surrounding fluid begin to increase. The surrounding fluid must behave as a semi infinite solid and must not begin to convect during the measurement period. The container must be sized to allow heat to diffuse in the radial direction and in the axial direction without reaching another material or system boundary. Equation 4.15 can be used to determine the thermal penetration depth to ensure that the semi-infinite condition is met. In order to avoid natural convection over the sensor face during measurement, a measurement period must be chosen such that the total measurement time is less than the time needed for onset of natural convection. The time needed for onset of natural convection can be computed as [98]:

$$t_{onset} = (9.52e^{-6}) \cdot \frac{\left(Pr^{0.456} \cdot Ra^{0.285}\right)}{\left(Q^{0.791} \cdot \beta^{0.830}\right)} \tag{4.17}$$

Should the measurement include time periods over which natural convection exists, the resultant solution for the thermal conductivity of the surrounding liquid will be artificially high. Thus, Equation 4.16 was developed in order to ensure that the period over which the measurement is

taken does not include the effects of natural convection. In order to develop an accurate and repeatable solution method for measuring the thermal conductivity of fluids using TPS method, a series of experiments were conducted. Table 12 summarizes the properties of salt hydrates used for commutating onset of convection.

Table 12: Thermo-physical properties of salt hydrates in liquid phase at 318K.

Salt Hydrates	*ρ (kg/m^3)*	*C_P (J/kg K)*	*α (m^2/s)*	*ν (m^2/s)*	*β (1/K)*	*Prandtl Number*
Lithium Nitrate Trihydrate [99]	1420	2760	1.49E-07	3.38E-06	3.50E-04	2.27E+01
Calcium Chloride Hexahydrate	1562	2100	1.65E-07	7.36E-06	3.03E-04	4.47E+01
Zinc Nitrate Hexahydrate	1828	2000	1.27E-07	5.36E-06	3.03E-04	4.22E+01
Glauber Salt	1458	2400	1.55E-07	5.36E-06	3.03E-04	3.45E+01

The effects of sensor power on onset of natural convection were computed and summarized in Figure 23. The TPS system allows user to set the measurement time and has 11-time periods (2.5, 5, 10, 20, 40, 80, 160, 320, 640, 1280 and 2560 s). It is expected that greatest accuracy can be obtained by maximizing the measurement time as it increases the number of data points collected without creating a situation where significant convection occurs. Small power input would increase the measurement uncertainty due to small temperature change. Therefore, based on Figure 23, the power input was selected between 0.06 to 0.1 watts which allowed for significant temperature change and maximized the number of data points collected, and minimized the effects of natural convection.

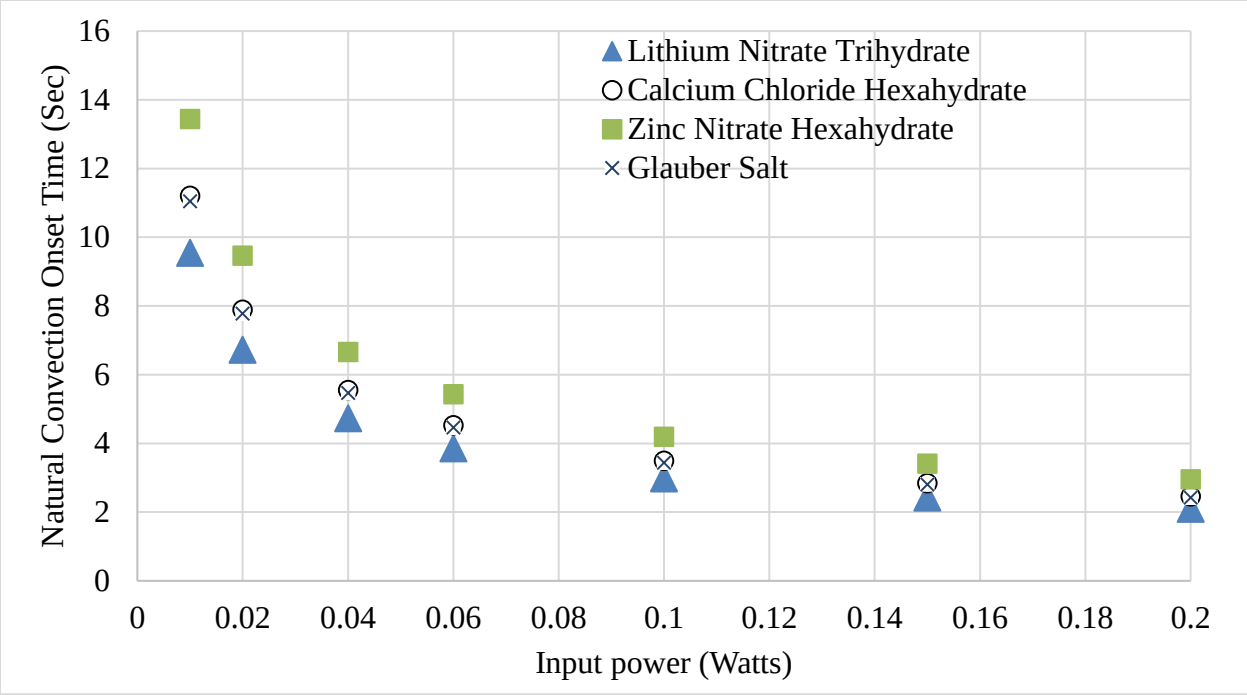

Figure 23: Time to the onset of convection with varying input power for each salt hydrates calculated per equation 17.

The setup of the liquid thermal conductivity measurement is shown in Figure 24. 30 ml glass beaker is filled with liquid salt hydrate and capped off with an insulation material with a cut-out for sensor placement. The glass beaker was sized to allow heat to diffuse 15 mm in the radial direction and 10 mm in the axial direction without reaching another material or system boundary. The sample was suspended in a water bath (Cole Parmer, StableTemp) at 40°C for an hour to reach steady state condition. The testing procedures and measurement uncertainties are listed in Table 13 .

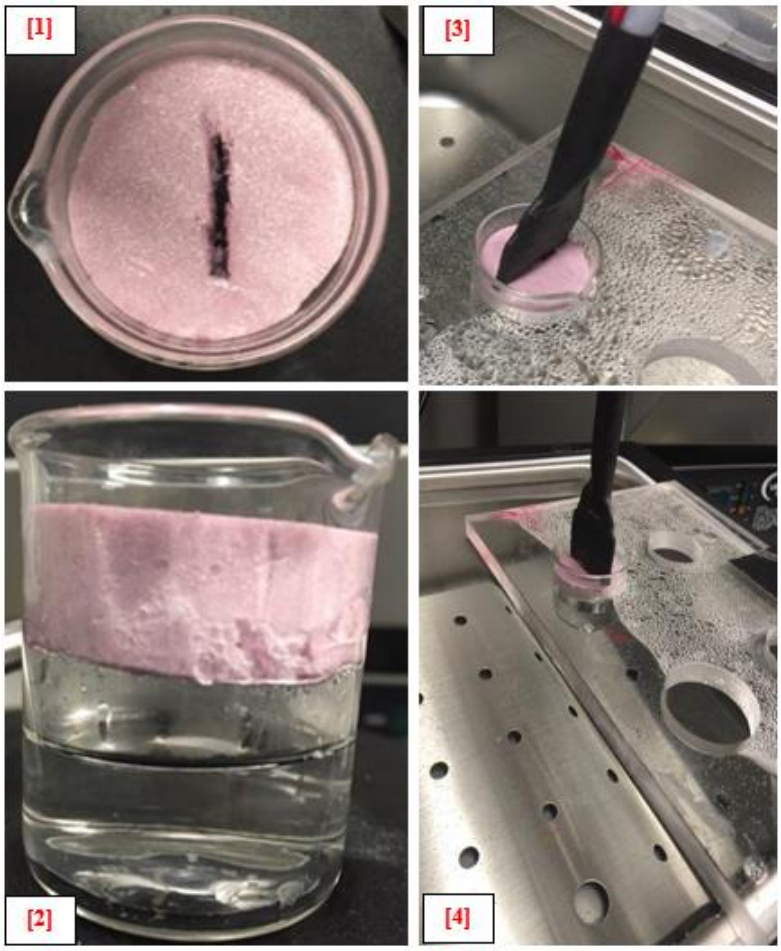

Figure 24: Liquid thermal conductivity measurement set-up in TPS. [1] Sensor mount; [2] Volume of sample; [3] Mounting of sensor in sample; [4] Sample and sensor placement in water bath to reach steady state temperature.

Table 13: Testing parameters for measuring thermal conductivity in liquid phase.

Experimental Parameter	***Condition***
Temperature of Measurement	40°C
Number of Measurements / Sample	5
Cooling period between each measurement	60 minutes
Calibration Uncertainty*	6.6%
Sensor Model	7577
Sensor Radius	2 mm
Penetration Depth	10mm (In Axial Direction)

*Measurement Uncertainty in liquid phase was analyzed using water as standard. The results of water thermal conductivity measurement are provided in Appendix A

4.2 Thermal Stability

Thermal stability of salt hydrates was determined by performing 1000 melt-freeze cycle on an in-house thermal cycle rig as shown in Figure 25. The water baths (Cole Parmer, Ploystat 12122-02 1C6) in the system were used as cooling and heating source. A digital temperature controller (OMEGA CN 310) and a relay (i.e. solenoid valve) is utilized to control the melting and freezing process, by receiving input signal from the samples and providing output signal to the relay for control. Plate heat exchanger was used as heat transfer system between bath working fluid and test rig working fluid. DI water was used as working fluid in both the test rig and bath.

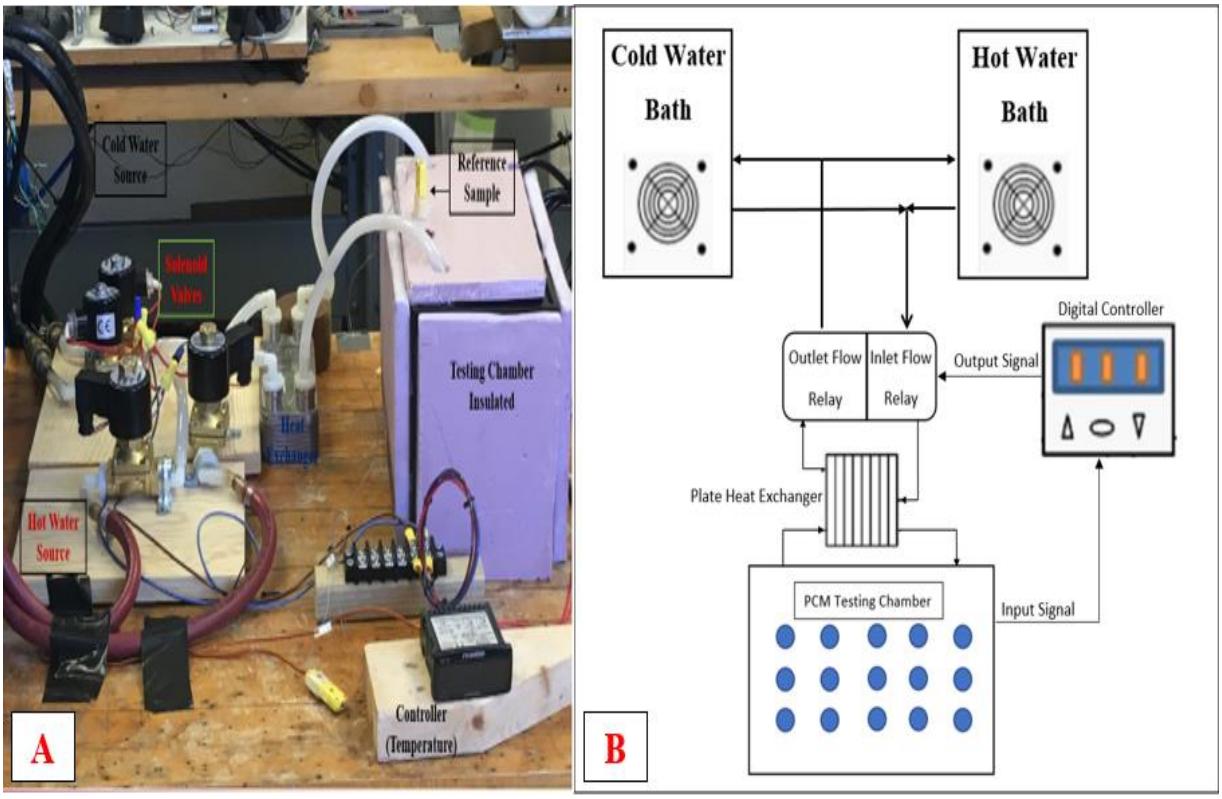

Figure 25: Thermal cycle set-up (a) Exploded view, (b) Schematic view.

The controller was tuned based on the reference sample n-octadecane and was tuned in way that the salt hydrates samples completely melts and solidifies in less than 2 hours as shown in Figure 26. Based on the tuning performance, the system was able to do 14 cycles/day and was able to complete 1000 melt-freeze cycles in 72 days. Considering that the material will undergo 365 melt-freeze cycles in a year, 1000 cycles was performed to access its utility for 2.5 consecutive years as an effective thermal energy storage material.

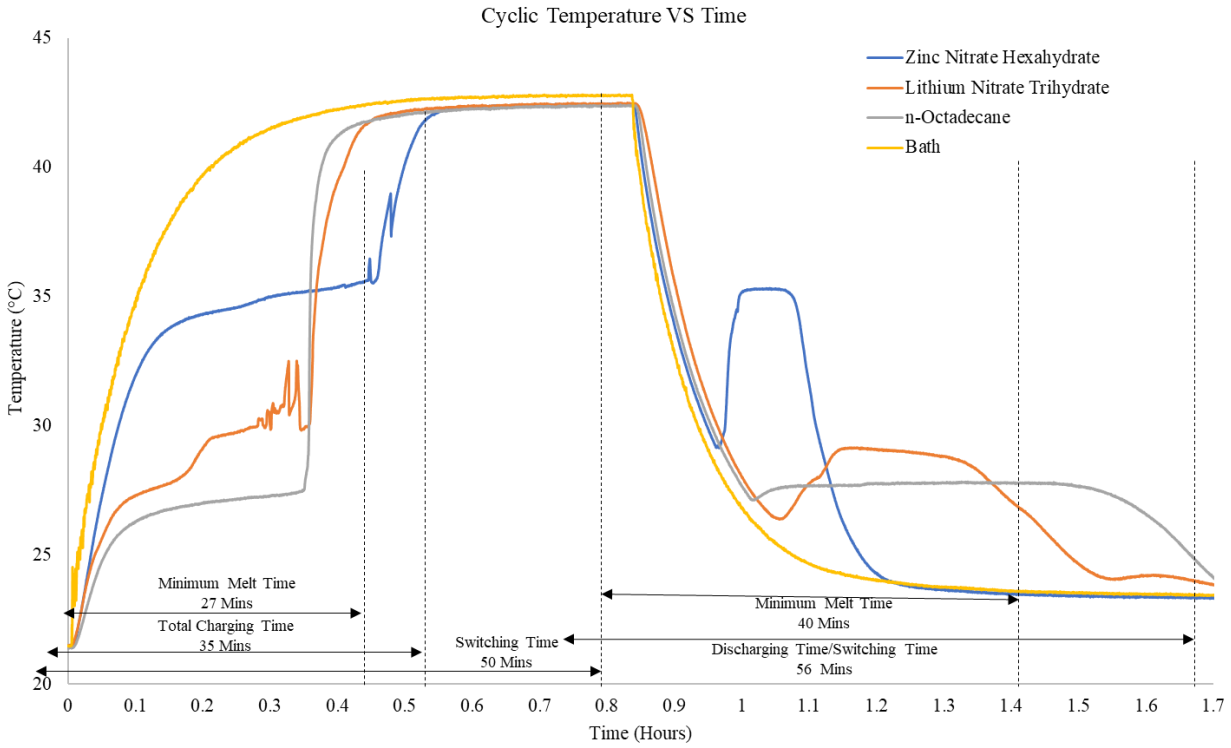

Figure 26: Cyclic temperature vs time for controller tuning during thermal cycles. The controller was tuned using n-octadecane as a reference due to their known thermal stability with cycles.

The candidate PCMs underwent complete melting and solidification thermo-cycling in the thermal cycle rig. The water baths were maintained at 42°C for melting cycle and 25°C for the solidification cycle. As synthesized salt hydrates were poured into a pyres glass test tube (VWR, PA) and capped off to prevent the effects of ambient on thermo-cycling. The sample preparation for thermal cycling is as shown in Figure 27. The samples were analyzed every 250 cycles for their thermal performance (i.e., latent heat, subcooled temperature, and phase transition temperature), change in mass, and physical changes. The thermal performances were characterized using temperature history method (T-History). A total of 12 samples for each PCM candidate were synthesized (i.e triplicate for every 250 cycles).

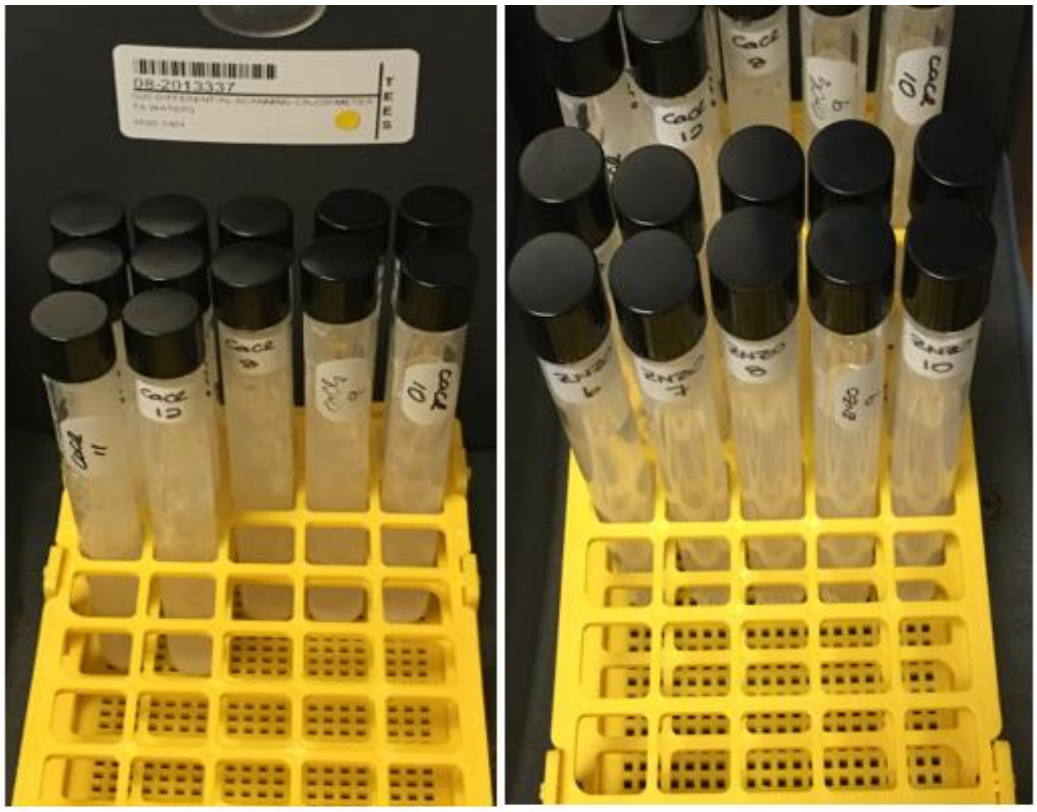

Figure 27: 1000 thermo-cycling sample preparation. The samples consist of lithium nitrate trihydrate, calcium chloride hexahydrate, and zinc nitrate hexahydrate.

The sample volumes were kept constant at 15 ml to a maintain a fixed heat transfer area during the thermo-cycling experiment. Individual PCM sample mass are summarized in Table 14 along with their energy storage capacity for fixed volume.

Table 14: The average mass of PCM candidate samples for thermo-cycling test.

Candidate PCMs	Nucleating Agent	Mass of Sample (g)	Energy Storage Capacity (kJ)	Density Ratio (ρ_s / ρ_l)
Lithium Nitrate Trihydrate ($LiNO_3.3H_2O$)	Zinc Nitrate Hydroxyl [$Zn(NO_3)_2(OH)_4$]	20	5.8	1.16
Calcium Chloride Hexahydrate ($CaCl_2.6H_2O$)	Strontium Chloride ($SrCl_2$)	27.7	4.0	1.06
Zinc Nitrate Hexahydrate [$Zn(NO_3)_2.6H_2O$]	Zinc Nitrate Hydroxyl [$Zn(NO_3)_2(OH)_4$] Zinc Oxide (ZnO)	23.7	4.3	1.10

As lithium nitrate trihydrate and calcium chloride hexahydrate samples were synthesized in house as discussed in later sections. Therefore, small mass quantities were withdrawn from the synthesized samples to evaluate water concentration through a dehydration process. Table 15 summarizes the water molar concentration in each individual sample.

Table 15: Summarizes of the water concentration in lithium nitrate trihydrate and calcium chloride hexahydrate samples.

Test Tube Nomenclature (Naming)	Concentration of Water (Moles) Lithium Nitrate Trihydrate	Concentration of Water (Moles) Calcium Chloride Hexahydrate
TT 1 and TT 2	3.05	5.95
TT 3 and TT 4	3.07	5.98
TT 5 and TT 6	3.05	6.01
TT 7 and TT 8	3.06	5.96
TT 9 and TT 10	3.07	6.03
TT 11 and TT 12	3.05	5.99

4.3 Aging Test

For a nucleation catalyst to be practical for applications, including its use with PCMs, it must be stable over long periods of time at relevant elevated temperatures. During aging test, the identified nucleating catalyst were mixed with salt hydrates (i.e. calcium chloride hexahydrate, lithium nitrate trihydrate, zinc nitrate hexahydrate) at varying mass concentration and aged at 45°C and 20°C for a period of 30 days. As synthesized salt hydrates and identified nucleating catalyst were mixed and poured into a Pyrex glass test tube (VWR, PA) and capped off to prevent the effects of ambient on aging test. As shown in Figure 28, the samples were placed in water baths maintained at 45°C and 20°C.

The samples were analyzed every 10 days for their thermal performance (i.e., latent heat, subcooled temperature, and phase transition temperature), change in mass, and physical changes. The thermal performances were characterized using temperature history method (T-History). A total of 9 samples of each PCM candidate were synthesized (i.e triplicate for every 10 cycles).

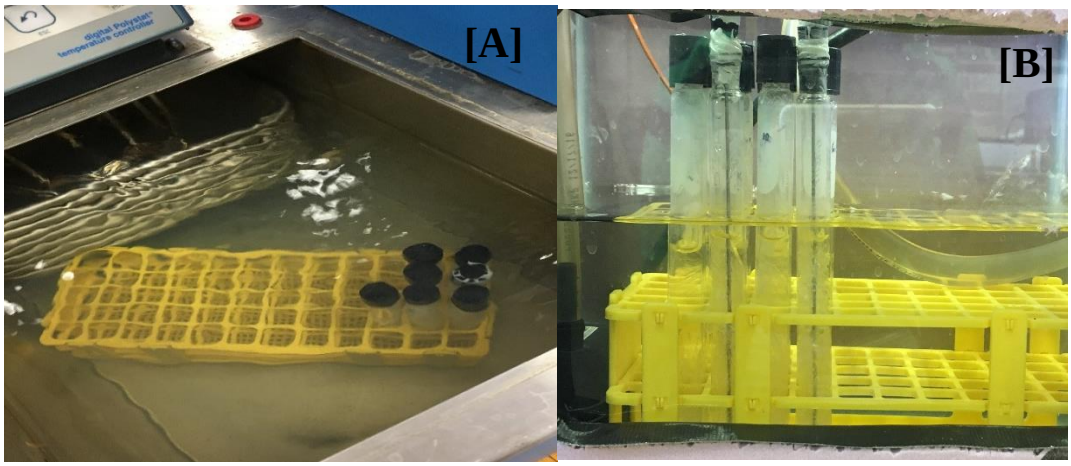

Figure 28: Aging experiment set-up [A] 45°C Water bath [B] 22°C Water Bath

4.4 “Cold Finger” Test

The “cold finger” thermo-cycling experiments were carried out to study the effects of incomplete melting (85% melting) on lithium nitrate trihydrate with and without additives. The experiment was designed for 1000 thermo-cycles. The only variation from the earlier set-up is that pure lithium nitrate trihydrate was used as the reference sample for the temperature controller due to simplicity in controller configurations necessary for cold finger experiment. The reference was sealed air tight to prevent mass gain due to water absorption as shown in Figure 29. Special attention was given to the sealing of the reference samples since mass gained could alter the performance of the PCM and therefore alter the initial controller configurations. The water baths in the flow loop apparatus were maintained at 40°C for the melting cycle and 26°C for solidification cycle. The PCM samples were sealed in a pyres glass test tube (VWR, PA). The mass of the samples was kept constant at ~17.5g. The samples were analyzed at every 250 cycles for their thermal performance (i e. latent heat, subcooled temperature, and phase transition temperature), change in mass, and physical changes. The thermal performances were characterized using the temperature history method (T-History). Total of 12 samples were synthesized for lithium nitrate trihydrate (i.e triplicate for every 250 cycles).

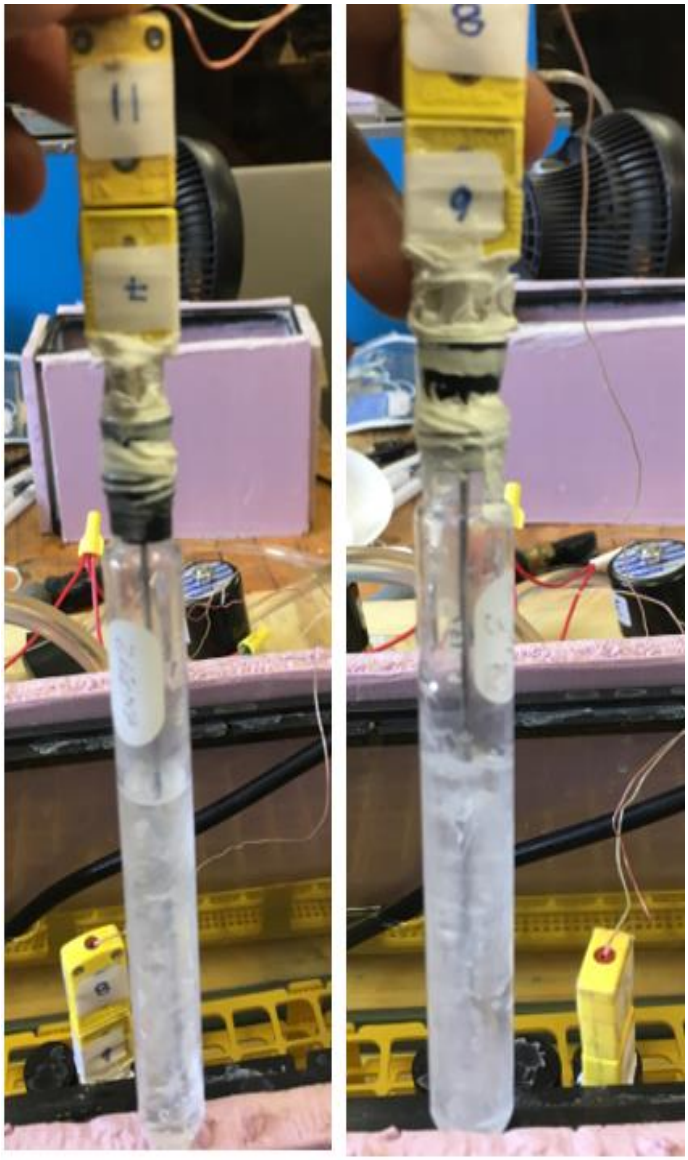

Figure 29: Reference samples for "Cold Finger" thermal cycling.

As shown in Figure 30, the complete melting of lithium nitrate trihydrate took around 27 mins. Based on the melting data the controller was programmed to run the melting process for 19 minutes before switching to solidification as shown in Figure 31. The samples were completely solidified at 30°C and then brought to a subcooled temperature of 26.4°C. Based on the results, each cycle took around 64 minutes. Therefore, a total of 23 cycles per day.

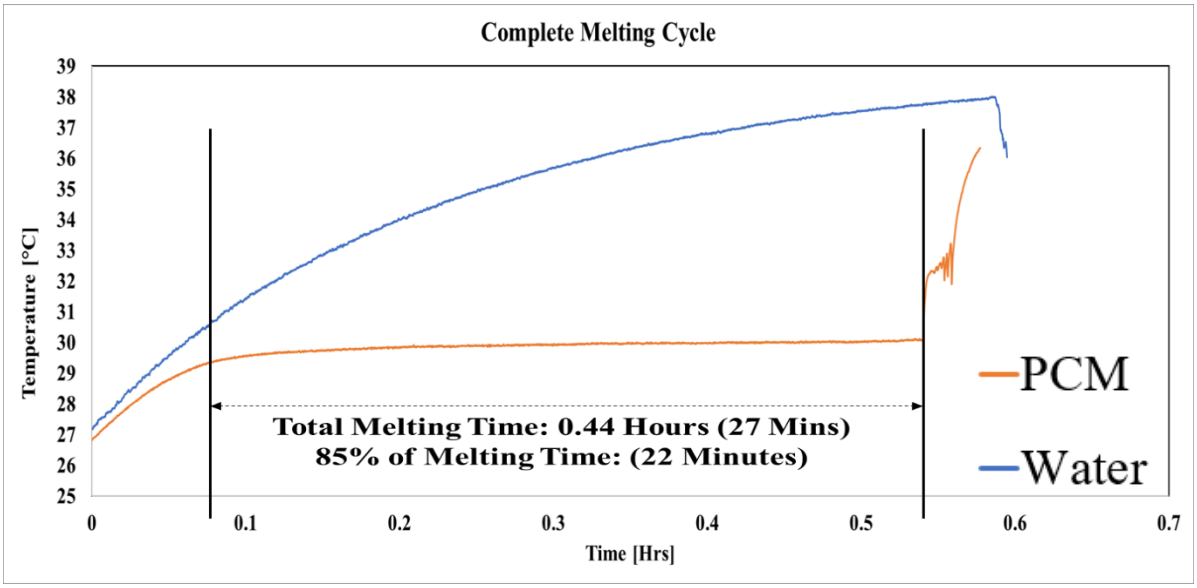

Figure 30: Complete melting of lithium nitrate trihydrate in water bath. Estimating the time for complete melting for lithium nitrate trihydrate to be inputted into controller.

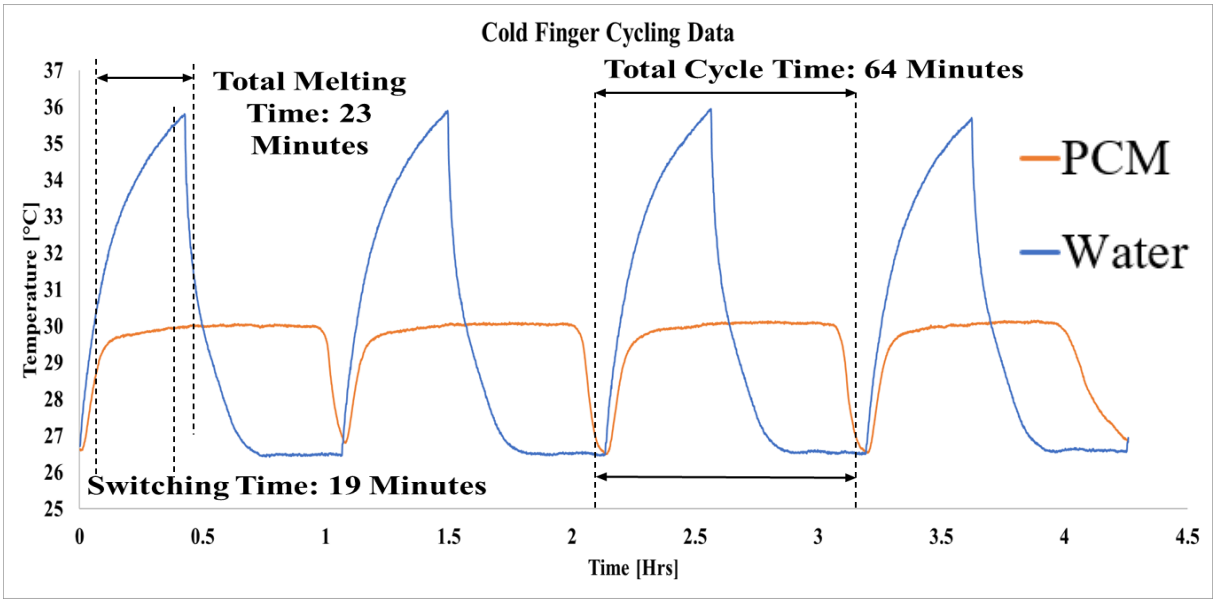

Figure 31: Example of controller validation "Cold Finger" thermo-cycling intervals.

As lithium nitrate trihydrate samples were synthesized in the laboratory. Small mass quantities were withdrawn from the synthesized samples to evaluate water molar concentration through a dehydration process. Table 16 summarizes the water of each samples of lithium nitrate trihydrate.

Table 16: Summarizes of the water concentration of each samples of lithium nitrate trihydrate for "Cold Finger experiment"

Test Tube Nomenclature (Naming)	Concentration of Water (Moles)
Reference 1 and Reference 2	3.03
TT 1 and TT 2	2.94
TT 3 and TT 4	2.94
TT 5 and TT 6	2.98
TT 7 and TT 8	2.97
TT 9and TT 10	3.11

The correlation for melt time and percentage was experimentally determined. The following paragraphs detail the process taken to experimentally determine the melt time and percentage of lithium nitrate trihydrate. A total of eight test tubes per trial were prepared using lithium nitrate trihydrate. Each glass test tube (VWR, PA) was filled with 17.5 grams of lithium nitrate trihydrate. Immediately after pouring liquid phase PCM, a rubber stopper was placed at the test tube opening to prevent moisture absorption. Once all test tubes were filled and sealed, sheathed K-type thermocouples were inserted and aligned along the center of the test tube. The sheathed thermocouples were fixated using a separate rubber stopper that contained a hole along its center which acted as a guide for the thermocouple. Once the thermocouple was inserted and fixated along the center using the rubber stopper, a generous amount of silicon was applied to all openings to prevent movement of the thermocouple and moisture absorption. This process was then repeated for the other seven samples. Next, complete solidification of all eight samples occurred in an environmental chamber. Once the samples were solidified, they were maintained at sub-cooled temperature of 26°C. The melting apparatus consisted of a water bath maintained at 38°C. Samples were melted individually for a predefined interval of time. Once the predefined melt duration of a sample was reached, the sample was taken out, data acquisition stopped, and

the amount of liquid phase PCM mass was directly measured by removing the solid state PCM attached to the thermocouple and carefully pouring liquid phase PCM into a beaker for measurement. For completion, the remaining solid state PCM mass was measured too. As shown in Figure 32, it takes 19 minutes to melt 85% of lithium nitrate trihydrate.

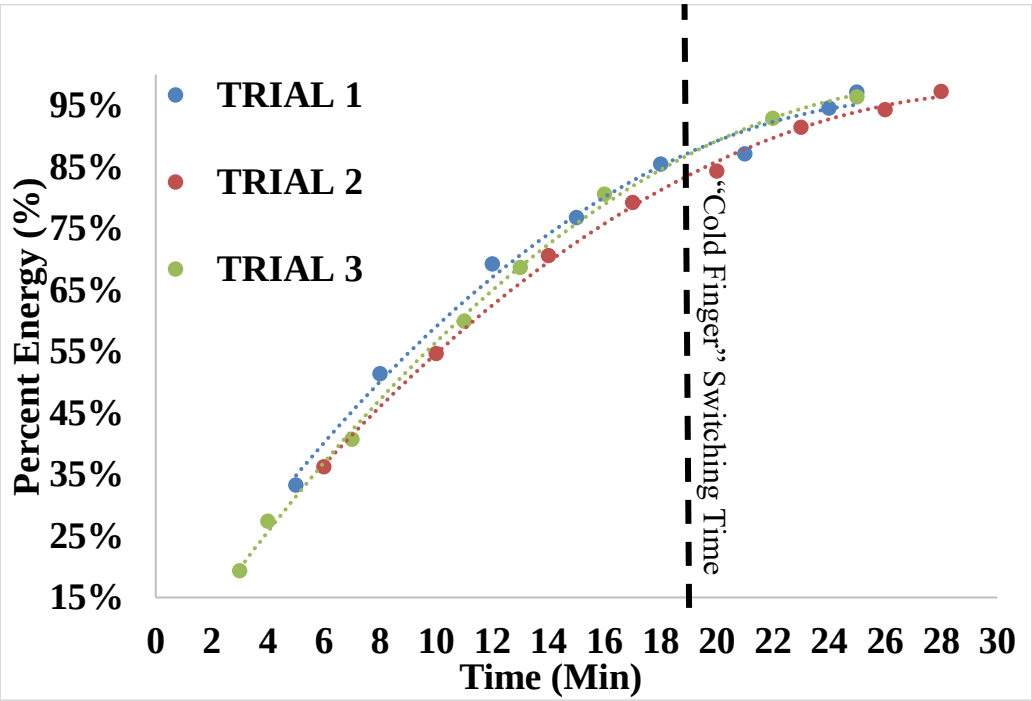

Figure 32: Computing the melt rate of lithium nitrate trihydrate in vertical glass tube to be implemented into "Cold Finger" technique. The melt rate was varied by experimentally measuring the liquid phase and solid phase after short interval of melts in a steady-state water bath.

4.5 Corrosion

The experimental methodology for corrosion can be divided into 5 steps:

- Preparation of the PCM and the nucleating additives
- Preparation of corrosion coupons
- Corrosion and degradation testing over prolonged time period
- Post-Corrosion sample descaling
- Sample examination and evaluation

Three salt hydrates formulations were analyzed. The three salt hydrates formulation are: lithium nitrate trihydrate with and without zinc hydroxyl nitrate, zinc nitrate hexahydrate with zinc hydroxyl nitrate and zinc oxide and calcium chloride with strontium chloride. The mass concentration of additives was kept at 3%. Lithium nitrate trihydrate and calcium chloride hexahydrate were synthesized in-house utilizing anhydrous lithium nitrate. Likewise, zinc hydroxyl nitrate, zinc oxide, and strontium chloride were synthesized in-house through decomposition technique. The properties of salt hydrates are summarized in Table 17.

Table 17: Properties of salt hydrates used in corrosion experiments.

Salt Hydrate	Melting Temp(°C)	Latent Heat	Ph (Liquid Phase)
Lithium Nitrate Trihydrate [$LiNO_3.3H_2O$]	29.6	254	8
With Nucleating Additives			
Lithium Nitrate Trihydrate [$LiNO_3.3H_2O$] With Zinc Hydroxyl Nitrate	29.6	254	8
Zinc Nitrate Hexahydrate [$Zn(NO_3)_2.6H_2O$] With Zinc Hydroxyl Nitrate	36	146	4
Calcium Chloride Hexahydrate [$CaCl_2.6H_2O$] With Strontium Chloride	29.2	180	6

Two different metals were selected as PCM containers; SS304 and Al 1100H. The stainless-steel coupons and aluminum coupons were purchased from Metal Samples Company in Alabama. The dimensions of the coupons are as shown in Figure 33. The composition of the metal is summarized in Table 18. All metal specimens were received as polished and cleaned with a surface finish of 120 grit.

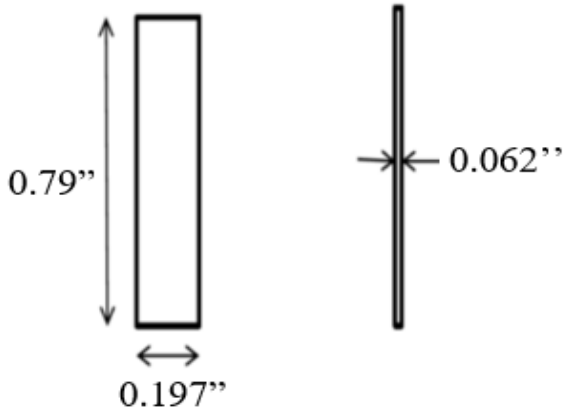

Figure 33: Corrosion test coupons.

Table 18: Chemical composition of the metals used in the experiments

Element/ Metal	Aluminum (Al 1100H)	Stainless Steel (SS347)
% Si	0.09	0.54
% Fe	0.57	70.426
% Mn	0.003	1.27
% Mg	0.003	-
% Cu	0.095	0.20
% Zn	0.002	-
% Cr	0.002	17.54
% It	0.01	-
% Pb	-	-
% Al	99.225	-
% C	-	0.04
% P	-	0.035
% S	-	0.0001
% Ni	-	9.23
% MO	-	0.18
% CB	-	0.57

Each metal coupon was cleaned with acetone in an ultrasonic bath for 10 minutes and rinsed off with isopropanol and DI water. The coupons were then air dried and placed in a desiccator overnight. The mass of the coupon was weighed and recorded the next day. Then the coupons were immersed in glass test tubes containing melted PCM as shown in Figure 34. All tubes were sealed with a plastic screw cap to avoid exposure to ambient and water. The test-tubes were submerged in a thermostatic water bath at a temperature of about 45°C. The volume of PCM in each test-tube was kept constant at 15 ml (±3%). The methodology implemented analyzed the metal-PCM after 6 weeks (42 days), 12 weeks (84 days), and 18 weeks (126 days). A total of 36 samples of each stainless steel and aluminum coupons were prepared. The corrosion testing was performed in triplicate for each test duration and sample.

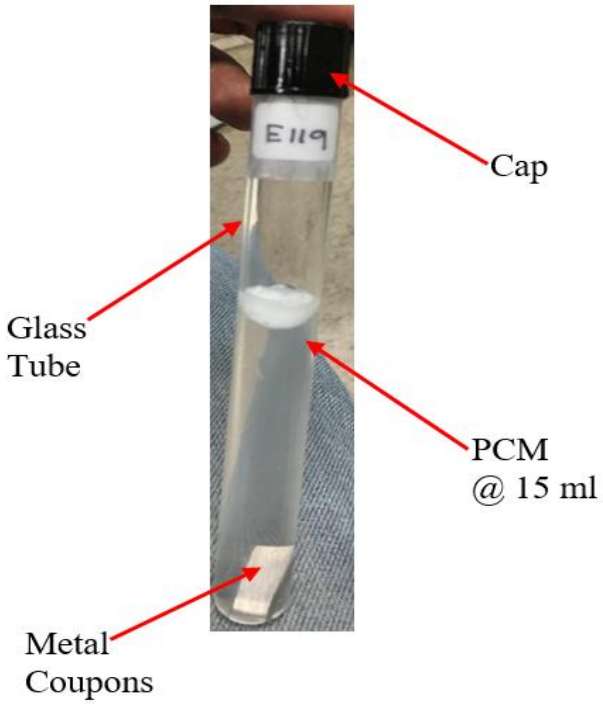

Figure 34: Example of Corrosion sample apparatus. The metal coupon was submerged into a glass test-tube with PCM and capped off. The volume of PCM in glass tubes was kept at 15 ml.

The ASTM G1-03 standard [100] was followed for the post-descaling process to treat the specimens (i.e., cleaning them with appropriate acid/alkaline solutions). After that, the coupons were dried with soft paper and weighed. The cleaning protocol for aluminum and stainless steel are summarized in Table 19. The guide for corrosion mass loss used in industry is summarized in Table 20.

Table 19: Corrosion removal protocol for stainless steel and aluminum alloy.

Metal Coupon	Solution	Time	Temperature
Stainless Steel	200g sodium hydroxide (NaOH) 30g Potassium Permanganate ($KMnO_4$) Reagent Water to make 1000 mL	5 Min	Boiling
	followed by		
	100g diammonium Citrate ($(NH_4)_2HC_6H_5O_7$) Reagent Water make 1000 mL	5 Min	80°C
Aluminum Alloy	50 mL phosphoric acid (H_3PO_4) 20 g chromium trioxide (CrO_3) Reagent Water to make 1000 mL	5 to 10 Min	90°C to Boiling

Table 20: Guide for corrosion weight loss used in industry. Adapted from [101].

mg/cm^2yr	Recommendation
>1000	Completely destroyed within days
100-999	Not Recommended for service greater than a month
50-99	Not Recommended for service greater than 1 yr.
0.3-9.9	Recommended for long term service
<0.2	No Corrosion, other than as a result of surface cleaning was evident

The corrosion evaluation procedure can be divided into 5 parts:

- The pH of the solutions was tested
- Change in solution appearance
- Change in metal coupons appearance
- Microscopic image of metal coupons
- Mass loss calculation in metal coupons

The gravimetric analysis prior to and following the corrosion tests provided the mass loss, Δm (mg), with respect to the initial mass:

$$\Delta \boldsymbol{m} = \boldsymbol{m_i} - \boldsymbol{m_f} \tag{4.18}$$

Measurement prior to and following the corrosion showed reduction in sample width and length (mm), therefore mass loss per unit area:

$$\frac{\Delta \boldsymbol{m}}{\boldsymbol{Area}} = \frac{\boldsymbol{m_i} - \boldsymbol{m_f}}{\boldsymbol{Width} \times \boldsymbol{Length}} \tag{4.19}$$

Corrosion rate CR (mg/cm^2 yr.) considers the mass loss (Δm), the area of the metal coupon, and the experimental time (t_o – t), as shown in the following:

$$\boldsymbol{CR} = \frac{\Delta \boldsymbol{m}}{\boldsymbol{A} \times (\boldsymbol{t_f} - \boldsymbol{t_i})} \tag{4.20}$$

4.6 Shell and Tube Heat Exchanger

The experimental set-up as shown in Figure 35, consists of several components that together make a controllable constant temperature thermal source that delivers heat to the centre of the cylindrical test sample. The water baths (Cole Parmar, Ploy stat 12122-02 1C6) in the system were used as cooling and heating source. 0.5” outer diameter tubing was used as a heat transfer medium between the HTF and PCM during charging and discharging. The 3-inch long tubing passed through the centre of the sample. Insulation around the tubing’s were utilized to minimize heat loss.

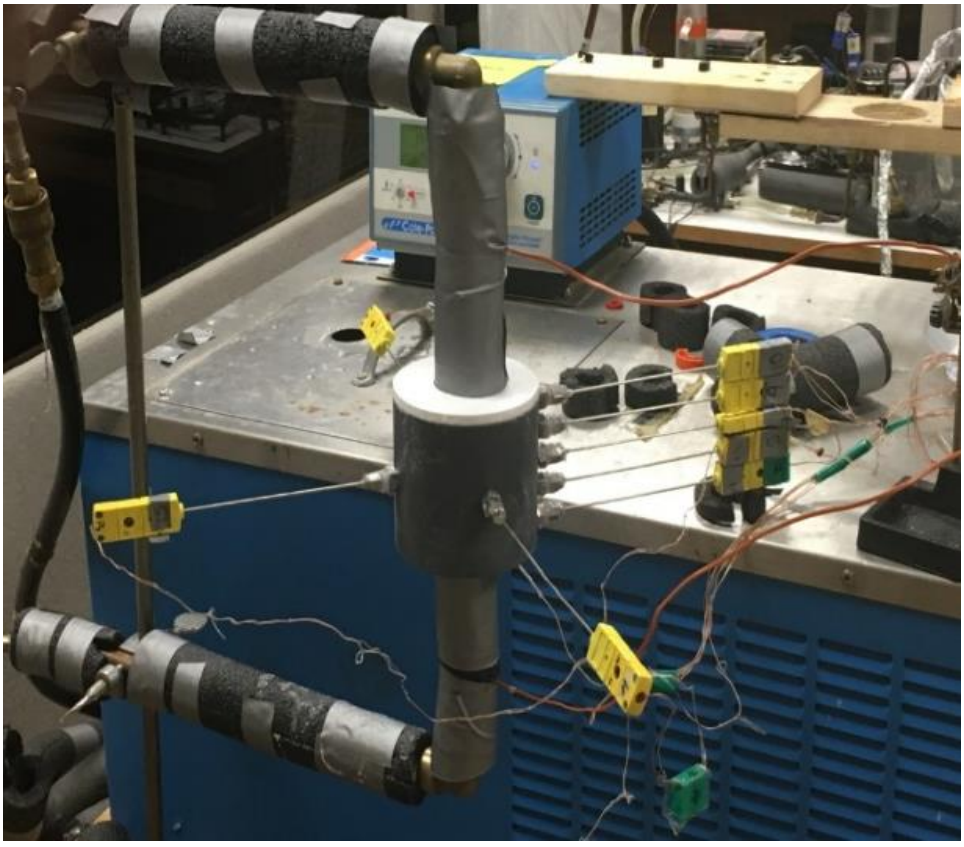

Figure 35: The Shell and Tube experimental set-up. The shell was vertically mounted and connected to water bath. The direction of water flow is against the gravity- top to bottom. The thermocouples were varied vertically and radially.

The test chamber (shell) was designed to encapsulate the PCM and insulate the boundary of the sample to minimize heat loss. The test chamber was manufactured using additive printing techniques. Different variations of thickness and fill volumes were tried out as shown in Figure 36 before deciding the final design. The shell section was 3D printed using Lulzbot Taz 5 with a build volume of 11.4 X 10.8 X 9.8 inch.

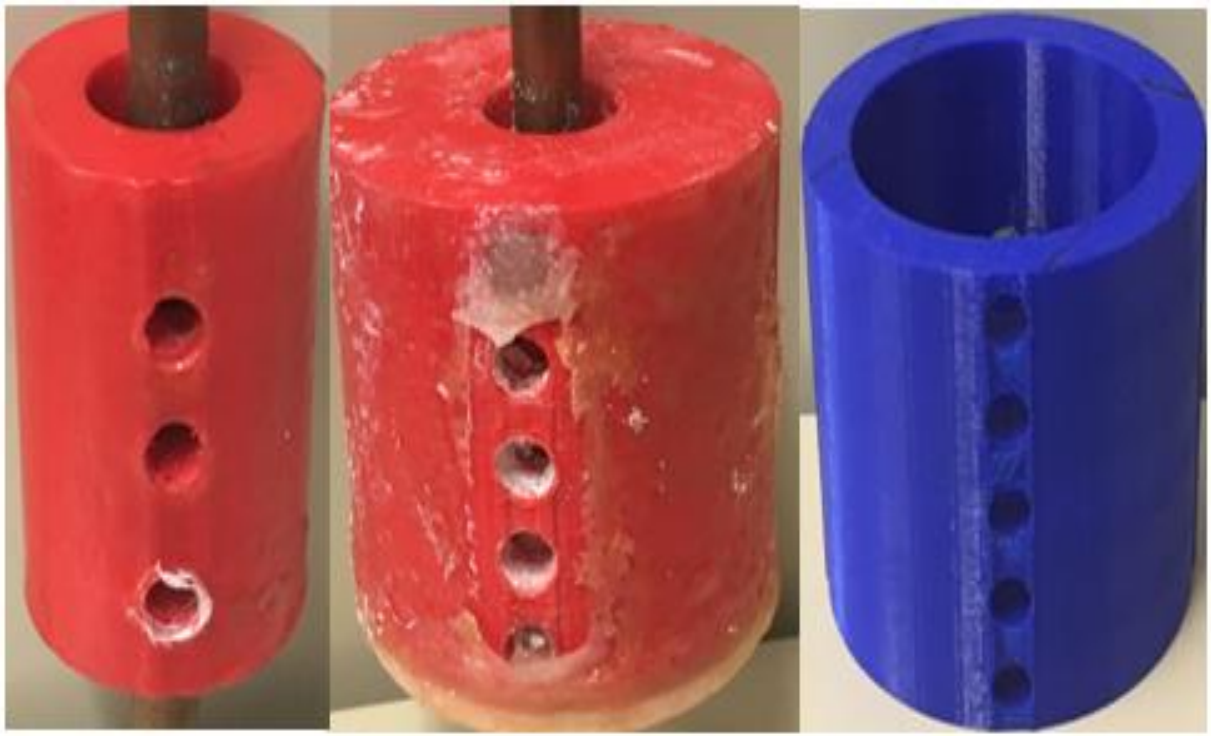

Figure 36: Different iterations of 3D Printed Shell for initial validation for structural and leakage stability.

Figure 37 shows the schematic and dimensions of the finalized design of the test chamber. The test chamber was 3D printed from 3mm filament ABS as it offers relatively low thermal conductivity (~0.1 W/m K). The chamber outer surfaces were coated with clear coat resin to provide a smooth and airtight finish.

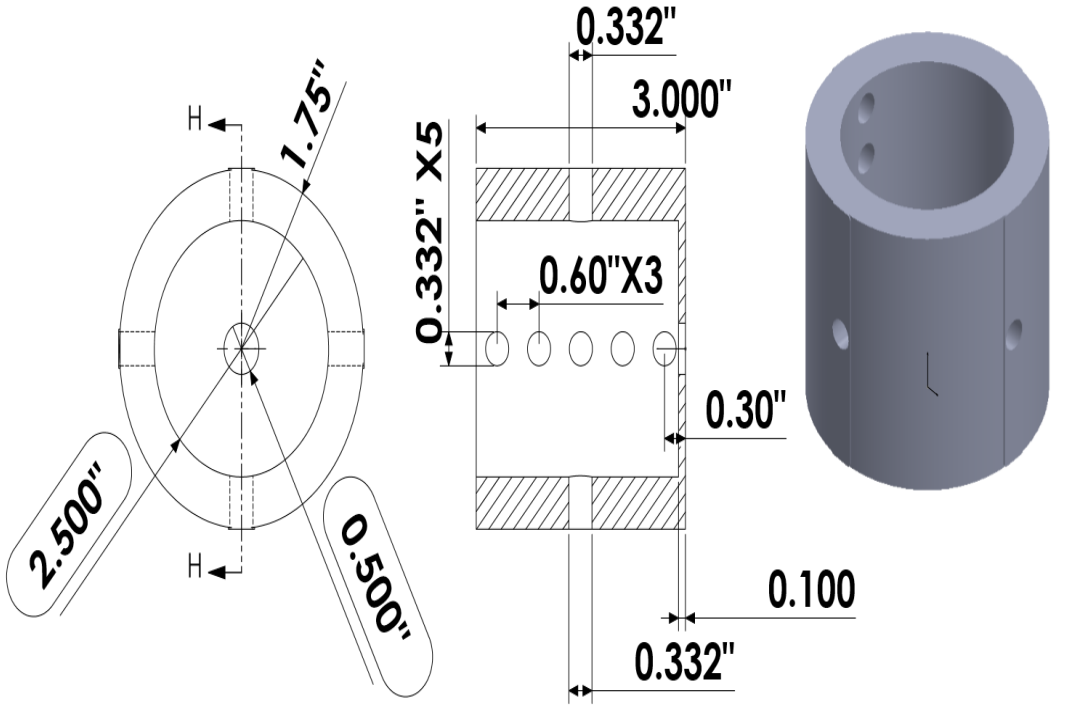

Figure 37: The Final shell and -tube HX design and the dimensional.

Thermocouple compression fittings (Sensor Connection, MI) were used to provide pass-through and precisely position of thermocouples. Sheathed "K"-type thermocouple (Omega, KMQXL-062G-6) were utilized with a measurement uncertainty of ± 0.24°C. The thermocouples were placed at same radial location with incremental depths in the samples to acquire the temperature profile as a function of depth, and after each successful run, the radial locations were changed in step of 0.15-inch. Thermocouples were also placed at equal depths (axial centre) at the four quadrants around the sample to verify symmetric heat flow, as seen in Figure 38. The axial locations of thermocouples and their symbolizations are shown in Figure 39.

Figure 38: Test chamber filled with PCM and location of thermocouples.

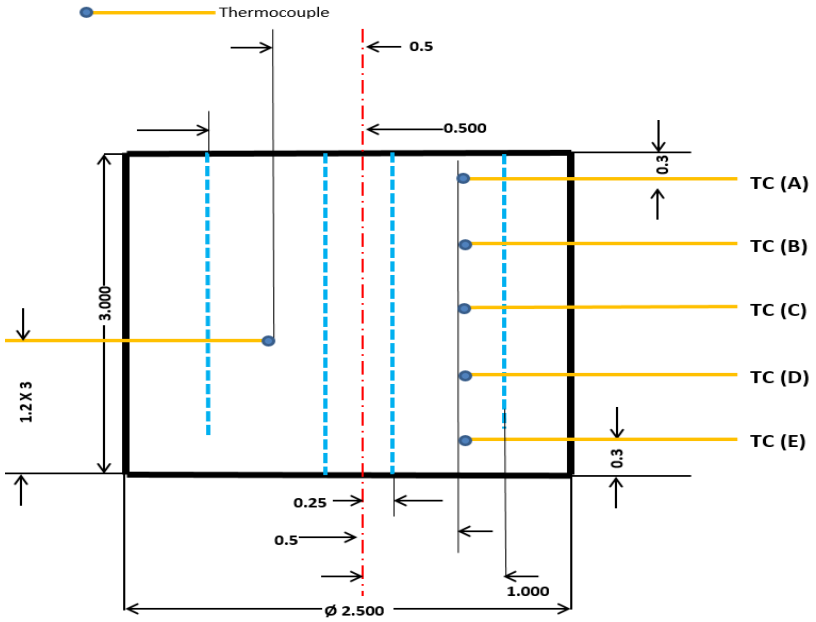

Figure 39: Schematic illustrating the thermocouple locations along the vertical and radial direction.

The inlet and outlet water temperatures were recorded using a wire “K” type thermocouple (Omega, Tt-K-36-SLE) with a measurement uncertainty of ±0.12°C. NI 9213 and Ni Instruments LabVIEW were utilized for data collection. The two water baths were maintained at 10°C and 40°C. The samples were equilibrated at 10°C initially. Once equilibrated at 10°C, the valves were adjusted to direct the hot flow at 40°C through the copper tubing, and the system is allowed to reach equilibrium. Once equilibrated at 40°C, the valves were switched back to redirect the cold-flow at 10°C. This is repeated for varying radial location and mass flowrate.

4.7 Chevron Plate Heat Exchanger

In the case of plate heat exchanger, no established methods for comparison purposes are available, therefore very different results can be interpreted and presented by authors for plate heat exchanger. The experimental evaluation of plate heat exchanger can be divided into system analysis and energy storage analysis. The system analysis considers the mass of metal (i.e. initial mass of Plate heat exchanger) and mass of PCM and the volume. In this way, it allows one to compare the sizes and masses of different systems. The energy storage analysis provides the deviation between the theoretical and actual energy stored, which are mainly due to heat transfer limitation, heat losses, and heat capacity of the metal itself. An example of temperature plot for plate heat exchanger is shown in Figure 40.

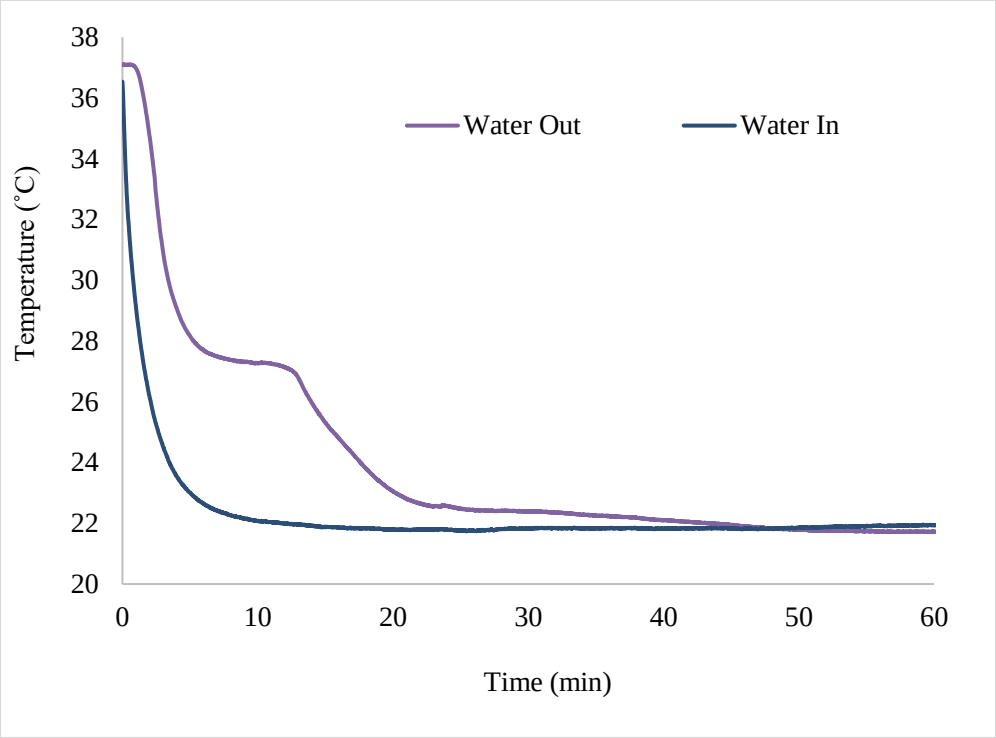

Figure 40: Example of temperature plot of heat transfer during solidification to illustrate the nomenclatures for data reduction.

The total energy storage was calculated by numerical integration of working fluid heat curve, as shown:

$$E_T = \dot{m}_{water} C_{p,water} \int_{t=0}^{t=final} T_{initial} - T_{final}\ dt \tag{4.21}$$

The total specific energy density of the storage is defined as the ratio between the energy stored and the mass of the overall system, as shown:

$$E_{TESS} = \frac{E_T}{m_{PCM} + m_{PCM}} \tag{4.22}$$

Specific energy density of the PCM is the ratio between energy stored (i.e. Total Energy – Sensible heat of Heat Exchanger) and the mass of PCM, as shown:

$$E_{PCM} = \frac{E_T - \left[m_{PHX} * C_{p,PHX} * \left(T_{final} - T_{initial}\right)\right]}{m_{PCM}} \tag{4.23}$$

Specific volumetric energy storage density is the ratio between the energy stored and the volume of the PCM, as shown:

$$E_V = \frac{E}{V_{STORAGE}} \tag{4.24}$$

Characteristic charge and discharge time are defined as the ratio between times needed to complete melting and solidification and the energy storage capacity of the system, as shown:

$$\tau_{charge/discharge} = \frac{t_{charge/discharge}}{E_T} \tag{4.25}$$

The power of the system can be classified as average power, as shown:

$$P_{average} = \frac{E}{t_{charge/discharge}} \tag{4.26}$$

The overall heat transfer coefficient is calculated as shown:

$$UA = \frac{P_{charge/discharge}}{T_{pcm} - \frac{(T_{in} + T_{out})}{2}} \tag{4.27}$$

The comparison between plate heat exchangers can be analyzed based on equations 4.21 - 4.27. The charge effectiveness during charging is calculated as the theoretical energy over the measured energy stored.

$$\varepsilon_{charging} = \frac{E_{th,charging}}{E_T} \tag{4.28}$$

The discharge effectiveness is calculated as the energy recovered over the theoretical energy.

$$\varepsilon_{discharge} = \frac{E_T}{E_{th,discharging}} \tag{4.28}$$

The test equipment used in the experiments consists of several components that together make a controllable constant temperature thermal source that delivers cold and heat to the heat exchanger for discharging and charging the PCM Respectively. Two different temperature-controlled water bath (Cole-Parmer 12111-11) delivers water at a constant temperature through the loop of plate heat exchanger. The flowrate of the working fluid was controlled by a needle valve and monitored through a vertical flowmeter (Omega FL-72 Series) with a precision uncertainty of ±0.5GPH. As shown in Figure 41.

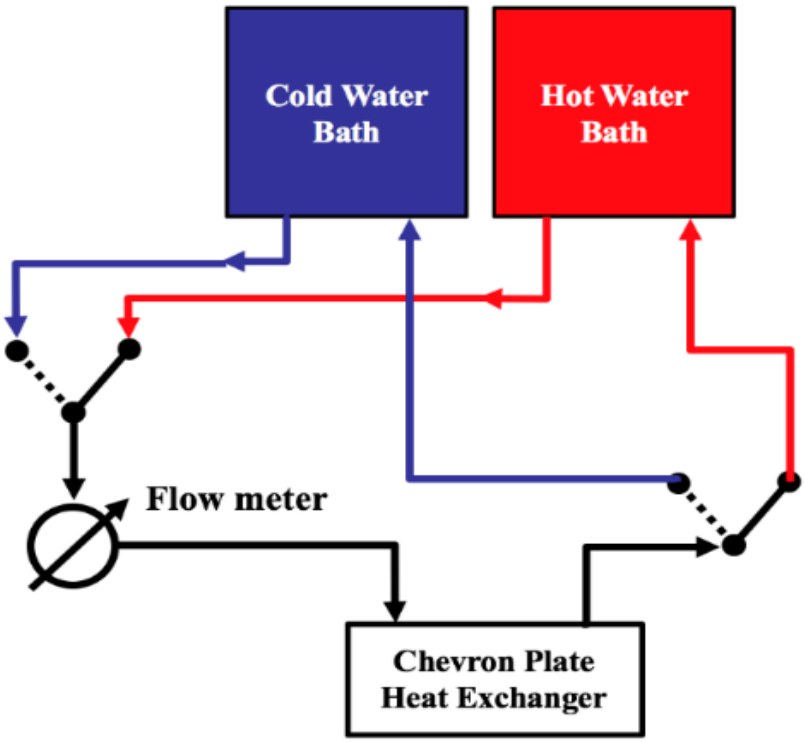

Figure 41: Schematic layout of chevron plate heat exchanger experimental set-up.

Wired "K"-type thermocouple (Omega, TT-K-24-SLE) were utilized with a measurement uncertainty of ± 0.35°C. The thermocouples were placed at the inlet and outlet side of the working fluid to measure the change in temperature in working fluid during charging and discharging. The thermocouples were also placed at the inlet and outlet of the top and bottom plates to study the melt and freeze propagation. Insulation were utilized to minimize heat loss during charging and discharging of the LHTESS system. NI 9213 and Ni Instruments LabVIEW were utilized for data collection. The final set-up and side view are as shown in Figure 42.

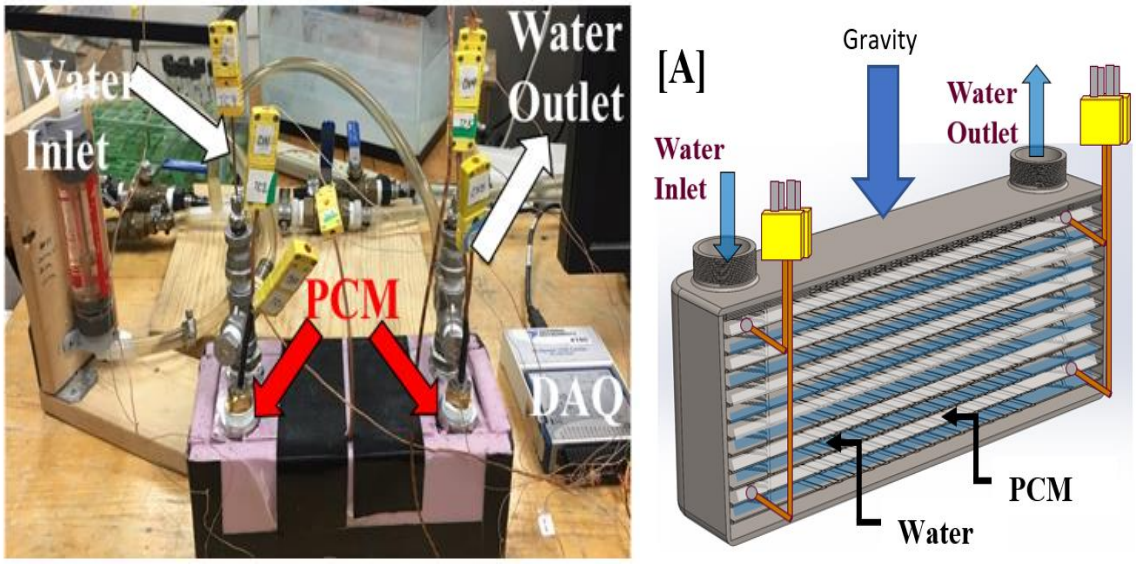

Figure 42: Image and cross-section view of chevron plate heat exchanger set-up. (Left) Complete set-up image. (Right) Cross-section view of heat exchanger highlighting the location of PCMs, thermocouples and flow direction.

The average heat capacity of the heat exchanger and the fittings were measured experimentally. The heat exchanger and its fittings were heated up in the environmental chamber to 60°C and 70°C and equilibrated at this temperature for 2 hours. A total of 5 thermocouples were attached to the heat exchanger. An insulated tank was filled with 6kg of water and equilibrated at room temperature. Then the heat exchanger was dunked into the water tank and the change in the temperature of the water and the heat exchanger was recorded using NI 9213 system. The experiment was repeated for total of three times. The average heat capacity of the heat exchanger was computed as follows:

$$Cp_{HX} = \frac{m_w Cp_w (T_{initial,water} - T_{final,,water})}{m_{HX}(T_{initial,HX} - T_{final,,HX})} \quad (4.30)$$

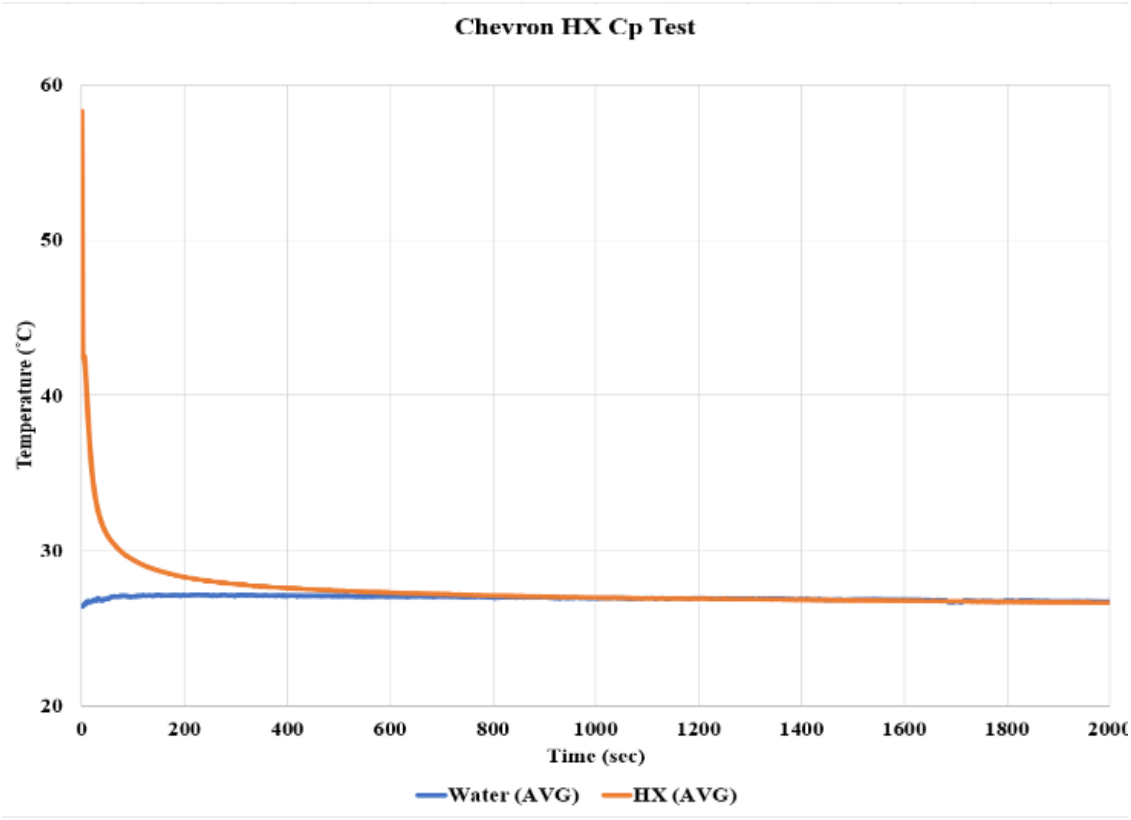

Figure 43: Experimental temperature measurement for computing average heat capacity of heat exchanger.

The two water baths were maintained at 20°C and 38°C. The initial conditions for the experiments have the sample equilibrate at 20°C using the cold-water bath. Once equilibrated at 20°C, the valves are adjusted to direct the hot flow at 38°C to start the charging process and the system is allowed to reach equilibrium. Then, the valves are switched to redirect the cold flow at 20°C to start the discharging process. This procedure was repeated for different mass flowrates and water bath temperatures as summarized in Table 21.

Table 21: Experimental test matrix for chevron plate heat exchanger charged with PureTemp 29 and lithium nitrate trihydrate.

Flow Rate [GPH, kg/s]	Temperature Range [°C]
5.00 (0.0053)	T_{hot} = 38 T_{cold} = 20
7.50 (0.0079)	T_{hot} = 34 T_{cold} = 24
10.00, (0.011)	T_{hot} = 32 T_{cold} = 26

Table 22 summarizes the LHTESS system size. In the current LHTESS system, the mass of PCM was only 10% of the total mass of the system and energy storage capacity of 30 Joules. The average heat capacity of the heat exchanger and the fittings was measured experimentally to be 0.323 kJ/kg. K.

Table 22: Chevron plate heat exchanger - LHTESS System Size and Scale

Totals	Value	Unit
Total Empty Weight	1.222	kg
Total Weight (Including PCM)	0.14469	kg
Heat Transfer Area Per Plate	0.01155	m^2
Average Heat Capacity HX	0.323	kJ/kg. K
Metal to PCM Ratio	8.5: 1	

4.8 Compact Heat Exchanger

The compact heat exchanger (CHX) LHTESS comprises of offset fins configuration on HTF regions and aluminum porous fin on the PCM regions. The compact heat exchange has five flow channels for HTF fluid flow and four hermetically sealed channels with encapsulated PCM. Lithium nitrate trihydrate is the PCM encapsulated in the LHTESS as illustrated in Figure 44.

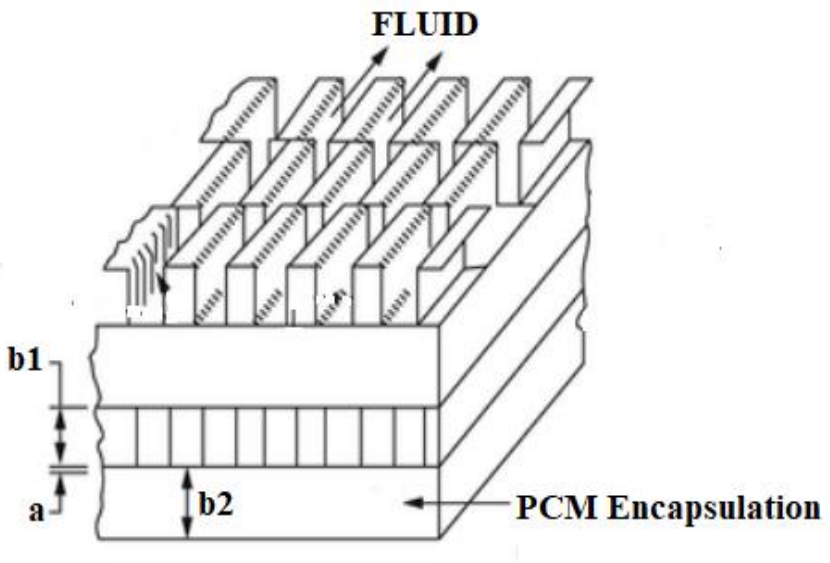

Figure 44: Compact heat exchanger-Latent Heat Energy Storage System (LHTESS). CHX comprises of nine regions. Five regions for fluid flow and four regions for encapsulating phase change material. The fluid flow region consists of offset fins and the PCM regions consists for aluminum porous medium. The vertical spacing in fluid flow region (b_1) is 0.081" and the spacing in the PCM region (b_2) is 0.25". The overall measurement of LHTESS is 1.83"x 2.65" x19.03". "Reprinted from [102] "

The HTF region of the CHX had an offset fin configuration fin configuration of 22 fins per inch; the offset fin configuration was selected due to their high surface area as illustrated in Figure 45. The offset fins and the CHX was manufactured using Al-3003 material. The PCM channels are brazed with aluminum porous fin as shown in Figure 46. The porous fin was impregnated with PCM -lithium nitrate trihydrate. The aluminum porous fin was formed by folding aluminum

porous screens. The idea aluminum porous fin is to enhance the effective thermal conductivity of PCM.

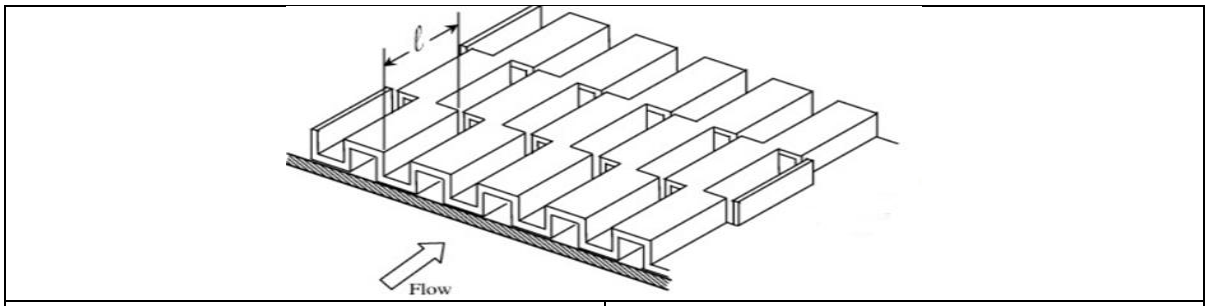

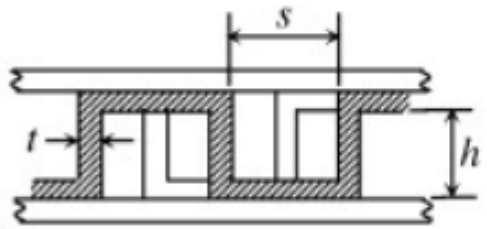

Parameter	Inches
h	.075
t	.006
s	0.0395
l	0.125
α (t/h)	.008
γ (t/s)	.048
δ (t/l)	.048

Figure 45: Offset fin configuration in compact heat exchanger-LHTESS. Top image illustrates the flow direction and layout of offset fin configuration in compact heat exchanger. Bottom left figure illustrates the nomenclature dimensions layout of offset fins and bottom right figure illustrates the design dimensions of offset fin. Reference for image. "Reprinted from [102]"

Material	Screen (in)	Porosity (%)	Thermal Conductivity (W/mK)
5056	200	34	117

Width (in)	Length (in)	Fin height (in)	FPI	Solid Factor (%)	Thermal Conductivity (W/mK)
1	1	0.25	100	27	32.1

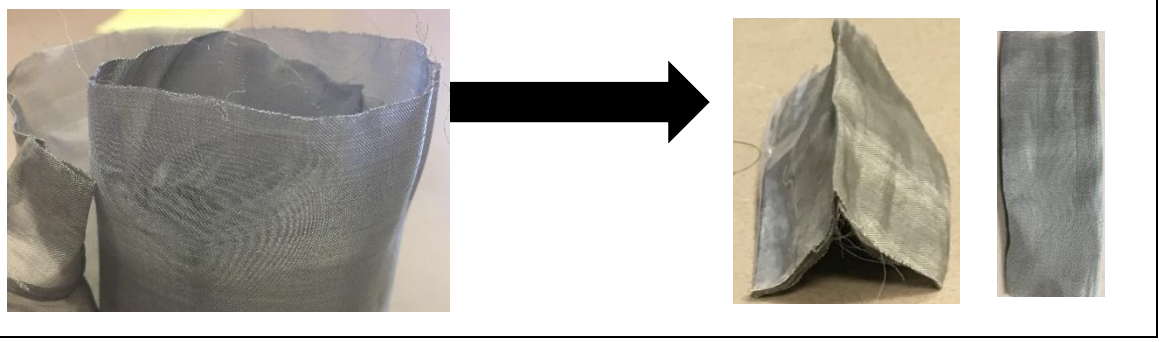

Figure 46: The porous aluminum sheet and fin for effective thermal conductivity enhancement of PCM. The top left table shows the properties of aluminum sheet as purchased and the top right table provides the dimensions of porous aluminum fin brazed into the CHX. The bottom image illustrates the porous screen and porous fin.

The CHX design allowed the center PCM channels to have increased in effective heat transfer area compared to top and bottom PCM channels as illustrated in Figure 47. Therefore, this resulted in faster charging and discharging in the center PCM channels in comparison to both the top and bottom PCM channels.

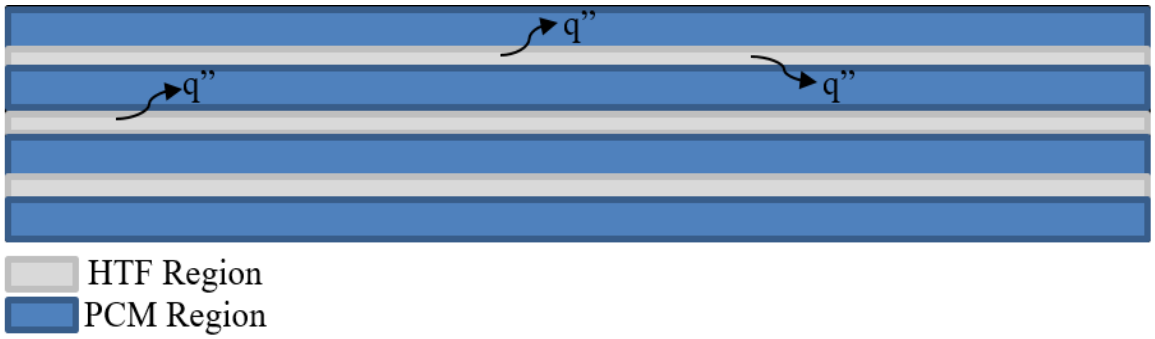

Figure 47: Heat transfer contribution from HTF region into PCM region during melting. The top and bottom PCM channels only had heat transfer in one direction, whereas the center PCM channels had heat transfer in two directions.

The CHX manufacturing and charging of PCM channels were outsourced to Allcomp Inc, in California. *Allcomp Inc* charged the PCM channels with lithium nitrate trihydrate using a propriety vacuum charging technique. *Allcomp* was able to charge 474 grams of lithium nitrate trihydrate into CHX system. With the latent heat of lithium nitrate trihydrate measured to be 275 J/g, the theoretical energy storage capacity of the LHTESS was rated to be 130 kJ. Lithium nitrate trihydrate was assumed to be distributed evenly throughout each channel at 68.7 J/channel. A spirit level was placed on the top of the heat exchanger to ensure level for even mass flowrate in each channel as well as uniform melting and solidification of the lithium nitrate trihydrate.

An experiment set-up of CHX is as shown in Figure 48. Due to the hygroscopic nature of lithium nitrate trihydrate, the compact heat exchanger apparatus was placed in a sealed plexiglass enclosure containing desiccants - calcium chloride and cobalt chloride to maintain a low humidity environment. The humidity in the enclosure was maintained at ~15% compared to an ambient humidity of 40~45%.

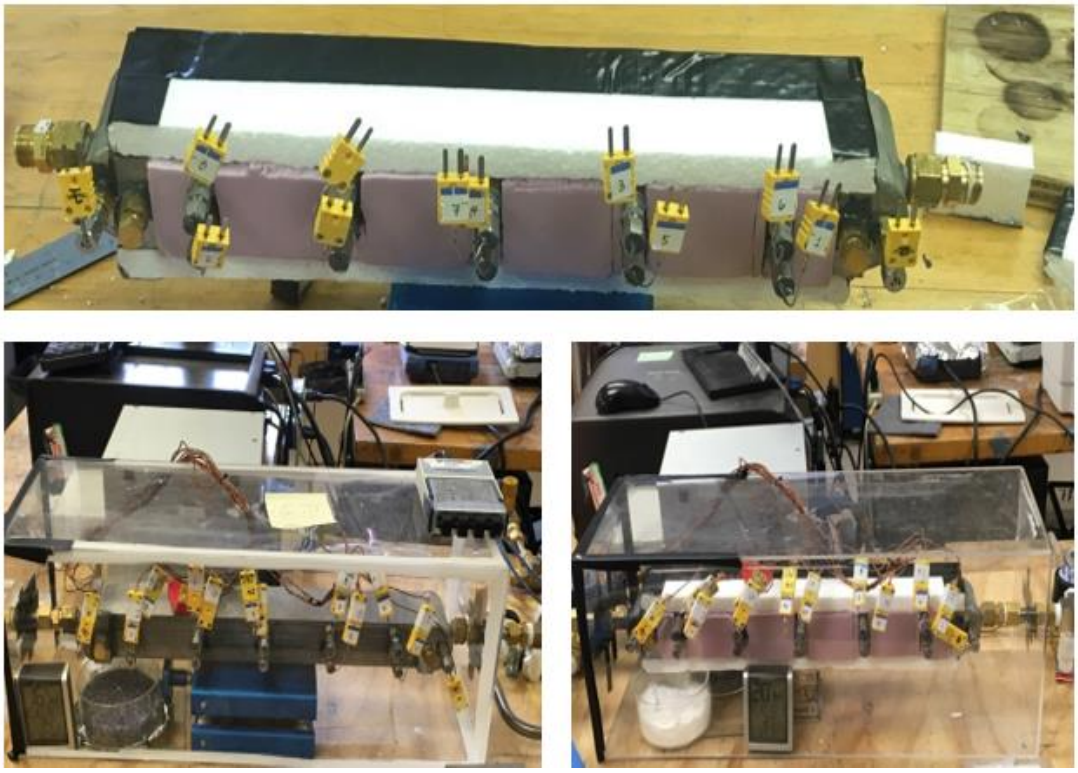

Figure 48: The CHX set-up with and without insulation. The top figure shows the insulation of CHX and bottom images shows the CHX enclosed in a desiccator with desiccants to reduce the effects of humidity on the experiment.

The melt front and freeze front of the PCM in the top and center channels were monitored by embedding thermocouples at predefined locations. The predefined locations correspond to 10%, 30%, 50%, 70%, and 90% melt fractions along the axial directions as illustrated in Figure 49. The temperature of the HTF (i.e. DI water) was measured at the inlet and outlet of the heat exchanger. Two different configurations – Configuration A and B were experimentally validated to study the efficacy of *"Cold Finger"* technique. *"Cold Finger"* techniques involve thermo-cycling protocols with complete solidification and incomplete melting of the PCM samples under consideration. The incomplete melting protocols enable a residue of PCM crystals to remain in the PCM sample - which in-turn act as nucleators (i.e., nucleation promoters). Prior studies have shown that this un-

melted phase of the PCM (i.e., the residue crystals) provide better efficacy for promoting nucleation (i.e., at subcooling less than 1 °C) than that of heterogeneous additives for promoting nucleation. To realize the full effectiveness of the *"Cold Finger"* techniques, the experiments were designed for the flow of HTF in to the CHX to be bi-directional. During melting the HTF flowed from left to right and during solidification the flow direction was reversed (i.e., right to left) as shown in Figure 49 – Configuration B. This enhances the efficacy of the residue crystals to initiate the nucleation and for the propagation of the solidification front in the melted phase of the PCM. The experiments were designed for the melting to proceed until 90% of the total latent heat energy storage capacity, thus allowing about 10% of the remaining PCM to be un-melted and remain in solid phase as dispersed crystals (i.e. as unused energy storage capacity). Thus, storage capacity is sacrificed marginally to enable better reliability of operation for the LHTESS. The variation in flow direction were manipulated with three-way valves and the valve configuration for melting and solidification are summarized in Appendix F.

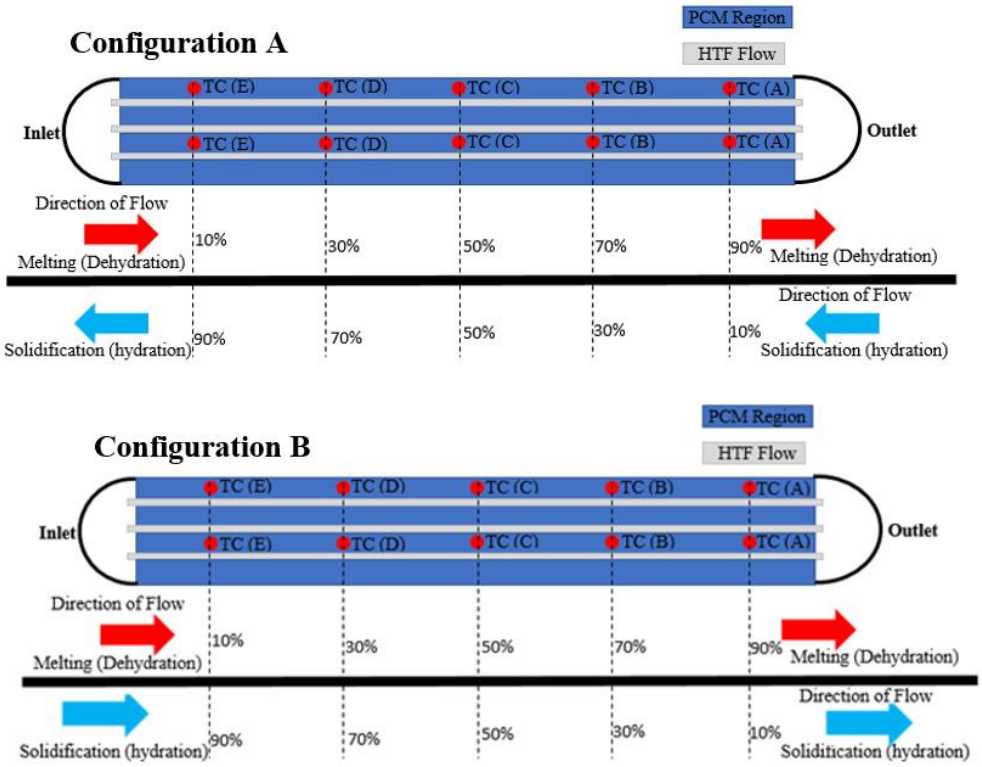

Figure 49: The schematic of predefined location of thermocouples to monitor the melt and freeze front during charging and discharging process. Two different HTF flow configuration during solidification. In configuration A, the flow of HTF during melting is from left to right, whereas during solidification the flow of HTF was reversed to flow from right to left (i.e. opposite direction during charging and discharging). In configuration B, the flow of HTF during melting and solidification is from left to right (i.e. same direction during charging and discharging).

Figure 50 illustrates the temperature profile of phase change material in top, and center channels and heat transfer fluid during melting. The "Cold Finger" protocols requires incomplete melting – melting up 90% only. Therefore, as shown in Figure 50A, the top PCM channel was referenced for the completion of 90% melt. The valves were switched to freezing when the temperature at 90% location of top channel read 30.5°. This allowed for maximization of the storage capacity and still implement "cold finger" technique.

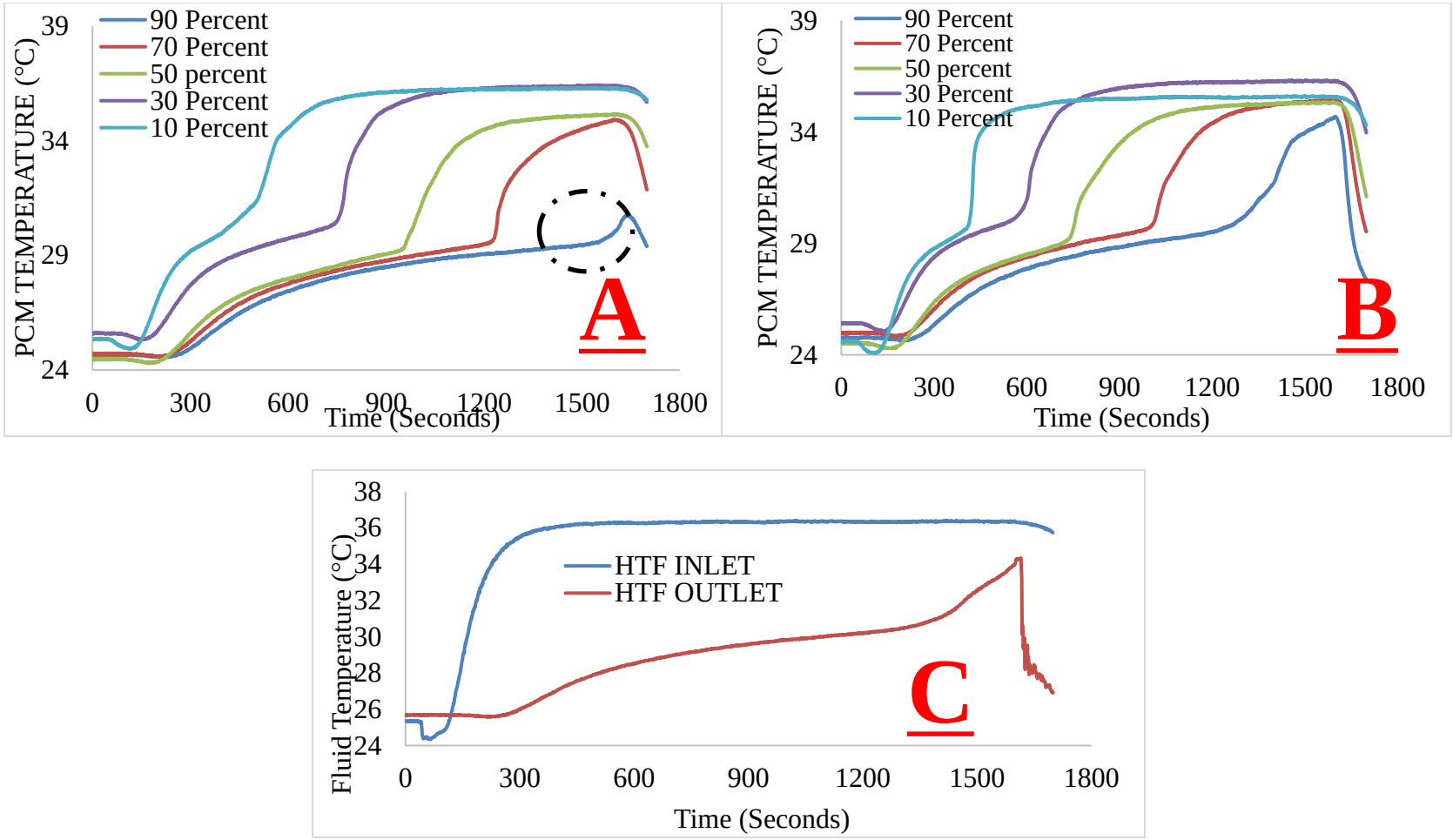

Figure 50: The "Cold Finger" melting plots. The volumetric flowrate during melting was 0.219 L/min (± 4.4%), and the temperature of Hot water bath was set at 37.4 °C (± 3.2%). A: The temperature profile of the top PCM channel, the dotted highlight is the completion of 90% melting and switching point to solidification. Top PCM channel was referenced for the 90% melt end. B: The temperature profile of the bottom PCM channel, where the 90% point completely melted and already in sensible heat region. C: The heat transfer fluid temperature profile during melting.

4.8.1 Experiment Equipment and Measurement Techniques

A charging and discharging temperature conditions were achieved using two different water baths. One water bath was kept at above phase transition temperature (i.e. T > 30°C) and the other water bath was kept below phase transition temperature. The water baths were brought from Cole-Parmer (Model: Polystat cooling/heating circulating baths, 2C15). The thermocouples utilized in the temperature measurements were K-Type (1/16" diameter) with hydro-thermic sheathed tip (Sheathing Material: SS 316, and Manufacturer: Temprel, Ohio). The tip of the thermocouple is located centrally along the width of the heat exchanger (1.5" from the edge). The thermocouples were calibrated in a water bath from 10 °C to 40 °C at an interval of 0.5 °C using an NIST Standard thermometer (Least Count: ± 0.25 °C and calibration uncertainty of 0.8%). After calibration, the uncertainty of the thermocouples was determined to be ±0.25 °C ~ ±0.35 °C. A high-speed data acquisition (DAQ) system was used for temperature recording. The DAQ consists of NI SCXI 1000 Chassis, and NI SCXI-1303 board. The temperature measurements were performed at 1 HZ frequency (i.e. 1 reading/second). The least count accuracy of DAQ system was 0.003 °C; therefore, the uncertainty from the DAQ can be considered negligible. Simultaneously, the voltage measurement from the flow meter was acquired using a NI USB 9162 DAQ at 1 HZ frequency. The HTF volumetric flow rate in the system was measured by an Omega FLR 1000 series flow meter (S/N 10981) which was calibrated for 0.2 L/min to 2 L/min by OMEGA. A sample calibration curves for thermocouple and flow meters are shown in Appendix F.

4.8.2 Experimental Procedure

The experimental procedure for CHX-LHTESS can divided into three parts:

1) Experimental validation of efficacy of "*Cold Finger*" technique in reducing sub-cooling during solidification cycles
2) Experimental validation of CHX-LHTESS thermal performance
3) Thermal cycling of lithium nitrate trihydrate in CHX-LHTESS for reliability validation

Efficacy of "*Cold Finger*" technique was experimentally validated in CHX-LHTESS. The *Cold Finger* protocol consisted of 90% melting of PCM — leaving 10% of PCM as solid crystals (and complete solidification of PCM). Furthermore, the flow direction of the was varied as shown in Figure 49 to experimentally study the sensitivity of flow direction on sub-cooling. The thermal performance of CHX-LHTESS were experimentally analyzed by varying (a) the flow rate of HTF during charging and discharging, (b) the inlet temperature of HTF during charging and discharging. The volumetric flowrate was varied between 3 and 5 GPH and HTF inlet temperature during melting was varied between 33 °C, 35 °C, and 37.4 °C. Similarly, during solidification, the HTF inlet temperature was varied between 20 °C and 25 °C. The design condition for the heat exchanger was 3 GPH with inlet temperature of 37.4 °C during melting and 25 °C during charging. The experiments were repeated two times with and without insulations for repeatability. The insulated and uninsulated cases allowed for comparison of parasitic heat loss to the environment during the melting and solidification process.

The experimental steps are listed as follows:

(1) Initially solidify PCM with HTF at cold inlet temperature;

(2) Close the cold HTF control valve and turn valves to direct the hot HTF;

(3) Open the hot HTF control valve and melt to the 90% mass fraction of un-melted PCM;

(4) Close hot HTF flow control valve and turn valves to direct the cold HTF;

(5) Completely solidify the PCM;

(6) Repeat steps (2) through (5) above for ensuring repeatability and for varying HTF mass flowrate and inlet temperature.

Thermal stability of lithium nitrate trihydrate and reliability of "*Cold Finger*" was determined by performing accelerated 1000 melt-freeze cycle in CHX-LHTESS set-up. The melt-freeze cycle was performed at 3 GPH with inlet temperature of 37.4 °C during melting and 25 °C during charging with a 90% PCM melt. The process was automated using solenoid valves and temperature controller as shown in. Each cycle took 80 minutes for completion. 1000 melt-freeze cycles took 56 days of continuous testing.

.

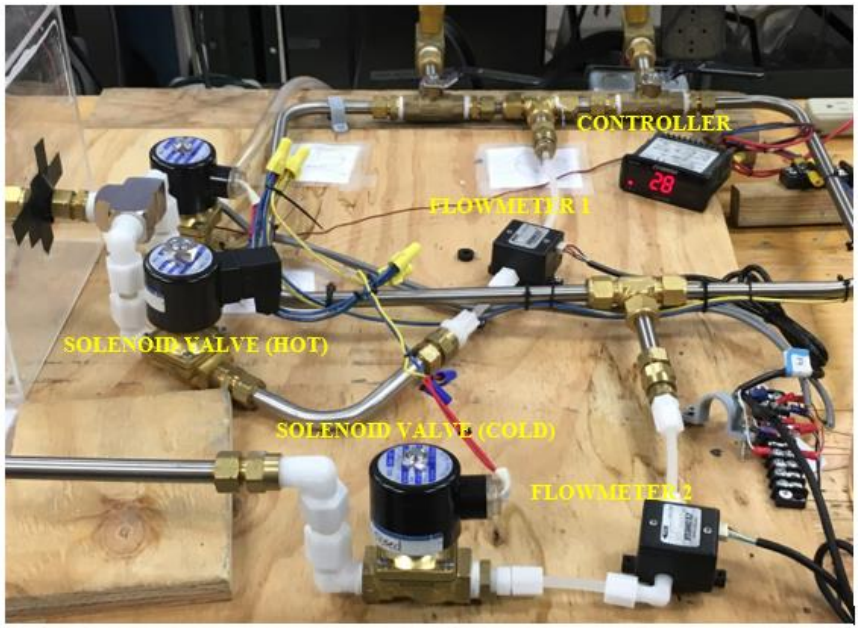

Figure 51: Automation of thermal cycling process in CHX-LHTESS system with the aid of solenoid valves and temperature controller. The temperature controller was programmed to close the HOT solenoid valve at when 90% melt front location reaches 31C and open COLD solenoid valves for the start of solidification process. Similarly, the COLD solenoid valves were programmed close when PCM temperature reaches 25C and open HOT solenoid valve. This procedure was repeated over 1000 thermal cycles.

4.8.3 Data Reduction and Measurement Uncertainty

This section summarizes the equations used for data analyses of thermal performance of CHX-LHTESS system. The measurement uncertainties were computed based on the Kline and McClintock Method. The temperature difference of the HTF between inlet and outlet was computed as follows:

$$\Delta \boldsymbol{T_{HTF}} = \boldsymbol{T_{outlet}} - \boldsymbol{T_{inlet}} \tag{4.31}$$

where, T_{outlet} is the HTF temperature measured at the outlet port of the heat exchanger and T_{inlet} is the inlet temperature measured at the inlet port of the heat exchanger. The measurement uncertainty of the ΔT_{HTF} was estimated by using the following equation:

$$\boldsymbol{u_{\Delta T_{HTF}} = \left[\left(\frac{\partial \Delta T_{HTF}}{\partial T_{outlet}}\right)^2 \left(u_{T_{out}}\right)^2 + \left(\frac{\partial \Delta T_{HTF}}{\partial T_{inlet}}\right)^2 \left(u_{T_{inlet}}\right)^2\right]^{1/2}} \tag{4.32}$$

where, u is the statistical uncertainty for each variable: ΔT_{HTF},T_{out}, and T_{inlet} . The calibrated uncertainty of thermocouples was determined to be ± 0.35 °C between 10 °C and 40 °C. The average uncertainty for ΔT_{HTF} is computed to be ± 0.49 °C. The effectiveness (ε) of the CHX-LHTESS was determined by Equation 4.33;

$$\boldsymbol{\varepsilon = \frac{T_{inlet} - T_{outlet}}{T_{inlet} - T_{PCM}}} \tag{4.33}$$

where, T_{PCM} is the temperature of the of the PCM at the 90% melt point in the heat exchanger (i.e. thermocouple E), T_{inlet} is the HTF inlet temperature, and T_{outlet} is the HTF outlet temperature. The uncertainty for the effectiveness was computed as shown:

$$\boldsymbol{u_{\varepsilon} = \left[\left(\frac{\partial \varepsilon}{\partial T_{inlet}}\right)^2 \left(u_{T_{inlet}}\right)^2 + \left(\frac{\partial \varepsilon}{\partial T_{outlet}}\right)^2 \left(u_{T_{outlet}}\right)^2 + \left(\frac{\partial \varepsilon}{\partial T_{PCM}}\right)^2 \left(u_{T_{PCM}}\right)^2\right]^{1/2}} \tag{4.34}$$

where, u is the statistical uncertainty for each variable; ε, $u_{T_{out}}$, T_{PCM} and T_{inlet} . The temperature average specific heat capacity (C_p) of the HTF was calculated using the following correlation, as shown in Equation 4.35:

$$\begin{aligned}\boldsymbol{C_p = \left[4 \times 10^{-13} T_{avg}^6 - 2 \times 10^{-10} T_{avg}^5 + 2 \times 10^{-8} T_{avg}^4 - 2 \times 10^{-6} T_{avg}^3 + \right.}\\ \boldsymbol{\left. 1 \times 10^{-4} T_{avg}^2 - 3.4 \times 10^{-3} T_{avg} + 4.2199\right] 1000}\end{aligned} \tag{4.35}$$

The temperature average density (ρ) of the HTF was calculated using the following correlation, as shown in Equation 4.36:

$$\boldsymbol{\rho = \left[1 \times 10^{-7} T_{avg}^{4} + 4 \times 10^{-5} T_{avg}^{3} + 7.5 \times 10^{-3} T_{avg}^{2} - 5.16 \times 10^{-2} T_{avg}\right] + 999.87} \tag{4.36}$$

The thermal storage capacity of the heat exchanger was calculated by using Equation 4.36, based on the measurements of the HTF temperature values and flow rates:

$$\boldsymbol{E = \int_{to}^{tf} \dot{m} c_p \Delta T_{HTF}\ dt} \tag{4.37}$$

where, ΔT_{HTF} is the difference between the temperature of the HTF at inlet and outlet, C_p is the average specific heat during each respective phase change, and $\dot{m}$ is the average mass flow rate of the HTF. t_o is the start of phase change, and t_f is the end of phase change. The uncertainty of the mass flow rate of the HTF is calculated as shown:

$$\boldsymbol{u_{\dot{m}} = \left[\left(\frac{\partial \dot{m}}{\partial \dot{V}}\right)^2 (u_{\dot{V}})^2 + \left(\frac{\partial \dot{m}}{\partial \rho}\right)^2 (u_{\rho})^2\right]^{1/2}} \tag{4.38}$$

where, $\dot{V}$ is the measured volumetric flow rate of the HTF and ρ is the density of the HTF. The uncertainty for the volumetric flow rate, $u_{\dot{V}}$, is determined to be 7.2×10^{-5} L/min. The extremely small uncertainty is due to the quality of the flow meter and is neglected in the thermal performance calculations. The uncertainty for the thermal energy (heat transfer) is then calculated using Equation 4.39, as follows:

$$\boldsymbol{u_E = \left[\left(\frac{\partial E}{\partial \dot{m}}\right)^2 (u_{\dot{m}})^2 + \left(\frac{\partial E}{\partial c_p}\right)^2 \left(u_{c_p}\right)^2 + \left(\frac{\partial E}{\int \partial \Delta T_{HTF}}\right)^2 (u_{\Delta T})^2 + \left(\frac{\partial E}{\partial t}\right)^2 (u_t)^2\right]^{1/2}} \tag{4.39}$$

where, t is time and u is the statistical uncertainty for each variable: $\dot{m}$, c_p, ΔT_{HTF} and t. For this experiment, u_{c_p} and u_t were considered to be negligible. The instantaneous power (P) for the CHX - LHTESS was calculated using Equation 4.40, as follows:

$$\boldsymbol{P = \dot{m} c_p \Delta T_{HTF}} \tag{4.40}$$

The measurement uncertainty for the estimates of the power rating of the LHTESS (for both melting and solidification) was calculated using Equation 4.41, as follows:

$$\boldsymbol{u_P = \left[\left(\frac{\partial P}{\partial \dot{m}} \right)^2 (u_{\dot{m}})^2 + \left(\frac{\partial P}{\partial c_p} \right)^2 \left(u_{c_p} \right)^2 + \left(\frac{\partial P}{\partial \Delta T_{HTF}} \right)^2 \left(u_{\Delta T_{HTF}} \right)^2 \right]^{1/2}} \tag{4.41}$$

Stefan number is defined as the ratio of the sensible heat to the latent heat. The average power of the system was calculated using Equation 4.42.

$$\boldsymbol{P_{average} = \frac{1}{time} \int_{to}^{tf} \dot{m} c_p \Delta T_{HTF} \; dt} \tag{4.42}$$

where, t is total time of phase change, t_o is the start of phase change, and t_f is the end of phase change. The Stefan number was calculated using Equation 4.43, as follows:

$$\boldsymbol{Stefan\ number = \frac{sensible\ heat}{latent\ heat} = \frac{c_p \Delta T_{HTF}}{h_{fs}}} \tag{4.43}$$

where, m is the mass of the PCM and h_{fs} is the latent heat value of the PCM.

CHAPTER V

RAW MATERIALS AND SYNTHESIS

This chapter provides a detail description of techniques for synthesizing salt hydrates and nucleators. Lithium nitrate trihydrate *($LiNO_3.3H_2O$),* calcium chloride hexahydrate *($CaCl_2.6H_2O$),* and sodium sulphate decahydrate *($Na_2SO_4.10H_2O$)* were synthesized in-house due to their hygroscopic nature. Zinc nitrate hexahydrate was "used as purchased" due to the difficulty in acquiring pure zinc nitrate and due its sensitivity to high temperature. In all synthesis high purity (>99%) base salts were utilized, as impurities could alter the thermal physical properties of salt hydrates. Zinc hydroxyl nitrate and zinc oxide were synthesized in-house as nucleators.

5.1 Salt Hydrates

In this section, the synthesis of salt hydrates is described in detail. The base salt of high purity (>99%) were utilized for synthesis of salt hydrates. As impurities could alter the thermal physical properties of salt hydrates.

5.1.1 Lithium Nitrate Trihydrate

Anhydrous lithium nitrate salt powders were procured commercially (Beantown Chemical, NH, Purity >99%) and hydration technique were utilized to synthesis lithium nitrate trihydrate in-house. The hygroscopic nature of lithium nitrate requires a careful and tedious hydration technique to minimize the effects of humidity on the sample. In the initial step lithium nitrate powders were dried in an oven for 12 hours at 150°C to remove moisture from lithium nitrate. After dehydration procedure, lithium nitrate samples were placed in a heated vacuum chamber overnight at 90°C as shown in Figure 52 .

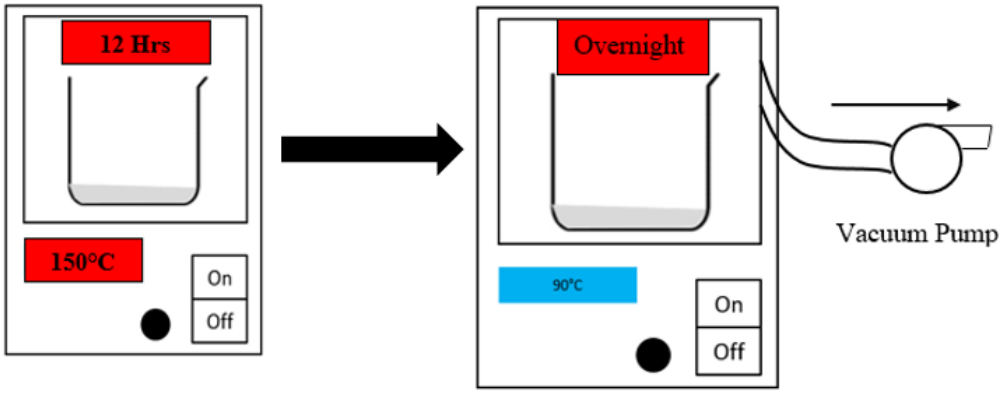

Figure 52: The initial dehydration process of lithium nitrate samples from supplier. The raw sample of lithium nitrate was dehydrated to remove any absorbed water from as-purchased samples.

The hydration step involved adding stoichiometric quantities of de-ionized water to anhydrous lithium nitrate at 35°C. The hydration was performed at 35°C (i.e. above the phase transition temperature) for homogenous formation of lithium nitrate trihydrate. The hydrated lithium nitrate (i.e. lithium nitrate trihydrate) should contain 44% mass of water and 56% mass of lithium nitrate salt as shown in Figure 53. Therefore, in the final step a small quantity of hydrated lithium nitrate was removed from the bulk mixture and dehydrated to validate the mole concentration of water. As the performance of lithium nitrate trihydrate trends to vary with lack or excess of hydration.

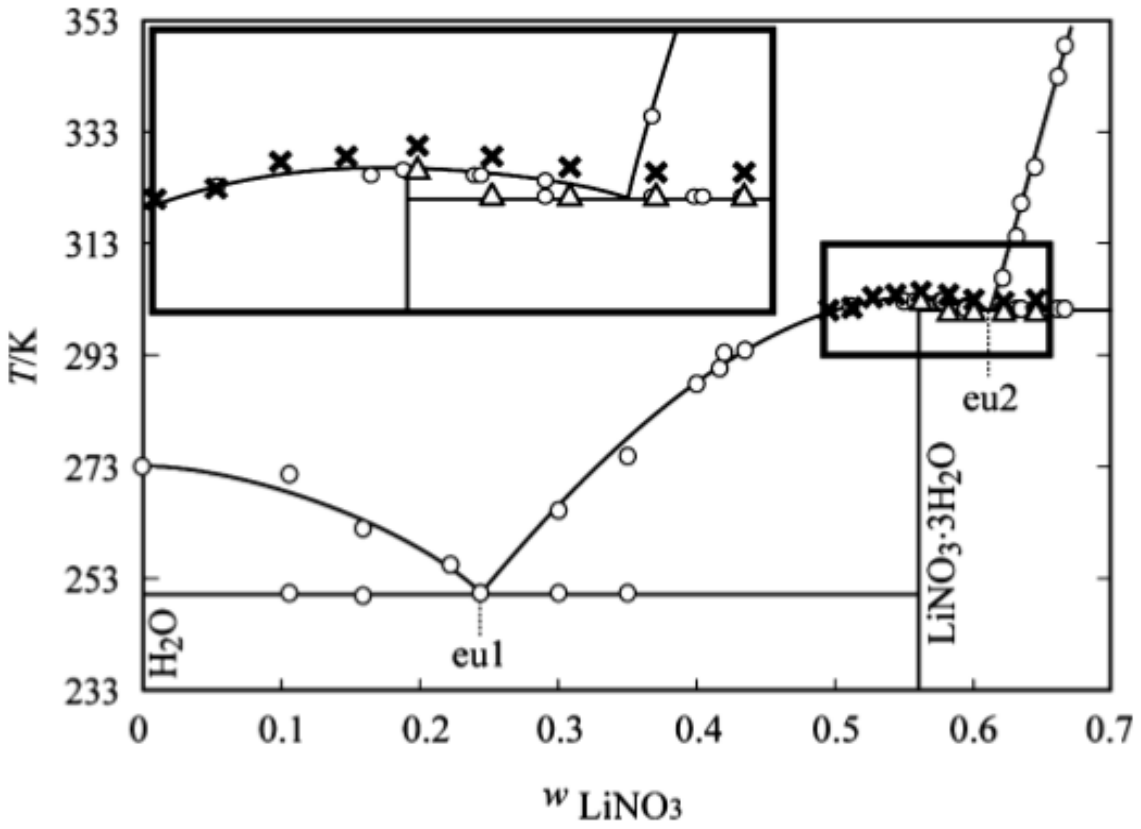

Figure 53: The binary phase diagram of lithium nitrate – water. The highlighted region shows the second eutectic point of lithium nitrate at 302.5 K. Lithium nitrate also has colder eutectic at 250 K. In this work only, eutectic point at 302.5 K was considered. ""Reprinted from [103]"

The lithium nitrate trihydrate with nucleating additives were synthesized using a two-step process for uniform distribution of nucleating additives. As shown in Figure 54, the dehydrated lithium nitrate and as synthesized zinc hydroxyl nitrate were added to distill water at ratio of 4:1 (lithium nitrate: H_2O). Then the sample was stirred for 40 minutes at 45°C on a hot plate and ultrasonicated for 2 hours at 45°C. In order to obtain dehydrated mixture of lithium nitrate and nucleating additives, the solution was evaporated on a hotplate at 150°C. The hydration step involved adding stoichiometric quantities of de-ionized water to anhydrous lithium nitrate mixture at 35°C.

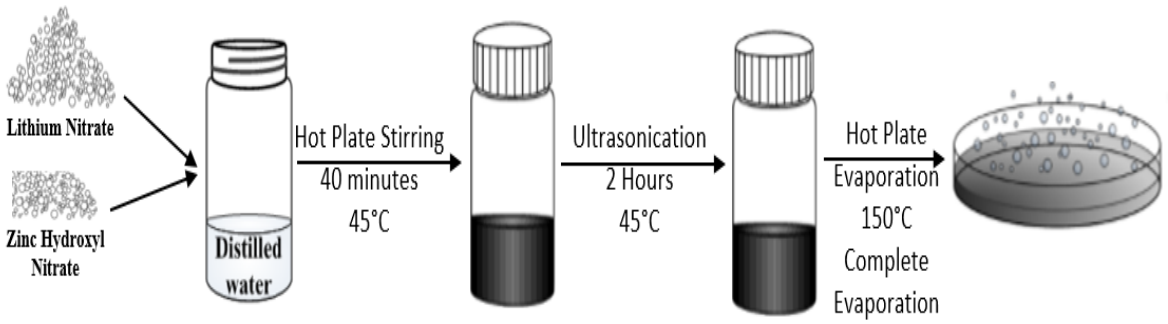

Figure 54: Uniform mixing technique of lithium nitrate with nucleating additives (Zinc Hydroxyl Nitrate). The uniform mixing technique allowed for homogenous distribution of nucleating additives into base lithium nitrate trihydrate. The uniform mixing technique was followed by a stoichiometric hydration step.

5.1.2 Calcium Chloride Hexahydrate

Anhydrous calcium chloride was procured commercially (Sigma Aldrich, MO, Purity >90%) and hydration techniques were utilized to synthesis calcium chloride hexahydrate in-house. Calcium chloride is both hygroscopic and deliquescent. Thus, under common ambient conditions, calcium chloride will absorb moisture from ambient until equilibrium is reached. Therefore, calcium chloride was dried in an oven for 12 hours at 190°C to remove absorbed moisture. The dehydrated calcium chloride was placed in a heated vacuum chamber overnight at 90°C similar to procedures as shown in Figure 52 . The hydration step involved adding stoichiometric quantities of de-ionized water to anhydrous calcium chloride at 35°C. The hydrated calcium chloride (i.e. calcium chloride hexahydrate) sample should contain 49.3% mass of water and 50.7% mass of anhydrous calcium chloride as shown in Figure 55. In the final step a small quantity of hydrated calcium chloride was removed from the bulk mixture and dehydrated to validate the mole concentration of water.

Calcium chloride hexahydrate with nucleating additives were synthesized using a two-step process for uniform distribution of nucleating additives. As shown in Figure 56, the dehydrated calcium chloride and strontium chloride were added to distill water at a ratio of 1:3 (calcium chloride: H_2O). Then the sample was stirred for 40 minutes at 45°C on a hot plate and ultrasonicated for 2 hours at 45°C. In order to obtain dehydrated mixture, the calcium chloride solution, was evaporated on a hotplate at 190°C. The hydration step involved adding stoichiometric quantities of de-ionized water to anhydrous calcium chloride mixture at 35°C.

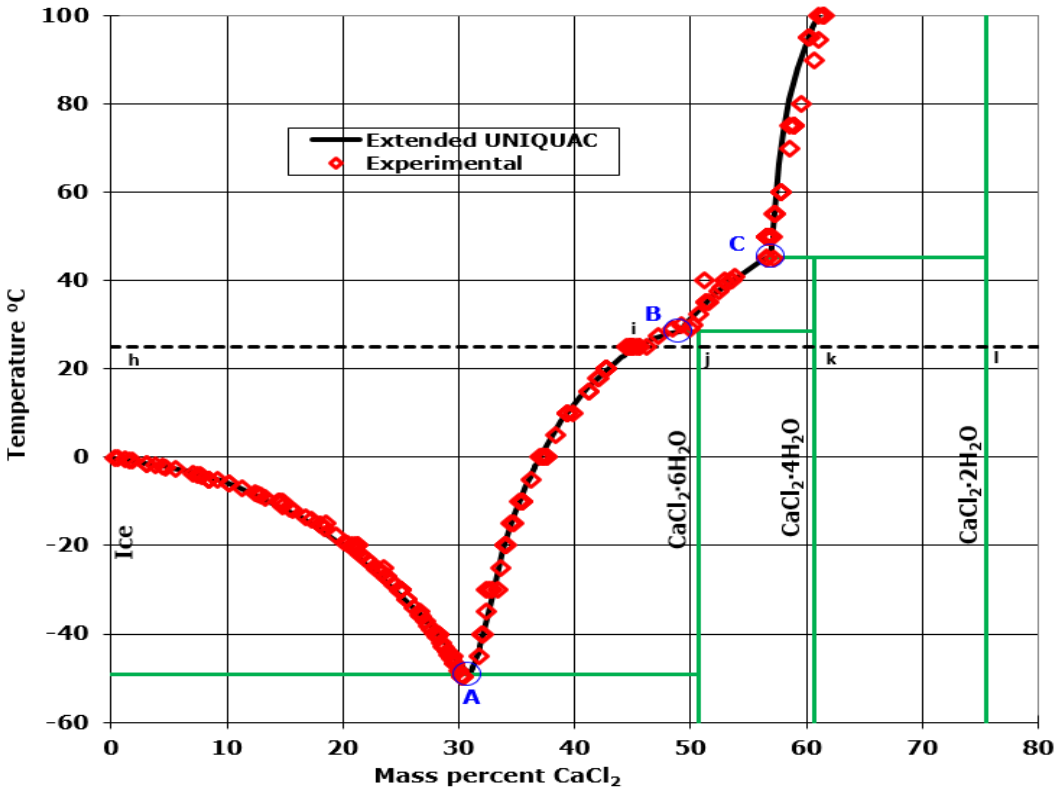

Figure 55: The binary phase diagram of calcium chloride – water. Calcium chloride could form different hydrates with varying concentration and temperature. In current application, only calcium chloride hexahydrate at 29°C (i.e. calcium chloride hexahydrate) will be considered. "Reprinted from [16]"

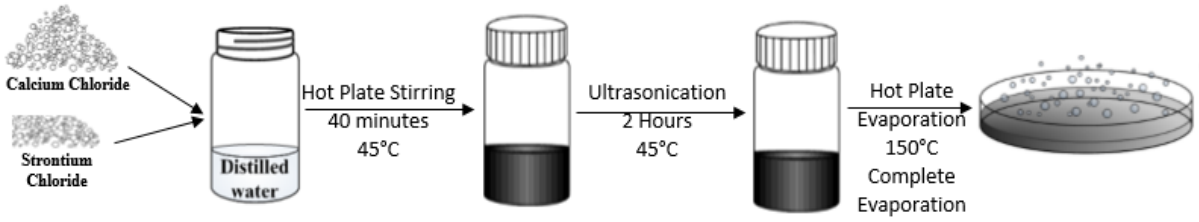

Figure 56: Uniform mixing technique of calcium chloride hexahydrate with nucleating additives. The uniform mixing technique allowed for homogenous distribution of nucleating additives into base calcium chloride hexahydrate. The uniform mixing technique was followed by a stoichiometric hydration step.

5.1.3 Zinc Nitrate Hexahydrate

Zinc Nitrate hexahydrate (Alfa Assar, MA, purity >99%) were used as purchased due to difficulty in sourcing high purity zinc nitrate and difficulty in synthesis anhydrous zinc nitrate. As shown in Figure 57, zinc nitrate hexahydrate and nucleating additives were stirred and ultrasonicated at 45°C for two hours for uniform distribution.

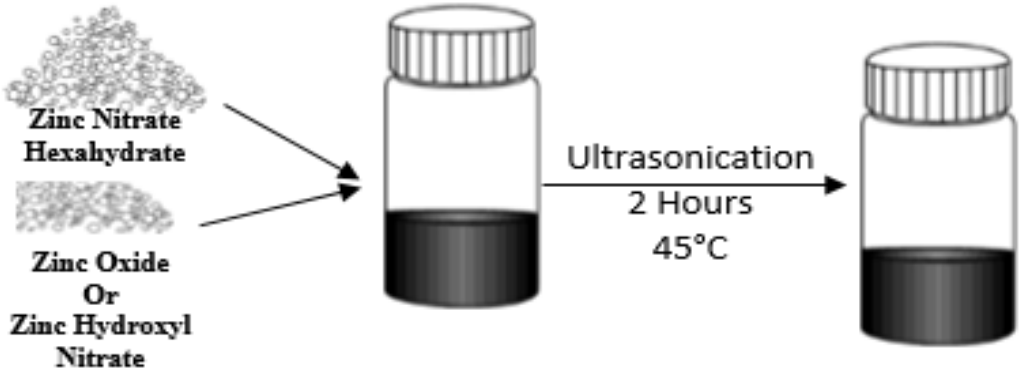

Figure 57: Uniform mixing technique of zinc nitrate hexahydrate with nucleating additives. Zinc nitrate hexahydrate (ZNH) uniform mixing step was accomplished using wet mixing technique.

5.1.4 Sodium Sulfate Decahydrate

During the initial characterization sodium sulfate decahydrate were used as purchased but during gelling and additive period of experimentation, sodium sulfate decahydrate were synthesized in lab using sodium sulfate. The initial step involves dehydration of as purchased sodium sulfate at 130°C for few hours until the mass is constant. Then stoichiometry water (Figure 58) of water with additives and gelling materials were added and stirred. The accuracy of water content in sodium sulfate could alter its phase transition temperature and magnify (lesser water content) or minimize (high water content) the effects of phase segregation.

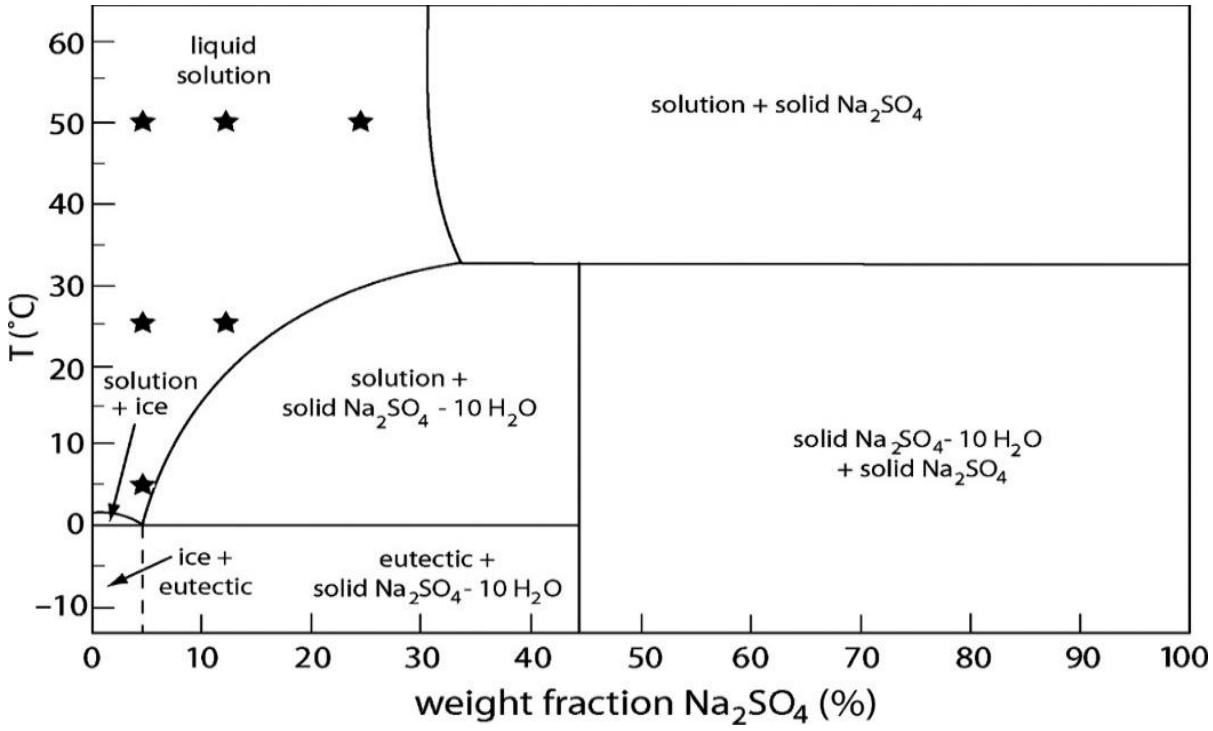

Figure 58: The binary phase diagram of sodium sulfate– water. Sodium sulfate forms a eutectic with water at 32°C – Sodium sulfate decahydrate. "Reprinted from [45]"

5.2 Nucleating Additives

In this section, the synthesis of nucleators are explained in greater detail, as the acquiring of zinc nitrate hydroxyl and zinc oxide nucleators were physically impossible. Therefore, the nucleators were manufactured in-house for better control and formation of correct crystal structure. Strontium chloride was synthesized from as-purchased strontium chloride hexahydrate.

5.2.1 Strontium Chloride

Strontium chloride ($SrCl_2$) nucleating additives could be synthesized by dehydrating strontium chloride hexahydrate ($SrCl_2.6H_2O$) as shown in Figure 59 TGA curve. Strontium chloride hexahydrate dehydrates into anhydrous strontium chloride at 160°C (i.e. 38.9% of mass) and melts at 880°C and rehydrates to form hexahydrate at 110°C. Therefore, strontium chloride is an ideal nucleating agent candidate for calcium chloride hexahydrate. As purchased strontium chloride hexahydrate (sigma Aldrich, MO, 99% purity) were dehydrated in a furnace (Thermo Scientific: FB1315M) at 190°C for an hour.

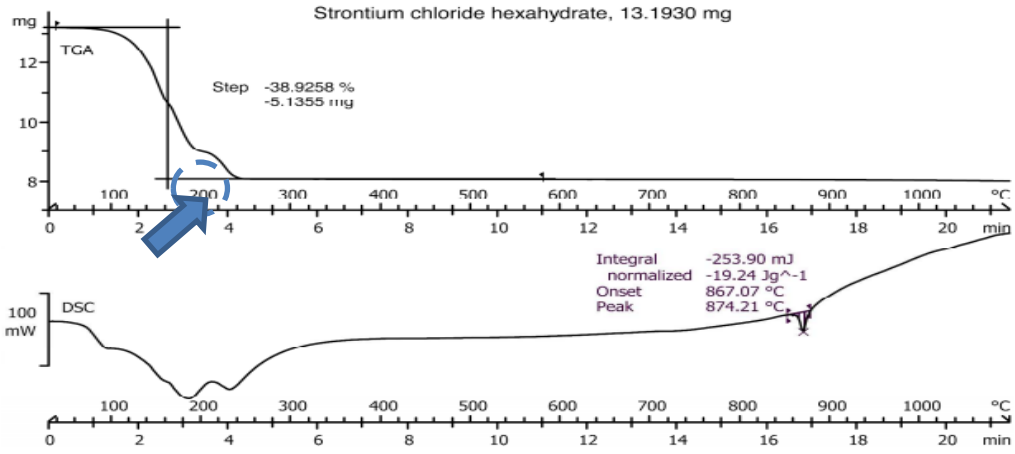

Figure 59: TGA curve of dehydration of strontium chloride hexahydrate to strontium chloride. Strontium chloride hexahydrate dehydrates into strontium chloride at around 160°C.

5.2.2 Zinc Hydroxyl Nitrate

Zinc hydroxyl nitrate ($Zn_3(OH)_4(NO_3)_2$) was synthesized in-house as nucleation catalyst for lithium nitrate trihydrate and zinc nitrate hexahydrate. As shown in Figure 60, the crystalline of zinc hydroxyl nitrate could be isolated from zinc nitrate hexahydrate [$Zn(NO_3)_2.6H_2O$] by isotherm heating at 105°C and evaporation of volatile constituents from the melted zinc nitrate hexahydrate. The decomposition of zinc nitrate hexahydrate to zinc hydroxyl nitrate takes around 4-5 days for completion and is thermally stable for period of about 4 weeks at this temperature [105]. Thermal changes occurring in the system of $Zn(NO_3)_2.6H_2O$ can be expressed as follows:

$Zn(NO_3)_2 \cdot 6H_2O$ (solid phase) → pseudo-melting → HNO_3–H_2O (solution 1:6) → evaporation (H_2O, HNO_3), hydrolysis, crystallization → $Zn(OH)NO_3 \cdot H_2O$ (solid phase) → polycondensation, evaporation (H_2O, HNO_3) → $Zn_3(OH)_4(NO_3)_2$.

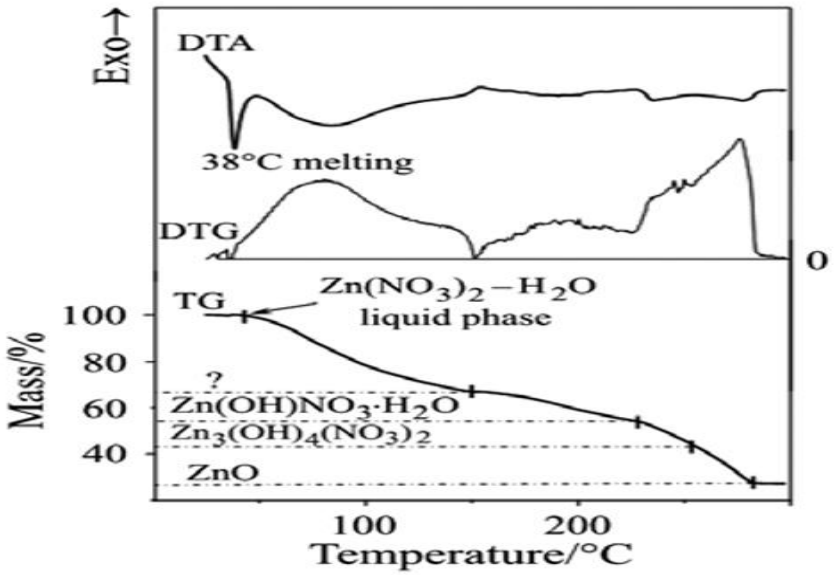

Figure 60: TG/DTG-DTA curves of thermal decomposition of zinc nitrate hexahydrate into zinc hydroxyl nitrate and zinc oxide. The thermal decomposition to zinc hydroxyl nitrate occurred at 115°C for three to five days. The decomposition to zinc oxide occurred at 250°C in an hour. "Reprinted from [105] "

As shown in Figure 61, the furnace (Thermo Scientific: FB1315M) was pre-baked at 115°C for 1 hour. 8 grams of zinc nitrate hexahydrate [Sigma Aldrich (228737), MO] was measured and placed in the furnace for 4 to 5 days in a 50ml glass beaker. The mass was measured daily. The targeted mass loss is around 15% - 20% as reported by the literature [105].

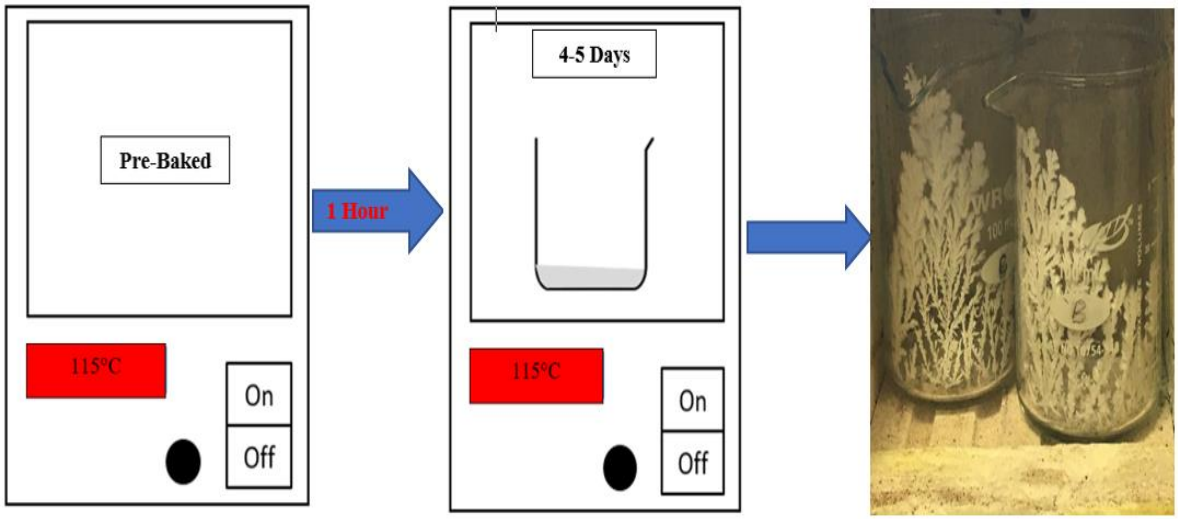

Figure 61: Partial Decomposition of zinc nitrate hexahydrate to zinc hydroxyl nitrate at 115°C over 4-5 days. The furnace was pre-baked without samples at 115°C for an hour.

As shown in Figure 62, upon synthesis the samples were examined under scanning electron microscopy (FE-SEM, FEI Quanta 600) for topology and element characterization using energy dispersive spectroscopy (EDS). The topology consists of short and long rods varying from 3 µm to 10 µm and only zinc, oxygen and nitrogen elements were present. The crystal structure lattice of the sample was analyzed using XRD and the parameters are summarized in Table 23.

Table 23: Lattice crystal structure parameters of zinc hydroxyl nitrate.

Phase	a [Å]	b [Å]	c [Å]	β [deg]
$Zn_3(OH)_4(NO_3)_2$	7.0527	9.6383	11.2244	100.73

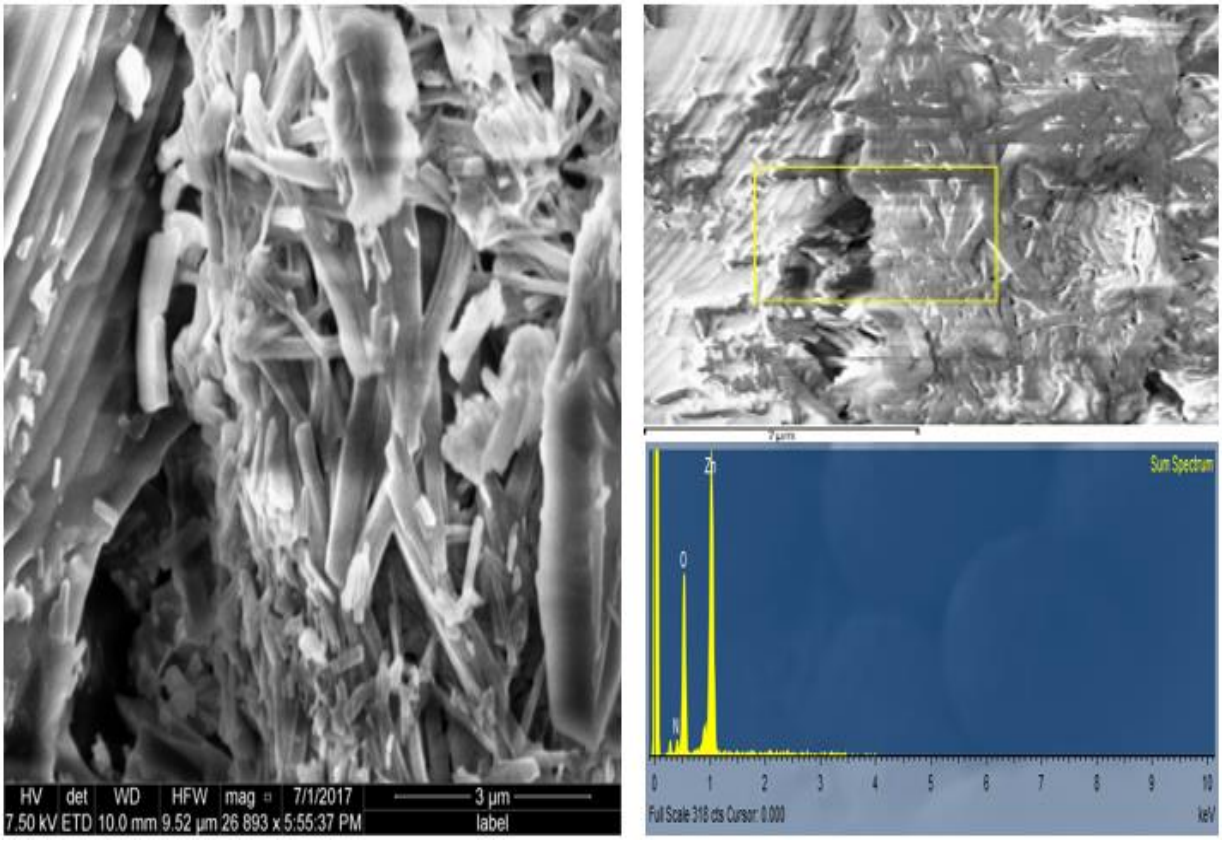

Figure 62: SEM images and EDS characterization of synthesized zinc nitrate hydroxyl (ZHN). The sample was imaged at 3µm.

5.2.3 Zinc Oxide

Zinc oxide (ZnO) was synthesized in-house as a nucleation catalyst for zinc nitrate hexahydrate. As shown in Figure 63 TGA Curve, the calcination of zinc nitrate hexahydrate [$Zn(NO_3)_2.6H_2O$] above 200°C forms crystalline of zinc oxide. The decomposition of zinc nitrate hexahydrate to zinc oxide usually takes around 24 hours.

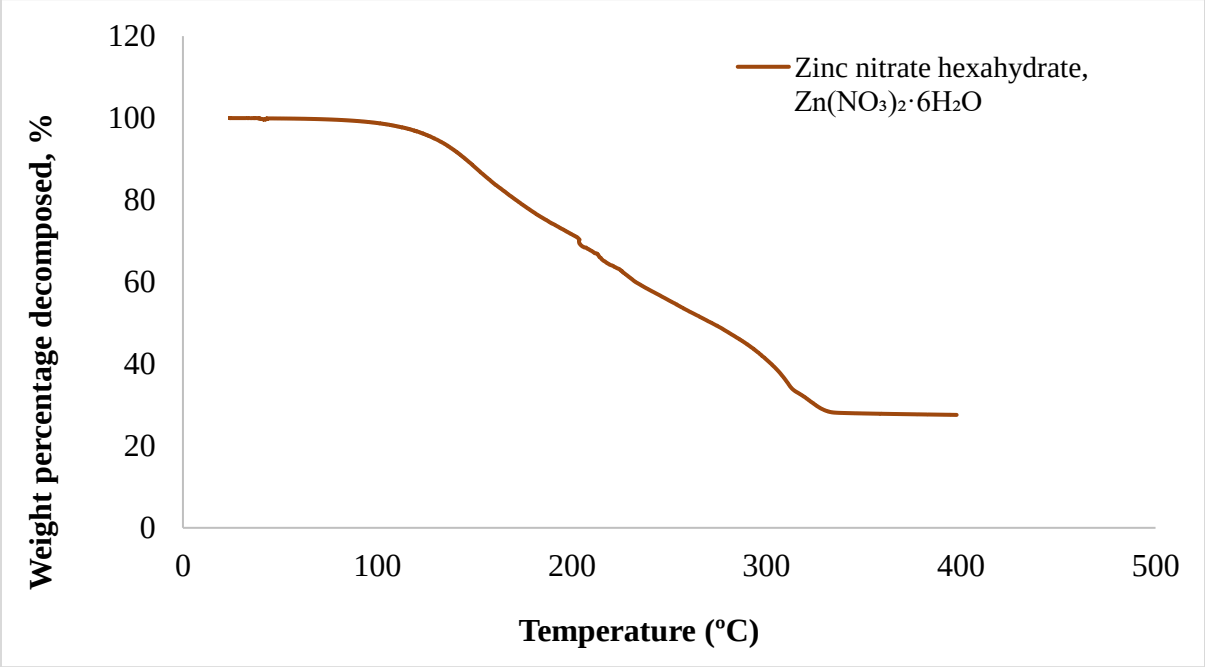

Figure 63: TGA decomposition curve of zinc nitrate hexahydrate above 160°C.

As shown in Figure 64, the furnace (Thermo Scientific: FB1315M) was pre-bake at 290°C for 1 hour.10g of Zinc Nitrate Hexahydrate [Sigma Aldrich (228737), MO] were prepared and placed in the furnace for 24 hours.

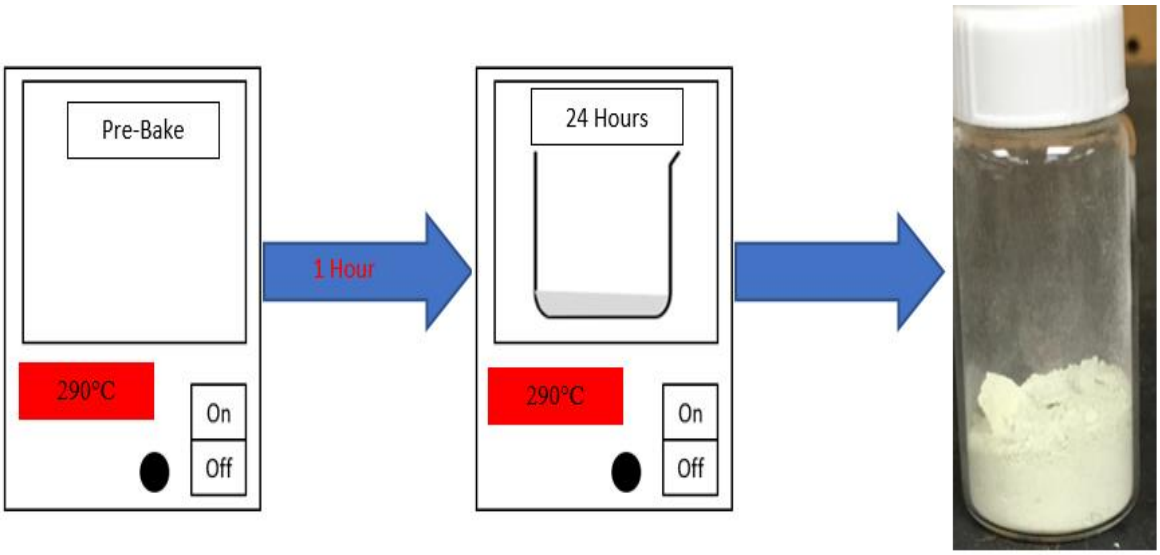

Figure 64: Decomposition of zinc nitrate hexahydrate into zinc oxide at a furnace temperature of 290°C for a day. The furnace was pre-baked without samples at 290°C for an hour.

As shown in Figure 65, upon synthesis the samples were examined under scanning electron microscopy (FE-SEM, FEI Quanta 600) for topology and element characterization using energy dispersive spectroscopy (EDS). The topology consists of needle like-structures and rod structures in a length scale range of 1 µm to 5 µm. The crystal structure lattice of the sample was analyzed using XRD and the parameters are summarized in Table 24. The lattice structures belong to the wurtzite group.

Table 24: Crystal Structure lattice parameters of zinc oxide.

Phase	a [Å]	b [Å]	c [Å]	β [deg]
ZnO	3.2	1.95	5.2	109.47

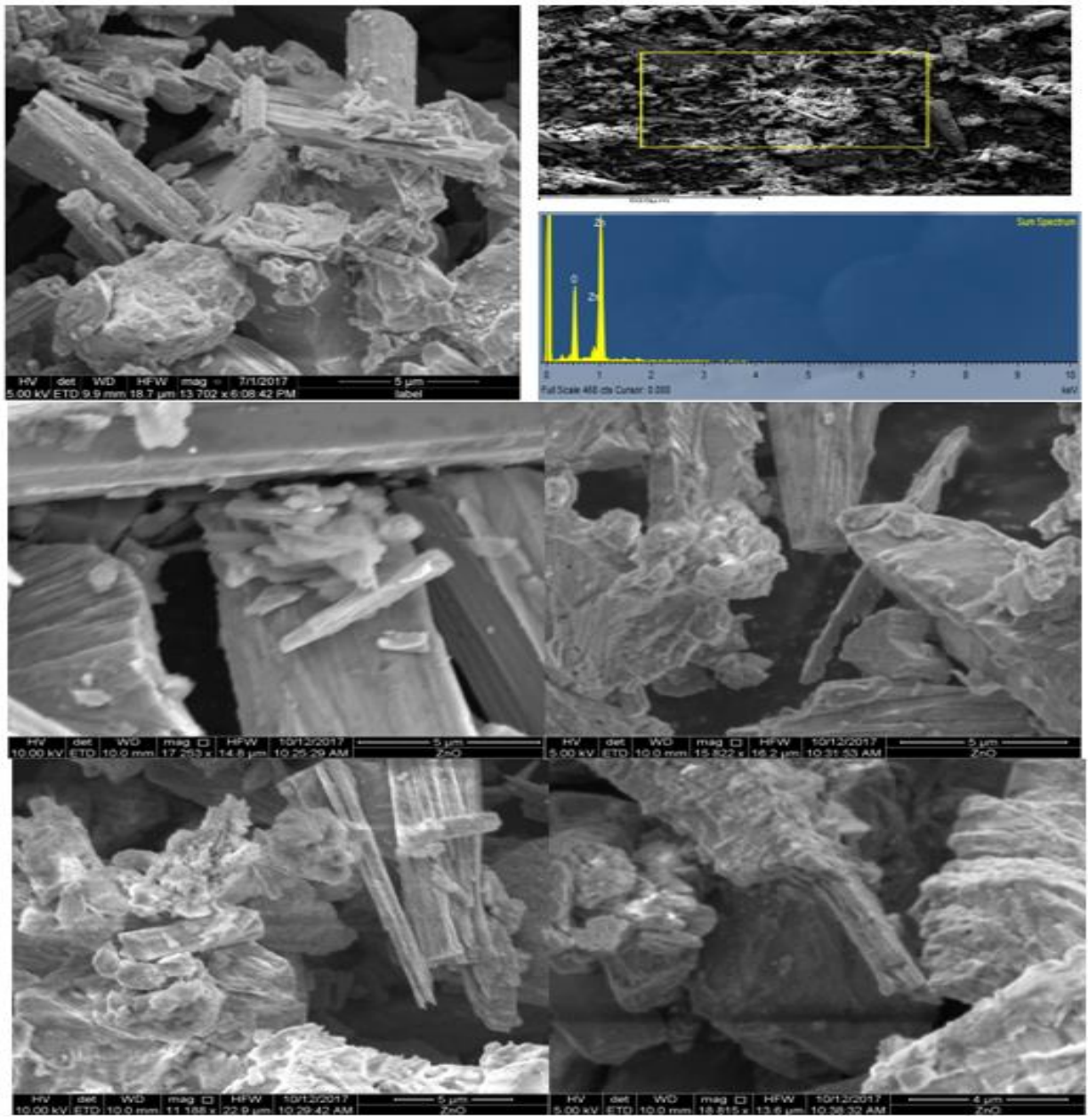

Figure 65: SEM images and EDS characterization of synthesized zinc oxide samples. The samples were imaged at 5µm and 4µm.

CHAPTER VI

CHARACTERIZATION OF LITHIUM NITRATE TRIHYDRATE

This chapter summarizes the thermal stability (i.e. latent heat, sub-cooled temperature, and phase transition temperature) of lithium nitrate trihydrate with and without nucleating agents with thermal cycling. This section is divided into two sections: initial thermal characterization, and thermal stability.

Lithium nitrate trihydrate without additives required sub-cooling in excess of 16°C for onset of nucleation. Zinc nitrate hydroxyl was investigated as additives for heterogenous nucleation. The performance of lithium nitrate trihydrate was vastly improved with the aid of heterogenous nucleation over 1000 melt-freeze cycles. The results have shown that, sub-cooling reduced by as much as 400% with heterogenous nucleators and remained constant with increasing mass concentration of zinc nitrate hydroxyl. Lithium nitrate trihydrate with 3% zinc hydroxyl nitrate survived 1000 melt-freeze cycles – with maximum energy storage density degradation of 5.3% (aft 1000 cycles) and maximum 1°C increment in sub-cooling (after 1000 cycles). When aged at 45°C, the sub-cooling increased by 1.1°C over 30 days, therefore zinc hydroxyl nitrate is sensitive to temperature above 40°C. Prolonged heating at higher temperature could degrade zinc nitrate hydroxyl faster. Increase in water concentration played a major part in degradation of energy storage capacity. "Cold finger" maintained a 0°C sub-cooling (without additives) over 1000 melt-freeze cycles, with a phase transition temperature of 30°C. However, if lithium nitrate trihydrate completely melts due to instrumentation failure, the system will not be able to self-recover as the sub-cooling was in excess of 16°C after 1000 melt-freeze cycle. Therefore, the solution, was "cold finger" technique with nucleating additives.

6.1 Initial Characterization

The initial characterization of lithium nitrate trihydrate was performed using T-History technique. The measurement was performed between 24°C and 40°C. As summarized in Table 25 , the energy storage capacity of lithium nitrate trihydrate was ~273 J/g for endothermic and ~234 J/g for exothermic, the measurement was within 6% of literatures using DSC measurement technique [99]. The difference in the energy storage capacity between endothermic and exothermic is mainly due to effects of sub-cooling and measurement uncertainty. Measurement accuracy of T-History was diminished during exothermic reaction, as heat transfer coefficient of reference was higher than PCM ($h_{ref} \neq h_{pcm}$), in sub-cooled cases. The phase transition occurred around 28.6°C with 5°C sub-cooling.

Table 25: Initial characterization of lithium nitrate trihydrate without additives utilizing T-history technique. The air temperature was maintained between 40°C for melting and 20°C for freezing.

	C_p Liquid (J/g k)	C_p Solid (J/g k)	MP (°C)	FP (°C)	Latent Heat (endothermic) (J/g)	Latent Heat (exothermic) (J/g)	ΔT °C
Initial Data	1.81	3.14	29.2	28.63	273	234	5
Uncertainty (Abs)	0.13	0.89	0.14	0.8	16	21	0.5

As summarized in Figure 66 , lithium nitrate trihydrate had a sub-cooling in excess of 16°C (aft 300 cycles). However, sub-cooling is not an intrinsic material property, and may be affected by experimental parameters which affect nucleation rates (e.g., cooling rates, sample volume, container material, vibration and sample purity). The increase in sub-cooling suggests that whatever heterogeneities may have initially existed in lithium nitrate hexahydrate dissolved, reacted or passivated during thermal cycling. Thus, sub-cooling remains problematic in lithium

nitrate trihydrate, and cannot be overcome simply by introducing an arbitrary solid particle into the mixture.

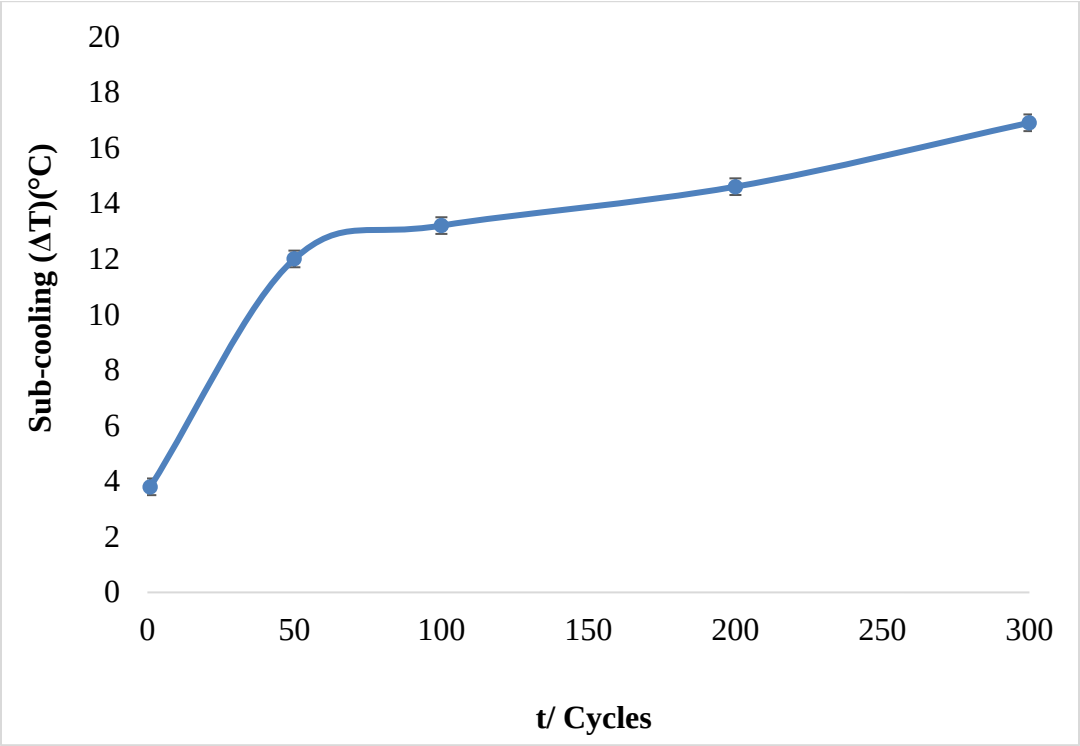

Figure 66: Effects of thermal cycling on sub-cooling of pure lithium nitrate hexahydrate. The sub-cooling in pure lithium nitrate trihydrate increased with thermal cycling. After 300 cycles the effective sub-cooling in lithium nitrate was around 16°C.

Candidate nucleation catalyst phases were experimentally screened to quantify their effect on sub-cooling in lithium nitrate trihydrate. The candidate nucleation catalyst may be crystals of a material which resembles the storage material in structure and lattice parameters. Generally, it is true that a lower lattice mismatch leads to a smaller degree of sub-cooling. The selected candidates with the lowest mismatch with lithium nitrate trihydrate was zinc hydroxyl nitrate. As shown in Figure 67, the mass concentration dependence of zinc hydroxyl nitrate on sub-cooling was quantified. Lithium nitrate trihydrate without nucleating agents showed sub-cooling in excess of

12°C at the end of 50 cycles, but with varying mass concentration of zinc nitrate hydroxyl, the sub-cooling was reduced by 8°C. The sub-cooling remained constant with increasing mass concentration of zinc nitrate hydroxyl. In conclusion, sub-cooling is insensitive to concentration of zinc nitrate hydroxyl. Therefore, moving forward 3% mass concentration of zinc nitrate hydroxyl were selected as target mass for nucleation.

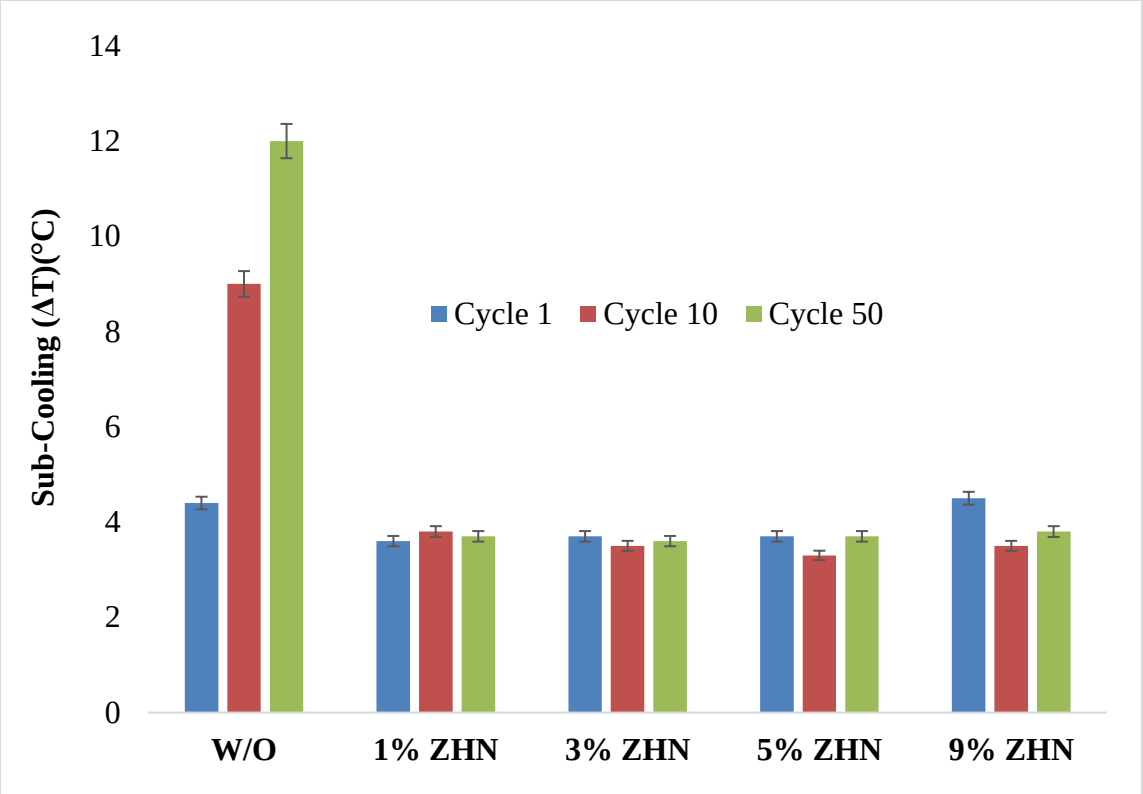

Figure 67: Effects of zinc hydroxyl nitrate nucleation additives concentration (mass %) on suppressing sub-cooling in lithium nitrate trihydrate. The increasing concentration of nucleating additives had negligible effect on suppressing sub-cooling. The additives even at low concentration was able to maintain a 3°C sub-cooling.

6.2 Thermal Stability

For a nucleation catalyst to be practical for certain applications, including its use with PCMs, it must be stable in the presence of the solid or liquid phase over large numbers of melt-freeze cycles and over long periods of time at elevated temperatures. Thermal stability experiments allow one to understand the degradation mechanisms. Potential degradation mechanisms include dissolution, agglomeration, oxidation, anion/cation substitution or any other form of reaction that could alter the physical or chemical properties. The following sections summarizes aging and thermal cycling results of lithium nitrate trihydrate with 3% (mass concentration) of zinc nitrate hydroxyl.

6.2.1 1000 Thermal Cycles

Thermal stability was determined by performing 1000 melt-freeze cycles. The thermo-physical properties of lithium nitrate trihydrate were measured by T-history technique after 250^{th},500^{th},750^{th},1000^{th} cycles and presented. As summarized in Figure 68 , the energy storage density remained constant at around 265 J/g (σ = 9 J/g) for endothermic process and 238 J/g (σ = 16 J/g) for exothermic process over 1000 melt-freeze cycle.

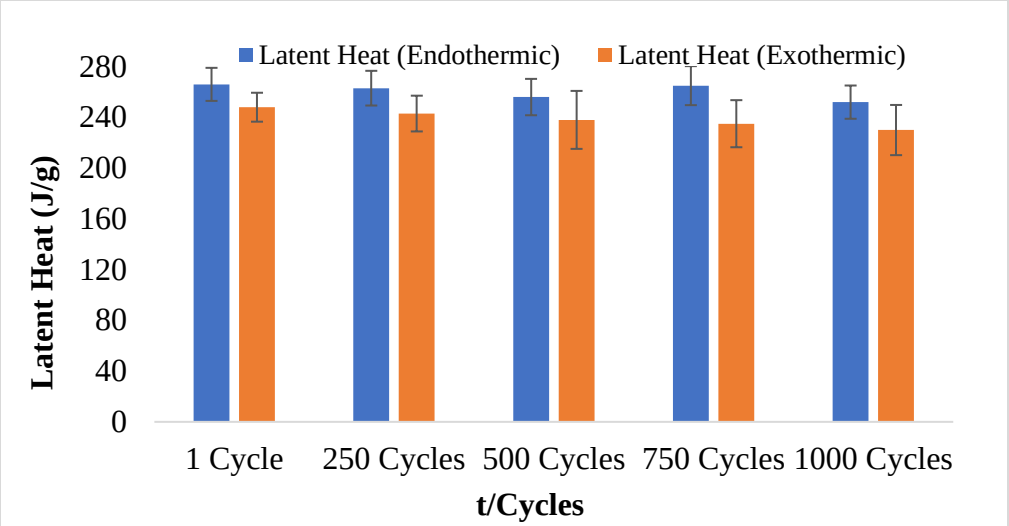

Figure 68: 1000 melt-freeze cycle on latent heat of lithium nitrate trihydrate with 3% zinc hydroxyl nitrate. The latent heat had negligible degradation with thermal cycling.

As summarized in Figure 69, sub-cooling remained constant for first 500 melt-freeze cycles, but 0.6°C and 0.9°C increments were observed after 750 and 1000 thermal cycles respectively. Therefore, with thermal cycling zinc nitrate hydroxyl is degrading.

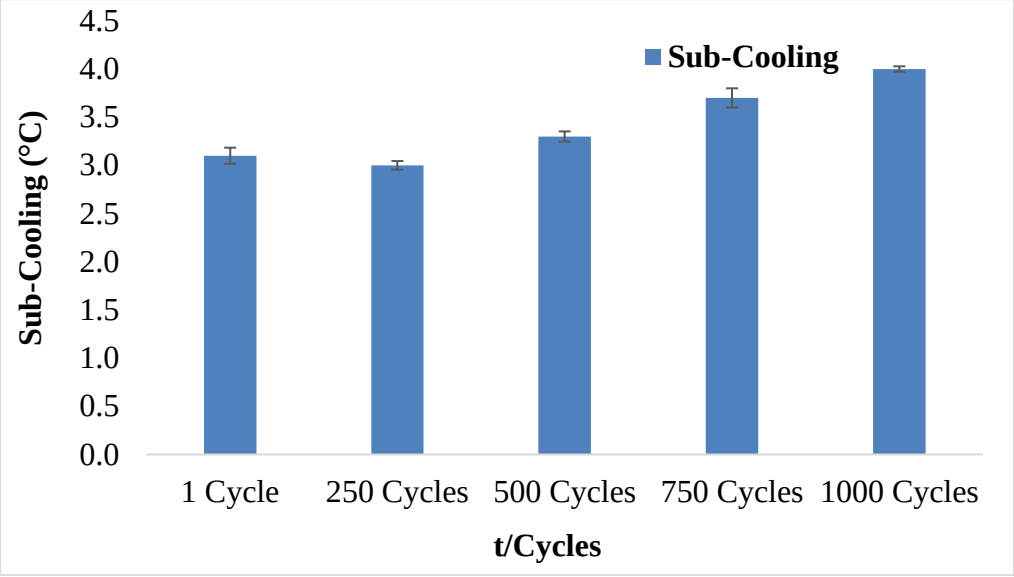

Figure 69: Effects of 1000 melt-freeze cycle on sub-cooling of lithium nitrate trihydrate with 3% zinc hydroxyl nitrate. The samples were able to maintain less than 4°C in sub-cooling over 1000 cycles.

Based on 1000 melt-freeze cycles, it could be acknowledged that the lithium nitrate trihydrate with 3% mass concentration of zinc hydroxyl nitrate survived 1000 cycles (i.e. 3.5 years) with a slight increase in sub-cooling at end of 750 cycles. Physical inspection of the samples showed no form of phase segregation with melt-freeze cycles. To further demonstrate the stability of the lithium nitrate trihydrate with additives, the samples underwent aging test.

6.2.2 Aging Test

Lithium nitrate trihydrate with 3% mass concentration of zinc hydroxyl nitrate underwent aging at 45°C (liquid phase) and 20°C (solid phase) for a period of 30 days. As summarized in Table 26, lithium nitrate trihydrate is not susceptible to aging at elevated temperatures. The latent storage capacity remained constant at around 277 J/g for a period of 30 days. Similarly, sub-cooling remained constant at around 3°C when aged at 20°C but increased by 0.9°C when aged at 45°C. Therefore, zinc hydroxyl nitrate is sensitive to temperature. Prolonged heating at high temperature (>45°C) could degrade zinc hydroxyl nitrate.

Table 26: Summary of aging test (30 days) on lithium nitrate hexahydrate with 3% zinc hydroxyl nitrate sample. The aging test was conducted at 20°C for solid phase and 45°C for liquid phase.

	Solid Phase Aging		Liquid Phase Aging	
Days	**Latent Heat (J/g)**	**Sub-Cooling (ΔT) (°C)**	**Latent Heat (J/g)**	**Sub-Cooling (ΔT) (°C)**
Initial	277 (±15)	3.1(±0.3)	277 (±15)	3.1 (±0.3)
10	277 (±14)	3 (±0.3)	267(±13)	3.5(±0.3)
20	279 (±14)	2.6(±0.3)	259(±13)	4.2(±0.3)
30	273(±14)	2.4(±0.3)	274(±15)	4(±0.3)

6.2.3 Effects of Water

Lithium nitrate is hygroscopic, hence during thermal cycling the sample could absorb moisture from the environment. Therefore, the effects of water on thermal performance were analyzed with thermal cycling. As shown in Figure 70 , increase in water concentration had negligible impact on sub-cooling contrary to literature [87], where a sample with 3% mass increase after 500 cycles had sub-cooling of 3°C whereas a sample with 1% mass increase after 750 cycles had sub-cooling of 3.5°C. These concludes that, the degradation of sub-cooling is mainly due to thermal cycling, and exposure to high temperatures ($T_{melting}$ =42°C) could have caused degradation in the nucleating agent.

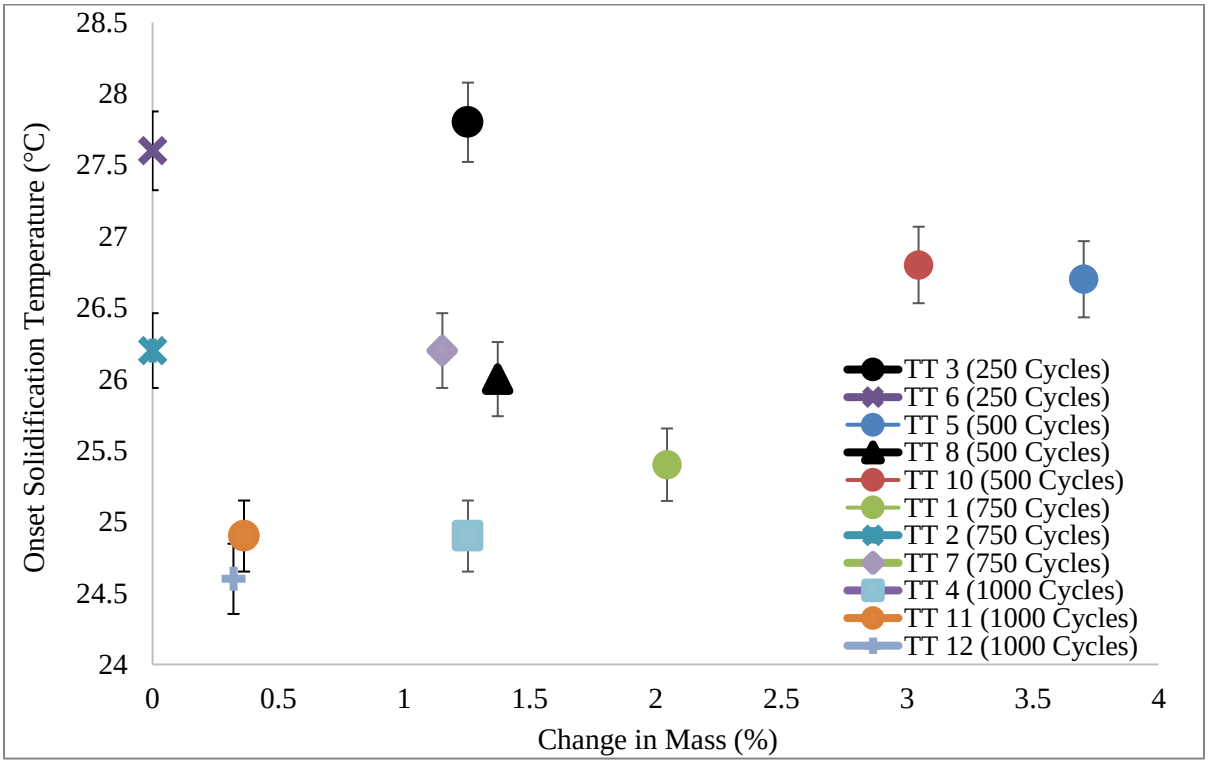

Figure 70: Effects of water absorption on sub-cooling with thermal cycling. During thermal cycling, the effects of water absorption on sub-cooling during solidification was analyzed.

As shown in Figure 71 , both thermal cycling and change in water concentration had an impact on the latent heat storage capacity. Samples without any mass change showed 7% degradation in storage capacity after 750 cycles, whereas a sample with 3.8% increment in mass after 500 cycles showed 16% degradation in storage capacity. Therefore, increase in water concentration played a major part in degradation of energy storage capacity.

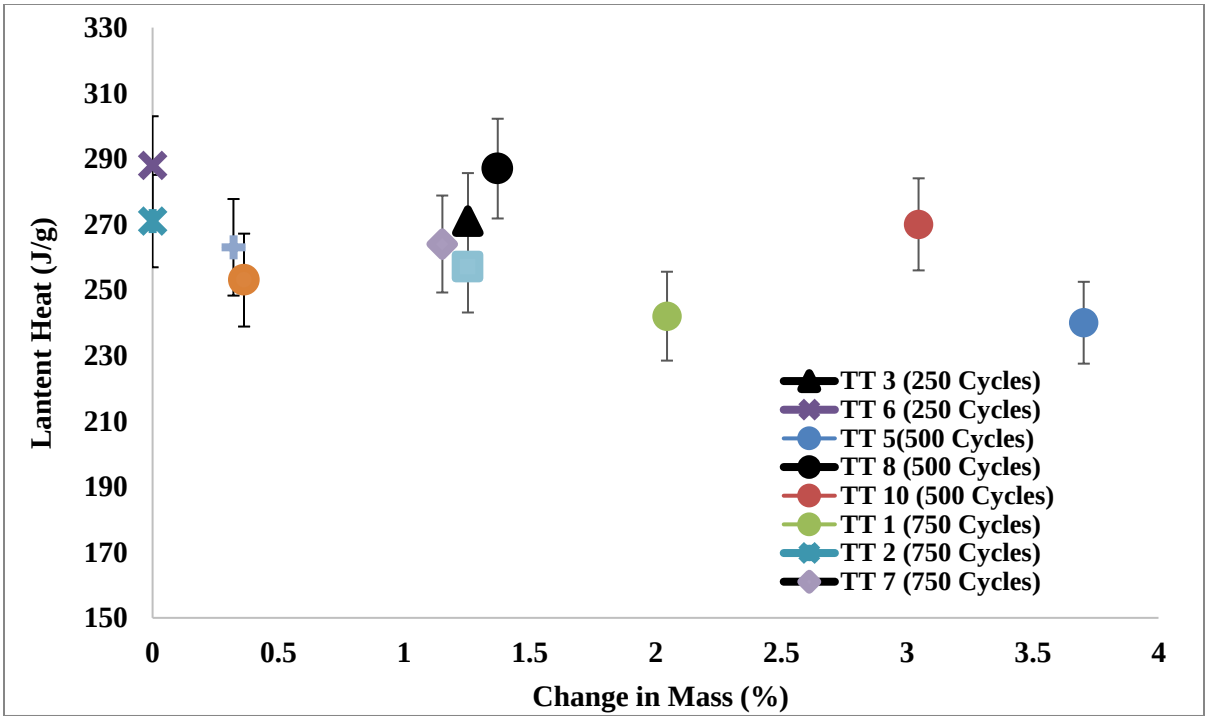

Figure 71: Effects of water absorption on endothermic latent heat with thermal cycling. During thermal cycling, the effects of water absorption on sub-cooling during solidification was analyzed.

6.3 "Cold Finger"

"Cold Finger" technique is a non-seeding technique to eliminate sub-cooling. "Cold finger" technique utilizes cold spots in the system, intentionally created by incomplete melting, to always have some solid PCM (i.e. hydrated crystals) left to act as homogenous nucleator. As shown in Figure 72, endothermic latent heat storage capacity remained constant at around 270 J/g over 1000 melt-freeze with a measurement uncertainty of 11 J/g. Similar trends were also observed during 1000 melt-freeze cycle of lithium nitrate trihydrate with 3% zinc hydroxyl nitrate. Therefore, lithium nitrate trihydrate could be considered to be reliable up to 1000 melt-freeze cycles.

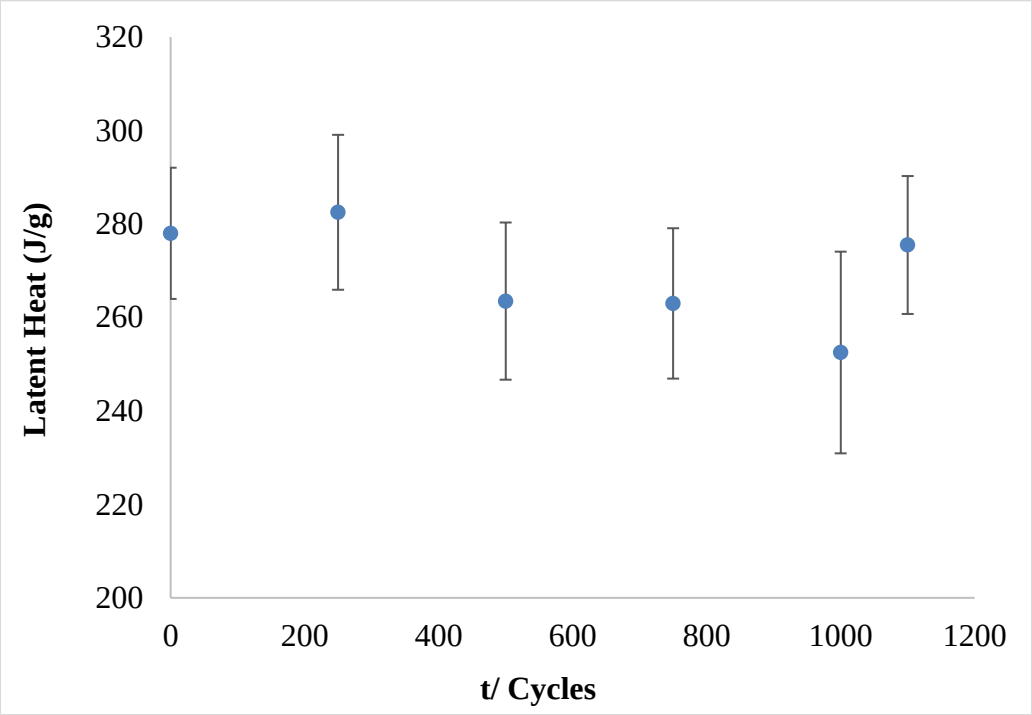

Figure 72: Effects of 1000 "Cold Finger" thermal cycling on endothermic latent heat storage capacity. The thermal cycling had negligible effect on latent heat.

The set-back of "cold finger" technique is the high sub-cooling in the system. If the system had a control failure and completely melts, then system will not be able to self- recover and cause catastrophic system failure. As shown in Figure 73, sub-cooling of lithium nitrate trihydrate increased by 300% at the end of 1000 melt-freeze cycles, when lithium nitrate trihydrate is allowed to completely melt. But the system maintains a 0°C sub-cooling over 1000 melt-freeze cycles when no complete melting occurs in the system as shown in Figure 74 .

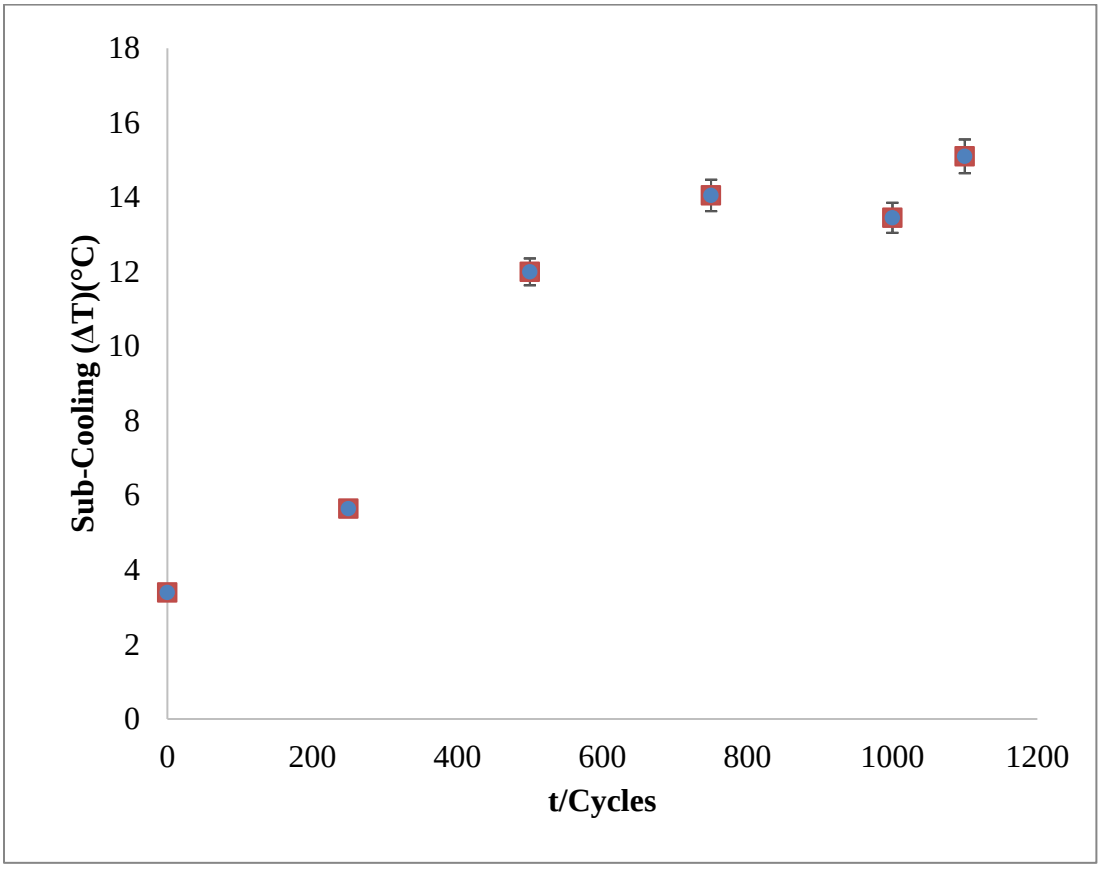

Figure 73: Effects of "Cold Finger" thermal cycling on sub-cooling of lithium nitrate trihydrate when complete melting occurs.

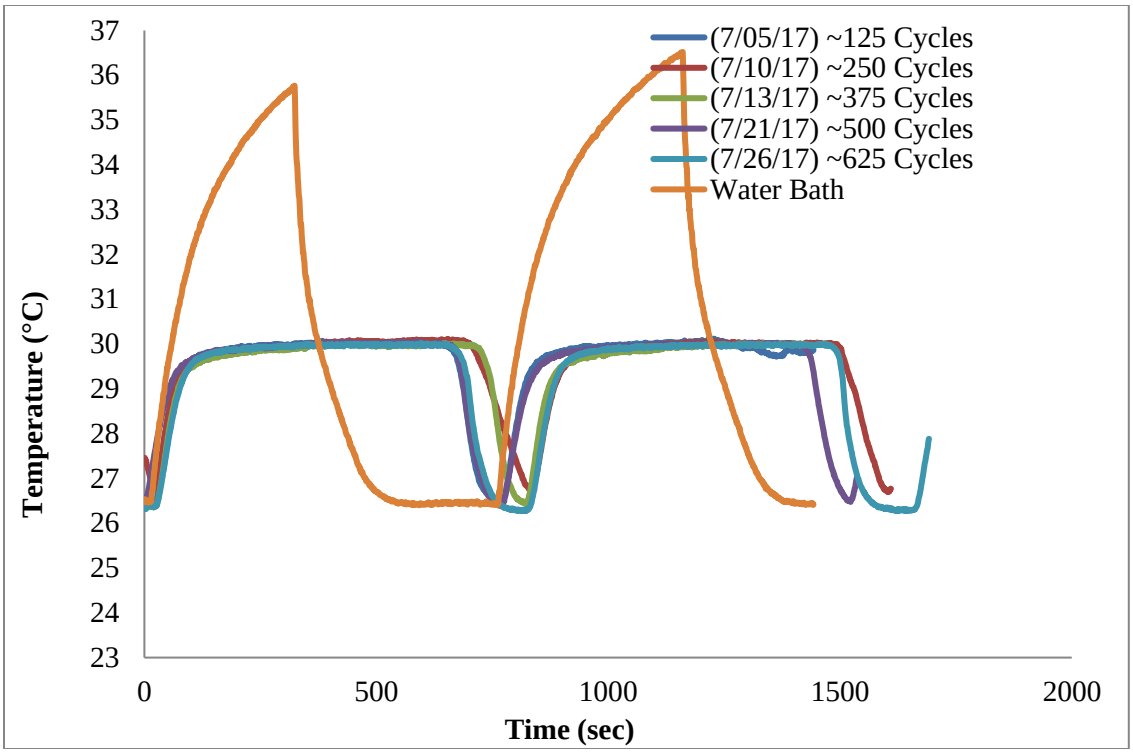

Figure 74: Effects of "Cold Finger" thermal cycling on sub-cooling of lithium nitrate trihydrate when no complete melting occurs.

The "cold finger" technique was repeated with 3% mass concentration of zinc hydroxyl nitrate, to prevent catastrophic system failure due to complete melting. As shown in Figure 75, with 3% mass concentration of zinc hydroxyl nitrate the sub-cooling remained constant at 3.5°C over 1000 "cold finger" melt-freeze cycle, when the samples were completely melted. A combination of nucleating additives and "cold finger" could help prevent catastrophic failure and maintain 0°C sub-cooling. The nucleating additives aids the system, when the sample is completely melted due to system and control failure by providing nucleating sites for rehydration. The latent heat energy storage capacities are summarized in Appendix B.

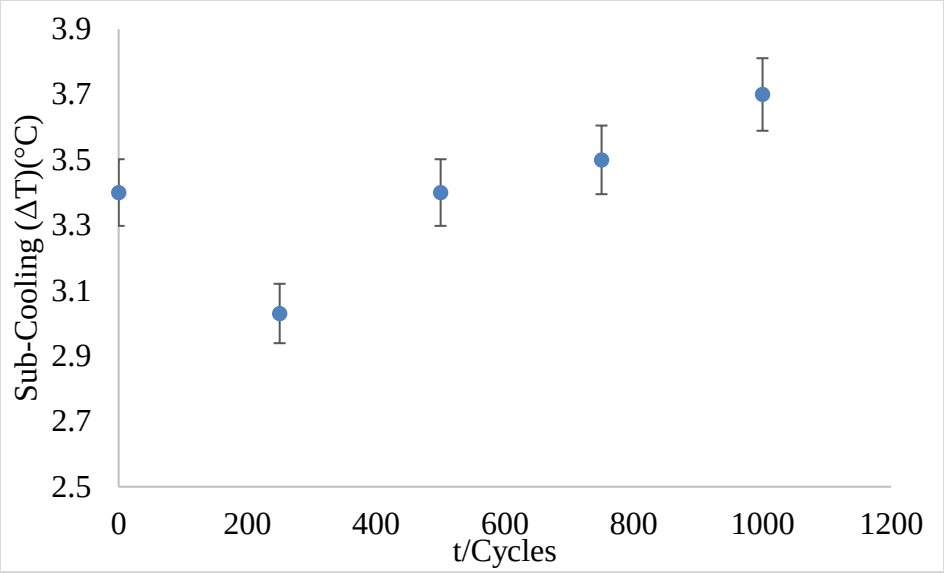

Figure 75: Effects of "Cold Finger" thermal cycling on sub-cooling of lithium nitrate trihydrate with 3% zinc hydroxyl nitrate when complete melting occurs.

Thermal conductivity for solid samples was measured using a 30mm diameter mold at room temperature of 21°C. Multiple samples were prepared to account for the hygroscopic nature of lithium nitrate trihydrate, as the testing was conducted in Material Characterization Facility located at TAMU Research Parkway. The water concentration in lithium nitrate trihydrate were analyzed before and after measurement. The depth of the mold was 10mm. The measured value of 0.868 W/m K varies by 4.2% in comparison to literature [99] at 21°C with a standard deviation of 5.0%. As summarized in Figure 76 , with 10% reduction in water concentration, increased thermal conductivity by 15%. Appendix B summarizes the experimental results on the effects of water concentration on thermal conductivity.

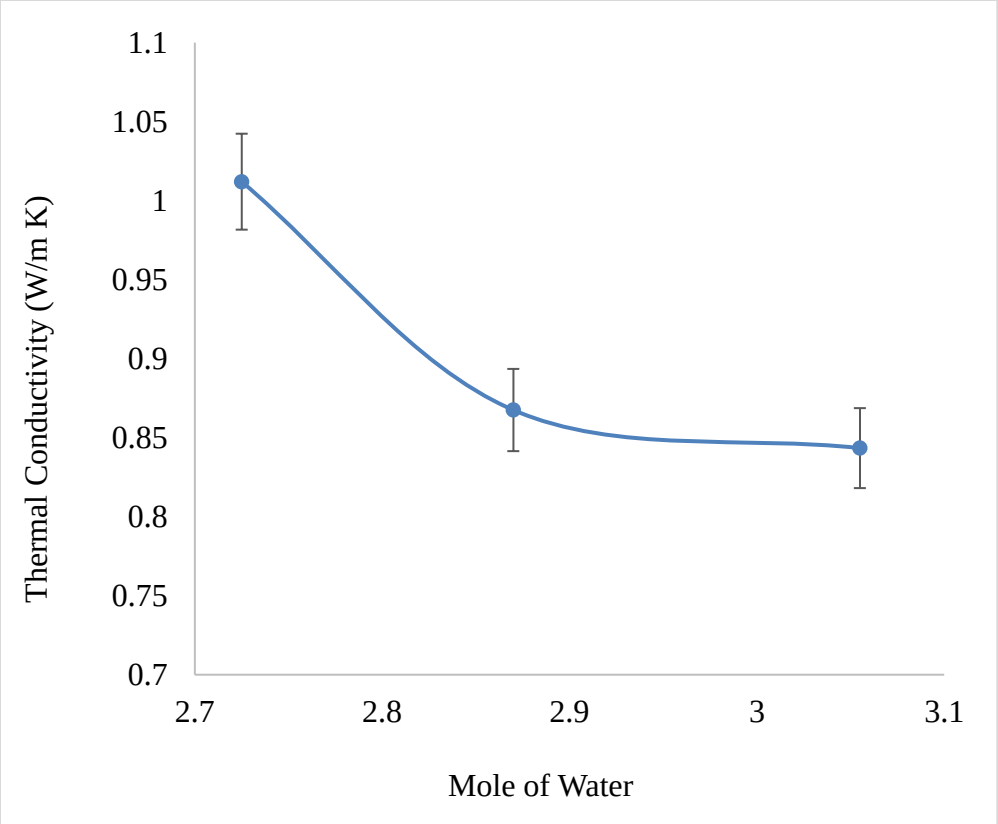

Figure 76: Thermal conductivity vs mole of water plot for lithium nitrate trihydrate.

6.4 Summary and Recommendation

In summary, the two main problems of lithium nitrate trihydrate is excess sub-cooling and long-term stability. The excess sub-cooling in lithium nitrate trihydrate can be controlled by addition of nucleating additives. With additives the sub-cooling remained constant over multiple melt-freeze cycles and at elevated temperature. The sub-cooling performance could be further improved with combine implementation of "cold finger" technique and nucleating additives. This method maintained a 0°C sub-cooling. Increase in water concentration in lithium nitrate trihydrate played a major role in degradation of energy storage capacity and the degradation was amplified with thermal cycling.

In conclusion, sub-cooling in lithium nitrate trihydrate was reduced by 4 times and maintained over 1000 melt freeze cycles. With implementation of "Cold Finger" technique the sub-cooling was negligible over 100 melt-freeze cycles. The maximum energy storage degradation with 1000 melt-freeze cycle was 5.3% which was below the measurement uncertainty. With aging test, it could be concluded that zinc hydroxyl nitrate is sensitive to temperatures, as zinc hydroxyl nitrate tends to lose its nucleation capability with prolonged exposure to elevated temperature above 40°C. Water absorption is the main contributor to degradation to energy storage capacity, variation in phase transition temperature, and had negligible effects on sub-cooling and phase transition temperature. Future recommendation is to understand and study different encapsulation techniques (e.g. Macro, Micro, Nano) to prevent or reduce water absorption. Secondly conduct to continuous melt-freeze cycle to failure, for documenting the actual failure rate and cause of failure. The current 1000 melt-freeze cycle does not provide a concise outcome on the actual failure rate or possible reasons for future failures.

CHAPTER VII

CHARACTERIZATION OF CALCIUM CHLORIDE HEXAHYDRATE

This section summarizes the thermal stability (i.e. latent heat, sub-cooled temperature, and phase transition temperature) of lithium nitrate trihydrate with and without nucleating agents with thermal cycling. This section is divided into two sections: initial thermal characterization, and thermal stability.

Calcium chloride hexahydrate without additives required sub-cooling (ΔT) in excess of 18°C after 300 melt-freeze cycles. Therefore, strontium chloride and sodium chloride were investigated as additives for heterogenous nucleation. The sub-cooling in calcium chloride hexahydrate was vastly improved with the aid of heterogenous nucleation. The results showed sub-cooling was reduced by 300% and remained constant at around 4°C over 300 thermal cycles. The reduction in sub-cooling (ΔT) was a function of mass concentration of nucleating additives. With increasing mass concentration, both sub-cooling and energy storage capacity reduced. Calcium chloride hexahydrate with 3% strontium chloride survived 1000 melt-freeze cycles – with a maximum energy storage density degradation of 5% (aft 1000 cycles) and maximum of 0.9°C increment in sub-cooling. When aged at elevated temperatures over 30 days, the samples with 3% mass concentration of strontium chloride showed no degradation in both latent heat storage capacity and sub-cooling. Therefore, strontium chloride and calcium chloride hexahydrate are stable at elevated temperature up 45°C. Increase in water concentration played a major part in degradation of energy storage capacity.

7.1 Initial Characterization

The initial characterization of calcium chloride hexahydrate was conducted using T-History technique. The measurement was performed between 24°C and 40°C. As summarized in Table 27, the energy storage capacity of calcium chloride hexahydrate was ~182 J/g for melting and ~158 J/g for solidification, the measurement error was within 10% of literatures using DSC measurement technique [6, 106]. The difference in the energy storage capacity between melting and solidification was due to the effects of sub-cooling. As heat transfer coefficient of reference is slightly higher than PCM in sub-cooled case. The phase transition occurred at 29.8°C with 6°C sub-cooling.

Table 27: Initial characterization of calcium chloride hexahydrate without additives utilizing T-history technique. The air temperature was maintained between 40°C for melting and 20°C for charging.

	Cp Solid	Cp Liquid	FP (°C)	MP (°C)	Latent Heat (Solidification) (J/g)	Latent Heat (Melting) (J/g)
T-History	1.67	2.32	23.9	29.8	158	182
Uncertainty (%)	4.8	6.6	1	1	9.3	4.3

However, undercooling is not an intrinsic material property, and may be affected by experimental parameters which affect nucleation rates (e.g., cooling rates, sample volume, container material, vibration and sample purity). Therefore, heterogenous nucleation were introduced to overcome sub-cooling in calcium chloride hexahydrate. The nucleation additives commonly utilized in calcium chloride hexahydrate were strontium chloride and sodium chloride [69, 107]. Previous studies lacked information regarding the effects of mass concentration and thermal cycling on sub-cooling and latent heat energy storage density. Figure 77 summarizes the mass concentration effects of nucleating agent on sub-cooling. As shown in Figure 77 , the degree of sub-cooling (ΔT)

reduced with increasing mass concentration of nucleating agent. 3% mass concentration of strontium chloride and sodium chloride reduced sub-cooling by 67% and 80% respectively. Therefore, both strontium chloride and sodium chloride could be suitable nucleating agent candidates for calcium chloride hexahydrate.

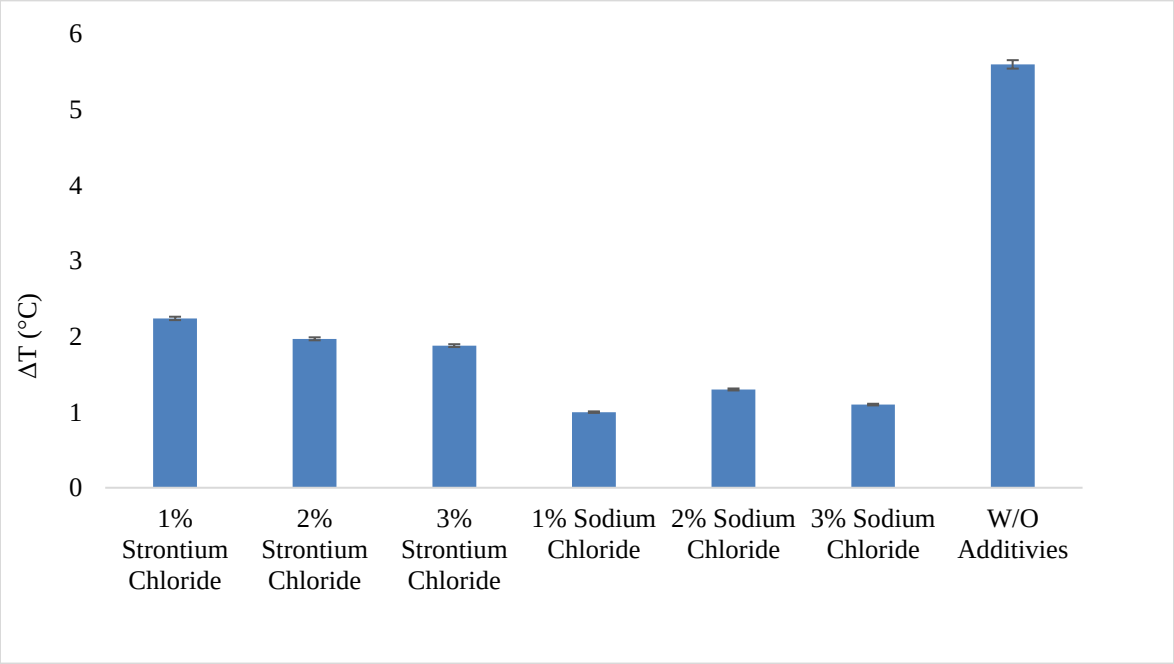

Figure 77: Effects of nucleating agent concentration (mass %) on sub-cooling of calcium chloride hexahydrate. The nucleating additives were strontium chloride and sodium chloride. Nucleating additives were added in 1,2,3 % mass concentration.

Figure 78 summarizes the effects of nucleating agent concentration on energy storage capacity. As shown in Figure 78, the energy storage capacity was reduced by 4% (Maximum) with additional of nucleating agents. Reduction in energy storage capacity was within the measurement uncertainty. The stability of the nucleating agents was analyzed through thermal cycling

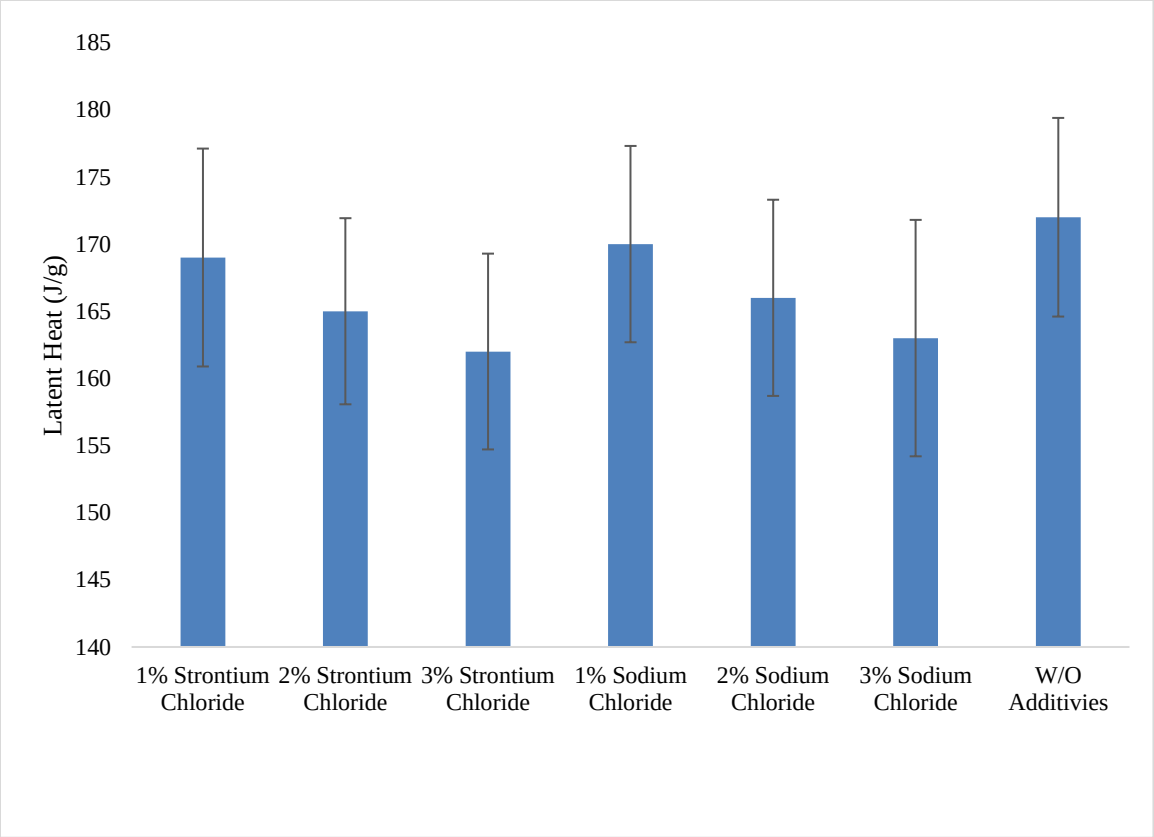

Figure 78: Effects of nucleating agent concentration (mass %) on energy storage capacity. The nucleating additives were strontium chloride and sodium chloride. Nucleating additives were added in 1,2,3 % mass concentration.

Figure 79 summarizes effects of 300 melt-freeze cycles on sub-cooling. As shown in Figure 79, the sample without nucleating agent showed 200% increase in sub-cooling after 300 melt-freeze cycles - ΔT of 17.2°C. Whereas, samples with 1% and 3% mass concentration of nucleating agents showed no degradation in sub-cooling, - remained constant at 2°C – 4°C. Therefore, addition of nucleating additives reduced sub-cooling by at least 300%.

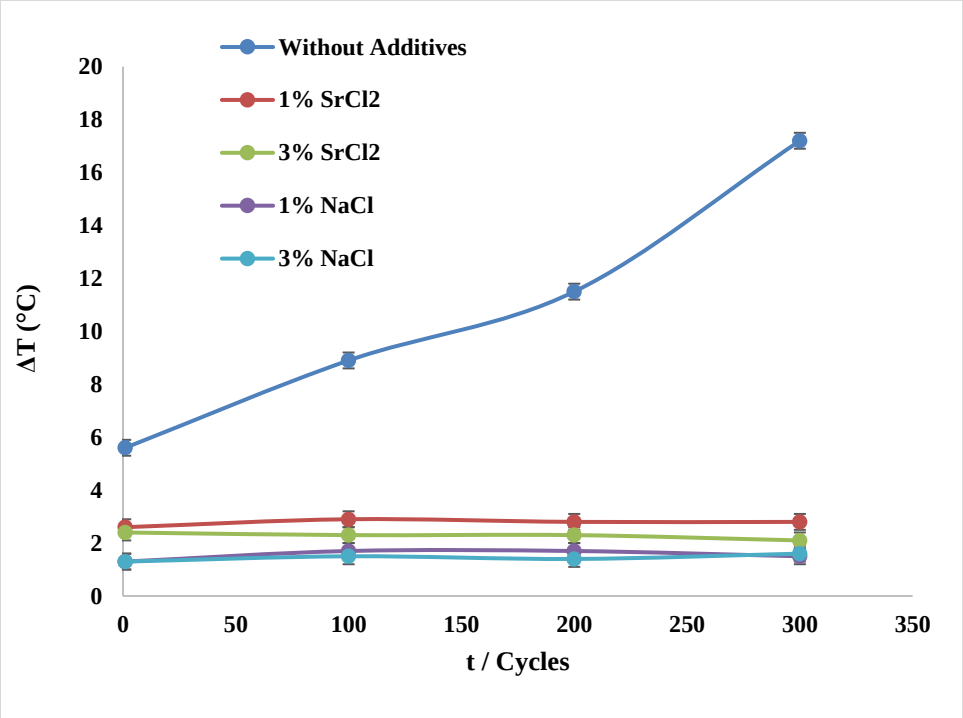

Figure 79: Effects of nucleating additives in controlling calcium chloride hexahydrate sub-cooling over 300 melt-freeze cycles.

Figure 80 summarizes the effects of 300 melt-freeze cycles on latent heat. As shown in Figure 80 , the samples showed no degradation in latent heat over 300 melt-freeze cycles.

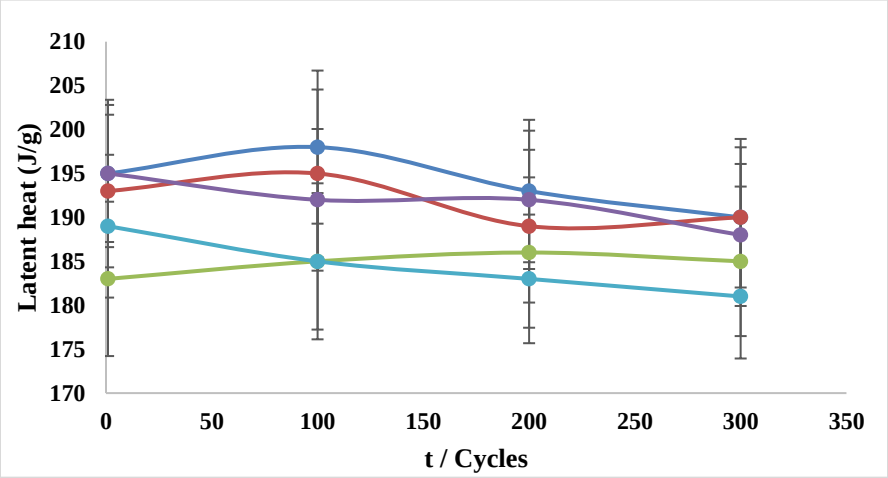

Figure 80: Effects of nucleating additives on calcium chloride hexahydrate energy storage capacity over 300 melt-freeze cycles.

After initial characterization, both strontium chloride and sodium chloride had potentials as nucleating agent candidates for calcium chloride hexahydrate. 3% mass concentration of strontium chloride and sodium chloride reduced sub-cooling (ΔT) to 2.8°C and 1.6°C respectively, and both nucleating agents survived 300 melt-freeze cycles without any degradation in sub-cooling and latent heat. Due to sodium chloride's corrosive nature, strontium chloride was selected as a nucleating agent candidate.

Thermal conductivity measurement for solid sample were measured using a 30mm diameter mold at room temperature of 19.7°C and the testing was conducted in TAMU Research Parkway. The water concentration of $CaCl_2.6H_2O$ were checked before and after measurement. The depth of the mold was 10mm. The literature data for Thermal conductivity at 23°C is 1.088 W/m K. and the measured value was 0.8606 W/m. K at 19.7°C. Table 28 summarizes the solid thermal conductivity results.

Table 28: Calcium chloride hexahydrate ($CaCl_2.6H_2O$) solid phase thermal conductivity measured using thermal plane source (TPS) Technique.

Run	Temp (°C)	Out. Power (mW)	Meas Time (sec)	Th. Conduct (W/mK)	Th. Diffusivity (mm^2/s)	Spec. Heat (MJ/m^3K)	Probing Depth (mm)	Temp Increment (K)
1	19.7	140	160	0.8569	0.3100	2.765	5.45	0.834
2	19.7	140	160	0.8606	0.3126	2.753	5.48	0.833
3	19.7	140	160	0.8641	0.3217	2.686	5.56	0.836
Average				0.8606	0.3148	2.735	5.50	0.834
Std.Dev(± **σ**)				0.0029	0.0050	0.035	0.4	0.001

7.2 Thermal Stability

For a nucleation additive to be practical for certain applications, including its use with PCMs, it must be stable in the presence of the solid or liquid phase over large numbers of melt-freeze cycles and over long periods of time at relevant elevated temperatures. Thermal stability testing allows one to understand the degradation mechanisms. Potential degradation mechanisms include dissolution, agglomeration, oxidation, anion/cation substitution or any other form of reaction that could alter the physical or chemical properties. In this chapter, I present results of selected aging and cycling experiments on nucleation catalyst/calcium chloride hexahydrate mixtures. Tyagi and Buddhi had already studied the effects of 1000 melt-freeze cycles on pure calcium chloride hexahydrate without nucleating additives [70].

7.2.1 1000 Thermal Cycles

Long-term thermal stability of calcium chloride hexahydrate was determined by performing 1000 melt-freeze cycles. The latent heat of fusion and sub-cooling (ΔT) was measured by T-history technique after 250^{th},500^{th},750^{th},1000^{th} cycles and are presented in Table 29 . As summarized in Table 29, the latent heat of fusion remained constant at 178 J/g (σ = 5 J/g) for melting and 181 J/g (σ = 7 J/g) for solidification over 1000 melt-freeze cycle. As the measurement uncertainty is higher than measurement standard deviation (σ) over 1000 cycles. Increase in sub-cooling is observed after 1000 melt-freeze cycles, which was approximately 3.6°C (σ = 12.8 %) but no increment in sub-cooling was noticed in earlier cycles.

Table 29: Effects of 1000 melt-freeze cycle on calcium chloride hexahydrate with 3% strontium chloride performance.

Number of Cycles	Latent Heat (J/g)		ΔT (°C)
	Melting	Solidification	
0	179 (±6)	183(±10)	2.4 (±0.2)
250	186(±7)	189(±9)	2.1 (±0.3)
500	177(±5)	185(±11)	2.3 (±0.3)
750	177(±8)	174(±10)	2.5 (±0.1)
1000	171(±8)	172(±12)	3.6 (±0.5)

Mass gained by calcium chloride hexahydrate was measured after 250th,500th,750th,1000th cycles and summarized in Figure 81. As shown in , mass gained by samples are observed to vary vastly. The average standard deviation of measurement over 1000 melt-freeze cycle was 77%. The main cause of fluctuation in mass change was due to capping of the test-tube. During the initial period of thermal cycling, the caps were not completely tightened due to expansion during thermal cycling.

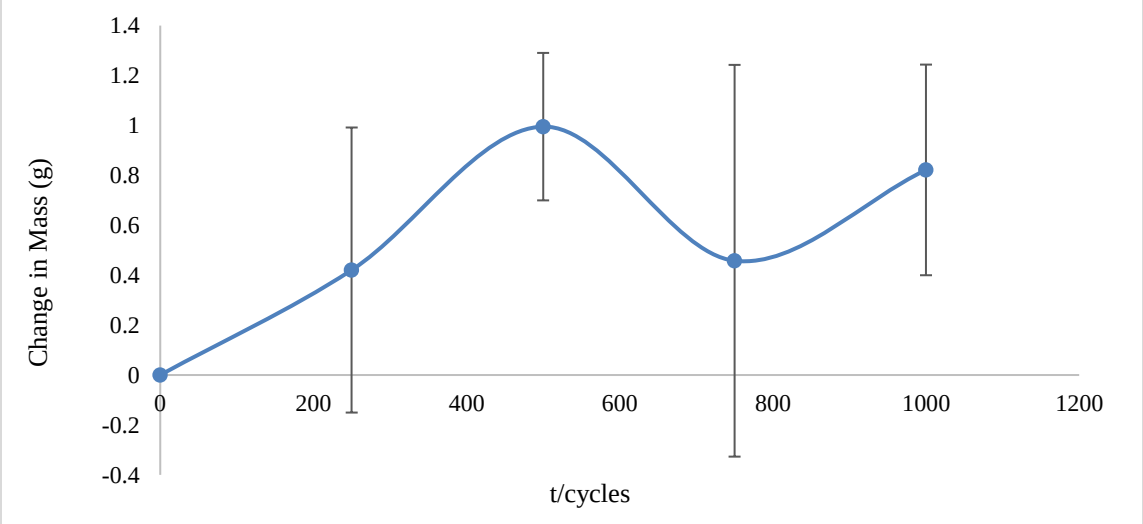

Figure 81: Effects of 1000 melt-freeze cycles on calcium chloride hexahydrate with 3% Strontium chloride mass.

Figure 82 summarizes the change in latent heat of fusion with and without nucleating agents over 1000 melt freeze cycles. The data for pure calcium chloride hexahydrate was obtained from literature [64]. Tyagi et al. studied the effects of 1000 melt-freeze cycles on pure calcium chloride hexahydrate performance in a DSC with a sample mass of 26.38 mg [70], and the authors did not present any results on the effects of thermal cycling on sub-cooling. The authors only utilized the endothermic plots for analyzes. As shown in Figure 82, the change in latent heat capacity did not differ much between samples with and without nucleating additives with thermal cycling. Therefore, we can conclude that the nucleating agents and 1000 melt-freeze cycles did not degrade the energy storage of calcium chloride hexahydrate.

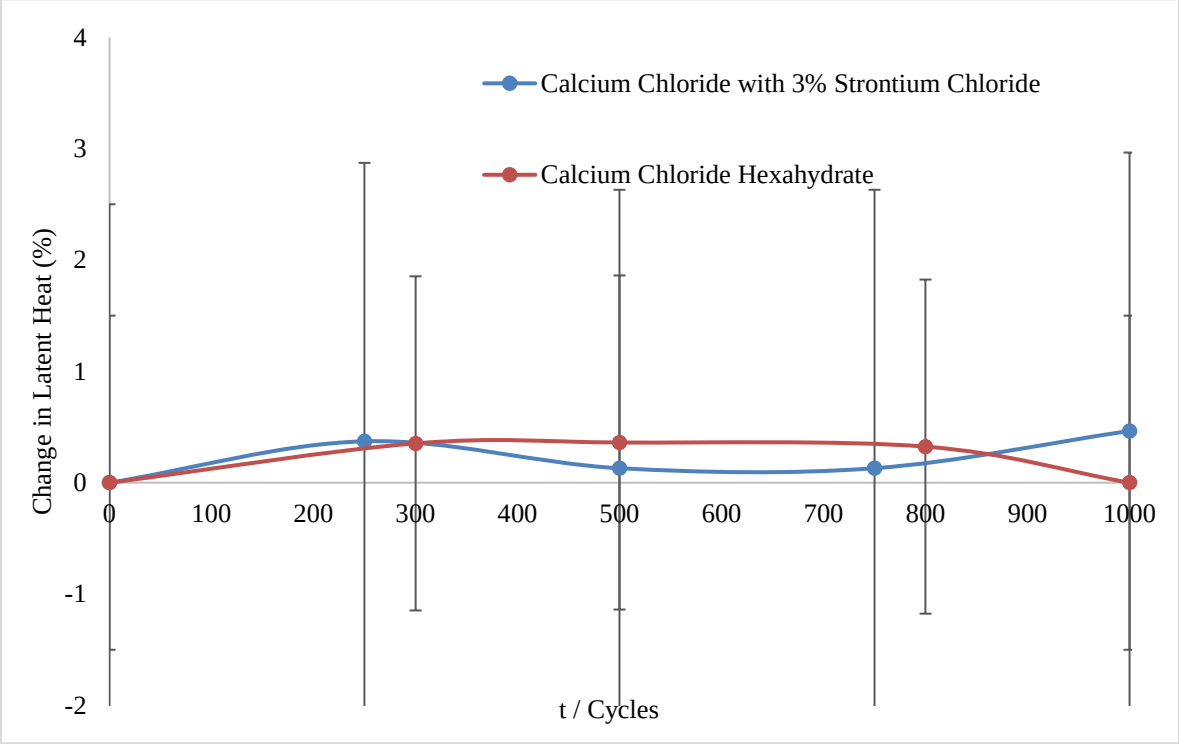

Figure 82: Comparison of change in latent heat of fusion with and without nucleating agents over 1000 melt-freeze cycle. Pure calcium chloride hexahydrate (Red Line) data were obtained from literature [64].

Based on 1000 melt-freeze cycles, it could be acknowledged that the calcium chloride hexahydrate with 3% mass concentration of strontium chloride survived 1000 melt-freeze cycles (i.e. 3.5 years) with a slight increase in sub-cooling at end of 1000 cycles. Physical inspection of the samples showed no form of phase segregation with melt-freeze cycles. To further demonstrate the stability of the calcium chloride hexahydrate with additives, the samples underwent aging test.

7.2.2 Aging Test

The most active nucleation agent strontium chloride was mixed with calcium chloride hexahydrate and aged at 45°C (liquid phase) and 20°C (solid phase) for a period of 30 days. The results demonstrate that calcium chloride hexahydrate with 3% mass concentration strontium chloride is not susceptible to aging in both liquid and solid phases. As summarized in Figure 83, latent heat energy storage capacity remained constant at around 185 J/g for a period of 30 days when aged at 45°C and 20°C. Similarly, sub-cooling remained constant at around 2.7°C when samples were aged at 45°C and 20°C for period of 30 days as summarized in Figure 84. The sudden increase in sub-cooling at end of 20 days is within the measurement uncertainty, therefore the materials did not degrade at end of 20 days.

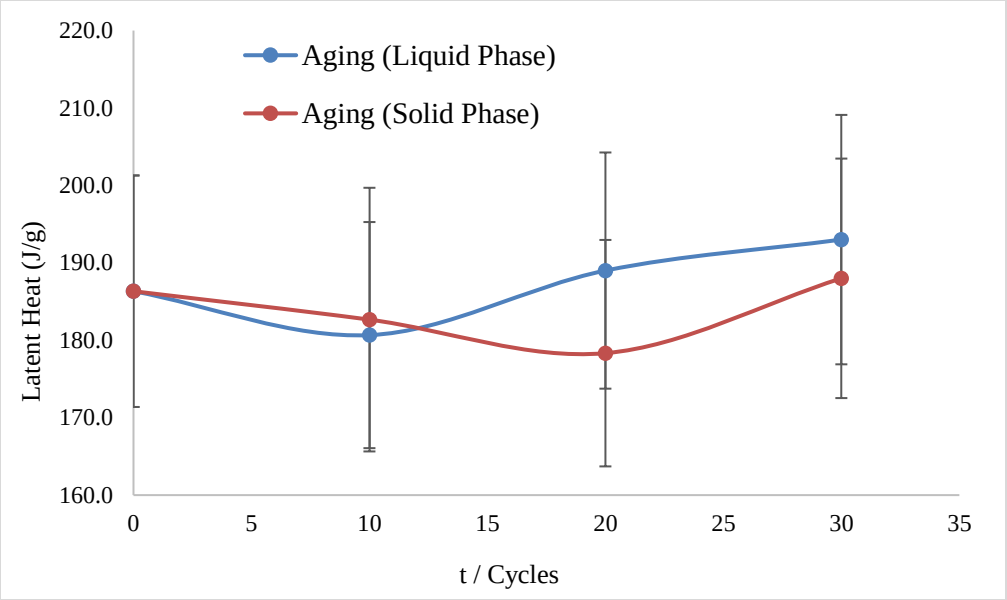

Figure 83: Effects of aging on calcium chloride hexahydrate with 3% strontium chloride's latent heat over a period of 30 days.

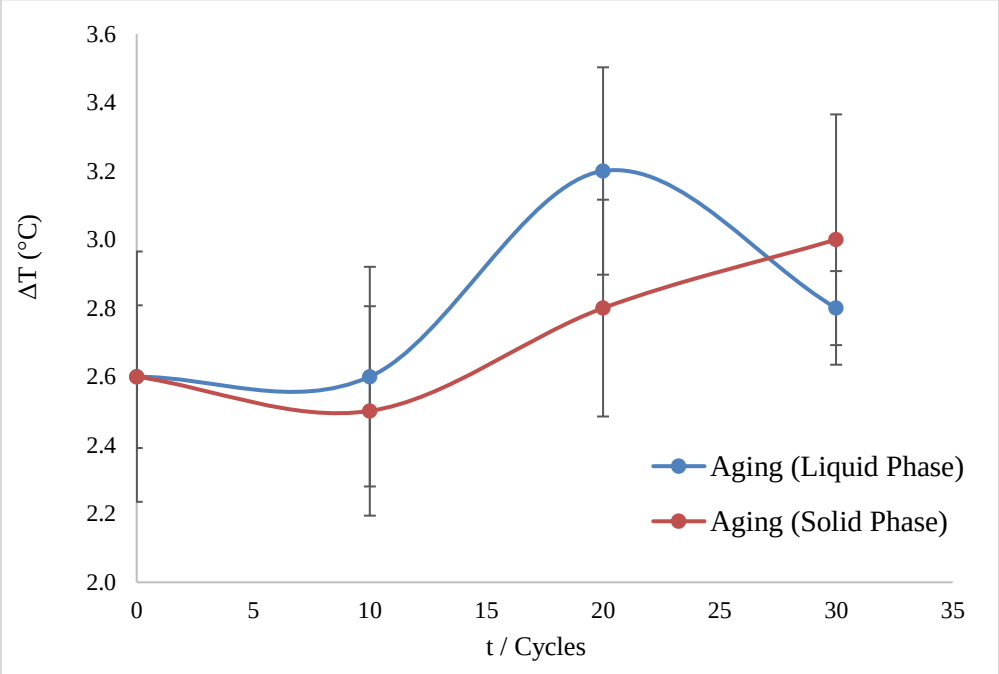

Figure 84: Effects of aging on calcium chloride hexahydrate with 3% strontium chloride's sub-cooling over a period of 30 days.

7.2.3 Effects of Water

Calcium chloride is hygroscopic, hence during thermal cycling the samples could absorb moisture from the environment to the point of equilibrium. Therefore, the effects of water on thermal performance were analyzed during thermal cycling. As shown in Figure 85 , increase in water concentration reduced sub-cooling slightly. But the reduction in sub-cooling is within the measurement uncertainty, therefore no concise conclusion could be derived. With 1% increment in water concentration the degree of sub-cooling was 2.2°C whereas at stichometry concentration the sub-cooling was measured to be 2.7°C, therefore that is 0.5°C reduction.

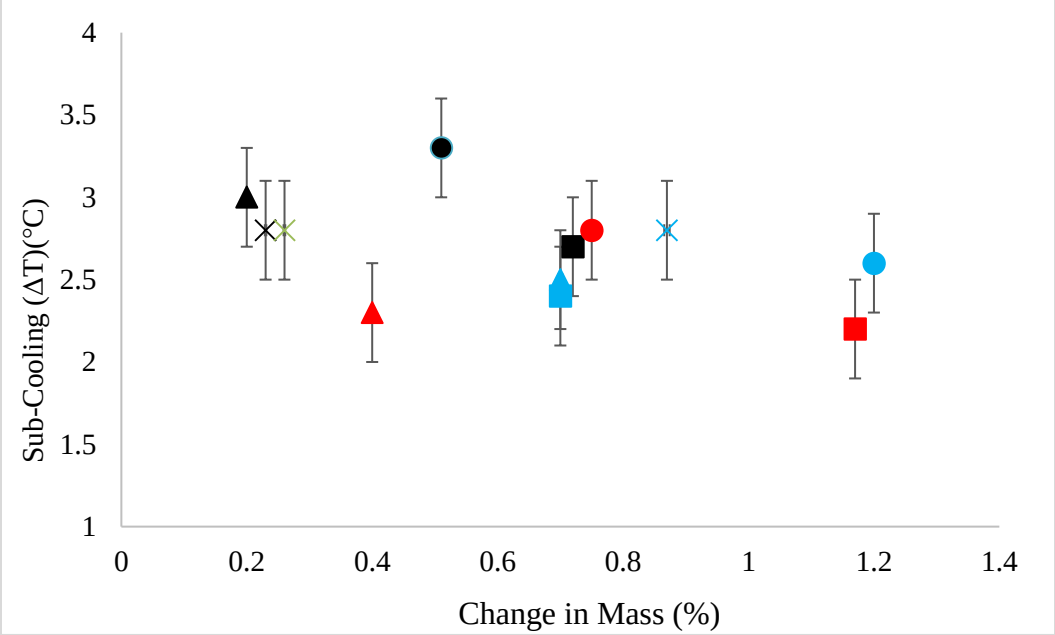

Figure 85: Effects of water absorption during thermal cycling on sub-cooling of calcium chloride hexahydrate.

As shown in Figure 86, both thermal cycling and change in water concentration had an impact on the latent heat storage capacity. Samples least mass change showed no variation in energy storage capacity, whereas samples with more than 0.4% change in mass concentration

showed 4% reduction in energy storage capacity whereas with 1% increment in mass, the energy storage capacity was rescued by 13% and the degradation was amplified with thermal cycling.

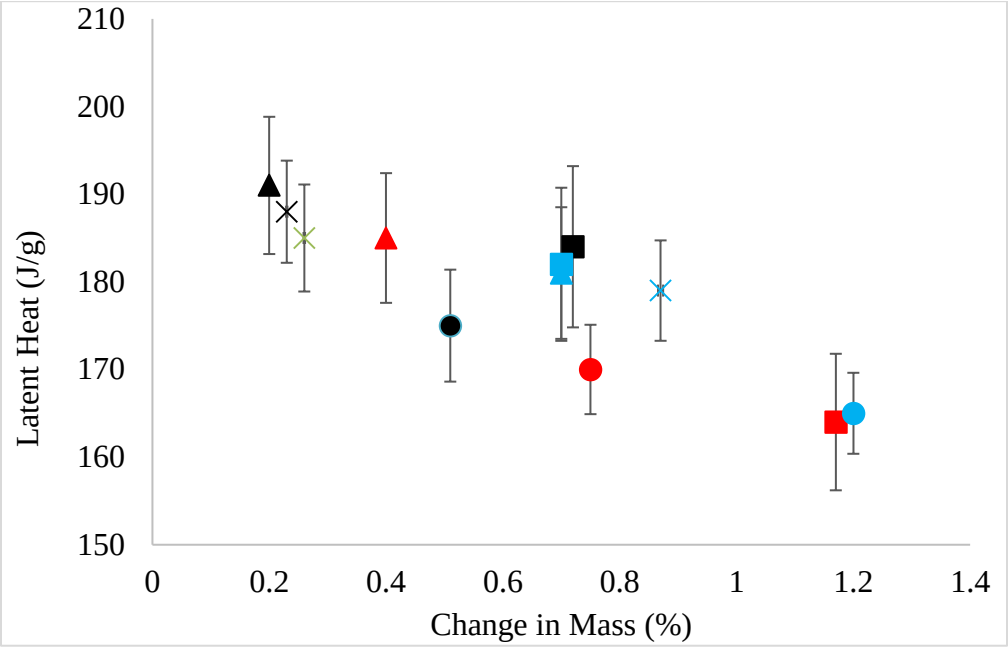

Figure 86: Effects of water absorption during thermal cycling on energy storage capacity of calcium chloride hexahydrate.

7.3 Summary and Recommendation

In summary, the main problem with calcium chloride hexahydrate was excess sub-cooling. The excess sub-cooling in calcium chloride hexahydrate can be controlled by addition of nucleation additives. The nucleating additives considered for calcium chloride hexahydrate was strontium chloride and sodium chloride. The 3% mass concentration of strontium chloride reduced sub-cooling in calcium chloride hexahydrate and remained constant over multiple melt-freeze cycles, and at elevated temperature without degradation in latent heat energy storage capacity. The degradation in energy storage density is comparable to data's available in literatures for pure calcium chloride hexahydrate. Therefore, calcium chloride hexahydrate with 3% mass concentration is a good candidate for latent heat thermal energy storage.

In conclusion, sub-cooling in lithium nitrate trihydrate was reduced by 3 times (i.e. 9.0°C to 2.6°C) and maintained over 1000 melt freeze cycles. The maximum energy storage degradation with 1000 melt-freeze cycle was 2.3% which was below the measurement uncertainty. With aging test, it could be concluded that both calcium chloride hexahydrate and strontium chloride are not sensitive when exposed to elevated temperatures and supercooled temperatures of 40°C and 20°C for prolonged periods. With thermal cycling analyzes, it was concluded that water absorption is the main contributor to degradation to energy storage capacity, variation in phase transition temperature, and had negligible effects on sub-cooling and phase transition temperature.

Future recommendation is to understand and study different encapsulation techniques (e.g. Macro, Micro, Nano) to prevent or reduce water absorption. Secondly conduct to continuous melt-freeze cycle to failure, for documenting the actual failure rate and cause of failure.

CHAPTER VIII

CHARACTERIZATION OF ZINC NITRATE HEXAHYDRATE

Phase change materials (PCM) store large quantities of energy in small form factors due to the high values of latent heat involved during phase change (e.g., from solid to liquid). However, they often require low temperatures (i.e., subcooling below the melting point) to initiate solidification. Heterogeneous nucleation enables reduction in the values of sub-cooling, $(\Delta T)_{sub}$, during the solidification of PCMs. Identification of material-specific nucleation promoters (or "nucleators") remains non-trivial. In this chapter we investigate heterogeneous nucleation in a chosen thermal energy storage material, Zinc nitrate hexahydrate, $Zn(NO_3)_2.6H_2O$. Previously recommended heterogeneous nucleators were zinc oxide (ZnO) and impurities [6] without any specific causality being identified that justifies the specific selection of this nucleator. In last 30 years, no systematic study was conducted to study the effects of different heterogenous nucleators on zinc nitrate hexahydrate. In one study, the heterogenous nucleators were selected based on the relation between subcooling and lattice mismatch between the planes of closely packed polyhedral sites of PCMs [28]. In this study, the operational performance of zinc nitrate hexahydrate as PCM candidate was improved through heterogenous nucleation and the stability was studied to ensure that the PCM survived over 1000 thermal cycles. The heterogeneous nucleators considered in this study were zinc oxide [ZnO] and zinc hydroxyl nitrate [$Zn_3(OH)_4(NO_3)_2$]. The results have shown that the heterogenous nucleators reduce sub cooling by as much as 100%, increased the energy storage and survived up to 1000 cycles of repeated melting and solidification.

---

*Part of this chapter is reprinted with permission from "Exploring additives for improving the reliability of zinc nitrate hexahydrate", by N. Kumar, D. Banerjee and R. Chavez, 2018, Journal of Energy Storage, Copyright 2018 by Rightslink License.

8.1 Initial Characterization

The initial characterization of zinc nitrate hexahydrate was conducted using T-history technique. The measurement was performed between 24°C and 45°C. As summarized in Figure 87 , the volumetric energy storage capacity of zinc nitrate hexahydrate was around ~290 MJ/m^3 for melting and ~246 MJ/m^3 for solidification, which is close to that of literature [6]. The phase transition occurred at 34.6°C. Therefore, zinc nitrate hexahydrate is an attractive PCM candidate since it has a low melting point, and relatively large latent heat of fusion as well as large volumetric heat of fusion. The volumetric energy storage density is approximately double the energy densities of comparable organic PCMs (such as paraffins) with similar melting point.

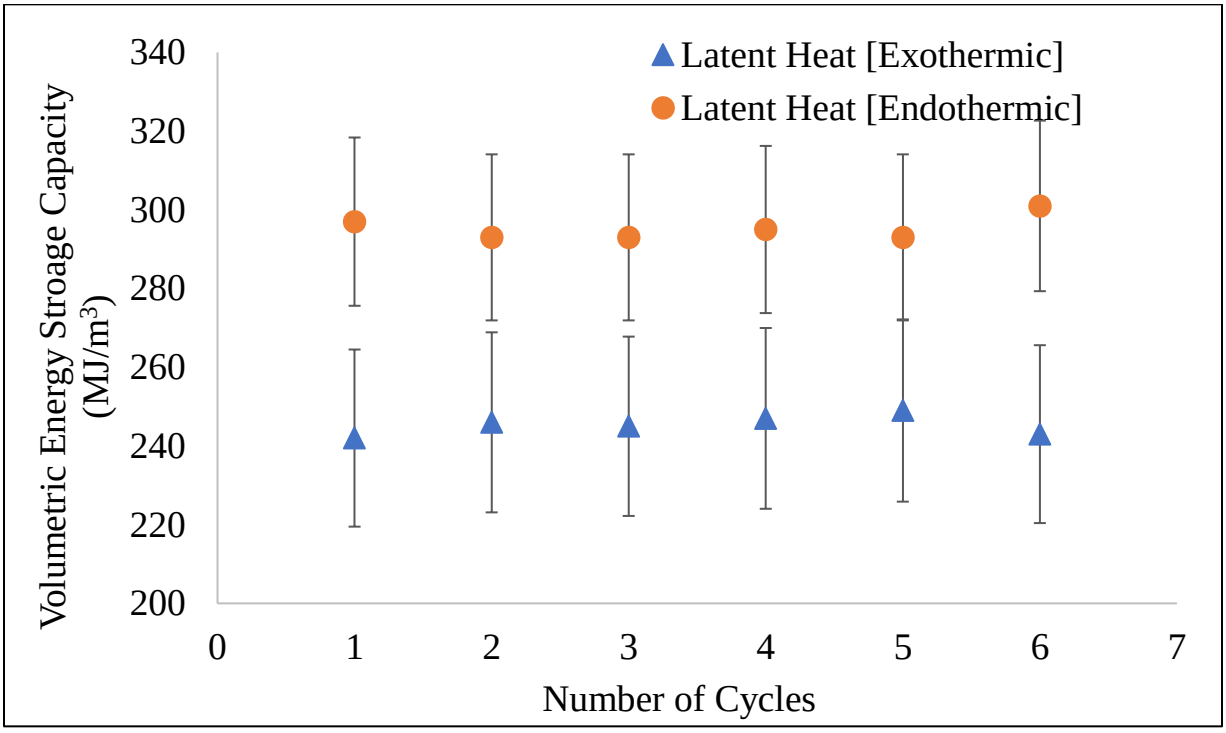

Figure 87: Initial characterization of zinc nitrate hexahydrate utilizing T-history technique. The air temperature was ramped between 45°C and 24°C.

Initial studies as summarized in Figure 88, suggests sub-cooling in excess of $\Delta T = 12°C$. However, undercooling is not an intrinsic material property, and may be affected by experimental parameters which affect nucleation rates (e.g., cooling rates, sample volume, container material, vibration and sample purity). The increase in sub-cooling suggests that whatever heterogeneities may have initially existed in the liquid zinc nitrate hexahydrate dissolved, reacted or passivated during thermal cycling. Thus, undercooling remains problematic in zinc nitrate hexahydrate, and cannot be overcome simply by introducing an arbitrary solid particle into the mixture.

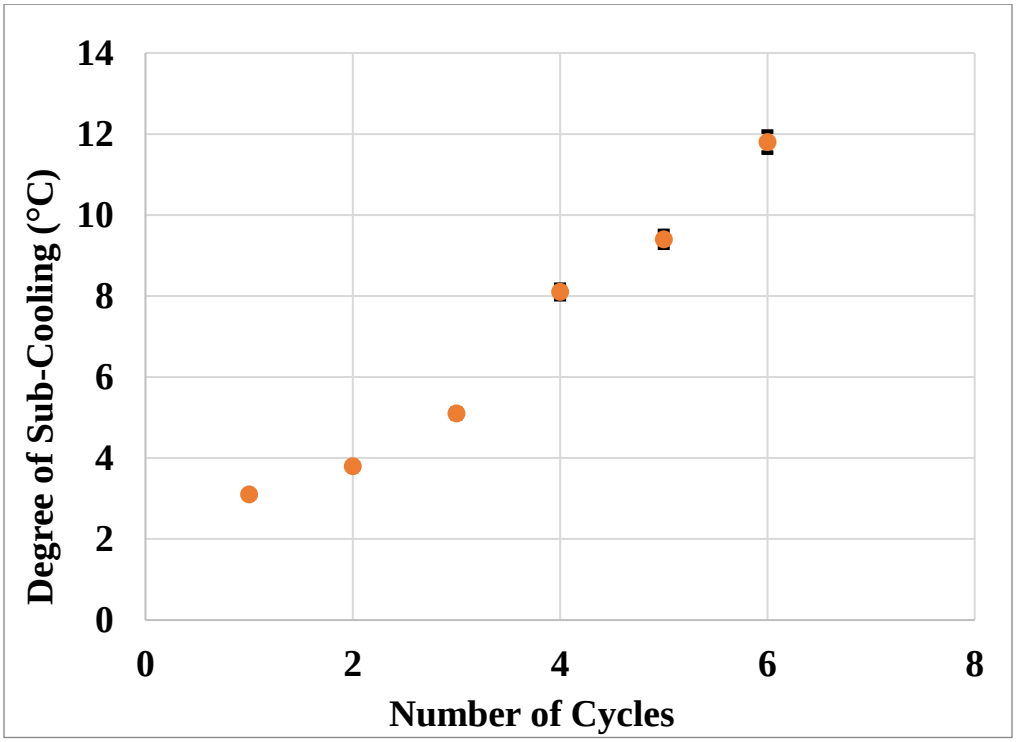

Figure 88: Degree of sub-cooling in zinc nitrate hexahydrate with 6 thermal cycles.

Candidate nucleation catalyst phases were experimentally screened to quantify their effect on sub-cooling in zinc nitrate hexahydrate. The candidate nucleation catalyst may be crystals of a material which resembles the storage material in structure and lattice parameters. Generally, it is

true that a lower lattice mismatch leads to a smaller degree of -sub-cooling. The selected candidates with the lowest mismatch were zinc hydroxyl nitrate and zinc oxide. Concentration dependence of sub-cooling was quantified for zinc hydroxyl nitrate as well as for zinc oxide. In the case of Zinc hydroxyl nitrate and zinc oxide, sub-cooling decreases monotonically with increasing concentration of nucleation agent to a sub-cooling of 3.6°C for zinc hydroxyl nitrate and 3.2°C for zinc oxide. In conclusion the degree of sub-cooling is insensitive to concentration if the concentration is more than 1% as shown in Figure 89.

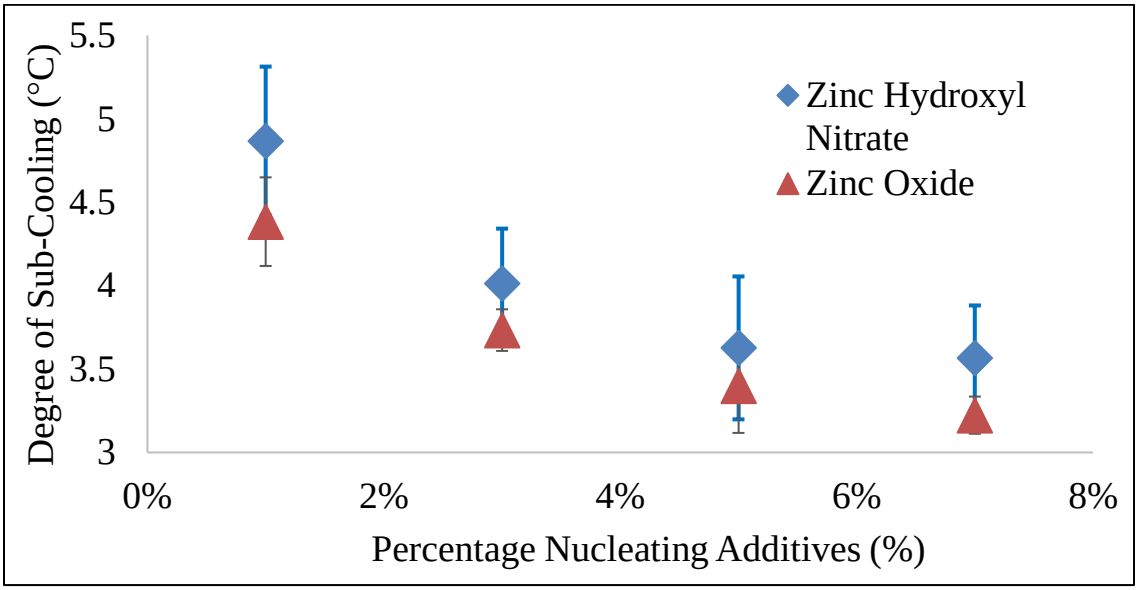

Figure 89: Effects of zinc hydroxyl nitrate and zinc oxide nucleation additives concentration (mass %) on suppressing sub-cooling in zinc nitrate hexahydrate. The increasing concentration of nucleating additives had negligible effect on suppressing sub-cooling. The additives even at low concentration was able to maintain a 3°C sub-cooling.

The initial characterization of zinc nitrate hexahydrate with and without additives showed reduction in energy storage capacity. As shown in Figure 90, the sample with nucleating agent showed 8% (maximum) degradation in the energy storage capacity. The decrease in thermal energy storage capacity is due to addition of 5% mass additives.

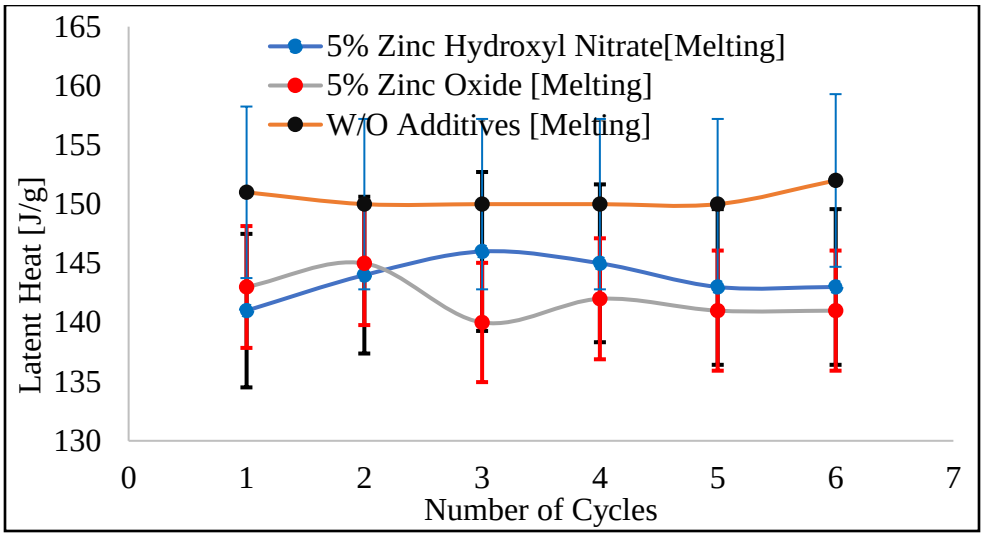

Figure 90: Effect of nucleating additive (zinc hydroxyl nitrate and zinc oxide) on energy storage capacity of zinc nitrate hexahydrate.

The energy storage capacity reduced by 8% with nucleating agents, the degree of sub-cooling was enhanced by 65%, as shown in Figure 91. The degree of sub-cooling remained constant over 6 thermal cycles, which wasn't the case for zinc nitrate hexahydrate without additives.

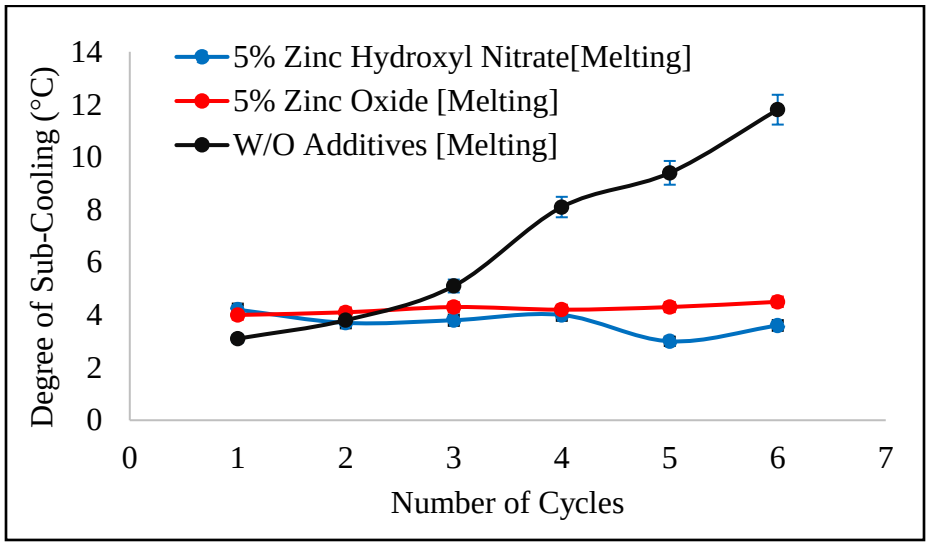

Figure 91: Effect of nucleating additive (zinc hydroxyl nitrate and zinc oxide) on sub-cooling capacity of zinc nitrate hexahydrate.

8.2 Thermal Stability

For a nucleation catalyst to be practical for certain applications, including its use with PCMs, it must be stable in the presence of the solid or liquid phase over large numbers of melt-freeze cycles and over long periods of time at relevant temperatures. Thermal stability testing allows one to understand the degradation mechanisms. Potential degradation mechanisms include dissolution, agglomeration, oxidation, anion/cation substitution or any other form of reaction that could alter the physical or chemical properties. In this chapter, I present results of selected aging and cycling experiments on pure zinc nitrate hexahydrate and nucleation catalyst/zinc nitrate hexahydrate mixtures.

8.2.1 1000 Thermal Cycles

Thermal stability was determined by performing 1000 melt-freeze cycles on an in-house thermal cycle test rig as shown in Figure 25. The value of the latent heat of fusion of zinc nitrate hexahydrate was measured by T-history technique after 250^{th},500^{th},750^{th},1000^{th} cycles and presented in Table 30. As can be seen from Table 30, the reduction in the latent heat of fusion of zinc nitrate hexahydrate with 5% zinc oxide is observed after 750 melt-freeze cycles which is approximately 16% and further reduction in latent heat of fusion of almost 21% after 1000^{th} cycle, similar trends are also noticed in zinc nitrate hexahydrate without additives and 5% zinc hydroxyl oxide. In the case zinc nitrate hexahydrate without additives, 24% reduction in latent heat of fusion was observed after 750 melt-freeze cycles and remained constant for 1000^{th} cycles, whereas zinc nitrate hexahydrate with 5% zinc hydroxyl nitrate 17% reduction in latent heat of fusion was observed after 750 melt-freeze cycles and remained constant.

Table 30: Latent heat of fusion of zinc nitrate hexahydrate with and without nucleating additives during the thermal cycle test. The nucleating additives (zinc hydroxyl nitrate and zinc oxide) were added at 5% mass concentration.

Cycle	Zinc Nitrate Hexahydrate without additives	Zinc Nitrate Hexahydrate with 5% Zinc Oxide	Zinc Nitrate Hexahydrate with 5% Zinc Hydroxyl Nitrate
0	143 (σ±1.4%)	145 (σ±2.9%)	143 (σ±1.4%)
250	138(σ±2.2%)	143 (σ±2.1%)	137 (σ±2.2%)
500	136(σ±4.9%)	143(σ±2.3%)	135 (σ±4.3%)
750	108 (σ±5.2%)	122 (σ±3.2%)	118(σ±3.5%)
1000	103 (σ±1.4%)	115 (σ±2.3%)	115(σ±3.6%)

The value of the sub-cooling of zinc nitrate hexahydrate was measured by T-history technique after 250^{th},500^{th},750^{th},1000^{th} cycles and presented in Table 31. As can be seen from Table 31, the increase in degree of sub-cooling of zinc nitrate hexahydrate with 5% zinc oxide is observed after 250 melt-freeze cycles which is approximately 19% but no further increment in degree of sub-cooling is subsequently noticed in between 500^{th},750^{th}, and 1000^{th} cycle and 0^{th} cycle. The increase in degree of sub-cooling of zinc nitrate hexahydrate with 5% zinc hydroxyl nitrate is observed after 1000 melt-freeze cycles which is approximately 0.6°C but no further increment in degree of sub-cooling is subsequently noticed in between 250^{th}, 500^{th},750^{th}, and 0^{th} cycle. Whereas for zinc nitrate hexahydrate without additives showed 340% increment in sub-cooling after 1000 melt-freeze cycle, which is approximately 17.6°C. Therefore, additives surpassed sub-cooling by as much as 86% and 75% with 5% mass concentration of zinc oxide and zinc hydroxyl nitrate respectively. Without nucleating agents, the system could undergo catastrophic failure, as the onset of nucleation temperature is below the system operation temperature after 250^{th} cycle.

Table 31: Degree of Sub-cooling (ΔT) of zinc nitrate hexahydrate with and without nucleating additives during the thermal cycle test. 5% mass concentration of zinc hydroxyl nitrate or zinc oxide were added.

Cycle	Zinc Nitrate Hexahydrate without additives	Zinc Nitrate Hexahydrate with 5% Zinc Oxide	Zinc Nitrate Hexahydrate with 5% Zinc Hydroxyl Nitrate
0	4.0 (σ±1.0%)	2.6 (σ±2.0%)	3.8 (σ±1.0%)
250	3.9(σ±3.0%)	3.1 (σ±1.8%)	2.9 (σ±1.6%)
500	11.6(σ±2.3%)	2.8(σ±1.0%)	3.4 (σ±0.8%)
750	15.1(σ±3.9%)	2.3(σ±1.6%)	3.9 (σ±1.9%)
1000	17.6(σ±3.4%)	2.4(σ±1.0%)	4.4 (σ±0.4%)

The value of the mass gained by zinc nitrate hexahydrate was measured after 250^{th},500^{th},750^{th},1000^{th} cycles and presented in Table 32. As can be seen from Table 32, mass gained by zinc nitrate hexahydrate with 5% zinc oxide is observed to be constant over 1000 melt-freeze cycle which is approximately 0.4%. Similar trends were also noticed with zinc nitrate hexahydrate without additives and with 5% zinc hydroxyl nitrate.

Table 32: Mass gained by zinc nitrate hexahydrate with and without nucleating additives during the thermal cycle test. The nucleating additives (zinc hydroxyl nitrate and zinc oxide) were added at 5% mass concentration.

Cycle	Zinc Nitrate Hexahydrate without additives	Zinc Nitrate Hexahydrate with 5% Zinc Oxide	Zinc Nitrate Hexahydrate with 5% Zinc Hydroxyl Nitrate
250	0.77 (σ±11.2%)	0.37 (σ±8.5%)	0.37 (σ±6.5%)
500	0.72 (σ±10.8%)	0.50 (σ±6.8%)	0.5 (σ±5.3%)
750	0.9 (σ±8.8%)	0.42 (σ±7.3%)	0.52(σ±7.7%)
1000	1.1 (σ±9.6%)	0.36 (σ±3.7%)	0.71(σ±6.1%)

Based on 1000 melt-freeze cycles, it could be acknowledged that the start degradation of zinc hydroxyl nitrate with and without additives starts after 500 and before 750 melt freeze cycles. The cause of degradation is not due to mass gain, as mass gain remained constant throughout the

1000 melt-freeze cycles. Therefore, the samples were physically analyzed for mode of degradation as shown in Figure 92. As can be seen from Figure 92, the phase segregation increased by 83% between 250th cycle to 1000th cycle (based on the measurement of change in height).

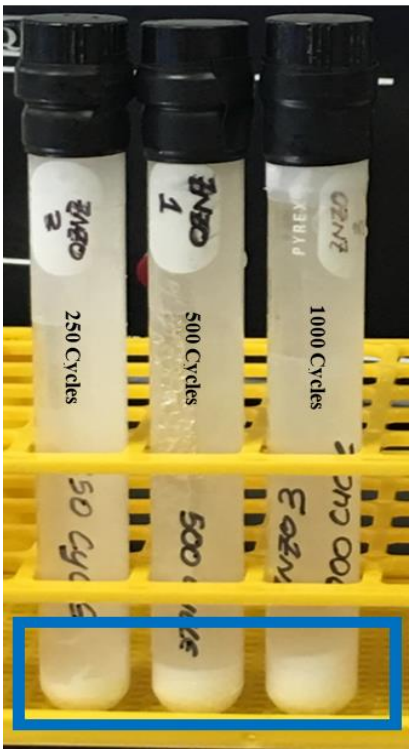

Figure 92: Phase segregation of zinc nitrate hexahydrate with 5% zinc oxide nucleating additives after 500 melt-freeze cycles.

Zinc nitrate hexahydrate were further evaluated with and without additives, the samples were re-analyzed at lower temperature by T-history technique after 750th and 1000th cycle. As shown in Figure 93, the samples when exposed to lower temperature (i.e. 15°C) a new secondary phase is formed with thermal cycling. This behavior closely follows the trends of phase segregation as shown in Figure 92. Due to the formation of secondary phase, latent heat of fusion was reduced 34 J/g in samples without additives and 22J/g in samples with additives after 750 cycles. in Appendix C shows the difference in visual appearance when solidified at 24°C and 15°C. To

further demonstrate the stability of the zinc nitrate hexahydrate with and without additives, the samples underwent aging test.

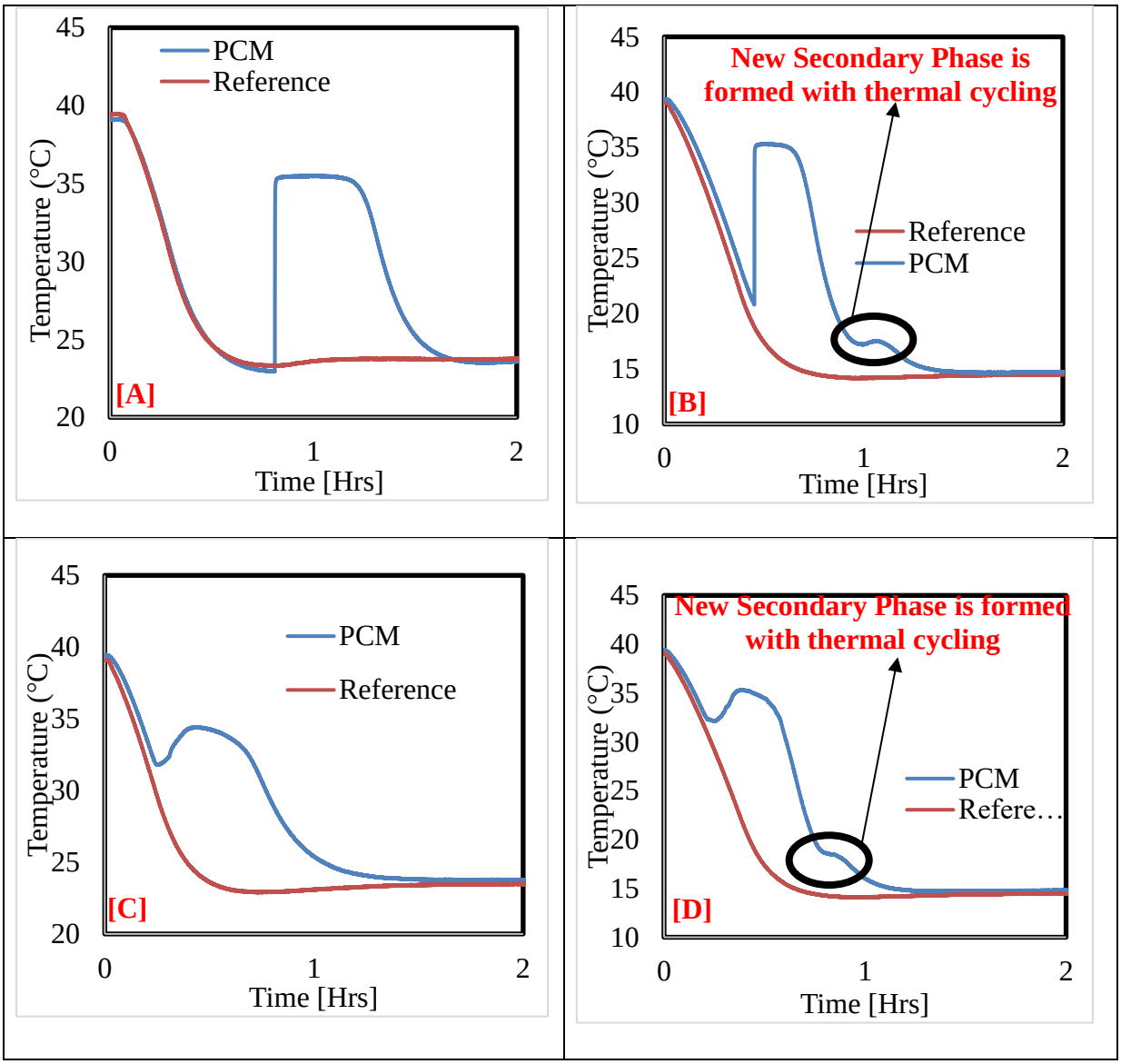

Figure 93: T-History of Zinc Nitrate Hexahydrate with and without additives after 750 cycles [A]: Without additives cooled at 24°C; [B]: Without additives cooled at 15°C; [C]: With 5% zinc hydroxyl nitrate cooled at 24°C; [D]: With 5% zinc hydroxyl nitrate cooled at 15°C.

8.2.2 Aging Test

The two most active nucleation agents (i.e. zinc oxide and zinc hydroxyl identified were mixed with zinc nitrate hexahydrate and aged at 45°C (liquid phase) and 24°C (solid phase) for a period of 30 days. Detail description on aging test is provided in section 4.3. Our results clearly demonstrate that zinc hydroxyl nitrate and zinc oxide are not susceptible to aging. As shown in Figure 94(A), aging at 45°C (i.e. liquid phase) showed no change in sub-cooling remained constant at around 3°C and 4.5°C for zinc oxide and zinc hydroxyl nitrate respectively. Whereas for aging at 20°C (i.e. solid phase) for periods of 30 days showed change in sub-cooling, sub-cooling for zinc oxide increased from ΔT = 3 - 4°C (33% increase), and sub-cooling for zinc hydroxyl nitrate reduced from ΔT = 4.5 - 2.9C (35% decrease). Agglomeration was clearly visible after prolonged aging in both liquid and solid phase. The degradation of zinc nitrate hexahydrate in nucleating additives has not been previously reported. Despite this, even after prolonged aging, sub-cooling is still significantly lower than neat zinc nitrate hexahydrate, and lower than observed with any other reported nucleation agent.

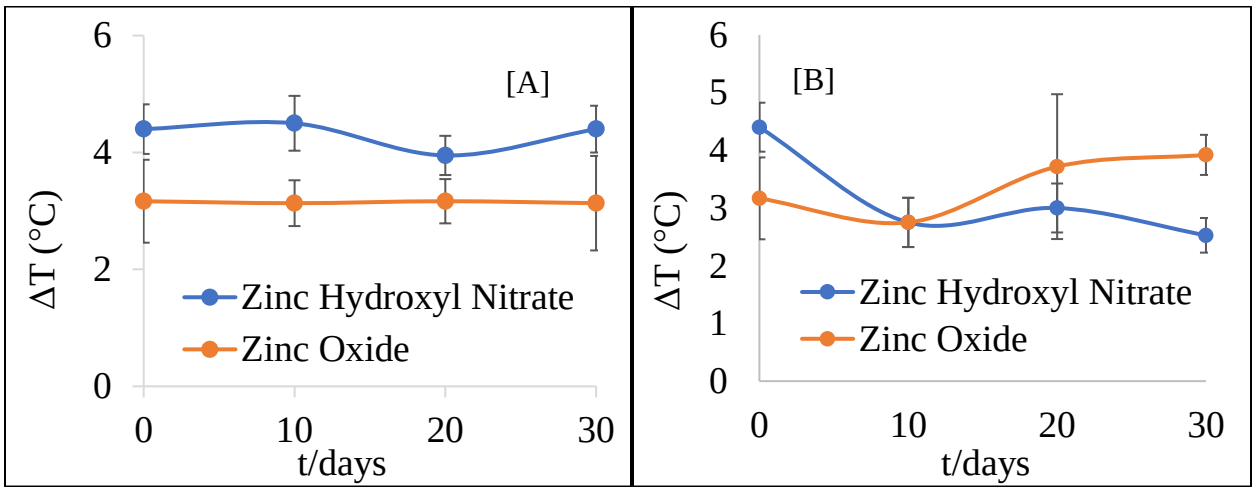

Figure 94: Degree of Sub-Cooling (°C) (A) Aging as a function of time held at 45°C (T > Tm of Zinc Nitrate Hexahydrate) and (B) Aging as a function of time held at 20°C (T < Tm of Zinc Nitrate Hexahydrate). Uncertainty bars represent σ variations observed over triplicate samples.

Our results as shown in Figure 95 (A) clearly demonstrates that energy storage density of zinc nitrate hexahydrate with zinc hydroxyl nitrate and zinc oxide is susceptible aging at 45°C (i.e. liquid phase). The energy storage density of zinc nitrate hexahydrate with zinc hydroxyl nitrate decreased from 143 to 95 J/g (34% decrease), whereas with zinc oxide the energy storage density decreased from 144 to 125 J/g (13% decrease). As summarized in Figure 95 (B), no change in energy densities were noticed in samples aged at 20°C (i.e. solid phase) for 30 days. The main cause of degradation in phase segregation as shown in Appendix C. At the end of 30 days, the phase segregation in both samples were 9%, therefore we lost 9% of energy storage capacity. Another reason for degradation of zinc nitrate hexahydrate with zinc hydroxyl nitrate due to dissolution of zinc hydroxyl nitrate into zinc nitrate hexahydrate and mass gained by sample during the thermal cycling. The mass gained by the samples are summarized in Figure 96, samples aged at 45°C (i.e. liquid) for 30 days showed a maximum mass gain of 1% and samples aged at 20°C (i.e. solid) for 30 days showed a maximum mass gain of 0.4%.

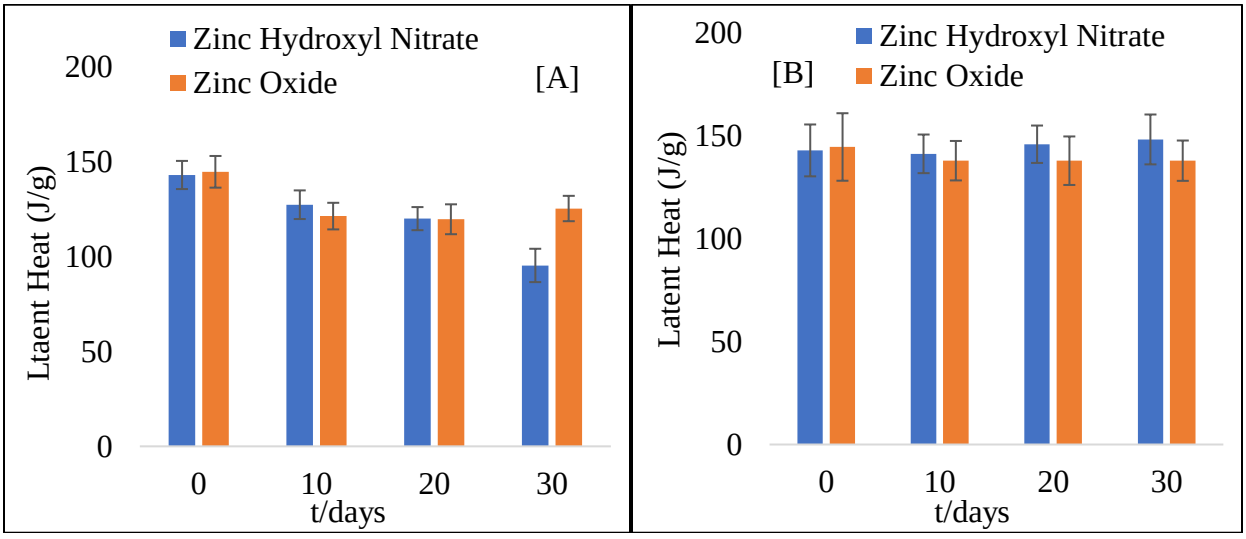

Figure 95: Latent Heat (J/g) (A) Aging as a function of time held at 45°C (T > Tm of Zinc Nitrate Hexahydrate) and (B) Aging as a function of time held at 20°C (T < Tm of Zinc Nitrate Hexahydrate). Uncertainty bars represent σ variations observed over triplicate.

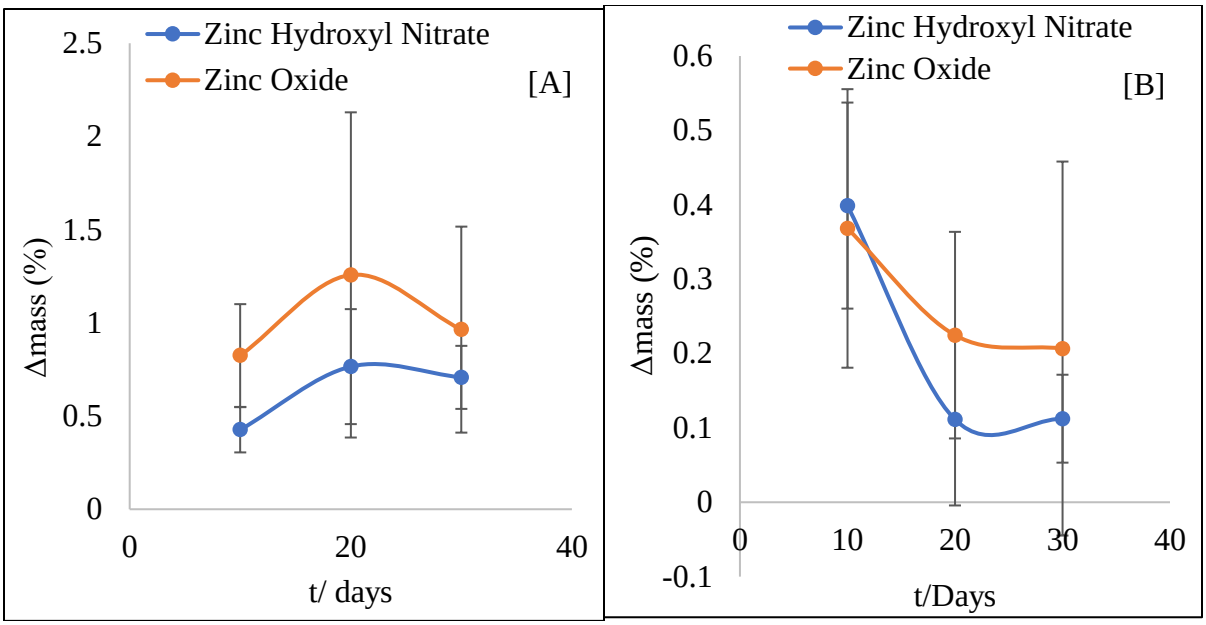

Figure 96: Change in mass (%) (A) Aging as a function of time held at 45°C (T > Tm of Zinc Nitrate Hexahydrate) and (B) Aging as a function of time held at 20°C (T < Tm of Zinc Nitrate Hexahydrate). Uncertainty bars represent σ variations observed over triplicate.

8.3 Summary and Recommendation

Zinc nitrate hexahydrate, Zn (NO3)2·6H2O is an attractive candidate as a Phase Change Material (PCM) since it has a low melting point (of 35 °C), and relatively large latent heat of fusion (145 J/g) as well as large volumetric heat of fusion (269 MJ/m3 ~ 284 MJ/m3). The volumetric energy storage density is approximately double the energy densities of comparable organics PCMs (such as paraffins) with similar melting points. Thus, zinc nitrate hexahydrate (ZNHH) is amenable for realizing compact and light-weight platforms for thermal energy storage (TES). However, ZNHH often requires high degree of sub-cooling to initiate solidification that has impeded the adoption of this PCM for conventional applications. Historically, very few nucleation agents have been found to be compatible with ZNHH that can reduce sub-cooling and are reliable (i.e., can survive a large number of thermal cycles). In this disclosure, the performance of ZNHH was measured experimentally for 1000 thermal-cycles of repeated melting and solidification by incorporating additives (nucleation promoters) into the PCM samples. The heterogeneous nucleation promoters (nucleators) considered in this study were zinc oxide (ZnO) and zinc hydroxyl nitrate (Zn3(OH)4(NO3)2 or "ZHN"). The material selection for the nucleators were based on the melting point mismatch as well as the affinity of the crystal lattice structures between the PCM and the nucleators.

The experimental measurements show that these nucleators reduced sub-cooling significantly (initially 5.6°C and finally 3.0°C for ZnO after 1000 cycles; initially 3.8 °C and 4.4°C after 1000 cycles for ZHN). However, pure ZNHH (without additives) suffered from the requirement for high sub-cooling (initially 3.5 °C and 17.6 °C after 6 cycles).

The additives minimized the degradation of thermal performance, i.e., energy storage capacity (20% degradation after 1000 cycles for ZnO; 20% after 1000 cycles for ZHN) and enhanced the reliability by ensuring the survival of the PCM for 500 ~ 1000 cycles (melt-freeze cycles). The degradation in latent heat storage density is due to phase segmentation and formation of another new phase at 15°C.Our results clearly demonstrate that zinc hydroxyl nitrate and zinc oxide are not susceptible to aging with no changes in degree of sub-cooling, but the energy storage density when held in liquid phase showed 23% degradation after 30 days. The degradation is due to phase segmentation.

CHAPTER IX

CHARACTERIZATION OF SODIUM SULFATE DECAHYDRATE

Latent Heat storage using phase change materials (PCMs) is one of the most efficient methods to store thermal energy. The usage of PCMs in thermal energy storage (TES) has been a main topic of research for last 20 years. PCMs have the capability to store energy in the form of sensible heat and latent heat. Therefore, PCMs are particularly attractive due to their ability to provide high energy storage capabilities. A suitable phase transition temperature and a large energy storage density are the two most vital requirements for selection of phase change materials. Inorganic materials, particularly salt hydrates cover a wide range of phase transition temperature. Among all the potential salt hydrate PCM candidates for thermal energy storage, sodium sulfate decahydrate ($Na_2SO_4.10H_2O$) also known as Glauber's salt are of particular interest due to their low phase transition temperature of 32°C and large latent heat storage density of 251 KJ/Kg. However, Glauber salts are susceptible to degree of sub cooling of more than 14°C and melts incongruently. The severity of incongruent melting increases with rising temperature, as the solubility of Na_2SO_4 decreases further, thus prevents the formation of a homogeneous liquid. Such melting and freezing behavior could severely reduce the latent heat storage density and alter the phase transition temperature. However, the advantages of Glauber's salt are so convincing that great deals of work are carried out to overcome its deficiencies. The aim of this paper is to study the effects of a gelling, thickening, and nucleating agent on Glauber's salt with thermal cycling. The initial thermal characterization measurements were evaluated using differential scanning Calorimetry (DSC) and the thermal cycling were evaluated using T-History method to eliminate the sample size variability.

9.1 Initial Characterization

The initial thermal characterization experiments for sodium sulfate decahydrate were performed using MDSC Q2000 and T-History. The sample mass was 14.306 mg and 25.940g respectively. The ramp rate of MDSC was pre-programmed at 5.2°C/min with a modulation of 0.48°C/min. The testing in MDSC were performed at 0°C to 60°C. Table 33 summarizes the MDSC results of sodium sulfate decahydrate. The measured latent heat during melting and solidification varies by 50%. The difference in latent heat measurement between T-History and MDSC is due to inherent sub-cooling and phase segregation in salt hydrates. It is shown Figure 97 the degree of sub-cooling is observed to be around 25°C and able to recover only 104 J/g of latent heat energy storage during the solidification phase. It is shown in Figure 98 , during endothermic reaction multiple peaks are observed. The peaks could be due to phase segregation in sodium sulfate decahydrate, causing intermediate and random phase transition. The measured average latent heat during endothermic was 210J/g.

Table 33: MDSC summary result of sodium sulfate decahydrate.

	Specific heat Liquid (J/g k) (ε_1)	**Specific heat Solid (J/g k) (ε_1)**	**MP (°C) (ε_1)**	**FP (°C) (ε_1)**	**Latent Heat [Endo] (J/g) (ε_1)**	**Latent Heat [Exo] (J/g) (ε_1)**
First Run	2.70 (3.1%)	2.65 (52.5%)	32.15 (0.2%)	7.98 (0.2 %)	135.82 (1%)	109 (1.8%)
Second Run	2.70 (3.0%)	1.63 (41.0%)	32.15 (0.2 %)	6.76 (0.2%)	233.46 (1.5%)	103 (1.8%)
Third Run	2.70 (3.0 %)	2.18 (6.9 %)	32.29 (0.2%)	6.38 (0.2%)	258.64 (1.5%)	104 (1.8%)
Average (ε_3)	2.70 0 %	2.15 23.7%	32.20 0.3%	7.04 11.9 %	209.31 3.1 %	104 4 %

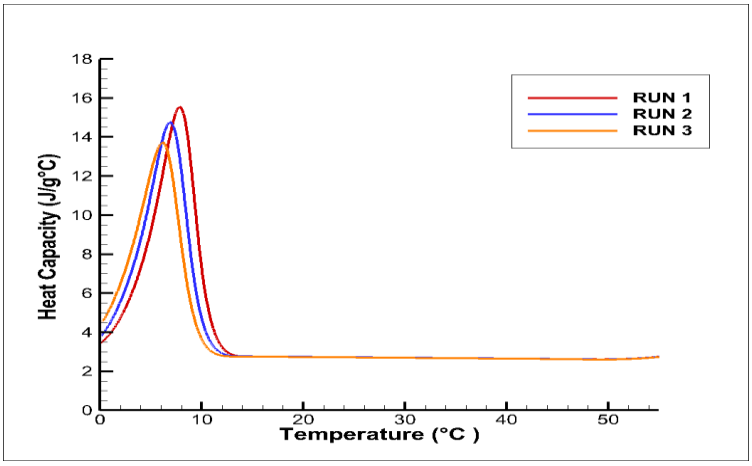

Figure 97:MDSC solidification result for sodium sulfate decahydrate.

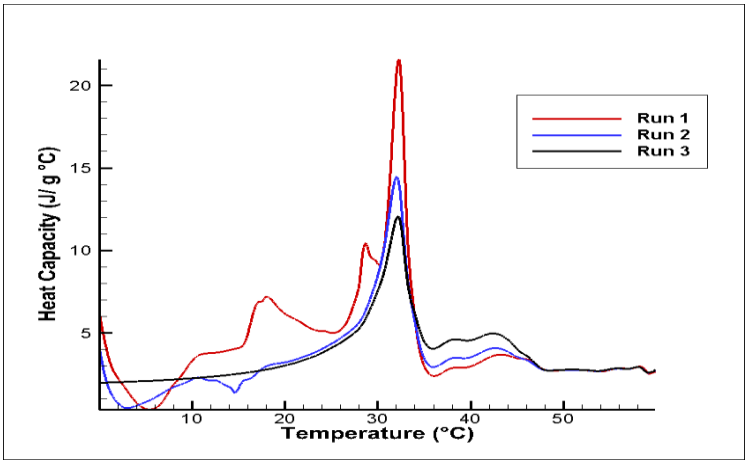

Figure 98: DSC melting result for sodium sulfate decahydrate.

The initial T-History measurements were performed at 15°C to 40°C did and not provide a concise result for pure sodium sulfate decahydrate due to sub-cooling. Therefore, the measurements were repeated again between 10°C and 40°C. The measured latent heat for pure sodium sulfate decahydrate was 147 J/g. The low recovery of latent heat storage capacity could be due to phase segregation. The effects of phase segregation magnify for larger sample mass. Whereas the degree of sub-cooling was reduced by 32%.

9.2 Effects of Additives

In the case of sodium sulfate decahydrate, both nucleating agent and gelling agent were required for performance enhancement. As reported previously, sodium sulfate decahydrate performance degraded due to sub-cooling and phase segregation. Borax (Sodium tetraborate decahydrate, $Na_2B_4O_7 \cdot 10H_2O$), was exploited as nucleating agent and gelatin as phase segregation agent. The borax mass fraction was varied from 1% and 3%. Figure 99 summarizes the effects of varying mass fraction of borax on reducing the degree of sub-cooling. The increasing mass fraction of borax did not significantly reduce the effects of sub-cooling.

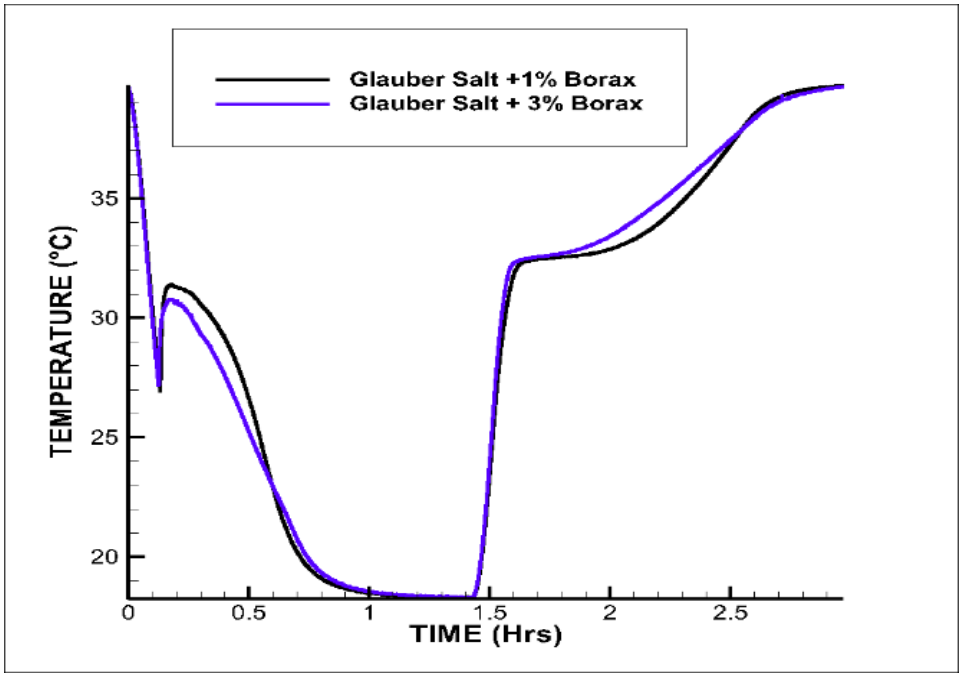

Figure 99: Mass concentration of nucleating additives of sodium sulfate decahydrate.

Table 34 summarizes the effect of borax and gelatin on sodium sulfate decahydrate performance. The addition of 1% borax, the degree of sub-cooling reduced by 84%, but the existence of incongruent melting prevented sodium sulfate decahydrate from solidifying

completely. The addition of gelatin with borax increased the energy storage capacity from 147 J/g to 210 J/g. Therefore, with gelling 89% of ideal energy capacity was achieved. The stability of nucleating and gelling additives was analyzed by conducting 300 thermal cycles and reported in the following chapter.

Table 34: Effects of borax and gelatin on sodium sulfate decahydrate performance.

	MP (°C) (ε)	**FP (°C) (ε)**	**Latent Heat (endothermic) (J/g) (ε)**	**Latent Heat (exothermic) (J/g) (ε)**	**Sub Cooling ΔT (°C)**
Pure Glauber Salt @ 10°C	23.6 (1.2%)	14.7 (3.4%)	147 (7.2%)	-	15.2 (0.5%)
Glauber Salt with 1% Borax	32.4 (0.8%)	30.9 (1.8%)	131 (13.8%)	170 (12.0%)	2.5 (6.7%)
Glauber Salt with 1% Borax and 10% Gelatin	30.3 (1.1%)	31.2 (2.1%)	210 (2.2%)	227 (3.6%)	3.1 (7.2%)

Figure 100 shows an image of the PCM samples (with and without additives). The image shows the effects of gelling additives on the solidification of the sodium sulfate decahydrate samples at room temperature (which is below the phase transition temperature of sodium sulfate decahydrate). The image shows that without gelling additives the phase segregation of the PCM samples is acute and no nucleation (or solidification) is observed. On mixing with 1% borax, phase segregation still exists but a limited amount of crystallization occurred. However, on mixing with 1% borax and 10% Gelatin the phase segregation was obviated and with complete solidification was achieved.

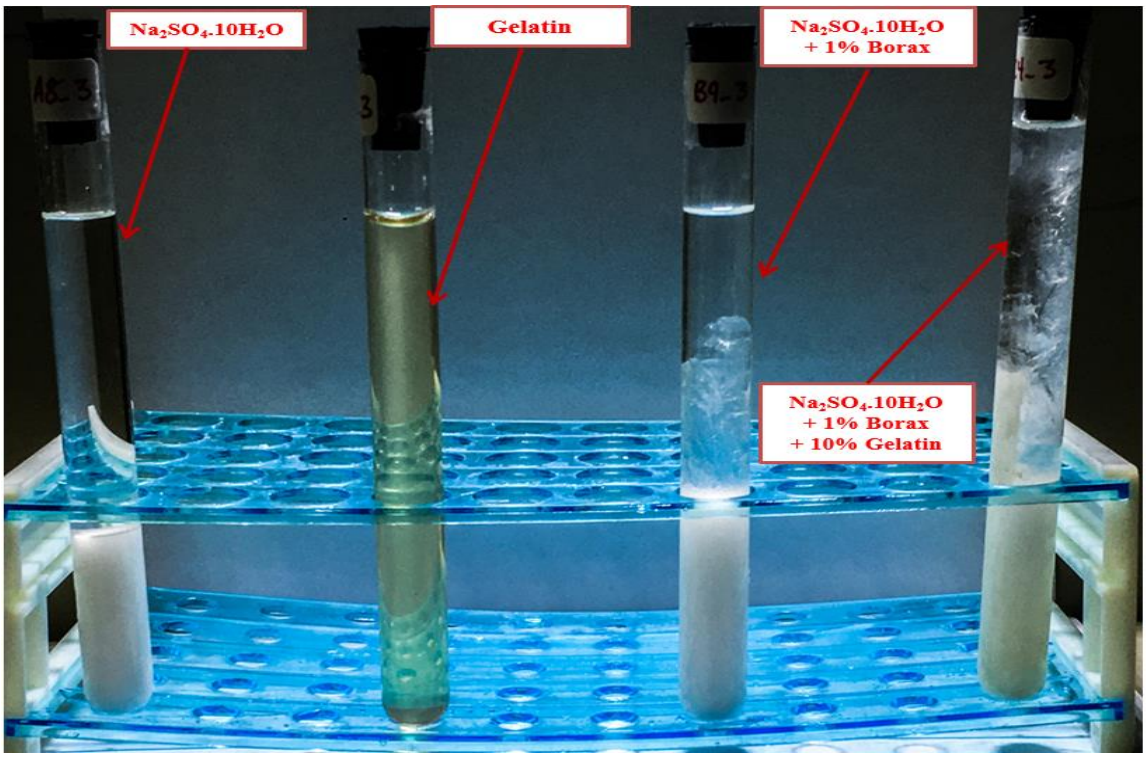

Figure 100: Image of sodium sulfate decahydrate samples with and without additives at room temperature.

In this chapter, the effects of additives on sub-cooling and phase segregation was described. The mass fraction of the different nucleating additives was varied to explore the effect of concentration on their efficacy in promoting nucleation as well as minimizing subcooling. The results show that these additives were successful in reducing the degree of sub-cooling by as much as 15% for sodium sulfate decahydrate.

9.3 Thermal Stability

The thermal cycling experiments for sodium sulfate decahydrate with and without additives were performed using T-History. The sample mass was 23g, and the thermal cycling experiment were performed at 15°C to 40°C. Table 35 summarizes the outcome of thermal cycling preformed on sodium sulfate decahydrate over 300 Cycles. The average latent heat energy storage capacity of pure sodium sulfate decahydrate was reduced by 83.5% at the end of 200 cycles. Therefore, clearly pure sodium sulfate decahydrate have failed the 300-thermal cycling test.

Table 35: Thermal cycling of sodium sulfate decahydrate.

	MP (°C) (ε)	Latent Heat Endo (J/g) (ε)	Sub Cooling ΔT (°C)
Initial	23.6(1.2%)	147(7.2%)	15.2 (0.5%)
100 Cycle	26.(4.5%)	108(11%)	15.5(1.2%)
200 Cycle	15.(1.0%)	24.3(10%)	14.7(0.9%)
300 Cycle	**No Crystallization**		

9.3.1 Sodium Sulfate Decahydrate with 1% Borax

Table 36 summarizes the outcome of thermal cycling preformed on sodium sulfate decahydrate with 1% Borax over 300 cycles. The average latent heat storage capacity declined as much as 11% after 300 cycles. In summary sodium sulfate decahydrate with 1% Borax could only recover 67.8% of the ideal latent heat energy storage capacity, but the degree of sub-cooling was sustained at 3.0°C for 300 cycles. The sodium sulfate decahydrate, with 1-3% borax additives had a mass loss of roughly a 2.6% to 3.0% mass loss at 300 cycles.

Table 36: Thermal Cycling of Sodium Sulfate Decahydrate with 1% Borax.

	MP (°C) (ε)	FP (°C) (ε)	Latent Heat (endothermic) (J/g) (ε)	Latent Heat (exothermic) (J/g) (ε)	Sub Cooling ΔT (°C)
Initial	32.4(0.8%)	30.9(1.8%)	131 (13.8%)	170(12.0%)	2.5(6.7%)
100 Cycle	32.2(0.8%)	30.8(1.5%)	134(13.6%)	175(12.9%)	2.7(10.4%)
200 Cycle	32 (1.5%)	30.8(1.6%)	118(4.3%)	150(15.8%)	3.0(8.7%)
300 Cycle	31.9(1.4%)	30.9(1.1%)	113(5.1%)	151(15.3%)	3.2(7.8%)

9.3.2 Sodium Sulfate Decahydrate with 1% Borax and 10% Gelatin

Table 37 summarizes the outcome of thermal cycling preformed on sodium sulfate decahydrate with 1% Borax and 10% Gelatin over 300 cycles. The average latent heat energy storage capacity of sodium sulfate decahydrate with 1% Borax and 10% Gelatin declined as much as 30% after 300 cycles but the transition temperature and degree of sub-cooling remained constant at 31.1 °C and 3.9°C respectively. Sodium sulfate decahydrate with 1% Borax and 10% Gelatin had a mass loss of 3.5%. The increase in mass loss could be due to degradation of gelatin, as gelatin itself contains water.

Table 37: Thermal Cycling of Sodium Sulfate Decahydrate with 1% Borax and 10% Gelatin.

	MP (°C) (ε)	FP (°C) (ε)	Latent Heat (endothermic) (J/g) (ε)	Latent Heat (exothermic) (J/g) (ε)	Sub Cooling ΔT (°C)
Initial	30.3(1.1%)	31.2(2.1%)	210(2.2%)	227(3.6%)	3.1(7.2%)
100 Cycle	30.8(2.9%)	31.6(2.3%)	215(8.2%)	226(10.0%)	3.5(6.5%)
200 Cycle	30.9(4.0%)	31.5(2.1%)	198(9.2%)	187(7.9%)	3.6(6.2%)
300 Cycle	32.0(0.5%)	31.4(2.2%)	165(18.4%)	160(2.3%)	3.9(6.7%)

9.4 Summary and Recommendation

The thermal characterization and thermal cycling of sodium sulfate decahydrate has shown that the concept of using a nucleating agent (borax) to compensate for the sub cooling in sodium sulfate decahydrate could result in a significant improvement in the energy storage capacity of over the pure sodium sulfate decahydrate. Nonetheless, there is still considerable room for further improvement in understanding the gelling methods to improve the thermal capacity of sodium sulfate decahydrate.

In conclusion, borax was efficient in suppressing sub-cooling in sodium sulfate decahydrate over 300 thermal cycles. With 3% mass concentration of borax, sub-cooling reduced by 5 times from 15°C to 3.2°C. The thickening of sodium sulfate decahydrate with gelatin was able to reduce phase segregation up to 300 cycles. As the energy storage density degraded more than 100% after 300 melt-freeze cycles due to phase separation. Therefore, the experiment was ended at 300 cycles.

Future recommendation is to understand and study different thickening techniques to stabilize sodium sulfate decahydrate over 1000 melt-freeze cycles. The direction could towards implementing carboxymethyl cellulose, hydroxyethyl cellulose, and fumed silica as cellulose and silica are able to increase the overall viscosity by 20 -30 times with small mass percentage and they are also thixotropic. High concentration of cellulose or silica could help in forming shape stabilized salt hydrate (i.e. acts like a solid-solid phase change). Studying the effects of melt length scale on phase segregation. As by reducing length scale of melt, the effects of phase segregation could be contained and the diffusion rate during freezing could be increased, therefore reducing the overall effects of phase segregation.

CHAPTER X

CHARACTERIZATION OF PURETEMP 29

The initial thermal characterization experiments for PureTemp 29 were performed using MDSC Q2000 and T-History. The sample mass was 10.5 mg and 16.810g respectively. The ramp rate of MDSC was pre-programmed at 3°C/min with a modulation of 0.48°C/min. The testing in MDSC were performed at 10°C to 40°C. Table 38 summarizes the MDSC results of PureTemp 29. The measured average peak melting and solidification temperatures are 28.7 °C and 22 °C respectively. The average latent heat for both exothermic and endothermic reactions is 195 J/g (±σ 0.4%). The difference in average peak melting and solidification temperature is due to thermal hysteresis. It is reported in multiple literatures ([11], [108]) that thermal hysteresis is inherent problem in paraffin wax. It is shown in Figure 101 that PureTemp 29 melts and solidifies over a range of temperature. The melting occurs in the region of 20°C to 32°C and solidifications occurs in the region of 23°C to 17°C. The effects of thermal hysteresis could have design implication of paraffin waxes in LHTESS with temperature sensitive applications.

Table 38: MDSC results summary of Puretemp 29.

	Specific heat Solid (J/g k) (ε_1)[4]	**Specific heat Liquid (J/g k) (ε_1)**	**MP (°C) (ε_1)**	**FP (°C) (ε_1)**	**Latent Heat (Endothermic) (J/g) (ε_1)**	**Latent Heat (Exothermic) (J/g) (ε_1)**
First	1.83 (2.2 %)	1.90 (0.8 %)	28.6 (0.2 %)	22.1 (0.4%)	192 (4.7 %)	198 (4.2%)
Second	1.76 (2.6 %)	1.89 (0.7 %)	28.54 (0.2 %)	21.9 (0.4%)	194 (4.4 %)	197 (4.2%)
Third	1.75 (2.6 %)	1.88 (0.7 %)	29.1 (0.2 %)	21.9 (0.4%)	194 (4.4 %)	198 (4.2%)
Average (ε_3)[5]	1.78 2.2 %	1.89 0.5%	28.7 1.1 %	22.0 0.5%	193 0.4 %	198 0.3%

[4] The measurement instrument uncertainty

[5] The Standard Deviation of three run

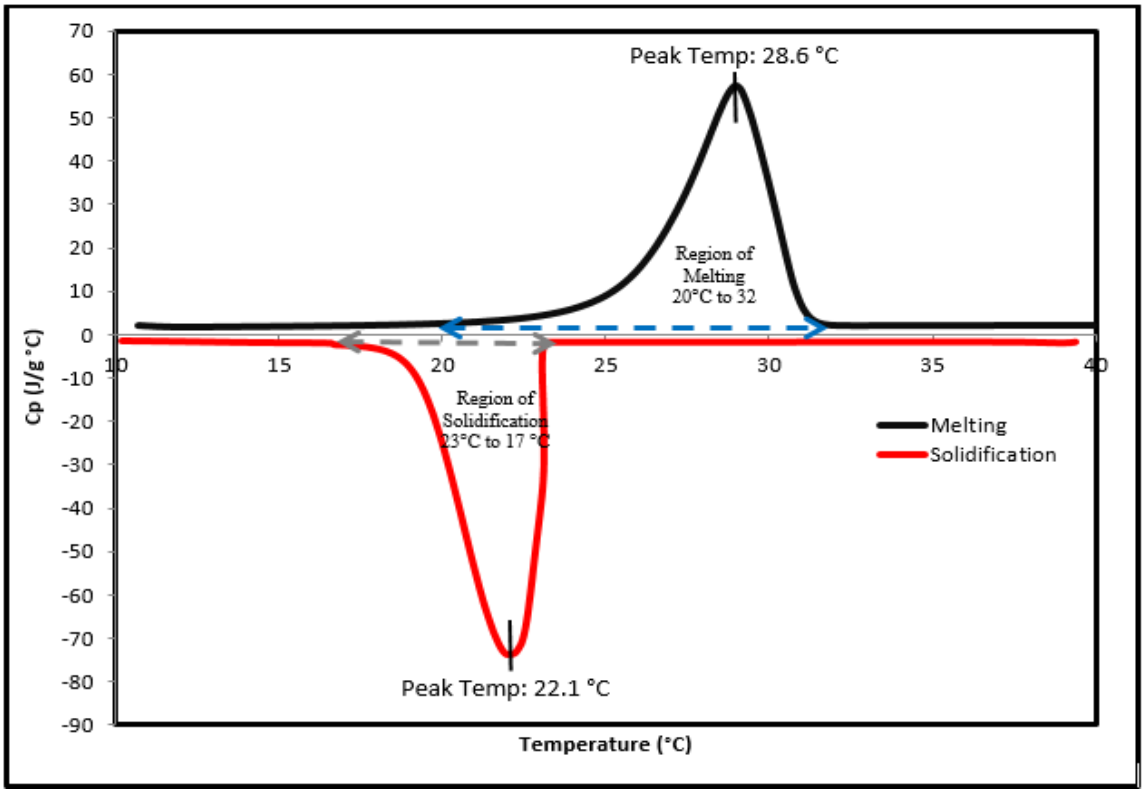

Figure 101: DSC curve of PureTemp 29.

Table 39 summarizes the initial characterization performed using T-History. During T-History Measurement the heating rate of PCM were maintained at 5.5°C/min during the phase transition. The measurement of latent heat performed using T-History and DSC differs by 3.6% for the exothermic reaction, and no difference were noted for endothermic reaction, in both cases the results are within the measurement uncertainties. Vast deviations are noted for the solidification temperature, and for the specific heat of liquid. Solidification temperature measured by DSC, and T-History are 22 °C (±0.64%) and 27.3 °C (± 1.1%) respectively. The variation in solidification temperature could be due sample size and heating rate. As the higher heating rate could reduce the thermal hysteresis. The inhomogeneity and the thermal hysteresis observed by a small sample mass is not representative of the larger sample mass. The liquid and solid specific

heat (Cp) measurements in T-History were analyzed using the freezing and melting curves respectively. Whereas for MDSC the specific heat (Cp) measurements for both liquid and solid was analyzed using both freezing and melting curves. For MDSC the results were identical in both instances. In comparison of T-History and MDSC the solid specific heat capacity (Cp) were within the measurement uncertainties but the liquid specific heat capacity (Cp) varied by 6% between T-History and MDSC.

Table 39: Summary of T-History Result for PureTemp29

Runs	C_p Solid (J/g k) (ε_1)	C_p Liquid (J/g k) (ε_1)	MP (°C) (ε_1)	FP (°C) (ε_1)	Latent Heat Endo (J/g) (ε_1)	Latent Heat Exo (J/g) (ε_1)
First	1.69 (3.8%)	2.00 (5.5%)	28.2 (0.9%)	27.34 (0.9%)	195 (8.2 %)	195 (8.2%)
Second	1.82 (3.3 %)	2.13 (5.4%)	28.3 (0.9%)	27.06 (0.9%)	191 (8.5%)	189 (8.6%)
Third	1.73 (3.2 %)	2.28 (5.7%)	28.3 (0.9%)	27.36 (0.9%)	197 (8.1 %)	191 (8.5%)
Fourth	1.79 (3.3 %)	2.19 (5.1%)	28.3 (0.9%)	27.39 (0.9%)	189 (8.4%)	192 (8.5%)
Fifth	1.74 (3.4 %)	2.37 (5.6%)	28.4 (0.9%)	27.54 (0.9%)	191 (8.5%)	190 (8.5%)
Average (ε_3)	1.75 (5%)	2.20 (6.5%)	28.3 (0.15%)	27.3 (0.6%)	193 (1.7%)	191 (1.1%)

Thermal conductivity measurement for solid sample were measured using a 30mm diameter mold in environmental temperature of 21°C. Thermal conductivity for the liquid sample were measured using a 50-ml beaker (Diameter: 39mm) filled with 30-ml of PT29 sample and submerged in a water bath maintained at 35°C. The testing parameters and the results for the solid and liquid measurements are shown in Table 40 and Table 41 respectively. The solid and liquid thermal conductivity were within 1.8% and 18.6% of the manufacturer data.

Table 40: PT29 solid thermal conductivity measurement.

Run	Temp (°C)	Out. Power (mW)	Meas Time (sec)	Th. Conduct (W/mK)	Th. Diffusivity (mm^2/s)	Spec.Heat (MJ/m^3K)
1	20.1	10	80	0.2493	0.1625	1.780
2	20.6	10	80	0.2453	0.1647	1.648
3	20.6	10	80	0.2447	0.1289	1.821
4	21	10	20	0.2413	0.1815	1.330
5	21	10	40	0.2422	0.1818	1.332
6	21	10	80	0.2504	0.1547	1.618
Average				0.2455 (1.5%)	0.1623 (11.0%)	1.5882 (12.3%)
Difference with Literature				**1.8%**	**8.2%**	**4.3%**

Table 41: PT29 liquid thermal conductivity measurement.

Run	Temp (°C)	Out. Power (mW)	Meas Time (sec)	Th. Conduct (W/mK)
1	35	30	3	0.1775
2	35	30	3	0.1763
3	35	30	3	0.1804
Average (Std. Dev ±σ)				0.1780 (0.9%)
Difference with Literature				**(0.15) 18.6%**

10.1 Thermal Cycling

The thermal cycling experiments for PureTemp 29 were performed using T-History. The sample mass was 18g and the testing were performed at 15°C to 40°C. Table 42 summarizes the outcome of thermal cycling preformed on PureTemp 29 over 300 Cycles. The change in the average latent heat energy storage capacity at the end of 300 cycles was 0.5% and it's within the measurement uncertainty. The phase transition temperature was altered by 0.1°C, and PureTemp29 had a mass loss of 1.6% at the end of 300 cycles as summarized in Figure 102. Therefore, it could be concluded that PureTemp 29 is reliable up to 300 cycles.

Table 42: Summarizing effects of thermal cycling on PureTemp 29.

	MP (°C) (ε_1)	**FP (°C) (ε_1)**	**Latent Heat Endo (J/g) (ε_1)**	**Latent Heat Exo (J/g) (ε_1)**	**% Mass Change**
Cycle 1	30.5 (0.5%)	26.8 (0.9%)	213 (7.6%)	203 (8.6%)	0
Cycle100	31.2 (0.5%)	26.7 (0.9%)	214 (7.6 %)	203 (8.6%)	0.71
Cycle200	31.5 (0.5%)	26.9 (0.8%)	215 (5.9%)	201 (8.6%)	0.94
Cycle300	31.5 (0.5%)	26.9 (0.8%)	217 (6.1%)	204 (8.6%)	1.27

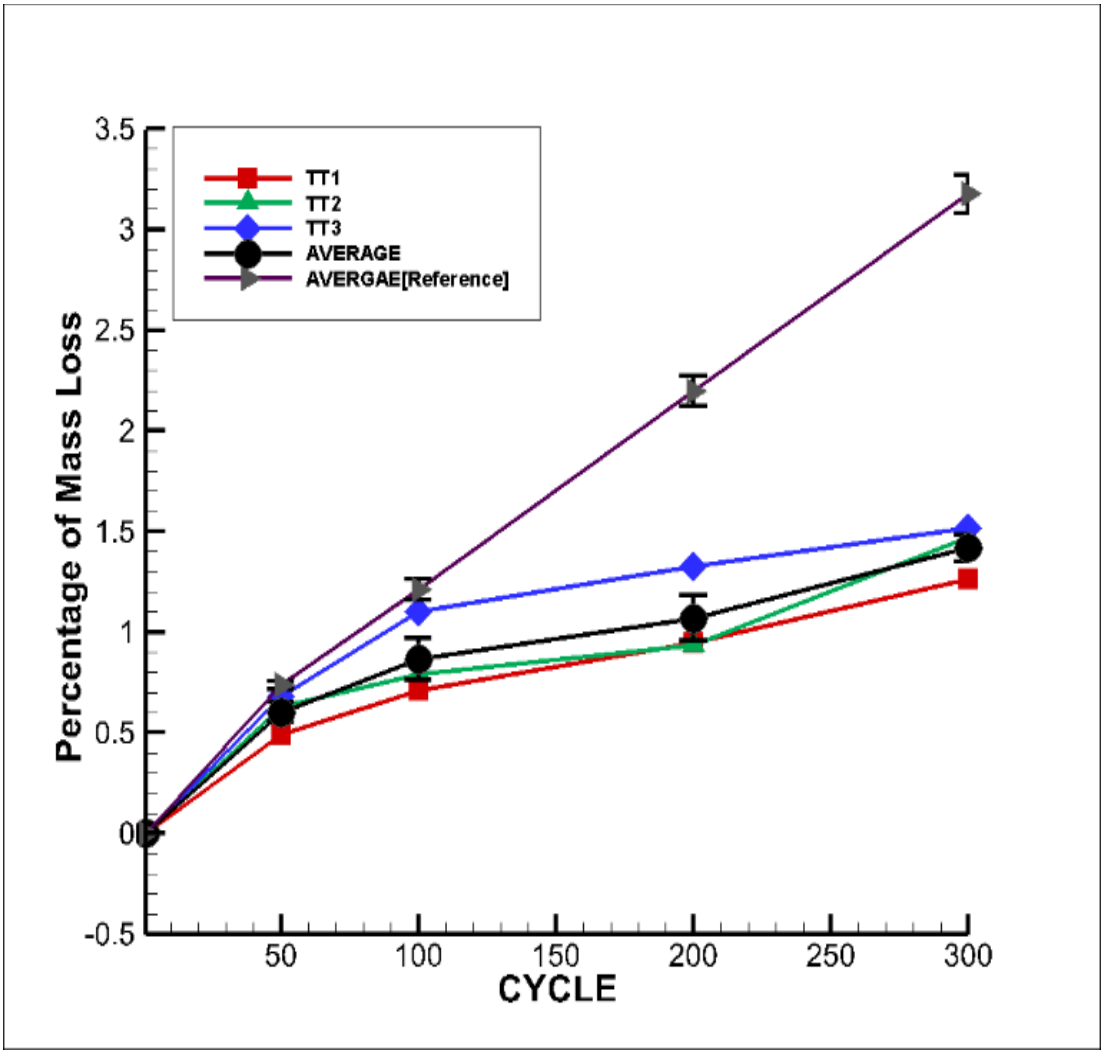

Figure 102: The mass loss of 3 samples of PT29 with thermal cycling.

10.2 Summary

In this chapter, the thermal stability of PCMs (with and without additives) was measured. The results show that Preterm 29 samples were thermally stable up to 300 cycles without the need for any additives. However, PureTemp 29 have low volumetric energy storage capacity due to their low-density values. PureTemp 29 also suffers from thermal hysteresis and low thermal conductivity. Unpredictable thermal hysteresis and low thermal conductivity could affect LHTESS design performance. The low volumetric energy storage density of paraffin wax could elevate the overall cost of LHTES as well.

CHAPTER XI

CORROSION

Phase Change Materials (PCMs) have gained popularity for their high energy storage densities, which makes them suitable for various applications including, as heat transfer fluids (HTF) for waste heat management and supplementary thermal energy storage (TES) systems for dry cooling enhancement. PCMs are also used for Latent Heat Thermal Energy Storage Systems (LHTESS). PCMs can be classified as organic (i.e. Paraffin, and Fatty acids) and inorganic (i.e. Salt hydrates, Eutectics). For a given volume, salt hydrates tend to have larger storage capacity due to their higher densities compared to that of organic PCMs. However, corrosive nature of salt hydrates towards various metals and alloys renders a challenge for their engineering applications. Corrosion could be further enhanced on addition of nucleating agents to the PCMs. Additives can affect the operational performance and efficacy of PCMs. The effect of additives on the corrosivity of these PCMs are currently lacking in the contemporary literature. Hence, in this study the effect of nucleating agents (additives) on the rate of corrosion is explored for applications in LHTESS. In this study, various PCMs in liquid phase (with or without nucleating additives) are exposed to a variety of test coupons. The test coupons are made from stainless steel (SS347) and aluminum (AL 1000 Series). The corrosion tests were performed in sealed glass test tubes. The PCM samples utilized in the corrosion tests are lithium nitrate trihydrate, zinc nitrate hexahydrate, and calcium chloride hexahydrate. The glass tubes were fully submerged in 45°C water bath for 6 ~ 18 weeks. The mass loss of the test coupon was measured at 6-week intervals. The results obtained in this study were compared to the literature data and the efficacy of the various PCM samples for TES applications were explored.

11.1 Experimental Analysis

The corrosion rate results (mg/cm^2 yr.) for individual PCM and metal combinations are presented in Table 43 after 6,12 and 18 weeks. After analyzing the data obtained from mass measurement, no similar pattern was observed for aluminum coupons. Therefore, each PCM-aluminum coupon must be treated independently. However, a common pattern is observed in stainless steel coupons, the rate of corrosion was less than < 2.4 mg/cm^2.yr, therefore stainless steel (SS 347) could be considered for long term service as per industry standard.

Table 43: Corrosion rate through time of metal coupons with all PCM combinations (mg/cm2.yr). The results were averaged over 18 weeks for stainless steel SS347 and aluminum AL 1100 samples.

	Stainless Steel SS347			**Aluminum AL 1100**		
	6 Weeks	**12 Weeks**	**18 Weeks**	**6 Weeks**	**12 Weeks**	**18 Weeks**
Lithium Nitrate Trihydrate	0.6	1.7	1.1	12	15	14
Lithium Nitrate Trihydrate with 5% ZHN	1.5	1.7	1.6	15	18	19
Zinc Nitrate Hexahydrate with 5% ZHN	2.1	1.6	1.2	50	73	71
Calcium Chloride Hexahydrate with 5% $SrCl_2$	2.4	1.5	2.4	131	158	127

Figure 103 illustrates that no surface corrosion effects are noticeable in SS 347 PCMs with any of the salt hydrate PCMs.

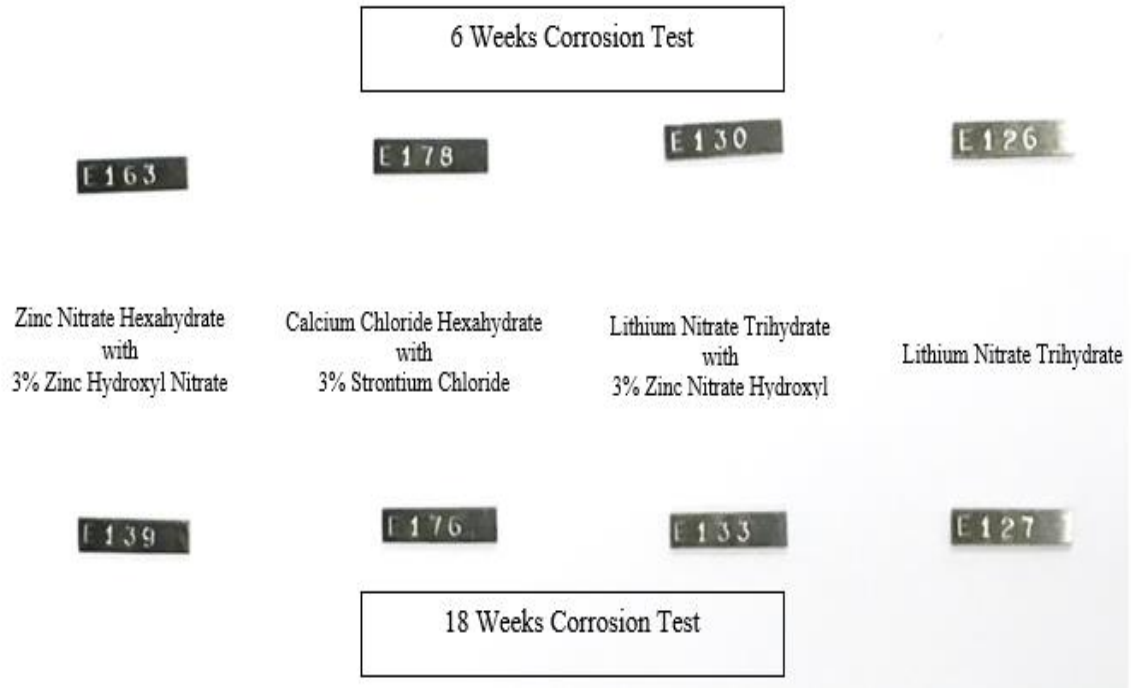

Figure 103: SS 347 Coupons surface image after 6 weeks and 18 weeks submerged corrosion testing.

The maximum rate of corrosion of lithium nitrate trihydrate with aluminum coupon was measured to be 15 mg/cm^2.yr at the end of 12 weeks and averaged about 13 mg/cm^2.yr over the 18-week period (Figure 104)Whereas, the sample with 5 % mass percentage of zinc hydroxyl nitrate showed 33% increment in the rate of corrosion. The rate of corrosion with additives reduced with time and remain constant after 12 and 18 weeks at around 18 mg/cm^2. yr. Therefore, lithium nitrate trihydrate with and without additives with aluminum coupons can be considered for long term service.

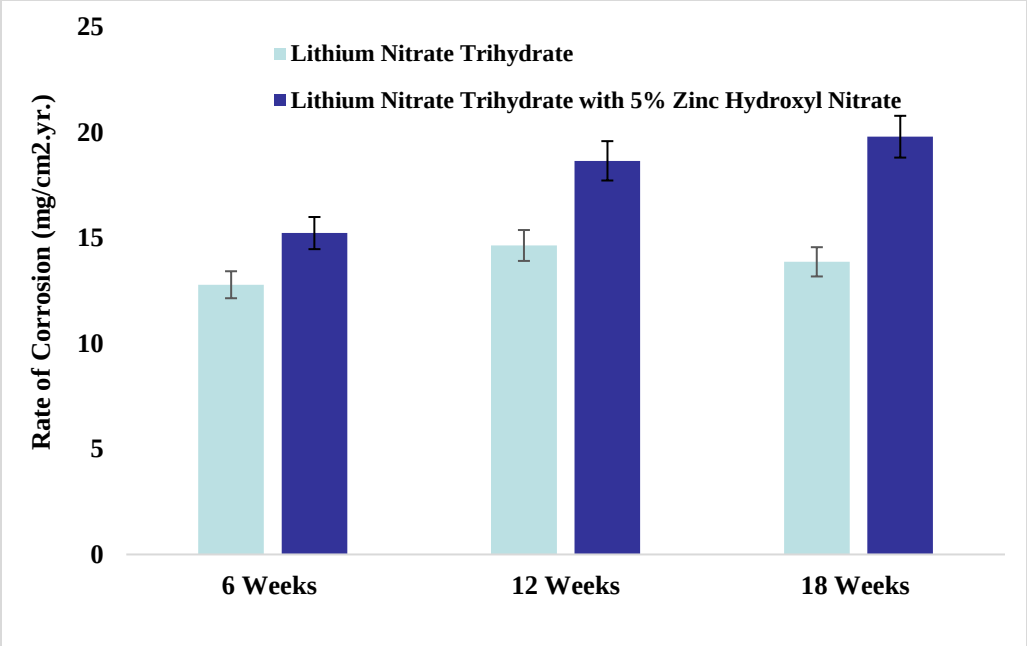

Figure 104: Effects of lithium nitrate trihydrate with and without nucleating additives on aluminum coupons corrosion rate. The rate of corrosion was averaged over three sample coupons for each test period and the standard deviation reported as error bars.

After 6 weeks, the aluminum coupons immersed in zinc nitrate hexahydrate with additives experienced two visible changes. First, the coupon had a layer of white precipitates on them. Second, the solution of zinc nitrate hexahydrate changed to yellowish in color with traces of white precipitate (Figure 105). The white precipitates are most likely an aluminum hydroxide $Al(OH)_3$ layer [109] due to aluminum oxidation.

Figure 105: Images illustrating post corrosion outcome of coupons and zinc nitrate hexahydrate. Left: yellowish zinc nitrate hexahydrate after 18 weeks corrosion test Right: White Precipitates on aluminum coupon – aluminum oxide.

At end of 18 weeks, the samples immersed in zinc nitrate hexahydrate were imaged under scanning electron microscopy (FEI Quanta 600) before descaling to analyze the white precipitates on the coupons (Figure 106:). The highly porous dense medium on surface covering most of corroded area showed high oxygen and aluminum concentration, concluding the assumption that the white precipitates are concentration of aluminum hydroxide Al $(OH)_3$ forming a protection layer. The corrosion rate of the aluminum coupons in zinc nitrate hexahydrate with 5% zinc nitrate hydroxyl was significant for the three corrosion periods, increasing and remaining constant with time (Figure 107). The most probable reason is the formation of an aluminum hydroxide layer, which is a self-protecting layer that aids in the reduction of corrosion. The constant rate of corrosion was around 71(mg/cm^2.yr). In thermal energy storage applications, PCMs can interfere in the formation of aluminum hydroxide formation and making layer making it porous.

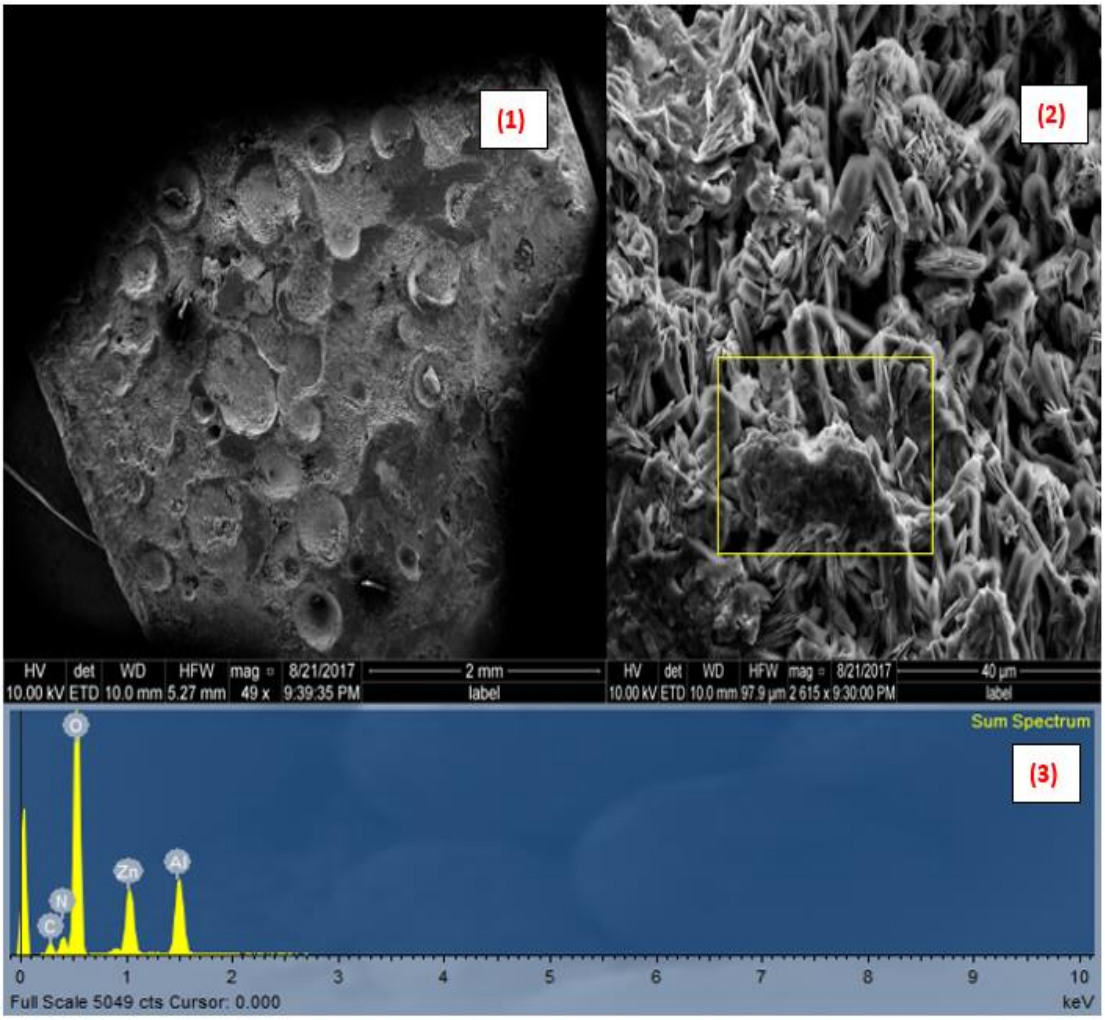

Figure 106: Scanning Electron Microscopy of the surface on an aluminum alloy 1100H specimens tested for 18 weeks at 45°C completely immersed in zinc nitrate hexahydrate with 3% zinc hydroxyl nitrate before descaling. (1) Imaging taken in a high porous deposit area; (2) Shows the magnified area of high porous region for spectrum analysis; (3) EDX spectrum corresponds to the analysis of particles in the region.

Likewise, continuous thermal cycling may cause the layer to flake off and cause an increase in corrosion [110]. Cabeza et al, 2001 [79] studied the rate of corrosion of pure zinc nitrate hexahydrate with Al 2007 (93.5% aluminum) coupons over a period of 75 days and reported the corrosion rate to be 81 ($mg/cm^2.yr$) compared to TAMU Al 100H (99.5% aluminum) experiment of around 71 ($mg/cm^2.yr$) for a period of 126 days. Therefore, the results are within the

measurement uncertainty and the addition of additives does not really affect the rate of corrosion even through the corrosion coupons are different.

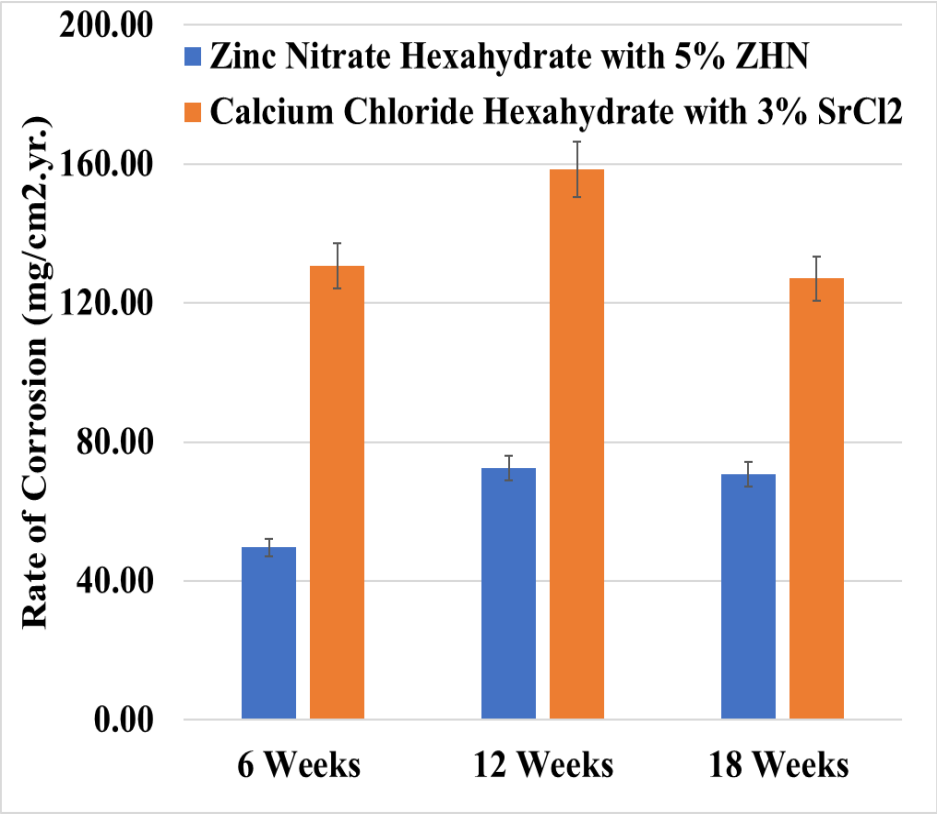

Figure 107: Rate of corrosion on aluminum coupons (AL 1100H) when submerged in zinc nitrate hexahydrate and calcium chloride hexahydrate with additives over a period of 18 weeks. The rate of corrosion was averaged over three sample coupons for each test period and the standard deviation reported as error bars.

At end of 18 weeks the aluminum sample immersed in zinc nitrate hexahydrate were imaged under scanning electron microscopy (FEI Quanta 600) after descaling to visually represent the surface topology (Figure 108). Large pits were observed under the scanning electron microscope after the removal of the aluminum oxide layer. Post cleaning further confirms that the white precipitate is aluminum hydroxide, as the oxygen and hydrogen concentration reduced after cleaning.

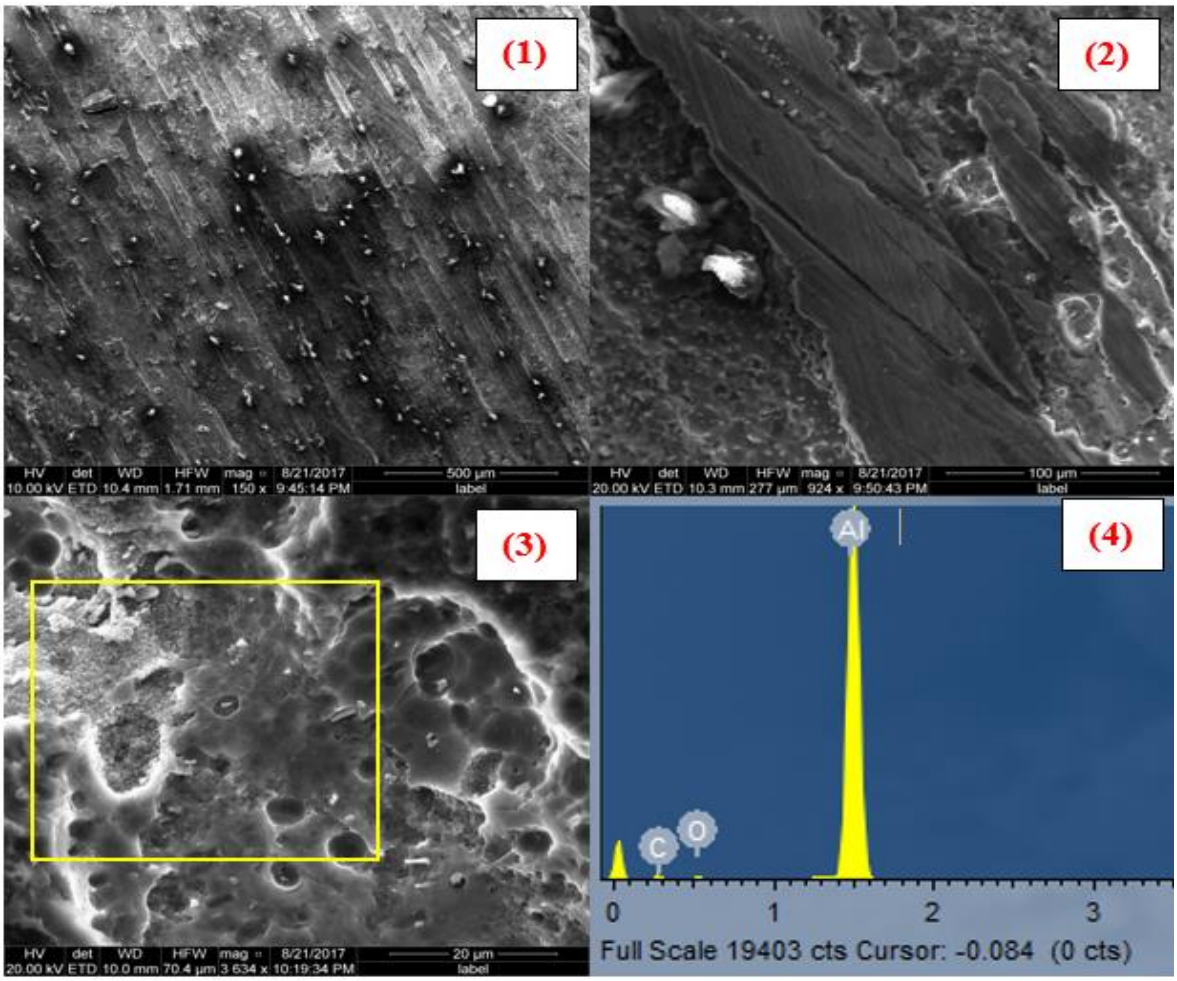

Figure 108: Scanning Electron Microscopy of the surface on an aluminum alloy 1100H specimens tested for 18 weeks at 45°C completely immersed in zinc nitrate hexahydrate with 3% zinc hydroxyl nitrate after descaling. (1) Imaging at 500 µm; (2) Imaging at 100 µm; (3) Imaging at 20 µm; (4) EDX spectrum corresponds to the analysis of particles in the region.

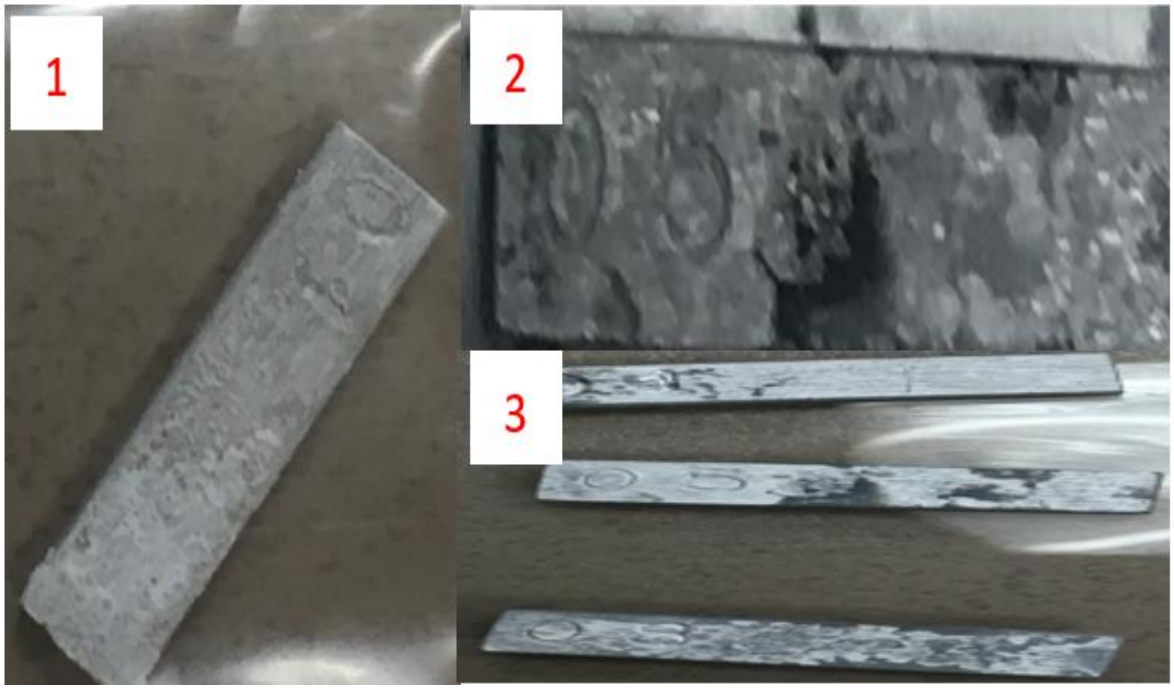

Figure 109: Aluminum Coupon descaling duration outcome. (1): Before chemical descaling; (2) Chemical descaling for 5 minutes; and (3) Chemical descaling for 15 minutes.

The post-cleaning of aluminum coupons immersed in calcium chloride hexahydrate with additives were descaled at different time intervals to reduce coupon mass loss due to descaling (Figure 109). Aluminum is known to suffer from pitting with chloride salts [101].The immersion of aluminum coupon in calcium chloride hexahydrate with 5% $SrCl_2$ experienced three visible changes. The coupons in the calcium chloride hexahydrate solution produced bubbles and changed to a dark bluish from a cloudy white solution near the region of the coupons (Figure 110 - Left) at the end of 6 weeks, 12 weeks and 18weeks. The coupons were completely covered with cloudy white precipitate (aluminum hydroxide $Al(OH)_3$) and can't be easily removed with water rinse (Figure 110 - Left). Longer corrosion period increased the amount of dark precipitates attached to the coupon.

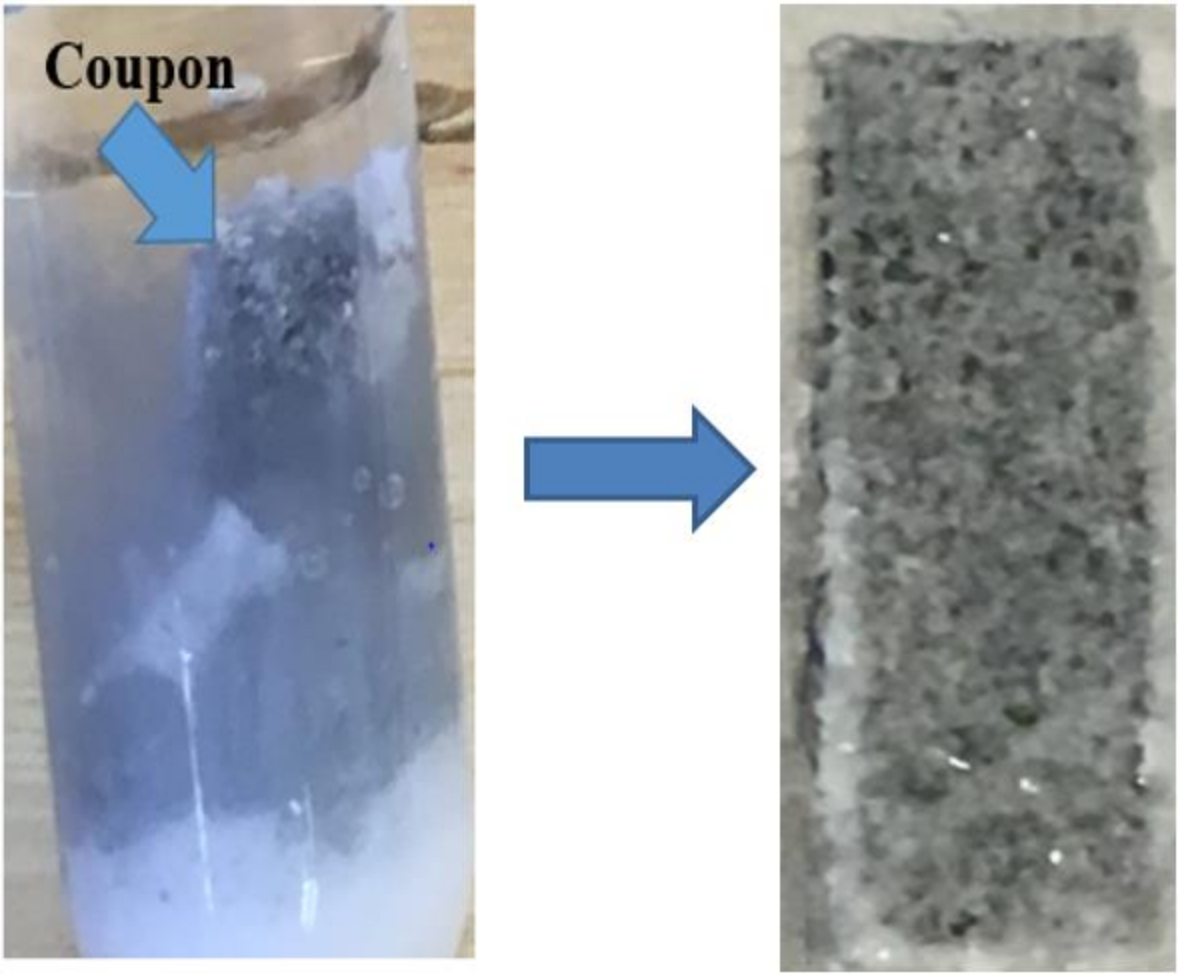

Figure 110: Images illustrating post corrosion outcome of coupons and calcium chloride hexahydrate. Left: Change of appearance of calcium chloride hexahydrate with corrosion (Aluminum Coupon), Right: White and dark Precipitates on aluminum coupon.

The SEM observation of the aluminium coupon before descaling showed some small zones of compact deposits 1-5µm depth, with a characteristically cracker feature (Figure 111) covering most of the coupon. The EDX analysis of the porous white precipitate contained a range of elements either leached from the alloy contained in the PCM itself, and especially high concentration of oxygen, aluminium and hydrogen, which could mean that the white precipitate is aluminum hydroxide Al $(OH)_3$ like samples immersed in zinc nitrate hexahydrate.

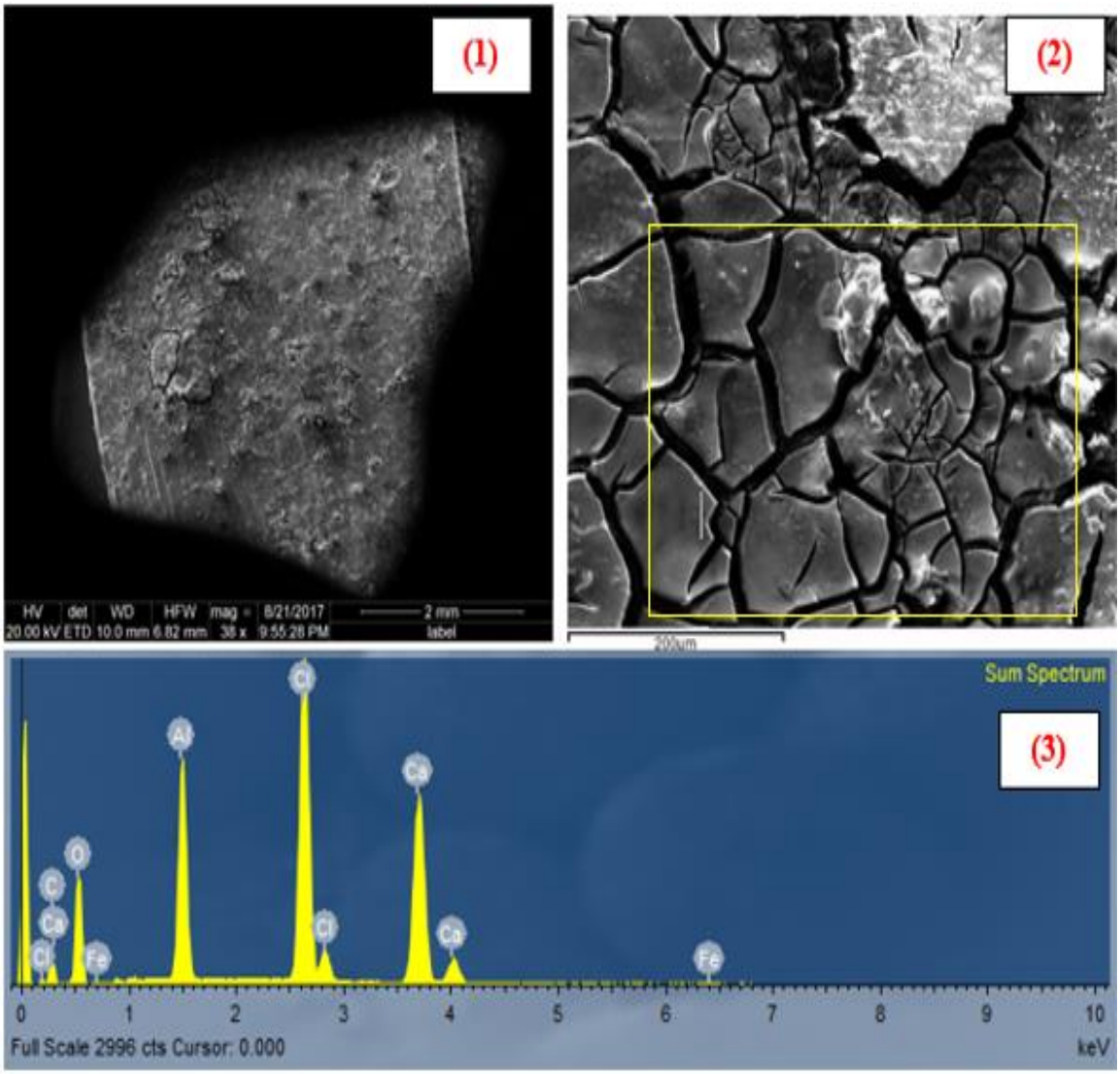

Figure 111: Scanning Electron Microscopy of the surface on an aluminum alloy 1100H specimens tested for 18 weeks at 45°C completely immersed in calcium chloride hexahydrate with 3% strontium chloride *before descaling*. (1) Imaging at 2mm (2) Shows the magnified region of the white precipitate (3) EDX spectrum corresponds to the analysis of particles in the region.

The corrosion rate of the aluminum coupons in calcium chloride hexahydrate with 5% strontium chloride was significant for the three corrosion periods. The maximum rate of corrosion occurred at the end of 12 weeks at the rate of 158 (mg/cm^2.yr) but reduced to 127 (mg/cm^2.yr) at the end of 18 weeks. The reduction in corrosion could be due to formation of aluminum completely covering the surface of the coupon.

During post-cleaning analysis, the surface topology was analyzed visually and under the scanning electron microscopy (FEI Quanta 600). Figure 112 illustrates the visual inspection of aluminum coupons after descaling.

Figure 112: Post cleaned samples aluminum coupons immersed in calcium chloride hexahydrate with 3% mass percentage of strontium chloride.

Figure 113 illustrates the surface topology under SEM. In both cases the large pits and dark deposits were observed in these coupons. In closer magnification of these coupons showed layers of uneven corrosion occurring on the surface (i.e. layers flaking off the surface). All these effects do clearly agree with pitting corrosion. Figure 114 illustrates the rate of corrosion of aluminium coupons with zinc nitrate hexahydrate and calcium chloride hexahydrate salt hydrates for both

short-term and long-term testing periods. The coupons utilized in the literature was Al 2007 (93.5% aluminium) while coupons utilized by TAMU was Al 1100H (99.5% aluminium).

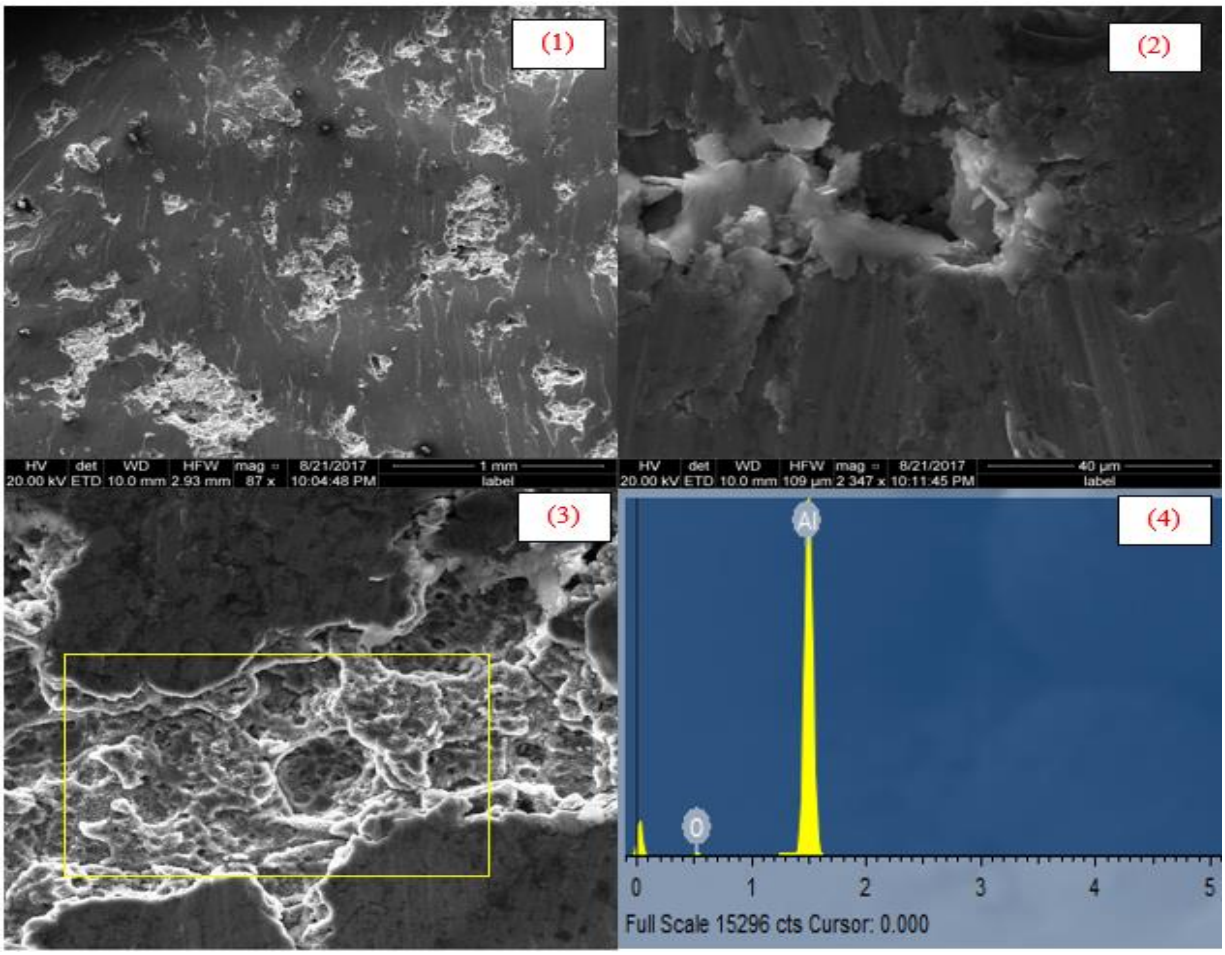

Figure 113: Scanning Electron Microscopy of the surface on an aluminum alloy 1100H specimens tested for 18 weeks at 45°C completely immersed in calcium chloride hexahydrate with 3% strontium chloride *after descaling*. (1) Imaging at 1 mm; (2) Imaging at 40 µm; (3) Imaging at 200 µm for EDX; (4) EDX spectrum corresponds to the analysis of particles in the region.

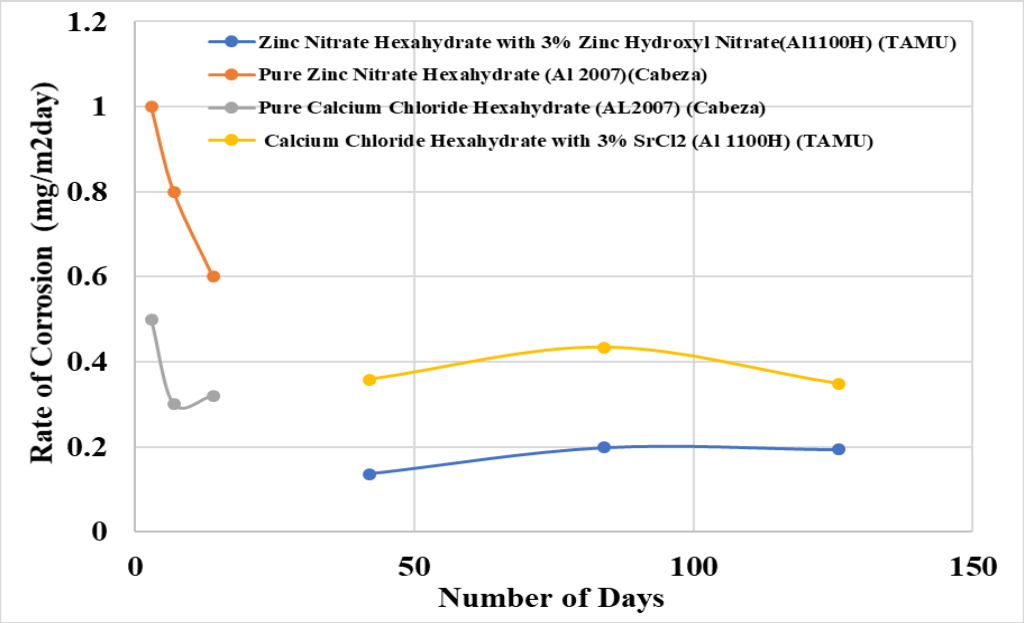

Figure 114: Comparison of short-term and long-term corrosion result for aluminum alloy submerged in zinc nitrate hexahydrate and calcium chloride hexahydrate. The short- term results were gathered from literature Cabeza et al [8].

All experimental results are summarized in Table 44. Now, the suitability of the reported weight loss for thermal energy storage applications has to be evaluated. There is a guide for industry concerning the suitability of materials regarding mass loss due to corrosion [101]. In Table 44 the results are interpreted with recommendations from industry standard. Also, visual changes in the solutions and metal pieces have been considered. Stainless steel is recommended in all cases. Only lithium nitrate trihydrate is recommended for aluminum

Table 44: Recommendation of the metal-PCM combination based on the 126 days continuous corrosion data.

Metal/PCM	Lithium Nitrate Trihydrate	Lithium Nitrate with 5% Zinc Nitrate Hydroxyl	Zinc Nitrate Hexahydrate with 5% Zinc Nitrate Hydroxyl	Calcium Chloride Hexahydrate with 3% $SrCl_2$
Aluminum	1.6 Recommended	3.4 Recommended	71 Caution Recommended	127 Not Recommended Gas Production
Stainless Steel	1.1 Recommended	1.6 Recommended	1.2 Recommended	2.4 Recommended

11.2 Summary and Recommendation

Corrosion tests of three different salt hydrates in combination with two commonly used metals were performed. Never in literature was corrosion ever conducted for lithium nitrate trihydrate and for a period of 126 days. When lithium nitrate trihydrate with and without additives is used as phase change material in a metal thermal energy storage, or in any other application, both stainless steel (SS 347) and aluminium (Al 1100H) are recommended. When zinc nitrate trihydrate is used, only stainless steel (SS 347) is recommended for long-term service and aluminium is only recommended for service up to a month at maximum. When calcium chloride hexahydrate is used as PCM only stainless steel (SS 347) is recommended for long-term service and aluminium is not at all recommended due to high corrosion rate and bubble formation. The study shows that long-term corrosion experiments provides more concise results than the short-term corrosion results found in current literature.Future recommendation is to study the effects of corrosion on other methods and even for longer duration.

CHAPTER XII

RESULTS OF CHEVRON PLATE HEAT EXCHANGER

Thermal energy storage (TES) platforms can help to improve the energy efficiency of various types of Thermal Management Systems (TMS) by actively modulating the transient response of these integrated thermal systems. A novel strategy for TES platforms involves the integration of Phase Change Materials (PCM) into various types of heat exchangers (HX). High performance, compact, and low cost HX platforms for TES involving PCM are often desired for applications ranging from power plants (to reduce their water usage and carbon footprint) to building thermal management to transportation technologies (e.g., aerospace and automotive vehicles) to high heat flux electronics cooling. These applications are often constrained by requirements for minimizing pressure loss (or pump penalty), miniaturizing the form factors (or reduced system size) and the need for easy scalability to large systems. This imposes steep challenges for design, fabrication and operation of these HX platforms. This also severely restricts the available options and material choices for PCM. In this experimental study, the transient performance of a Plate Heat Exchanger (PHX) integrated with various types of PCM were analyzed for realizing a Latent Heat Storage Unit (LHSU). This study enabled a detailed experimental characterization of the efficacy of the LHSU realized in a PHX (model: SWEP B5T). The inner volume of the PHX was filled up with PCM. The PCMs considered were PureTemp 29 and lithium nitrate trihydrate with phase transition temperatures of 29 ºC and 29.5°C respectively. The temperature of the heat transfer fluid (HTF) was varied from 32 ºC- 38 ºC for melting and 20 ºC - 26 ºC for solidification. The HTF used in this study was water. The volumetric flow-rate ranged from 5, 7.5 and 10 GPH. Experimental validation for the transient response of the LHSU (i.e., the charging and discharging time periods) were performed.

12.1 Experimental Analysis

The dynamic and energy storage capacity performance of plate heat exchanger were experimentally analyzed with varying flowrate and working fluid inlet temperature. All the above-mentioned parameters are computed and summarized in Appendix E. As shown in Figure 115, the effectiveness during charging and discharging were analyzed for varying flowrate and temperature. In the case of melting (Figure 115A), the effectiveness of the system is a function of both flowrate and inlet temperature. Increasing the flowrate from 5 GPH to 10 GPH, increased the effectiveness by 1.5 times, whereas the increase in inlet temperature from 32°C to 38°C increased the effectiveness by around 60%.

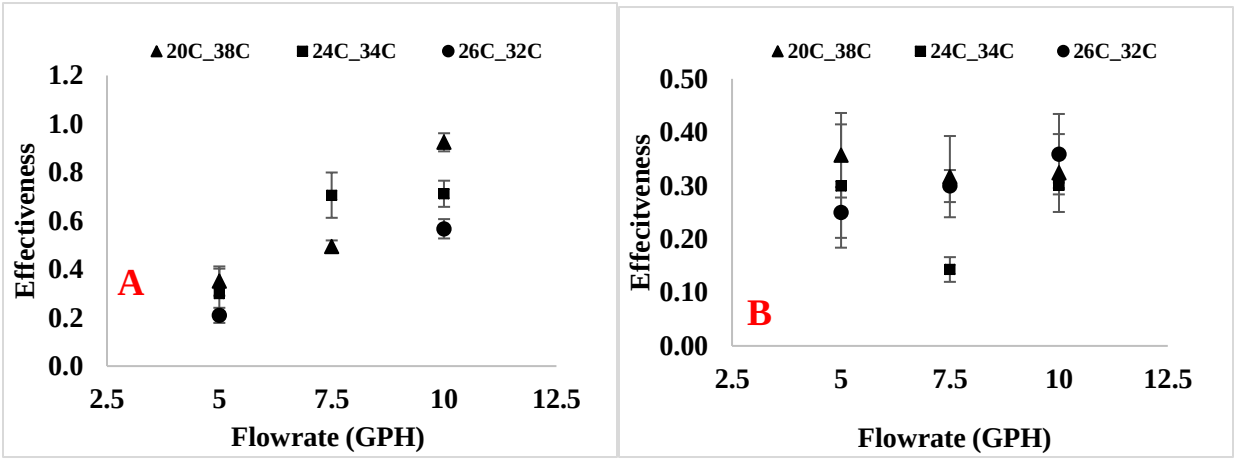

Figure 115: Effectiveness of plate heat exchanger for [A]Charging (melting) [B]Discharging (solidification).

In the case of solidification (Figure 115B), the effectiveness remained constant at around 0.35 above 5 GPH and no variation with decreasing inlet temperature. For the case of 5 GPH, the effectiveness increased with decreasing inlet temperature. When inlet temperature decreases from 26°C to 20°C, the effectiveness increased by 40%. The average effectiveness across the flowrate and temperature was 0.294 with a standard deviation of 0.07. Therefore, solidification is

independent of flowrate and inlet temperature. The outcome is due to low thermal conductivity of Puretemp 29.

The heat transfer within the LHTESS is controlled by two groups of thermal resistance, the thermal resistance of the heat exchanger (i.e. h_{fluid}, k_{plate}) and the thermal resistance of PCM. The thermal resistance circuit of plate heat exchanger LHTESS can be represented as shown in Figure 116. The thermal resistance of PCM is a function of time, as the thickness of PCM (Tpcm) changes with time. k_{pcm} is the effective thermal conductivity of the PCM. Therefore, if the thermal resistance of PCM is small, then thermal resistance of the heat transfer fluid contributes, which causes a plateau in outlet temperature as a function of time. Similarly, when thermal resistance of PCM is high, then the overall resistance changes with time, as resistance increases with time. Therefore, outlet temperature reduces gradually as shown in Figure 117 and Figure 118 summaries the temperature profile of lithium nitrate trihydrate during melting and solidification with varying volumetric flowrate. Figure 118 summaries the temperature profile of lithium nitrate trihydrate during melting and solidification with varying volumetric flowrate, and Figure 117 summaries the temperature profile of lithium nitrate trihydrate during melting and solidification with varying volumetric flowrate. In the case of solidification, the effectively thermal conductivity of PureTemp 29, lithium nitrate trihydrate is around 0.25 W/m. K and 0.868 W/m. K, whereas during melting the effective thermal conductivity is enhanced due to the onset of natural convection.

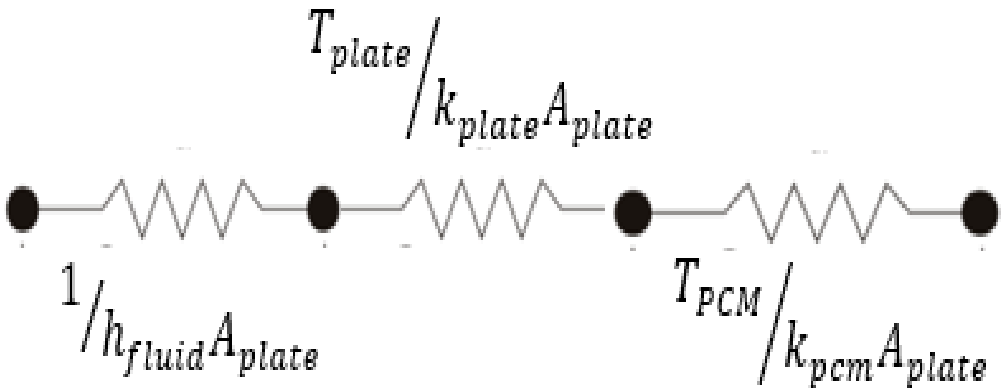

Figure 116: The thermal resistance circuit of plate heat exchanger LHTESS.

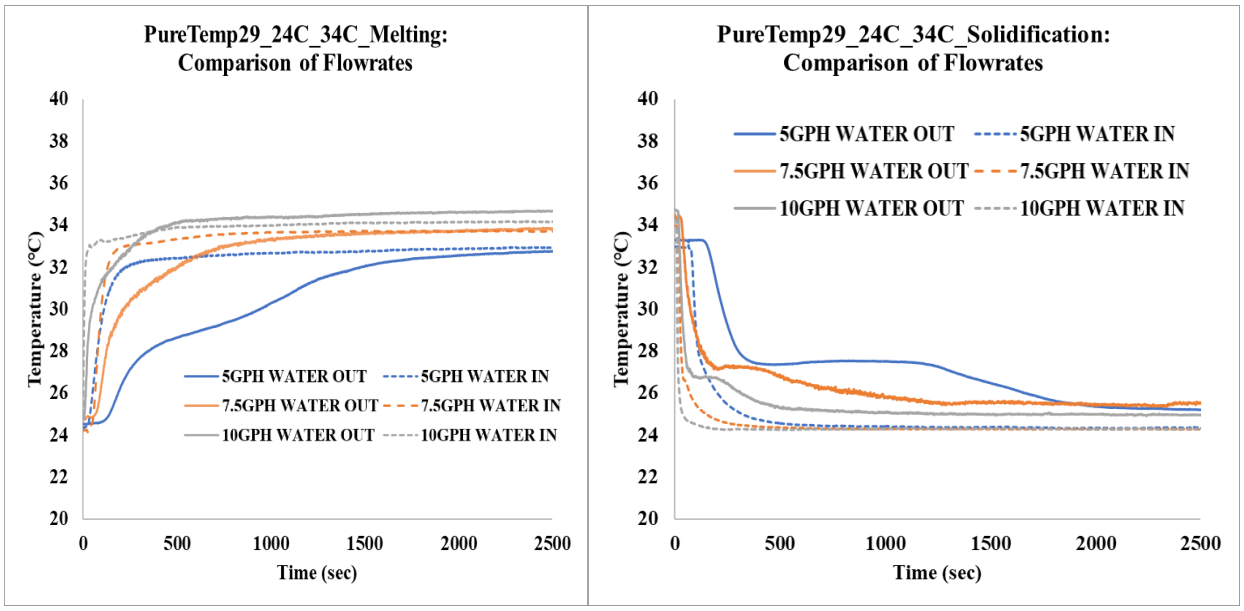

Figure 117: The experiment was conducted between 24°C and 34°C at varying volumetric flow. The volumetric flow was varied from 5GPH to 10 GPH. [Left] Charging [Right] Discharging.

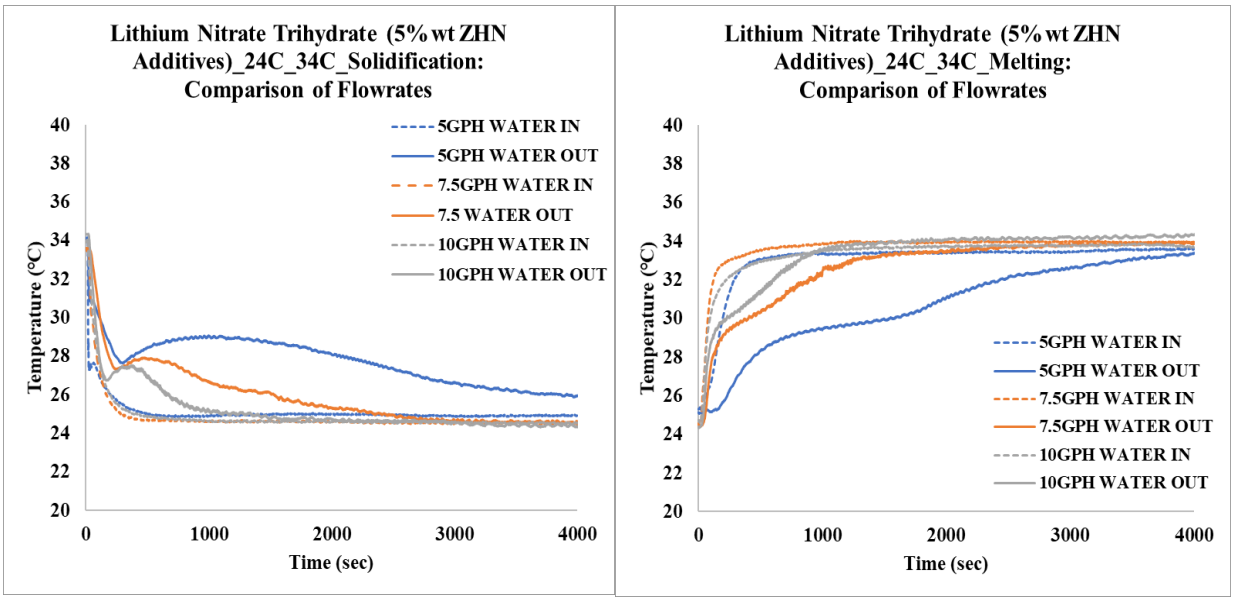

Figure 118: Lithium nitrate trihydrate with 5% zinc nitrate hydroxyl as nucleating additives. The experiment was conducted between 24°C and 34°C at varying volumetric flow. The volumetric flow was varied from 5GPH to 10 GPH. [Left] Charging [Right] Discharging.

In the case of solidification, the heat transfer is limited by the thermal resistance of PCM, therefore even reduction in inlet temperature or increase in mass flowrate will not enhance the effectiveness of the system. Whereas for melting, the heat transfer is still limited by the thermal resistance of PCM, but contribution of natural convection is a function of wall temperature. The wall temperature influenced by mass flowrate and inlet temperature. This trend can be further established by analyzing the thermal resistance (UA) of the system. During solidification, UA averaged around 16.3 with varying flowrate and temperature with a standard deviation of 5.9, whereas during melting UA varied with increasing mass flowrate and inlet temperature. The UA varied from 40 at 5 GPH to 140 at 10 GPH. Even at the lowest flowrate the heat transfer during melting is 2 times higher than solidification. The characteristics time (τ) provides an average charging and discharging time per KJ. The characteristic time provides a means of estimating the average charging and discharging time for given storage capacity. In most cases, the charging

needs to be quicker than discharging. The average ratio of discharging to charging is 1.32 (±σ: 0.08) at 5 GPH and 1.68 (±σ: 0.41) at 10 GPH. Therefore, the selection of flow-rate purely depends on the duration of charging and discharging. Based on the current results, we could conclude that plate heat exchanger is ineffective as LHTESS for two main reasons, the effectiveness during solidification is very low. Figure 119 illustrates the performance on Puretemp 29 and lithium nitrate trihydrate. The energy storage capacity affects the length time for solidification and melt. Lithium nitrate trihydrate has a high-power rating in comparison to PureTemp 29.

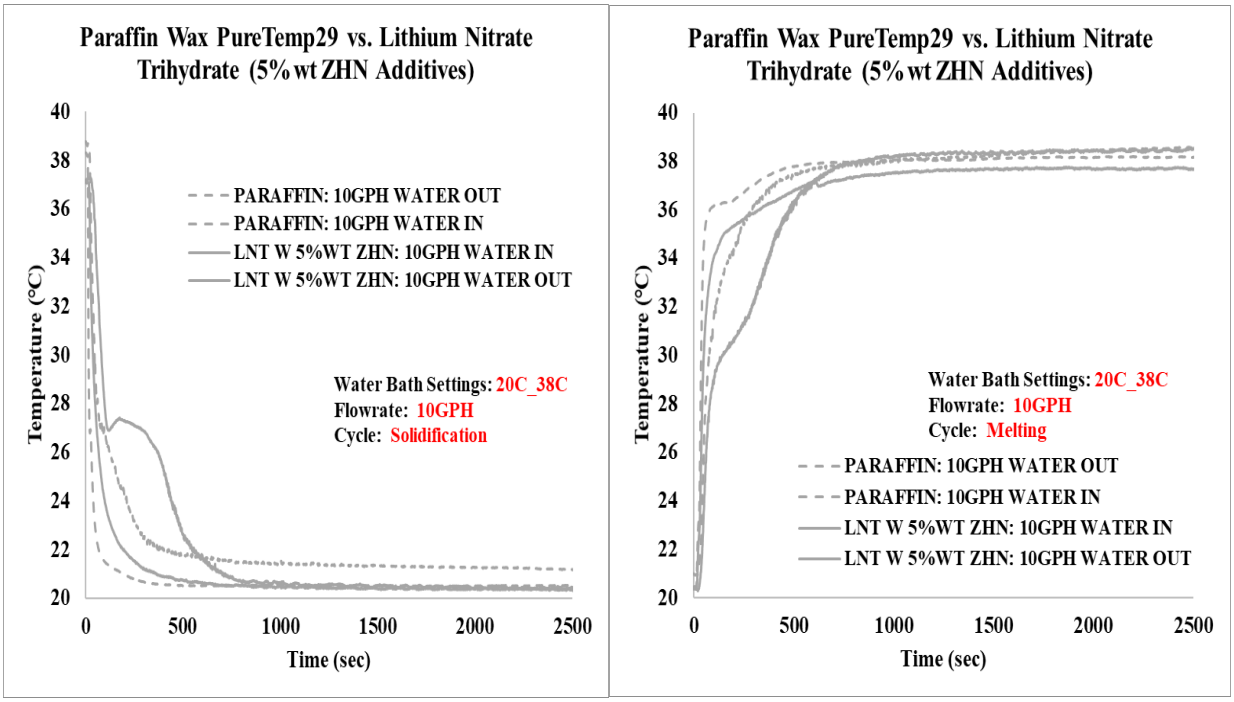

Figure 119: Comparison of results between PureTemp and Lithium Nitrate Trihydrate. The comparison was done at solidification temperature of 20°C and melting temperature of 38°C at a volumetric flowrate of 10 GPH.

12.2 Summary and Recommendation

An experiment is conducted to understand the performance of a plate heat exchanger as a latent heat thermal energy storage system, using biodegradable PCM (i.e. Puretemp 29) as the PCM. The aim of the experiment is to characterize and benchmark the energy storage and dynamic performance of the system. The experiments demonstrate that during charging higher transfer efficiency could be correlated to increasing flowrate and working fluid temperature, whereas during discharging only flowrate influenced the performance. This is can be related to effects of natural convection during charging and low thermal conductivity during discharging. Accordingly, it can be stated that, for further work, it would be necessary to properly design and realize the maximum optimized performance of plate heat exchanger and with increased energy storage density.

In conclusion, chevron plate heat exchanger is ineffective as a LHTESS due to the low efficiency during solidification – limited by low solid thermal conductivity of PCMs, high metal to PCM ratio – high transient parasitic loss. The beneficial outcome of chevron plate heat exchanger as a LHTESS is the high thermal power during melting. As 115W of thermal power was achieved with 5GPH flowrate during melting. In the case of melting, the power could be correlated to increasing flowrate and inlet fluid temperature, whereas for solidification, the power is not related to flowrate but more of a function of solid thermal conductivity of PCM and inlet temperature of fluid.

Future recommendation is implementation of thermal conductivity enhancement techniques (i.e. fins, foams etc.) to reduce the thermal resistance during freezing and increase the overall power of the system. Implementation of "cold finger" to reduce sub-cooling in the system.

CHAPTER XIII

RESULTS OF SHELL AND TUBE HEAT EXCHANGER

Experimental validation was performed in this study to verify the efficacy of numerical models for predicting the location of solid-liquid interface in an axis-symmetric configuration during both melting and solidification in a Latent Heat Storage Unit (LHSU). Development of analytical solutions for predicting the location of the solid-liquid interface is often intractable in LHSU due to non-linear temperature distribution in the Phase Change Material (PCM). This is further complicated by the moving boundary problem with free convection within the liquid phase of the PCM. Analytical solutions available in the contemporary literature are based on simplified transient heat conduction models and often fail to reliably predict the charging and discharging time constants for LHSU with complex configurations. This study is designed with the goal of developing more sophisticated numerical models for the estimation of transient thermal performance of an LHSU with a simple configuration involving a shell and tube heat exchanger (HX).

The LHSU utilized in this study is realized by integrating various types of Phase Change Materials (PCM) contained in the shell side of a HX. The LHSU is charged or discharged by pumping hot or cold fluids in the tube side of the HX (i.e., by pumping water at a fixed inlet temperature from a commercial chiller apparatus). This study enabled the characterization of the transient response of a LHSU subjected to conduction and forced convection heat transfer. The PCM used in this material was paraffin wax (PURETEMP 29). The HX in the LHSU consisted of a single pass straight tube (½ inch copper pipe) mounted within a single shell configuration. The shell was fabricated from plastic material using additive manufacturing (i.e., “3D Printing”). The

HX assembly was performed by inserting a tube into the shell. The shell was filled with PCM and sealed to prevent leaks. The temperature variation during melting and solidification of the PCM were measured at different radial and axial locations within the cylindrical shell that was mounted vertically. A commercial chiller unit was used to pump water into the tube and the mass flow rate of the working fluid (water) was fixed at 4 GPH (gallons per hour) and 6 GPH. The inlet temperature of water was maintained at 40 ºC and 45ºC (for melting) as well as 10ºC (for solidification). The experiment results show that the transient response of the LHSU for charging and discharging (i.e., time required for melting and solidification of the PCM) vary significantly. Comparison of the experimental data with analytical results (involving quasi-stationary models for phase change) demonstrate that natural convection is the dominant mode during the melting process, while conduction is the dominant mode during the solidification process.

13.1 Experimental Analysis

The thermal performance of the shell-and-tube hx is established by measuring the temperature variation at different radial and axial locations within the cylindrical shell during melting and solidification. FIGURE 120 and Figure 121 shows the temperature distribution near the heat source and the mid-plane during the melting process. The temperature distribution shown in FIGURE 120 and Figure 121 is for mass flowrate of 0.007 kg/sec and fluid inlet temperature of 40° C. The temperature of PT29 at location e is higher than that of location a and b at the initial stage. The melting at location ends at 0.5 hours and around 2.5 hours at location b. It is further observed that location a has a sudden and rapid increase to the steady temperature of 36°C, this could be due to the density difference between solid and liquid, an empty void is formed at the top of the shell filled with air as shown in Figure 38. After 0.6 hours, the air at top is sufficiently heated and aids in heat transfer at the top due to natural convection and the initial temperature rise is due to the temperature gradient between the pcm and the heat source. Secondly it could also be noted from that a constant temperature line is observed after 1.3 hours near the HTF pipe at thermocouple location a, this indicates that more heat transfer is towards the adjacent layer of the solid pcm. This could be justified by examining Figure 121. After 1.3 hours, the temperature at the middle of thermocouple location a is observed to increase significantly. Similar observations could also be made for all other sections. It is also observed that in pt29 phase transition does not occur isothermally but occurs over a range of temperature.

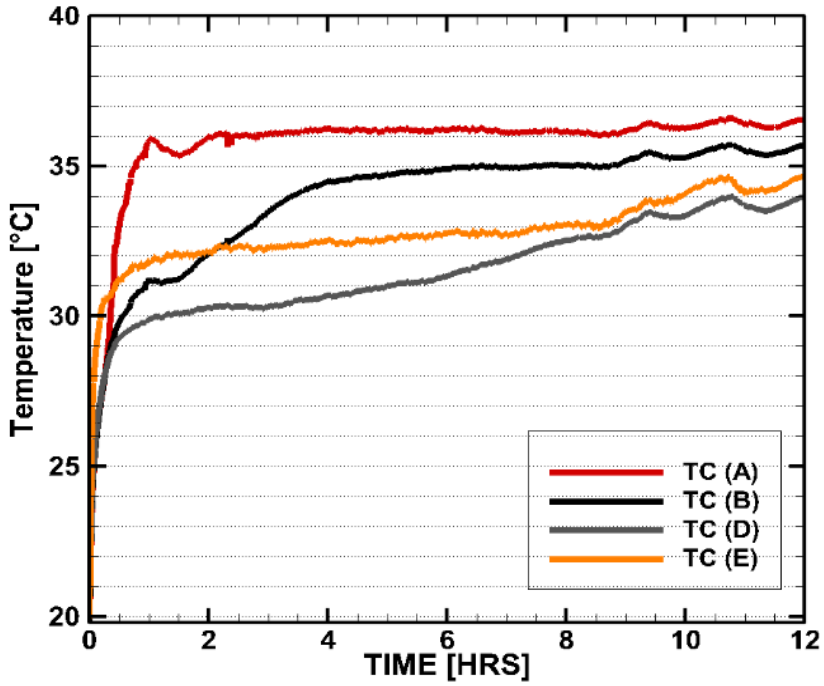

Figure 120: Temperature distribution of PT29 along the axial direction near the HTF pipe (0.0625" away during melting).

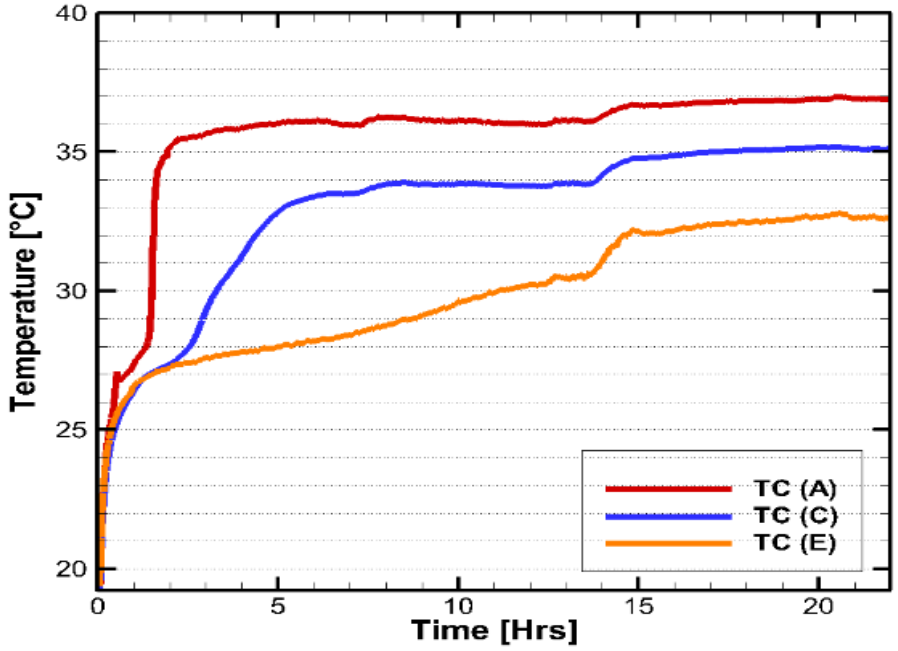

Figure 121: Temperature distribution of PT29 along the axial direction at the mid plane during melting.

Figure 122 shows the axial variation of temperature at the mid-plane as a function of time. Initially the temperature of PT 29 is constant along the axial direction. After two hours, the temperature at the bottom at bottom of the shell reaches 24°C and increased to 26°C after 11 hours, while the temperature at top rises rapidly to 30°C within 3 hours. Another reason for the rapid rise in the temperature the top could be due to initiation of natural convection. The motion of molten PT29 near the heat source is started due to buoyancy force induced by the density gradient.

In summary, it was observed that melting occurs in axial and radial direction. The similar trends of temperature distribution during melting has been reported by [91]. Secondly, it was also observed that the melting front does not move with the same radial velocity along the axial direction. Therefore, it appears that conduction is the dominant transport mechanism at very early times, and thereafter, natural convection comes into play and takes over.

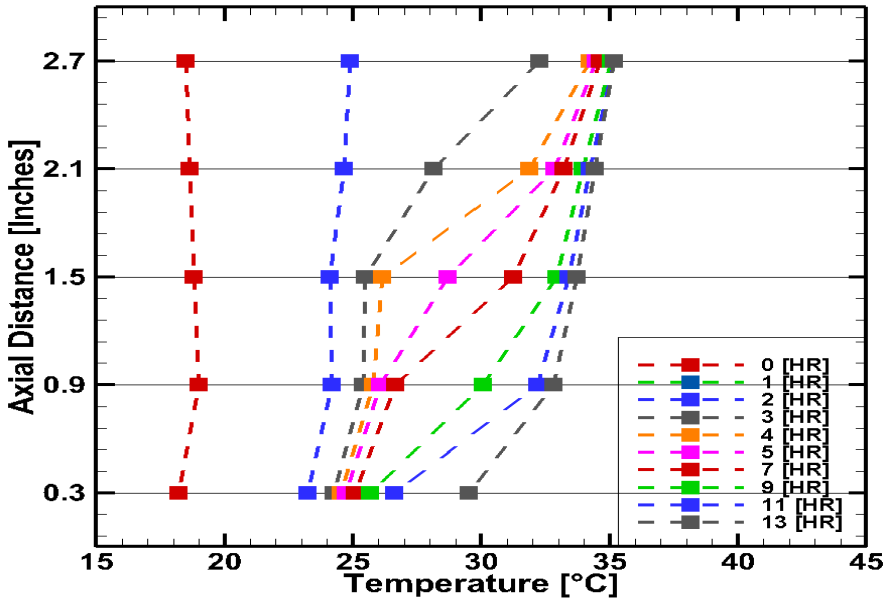

Figure 122: Axial temperature variation along the height of the shell at mid-plane during melting over 13 hours period.

After the charging (endothermic) the PCM, the discharging process was started immediately by-passing cold water through the copper pipe. Figure 123 and Figure 124 shows the temperature distribution near the heat source and the mid-plane during solidification. Molten PT29 gets solidified more rapidly near the copper pipe as seen in Figure 123, because of the large initial temperature gradient between wall of the copper tube and PCM. As observed in , the onset of solidification is around 27°C. It is observed that during solidification process, heat transfer (energy release) is a slow process in contrast melting (energy absorption). The temperature reduces rapidly once PCM solidifies completely.

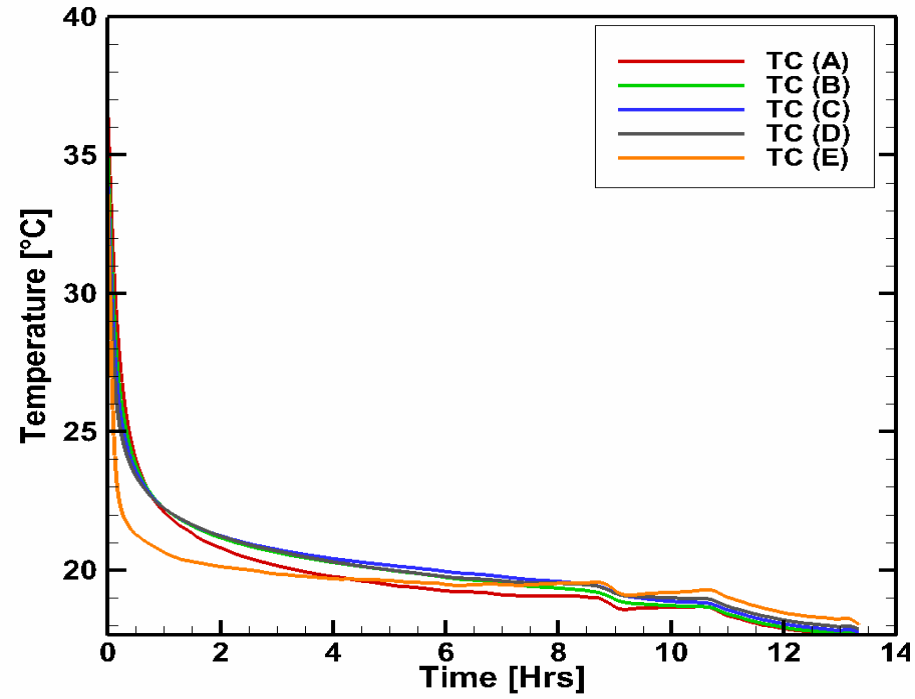

Figure 123: Temperature distribution of PT29 along the axial direction near the HTF pipe (0.0625" away) during solidification.

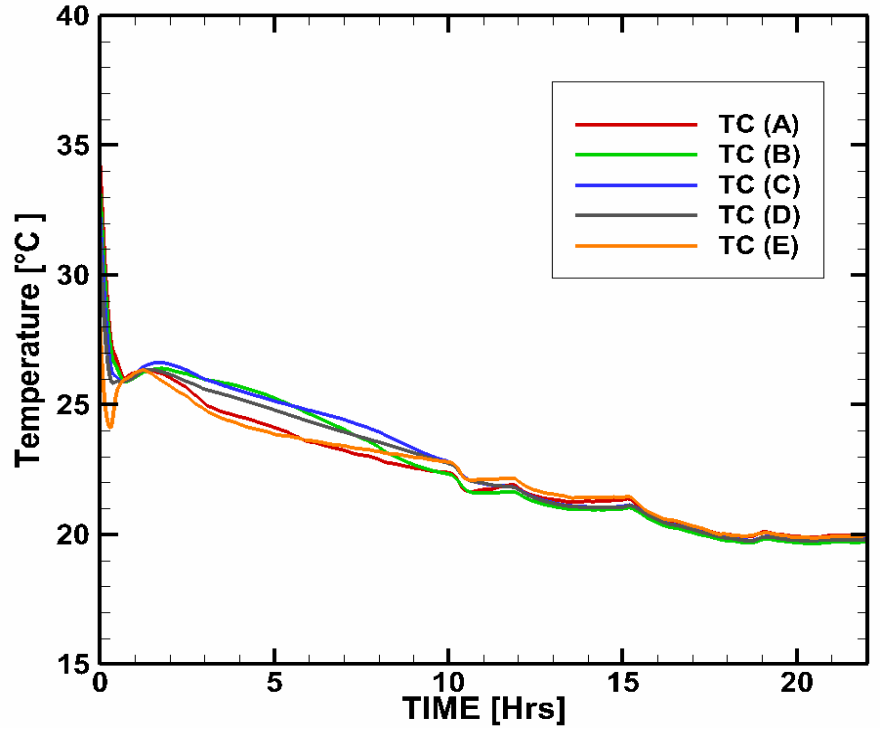

Figure 124: Temperature distribution of PT29 along the axial direction at the mid plane during melting.

As seen Figure 125 in little temperature variation is observed along the axial direction during the initial 2-hour period. After the 2 hours, rapid temperature decline is observed at the top, this could be due to the additional heat losses at the top due to the air gap above PCM after complete solidification.

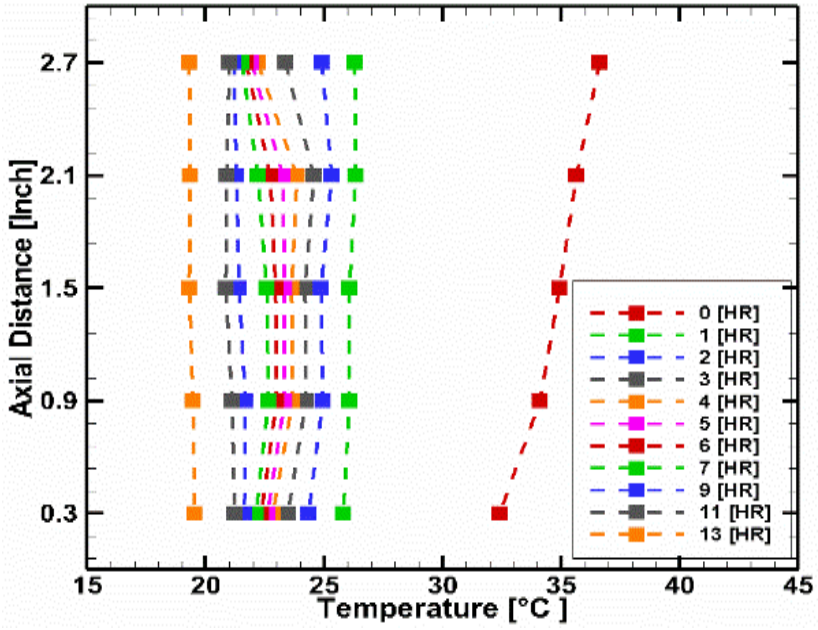

Figure 125: Axial variation of temperature as a function of temperature at mid-plane during solidification

In summary, it was observed that solidification front only moves in radial direction and conduction is the dominant mode of heat transfer. Therefore, solidification front could be simply represented by the thermal conduction resistance as given by the following equation:

$$R_{t,cond} = \frac{\ln\left(\frac{r(t)}{r_{inner}}\right)}{2\pi Lk} \tag{13.1}$$

Where r(t) is location of solidification front, r_{unner} is the outer radius of the copper tube, L is the length of the test shell, and k is the thermal conductivity (solid) of PCM. This thermal conduction resistance depends purely of the locus of the solidification front. As solidification, front moves outwards, the thermal resistance increases, thus reducing the rate of heat transfer. Hence the heat transfer is higher near the pipe and reduces along the radial direction, and similar trends were observed in the experimental study. The total time taken for solidification is 11 hours, in contrast melting was completed in 6.5 hours.

Figure 126 shows the comparison of the analytical solution to the experimental result. The derivations for the analytical solution are shown in equation 1 to 7. Based on the experimental and analytical result, it could be concluded that Quasi-Stationary 1-D analytical solutions predicts the solidification time to higher precision than the melting.

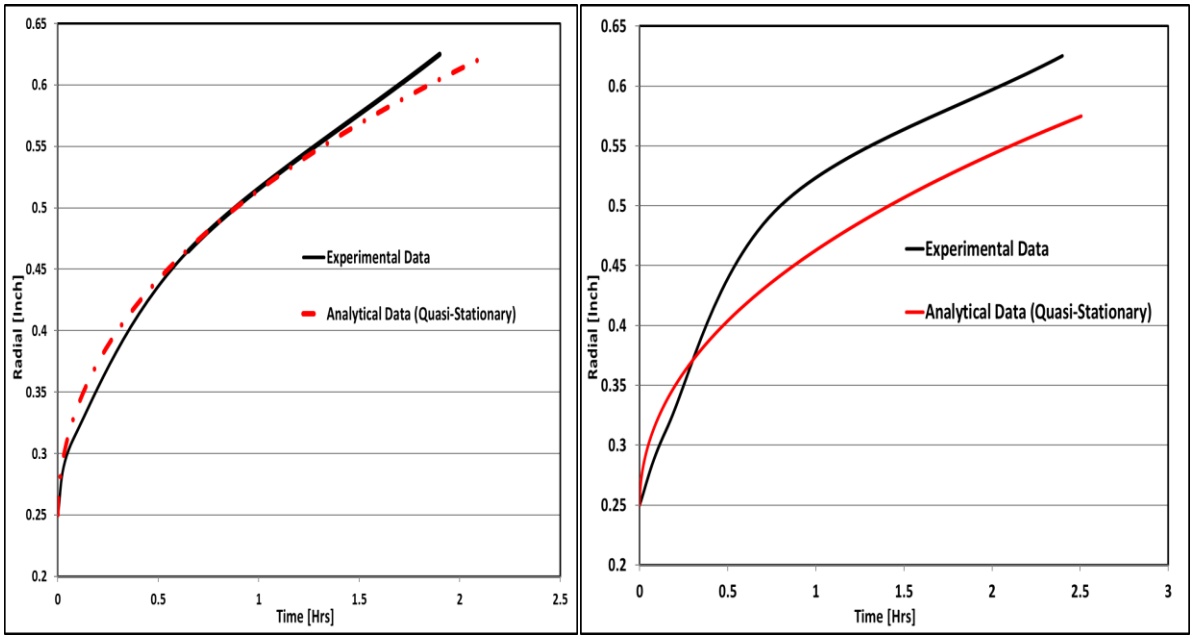

Figure 126: Comparison with Analytical Solution [Top: Solidification; Bottom: melting].

13.2 Summary

Experimental validation was performed in this study to verify the efficacy of numerical models for predicting the location of solid-liquid interface in an axi-symmetric configuration during both melting and solidification in a Latent Heat Storage Unit (LHSU). Comparison of the experimental data with analytical results (involving quasi-stationary models for phase change) demonstrate that natural convection is the dominant mode during the melting process, while conduction is the dominant mode during the solidification process. One can say that the analytical solutions available in the contemporary literature are based on simplified transient heat conduction models often fail to reliably predict the charging time constants for LHSU with complex configurations. Future studies would be conducted to analyze the effects of different bath temperature and flowrate on the melting and solidification in depth.

CHAPTER XIV

RESULTS OF 100 KJ COMPACT HEAT EXCHANGER

The aim of this section is to perform experimental validation of the effectiveness of compact heat exchangers (filled with aluminum porous foam impregnated with phase change materials/ PCM). The objective of the experiments is to ascertain the efficacy of the compact heat exchanger (CHX) platform as a part of a latent heat thermal energy storage system (LHTESS) for various types of loading cycles. The PCM used in this study was pure Lithium Nitrate Trihydrate (LNT). The net energy storage capacity of this LHTESS was theoretically rated to be 130 kJ. This rating was based on the total mass of LNT loaded in the CHX (i.e. the total mass of LNTH was estimated to be 474 grams based on the total mass of the CHX after charging with PCM and as received at TAMU after it was shipped by the vendor (Allcomp Inc., City of Industry, CA). The latent heat of melting, i.e., the phase change enthalpy (H_{fs}), of LNTH is assumed to be 275 J/g.

The primary aim of the study was to verify if the melting and solidification could be achieved in a specified amount of time (i.e., to enable comparison with predictions from numerical simulations). The experimental design was geared to enable the heat transfer fluid (HTF) to attain a 5°C temperature differential during cooling of the HTF which corresponds to the melting cycle (i.e., dehydration). This was designed for a duration of 30 minutes for an inlet temperature of 37.4°C of the HTF at a mass flowrate of 0.0035 kg/sec (approximately 3 gallons per hour, or 3 GPH). The HTF chosen for this study was de-ionized water (DIW). During the solidification cycle of the PCM (i.e. hydration process) the experiments were designed for completion of solidification of the PCM in less than hour for an inlet temperature of 25°C at a mass flow rate of 0.0035 kg/sec. Second aim of the study was to implement “Cold Finger” experimental protocol and verify the

efficacy of this protocol for many thermocycles involving complete solidification and partial melting of the total mass of PCM in the CHX. The goal of the "Cold Finger" experiments was to achieve subcooling of less than 1°C (without the aid of nucleating additives) for initiating solidification of the PCM. This was also expected to enhance the reliability of operation of the LHTESS.

"Cold Finger" techniques involve thermo-cycling protocols with complete solidification and incomplete melting of the PCM samples under consideration. The incomplete melting protocols enable a residue of PCM crystals to remain in the PCM sample - which in-turn act as nucleators (i.e., nucleation promoters). Prior studies by the research team at TAMU have shown that this un-melted phase of the PCM (i.e., the residue crystals) provide better efficacy for promoting nucleation (i.e., at subcooling less than 1 °C) than that of heterogeneous additives for promoting nucleation. To realize the full effectiveness of the "Cold Finger" techniques, the experiments were designed for the flow of HTF in to the CHX to be bi-directional. During melting the HTF flowed from left to right and during solidification the flow direction was reversed (i.e., right to left). This enhances the efficacy of the residue crystals to initiate the nucleation and for the propagation of the solidification front in the melted phase of the PCM. The experiments were designed for the melting to proceed until 90% of the total latent heat energy storage capacity, thus allowing about 10% of the remaining PCM to be un-melted and remain in solid phase as dispersed crystals (i.e. as unused energy storage capacity). Thus, storage capacity is sacrificed marginally to enable better reliability of operation for the LHTESS.

14.1 Efficacy Of "Cold Finger" Technique

As reported by previous studies sub-cooling ($\Delta T_{sub\text{-}cooling}$) could be as high as 30°C without nucleators and reduce less than 5°C without nucleators, but nucleators are susceptible to degradation with thermal cycling. A $\Delta T_{sub\text{-}cooling}$ of more than 5°C is not acceptable in LHTESS applications. Therefore, the efficacy of *"Cold Finger"* technique was experimentally validated to suppress sub-cooling to less than 1°C without the aid of nucleating additives for initiating freezing, therefore enhancing the overall reliability of the LHTESS. The *"Cold Finger"* technique was validated in two different configurations (Figure 49). In configuration A, the flow direction of Heat Transfer Fluid (HTF) was reversed during melting and solidification phase. During melting phase, the flow of HTF was from left to right, whereas during solidification the direction was reversed to flow from right to left. In configuration B, the direction during melting and solidification was fixated to flow from left to right.

"Cold Finger" technique implemented involve thermal-cycling protocols with complete solidification and incomplete melting of the PCM samples under consideration. The incomplete melting protocols enable a residue of PCM crystals to remain in the PCM sample - which in-turn act as nucleators (i.e., nucleation promoters). Prior studies have shown that this un-melted phase of the PCM (i.e., the residue crystals) provide better efficacy for promoting nucleation (i.e., at subcooling less than 1 °C) than that of heterogeneous additives for promoting nucleation. To realize the full effectiveness of the "Cold Finger" techniques, the experiments were designed for the flow of HTF in to the CHX to be bi-directional. This enhances the efficacy of the residue crystals to initiate the nucleation and for the propagation of the solidification front in the melted phase of the PCM. The experiments were designed for the melting to proceed until 90% of the

total latent heat energy storage capacity, thus allowing about 10% of the remaining PCM to be un-melted and remain in solid phase as dispersed crystals (i.e. as unused energy storage capacity). Thus, storage capacity is sacrificed marginally to enable better reliability of operation for the LHTESS.

Configuration A and B freezing temperature profiles during "Cold Finger" is as shown in Figure 127. In the case of configuration, A, the maximum sub-cooling was measured to be 3.3°C at the 10% and 30% freeze front, with an average 2.1°C temperature suppressing in HTF during the sub-cooling period of 5 minutes. Whereas in configuration B, by reversing the flow direction during melting and freezing, the max sub-cooling was measured to be less than 0.5°C, with negligible temperature suppressing in HTF. Therefore, the results summarize that, *"Cold Finger"* technique permits one to maintain $\Delta T_{sub\text{-}cooling}$ less 5°C without the aid of any nucleators with a 10% loss in energy storage capacity. When the HTF flow direction is are reversed during melting and freezing, the system is able to achieve $\Delta T_{sub\text{-}cooling}$ of less than 1°C, which can't be achieved with aid of nucleators.

The effectiveness of the *Cold Finger* technique was experimentally ascertained in both co-Configuration A and B. In the case of the configuration A, maximum subcooling during solidification was 3 °C as shown in Figure 127, whereas in the case of configuration B the maximum subcooling during solidification was 0.5 °C as shown in Figure 127. In the case of configuration B, the direction of nucleation (i.e. crystal growth) was in the same direction as the flow, thus creating a favorable orientation of the nucleation spot, as portrayed in Figure 129.

In configuration A, due to lack of a cold spot in the flow direction, the effectiveness of the *Cold Finger* technique (i.e., in both minimizing subcooling while enhancing the power rating) was

diminished. Therefore, based on the flow directions (in melting and solidification), the subcooling in the PCM (i.e. 90% freeze front location) is enhanced without the aid of cold spots and decreases when there is presence of a cold spot (i.e. at the 10 % freeze location), as shown in Figure 128. Figure 128 and Figure 129 illustrates the schematic explanation of nucleation in configuration A and B respectively. The rate of nucleation or crystal growth is a function of heat removal (o_{ut}) from the PCM. The rate is heat removal at any axial location is increased with increasing ΔT ($T_{PCM} - T_{HTF}$). As illustrated in Figure 128 for configuration A, the HTF fluid increases in temperature along the axial direction through sensible heat from PCM towards the un melted region (remaining crystal – 90% location), therefore T_{HTF} at 90% location is more than 25°C. Whereas as illustrated in Figure 129 for configuration B, T_{HTF} at 90% location is at 25°C. Therefore, the rate of crystallization is faster in configuration B than configuration A. Due to the slow rate of crystallization in configuration A, the PCM is sub-cooled to below the phase transition temperature, thus creating two nucleation spots randomly at the sub-cooled temperature. Whereas in configuration B, direction crystallization growth and cooling of PCM was from right to left thus preventing any sub-cooling along the axial direction, as the cooling rate and crystallization rate is predicted to be in same magnitude.

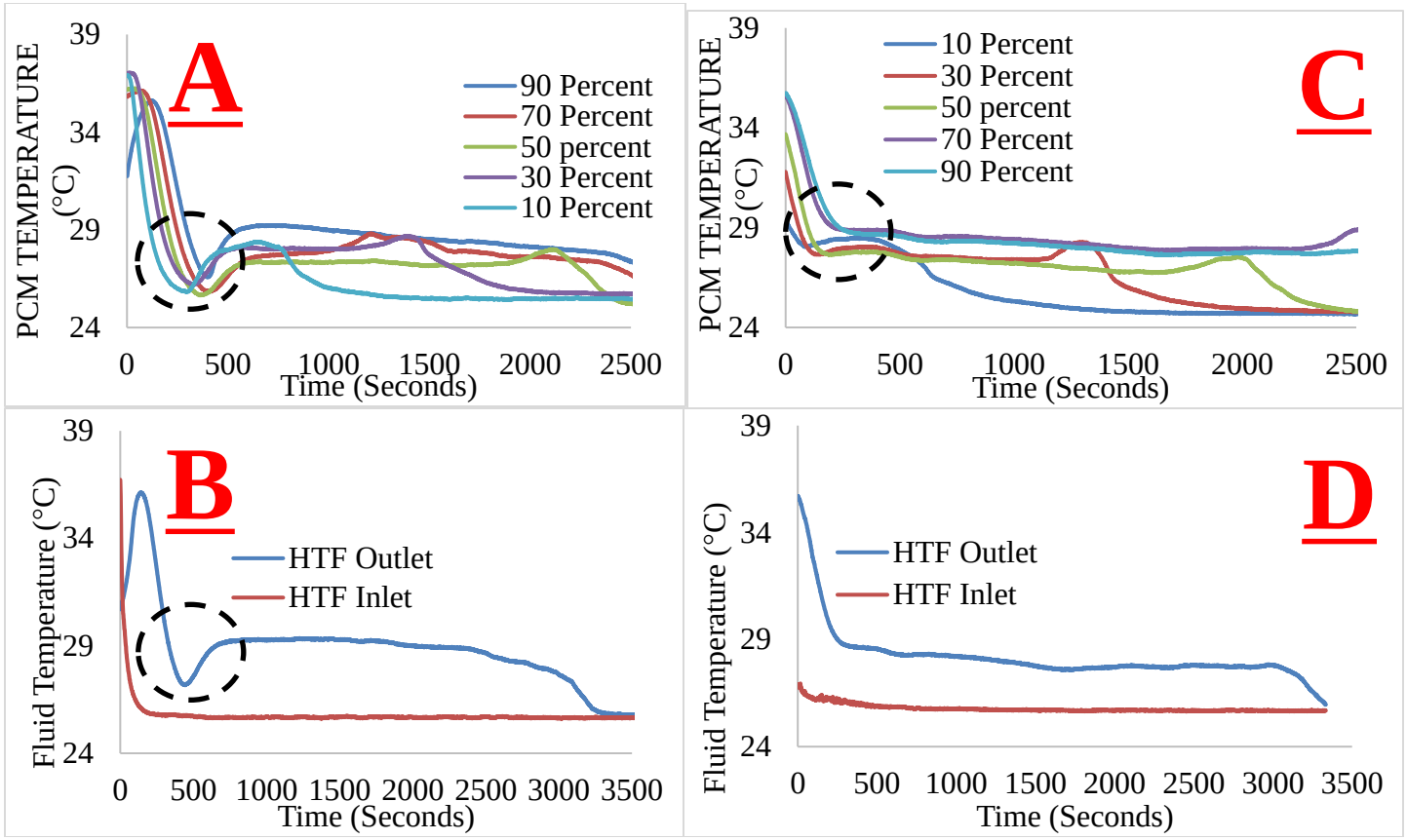

Figure 127: The temperature profile of "Cold Finger" configuration A and B with 90% melt in the top PCM channel. Plot A and B illustrates the temperature profile of PCM top channel and HTF during solidification in configuration B format. The volumetric flowrate in configuration B during solidification was 0.218 L/min (± 4.5%), and Cold- water bath temperature was set a 25°C (± 3.2%). Plot C and D illustrates the temperature profile of PCM top channel and HTF during solidification in configuration B format. The volumetric flowrate in configuration A during solidification was 0.229 L/min (± 4.3%), and Cold -water bath temperature was set a 25°C (± 3.2%). The highlighted region in plot A, B, and C shows the sub-cooling requirement in configuration A and B. In configuration B format, the maximum sub-cooling was measured to be 3.3°C (Plot A) and average effective sub-cooling of 2.1°C (Plot B), whereas in configuration B, the maximum sub-cooling was measured to be 0.5°C (Plot C) and average effective sub-cooling of 0°C (Plot D).

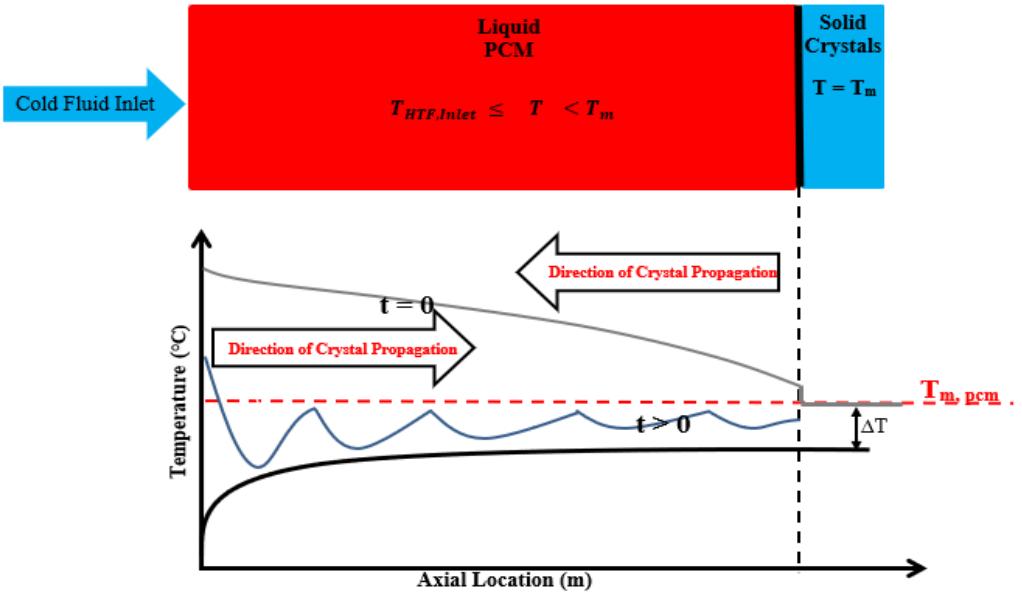

Figure 128: A schematic explanation of nucleation in configuration A. The solid black line represents HTF temperature profile along the axial direction. The dotted red line represents the phase transition temperature of the PCM. The solid grey line represents the axial temperature profile of PCM at time equals to 0 (immediately after the completion of 90% melt). The solid blue line represents the onset of nucleation at some time after initiation of solidification. ΔT is temperature difference between HTF and PCM along the axial direction.

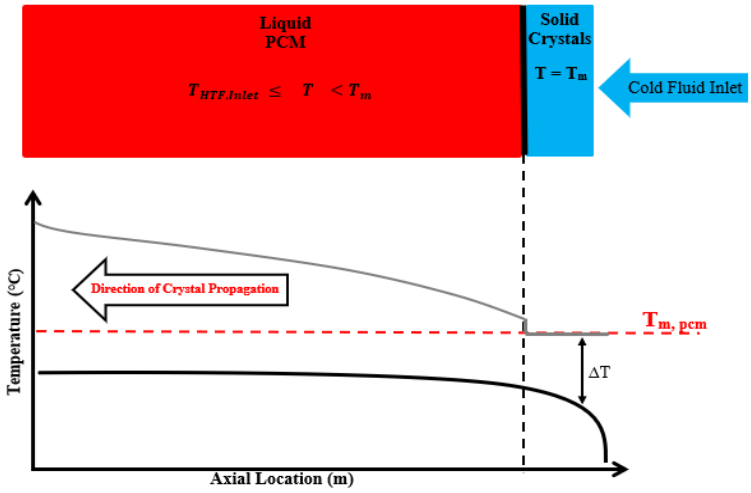

Figure 129: A schematic explanation of nucleation in configuration B. The solid black line represents HTF temperature profile along the axial direction. The dotted red line represents the phase transition temperature of the PCM. The solid grey line represents the axial temperature profile of PCM at time equals to 0 (immediately after the completion of 90% melt). ΔT is temperature difference between HTF and PCM along the axial direction.

14.2 Design Condition Analysis

The primary aim of the design condition was to verify if the melting and solidification could be achieved in a specified amount of time (i.e., to enable comparison with predictions from numerical simulations). The experimental design was geared to enable the heat transfer fluid (HTF) to attain a 5°C temperature differential during cooling of the HTF which corresponds to the melting cycle (i.e., dehydration). This was designed for a duration of 30 minutes for an inlet temperature of 37.4°C of the HTF at a mass flowrate of 0.0035 kg/sec (approximately 3 gallons per hour, or 3 GPH). During the solidification cycle of the PCM (i.e. hydration process) the experiments were designed for completion of solidification of the PCM in less than hour for an inlet temperature of 25°C at a mass flow rate of 0.0035 kg/sec.

The thermal effectiveness of the LTHESS obtained in these experiments are listed in Table 45. At design condition (i.e. Case A – design condition), the system was able to provide 6.9°C of cooling to HTF during melting (i.e. dehydration) phase: which meets the project deliverable of cooling in excess 5°C. The CHX was able to sustain the cooling capability for 28 minutes. This shows that the energy storage capacity was 121 KJ (i.e., for an estimated mass fraction of 90% of the PCM that was melted). For the case of solidification (i.e. hydration), the PCM sample was completely solidified in 50 minutes: which meets the project deliverable of cooling within 60 minutes, at this design condition. The effectiveness of LHTESS during melting and solidification was 0.88 and 1 respectively.

Table 45: Summary of Experimental Validation of Compact Heat Exchanger LHTESS with varying flowrate, melting (i.e. dehydration) and solidification (i.e. hydration) conditions.

CASE	CASE A		CASE B	
	Melting (Dehydration)	**Solidification (Hydration)**	**Melting (Dehydration)**	**Solidification (Hydration)**
Inlet Temperature (°C)	37.4	25	35	25
Mass Flowrate (kg/sec)	0.0034 (±3.5%)	0.0035 (±3.5%)	0.0035 (±3.2%)	0.0033 (±4.1%)
$\Delta T_{HTF,\ Average}$ (°C)	6.9 (±1.4%)	2.5 (±4%)	4.8 (±2.1%)	2.3 (±4.5%)
Storage Capacity (kJ)	125(±4.8%)	121 (±7.3%)	122(±5.3%)	124 (±8.3%)
Average Power (kW)	0.074(±4.8%)	0.037 (±7.3%)	0.070 (±5.3%)	0.034 (±8.3%)
Duration of Phase Change (Minutes)	28	50	33	62
Stefan Number	0.01	0.006	0.01	0.008
Effectiveness	0.88	1.0	0.70	1.0

14.3 Effects of Varying Parameter on Thermal Performance

The LHTESS is effectively a thermal battery (i.e., for delivering and storing heat at different duty cycles). Therefore, it is important to analyze the instantaneous power performance and the average power output during melting and solidification to validate the thermal performance of the LHTESS. In the case of an electric battery, instantaneous power is typically constant (slight line) during both charging and discharging process. In contrast, for thermal battery the power ratings could vary drastically during charging and discharging due to the influences of natural convection and thermal conductivity. Figure 130 illustrates the instantaneous power during melting and solidification for varying volumetric flowrate, melting and solidification temperature. The volumetric flowrate was varied from 3 GPH to 5 GPH. The melting temperature was varied between 37.4°C and 35°C. The solidification temperature was varied between 20°C and 25°C. As summarized, for thermal battery the power is not constant during melting but is constant throughout solidification. During melting the power peaks initially due to onset of melting and sudden cooling of HTF, as melting starts along the axial direction at the same time, and the power decreases gradually as the energy storage capacity is reduced. This concludes that during melting high influx of power is absorbed during the initial period of 4 to 6 minutes and then power gradually reduces through the remaining melt front. Whereas in the case of solidification the instantaneous power remains constant, acting an electric battery. The reason for variation in power behavior during melting and solidification is mainly due to the heat transfer mechanism. During melting the heat transfer into the PCM is through natural convection, and conduction, whereas during solidification, the heat transfer from the PCM is mainly dominated by conduction.

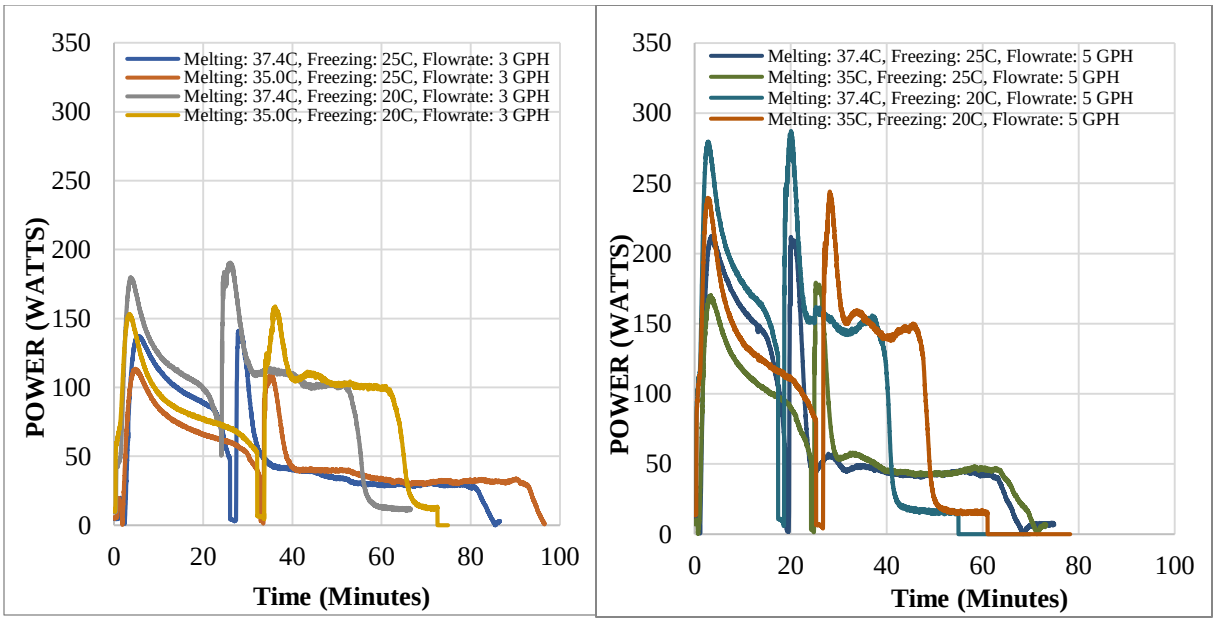

Figure 130: Instantaneous power for the melting and solidification. [Left] Volumetric Flowrate of 3GPH with melting temperatures of 37.4°C, 35.0°C and solidification temperature of 25°C and 20°C. [Right] Volumetric Flowrate of 5GPH with melting temperatures of 37.4°C, 35.0°C and solidification temperature of 25°C and 20°C.

Figure 131 summarizes the values of the average power rating for varying flowrate and inlet temperatures for both during melting and solidification. The average power is a function of mass flowrate, specific heat capacity of HTF, and the temperature difference of HTF between inlet and outlet. Due to temperature gradient, there is marginal change in specific heat capacity of the experiment, but it could be assumed constant. Therefore, the contribution on the effects of average power is mainly from change in mass flowrate and inlet temperature during melting and solidification. In the case of solidification, when the inlet temperature is 25°C, the average increased by 25% by increasing the volumetric flowrate from 3 GPH to 5 GPH with a 18% reduction in freezing as summarized in Figure 133and with negligible variation in ΔT of heat transfer as summarized in Figure 134. Therefore, the increase in average power in mainly contribute due to the increase in mass flowrate due to shorter freezing time, as the energy capacity remained constant at around 123 KJ as summarized in the solidification plot of Figure 132.

Starting temperature (i.e. previous melting temperature) had negligible effect on power, energy storage capacity, freeze time and ΔT of heat transfer fluid. Whereas when the freezing temperature was reduced to 20°C, the average power was roughly increased by 2X and 3X for 3 GPH and 5 GPH respectively. At lower freezing temperature the energy storage capacity was increased by 40% in comparison to energy storage capacity at 25°C freezing. The cause for variation on storage capacity during freezing at 20°C could be attributed to the heat loss. The PCM section of the heat exchanger was insulated, but the water manifold was not insulated. The heat exchanger was kept in enclosed environment at a temperature of 22 to 24°C. Therefore, at lower temperature the heat gained from the ambient increased the overall storage capacity. By reducing the freezing temperature from 25°C to 20°C the ΔT increased was 3 times, therefore the power was increased by 3 times. This power increase is not 100% due to lowering of freezing temperature, the parasite heat gained also contributed to the power increase. The parasite heat loss along the PCM section is negligible as it was insulated, and the time to complete freeze was reduced by 50% with 5°C drop in freezing temperature, therefore based on time of freeze the average power is enhanced by 50%. Therefore, the remaining increase in power is contributed by parasite heat gained. Increasing the volumetric flowrate reduced the freezing time roughly by 20%. Therefore, both inlet temperature and volumetric flowrate plays an important role in determining the thermal performance of LHTESS during freezing. A 20% reduction (25°C to 20°C) in freezing time increased the average power by 50%, whereas a 67% increase (3 GPH to 5 GPH) only increased the average power by 20%. In actual application, inlet temperature can't be predetermined as depends on daily weather condition, therefore the only thermal performance control availability is volumetric flowrate.

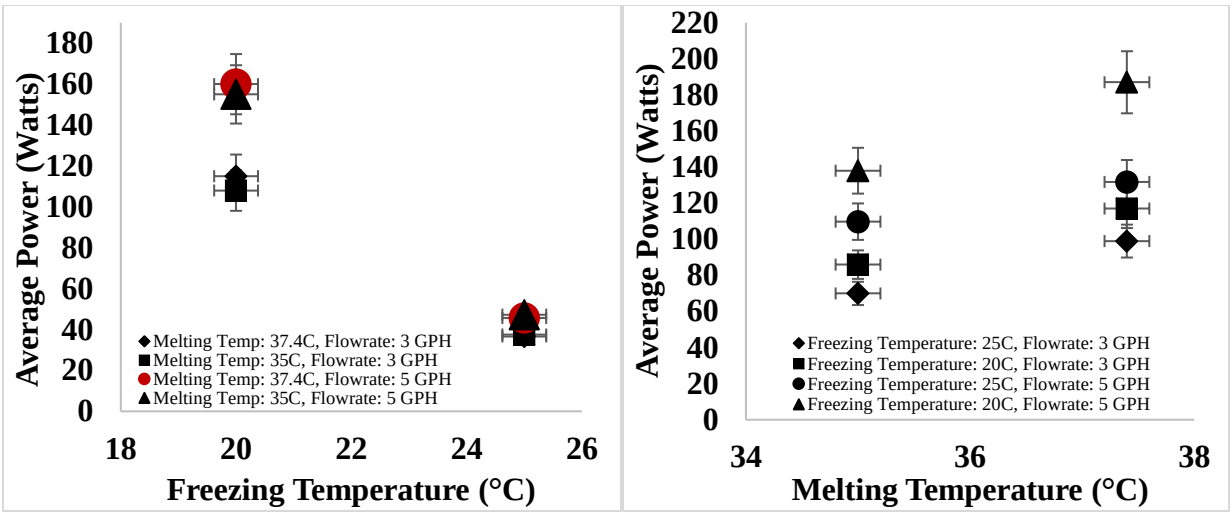

Figure 131: The average power of LHTESS during melting and solidification. [Left] Average power during solidification with varying flowrate and varying starting temperature. [Right] average power during melting with varying flowrate and varying temperature.

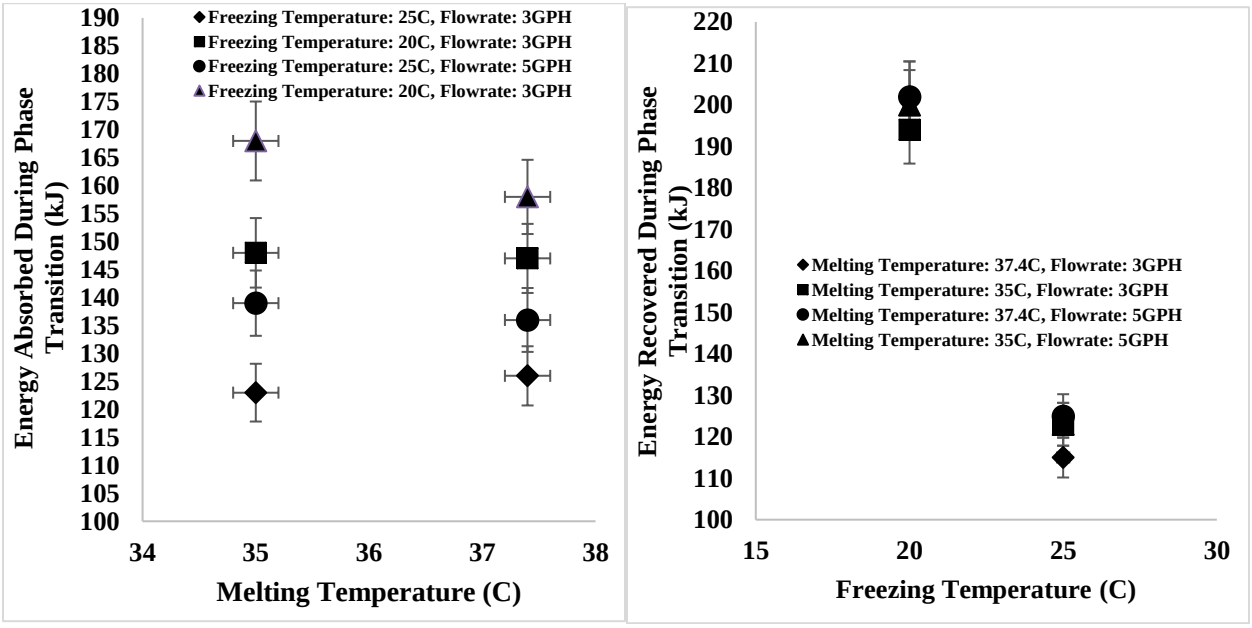

Figure 132: The energy capacity during melting and solidification. [Left] Energy absorbed by PCM during melting with varying flowrate and varying starting temperature. [Right] Energy recovered by HTF from PCM during solidification with varying flowrate and varying starting temperature.

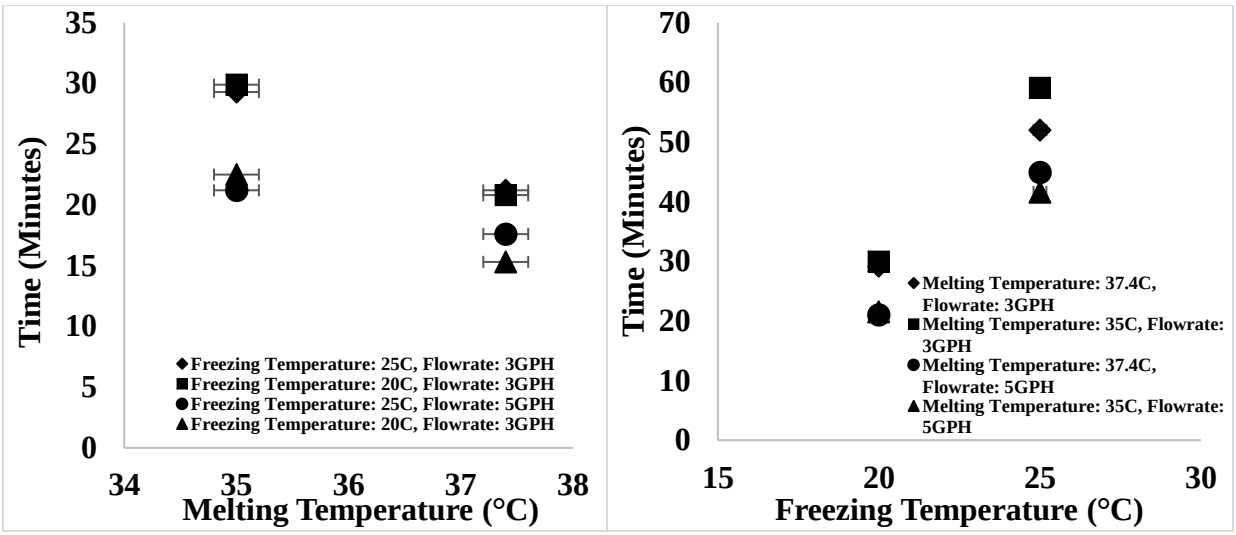

Figure 133: The time taken for 90% melting and solidification. [Left] Time taken to complete 90% melting based on the top plate. [Right] Time taken to complete 90% solidification based on top plate.

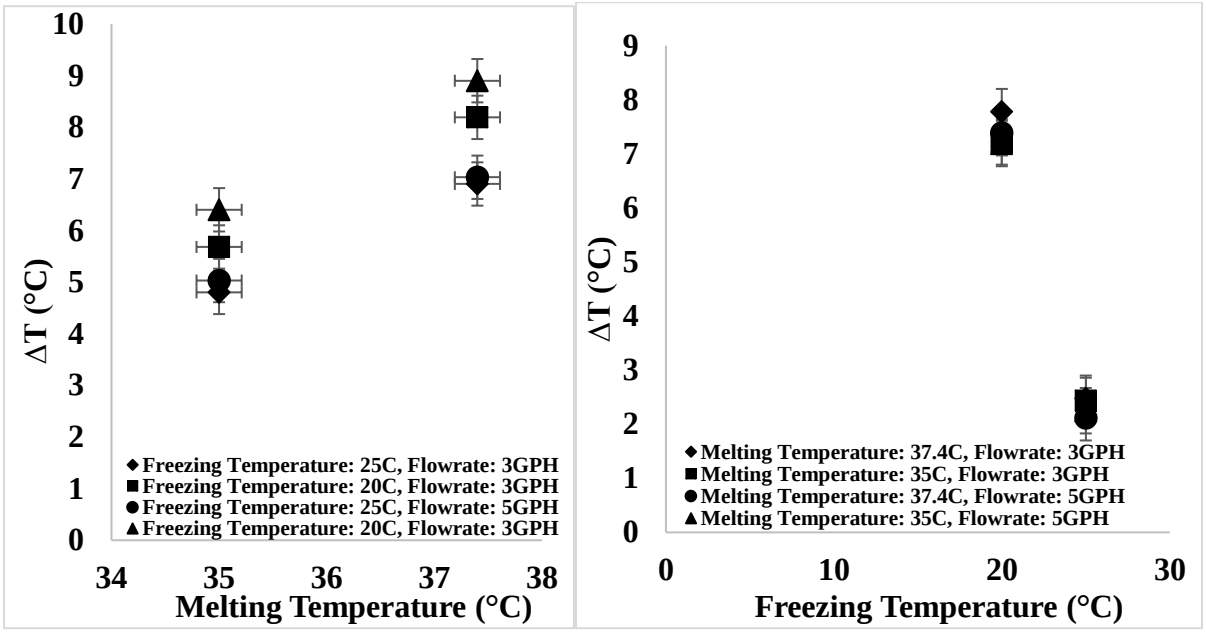

Figure 134: The average temperature (ΔT) of heat transfer fluid during melting and solidification process. [Left] ΔT of heat transfer fluid during melting [Right] ΔT of heat transfer fluid during solidification.

In the case of melting, the thermal performance was function of mass flowrate and starting temperature (i.e. previous freezing temperature). When the inlet temperature was37.4°C, the power

increased was roughly around 33% and 50% when the volumetric flowrate was increased from 3GPH to 5GPH at starting temperature (i.e. previous freezing temperature) of 25°C and 20°C respectively. The energy capacity of LHTESS increased by 7% when the volumetric flowrate was increased, and by 16% the starting temperature. The time taken to complete 90% melting was reduced by 17% (initial temperature 25°C) and 26% (initial temperature 20°C) by increasing the volumetric flowrate. In both starting conditions, the increase in ΔT was less than 5% with a measurement uncertainty of 5%. When the inlet temperature was reduced to 35°C, the power was reduced by 30% and similar trends to 37.4°C were seen with varying volumetric flowrate and starting condition.

14.4 “COLD FINGER” Thermal Cycling in Compact Heat Exchanger

The melt-freeze cycle was automated to run 1000 melt-freeze cycles as shown in Figure 51. Although the system was designed for 1000 melt-freeze cycle, only total of 895 thermal cycles were completed before the lithium nitrate trihydrate leaked from the charging ports. More detail on the failure of the charging port is provided in Appendix G. The thermal cycle performance of LHTESS system was validated at every 100 cycles for their ability in retaining the energy storage capacity. Figure 135 summarizes the energy storage capacity of LHTESS -compact heat exchanger during melt – freeze cycles. During the first 700 melt -freeze cycles no degradation in energy storage capacity were observed during the melt and freeze cycles. The variation in results were within the measurement uncertainty. At the end of 800 cycles reduction in energy storage capacity in melt cycles were observed. The energy storage capacity was observed to degrade by 6%. By the end 895 melt-freeze cycles, the LHTESS system had already lost 15% of energy storage capacity. Therefore, the leakage in the LHTESS system occurred between 800 to 895 cycles.

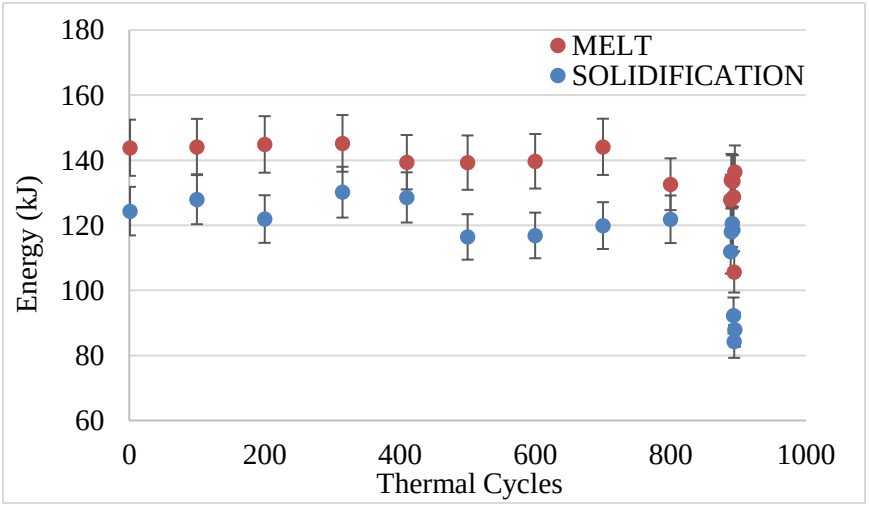

Figure 135: The calculated energy storage capacity of LHTESS -compact heat exchanger charged with lithium nitrate trihydrate as a latent heat storage medium. The LHTESS system underwent 895 melt-freeze cycles. The mass flowrate during melt and freeze was 0.0035 kg/sec. The mass flowrate during first 200 cycle of melt was 0.0044 kg/sec. The inlet temperature during melt and freeze were 37.4°C and 25°C. he results were analyzed after every 100 melt -freeze cycles.

The power of melt and freeze were analyzed during the thermal cycles. The power allowed one to monitor the degradation of lithium nitrate trihydrate, as any change in time will alter the average power of the system which is directly related to lithium nitrate trihydrate. Figure 136 summarizes the average power of LHTESS system over 895 melt-freeze cycles. The average power during melt phases varies between the first 200 cycles and the remaining cycles. This reduction in power is not due thermal stability degradation of lithium nitrate trihydrate, its due to variation in mass flowrate between cycles. During the first 200 cycles the mass flowrate during melt cycle was set at 0.0042 kg/sec and was altered to 0.0035 kg/sec for the remaining 695 cycles. The variation in the melt mass flowrate during the first 200 cycles, was due to tuning, as the flowmeter and needle valve had to be tuned to accuracy. The mass flowrate during the freeze cycle was set to 0.0035 kg/sec for the first 890 cycles and altered to 0.008 kg/sec during the last 6 cycles. The adjustment in flowrate was made to achieve an equal melt and solidification time. An equal melt and solidification time were determined to be ~24 minutes. Figure 137 summarizes the measured mass flowrate of HTF during the melt and freeze phases during thermal cycles. Accounting for the varying mass flowrate, negligible degradation in power were observed over 800 melt – freeze cycles.

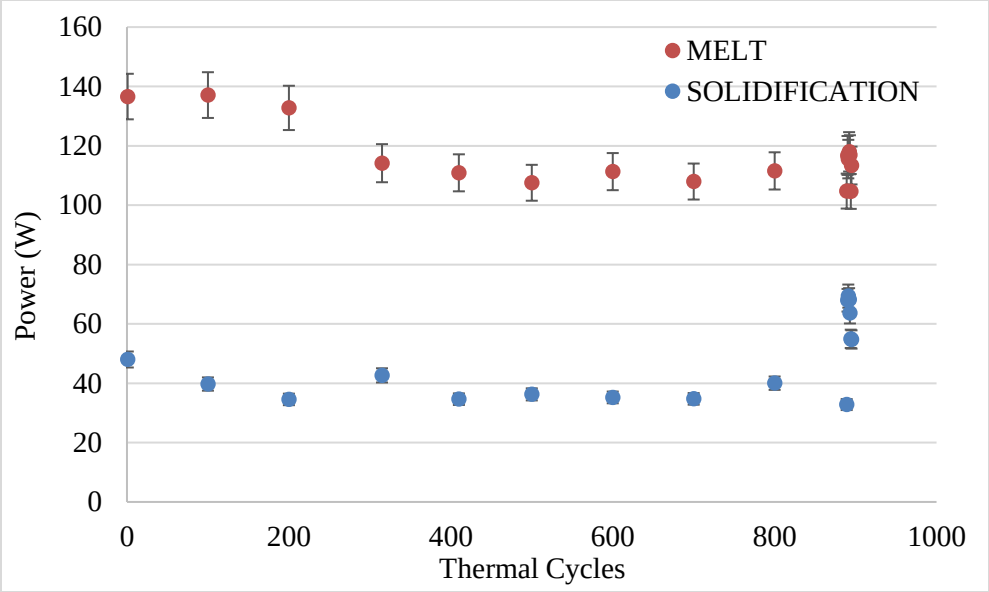

Figure 136: The calculated average power of LHTESS -compact heat exchanger charged with lithium nitrate trihydrate as a latent heat storage medium. The LHTESS system underwent 895 melt-freeze cycles. The mass flowrate during melt and freeze was 0.0035 kg/sec. The mass flowrate during first 200 cycle of melt was 0.0044 kg/sec. The inlet temperature during melt and freeze were 37.4°C and 25°C. The results were analyzed after every 100 melt -freeze cycles.

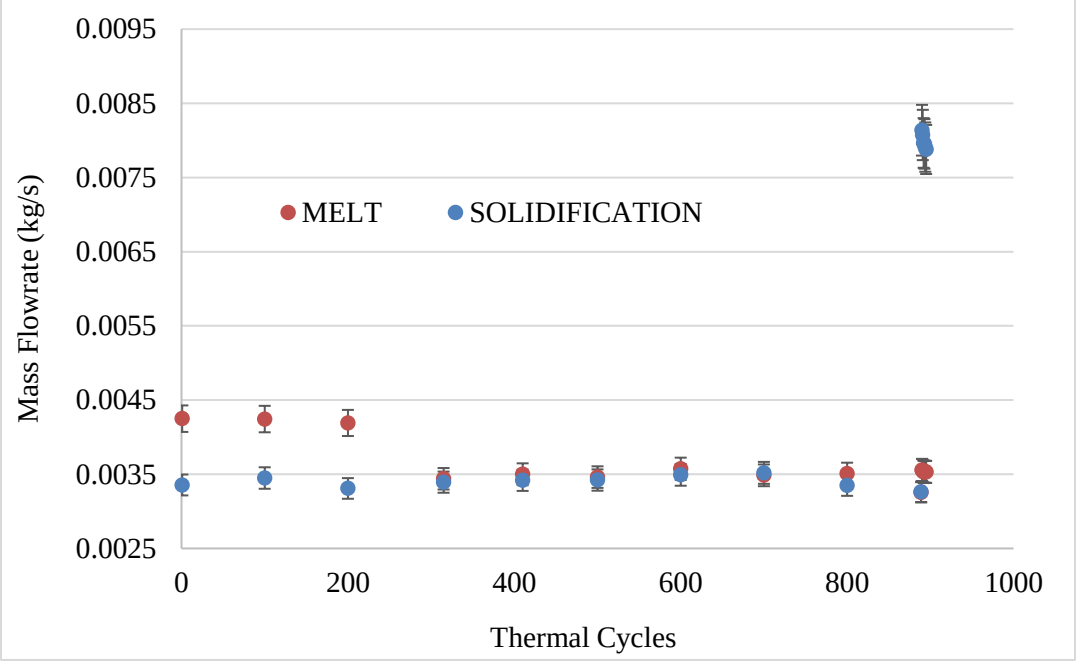

Figure 137: The measured flowrate of HTF of LHTESS -compact heat exchanger during melt and solidification cycle. The LHTESS system underwent 895 melt-freeze cycles. The flowrate was measured using a volumetric flowrate meter (OMEGA FLR1011 and FLR1010) and converted to mass flowrate.

The 895 thermal cycles were accomplished with 90% melting and complete solidification. During the thermal cycles, the efficacy of "Cold Finger" was validated in reducing sub-cooling. Figure 138 summarizes the measured onset of nucleation temperature during freezing. Based on the measurement, "Cold Finger" technique was very efficient in maintaining a 0.5°C sub-cooling without the aid of nucleators. Sub-cooling of 0.5°C was maintained over 800 freeze cycles. When the freeze flowrate was increased, the sub-cooling increased to 2°C. The increase in sub-cooling could be due to increase in flowrate that alters the nucleation growth rate, or it could due to the leakages.

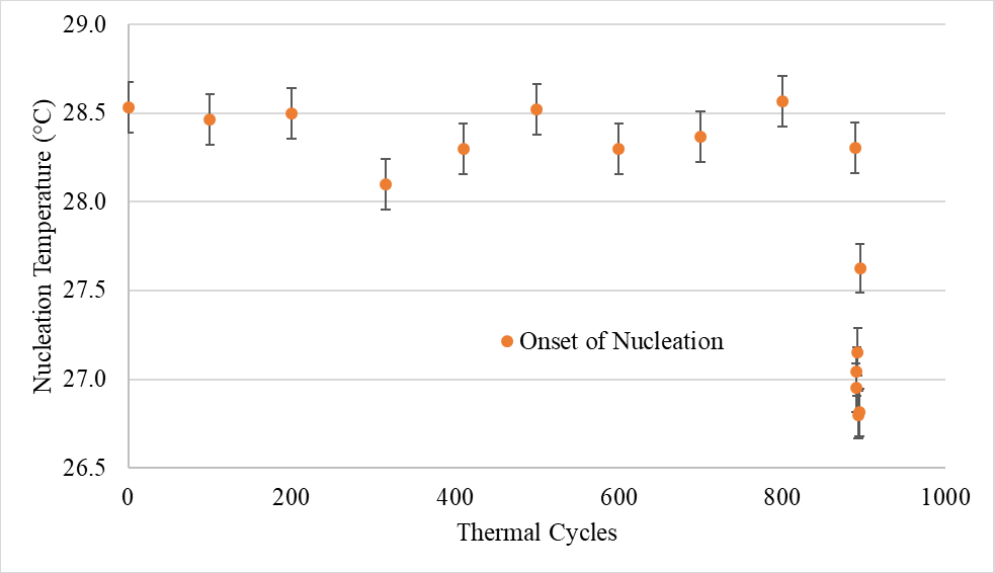

Figure 138: The measured onset of nucleation with "Cold Finger" was monitored over 895 thermal cycles. In "Cold Finger" thermal cycle, 90% melting was accomplished with complete solidification.

14.5 Summary and Recommendation

In summary, the instantaneous power during melting is not constant like an electric battery but reduces with time, whereas during freezing the power remained constant. In both cases the thermal performance of the heat exchanger is a function of both volumetric flowrate and inlet temperature. During freezing, the starting condition had negligible effect on the thermal performance, whereas during melting starting condition played a part on the thermal performance of the heat exchanger. During melting, starting at a lower temperature increased the average power capacity of the heat exchanger. During solidification, the inlet temperature had bigger impact on thermal performance then volumetric flowrate. Whereas during melting, both inlet temperature and volumetric flowrate have equal contribution to thermal performance. These is due the heat transfer mechanism. During solidification, the heat transfer from the PCM to HTF is limited by the effective thermal conductivity, therefore limiting the resistance is not the heat transfer coefficient on the HTF side but the thermal conductivity on PCM side, whereas by reducing the inlet temperature a bigger thermal gradient aids in the rate of solidification. During melting heat transfer from HTF to PCM is dominated by natural convection on the PCM side, therefore by increasing volumetric flowrate could further reduce the thermal resistance on HTF side and enhance the heat transfer rate, similarly by increasing the inlet temperature a big temperature gradient increases the rate. In actual application, inlet temperature can't be predetermined as depends on daily weather condition, therefore the only thermal performance control availability is volumetric flowrate. The thermal cycling of LHTESS showed that lithium nitrate trihydrate is reliable and thermal stable up to 800 melt freeze cycles and "Cold Finger" is an efficient technique to reduce sub-cooling without the aid of nucleators in the system level.

CHAPTER XV

CONCLUSION AND RECOMMENDATION

Conventional electric power production primarily relies on water cooling technologies to remove low grade heat from the steam exiting from turbines in thermal power-plants. It is anticipated that in the next two to three decades - these conventional techniques for water cooling of thermal power-plants will become unsustainable in various geographical regions that have scarcity of water resources. This is expected to arise from a combination of environmental concerns, increased water demand due to population growth, and the impact of climate change. Hence, these factors are expected to significantly constrain the available water supply that can be allocated to power plant cooling. It is also anticipated that smaller scale distributed electric power generation will continue to penetrate the market, including in regions where water cooling for low-grade heat removal is not feasible. Therefore, air-cooled platforms are the obvious replacement for water-cooled platforms. With current air-cooled technology, power producers are reluctant to use dry-cooling systems for two principle reasons: (1) the low air-side heat transfer coefficient necessitates heat exchangers that are costly and require a larger footprint (with concomitant land usage and real-estate issues); and (2) air cooling imposes a performance penalty when ambient temperatures are high, and therefore imposes several challenges.

The purpose of this study to reduce the performance penalty arising from the ambient temperature excursions during the hottest period of the day. In this study the technical feasibility of a latent heat thermal energy storage supplemental cooling system (LHTESS) was demonstrated. To further extend the viability of the concepts demonstrated in this study, various types of phase change materials (PCM) were explored as potential medium for LHTESS (including salt-hydrates)

due to their high volumetric energy storage capacity, and non-flammability properties, although they suffer from inherent kinematics and chemical instabilities.

A list of candidates for various PCMs are explored in this study to validate their thermos-physical properties. Additional studies are performed for these PCMs with the goal of improving their thermo-physical properties (e.g., by mixing with additives), determining their material compatibility with various metals/ alloys (that are typically used for constructing heat exchangers) and their reliability of operation when subjected to repeated thermal cycling. Both organic materials and inorganic materials (salt hydrates) were explored as candidate PCMs. The candidate PCMs explored in this study include: (a) paraffin wax (PureTemp29); (b) lithium nitrate trihydrate; (c) calcium chloride hexahydrate; (d) sodium sulfate decahydrate (Glauber's salt); (e) zinc nitrate hexahydrate.

A significant segment of this study was therefore focused on improving the chemical-kinetics and associated material properties of salt hydrates used as PCM candidates in this study. This achieved by mixing each of the selected PCMs with various types of additives (e.g., nucleation promoters to minimize subcooling, precursors for forming gels to obviate phase-segregation, etc.). The nucleators were selected based on lattice mis-match techniques. It was discovered that zinc nitrate hydroxyl was successful in reducing the degree of sub-cooling for initiating solidification in lithium nitrate trihydrate from 17°C to 4°C. In another embodiment of this approach, sodium chloride and strontium chloride reduced the degree of sub-cooling in calcium chloride hexahydrate from 6°C to 3°C.

Another new technique "Cold Finger" was designed as an active technique to obviate sub-cooling in salt hydrates. "*Cold Finger"* technique was designed as a localized cooling technique where a cold spot is created intentionally in the vicinity of the PCM sample such that a portion of

the sample is always maintained in solid state. This technique was tested with lithium nitrate trihydrate and proved that it's more efficient than nucleators in reducing sub-cooling. The results observed shows that one could maintain a 0°C – 0.5°C sub-cooling in lithium nitrate trihydrate. Such low values of sub-cooling have never been achieved with nucleators before for any salt hydrates. Therefore, "Cold Finger" technique is a viable option for improving the radiality of LHTESS.

Material stability of the candidate PCM samples and additives were analyzed by subjecting them to thermo-cycling consisting of repeated cycles of melting and solidification. In the case of lithium nitrate trihydrate and calcium chloride hexahydrate, the additives and the base material survived up 1000 thermo – cycles and 30 days of elevated aging test, with less than 6% degradation in latent heat capacity and with negligible changes in nucleation temperature and phase transition temperature. Similarly, for zinc nitrate hexahydrate, the nucleators (zinc oxide and zinc hydroxyl nitrate) reduced sub-cooling significantly but with thermo cycling zinc nitrate hexahydrate was susceptible to phase segregation and caused rapid deterioration in the values of latent heat capacity. Nucleators reduced the sub-cooling from 12°C to 3°C and deterioration in latent heat capacity started occurring after 500 cycles, with a 20% reduction in energy storage capacity by the end of 1000 cycles. For the sodium sulfate decahydrate samples - an additive (borax) reduced the degree of sub-cooling significantly but the debilitating effects arising from phase segregation reduced the overall energy storage due to rapid deterioration in the values of latent heat capacity. Additives to promote formation of gels ("gelling techniques") were explored and showed significant improvement in preventing phase segregation in these samples of salt hydrates. However, the gelling technique was found to be unsuitable since the material properties of these PCM samples

with these chosen additives deteriorated rapidly within 300 cycles of the imposed thermocycling protocol.

In addition, corrosion experiments for evaluating the material compatibility of the chosen list of salt hydrates with candidate materials used in construction of LHTESS were analyzed. The corrosion testing was contacted over 18 weeks. Stainless steel SS347 turned out to be the best option for a salt hydrate based LHTESS system.

The incorporation of candidate PCMs in various heat exchanger configurations and validating their thermal performance in reaching the goals of ARID program. The heat exchanger configuration consists of shell- and tube, chevron plate heat exchanger and compact heat exchanger. Thermal conductivity enhancement techniques were explored in compact heat exchanger.

A set of experiments were conducted to study the thermal performance of a plate heat exchanger as a latent heat thermal energy storage system, using biodegradable PCM (i.e. Puretemp 29) and lithium nitrate trihydrate. The experiments demonstrate that during charging higher transfer efficiency could be correlated to increasing flowrate and working fluid temperature, whereas during discharging only flowrate influenced the performance. This can be related to the dominance of natural convection during melting (causing higher rates of heat transfer than that of freezing) and dominance of thermal conduction (due to low values of the overall thermal conductivity) during solidification.

A set of experiments were conducted to study the performance of compact heat exchanger as a latent heat thermal energy storage system with aluminum porous fins, using lithium nitrate trihydrate as PCM. The aim of the study is to perform experimental measurement of the effectiveness of compact heat exchangers (filled with aluminum porous foam impregnated with

phase change materials/ PCM). The objective of the experiments was to ascertain the efficacy of the compact heat exchanger (CHX) platform as a part of a latent heat thermal energy storage system (LHTESS) for various types of loading cycles. The thermal effectiveness of the LTHESS was proved at design condition by being able to provide 6.9°C of cooling to HTF during melting (i.e. dehydration) phase: which meets the project deliverable of cooling in excess 5°C. The CHX was able to sustain the cooling capability for 28 minutes. This shows that the energy storage capacity was 127 KJ. For the case of solidification (i.e. hydration), the PCM sample was completely solidified in 50 minutes: which meets the project deliverable target of cooling within 60 minutes, at this design condition. The effectiveness of "Cold Finger" technique in suppressing sub-cooling in LHTESS were also validated. With implementation of "Cold Finger" technique solidification occurred at phase transition temperature of ~28°C, i.e., without requiring any additional sub-cooling. The efficacy of "Cold Finger" was further enhanced when the direction of HTF flow and nucleation crystal growth are on the same side. As it creates a favorable orientation of the nucleation spot.

In summary compact heat exchanger LHTESS with porous metal fins charged with lithium nitrate trihydrate as latent heat storage medium is the idea system for enhancing the thermal performance of air-cooled power-plants during temperature excursions. The current system could accomplish AIRD program targets of:

- Achieved more than 5°C of cooling for the HTF during melting of the PCM.
- Achieved more than total energy storage capacity of 250 kWh (i.e., $P_{ool} > 250$ kWh).
- Achieved complete solidification (Recharging duration) in less than 1 hour (after the melting cycle was stopped after the melted mass fraction of the PCM was estimated to be at 90%, which corresponds to the Location A of the thermocouple array).

- “Cold Finger” technique enabled the sub-cooling to be restricted to less than 0.5 °C.
- The “Cold Finger” technique was most effective when the flow directions for the HTF were reversed between the melting and solidification portions of the thermo-cycling experiments.

REFERENCES

[1] H. Mehling and L. F. Cabeza, Heat and cold Storage with PCM, Berlin (Germany): Springer-Verlag, 2008.

[2] A. Solomon, "On the melting time of a simple body with a convection boundary condition," *Letters In Heat and Mass Transfer*, vol. 7, pp. 183-188, 1980.

[3] P. Theunissen and J. Buchlin, "Numerical Optimization of a solar air heating system based on encapsulated PCM storage," *Solar Energy*, vol. 31, pp. 271-277, 1983.

[4] W. Humphries, "Performance of finned thermal capacitors," NASA-TN-D-7690, 1978.

[5] W. Humphries and E. Griggs, "A design Handbook for phase change thermal control and energy storage devices (NASA-TP-1074)," *NASA Technical Paper*, 1977.

[6] A.Abhat, ""Low Temperature latent heat temperature energy storage: heat storage materials"," *Solar Energy*, vol. 30, no. 4, pp. 313-332, 1983.

[7] G. Lane, ""Background and Scientific Principles"," in *"Solar Heat Storage: Latent Heat Material, vol.I"*, Florida, CRC Press, 1983.

[8] M. Rosen and Ibrahim Dincer, "Thermal Energy Storage, Systems, and Applications", Chichester (England): Johm Wiley & Sons, 2002.

[9] A. Sharma, V. V. Tyagi, C. R. Chen and D. Buddhi, "Review on thermal energy storage with phase change materials and applications," *Renewable and Sustainable Energy Reviews* , pp. 318-345, 2009.

[10] M. A. Shamseldin, F. A. Al_Sulaiman, N. I. Ibrahim and A. Z. Sahin, "A review on current status and challenges of inorganic phase change materials for thermal energy

storage systems," *Renewable and Sustainable Energy Reviews,* vol. 70, pp. 1072-1089, 2017.

[11] A. S.Fleicher, Thermal Energy Storage Using Phase Change Materials Fundamentals and Applications, New York: SpringerBriefs in Thermal Engineering and Applied Science, 2015.

[12] Z. Khan, Z. Khan and A. Ghafoor, "A review of performance enhancement of PCM based latent heat storage system within the context of materials, thermal stability and compatibility," *Energy Conversion and Management,* pp. 132-158, 2016.

[13] B. Owens, "Owens, Brandon. "The Rise of Distributed Power"," General Electric, 2014.

[14] E. Williams and J. Simmons, "Water in the Energy Industry," BP, 2013.

[15] K. Birkinshaw, M. Marwan and R. L. Therkelsen, "Comparsion of Alternate Cooling Technologies for California Power Plants Economic, Environmental and Other Tradeoffs," California Energy Commission, 2002.

[16] Department of Energy, "ARPA-E Energy," [Online]. Available: https://arpa-e.energy.gov/sites/default/files/documents/files/ARID_ProgramOverview.pdf. [Accessed 04 05 2017].

[17] S. Bushart, "CornerStone," 11 April 2014. [Online]. Available: http://cornerstonemag.net/advanced-cooling-technologies-for-water-savings-at-coal-fired-power-plants/. [Accessed 1 May 2017].

[18] U.S. Department of Energy, ""The Water-Energy Nexus: Challenges and Opportuinities".," 2014.

[19] Z. Yinping, J. Yi and J. Yi, "A Simple method, the T-History method, of determining the heat of fusion, specific heat and thermal conductivity of phase change materials," *Measurement Science Technology*, vol. 10, pp. 201-205, 1999.

[20] X. Y. Liu, "Heterogenous nucleation or homogeneous nucleation," *American Institute of Physics*, vol. 112, no. 22, pp. 9949-9955, 2000.

[21] M. Faucheux, G. Muller, M. Havet and A. LeBail, "Influence of surface roughness on the supercooling degree: Case of selected water/ethanol solutions frozen on aluminium surfaces," *International Journal of Refrigeration*, vol. 29, no. 7, pp. 1218-1224, November 2006.

[22] R. A. Taylor, N. Tsafnat and A. Washer, "Experimental Characterisation of Sub-cooling in hydrated salt phase change materials," *Applied Thermal Engineering*, no. 93, pp. 935-938, 2016.

[23] A. Romero, G. Diarce, J. Ibarretxe, A. Urresti and J. Sala, "Influence of Experimental Conditions on the sub-cooling of Glauber's Salt when used as PCM," *Solar Energy Materials & Solar Cells*, vol. 3, no. 102, pp. 189-195, 2012.

[24] D. Porter and K. Easterling, Phase Transformations in Metals and Alloys, Cheltenham, UK: Chapman & Hall, 1992.

[25] G. Plascencia and D. Jaramillo, "Phase Equilibria I," in *Basic Thermochemistry in Materials Processing*, Springer International, 2017, pp. 43-63.

[26] J. A. Kalb, "Crystallization Kinetics," in *Phase Change Materials Science and Applications*, Boston, Ma: Springer, 2009, pp. 125-148.

[27] A. Mariaux and M. Rappaz, "Influence of anisotropy on hetergenous nucleation," *Acta Materialia,* vol. 59, no. 3, pp. 927-933, 2011.

[28] P. J. Shamberger and M. J. O'Malley, "Heterogeneous nucleation of thermal stroage material LiNO3.3H2O from stable lattice-matched nucleation catalysts," *ACta Materialia,* pp. 265-274, 2015.

[29] M. Hoover, P. Grodzka and M. O'Neill, "Space Thermal Control Development, Lockhead Missiles & Space Company.," NASA/CR-150724, Huntsville,Al, 1971.

[30] B. C. Shin, S. D. Kim and W.-H. Park, "Phase separation and supercooling of a latent heat-storage material," *Energy,* vol. 14, pp. 921-930, 1989.

[31] J. Schroder and K. Gawron, "Heat Stroage Material Comprising Calcium Chloride-Hexahydrate and a Nucleating Agent". Germany Patent US 4189394, 19 Feb 1980.

[32] H. Kimura and J. Kai, "Phase Change Stability of CaCl2.6H2O," *Solar Energy,* vol. 1, pp. 49-55, 1984.

[33] G. A. Lane, "Phase Change Materials for Energy Stroage Nucleation to Prevent Supercooling," *Solar Energy Materials and Solar Cells,* vol. 27, pp. 135-160, 1992.

[34] H. W. Ryu, S. W. Woo, B. C. Shin and S. D. Kim, "Prevention of Supercooling and stabilization of inorganic salt hydrates as latent heat storage materials," *Solar Energy Materials and Solar Cells,* vol. 27, no. 2, pp. 161-172, 1992.

[35] M. M. Farid, A. M. Khudhair, S. A. K. Razack and S. Al-Hallaj, "A Review on Phase Change Energy Stroage: Materials and Applications," *Energy Conversion and Management,* vol. 45, no. 9-10, pp. 1597-1615, 2004.

[36] L. F. Cabeza, G. Svensson, S. Hiebler and H. Mehling, "Thermal performance of sodium acetate trihydrate thickened with different materials as phase change energy storage material," *Applied Thermal Engineering,* vol. 23, pp. 1697-1704, 2003.

[37] B. G. Ramirez, C. Glorieux, E. S. M. Martinez and J. F. Cuautle, "Tuning of Thermal Properties of Sodium Acetate Trihydrate by blending with polymer and Silver nanopartilces," *Applied Thermal Engineering,* vol. 62, no. 2, pp. 838-844, 2014.

[38] A. Abhat, "Development of a Modular Heat Exchnager with Intergrated Latent Heat Stroeg (in German).," German Ministry for Science and Technology, Germany, 1981.

[39] J. Schroder, "Systems for Thermal Energy Stroage in temperature range from -25°C to 150°C," in *Seminar New Ways to Save Energy,* Brussels, 1980.

[40] V. N. Danilin.USSR Patent USSR Patent Number: 842094, 1981.

[41] G. A. Lane and H. E. Rossow, "Hydrated Mg(NO3)2 Reversible Phase Change Compositions". USA Patent US4271029 A, 1979.

[42] H. Garg, S. Mullick and A. Bhargava, Solar Thermal Energy Storage, Holland, Netherlands: D.Reidel Publishing Company, 2012.

[43] J. Meseguer, I. Perez-Grande and A. Sanz-Andres, "Phase Change Capacitors," in *Spacecraft Thermal Control,* Cambridge, Woodhead Publishing Limited, pp. 209-223.

[44] E. Gunther, H. Mehling and M. Werner, "Melting and Nucleation Temperatures of Three Salt Hydrates phase change materials under static pressures up to 800 MPA," *Journal of Physics: Applied Physics,* vol. 40, pp. 4636-4641, 2007.

[45] U. Al, "Why does Sodium Sulfate have an unusual solubility-temperature curve," Stack Exchange, 17 April 2016. [Online]. Available:

http://chemistry.stackexchange.com/questions/10457/why-does-sodium-sulfate-have-an-unusual-solubility-temperature-curve. [Accessed 27 March 2017].

[46] S. B. Marks, "The Effects of Crystal Size on the Thermal Enrgy Storage Capacity of Thickened Glauber's Salt," *Solar Energy,* vol. 30, no. 1, pp. 45-49, 1982.

[47] K. K. MEISINGSET and F. GR0NVOLD , "Thermodynamic properties and phase transitions of salt hydrates between 270 and 400 K II I. CH,CO,Na l 3H,O, CH,CO,Li 9 2H,O,," *Journal of Chem.Thermodynamics,* vol. 16, pp. 523-536, 1984.

[48] P. Hu, D.-J. Lu, X.-Y. Fan, X. Zhou and Z.-S. Chen, "Phase change performance of sodium acetate trihydrate with AlN nanoparticles and CMC,," *Solar Energy Materials and Solar Cells,* vol. 95, no. 9, pp. 2645-2649, 2011.

[49] S. Marks, "An investigation of the thermal energy storage capacity of Glauber's salt with respect to thermal cycling," *Solar Energy,* vol. 25, no. 3, pp. 255-258, 1980.

[50] S. F. Kenji Saita, "Heat storage composition". Japan Patent EP 0141550 A1, 15 May 1985.

[51] C. P. Georg Grubmueller, "Solar collector based on Glauber's salt contg. borax - thickened with amorphous silica, preventing storage capacity loss through sedimentation". Germany Patent DE 2643895 A1, 30 Mar 1978.

[52] K. H. Duane G.Chadwick, "Design Considerations in the Use of Glauber Salt," Utah State University/Utah Water Research Laboratory, Utah, 1981.

[53] H. W. Ryu, S. W. Woo, B. C. Shin and S. D. Kim, "Prevention of supercooling and stabilization of inorganic salt hydrates as lantent heat storage materials," *Solar Energy Materials and Solar Cells,* no. 27, pp. 161-172, 1992.

[54] P. J. Kent and J. K. Page, "Thermal energy storage material comprising hydrated compound and water-swollen cross-linked polymer". Patent US 4273667 A, 16 June 1981.

[55] D. R. Biswas, "Thermal Energy Storage Using Sodium Sulfate Decahydrate and Water," *Solar Energy*, vol. 19, pp. 99-100, 1977.

[56] S. Furbo, "Heat Stroage With An Incongruently Melting Salt Hydrate as Stroage Medium Based on the Extra Water Principle," *Thermal Storage of Solar Energy*, pp. 135-137, 5 11 1980.

[57] Y. Wu and T. Wang , "Preparation and Characterization of hydrated salts/silica composite as shape-stabilized phase chnage material via sol-gel process," *Thermochim ACTA*, vol. 591, pp. 10-15, 2014.

[58] Y. Wu and T. Wang, "Hydrated Salts/expanded graphite composite with high thermal conductivity as a shape-stabilized phase change material for thermal energy stroage," *Energy Convers Management*, vol. 101, pp. 164-171, 2015.

[59] Y. E. Milian, A. Gutierrez, M. Grageda and S. Ushak, "A Review on encapsulation techniques for inorganic phase chnage materials and the influence on their thermpohysical properties," *Renewable and Sustainable Energy Reviews*, vol. 73, pp. 983-999, 2017.

[60] R. Tamme, "Lowe-Temperature Energy Stroage," *Chemtech* , vol. 17, pp. 496-500, 1987.

[61] B. Zalba, J. Marin, L. F. Cabeza and H. Mehling, "Review on thermal energy storage with phase change: materials, heat transfer analysis and applications," *Applied Thermal Engineering*, pp. 251-283, 2003.

[62] K. Pielichowska and K. Pielichowski, "Phase Change Materials for Thermal Energy Stroage," *Progress in Materials Science* , vol. 65, pp. 67-123, 2014.

[63] A. Shukla, D. Buddhi and R. Sawhney, "Thermal Cycling test of few selected inorganic and organic phase chnage materials," *Renewable Energy,* vol. 33, no. 12, pp. 2606-2614, 2008.

[64] V. Tyagi and D. Buddhi, "Thermal Cycle testing of Calcium Chloride Hexahydrate as Possible PCM for Latent Heat Storage," *Solar Energy Materials and Soalr Cells,* vol. 92, no. 8, pp. 891-899, 2008.

[65] H. Kimura and J. Kai, "Mixtures of Calcium Chloride Hexahydrate with Some Salt Hydrates or Anhydrous Salts as Latent Heat Stroage Materials," *Energy Conversion,* vol. 28, no. 3, pp. 197-200, 1988.

[66] K. Ting, P. Giannakakos and S. Gibert, "Durability of Latent Heat Storage Tube-Sheets," *Solar Energy,* vol. 39, no. 2, pp. 79-85, 1987.

[67] T. Wada, R. Yamamoto and M. Yoshihiro, "Heat Storage Capacity of Sodium Acetate Trihydrate During Thermal Cycling," *Solar Energy,* vol. 33, no. 3/4, pp. 373-375, 1984.

[68] K. Nagano, K. Ogawa, T. Mochida, K. Hayashi and H. Ogoshi, "Thermal Characterization of Magnesium Nitrate Hexahydrate and magnesium Chloride Hexahydrate mixture as a phase change material for effective utilization of urban waste heat," *Applied Thermal Engineering,* vol. 24, pp. 221-232, 2004.

[69] H. Fellchenfeld and S. Sarig, "Calcium Chloride Hexahydrate : a Phase changing material for energy storage," *Ind Eng Chem Prod Res Dev,* vol. 24, pp. 130-133, 1985.

[70] V.V.Tyagi and D. Buddhi, "Thermal Cycle testing of Calcium Chloride Hexahydrate as a possbile PCM for latent heat storage," *Solar Energy Materials and Solar Cells,* vol. 92, pp. 891-899, 2008.

[71] F. Porosini, "Salt Hydrates used for latent heat storage: corrosion of metals and relaiablity of thermal performance," *Solar Energy,* vol. 41, pp. 193-197, 1988.

[72] A. A. El-Seball, S. AL-Amir, F. M. AL_Marzouki, A. S. Faidah, A. A. AL-GHAMDI and S. AL-Henitis, "Fast termal cycling of acetanilide and magnesium chloride hexahydrate for indoor solar cooking," *Energy Conversion and Management,* vol. 50, pp. 3104-3111, 2009.

[73] H. Kimura and J. Kai, "Feasibility of trichlorofluoromethane (CCl3F, R11) heptadecahydrate as a heat storage material," *Energy Conversation Management,* vol. 25, no. 2, pp. 179-186, 1985.

[74] J. K. Hiroshi Kimura, "Phase change stability of sodium acetate trihydrate and its mixtures," *Solar Energy,* vol. 35, no. 6, pp. 527-534, 1985.

[75] G. Ferrer, A. Sole, C. Barreneche, I. Martorell and L. F. Cabeza, "Review on the methodology used in thermal stability characterization of phase change materials," *Renewable and Sustainable Energy Reviews,* vol. 50, pp. 665-685, 2015.

[76] G. I. F. Q. A. a. C. E.V., "Quality Assurance (RAL-GZ-896)," in *Phase Change Materials,* Sankt Augustin , RAL Deutsches Institut, 2009.

[77] Z. Yinping, J. Yi and J. Yi, "A Simple method, the T-History method, of determining the heat of fusion, specific heat and thermal conductivity of phase-change materials," *Measurement Science Technology,* no. 10, pp. 201-205, 1999.

[78] P. A. Schweitzer, Corrosion and Protection Handbook, New York: Marcel Dekker, 1988.

[79] L. F. Cabeza, J. lla, J. Roca, F. Badia and H. Mehling, "Middle term immersion corrosion tests on metal-salt hydrates paris used for latent heat stroage in the 32 to 36°C temperature range," *Materials and Corrosion,* vol. 52, pp. 748-754, 2001.

[80] L. Cabeza, J. Illa, J. Roca, F. Badia, H. Mehling, S. Hiebler and F. Ziegler, "Immersion corrosion tests on metal-salt hydrate pairs used for latent heat stroage in the 32 to 36 Deg temperature range," *Marterials Corrosion,* vol. 52, pp. 748-754, 2001.

[81] A. J. Farrell, B. Norton and D. M. Kennedy, "Corrosive effects of salt hydrates phase change materials used with aluminium and copper," *Journal of Materials Processing Technology,* vol. 175, no. 1-3, pp. 198-205, 2006.

[82] K. Gawron and J. Schroder, "VDI Berichte," VDI0Verlag, Dusseldorf, 1977.

[83] D. Chahroudi, "Workshop on Solar Energy Subsystem for Heating and Cooling of Building," *Workshop on Solar Energy Subsystem for Heating and Cooling of Building,* pp. 56-57, 1975.

[84] S. N. Trushevskii, " Geliotekhnika," *Applied Solar Energy,* vol. 5, pp. 38-42, 1979.

[85] J. Schroder, " Proc. Seminar New Ways to Save Energy," *Proc. Seminar New Ways to Save Energy,* pp. 495-504, 1980.

[86] H. Kimura and J. Kai, "Phase Chnage Stability of CaCl2.6H2O," *Solar Energy,* vol. 1, pp. 49-55, 1984.

[87] R. Tamme, "Low-Temperature Energy Stroage," *Chemtech,* vol. 17, pp. 496-500, 1987.

[88] L. Cabeza, J. Roca, M. Nogues, F. Badia, H. Mehling and S. Hiebler, "Immersion corrosion tests on metal-salt hydrate pairs used for latent heat storage in the 48 to 58 Deg Celsius Temperature Range," *Materials Corrosion,* vol. 53, pp. 902-907, 2002.

[89] F. Agyenim, N. Hewitt, P. Eames and M. Smytha, "A review of materials, heat transfer and phase change problem formulation for latent heat thermal energy storage systems (LHTESS)," *Renewable and Sustainable Energy Reviews,* vol. 14, no. 2, pp. 615-628, 2010.

[90] A. Regin, S. Solanki and J. Saini, "Heat transfer characteristics of thermal energy storage system using PCM capsules: A review," *Renewable and Sustainable Energy Reviews,* vol. 12, no. 9, pp. 2438-2458, 2008.

[91] M. K. Rathod and J. Banerjee, "Thermal Performance of a Phase Change Material-Based Latent Heat Thermal Storage Unit," *Heat Transfer-Asian Research,* vol. 43, no. 8, pp. 706-719, 2014.

[92] N. Kousha, M. Hosseini, M. Aligoodarz, R. Pakrouh and R. Bahrampoury, "Effect of inclination angle on the performance of a shell and tube heat storage unit - An experimental study," *Applied Thermal Engineering,* vol. 112, pp. 1497-1509, 2017.

[93] S. Seddegh, M. M. Joybari, X. Wang and F. Haghighat, "Experimental and numerical characterization of natural convection in a vertical shell-and-tube latent thermal energy storage system," *Sustainable Cities and Society,* vol. 35, pp. 13-24, 2017.

[94] A. Agarwal and R. Sarviya, "An experimental investigation of shell and tube latent heat storage for solar dryer using paraffin wax as heat storage material," *Engineering Science and Technology,* vol. 19, no. 1, pp. 619-631, 2016.

[95] N. I. Ibrahim, F. A. Al-Sulaiman, S. Rahman, B. S. Yilbas and A. Z. Sahin, "Heat transfer enhancement of phase change materials for thermal energy storage applications: A critical review," *Renewable and Sustainble Energy Reviews,* vol. 74, pp. 26-50, 2017.

[96] K. Merlin, D. Delaunay, J. Soto and L. Traonvouez, "Heat transfer enhancement in latent heat thermal storage systems: comparative study of different solutions and thermal contact investigation between the exchanger and the PCM," *Applied Energy,* vol. 166, pp. 107-116, 2016.

[97] Y. He, "Rapid Thermal Conductivity Measurement with a hot disk sensor Part 1: Theoretical Considerations," *Thermochimica Acta,* no. 436, pp. 122-129, 2005.

[98] R. J. Warzoha and A. S. Fleischer, "Determing the thermal conductivity of liquids using the transient hot disk method. Part 11: Establishing an accurate and repeatable experiment methodolody," *International Journal of Heat and Mass Transfer,* vol. 71, pp. 790-807, 2014.

[99] P. J. Shamberger and T. Reid, "Thermophyiscal Propeorties of Lithium Nitrate Trihydrate from (253 to 353) K," *Journal of Chemical & Engineering Data,* vol. 57, pp. 1404-1411, 2012.

[100] ASTM International, "G1-03. Standard Practice for preparing, cleaning and evaluating corrosion test specimens," ASTM International, 2011.

[101] V. Sastri , E. Ghali and M. Elboujdaini, "Corrosion, prevention and protection," in *Practical Solutions,* John Wiley & Sons, 2007.

[102] K.-S. Lee and H. Bhowmik, "Aalysis of heat transfer and pressure drop characteristics in an offset strip fin heat exchanger," *International Communications in Heat and Mass Transfer,* no. 36, pp. 259-263, 2009.

[103] P. J.Shamberger and T. Reid, "Thermophysical Properties of Lithium Nitrate Trihydrate from (253 to 353) K," *Journal of Chemical & Engineering Data,* vol. 57, no. 5, pp. 1404-1411, 2012.

[104] D. Biswas, "Thermal Energy stroage using sodium sulphate decahydrate and water," *Solar Energy,* vol. 19, pp. 99-11, 1977.

[105] A. Kozak, K. Wieczorek-Ciurowa and A. Kozak, "The Thermal Transformations in Zn(NO3)2-H2O (1:6) System," *Journal of Thermal Analysis and Calorimetry ,* pp. 497-502, 2003.

[106] H. W. Ryu, S. W. Woo, B. C. Shin and S. D. Kim, "Prevention of Supercooling and stabilization of inorganic salt hydrates as latent heat storage materials," *Solar Energy Materials and Solar Cells,* vol. 27, no. 2, pp. 161-172, 1992.

[107] G. A. Lane, ""Phase change materials for energy storage nucleation to prevent supercooling"," *Solar Energy Materials and Solar Cells,* vol. 27, no. 2, pp. 135-180, 1992.

[108] L. Ying , B.-Y. Chen, C.-c. Sun and X.-H. Zhang, "Study on Influence Factors of Thermal Hysteresis in Parafin Actuator," in *IEEE Computer Society,* 2008.

[109] L. Cabeza, J. Illa, J. Roca, F. Badia, H. Mehling, S. Hiebler and F. Ziegler, "Immersion corrosion tests on metal-salt hydrate paris used for latent heat stroage in 32 to 36 Deg temperature range," *Material Corrosion,* vol. 52, pp. 140-146, 2001.

[110] G. A. Lane, "Latent Heat Material," in *Solar Heat Storage*, Boca Raton, CRC Press Inc.

[111] B. Zuberi, A. K. Bertram, C. A. Cassa, L. T. Molina and M. J. Molina , "Hetergenous nucleation of ice in (NH4)2SO4 - H2O particles with mineral dust immersions," *Geophyscial Research Letters*, vol. 29, no. 10, pp. 142-1 -142-4, 2002.

[112] X. Zhang, Y. Fan, X. TAO and K. YICK, "Fabricationa and properties of microcapsules and nanocapsules cantaining n-octadecane," *Materials Chemistry and Physics*, vol. 88, no. 2-3, pp. 300-307, 2004.

[113] P. Zhang, Z. Ma, X. Shi and X. Xiao, "Thermal conductivity measurements of a phase change material slurry under the influence of phase change," *International Journal of Thermal Sciences*, vol. 78, pp. 56-64, 2014.

[114] M. X. Zhang and P. Kelly, "Metall," *Mater.Trans A*, vol. 37, p. 833, 2006.

[115] M. Yamaguchi and T. Nogi, The Stefan Problem, Tokyo: Sangyo-Tosho, 1977.

[116] L. Xia, P. Zhang and R. Wang, "Preparation and thermal characterization of expanded graphite/paraffin composite phase change material," *CARBON*, vol. 48, pp. 2538-2548, 2010.

[117] R. Warzoha and A. Fleischer, "Improved heat recovery from paraffin-based phase change materials due to the presence of percolating graphene networks," *International Journal of Heat and Mass Transfer*, vol. 79, pp. 324-333, 2014.

[118] J.-P. Wang , X.-p. Zhao, H.-l. Guo and Q. Zheng, "Preparation of Microcapsulaes containing two phase core materials," *Langmuirl* , vol. 20, pp. 10845-10850, 2004.

[119] X. e. a. Wang, "Nano-encapsulated PCM via Pickering Emulsification," *Scientific Reports* , vol. 5, p. 13357, 2015.

[120] J. Wang, H. Xie and Z. Xin, "Thermal properties of paraffin based composites containing multi-walled carbon nanotubes," *Thermochimica Acta,* vol. 488, pp. 39-42, 2009.

[121] J. Wang, H. Xie and Z. Xin, "Thermal properties of paraffin based composites containing multi-walled carbon nanotubes," *Thermochimica Acta,* vol. 488, pp. 39-42, 2009.

[122] B. Vonnegut, "The nucelation of Ice Formation by Silver Iodide," *Journal of Applied Physics,* vol. 18, p. 593, 1947.

[123] B. Vonnegut and H. Chessin, "Ice Nucleation by coprecipitated silver iodide and silver bromide," *Science,* vol. 174, no. 4012, pp. 945-946, 1971.

[124] V. V. Tyagi and D. Buddhi, "PCM Thermal Stroage in Buildings: A State of Art," *Renewable & Sustainable Energy Reviews,* vol. 11, pp. 1146-116, 2007.

[125] V. Tyagi, S. Kaushik and T. Akiyama, "Development of phase change materials based microencapsulated technology for buildings: A review," *Renewable and Sustainable Energy Reviews,* vol. 15, pp. 1373-1391, 2011.

[126] D. Turnbull and B. Vonnegut, "Nucleation Catalysis," *Indutrial and Engineering Chemistry,* vol. 44, no. 6, pp. 1292-1298, 1952.

[127] A. Trp, K. Lenic and B. Frankovic, "Analysis of the Influence of operating conditions and geometric parameters on heat transfer in water-paraffin shell-and-tube latent thermal storage unit," *Applied Thermal Engineering,* vol. 26, no. 16, pp. 1830-1839, 2006.

[128] M. P. Trammell, "Evaluation of the transient thermal performance of a graphite foam/phase change material composite," University of Tennessee, Knoxville, 2013.

[129] L. C. Thomas, Modulated DSC Basics: Calculation and Calibration of MDSC Signals, DE: TA Instruments, 2005.

[130] M. Telkes, ""Nucleation of supersaturated inorganic salt solutions"," *Journal od Industrial and Engineering Chemistry,* vol. 44, pp. 1308-1310, 1952.

[131] M. Telkes.USA Patent 3986969, 1975.

[132] R. F. Speyer, Thermal Analysis of Materials,, New York: Marcl Dekker, 1994.

[133] R. Solthin and G. Chadwick, "Heterogeneous nucleation in solidifying metals," *Acta Metallurgica,* vol. 26, no. 2, pp. 223-231, 1978.

[134] N. Singh and D. Banerjee, Nanofins: Science and Applications, 1 ed., New York: Springer , 2013.

[135] A. Sari, C. Alkan, A. Karaipekli and O. Uzum, "Microencapsulated n-octadecane as phase change material for thermal energy storage," *Journal of Solar Energy,* vol. 83, pp. 1757-1763, 2009.

[136] A. Safari, A. Saidur, F. Sulaiman, Y. Xu and J. Dong, "A Review on Supercooling of Phase Change Materials in thermal energy storage systems," *Renewable and Sustainable Energy Reviews,* vol. 70, pp. 905-919, 2017.

[137] H. W. Ryu, S. W. Woo, B. C. Shin and S. D. Kim, "Prevention of supercooling and stabilization of inorganic salt hydrates as lantent heat storage materials," *Solar Energy Materials and Solar Cells,* no. 27, pp. 161-172, 1992.

[138] A. G. Romero, G. Diarce, J. Ibarretxe, A. Urresti and J.M Sala, "Influence of the experiemntal conditions on the subcooling of Glauber's salt when used as PCM," *Solar Energy Materials & Solar Cells,* vol. 102, pp. 189-195, 2012.

[139] D. Riley, F. SMITH and G. POOTS, "THE INWARD MELTING OF SPHERES AND CIRCULAR CYLINDERS," *INT.J.Heat Mass Transfer,* vol. 17, pp. 1507-1516, 1974.

[140] RAL, *Phase Change Material [Quality Assurance],* Berlin: RAL Deutsches Institut, 2009.

[141] R. Perry and D. Green, "Corrosion and its Control," in *Perry's Chemical Engineering Handbook*, New York, McGraw-Hill International Editions , 1984, p. 23.

[142] S. Pendyala, "Macroencapsulation of Phase Change Materials for Thermal Energy Storage," University of South Florida, Florida, 2012.

[143] B. Norton and D. Kennedy, "Corrosive effects of salt hydrate phase change materials used with aluminium and copper," *Journal of Materials Processing Technology*, pp. 198-205, 2006.

[144] R. Naumann and H. H. Emons, "Results of thermal analysis for investigation of salt hydrates as latent heat-storage materials," *Thermal Analysis,* no. 35, pp. 1009-1031, 1989.

[145] M. Nabil and J. Khodadadi, "Experimental determination of temperature-dependent thermal conductivity of solid eicosane-based nanostructure-enhanced phase change materials," *International Journal of ,* vol. 67, pp. 301-310, 2013.

[146] H. Mehling , S. Heibler and F. Ziegler, "Latent heat storage using a PCM-graphite composite material," Stuuttgrat, 2000.

[147] B. Mehalic, "Home Power," August 2009. [Online]. Available: https://www.homepower.com/articles/solar-water-heating/equipment-products/flat-plate-evacuated-tube-solar-thermal-collectors. [Accessed 1 March 2017].

[148] J. Marin, B. Zalba, L. Cabeza and H. Mehling, "Determination of enthalpy-temperature curves of phase change materials with the T-History method-improvements to

temperature dependent properties," *Measurement Science Technology,* vol. 14, no. 184, pp. 184-189, 2003.

[149] J. Marin, B. Zalba, L. Cabeza and H. Mehling , "Determination of enthalpy-temperature curves of phase change mateirals with temperature-history method: improvement to temperature dependent properties," *Measurement Science Technology,* vol. 14, pp. 184-189, 2003.

[150] J. Li, Y. Zeng and Z. Luo, "Simultaneous enhancement of latent heat and thermal conductivity of docoasane based phase change materials in the presence of spongy graphene," *Solar Energy Materials Solar Cells,* vol. 128, pp. 48-51, 2014.

[151] S. Latibari, M. Mehrali and T. Mahlia, "Synthesis,characterization and thermal properties of nanoencapuslated phase change materials via sol-gel method," *Solar Energy,* vol. 61, pp. 664-672, 2013.

[152] C. J. Lasance, "Electronics Cooling," 1 May 2001. [Online]. Available: https://www.electronics-cooling.com/2001/05/the-thermal-conductivity-of-unfilled-plastics/. [Accessed 03 02 2017].

[153] H. Kwon and J. Kim, "Preparation of n-octadecane nanocapsules by using interfacial redox initiation in miniemulsion ploymerization," *Macromol Res,* vol. 18, pp. 923-926, 2015.

[154] N. Kumar and D. Banerjee, "Characterization Phase Change Materials (PCM) Using T-History Method," in *ASME.Heat Transfer Summer Conference*, Washington,DC, 2016.

[155] E. D. Kravvaritis, K. A. Antonopoulos and C. Tzivanidis, "Improvements to the measurement of the thermal properties of phase chnage materials," *Measurement Science Technology,* vol. 21, pp. 1-9, 2010.

[156] E. D. Kravvaritis, K. A. Antonopoulos and C. Tzivanidis, "Improvements to the measurement of the thermal properties of phase change materials," *Measurement Sicience Technology,* vol. 21, pp. 1-99, 2010.

[157] H. Kimura and J. Kai, "Phase Change Stability of CaCl2.6H2O," *Solar Energy,* vol. 33, pp. 557-563, 1984.

[158] R. Kandasamy, X.-Q. Wang and A. S. Mujumdar, "Application of Phase change materials in thermal management of electronics," *Applied Thermal Engineering,* vol. 27, no. 17-18, pp. 2822-2382, 2007.

[159] P. Johansson, A. S. Kalagasidis and H. Jansson, "Investigating PCM Activation using Transient Plane Source Method," IBPC, 2015.

[160] A. Jameskhorshid, S. Sadrameli and M. Farid, "A Review of microencapsulation methods of phase change materials (PCMs) as a thermal energy storage (TES) medium," *Renewable and Sustainable Energy Reviews,* vol. 31, pp. 531-542, 2014.

[161] H. Inaba and P. Tu, "Evaluation of thermophysical characteristics on shape-stabilized paraffin as a solid-liquid phase change material," *Heat and Mass Transfer,* vol. 32, pp. 307-312, 1997.

[162] K. Hermansson, J. Thomas and I. Olovsson, "Acta Crystallogr. Sect. B Struct. Crystallogr," *Crystal Chemical,* vol. 36, p. 1032, 1980.

[163] Y. He, "Rapid Thermal Conductivity conducitivty measurement with a hot-disk sensor: Part 1. Theoretical considerations," *Thermochimica Acta,* vol. 436, pp. 122-129, 2005.

[164] Y. He, "Papid thermal conductivity measurement with a hot disk sensor Part 1. Theoretical considerations," *Thermochimica Acta,* pp. 122-129, 2005.

[165] A. Hasan, "Phase Change Material Energy storage system Employing Palmitic acid," *Solar Energy,* vol. 52, pp. 143-154, 1994.

[166] M. Hadis and U. Ozgur, "Crystal Structure," in *Zinc Oxide: Fundamental, Materials and Device Technology,* Verlag, Wiley , 2009, pp. 1-10.

[167] A. Garcia-Romero, G. Diarce, J. Ibarretxe, A. Urresti and J. Sala, "Influence of the experimental conditions on the subcooling of Glauber's Salt when used as PCM," *Solar Energy Materials & Solar Cells,* vol. 102, pp. 189-195, 2012.

[168] A. E. Fouda, G. J. Despault, J. B. Taylor and C. E. Capes, "Characterisitcs of polot systems operating with sodium sulphate solution," *Solar Energy,* vol. 32, pp. 57-65, 1984.

[169] L.-W. X. F. X. W. Y. Z. Y.-Q. X. Z.-T. Y. X. X. Y.-C. H. a. K.-F. C. Fan, "Effects of various carbon nonofillers on the thermal conductivity and energy storage properties of paraffin-based nanocomposite phase change materials," *Applied Energy,* vol. 110, pp. 163-172, 2013.

[170] M. A. Ezan, M. Ozdogan and A. Erek, "Experimental Study on charging and discharging periods of water in a latent heat stroage unit," *International Journal of Thermal Sciences,* vol. 50, no. 11, pp. 2205-2219, 2011.

[171] A. Elgafy and K. Lafdi, "Effect of carbon nonofiber additives on thermal behaviour of phase change materials," *Carbon,* vol. 43, pp. 3067-3074, 2005.

[172] F. D. Donnan and B. C. Burt, "The Solubilities and Transition-Points of Lithium Nitrate and its Hydrates," *Journal of the Chemical Society,* pp. 335-342, 1983.

[173] L. Desgrosseilliers, D. Groulx and M. A. White, "Heat Conduction in laminate multilayer bodies with applied finite heat source," *International Journal of Thermal Science,* vol. 72, pp. 47-59, 2013.

[174] Y. Deng, "Thermal conductivity enhancement of ployethylene glycol/expanded vermicilite shape-stabilized composite phase change material with silver nanowire for thermal enegry storage," *Chemical Engineering Journal,* vol. 295, pp. 427-435, 2016.

[175] D. Delaunay and P. Carre, "Dispositif de mesure automatique de la conductivité thermique des matériaux à changement de phase," *Rev. Phys. Appl,* vol. 17, pp. 209-215, 1982.

[176] A. D.Owens, "What Is Experiential Learning," STEMJOBS, 03 NOV 2015. [Online]. Available: http://edu.stemjobs.com/what-is-experiential-learning/. [Accessed 08 March 2017].

[177] A. D.Fedden, "Graphitzed Carbon Foam with Phase Change Material," Air Force Insitute of Technology, Ohio, 2006.

[178] H. S. Choi, B. C. Shin and S. D. Kim, "Heat Transfer in a latent heat-stroage system," *Energy,* vol. 14, no. 9, pp. 513-524, 1989.

[179] K. Chintakrinda, R. Weinstein and A. S. Fleischer, "A direct comparsion of three different material enhancement methods on the transient thermal response of paraffin phase change material exposed to high heat fluxes," *Internation Journal of Thermal Science,* vol. 50, pp. 1639-1647, 2011.

[180] L. Cabeza, J. Roca, M. Noguees, H. Mehling and S. Hiebler, "Long term immersion corrosion tests on metal-PCM pairs used for latent heat stroage in the 24 to 29 Deg Celsius temperature range," *Material Corrosion,* vol. 56, pp. 33-38, 2005.

[181] D. Buddhi and R. Sawhney, in *Thermal Energy Storage and Energy Conversion*, 1994.

[182] M. Bareiss and H. Beer, "An analytical solution of the heat transfer process during melting of an unfixed solid phase chnage material inside a horizontal tube," *International Journal of Heat and Mass Transfer,* vol. 27, no. 5, pp. 739-746, 1984.

[183] C. Alkan, A. Sari, A. Karaipekil and O. Uzun, "Preparation, characterization, and thermal properties of microencapsulated phase change material for thermal energy storage," *Solar Energy Materials and Solar Cells,* vol. 93, no. 1, pp. 143-147, 2009.

[184] V. Alexiades and A. D. Solomon , "Problems With Explict Solutions," in *Mathematical Modeling of Melting and Freezing Processes*, Washington,DC, Taylor and Francis, 1993, pp. 33-44.

[185] V. Alexiades and A. Solomon, Mathemtical Modelling of Melting and Freezing process, Washington,Dc: Taylor & Francis, 1993.

[186] "EGR AEROSAPCE," [Online]. Available: http://www.ergaerospace.com/project-gallery.htm. [Accessed 29 4 2016].

[187] H. Felichenfeld and S. Sarig, "Calcium Chloride Hexahydrate: A Phase-Changing Material for Energy Storage," *American Chemical Society*, vol. 24, pp. 130-133, 1985.

APPENDIX A

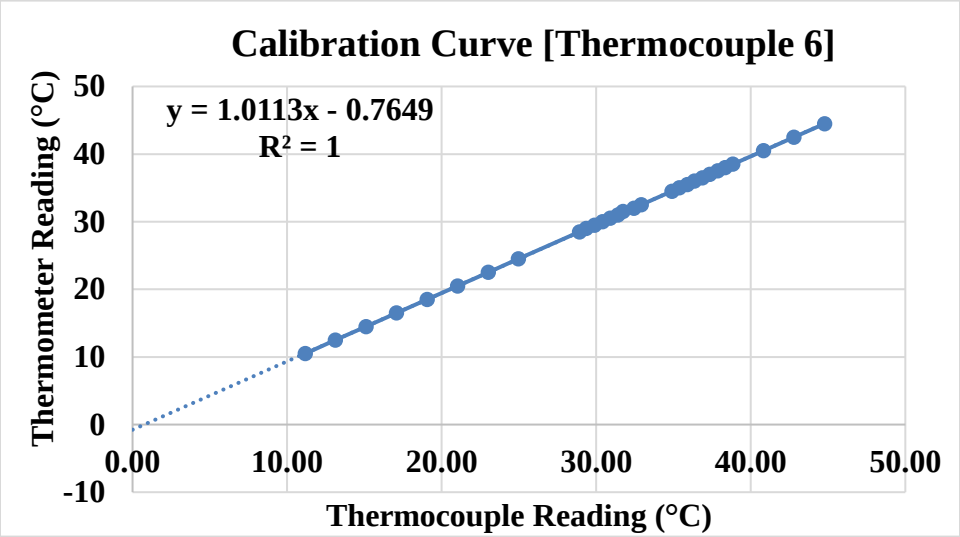

Figure 139: Thermocouple 6 Calibration Curve.

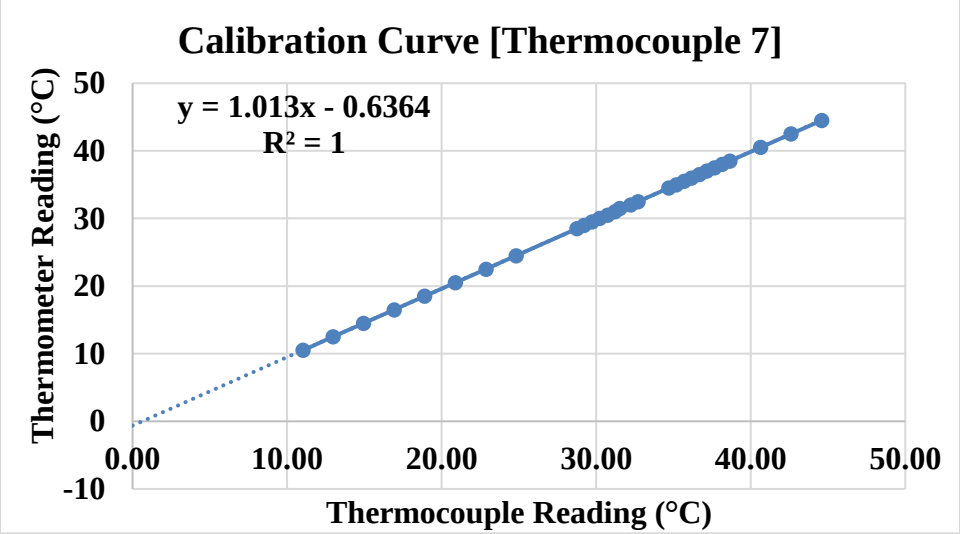

Figure 140: Thermocouple 7 Calibration Curve.

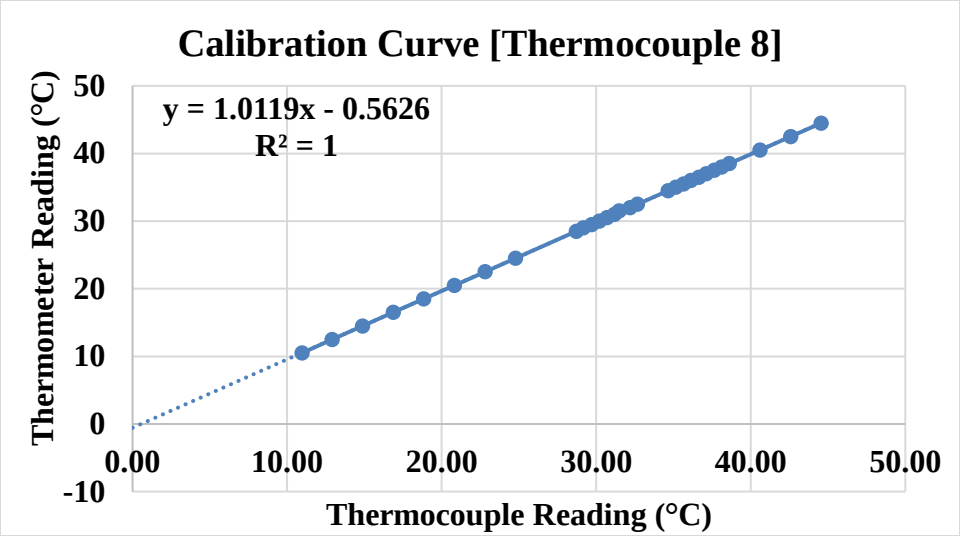

Figure 141: Thermocouple 8 Calibration Curve.

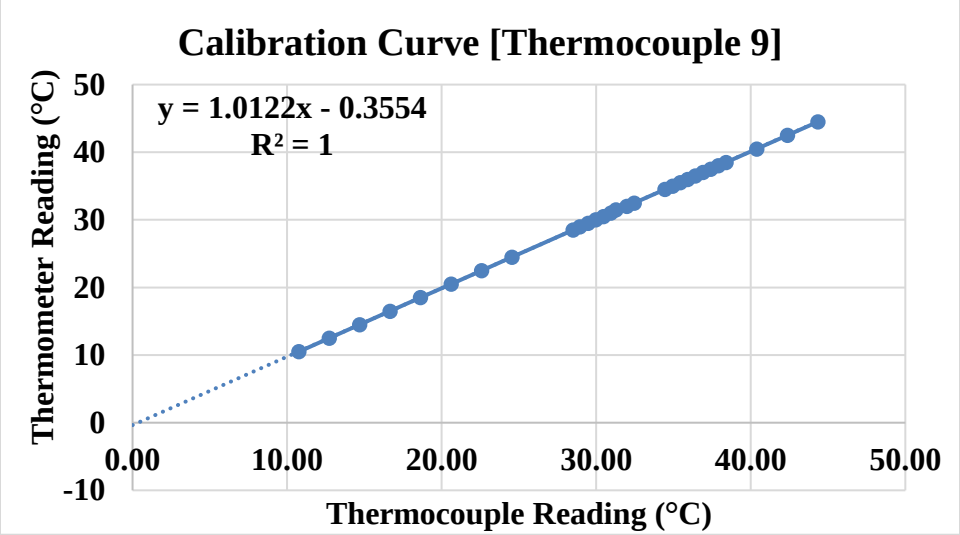

Figure 142: Thermocouple 9 Calibration Curve.

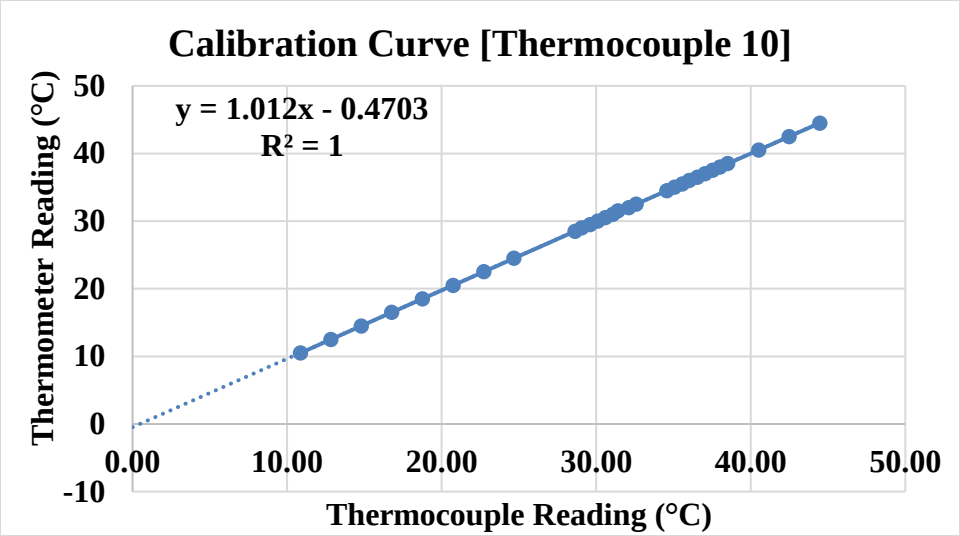

Figure 143: Thermocouple 10 Calibration Curve.

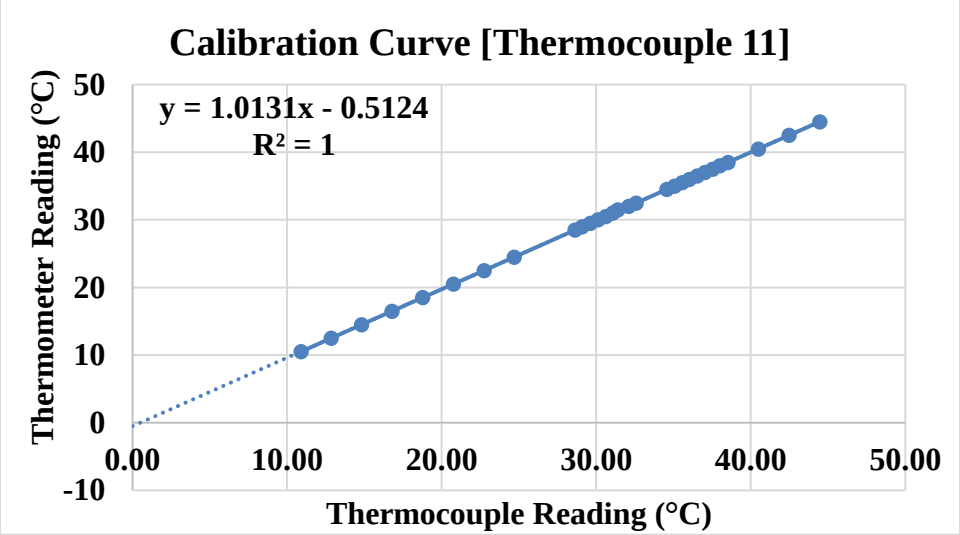

Figure 144: Thermocouple 11 Calibration Curve.

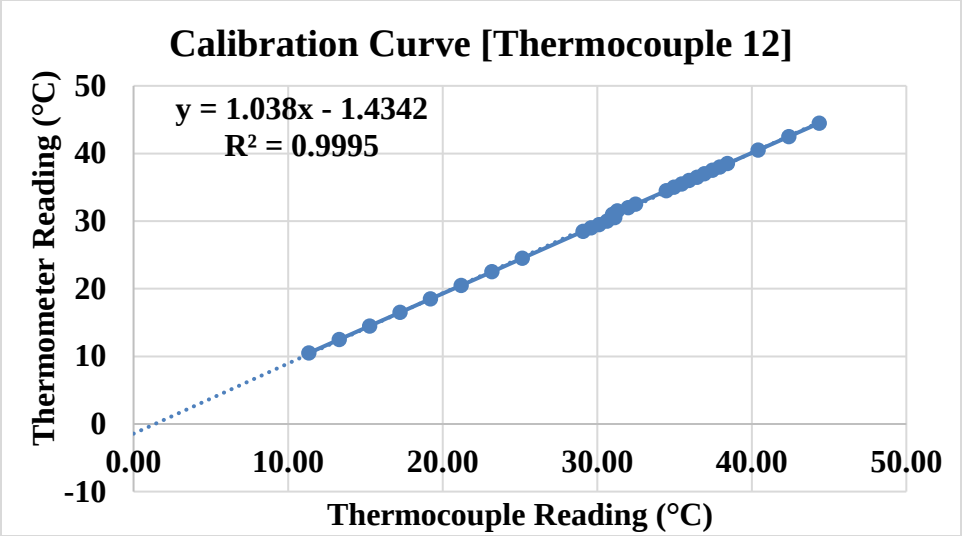

Figure 145: Thermocouple 12 Calibration Curve.

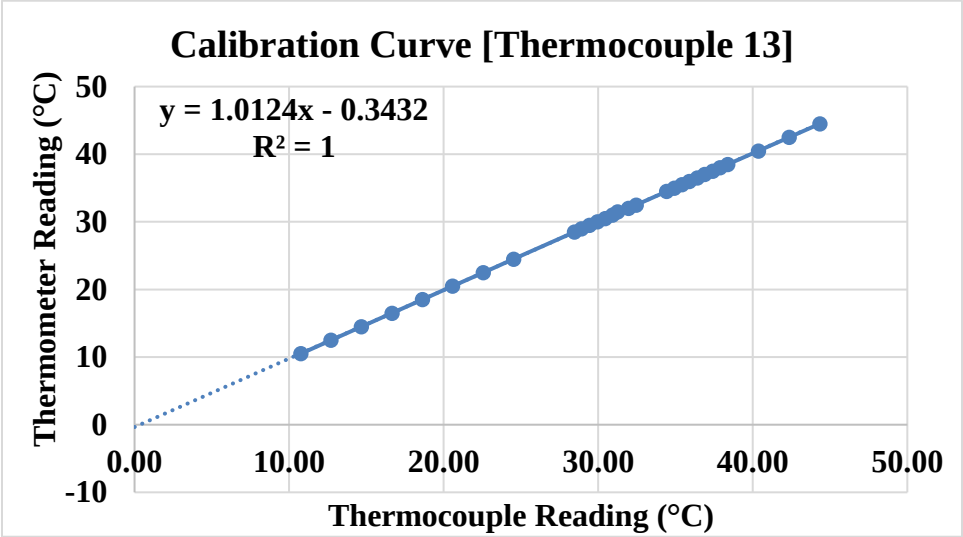

Figure 146: Thermocouple 13 Calibration Curve.

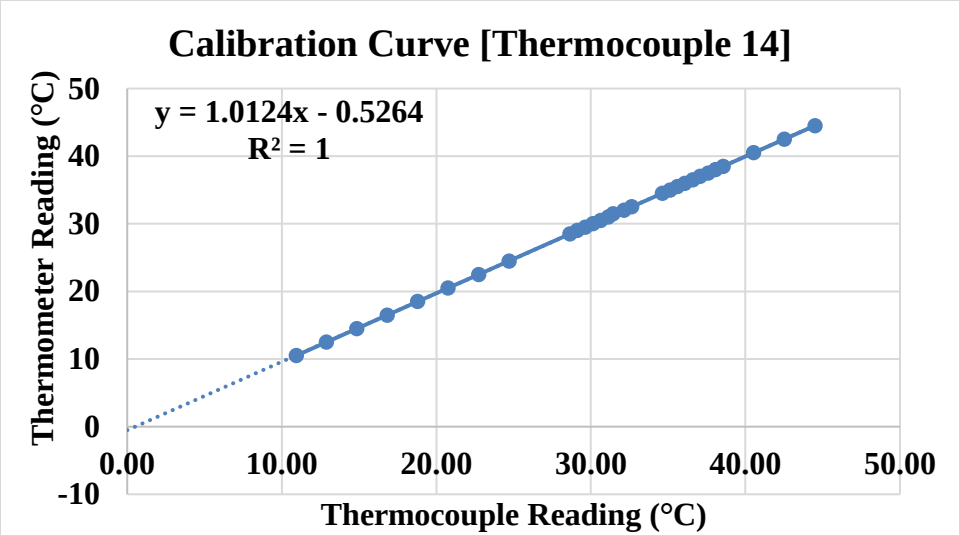

Figure 147: Thermocouple 14 Calibration Curve.

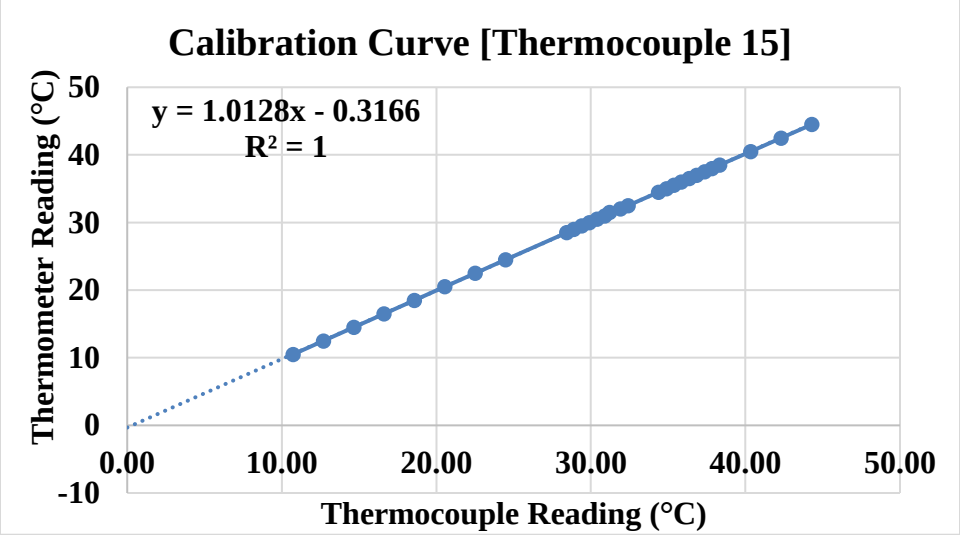

Figure 148: Thermocouple 15 Calibration Curve.

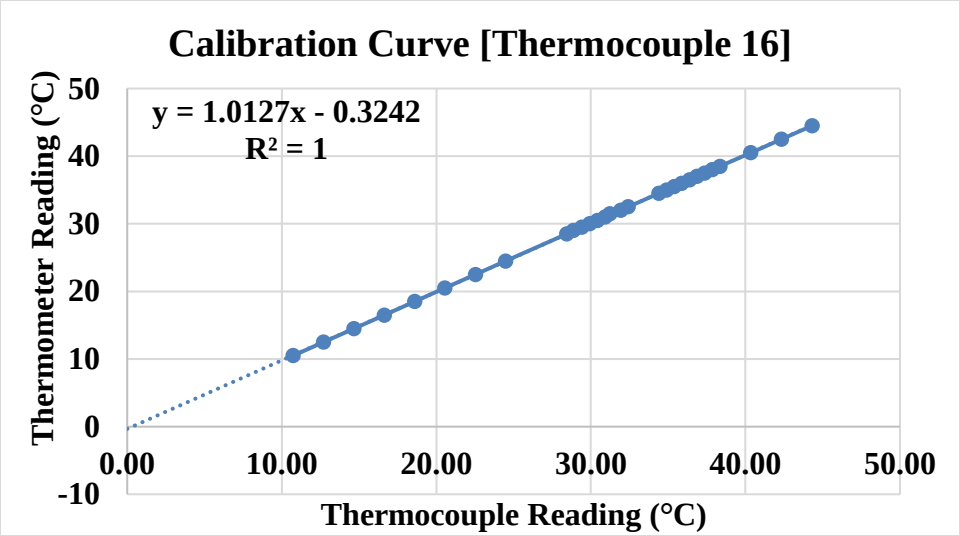

Figure 149: Thermocouple 16 Calibration Curve.

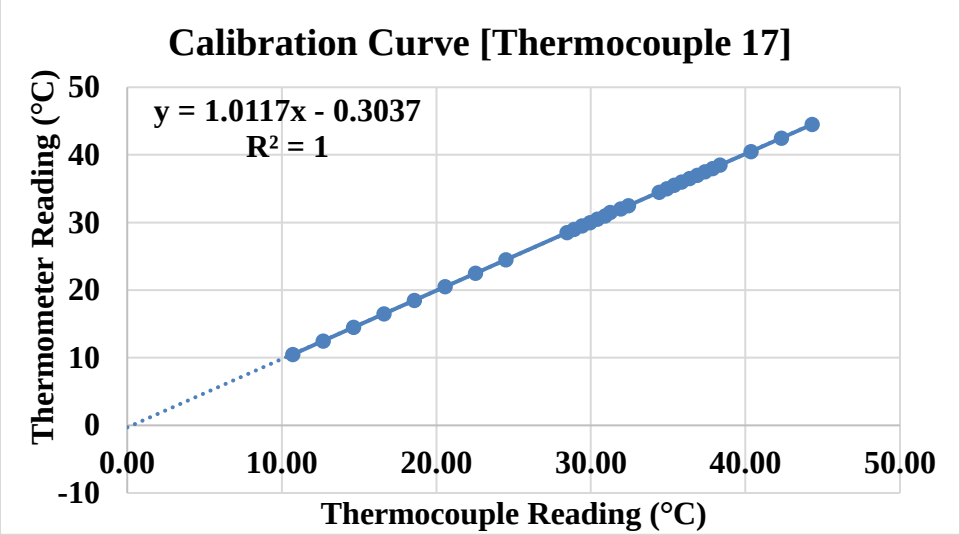

Figure 150: Thermocouple 16 Calibration Curve.

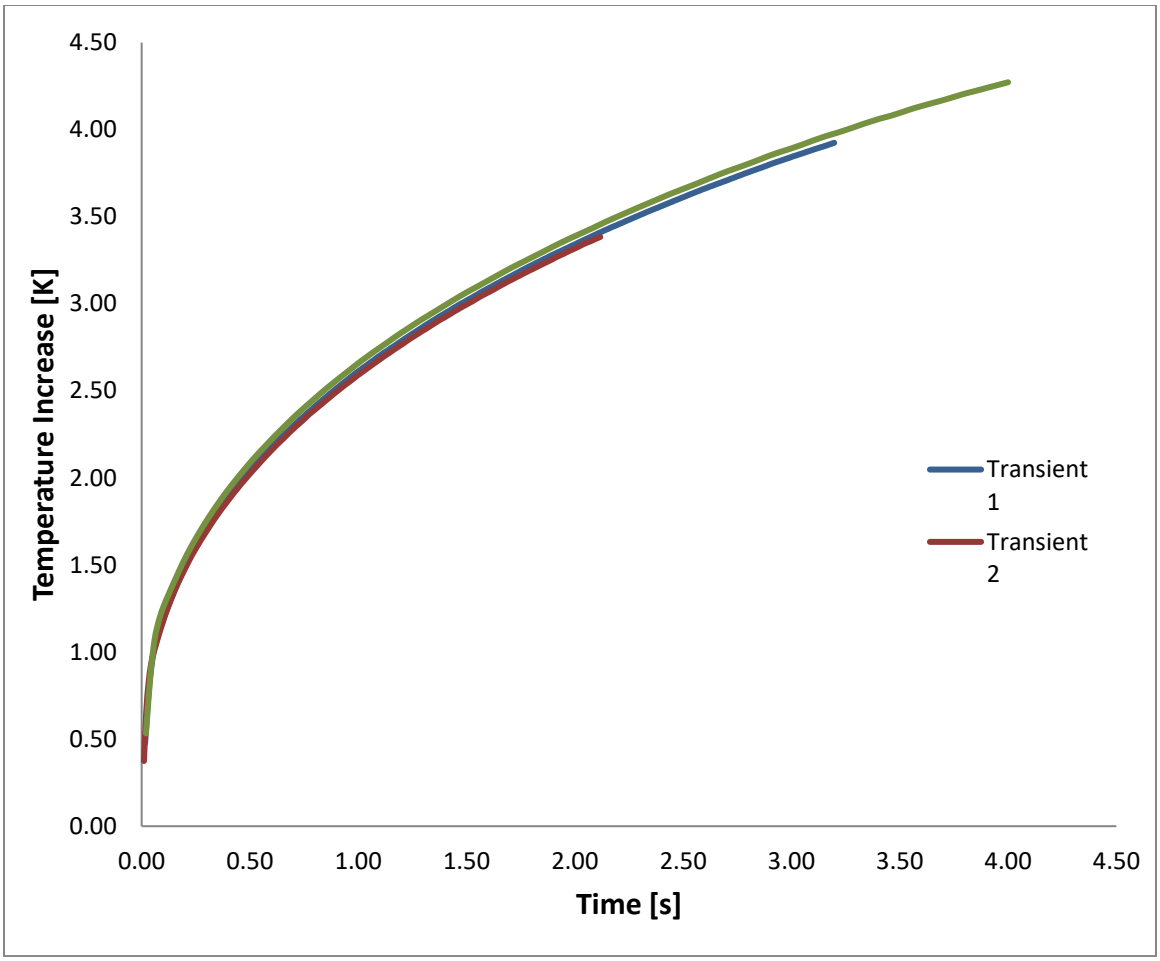

Figure 151: Transient Response of water (Calibration Standard) at a power input of 0.1-watt, measurement time of 3sec, 2sec and 4sec respectively at 20°C.

Table 46: Results of thermal conductivity of water (Calibration Standard) measured a power input of 0.1-watt and measurement time of 3sec, 2sec and 4sec respectively at 20°C.

	Temp (°C)	Th. Conductivity (W/ mK)	Th. Diffusivity (mm^2/s)	Spec. Heat (MJ/m^3K)	Pr. Depth (mm)	Temp Incr (K)
	19.8 °C	0.5618	0.1338	4.200	1.06	2.03
	19.8 °C	0.5604	0.1334	4.200	1.06	2.18
	19.8 °C	0.5870	0.1398	4.200	1.50	2.73
Average	19.8	0.6	0.1	4.2	1.2	2.3
Std.Dev	0	0.015	0.003	6.280E-16		
% Std.Dev	0	2.6	2.6	1.4E-14		

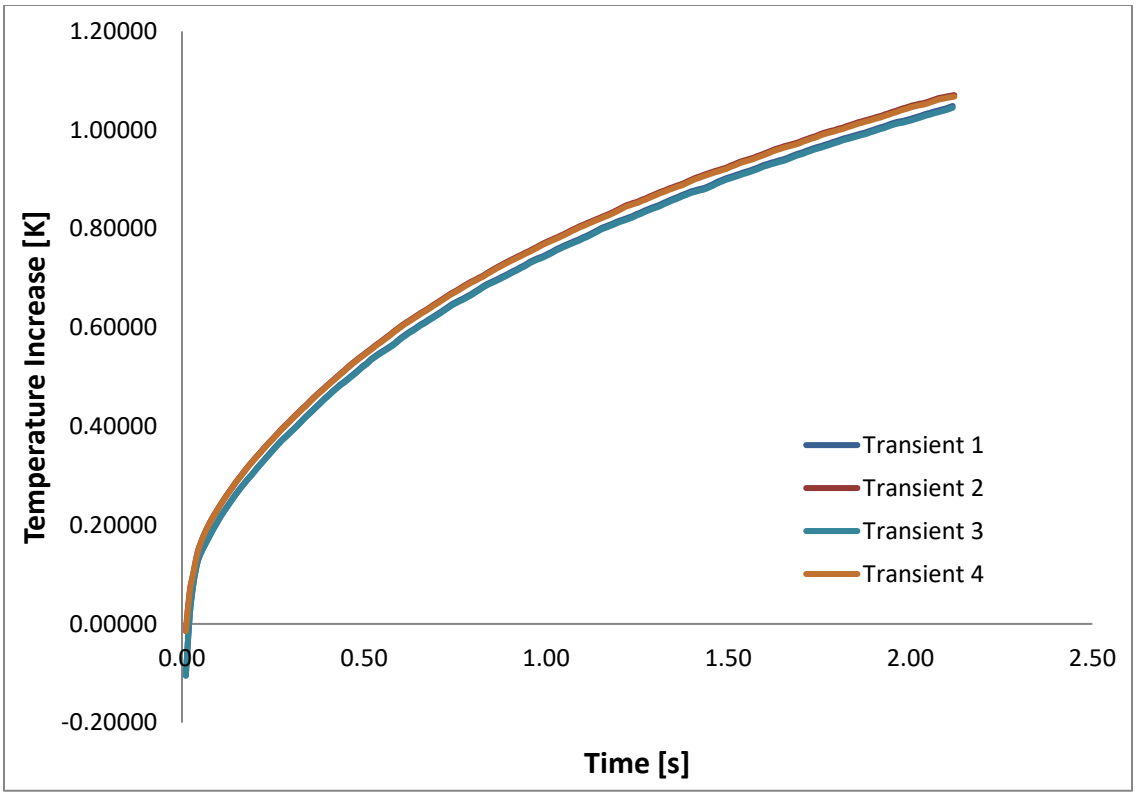

Figure 152: Transient Response of water (Calibration Standard) at a power input of 0.1-watt, measurement time of 2 sec at 50°C.

Table 47: Results of thermal conductivity of water (Calibration Standard) measured a power input of 0.1-watt and measurement time of 2sec. The thermal conductivity was measured at an ambient temperature of 50°C.

	Temp (°C)	Th. Conductivity (W/ mK)	Th. Diffusivity (mm^2/s)	Spec. Heat (MJ/m^3K)	Pr. Depth (mm)	Temp Incr (K)
	51.4 °C	0.6143	0.1939	4.200	0.906	0.458
	51.4 °C	0.6927	0.1887	4.200	0.895	0.457
	51.4 °C	0.6546	0.1797	4.200	0.714	0.378
	51.4 °C	0.6503	0.1786	4.200	0.769	0.450
Average	51.4	0.65	0.2	4.2	0.8	0.4
Std.Dev	0	0.032	0.007	8.881E-16		
% Std.Dev	0	4.9	3.8	2.1E-14		

Table 48: Measurement uncertainty for measuring liquid thermal conductivity using thermal plane source technique. Standard medium was distilled water.

Temperature	TPS Measured Thermal Conductivity	Literature Thermal Conductivity (NIST)	Std.Dev	Percentage Difference	Overall Measurement Uncertainty
19.8	0.6 W/mK	0.5984 W/mK	2.6%	0.3%	2.6%
51.4	0.65 W/mK	0.6825 W/mK	3.8%	4.7%	6%

APPENDIX B

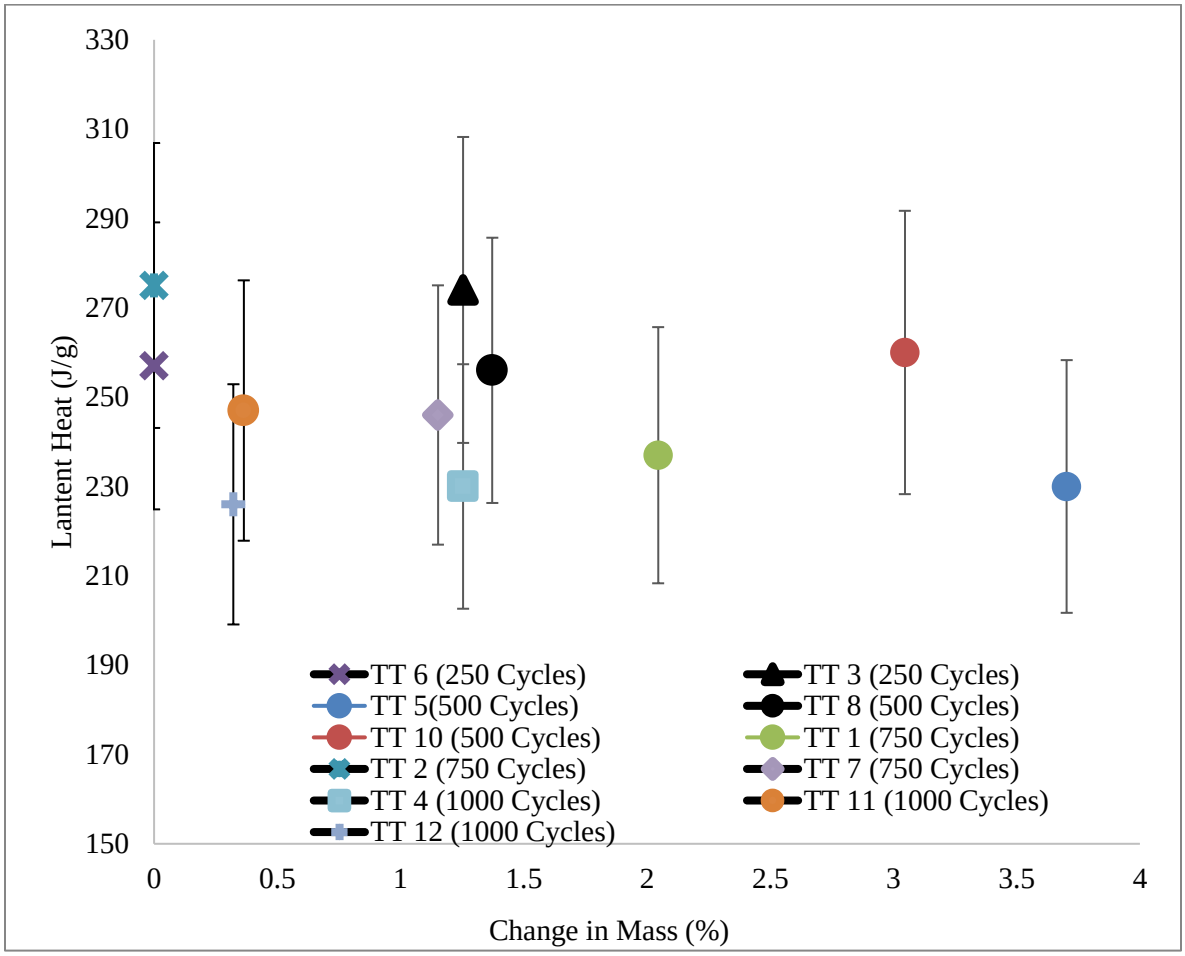

Figure 153: Effects of water absorption on endothermic latent heat with thermal cycling in lithium nitrate trihydrate.

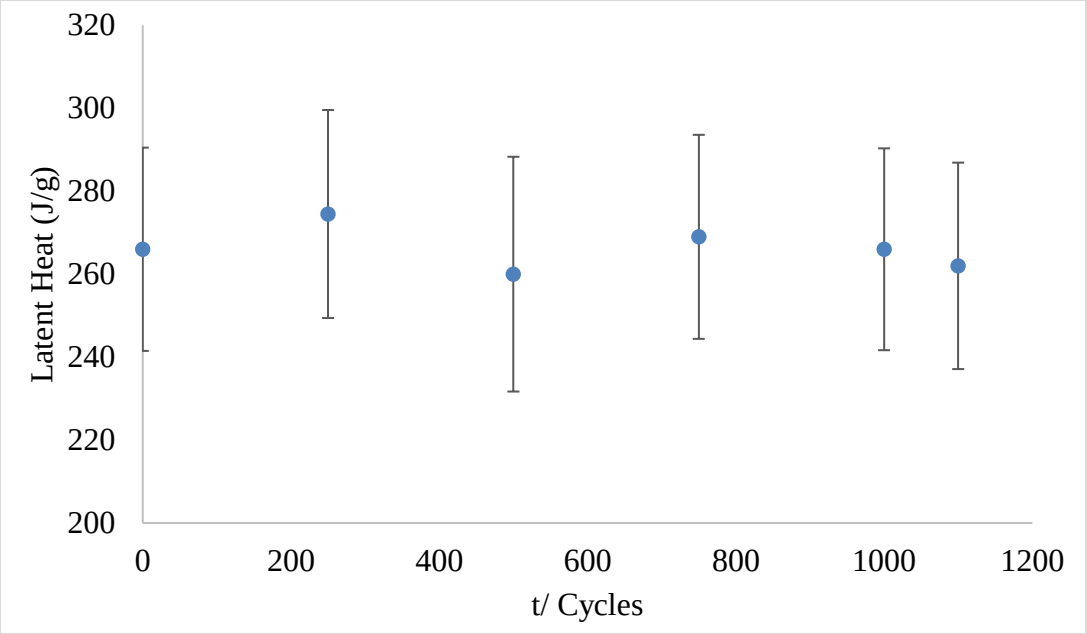

Figure 154: Effects of "Cold Finger" thermal Cycling on exothermic latent heat storage capacity of lithium nitrate trihydrate.

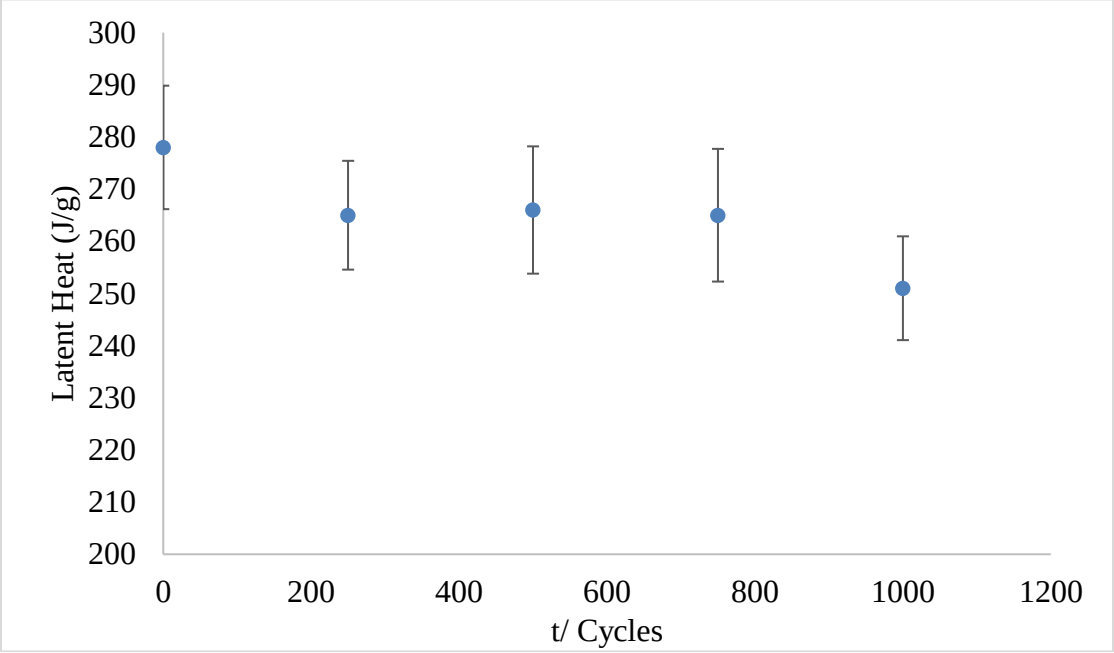

Figure 155: Effects of "Cold Finger" Thermal Cycling on endothermic latent heat storage capacity with 3% mass concentration of zinc hydroxyl nitrate.

Figure 49: Solid Thermal Conductivity Measurement of lithium nitrate trihydrate ($LiNO_3.3H_2O$) sample A (2.70 Mole of H_2O).

Run	*Temp (°C)*	*Out. Power (mW)*	*Meas Time (sec)*	*Th. Conduct (W/mK)*	*Th. Diffusivity (mm^2/s)*	*Spec. Heat (MJ/m^3K)*	*Probing Depth (mm)*	*Temp Increment (K)*
1	20.8	30	80	1.004	0.4145	2.422	6.76	1.64
2	20.8	30	80	1.014	0.3477	2.917	6.71	1.68
3	20.8	30	80	1.012	0.3397	2.980	6.63	1.78
4	20.8	30	80	1.016	0.3311	3.069	6.55	1.87
Average				1.012	0.3582	2.847	6.67	1.74
Std.Dev(± σ)				0.005	0.0330	0.251	0.08	0.09
Before Testing: $LiNO_3 + 2.70H_2O = LiNO_3.\ 2.70H_2O$								
After Testing: $LiNO_3 + 2.75H_2O = LiNO_3.\ 2.75H_2O$ **Change in Mass: 1.86%**								

Table 50: Solid Thermal Conductivity Measurement of lithium nitrate trihydrate ($LiNO_3.3H_2O$) sample B (2.92 Mole of H_2O).

Run	*Temp (°C)*	*Out. Power (mW)*	*MeasTime (sec)*	*Th. Conduct (W/mK)*	*Th. Diffusivity (mm^2/s)*	*Spec. Heat (MJ/m^3K)*	*Probing Depth (mm)*	*Temp Increment (K)*
1	21	100	80	0.8814	0.2970	2.967	7.65	0.872
2	21	100	80	0.8511	0.2798	3.042	7.42	0.887
3	21	100	80	0.8738	0.2952	2.960	7.62	0.876
4	21	100	80	0.8638	0.2834	3.048	7.47	0.881
Average				0.8675	0.288	3.004	7.54	0.879
Std.Dev(± σ)				0.0114	0.0074	0.041	0.1	0.006
Before Testing: $LiNO_3 + 2.82H_2O = LiNO_3.\ 2.82H_2O$								
After Testing: $LiNO_3 + 2.92H_2O = LiNO_3.\ 2.92H_2O$ **Change in Mass: 4.9%**								

Table 51: Solid Thermal Conductivity Measurement of lithium nitrate trihydrate ($LiNO_3.3H_2O$) sample C (3.09 Mole of H_2O).

Run	*Temp (°C)*	*Out. Power (mW)*	*MeasTime (sec)*	*Th. Conduct (W/mK)*	*Th. Diffusivity (mm^2/s)*	*Spec. Heat (MJ/m^3K)*	*Probing Depth (mm)*	*Temp Increment (K)*
1	20.6	100	160	0.8473	0.3589	2.361	9.59	0.632
2	20.6	100	160	0.8428	0.3633	2.320	9.64	0.637
3	20.6	100	160	0.8410	0.3636	2.313	9.65	0.639
4	20.6	100	160	0.8424	0.3630	2.301	9.68	0.637
Average				0.8434	0.3630	2.324	9.64	0.636
Std.Dev(± σ)				0.0024	0.0026	0.022	0.03	0.03
Before Testing: $LiNO_3 + 3.02H_2O = LiNO_3.\ 3.02H_2O$								
After Testing: $LiNO_3 + 3.09H_2O = LiNO_3.\ 3.09H_2O$ **Change in Mass: 2.3%**								

APPENDIX C

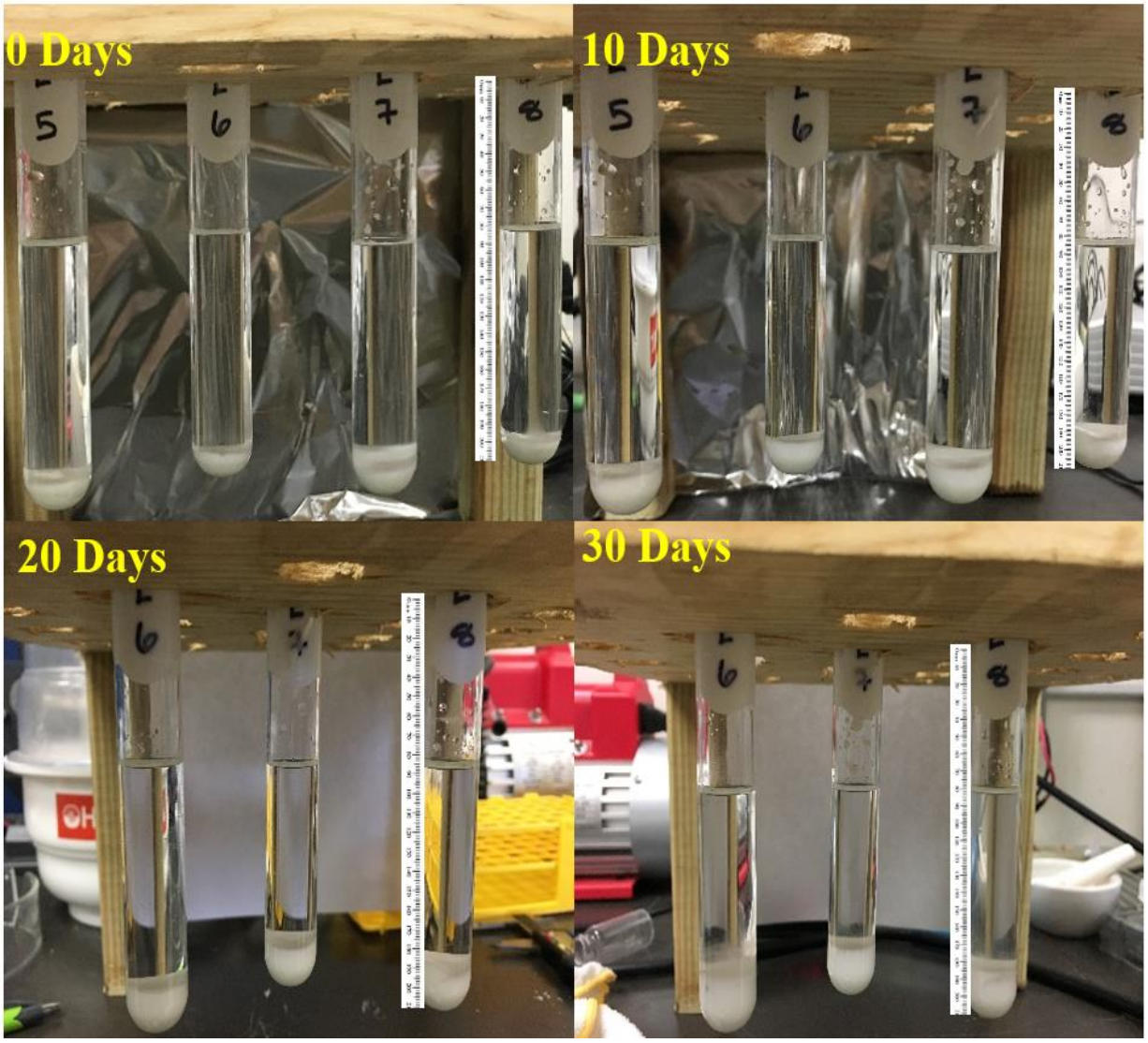

Figure 156: Effects of phase segregation with aging as function of time held at 45°C (T > Tm) with zinc nitrate hexahydrate with zinc oxide.

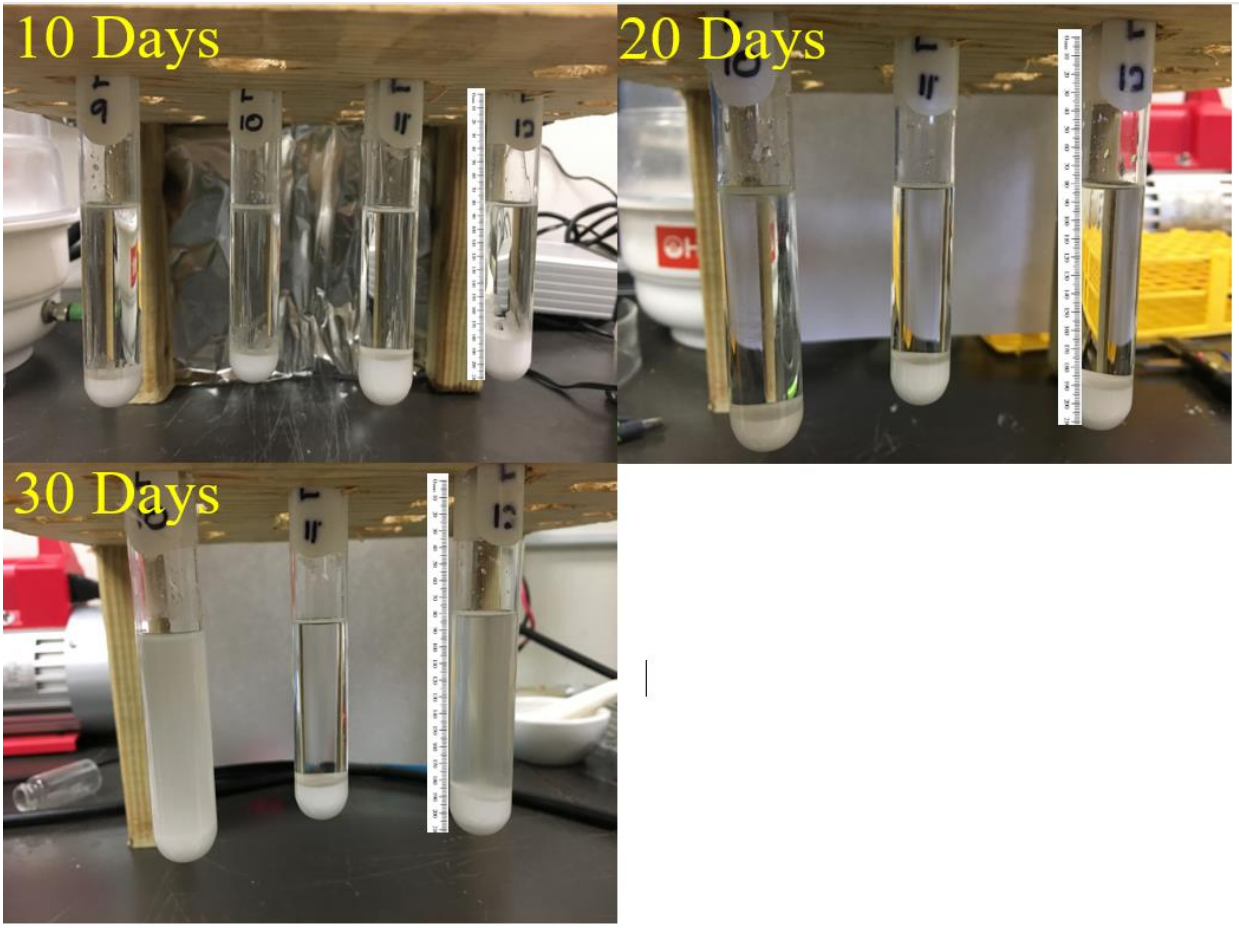

Figure 157: Effects of phase segregation with aging as function of time held at 45°C (T > Tm) with zinc nitrate hexahydrate with zinc hydroxyl nitrate.

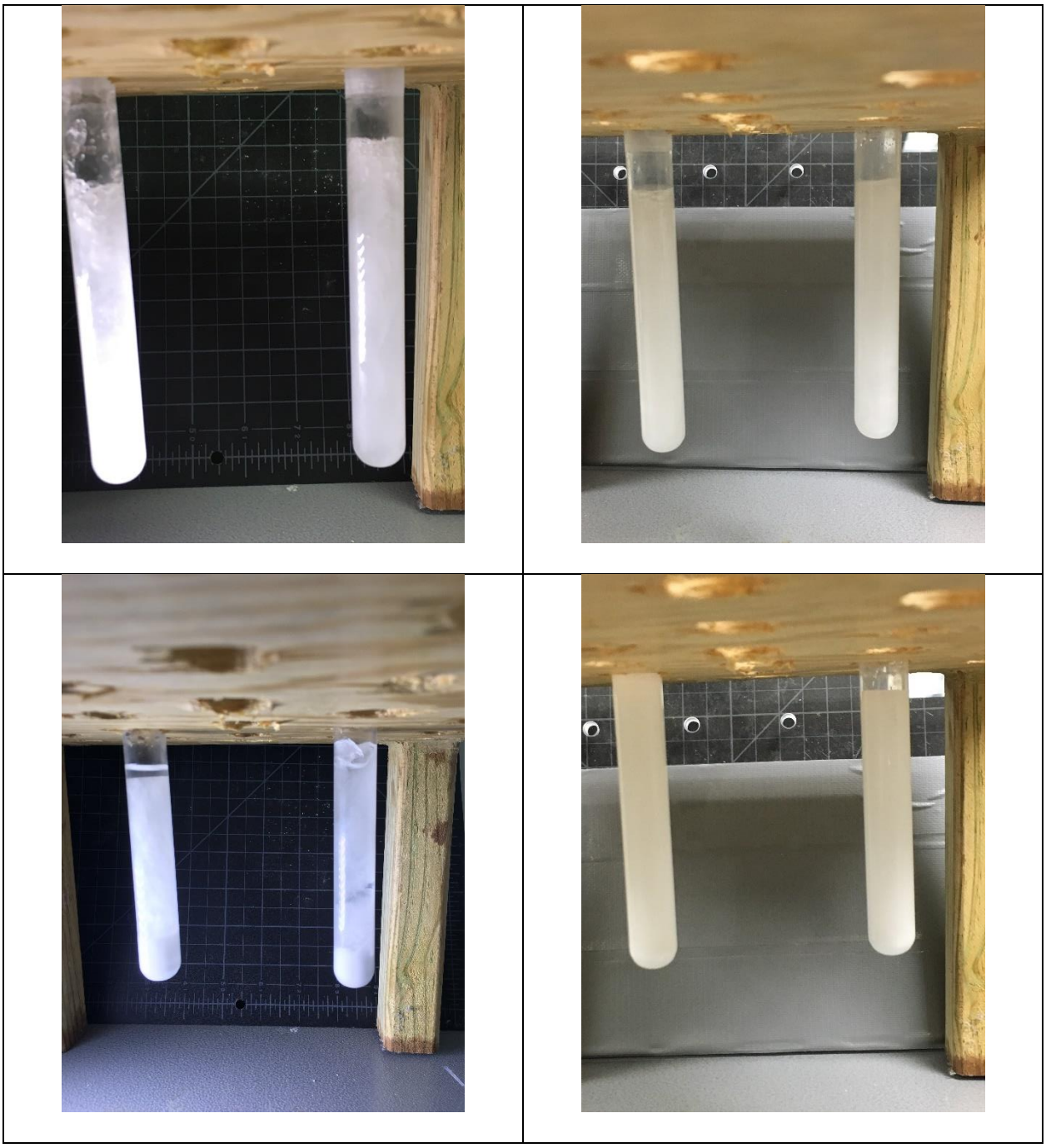

Figure 158: T-History of zinc nitrate hexahydrate with and without additives after 750 cycles [A]: Without additives cooled at 24°C; [B]: without additives cooled at 15°C; [C]: with 5% zinc hydroxyl nitrate cooled at 24°C; [D]: with 5% zinc hydroxyl nitrate cooled

APPENDIX D

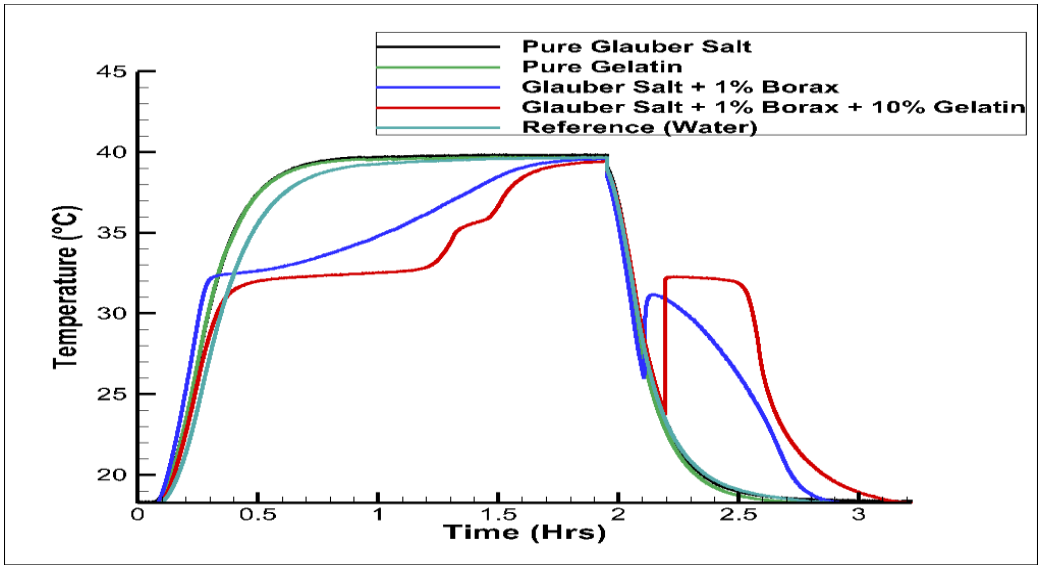

Figure 159: Initial thermal characterization of sodium sulfate decahydrate (Glauber Salt) with additives.

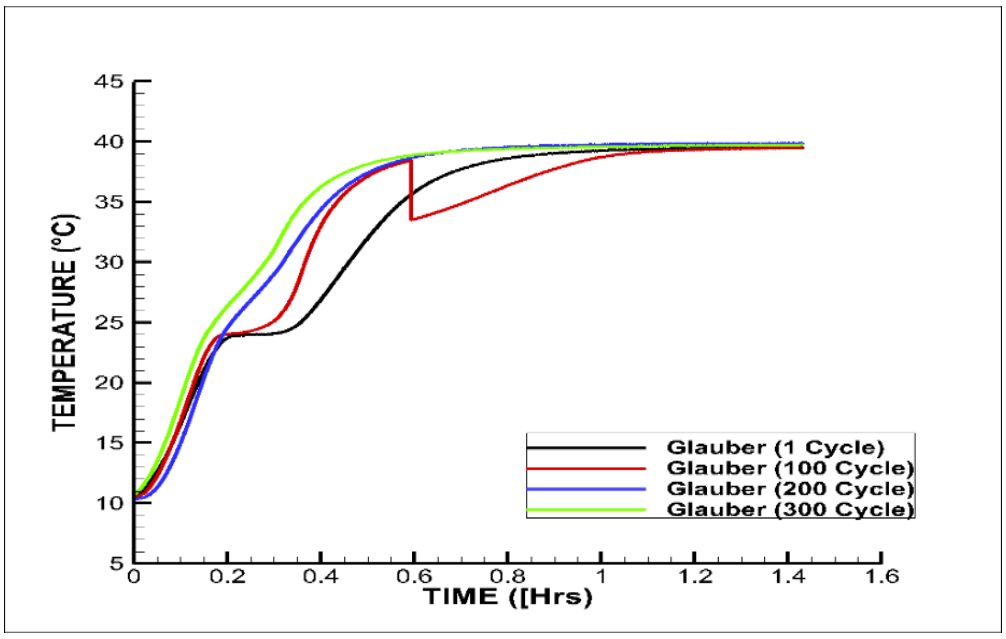

Figure 160: 300 thermal cyclic testing of sodium sulfate decahydrate (Glauber Salt) (Melting).

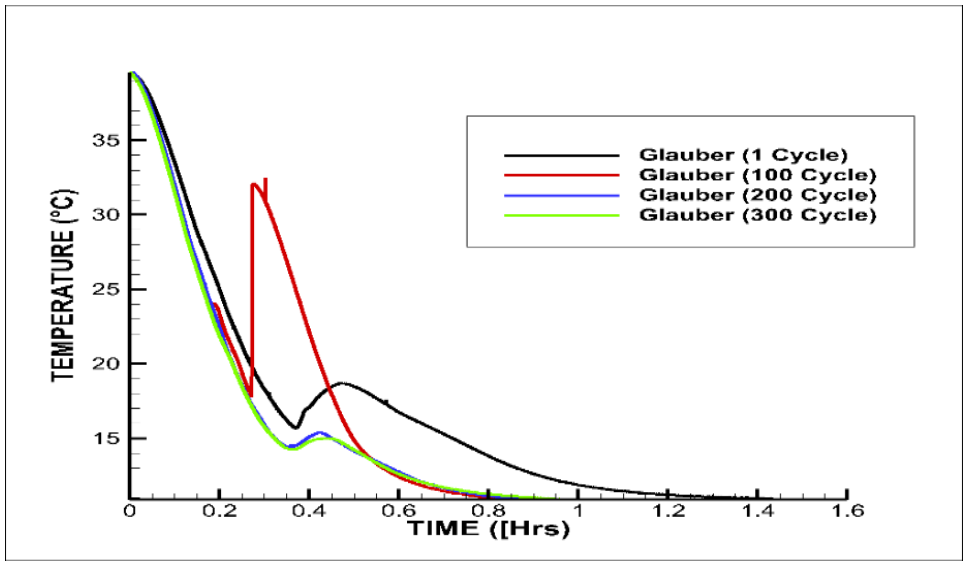

Figure 161: 300 thermal cyclic testing of sodium sulfate decahydrate (solidification)

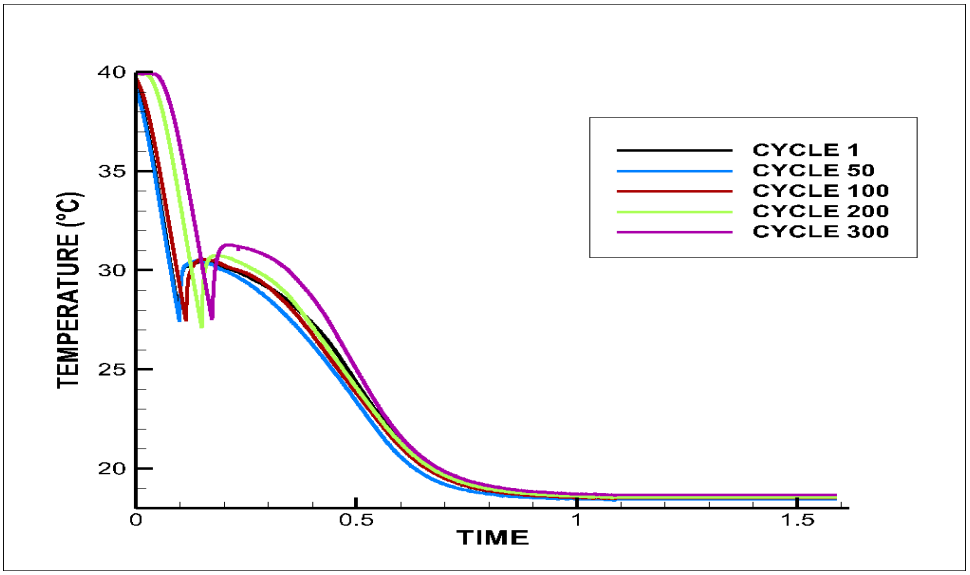

Figure 162: 300 Thermal cyclic testing of sodium sulfate decahydrate (Glauber Salt) with 1% Borax (melting).

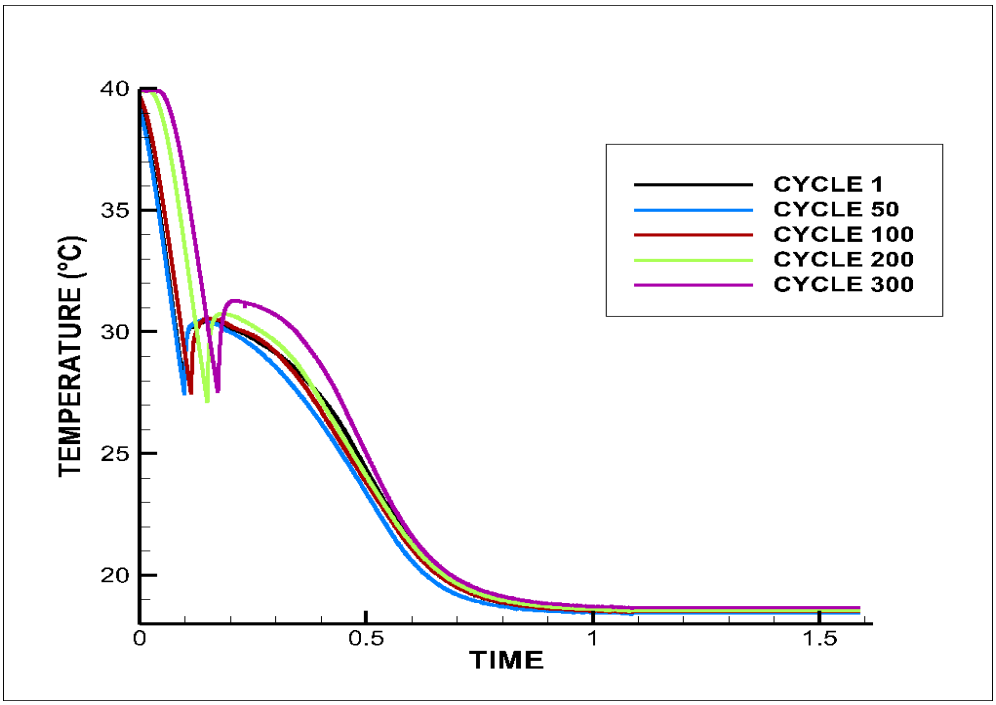

Figure 163: 300 thermal cyclic testing of sodium sulfate decahydrate (Glauber Salt) with 1% borax (solidification).

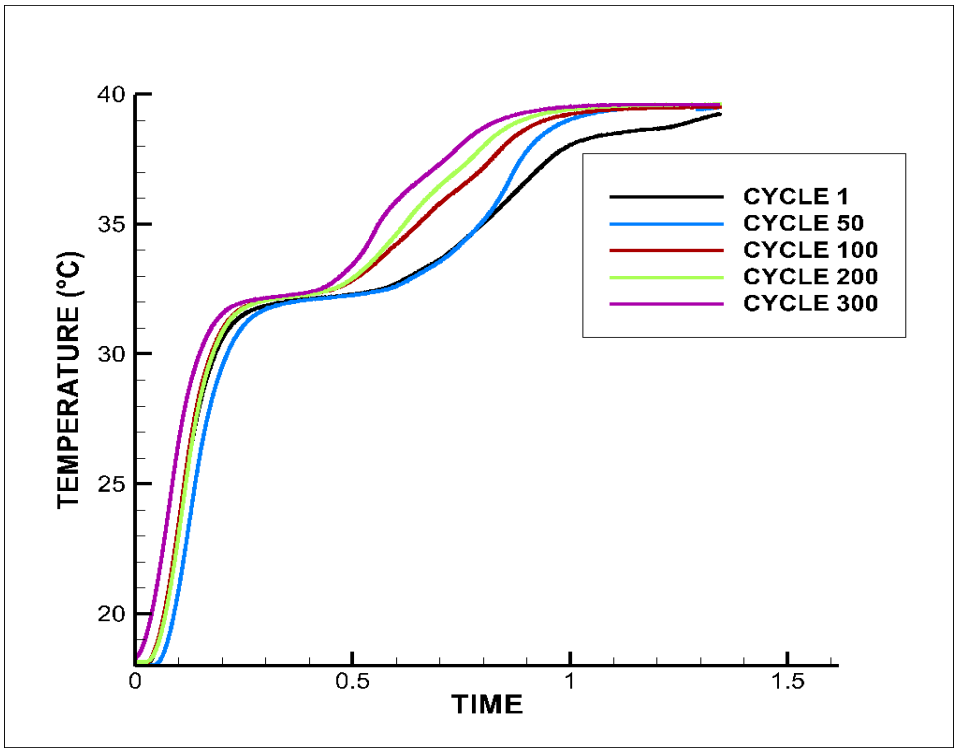

Figure 164: 300 thermal cyclic testing of sodium sulfate decahydrate (Glauber Salt) with 1% borax + 10% gelatin (melting).

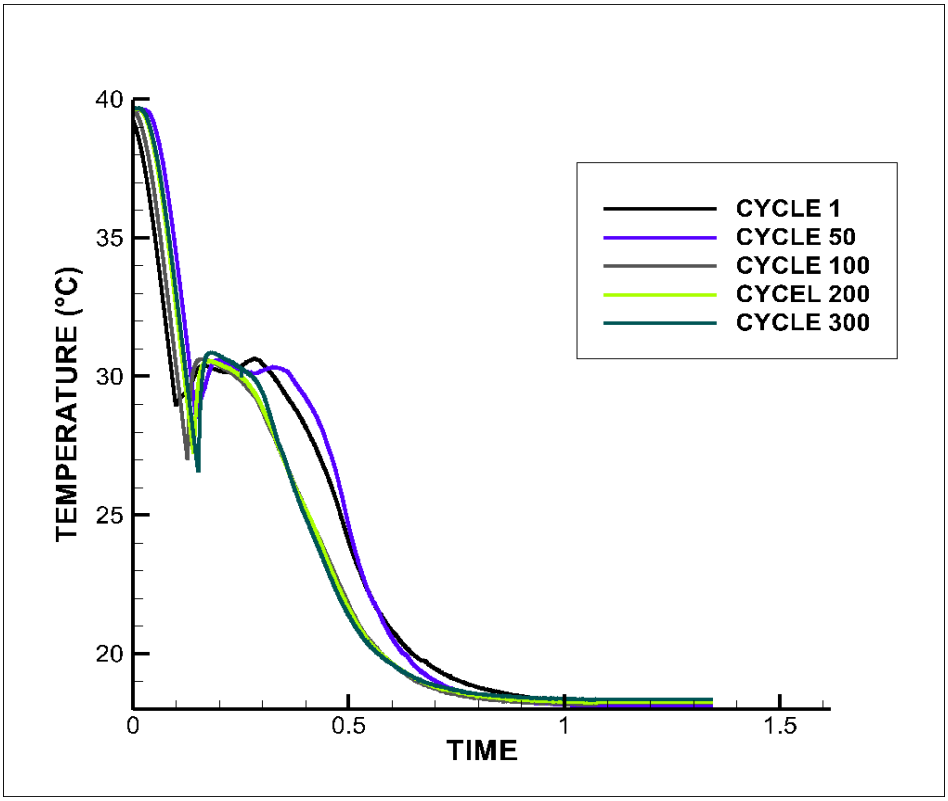

Figure 165: Thermal cyclic testing of sodium sulfate decahydrate (Glauber Salt) with 1% borax + 10% gelatin (solidification).

APPENDIX E

Table 52: Comparison of the heat storage during discharging and charging.

Flow Rate	T hot	T cold	Process	Total Time	Energy Total	Energy PCM	τ	Average Power	UA	NTU
GPH	deg C	deg C		sec	kJ	kJ	sec/kJ	kW	W/K	
5	38	20	Discharging	2294	97	764	18.6	0.057	20.28	461.22
5	34	24		3754	130	868	29.4	0.034	16.93	385.11
5	*32*	*26*		*4692*	*135*	*914*	*35.1*	*0.029*	*26.26*	*597.19*
7.5	*38*	*20*		*2633*	*140*	*906*	*18.4*	*0.055*	*9.67*	*219.98*
7.5	*34*	*24*		*6467*	*261*	*1769*	*24.8*	*0.040*	*14.89*	*338.50*
10	*38*	*20*		*2467*	*136*	*880*	*18.0*	*0.056*	*11.15*	*253.60*
10	*34*	*24*		*2850*	*121*	*806*	*23.5*	*0.043*	*13.71*	*311.87*
10	*32*	*26*		*2357*	*96*	*644*	*24.4*	*0.041*	*21.55*	*490.00*
5	*38*	*20*	*Charging*	*1752*	*81*	*767*	*14.9*	*0.067*	*32.03*	*728.33*
5	*34*	*24*		*2852*	*130*	*869*	*20.9*	*0.049*	*40.18*	*913.84*
5	*32*	*26*		*4240*	*159*	*1080*	*26.5*	*0.038*	*45.72*	*1039.61*
7.5	*38*	*20*		*736*	*81*	*511*	*9.1*	*0.117*	*166.72*	*3791.26*
7.5	*34*	*24*		*1342*	*50*	*320*	*25.3*	*0.046*	*173.30*	*3941.07*
10	*38*	*20*		*360*	*42*	*243*	*8.6*	*0.116*	*144.56*	*3561.53*
10	*34*	*24*		*340*	*25*	*145*	*13.8*	*0.073*	*141.22*	*3130.16*
10	*32*	*26*		*347*	*18*	*113*	*19.3*	*0.052*	*145.81*	*3315.77*

APPENDIX F

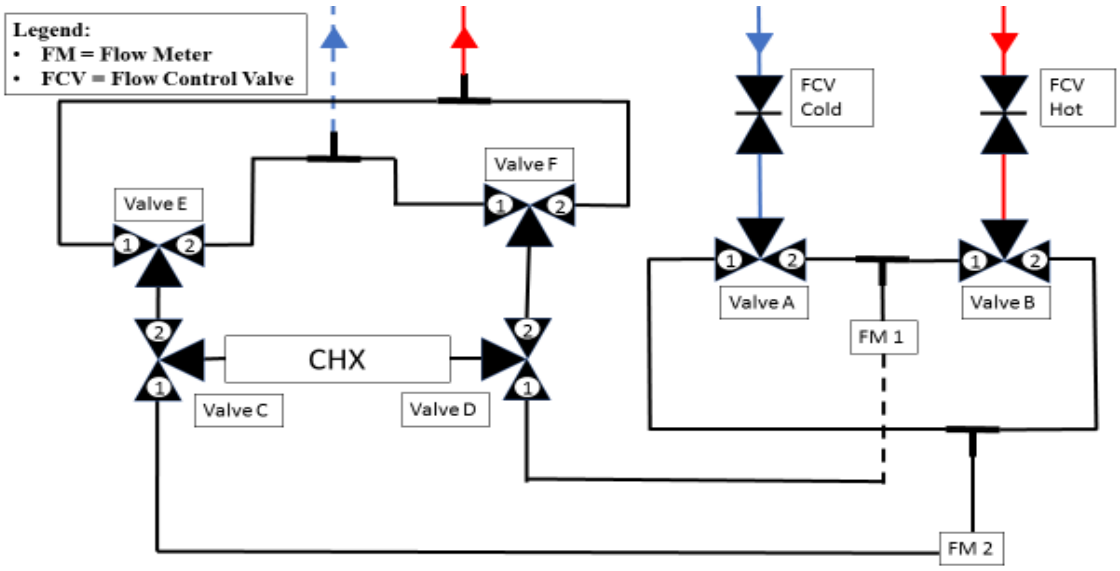

Figure 166: Schematic of heat exchanger flow loop for both configuration A and configuration B; showing the valve configurations for achieving both co-current and counter-current arrangements.

Table 53: Valve position for activating configuration A for charging and discharging for the LHTESS.

Valve	Location for Melting	Location for Solidification
A	2	2
B	2	2
C	1	2
D	2	1
E	N/A	1
F	2	N/A

Table 54: Valve position for activating configuration B for charging and discharging for the LHTESS.

Valve	Location for Melting	Location for Solidification
A	2	1
B	2	2
C	1	1
D	2	2
E	N/A	N/A
F	2	1

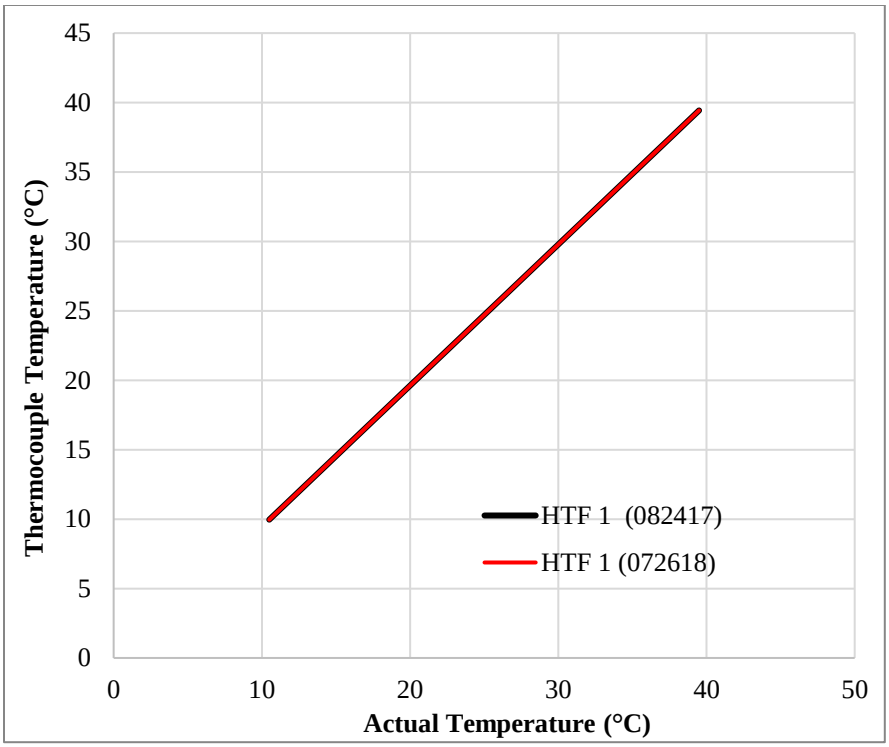

Figure 167: Sample thermocouple calibration curve for HTF inlet thermocouple before and after experiment for compact heat exchanger. The calibration was conducted in a water bath from 10°C to 40°C at an interval of 1°C and 0.5°C.

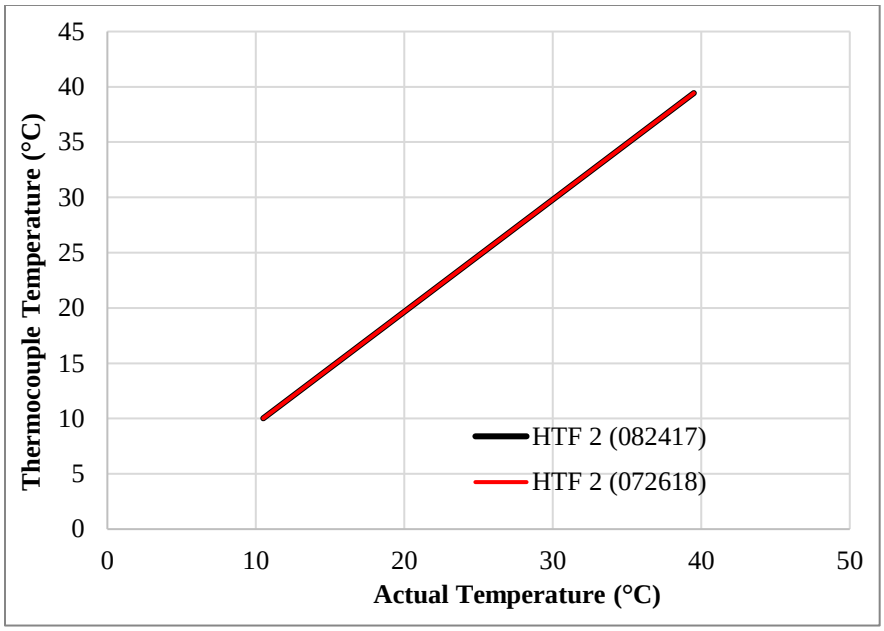

Figure 168: Sample thermocouple calibration curve for HTF outlet thermocouple before and after experiment for compact heat exchanger. The calibration was conducted in a water bath from 10°C to 40°C at an interval of 1°C and 0.5°C.

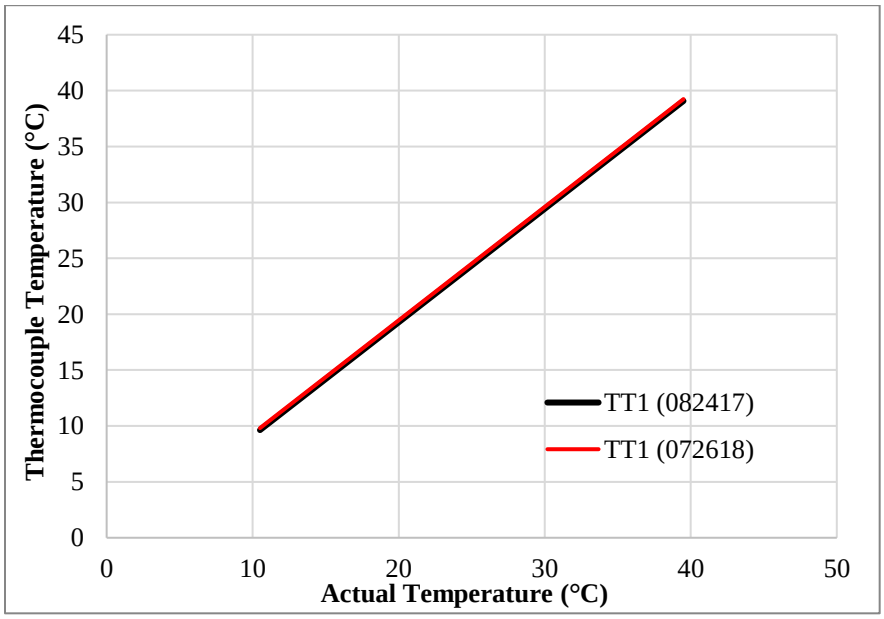

Figure 169: Sample thermocouple calibration curve for thermocouple 1 before and after experiment. The calibration was conducted in a water bath from 10°C to 40°C at an interval of 1°C and 0.5°C.

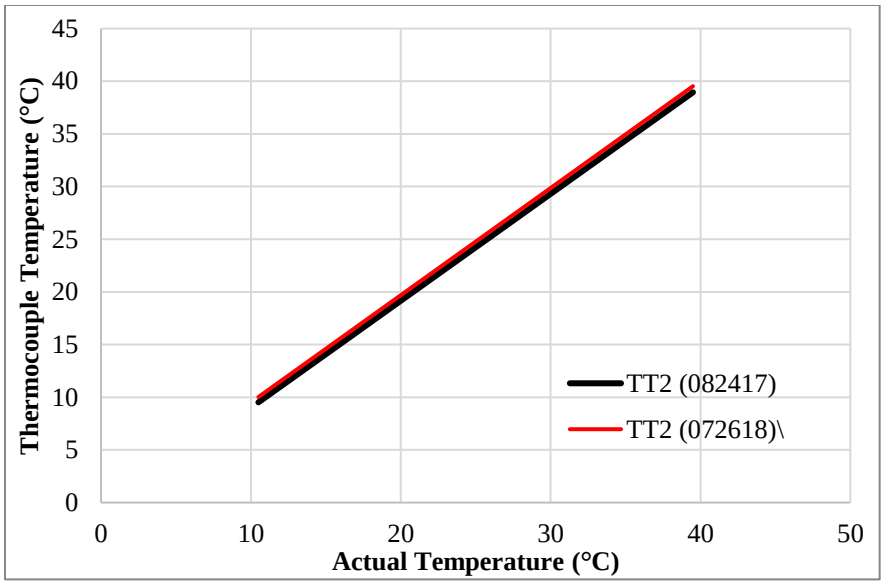

Figure 170: Sample thermocouple calibration curve for thermocouple 2 before and after experiment. The calibration was conducted in a water bath from 10°C to 40°C at an interval of 1°C and 0.5°C.

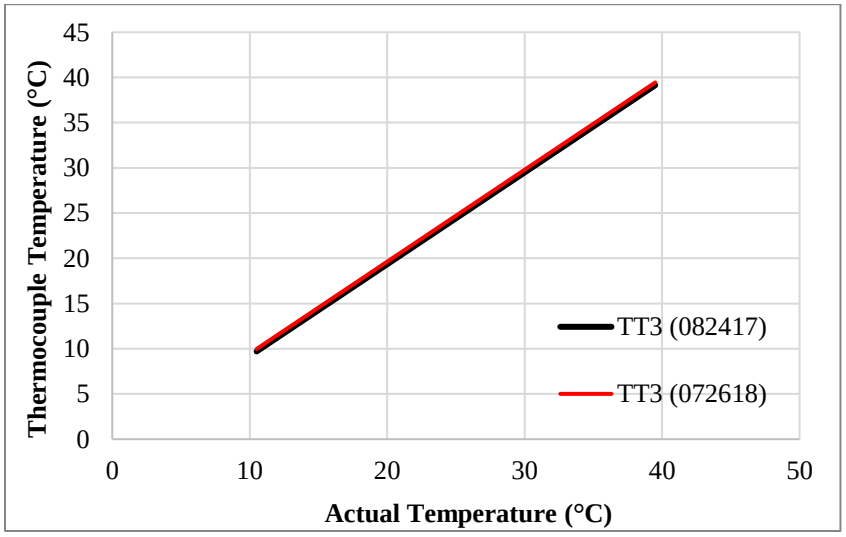

Figure 171: Sample Thermocouple Calibration Curve for Thermocouple 3 before and after experiment. The calibration was conducted in a water bath from 10°C to 40°C at an interval of 1°C and 0.5°C.

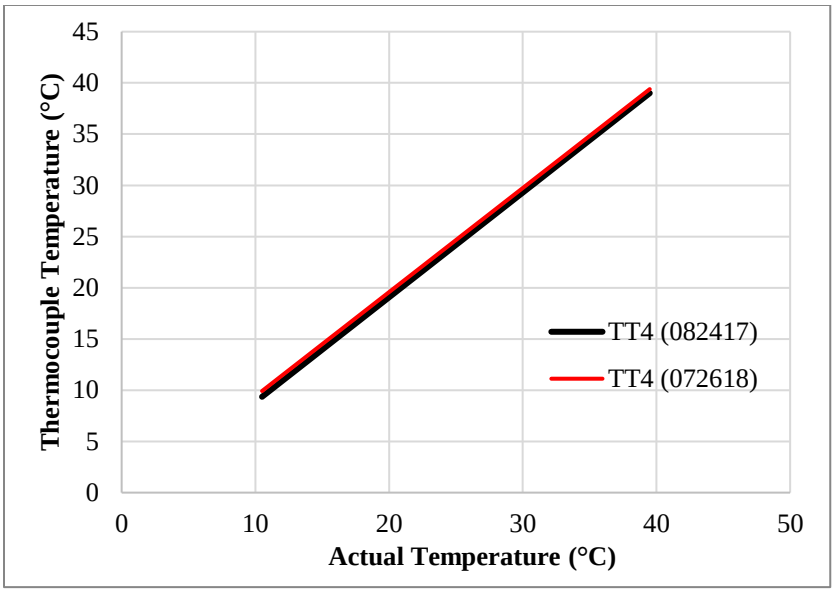

Figure 172: Sample thermocouple calibration curve for thermocouple 4 before and after experiment. The calibration was conducted in a water bath from 10°C to 40°C at an interval of 1°C and 0.5°C.

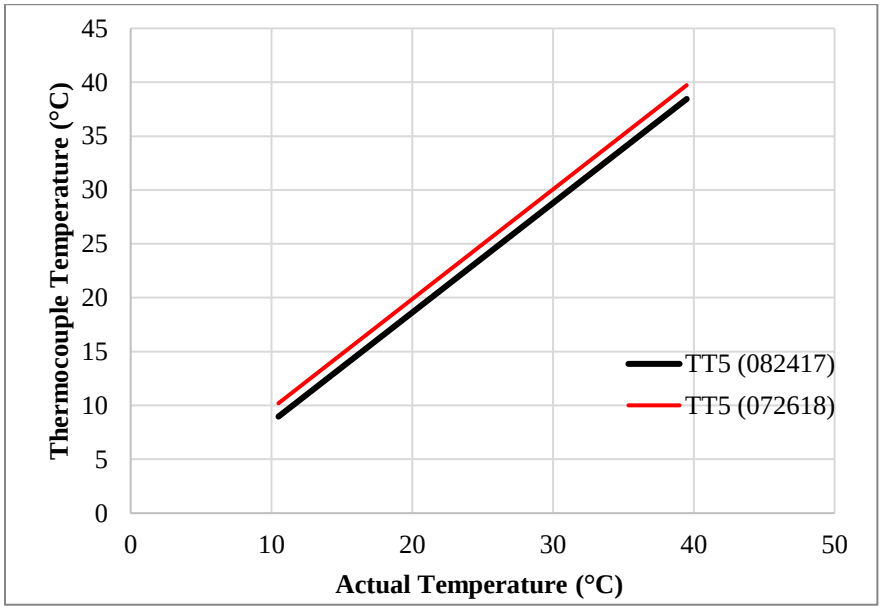

Figure 173: Sample thermocouple calibration curve for thermocouple 5 before and after experiment. The calibration was conducted in a water bath from 10°C to 40°C at an interval of 1°C and 0.5°C.

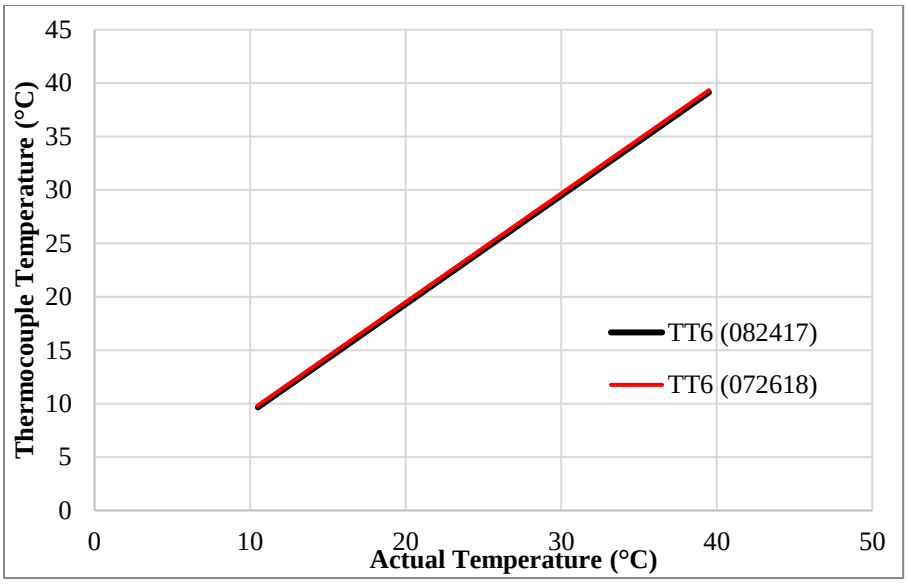

Figure 174: Sample thermocouple calibration curve for thermocouple 6 before and after experiment. The calibration was conducted in a water bath from 10°C to 40°C at an interval of 1°C and 0.5°C.

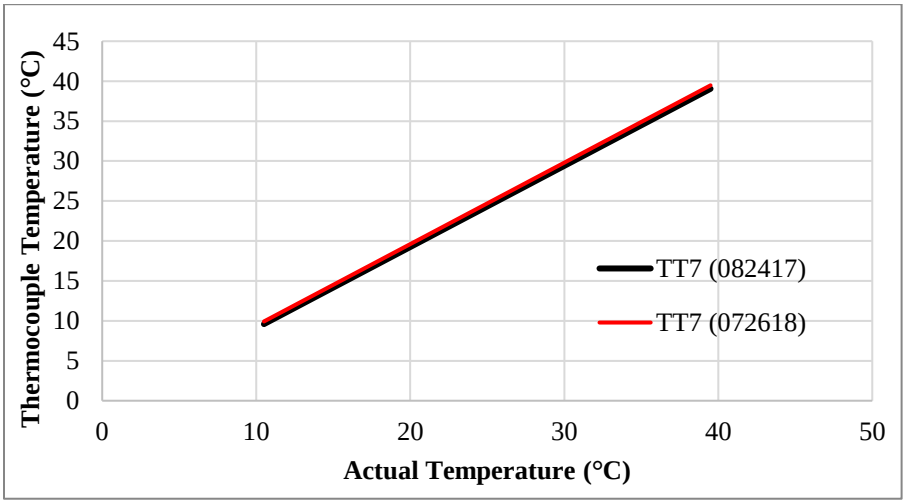

Figure 175: Sample thermocouple calibration curve for thermocouple 7 before and after experiment. The calibration was conducted in a water bath from 10°C to 40°C at an interval of 1°C and 0.5°C.

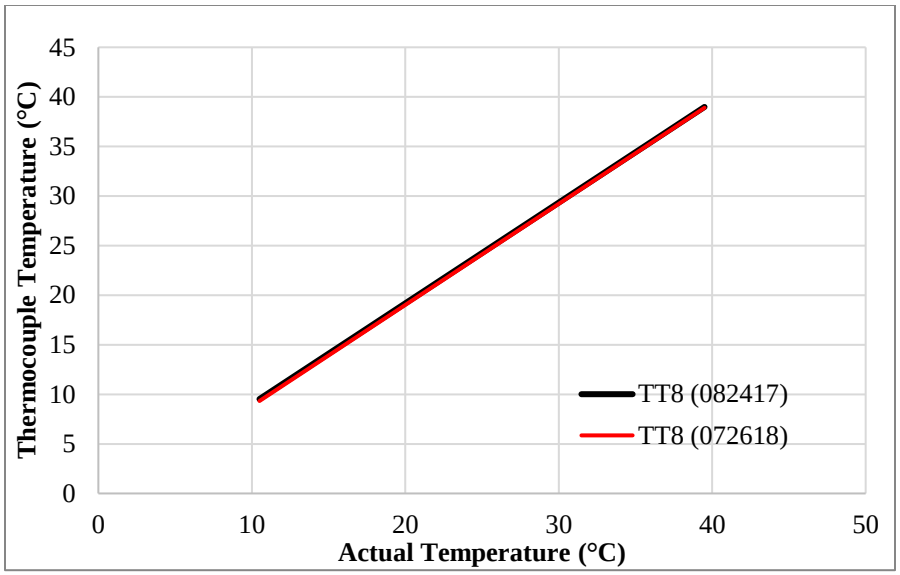

Figure 176: Sample thermocouple calibration curve for thermocouple 8 before and after experiment. The calibration was conducted in a water bath from 10°C to 40°C at an interval of 1°C and 0.5°C.

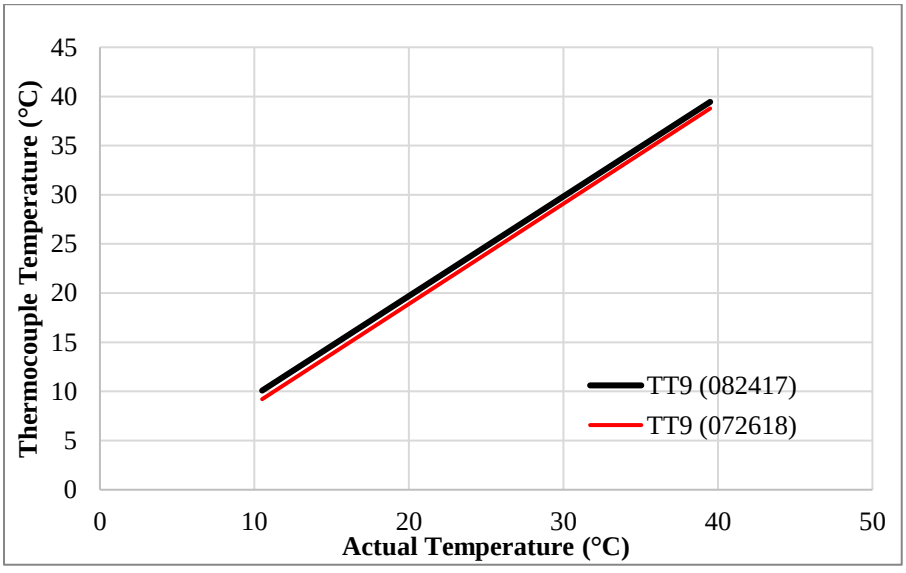

Figure 177: Sample thermocouple calibration curve for thermocouple 9 before and after experiment. The calibration was conducted in a water bath from 10°C to 40°C at an interval of 1°C and 0.5°C.

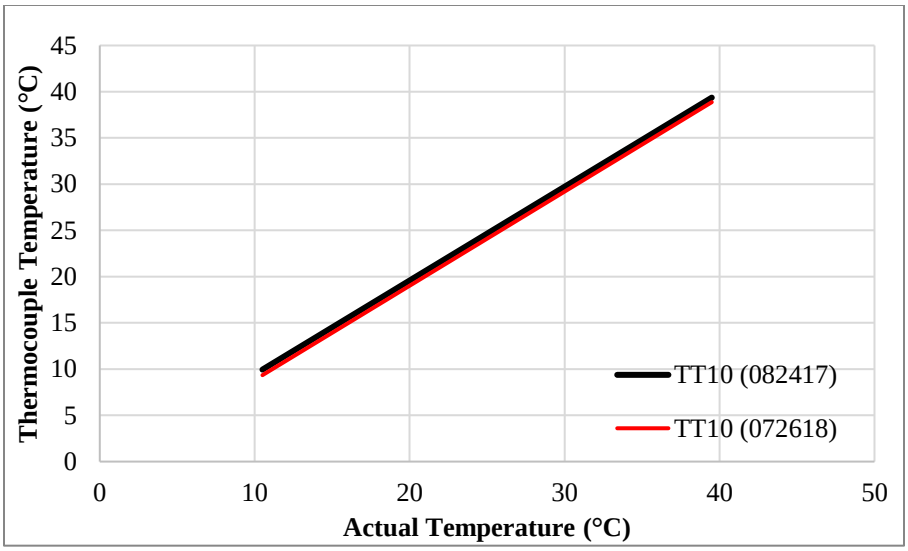

Figure 178: Sample thermocouple calibration curve for thermocouple 9 before and after experiment. The calibration was conducted in a water bath from 10°C to 40°C at an interval of 1°C and 0.5°C.

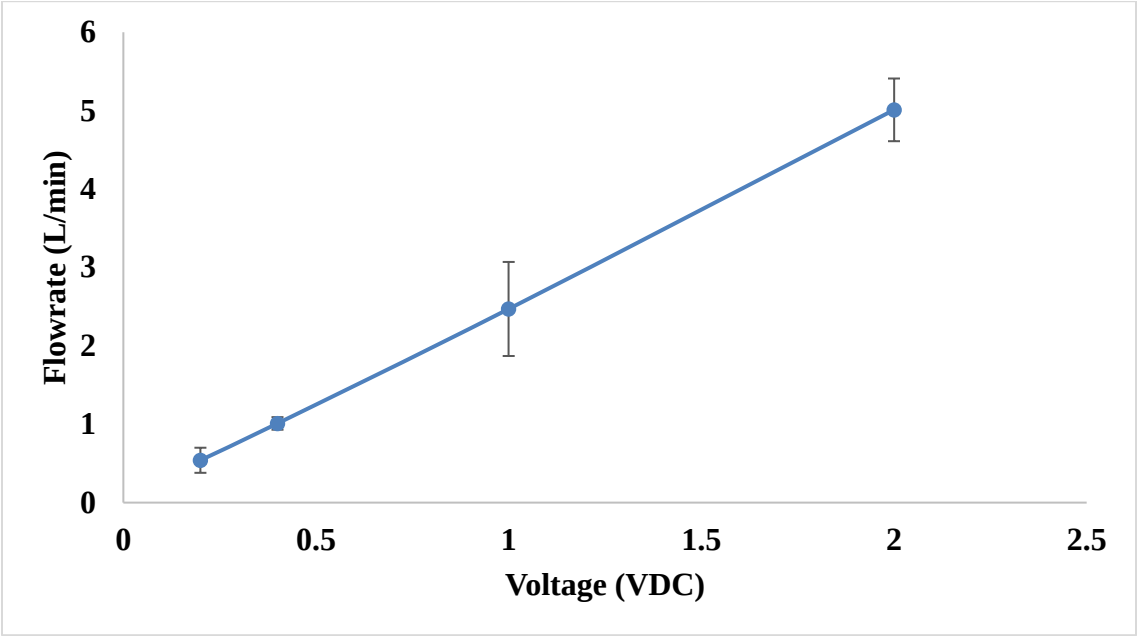

Figure 179: Sample flowmeter calibration curve for compact heat exchanger. Flowmeter model OMEGA FLR 1011.

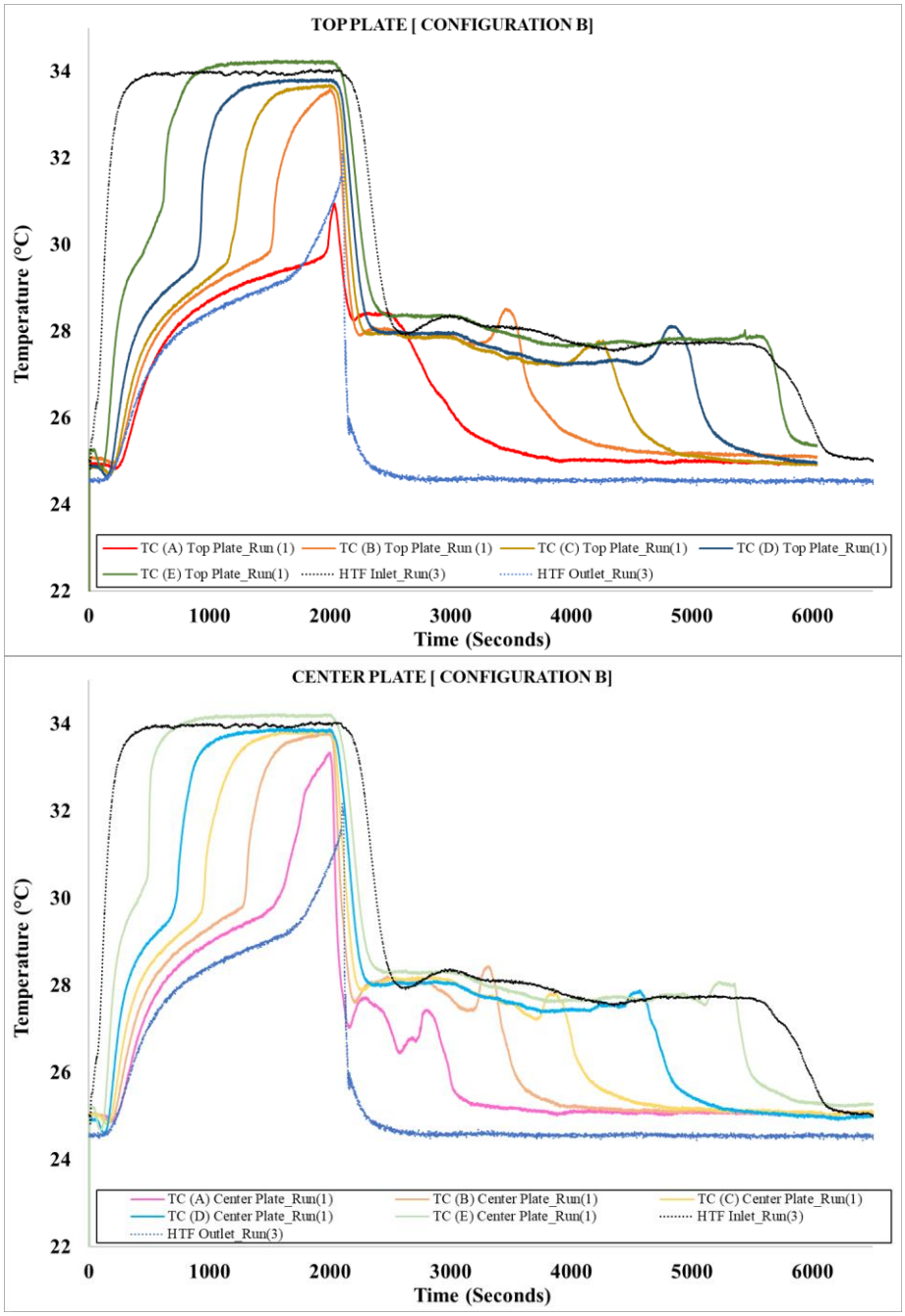

Figure 180: Temperature profile of PCM during melting and freezing cycle in configuration B layout. The inlet temperature of HTF during melting was 35°C, and the inlet temperature of HTF during freezing was 25°C at 3 GPH. Top image illustrates the temperature profile of top plate and bottom image illustrates the temperature profile of bottom plate.

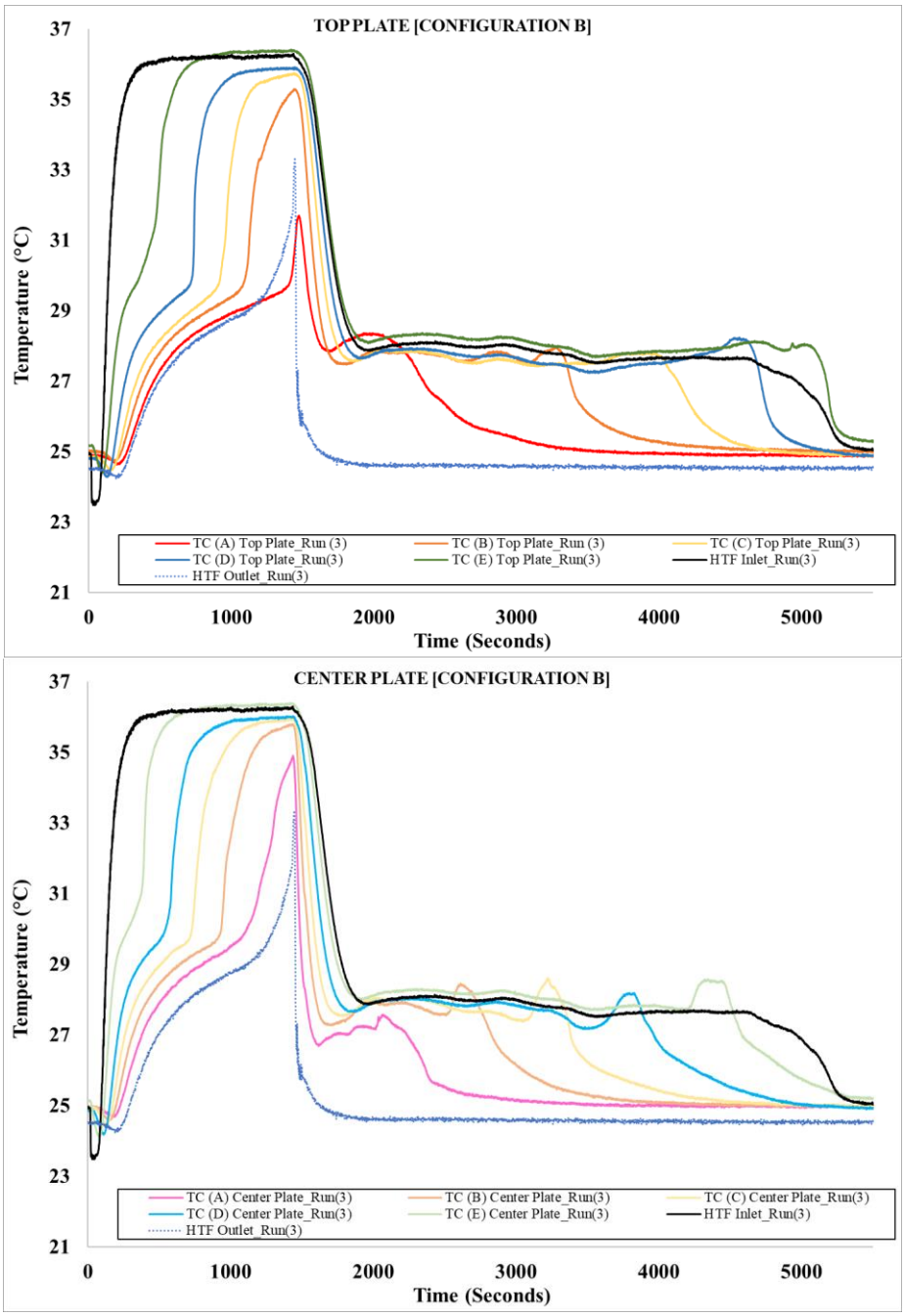

Figure 181: Temperature profile of PCM during melting and freezing cycle in configuration B layout. The inlet temperature of HTF during melting was 37.4°C, and the inlet temperature of HTF during freezing was 25°C at 3 GPH. Top image illustrates the temperature profile of top plate and bottom image illustrates the temperature profile of bottom plate.

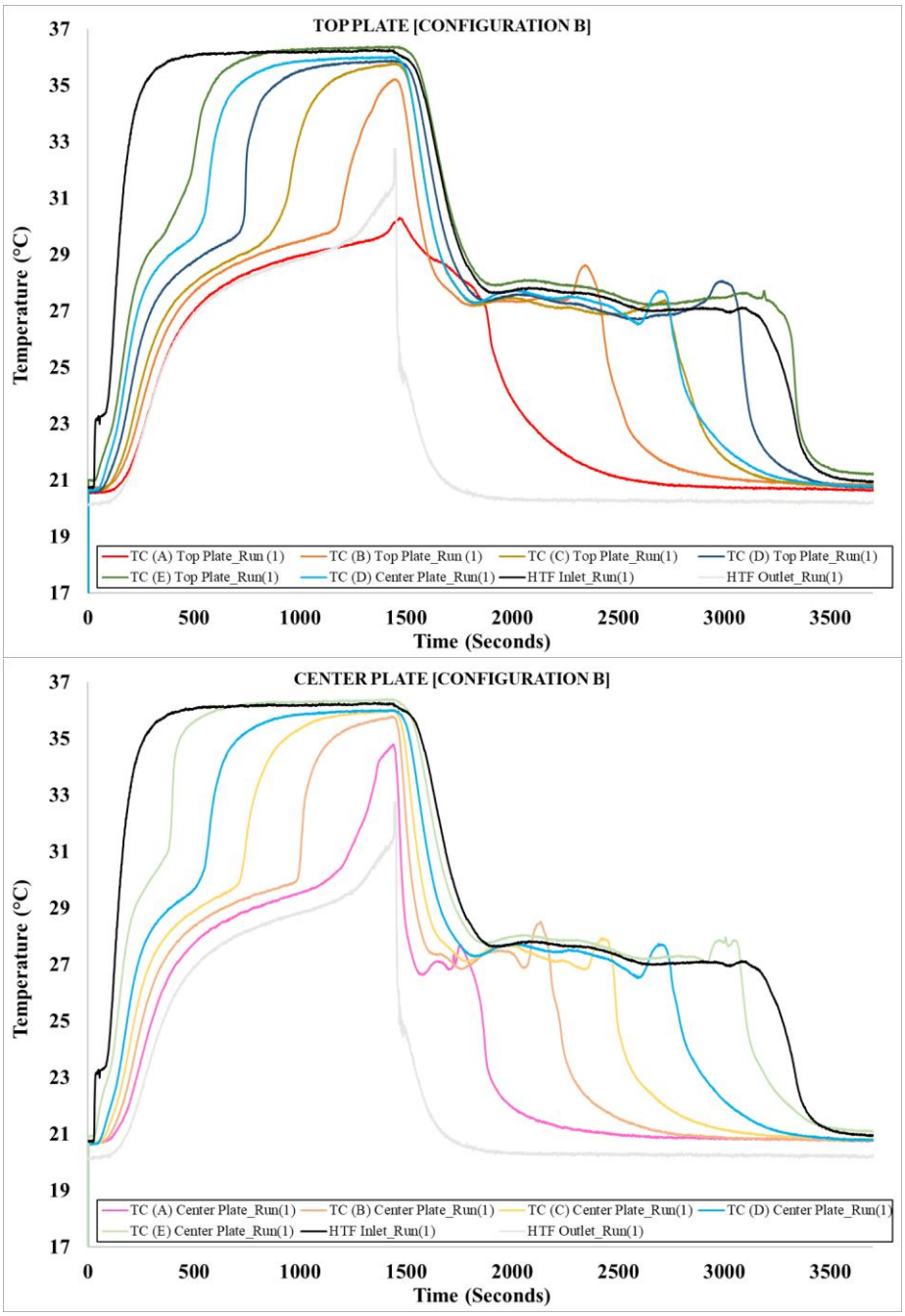

Figure 182: Temperature profile of PCM during melting and freezing cycle in configuration B layout. The inlet temperature of HTF during melting was 37.4°C, and the inlet temperature of HTF during freezing was 20°C at 3 GPH. Top image illustrates the temperature profile of top plate and bottom image illustrates the temperature profile of bottom plate.

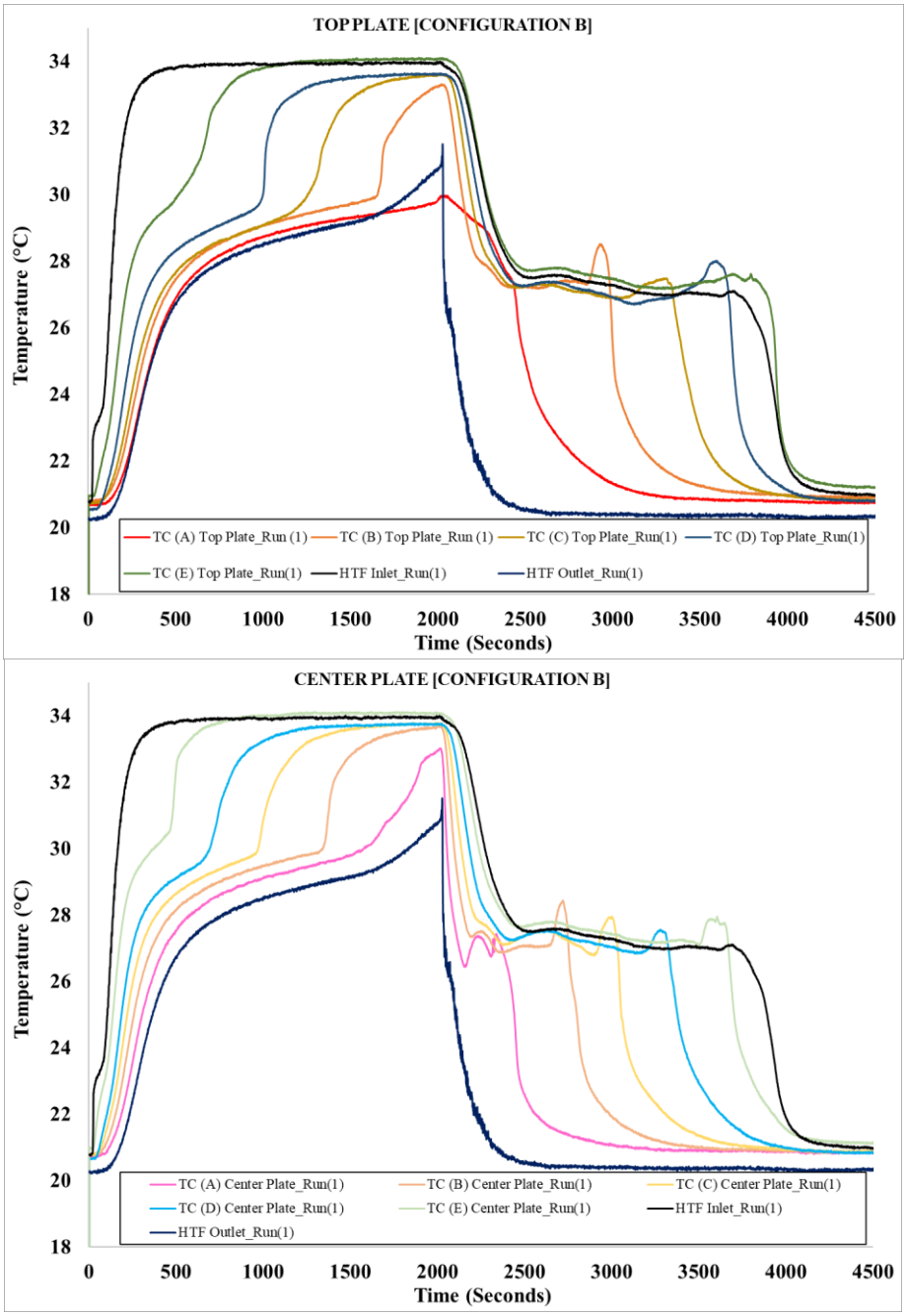

Figure 183: Temperature profile of PCM during melting and freezing cycle in configuration B layout. The inlet temperature of HTF during melting was 35°C, and the inlet temperature of HTF during freezing was 20°C at 3 GPH. Top image illustrates the temperature profile of top plate and bottom image illustrates the temperature profile of bottom plate.

Figure 184: Image shows the extent of the leakage. Prior to incident, anhydrous Calcium Chloride was used as a desiccant to reduce humidity within the acrylic chamber. This image shows the result of liquid state Lithium Nitrate Trihydrate (LNT) dripping into the Calcium Chloride dish. Notice the LNT crystal grasping the insulation layer indicating where the majority of LNT fell.

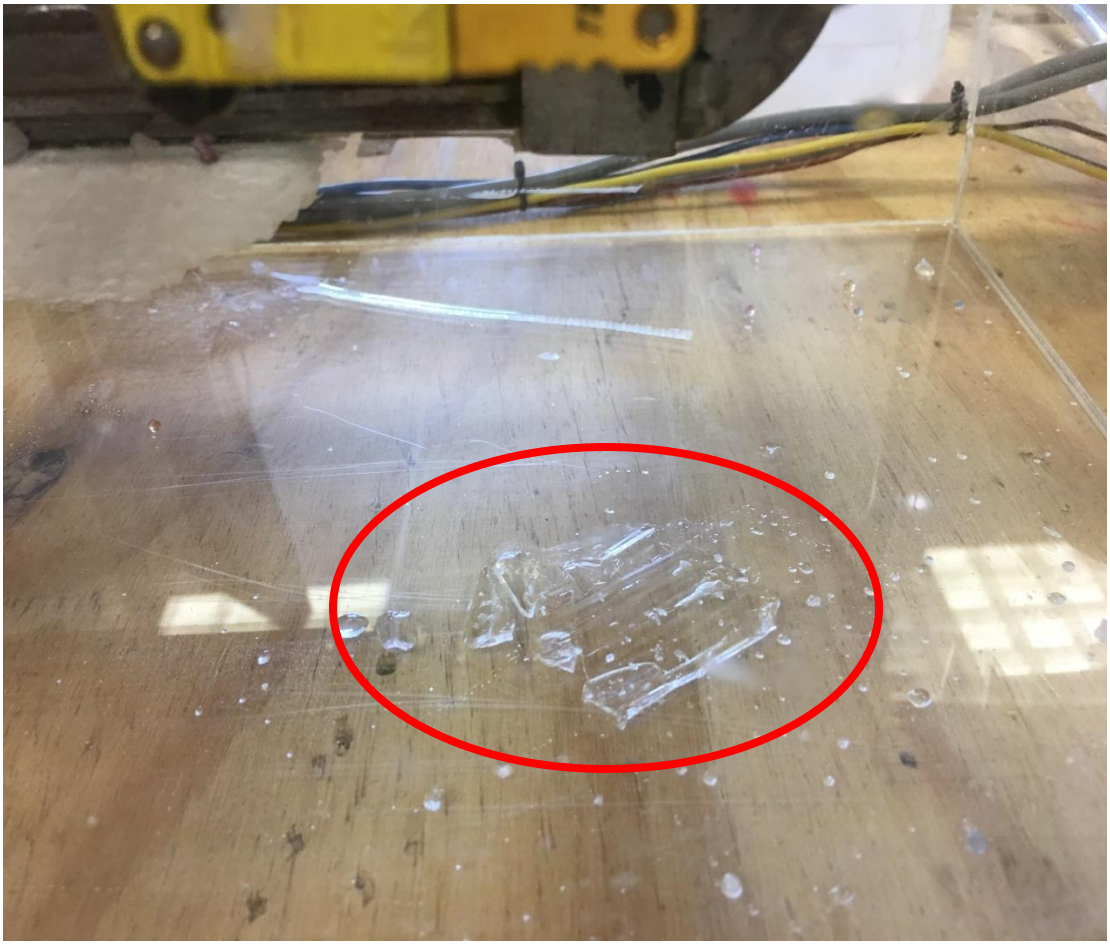

Figure 185: Image shows an additional leak, occurring on the opposite end of the heat exchanger. Notice the LNT crystal on the floor of the acrylic container.

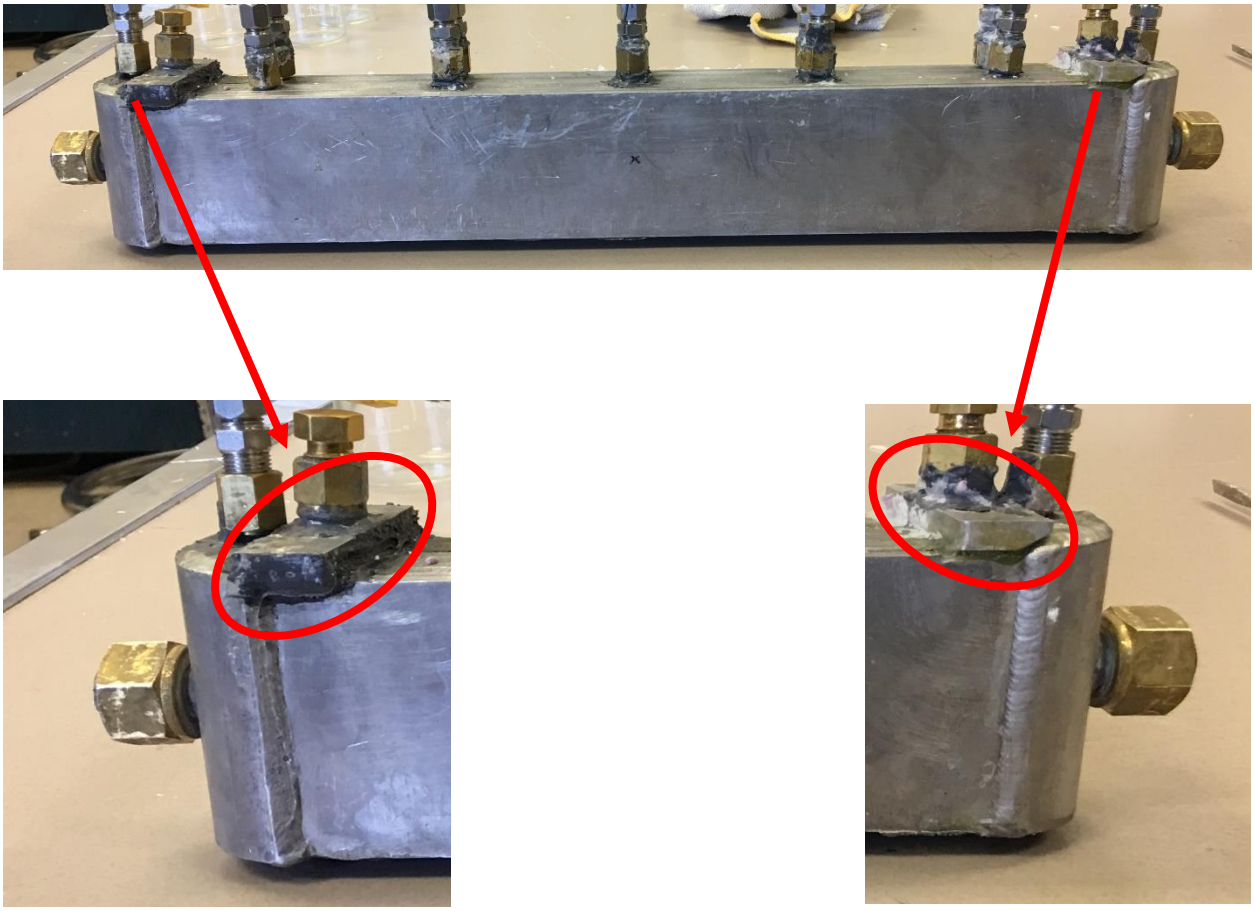

Figure 186: Image shows a likely source of the leaks. A dark gray epoxy (JB Weld) was applied in lab upon receiving the heat exchanger after accessing initial leaks. An unknown clear adhesive/epoxy, shown on the right, was used to seal the interface of a small rectangular plate located at the charging (filling) ports. Leaks were found directly below the inlet and outlet filling ports. Therefore, it is likely that the adhesive or epoxy failed to seal this interface which caused the leak.

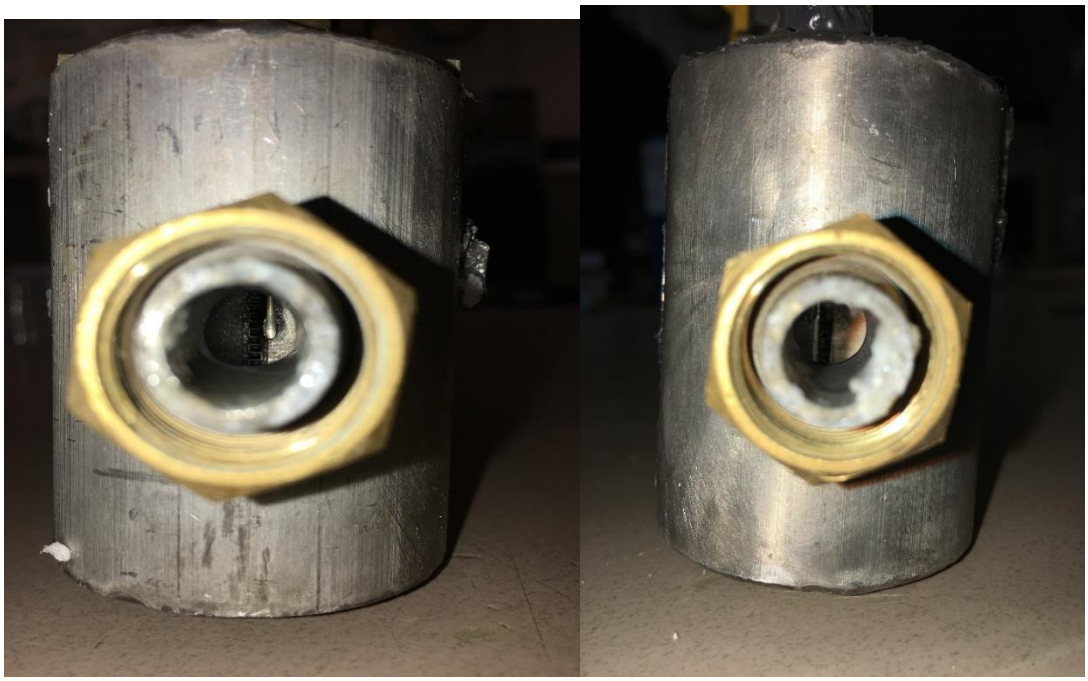

Figure 187: Image shows HTF inlet/outlet ports. Distilled water was used as HTF. A thin layer of fouling can be seen along the inside of the ports.

APPENDIX G

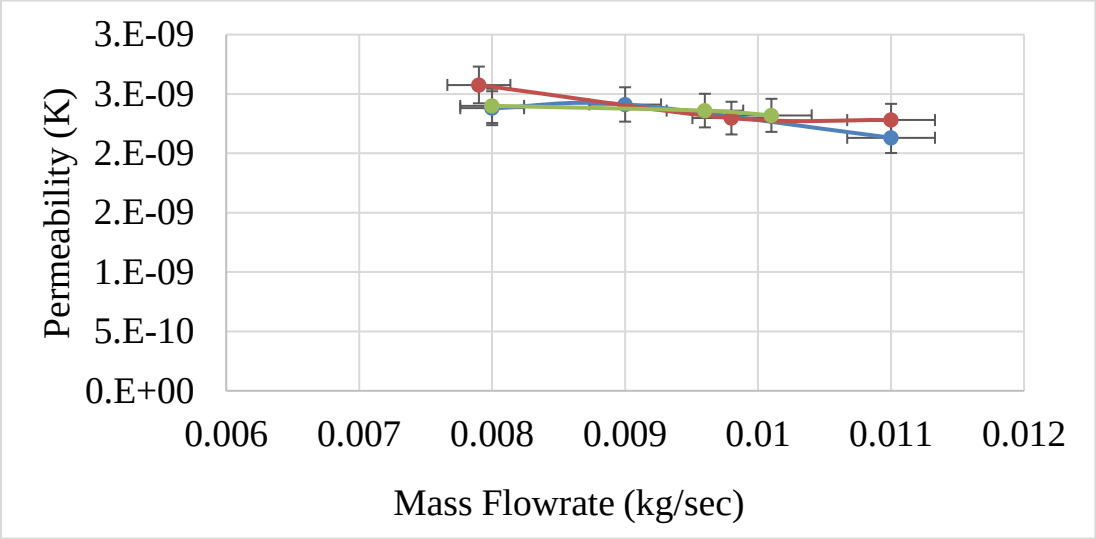

Figure 188: The Permeability testing of aluminum porous fin in water flow. The pressure difference was measured, and the permeability was calculated for varying flowrate.

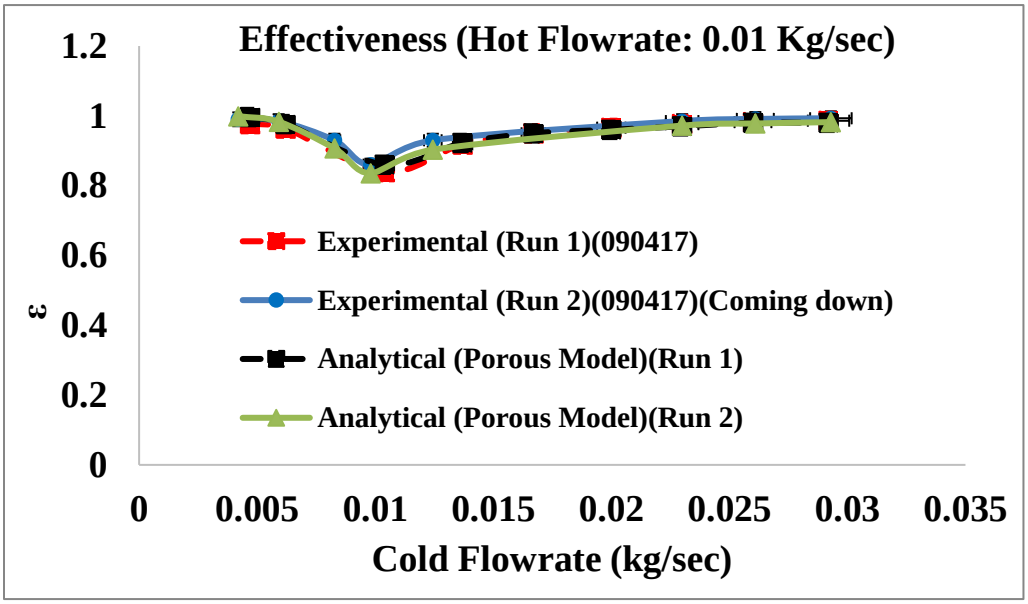

Figure 189: The effectiveness of compact heat exchanger with varying cold fluid side flowrate and compared to analytical solutions. The hot fluid side was maintained at 0.01 kg/sec.

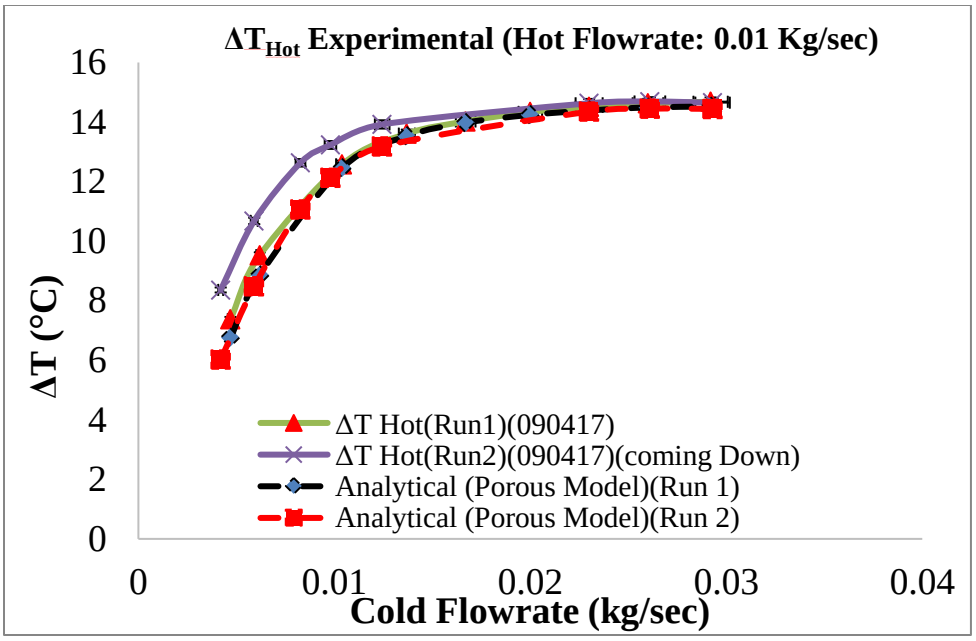

Figure 190: The ΔT_{Hot} of compact heat exchanger with varying fluid side flowrate and compared to analytical solutions.

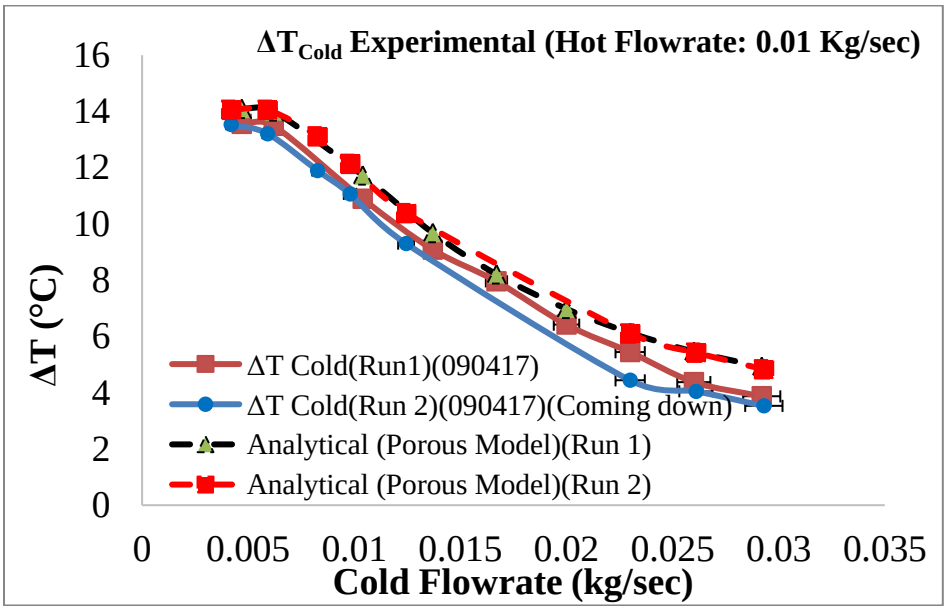

Figure 191: The ΔT_{Cold} of compact heat exchanger with varying fluid side flowrate and compared to analytical solutions.

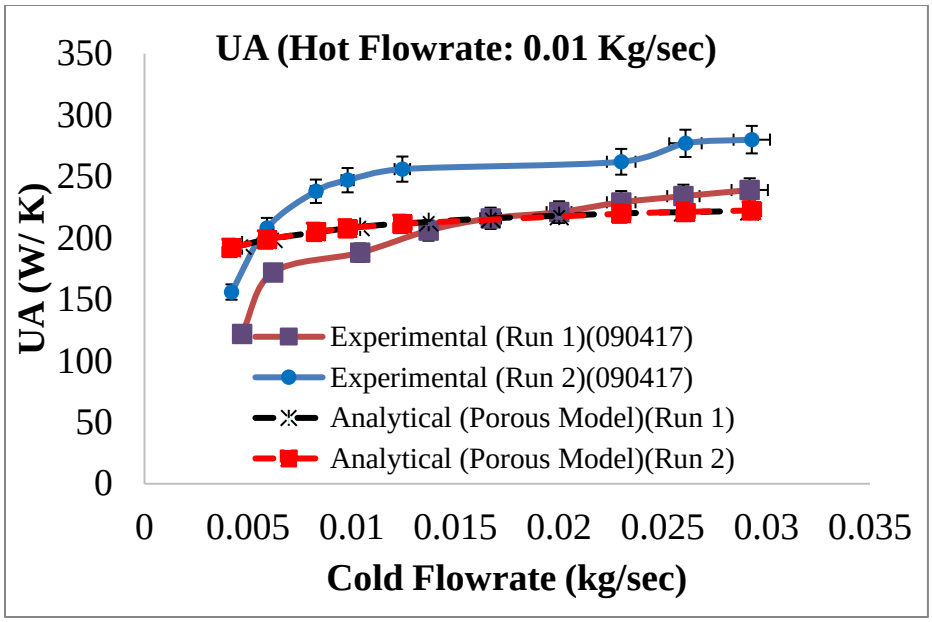

Figure 192: The UA of compact heat exchanger with varying fluid side flowrate and compared to analytical solutions.

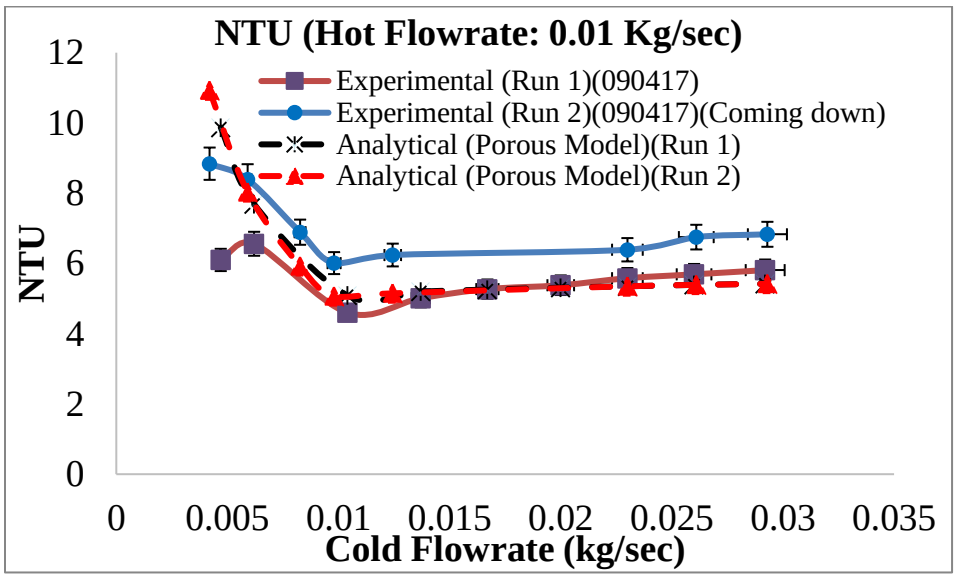

Figure 193: The NTU of compact heat exchanger with varying fluid side flowrate and compared to analytical solutions.

APPENDIX H

Table 55: Summary of experimental validation of compact heat exchanger with varying flow arrangement, flow rate, melting and solidification temperatures.

	nu.	Case	Flow Type	Flow Rate (GPH)	Melt Temperature (°C)	Solidification Temperature (°C)
Non - Insulated	1	Case A	Co - Current	3	35	25
	2	Case B	Co - Current	3	37.4	25
	3	Case C	Co - Current	5	35	25
	4	Case D	Co - Current	5	37.4	25
	5	Case E	Counter - Current	3	33	25
	6	Case F	Counter - Current	3	35	25
	7	Case G	Counter - Current	3	37.4	25
	8	Case H	Counter - Current	5	33	25
	9	Case I	Counter - Current	5	35	25
	10	Case J	Counter - Current	5	37.4	25
	11	Case K	Counter - Current	3	35	20
	12	Case L	Counter - Current	3	37.4	20
	13	Case M	Counter - Current	5	35	20
	14	Case N	Counter - Current	5	37.4	20
Insulated	15	Case O	Counter - Current	3	35	20
	16	Case P	Counter - Current	3	37.4	20
	17	Case Q	Counter - Current	3	35	25
	18	Case R	Counter - Current	3	37.4	25
	19	Case S	Counter - Current	5	35	20
	20	Case T	Counter - Current	5	37.4	20
	21	Case U	Counter - Current	5	35	25
	22	Case V	Counter - Current	5	37.4	25

Table 56: Summary of experimental measurements and calculations for 90%, 70 %, 50%, 30%, and 10% melts. At a flow rate of 3 GPH (configuration A), inlet temperature of HTF during melting is 35 °C and during solidification is 25 °C (Case A).

Melt Fraction	90 %		70 %		50 %		30 %		10%	
Case A	**Melting**	**Solidification**	**Melting**	**Solidification**	**Melting**	**Solidification**	**Melting**	**Solidification**	**Melting**	**Solidification**
Inlet Temperature (°C)	35	25	35	25	35	25	35	25	35	25
Average Mass Flowrate (kg/sec)	0.0036	0.0037	0.0036	0.0037	0.0036	0.0037	0.0036	0.0037	0.0037	0.0037
ΔT_{HTF}, Average (°C)	4.70 (± 10.4 %)	3.78 (± 13 %)	5.30 (± 9.3 %)	3.69 (± 13.3 %)	5.67 (± 8.6 %)	3.76 (± 13 %)	6.14 (± 8 %)	3.78 (± 13 %)	6.58 (± 7.5 %)	3.90 (± 12.6 %)
Total Energy Storage Capacity (kJ)	147.33 (± 4.5 %)	155.61 (± 4.5 %)	100.92 (± 4.5 %)	143.62 (± 4.5 %)	64.19 (± 4.5 %)	107.97 (± 4.5 %)	50.32 (± 4.6 %)	87.19 (± 4.6 %)	28.80 (± 4.6 %)	67.29 (± 4.6 %)
Duration of Phase Change (Seconds)	2107	2099	1390	2060	1003	1447	701	1074	467	747
Duration of Phase Change (Minutes)	35.11	34.98	23.17	34.33	16.72	24.12	11.68	17.90	7.78	12.44
Average Power (W)	71.35 (± 10.5 %)	57.52 (± 13 %)	80.49 (± 9.3 %)	56.19 (± 13.3 %)	86.15 (± 8.7 %)	57.26 (± 13.1 %)	93.34 (± 8 %)	57.64 (± 13 %)	100.04 (± 7.5 %)	59.40 (± 12.6 %)
Effectiveness	.8	1	.8	1	.8	1	.8	1	.8	1
Stefan Number	0.022	0.038	0.020	0.036	0.018	0.031	0.015	0.027	0.011	0.022

(± ε) is measurement uncertainty

Table 57: Summary of experimental measurements and calculations for 90%, 70 %, 50%, 30%, and 10% melts. At a flow rate of 3 GPH (configuration A), inlet temperature of HTF during melting is 35 °C and during solidification is 25 °C (Case B).

Melt Fraction	90 %		70 %		50 %		30 %		10%	
Case B	**Melting**	**Solidification**	**Melting**	**Solidification**	**Melting**	**Solidification**	**Melting**	**Solidification**	**Melting**	**Solidification**
Inlet Temperature (°C)	37.4	25	37.4	25	37.4	25	37.4	25	37.4	25
Average Mass Flowrate (kg/sec)	0.0036	0.0037	0.0036	0.0037	0.0036	0.0037	0.0036	0.0037	0.0036	0.0037
ΔT_{HTF}, Average (°C)	8.25 (± 5.9%)	3.14 (± 15.6 %)	8.75 (± 5.6 %)	3.69 (± 13.3 %)	9.30 (± 5.3 %)	3.34 (± 14.7 %)	9.70 (± 5.1 %)	3.30 (± 14.8 %)	10.22 (± 4.8 %)	3.27 (± 15 %)
Total Energy Storage Capacity (kJ)	154.19 (± 4.6 %)	166.74 (± 4.6 %)	112.89 (± 4.6 %)	133.83 (± 4.6 %)	80.09 (± 4.6 %)	101.30 (± 4.6 %)	60.89 (± 4.6 %)	76.99 (± 4.6 %)	28.20 (± 4.6 %)	45.82 (± 4.6 %)
Duration of Phase Change (Seconds)	1216	2678	918	1915	644	1550	446	1108	231	644
Duration of Phase Change (Minutes)	20.27	44.63	15.29	31.91	10.73	25.83	7.43	18.46	3.84	10.73
Average Power (W)	125.29 (± 6 %)	47.85 (± 15.7 %)	132.80 (± 5.6 %)	56.19 (± 13.3 %)	141.22 (± 5.3 %)	50.93 (± 14.7 %)	147.26 (± 5.1 %)	50.30 (± 14.9 %)	155.36 (± 4.8 %)	49.86 (± 15 %)
Effectiveness	.8	1	.8	1	.8	1	.8	1	.8	1
Stefan Number	.028	.047	.022	.041	.024	.033	.020	.028	.016	.020

(± ε) is measurement uncertainty

Table 58: Summary of experimental measurements and thermal efficiency calculations for varying melt fraction. At a flow rate of 3 GPH (configuration A), inlet temperature of HTF during melting is 35 °C and during solidification is 25 °C (Case C).

Melt Fraction	90 %		70 %		50 %		30 %		10%	
Case C	Melting	Solidification	Melting	Solidification	Melting	Solidification	Melting	Solidification	Melting	Solidification
Inlet Temperature (°C)	35	25	35	25	35	25	35	25	35	25
Average Mass Flowrate (kg/sec)	0.0052	0.0052	0.0052	0.0052	0.0052	0.0052	0.0052	0.0052	0.0052	0.0052
ΔT_{HTF}, Average (°C)	4.98 (± 9.9 %)	3.42 (± 14.3 %)	5.55 (± 8.8 %)	3.71 (± 13.2 %)	5.85 (± 8.4 %)	3.80 (± 12.9 %)	6.07 (± 8.1 %)	3.99 (± 12.3 %)	6.64 (± 7.4 %)	4.18 (± 11.7 %)
Total Energy Storage Capacity (kJ)	150.99 (± 4.5 %)	184.85 (± 4.5 %)	118.28 (± 4.5 %)	161.80 (± 4.5 %)	89.39 (± 4.5 %)	133.90 (± 4.5 %)	69.13 (± 4.6 %)	112.95 (± 4.6 %)	35.27 (± 4.6 %)	82.40 (± 4.6 %)
Duration of Phase Change (Seconds)	1449	1922	1083	1632	861	1263	703	1024	426	686
Duration of Phase Change (Minutes)	24.15	32.03	18.04	27.19	14.34	21.04	11.72	17.07	7.09	11.43
Average Power (W)	108.56 (± 6.9 %)	74.78 (± 10 %)	121.03 (± 6.2 %)	81.15 (± 9.2 %)	127.57 (± 5.9 %)	83.07 (± 9 %)	132.43 (± 5.7 %)	87.30 (± 8.6 %)	144.91 (± 5.2 %)	91.55 (± 8.2 %)
Effectiveness	.8	1	.8	1	.8	1	.8	1	.8	1
Stefan Number	0.022	0.042	0.021	0.038	0.018	0.034	0.016	0.030	0.014	0.023

(± ε) is measurement uncertainty

Table 59: Summary of experimental measurements and thermal efficiency calculations for varying melt fraction. At a flow rate of 3 GPH (configuration A), inlet temperature of HTF during melting is 35 °C and during solidification is 25 °C (Case D).

Melt Fraction	90 %		70 %		50 %		30 %		10%	
Case D	Melting	Solidification	Melting	Solidification	Melting	Solidification	Melting	Solidification	Melting	Solidification
Inlet Temperature (°C)	37.4	25	37.4	25	37.4	25	37.4	25	37.4	25
Average Mass Flowrate (kg/sec)	0.0052	0.0052	0.0052	0.0052	0.0052	0.0052	0.0052	0.0052	0.0052	0.0052
ΔT_{HTF}, Average (°C)	7.16 (± 6.8 %)	3.48 (± 14.1 %)	7.81 (± 6.3 %)	3.30 (± 14.8 %)	8.01 (± 6.1 %)	3.90 (± 12.6 %)	8.47 (± 5.8 %)	3.71 (± 13.2 %)	8.88 (± 5.5 %)	3.99 (± 12.3 %)
Total Energy Storage Capacity (kJ)	160.86 (± 4.5 %)	186.67 (± 4.5 %)	125.27 (± 4.5 %)	160.00 (± 4.5 %)	87.31 (± 4.5 %)	131.01 (± 4.5 %)	71.91 (± 4.6 %)	110.23 (± 4.6 %)	39.75 (± 4.6 %)	76.87 (± 4.6 %)
Duration of Phase Change (Seconds)	1074	1826	807	1820	623	1209	467	1058	277	692
Duration of Phase Change (Minutes)	17.89	30.43	13.44	30.33	10.38	20.14	7.78	17.63	4.62	11.53
Average Power (kW)	156.19 (± 4.8 %)	76.09 (± 9.8 %)	170.38 (± 4.4 %)	72.31 (± 10.4 %)	174.63 (± 4.3 %)	85.25 (± 8.8 %)	184.81 (± 4.1 %)	81.26 (± 9.2 %)	193.90 (± 3.9 %)	87.28 (± 8.6 %)
Effectiveness	.8	1	.8	1	.8	1	.8	1	.8	1
Stefan Number	0.028	0.048	0.026	0.044	0.022	0.036	0.020	0.032	0.015	0.022

(± ε) is measurement uncertainty

Table 60: Summary of experimental measurements and thermal efficiency calculations for varying melt fraction . At a flow rate of 3 GPH (Configuration B), inlet temperature of HTF during melting is 33 °C and during solidification is 25 °C (Case E).

Melt Fraction	90 %		70 %		50 %	
Case E	Melting	Solidification	Melting	Solidification	Melting	Solidification
Inlet Temperature (°C)	33	25	33	25	33	25
Average Mass Flowrate (kg/sec)	0.0036	0.0036	0.0036	0.0036	0.0036	0.0036
ΔT_{HTF}, Average (°C)	3.98 (± 12.3 %)	3.38 (± 14.5 %)	4.38 (± 11.2 %)	3.45 (± 14.2 %)	4.65 (± 10.5 %)	3.47 (± 14.1 %)
Total Energy Storage Capacity (kJ)	173.57 (± 4.7 %)	189.52 (± 4.7 %)	142.99 (± 4.7 %)	162.47 (± 4.7 %)	131.79 (± 4.8 %)	139.09 (± 4.8 %)
Duration of Phase Change (Seconds)	2802	3412	1971	2987	1721	2490
Duration of Phase Change (Minutes)	46.69	56.86	32.84	49.78	28.68	41.51
Average Power (W)	60.52 (± 12.4 %)	50.96 (± 14.7 %)	66.64 (± 11.2 %)	51.60 (± 14.5 %)	70.62 (± 10.6 %)	51.75 (± 14.5 %)
Effectiveness	.8	1	.8	1	.8	1
Stefan Number	0.016	0.031	0.013	0.024	0.009	0.018

(± ε) is measurement uncertainty

Table 61: Summary of experimental measurements and thermal efficiency calculations for varying melt fraction. At a flow rate of 3 GPH (Configuration B), inlet temperature of HTF during melting is 35 °C and during solidification is 25 °C (Case F).

Melt Fraction	90 %		70 %		50 %		30 %		10%	
Case F	**Melting**	**Solidification**	**Melting**	**Solidification**	**Melting**	**Solidification**	**Melting**	**Solidification**	**Melting**	**Solidification**
Inlet Temperature (°C)	35	25	35	25	35	25	35	25	35	25
Average Mass Flowrate (kg/sec)	0.0036	0.0037	0.0036	0.0037	0.0036	0.0037	0.0036	0.0037	0.0037	0.0037
ΔT_{HTF}, Average (°C)	5.17 (± 9.5 %)	2.69 (± 18.9 %)	5.66 (± 8.7 %)	2.79 (± 18.3 %)	5.96 (± 8.3 %)	2.86 (± 17.8 %)	6.20 (± 7.9 %)	2.87 (± 17.8 %)	6.81 (± 7.2 %)	3.31 (± 15.1 %)
Total Energy Storage Capacity (kJ)	152.63 (± 4.7 %)	166.33 (± 4.7 %)	135.01 (± 4.7 %)	138.14 (± 4.7 %)	120.16 (± 4.8 %)	118.99 (± 4.8 %)	99.51 (± 4.8 %)	96.95 (± 4.8 %)	63.27 (± 4.8 %)	61.90 (± 4.8 %)
Duration of Phase Change (Seconds)	1861	3590	1405	3210	1085	2636	820	2069	458	1041
Duration of Phase Change (Minutes)	31.01	59.83	23.41	53.51	18.08	43.93	13.67	34.49	7.63	17.36
Average Power (W)	78.56 (± 9.6 %)	41.05 (± 18.9 %)	86.02 (± 8.8 %)	42.55 (± 18.3 %)	90.57 (± 8.3 %)	43.71 (± 17.7 %)	94.24 (± 8 %)	44.06 (± 17.7 %)	103.62 (± 7.3 %)	50.91 (± 15 %)
Effectiveness	.8	1	.8	1	.8	1	.8	1	.8	1
Stefan Number	0.019	0.035	0.015	0.030	0.014	0.028	0.012	0.025	0.008	0.021

(± ε) is measurement uncertainty

Table 62: Summary of experimental measurements and thermal efficiency calculations for varying melt fraction. At a flow rate of 3 GPH (Configuration B), inlet temperature of HTF during melting is 37.4 °C and during solidification is 25 °C (Case G).

Melt Fraction	90 %		70 %		50 %		30 %		10%	
Case G	Melting	Solidification	Melting	Solidification	Melting	Solidification	Melting	Solidification	Melting	Solidification
Inlet Temperature (°C)	37.4	25	37.4	25	37.4	25	37.4	25	37.4	25
Average Mass Flowrate (kg/sec)	0.0036	0.0037	0.0036	0.0037	0.0036	0.0037	0.0036	0.0037	0.0036	0.0037
ΔT_{HTF}, Average (°C)	7.22 (± 6.8 %)	2.75 (± 18.3 %)	7.82 (± 6.3 %)	2.98 (± 16.9 %)	8.21 (± 6 %)	3.02 (± 16.6 %)	8.49 (± 5.8 %)	3.08 (± 16.2 %)	8.86 (± 5.5 %)	3.32 (± 15.2 %)
Total Energy Storage Capacity (kJ)	156.56 (± 4.7 %)	162.13 (± 4.7 %)	140.61 (± 4.8 %)	146.64 (± 4.8 %)	121.21 (± 4.8 %)	120.57 (± 4.8 %)	96.16 (± 4.8 %)	96.58 (± 4.8 %)	62.25 (± 4.8 %)	60.62 (± 4.8 %)
Duration of Phase Change (Seconds)	1385	3278	1039	3111	802	2484	585	1881	327	983
Duration of Phase Change (Minutes)	23.09	54.63	17.31	51.84	13.37	41.40	9.75	31.36	5.45	16.38
Average Power (W)	109.62 (± 6.9 %)	42.30 (± 18.2 %)	118.78 (± 6.3 %)	45.75 (± 16.8 %)	124.73 (± 6 %)	46.40 (± 16.6 %)	128.91 (± 5.8 %)	47.66 (± 16 %)	134.72 (± 5.6 %)	50.75 (± 15.2 %)
Effectiveness	.8	1	.8	1	.8	1	.8	1	.8	1
Stefan Number	0.023	0.040	0.020	0.035	0.015	0.031	0.012	0.023	0.010	0.022

(± ε) is measurement uncertainty

Table 63: Summary of experimental measurements and thermal efficiency calculations for varying melt fraction. At a flow rate of 3 GPH (Configuration B), inlet temperature of HTF during melting is 33 °C and during solidification is 25 °C (Case H).

Melt Fraction	90 %		70 %		50 %	
Case H	Melting	Solidification	Melting	Solidification	Melting	Solidification
Inlet Temperature (°C)	33	25	33	25	33	25
Average Mass Flowrate (kg/sec)	0.0052	0.0053	0.0052	0.0053	0.0052	0.0053
ΔT_{HTF}, Average (°C)	4.06 (± 12.1 %)	3.25 (± 15.1 %)	4.36 (± 11.2 %)	3.21 (± 15.3 %)	4.73 (± 10.4 %)	3.28 (± 14.9 %)
Total Energy Storage Capacity (kJ)	185.48 (± 4.7 %)	196.88 (± 4.7 %)	160.26 (± 4.8 %)	181.64 (± 4.8 %)	140.30 (± 4.8 %)	152.54 (± 4.8 %)
Duration of Phase Change (Seconds)	2077	2627	1595	2470	1136	1986
Duration of Phase Change (Minutes)	34.62	43.78	26.58	41.16	18.94	33.10
Average Power (W)	88.57 (± 8.5 %)	71.44 (± 10.5 %)	95.27 (± 7.9 %)	70.51 (± 10.6 %)	103.31 (± 7.2 %)	72.57 (± 10.3 %)
Effectiveness	.8	1	.8	1	.8	1
Stefan Number	0.011	0.030	0.013	0.029	0.012	0.028

(± ε) is measurement uncertainty

Table 64: Summary of experimental measurements and thermal efficiency calculations for varying melt fraction. At a flow rate of 3 GPH (Configuration B), inlet temperature of HTF during melting is 35 °C and during solidification is 25 °C (Case I).

Melt Fraction	90 %		70 %		50 %		30 %		10%	
Case I	**Melting**	**Solidification**	**Melting**	**Solidification**	**Melting**	**Solidification**	**Melting**	**Solidification**	**Melting**	**Solidification**
Inlet Temperature (°C)	35	25	35	25	35	25	35	25	35	25
Average Mass Flowrate (kg/sec)	0.0052	0.0053	0.0052	0.0053	0.0052	0.0053	0.0052	0.0053	0.0052	0.0053
ΔT_{HTF}, Average (°C)	5.40 (± 9.1 %)	2.50 (± 20 %)	5.87 (± 8.4 %)	2.72 (± 18.4 %)	6.18 (± 8 %)	2.69 (± 18.6 %)	6.46 (± 7.6 %)	2.85 (± 17.6 %)	6.91 (± 7.1 %)	3.25 (± 15.3 %)
Total Energy Storage Capacity (kJ)	168.56 (± 4.7 %)	160.63 (± 4.7 %)	152.00 (± 4.7 %)	143.10 (± 4.7 %)	137.94 (± 4.8 %)	124.32 (± 4.8 %)	119.14 (± 4.8 %)	105.67 (± 4.8 %)	78.37 (± 4.8 %)	70.23 (± 4.8 %)
Duration of Phase Change (Seconds)	1391	2550	1100	2371	853	2075	665	1639	394	863
Duration of Phase Change (Minutes)	23.18	42.51	18.33	39.51	14.22	34.58	11.08	27.32	6.56	14.38
Average Power (W)	117.74 (± 6.4 %)	54.99 (± 13.9 %)	128.09 (± 5.9 %)	59.79 (± 12.8 %)	134.92 (± 5.6 %)	59.37 (± 12.9 %)	140.98 (± 5.3 %)	62.44 (± 12.2 %)	150.81 (± 5 %)	71.34 (± 10.7 %)
Effectiveness	.8	1	.8	1	.8	1	.8	1	.8	1
Stefan Number	0.020	0.035	0.018	0.033	0.016	0.031	0.015	0.029	0.012	0.024

(± ε) is measurement uncertainty

Table 65: Summary of experimental measurements and thermal efficiency calculations for varying melt fraction. At a flow rate of 3 GPH (Configuration B), inlet temperature of HTF during melting is 37.4 °C and during solidification is 25 °C (Case J).

Melt Fraction	90 %		70 %		50 %		30 %		10%	
Case J	Melting	Solidification	Melting	Solidification	Melting	Solidification	Melting	Solidification	Melting	Solidification
Inlet Temperature (°C)	37.4	25	37.4	25	37.4	25	37.4	25	37.4	25
Average Mass Flowrate (kg/sec)	0.0052	0.0053	0.0052	0.0053	0.0052	0.0053	0.0052	0.0053	0.0052	0.0053
ΔT_{HTF}, Average (°C)	7.36 (± 6.7 %)	2.46 (± 20.6 %)	8.16 (± 6 %)	2.81 (± 17.9 %)	8.12 (± 6 %)	2.45 (± 20 %)	8.71 (± 5.6 %)	2.89 (± 17.4 %)	8.90 (± 5.5 %)	2.91 (± 16.8 %)
Total Energy Storage Capacity (kJ)	177.18 (± 4.7 %)	174.59 (± 4.7 %)	160.52 (± 4.8 %)	152.50 (± 4.8 %)	137.95 (± 4.8 %)	110.71 (± 4.8 %)	122.80 (± 4.8 %)	106.00 (± 4.8 %)	83.17 (± 4.8 %)	64.17 (± 4.8 %)
Duration of Phase Change (Seconds)	1058	2700	785	2422	645	2057	502	1634	323	909
Duration of Phase Change (Minutes)	17.63	45.01	13.09	40.37	10.75	34.28	8.37	27.23	5.38	15.14
Average Power (W)	160.60 (± 4.7 %)	53.97 (± 14.4 %)	177.92 (± 4.2 %)	61.65 (± 12.5 %)	177.06 (± 4.2 %)	53.60 (± 14 %)	190.10 (± 4 %)	63.20 (± 12.2 %)	193.86 (± 3.9 %)	63.72 (± 11.8 %)
Effectiveness	.8	1	.8	1	.8	1	.8	1	.8	1
Stefan Number	0.028	0.043	0.024	0.039	0.023	0.036	0.018	0.032	0.015	0.024

(± ε) is measurement uncertainty

Table 66: Summary of experimental measurements and thermal efficiency calculations for varying melt fraction. At a flow rate of 3 GPH (Configuration B), inlet temperature of HTF during melting is 35 °C and during solidification is 20 °C (Case K).

Melt Fraction	90 %		70 %		50 %	
Case K	Melting	Solidification	Melting	Solidification	Melting	Solidification
Inlet Temperature (°C)	35	20	35	20	35	20
Average Mass Flowrate (kg/sec)	0.0036	0.0036	0.0036	0.0036	0.0037	0.0036
ΔT_{HTF}, Average (°C)	5.89 (± 8.3 %)	7.09 (± 6.9 %)	6.45 (± 7.2 %)	7.23 (± 6.8 %)	7.04 (± 7 %)	7.23 (± 6.8 %)
Total Energy Storage Capacity (kJ)	179.46 (± 5.1 %)	208.21 (± 5.1 %)	175.39 (± 5.1 %)	183.50 (± 5.1 %)	155.79 (± 5.2 %)	158.00 (± 5.2 %)
Duration of Phase Change (Seconds)	1881	1736	1487	1711	1093	1345
Duration of Phase Change (Minutes)	31.34	28.93	24.78	28.52	18.21	22.41
Average Power (W)	89.57 (± 8.4 %)	105.55 (± 7.1 %)	97.98 (± 7.6 %)	108.22 (± 6.9 %)	107.15 (± 7 %)	108.00 (± 6.9 %)
Effectiveness	.8	1	.8	1	.8	1
Stefan Number	0.034	0.055	0.034	0.052	0.031	0.053

(± ε) is measurement uncertainty

Table 67: Summary of experimental measurements and thermal efficiency calculations for varying melt fraction. At a flow rate of 3 GPH (Configuration B), inlet temperature of HTF during melting is 37.4 °C and during solidification is 20 °C (Case L).

Melt Fraction	90 %		70 %		50 %	
Case L	Melting	Solidification	Melting	Solidification	Melting	Solidification
Inlet Temperature (°C)	37.4	20	37.4	20	37.4	20
Average Mass Flowrate (kg/sec)	0.0036	0.0036	0.0036	0.0036	0.0036	0.0036
ΔT_{HTF}, Average (°C)	8.36 (± 5.9 %)	7.69 (± 6.4 %)	8.99 (± 5.4 %)	7.55 (± 6.5 %)	9.47 (± 5.2 %)	7.37 (± 6.7 %)
Total Energy Storage Capacity (kJ)	176.37 (± 5.2 %)	223.00 (± 5.2 %)	171.95 (± 5.2 %)	199.82 (± 5.2 %)	152.66 (± 5.3 %)	161.79 (± 5.3 %)
Duration of Phase Change (Seconds)	1301	1793	1058	1647	786	1360
Duration of Phase Change (Minutes)	21.68	29.88	17.63	27.45	13.09	22.66
Average Power (W)	127.04 (± 5.9 %)	115.64 (± 6.5 %)	136.52 (± 5.5 %)	113.69 (± 6.6 %)	143.68 (± 5.2 %)	110.10 (± 6.8 %)
Effectiveness	.8	1	.8	1	.8	1
Stefan Number	0.042	0.062	0.039	0.057	0.035	0.055

(± ε) is measurement uncertainty

Table 68: Summary of experimental measurements and thermal efficiency calculations for varying melt fraction. At a flow rate of 3 GPH (Configuration B), inlet temperature of HTF during melting is 35 °C and during solidification is 20 °C (Case M).

Melt Fraction	90 %		70 %		50 %	
Case M	Melting	Solidification	Melting	Solidification	Melting	Solidification
Inlet Temperature (°C)	35	20	35	20	35	20
Average Mass Flowrate (kg/sec)	0.0052	0.0052	0.0052	0.0053	0.0052	0.0053
ΔT_{HTF}, Average (°C)	6.07 (± 8.1 %)	7.07 (± 6.9 %)	6.54 (± 7.5 %)	7.23 (± 6.8 %)	7.09 (± 6.9 %)	7.17 (± 6.8 %)
Total Energy Storage Capacity (kJ)	213.40 (± 5.1 %)	212.85 (± 5.1 %)	191.37 (± 5.1 %)	195.74 (± 5.1 %)	176.53 (± 5.2 %)	174.08 (± 5.2 %)
Duration of Phase Change (Seconds)	1497	1218	1151	1129	851	973
Duration of Phase Change (Minutes)	24.95	20.29	19.18	18.81	14.18	16.21
Average Power (W)	132.45 (± 5.7 %)	154.24 (± 4.9 %)	142.67 (± 5.3 %)	159.28 (± 4.7 %)	154.64 (± 4.8 %)	158.65 (± 4.7 %)
Effectiveness	.8	1	.8	1	.8	1
Stefan Number	0.037	0.058	0.036	0.055	0.034	0.054

(± ε) is measurement uncertainty

Table 69: Summary of experimental measurements and thermal efficiency calculations for varying melt fraction. At a flow rate of 3 GPH (Configuration B), inlet temperature of HTF during melting is 37.4 °C and during solidification is 20 °C (Case N).

Melt Fraction	90 %		70 %		50 %	
Case N	Melting	Solidification	Melting	Solidification	Melting	Solidification
Inlet Temperature (°C)	37.4	20	37.4	20	37.4	20
Average Mass Flowrate (kg/sec)	0.0052	0.0053	0.0052	0.0052	0.0052	0.0053
ΔT_{HTF}, Average (°C)	8.55 (± 5.7 %)	7.44 (± 6.6 %)	9.03 (± 5.4 %)	7.33 (± 6.7 %)	9.35 (± 5.2 %)	7.48 (± 6.5 %)
Total Energy Storage Capacity (kJ)	203.51 (± 5.2 %)	220.81 (± 5.2 %)	199.94 (± 5.3 %)	202.65 (± 5.3 %)	176.40 (± 5.3 %)	167.72 (± 5.3 %)
Duration of Phase Change (Seconds)	1010	1268	864	1128	641	934
Duration of Phase Change (Minutes)	16.83	21.13	14.39	18.79	10.68	15.56
Average Power (W)	186.46 (± 4 %)	163.55 (± 4.6%)	196.91 (± 3.8 %)	160.63 (± 4.7 %)	203.96 (± 3.7 %)	164.87 (± 4.5 %)
Effectiveness	.8	1	.8	1	.8	1
Stefan Number	0.044	0.065	0.044	0.061	0.038	0.057

(± ε) is measurement uncertainty

Table 70: Summary of experimental measurements and thermal efficiency calculations for 90% melt fraction. At a flow rate of 3 GPH (Configuration B), inlet temperature of HTF during melting is 35 °C and during solidification is 20 °C (Case O).

Melt Fraction	90 %	
Case O	Melting	Solidification
Inlet Temperature (°C)	35	20
Average Mass Flowrate (kg/sec)	0.0036	0.0037
ΔT_{HTF}, Average (°C)	5.95	7.18
Total Energy Storage Capacity (kJ)	175.19	184.78
Duration of Phase Change (Seconds)	1817	1356
Duration of Phase Change (Minutes)	30.28	22.60
Average Power (W)	90.39	111.37
Effectiveness	.8	1
Stefan Number	0.035	0.058

Table 71: Summary of experimental measurements and thermal efficiency calculations for 90% melt fraction. At a flow rate of 3 GPH (Configuration B), inlet temperature of HTF during melting is 37.4 °C and during solidification is 20 °C (Case P).

Melt Fraction	90 %	
Case P	Melting	Solidification
Inlet Temperature (°C)	37.4	20
Average Mass Flowrate (kg/sec)	0.0036	0.0036
ΔT_{HTF}, Average (°C)	8.55	7.62
Total Energy Storage Capacity (kJ)	169.80	221.20
Duration of Phase Change (Seconds)	1158	1722
Duration of Phase Change (Minutes)	19.29	28.70
Average Power (W)	129.82	115.72
Effectiveness	.8	1
Stefan Number	0.044	0.065

Table 72: Summary of experimental measurements and thermal efficiency calculations for 90% melt fraction. At a flow rate of 3 GPH (Configuration B), inlet temperature of HTF during melting is 35 °C and during solidification is 25 °C (Case Q).

Melt Fraction	90 %	
Case Q	Melting	Solidification
Inlet Temperature (°C)	35	25
Average Mass Flowrate (kg/sec)	0.0036	0.0037
ΔT_{HTF}, Average (°C)	5.81	3.34
Total Energy Storage Capacity (kJ)	152.66	187.90
Duration of Phase Change (Seconds)	1681	3327
Duration of Phase Change (Minutes)	28.02	55.46
Average Power (W)	88.31	51.30
Effectiveness	.8	1
Stefan Number	0.018	0.037

Table 73: Summary of experimental measurements and thermal efficiency calculations for 90% melt fraction. At a flow rate of 3 GPH (Configuration B), inlet temperature of HTF during melting is 37.4 °C and during solidification is 25 °C (Case R).

Melt Fraction	90 %	
Case R	Melting	Solidification
Inlet Temperature (°C)	37.4	25
Average Mass Flowrate (kg/sec)	0.0036	0.0037
ΔT_{HTF}, Average (°C)	7.76	3.44
Total Energy Storage Capacity (kJ)	152.79	195.23
Duration of Phase Change (Seconds)	1245	3372
Duration of Phase Change (Minutes)	20.74	56.21
Average Power (W)	117.83	53.52
Effectiveness	.8	1
Stefan Number	0.024	0.042

Table 74: Summary of experimental measurements and thermal efficiency calculations for 90% melt fraction. At a flow rate of 3 GPH (Configuration B), inlet temperature of HTF during melting is 35 °C and during solidification is 20 °C (Case S).

Melt Fraction	90 %	
Case S	Melting	Solidification
Inlet Temperature (°C)	35	20
Average Mass Flowrate (kg/sec)	0.0052	0.0053
ΔT_{HTF}, Average (°C)	6.30	7.06
Total Energy Storage Capacity (kJ)	196.64	209.53
Duration of Phase Change (Seconds)	1316	1110
Duration of Phase Change (Minutes)	21.93	18.51
Average Power (W)	137.53	156.39
Effectiveness	.8	1
Stefan Number	0.038	0.060

Table 75: Summary of experimental measurements and thermal efficiency calculations for 90% melt fraction. At a flow rate of 3 GPH (Configuration B), inlet temperature of HTF during melting is 37.4 °C and during solidification is 20 °C (Case T).

Melt Fraction	90 %	
Case T	Melting	Solidification
Inlet Temperature (°C)	37.4	20
Average Mass Flowrate (kg/sec)	0.0052	0.0053
ΔT_{HTF}, Average (°C)	8.68	7.46
Total Energy Storage Capacity (kJ)	189.42	217.73
Duration of Phase Change (Seconds)	910	1251
Duration of Phase Change (Minutes)	15.17	20.86
Average Power (W)	189.26	164.17
Effectiveness	.8	1
Stefan Number	0.045	0.068

Table 76: Summary of experimental measurements and thermal efficiency calculations for 90% melt fraction. At a flow rate of 3 GPH (Configuration B), inlet temperature of HTF during melting is 35 °C and during solidification is 25 °C (Case U).

Melt Fraction	90 %	
Case U	Melting	Solidification
Inlet Temperature (°C)	35	25
Average Mass Flowrate (kg/sec)	0.0052	0.0053
ΔT_{HTF}, Average (°C)	6.04	3.08
Total Energy Storage Capacity (kJ)	179.63	191.63
Duration of Phase Change (Seconds)	1275	2590
Duration of Phase Change (Minutes)	21.25	43.16
Average Power (W)	131.77	68.12
Effectiveness	.8	1
Stefan Number	0.020	0.040

Table 77: Summary of experimental measurements and thermal efficiency calculations for 90% melt fraction. At a flow rate of 3 GPH (Configuration B), inlet temperature of HTF during melting is 37.4 °C and during solidification is 25 °C (Case V).

Melt Fraction	90 %	
Case V	Melting	Solidification
Inlet Temperature (°C)	37.4	25
Average Mass Flowrate (kg/sec)	0.0052	0.0053
ΔT_{HTF}, Average (°C)	8.13	3.10
Total Energy Storage Capacity (kJ)	177.18	205.73
Duration of Phase Change (Seconds)	951	2540
Duration of Phase Change (Minutes)	15.85	42.34
Average Power (W)	177.22	68.71
Effectiveness	.8	1
Stefan Number	0.028	0.045

APPENDIX I

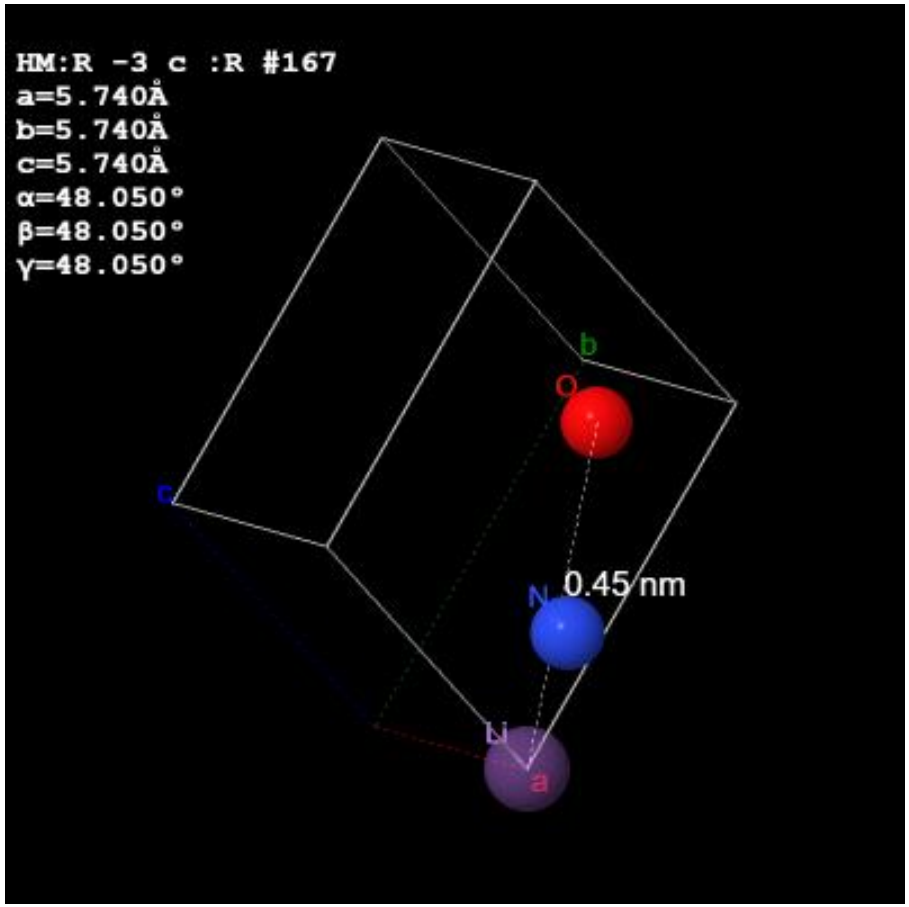

Figure 194: Crystallographic Information File (CIF) of Lithium Nitrate *($LiNO_3$)*. The images portray the crystal structure layout and the corresponding lattice mis-match.

Table 78: The Crystallographic information of Lithium Nitrate *($LiNO_3$)*. The table summarizes the lattice mismatch and Space Group.

Chemical Name	Lithium Nitrate
Formula	Li N O3
a	5.74 ± 0.02 Å
b	5.74 ± 0.02 Å
c	5.74 ± 0.02 Å
α	48.05 ± 0.17°
β	48.05 ± 0.17°
γ	48.05 ± 0.17°
Cell Volume	95.8 $Å^3$
Number of Distinct Elements	3
Hermann - Gauguin Symmetry Space Group	R -3 c : R
Hall symmetry Space Group	-P 3* 2n

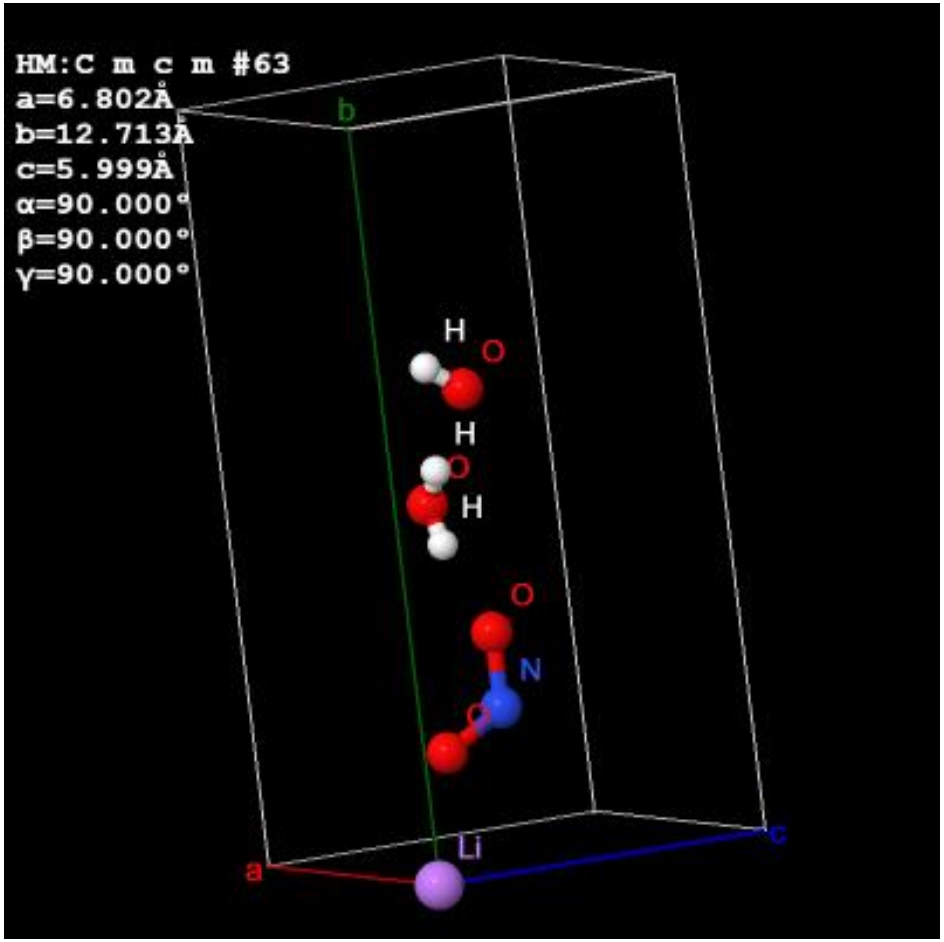

Figure 195: Crystallographic Information File (CIF) of Pure Lithium Nitrate Trihydrate *(LiNO3. 3H2O)*. The images portray the crystal structure layout and the corresponding lattice mis-match.

Table 79: The Crystallographic information of Lithium Nitrate Trihydrate ($LiNO_3$. 3H2O). The table summarizes the lattice mismatch and Space Group

Chemical Name	Lithium Nitrate Trihydrate
Formula	H6 Li N O6
a	6.8018 Å
b	12.7132 Å
c	5.999 Å
α	90°
β	90°
γ	90°
Cell Volume	518.749 $Å^3$
Number of Distinct Elements	4
Hermann - Mauguin Symmetry Space Group	C m c m
Hall symmetry Space Group	-C 2c 2

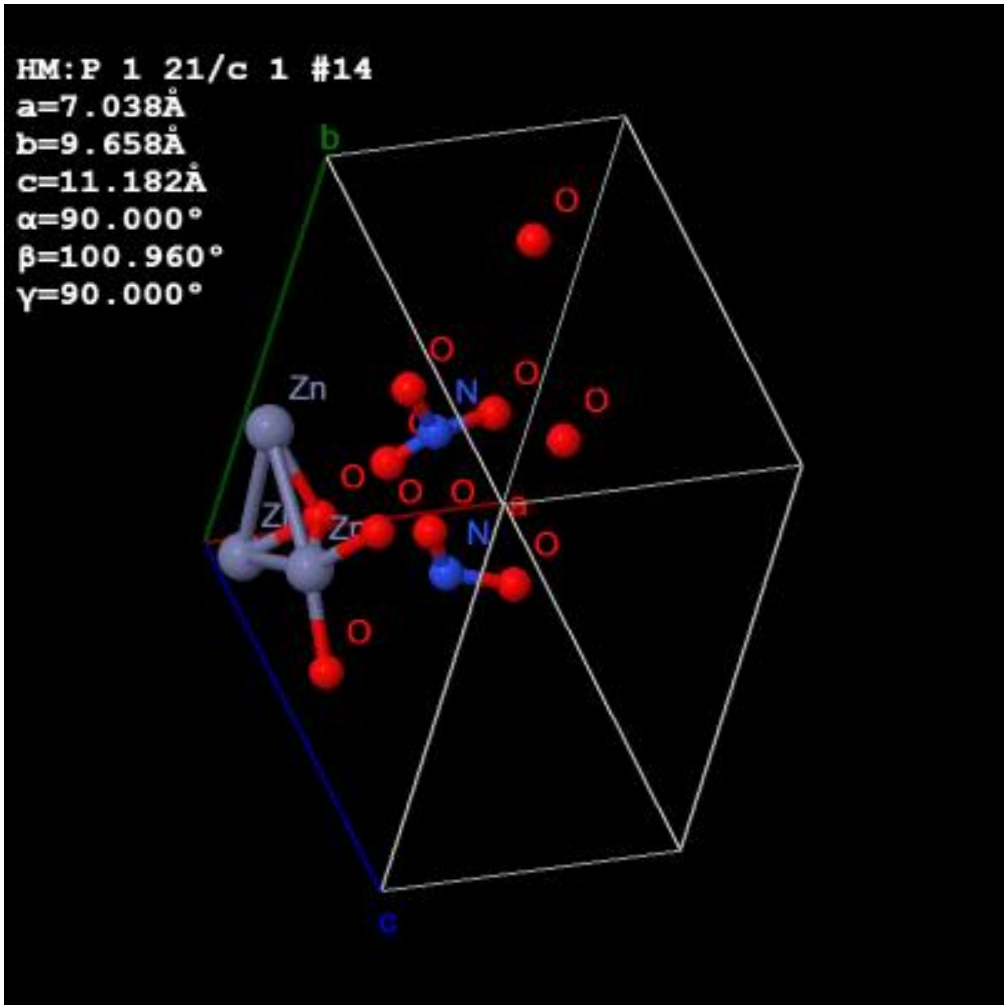

Figure 196: Crystallographic Information File (CIF) of Zinc Hydroxyl Nitrate. The images portray the crystal structure layout and the corresponding lattice mis-match.

Table 80: The Crystallographic information of Zinc Hydroxyl Nitrate. The table summarizes the lattice mismatch and Space Group.

Chemical Name	Zinc Hydroxyl Nitrate
Formula	$Zn3\ (OH)_{4\ (}N\ O_3)_2$
a	7.038 Å
b	9.658 Å
c	11.182 Å
α	90°
β	100.96°
γ	90°
Cell Volume	746.21 $Å^3$
Number of Distinct Elements	4
Hermann - Mauguin Symmetry Space Group	P 1 21/c 1
Hall symmetry Space Group	-P 2ybc

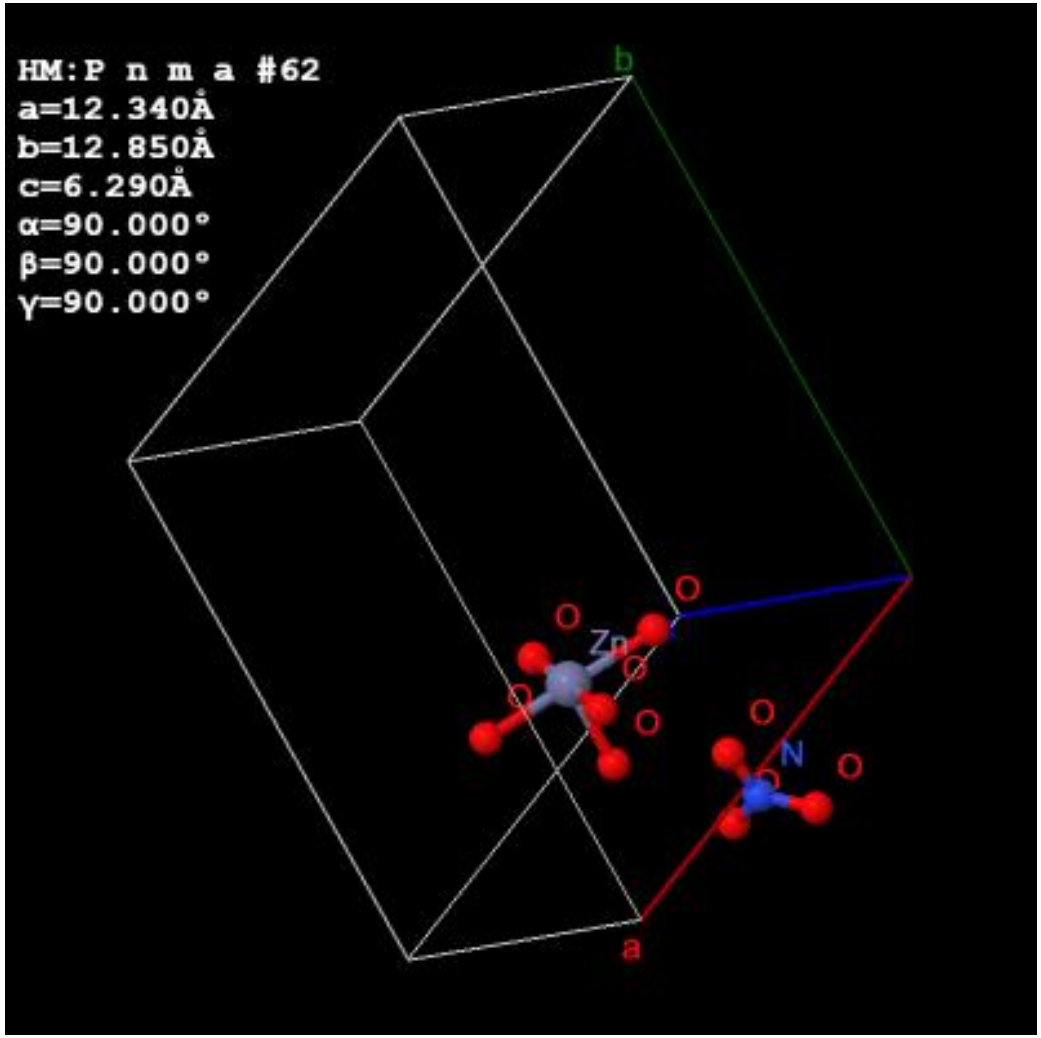

Figure 197: Crystallographic Information File (CIF) of Zinc Nitrate Hexahydrate *($Zn(NO_3)_2.\ 6H_2O$)*. The images portray the crystal structure layout and the corresponding lattice mis-match.

Table 81: The Crystallographic information of Zinc Nitrate Hexahydrate. The table summarizes the lattice mismatch and Space Group.

Chemical Name	Zinc Nitrate Hexahydrate
Formula	$Zn\ (NO_3)_2\ 6(H_2O)$
a	12.34 Å
b	12.85 Å
c	6.29 Å
α	90°
β	90°
γ	90°
Cell Volume	997.399 $Å^3$
Number of Distinct Elements	4
Hermann - Mauguin Symmetry Space Group	P n m a
Hall symmetry Space Group	-P 2ac 2n

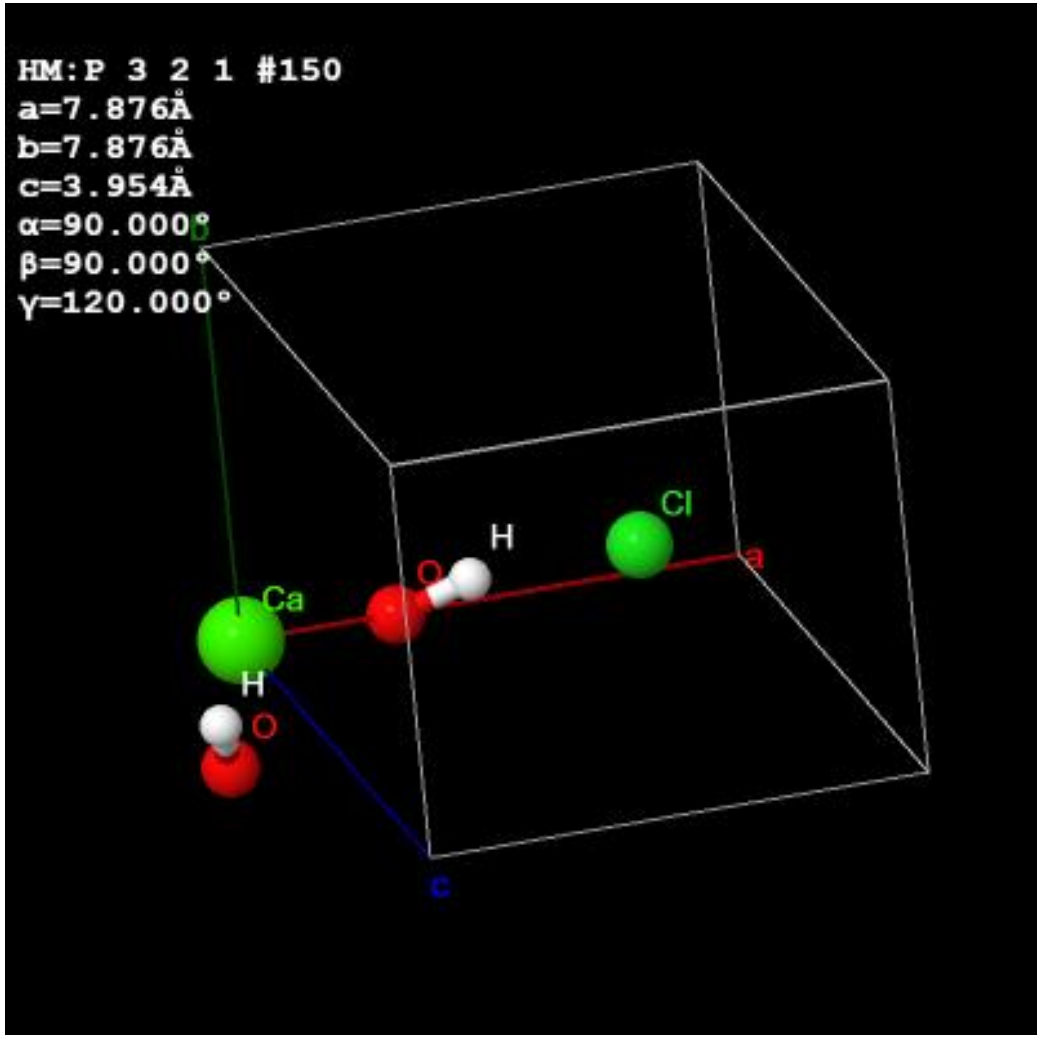

Figure 198: Crystallographic Information File (CIF) Calcium Chloride Hexahydrate *($CaCl_2$. $6H_2O$)*. The images portray the crystal structure layout and the corresponding lattice mis-match.

Table 82: The Crystallographic information of calcium chloride Hexahydrate. The table summarizes the lattice mismatch and Space Group.

Chemical Name	Calcium Chloride Hexahydrate
Formula	$Ca\ Cl_2\ 6(H_2O)$
a	7. 876 Å
b	7. 876 Å
c	3.954 Å
α	90°
β	90°
γ	120°
Cell Volume	212.4 $Å^3$
Number of Distinct Elements	4
Hermann - Mauguin Symmetry Space Group	P 3 2 1
Hall symmetry Space Group	P 3 2”
Symmetry Class	Trigonal
Structure type	Antarctictite

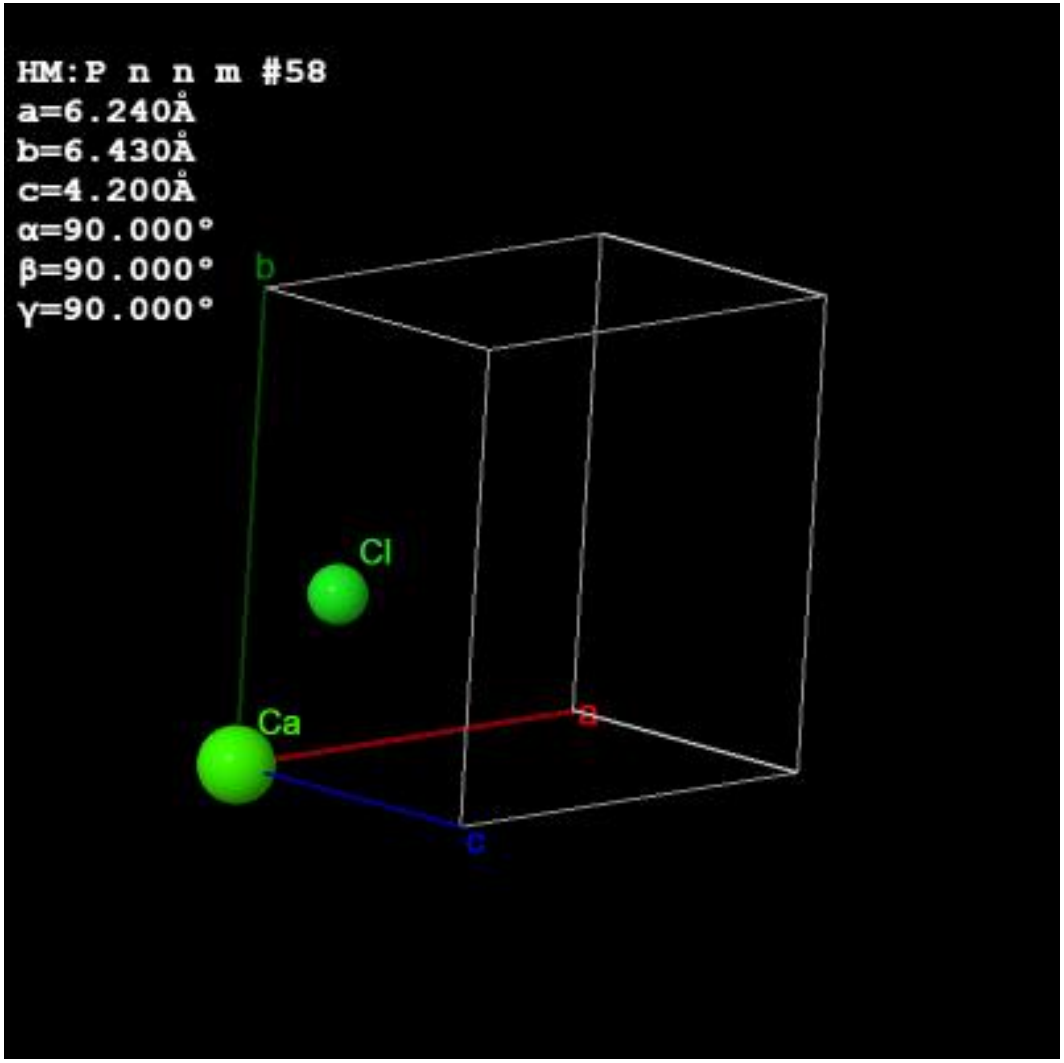

Figure 199: Crystallographic Information File (CIF) Calcium Chloride *($CaCl_2$).* The images portray the crystal structure layout and the corresponding lattice mis-match.

Table 83: The Crystallographic information of Calcium Chloride. The table summarizes the lattice mismatch and Space Group.

Chemical Name	Calcium Chloride
Formula	$Ca\ Cl_2$
a	6.24 Å
b	6.43 Å
c	4.2 Å
α	90°
β	90°
γ	90°
Cell Volume	168.5 $Å^3$
Number of Distinct Elements	4
Hermann - Mauguin Symmetry Space Group	P n n m
Hall symmetry Space Group	-P 2 2n
Symmetry Class	Orthorhombic
Structure type	Rutile – Distorted

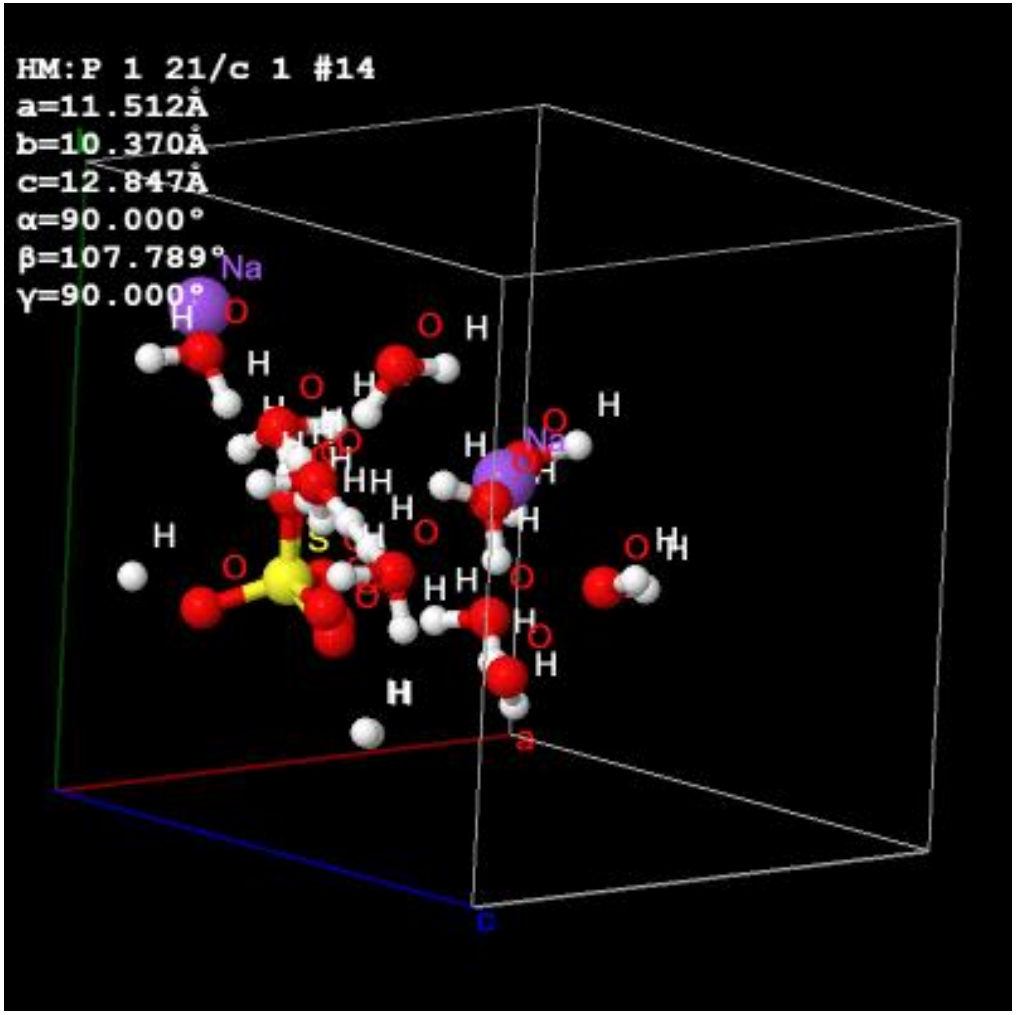

Figure 200: Crystallographic Information File (CIF) Sodium Sulfate Decahydrate *(Na_2 (SO_4))*. The images portray the crystal structure layout and the corresponding lattice mis-match.

Table 84: The Crystallographic information of Calcium Chloride. The table summarizes the lattice mismatch and Space Group.

Chemical Name	Sodium Sulfate Decahydrate
Formula	H_2O Na2 O_{14} S
a	11.512 Å
b	10.37 Å
c	12.847 Å
α	90°
β	107.789 °
γ	90°
Cell Volume	1460.3 $Å^3$
Number of Distinct Elements	4
Hermann - Mauguin Symmetry Space Group	P 1 21/ C 1
Hall symmetry Space Group	-P 2ybc
Symmetry Class	Monoclinic -beta
Structure type	mirabilite

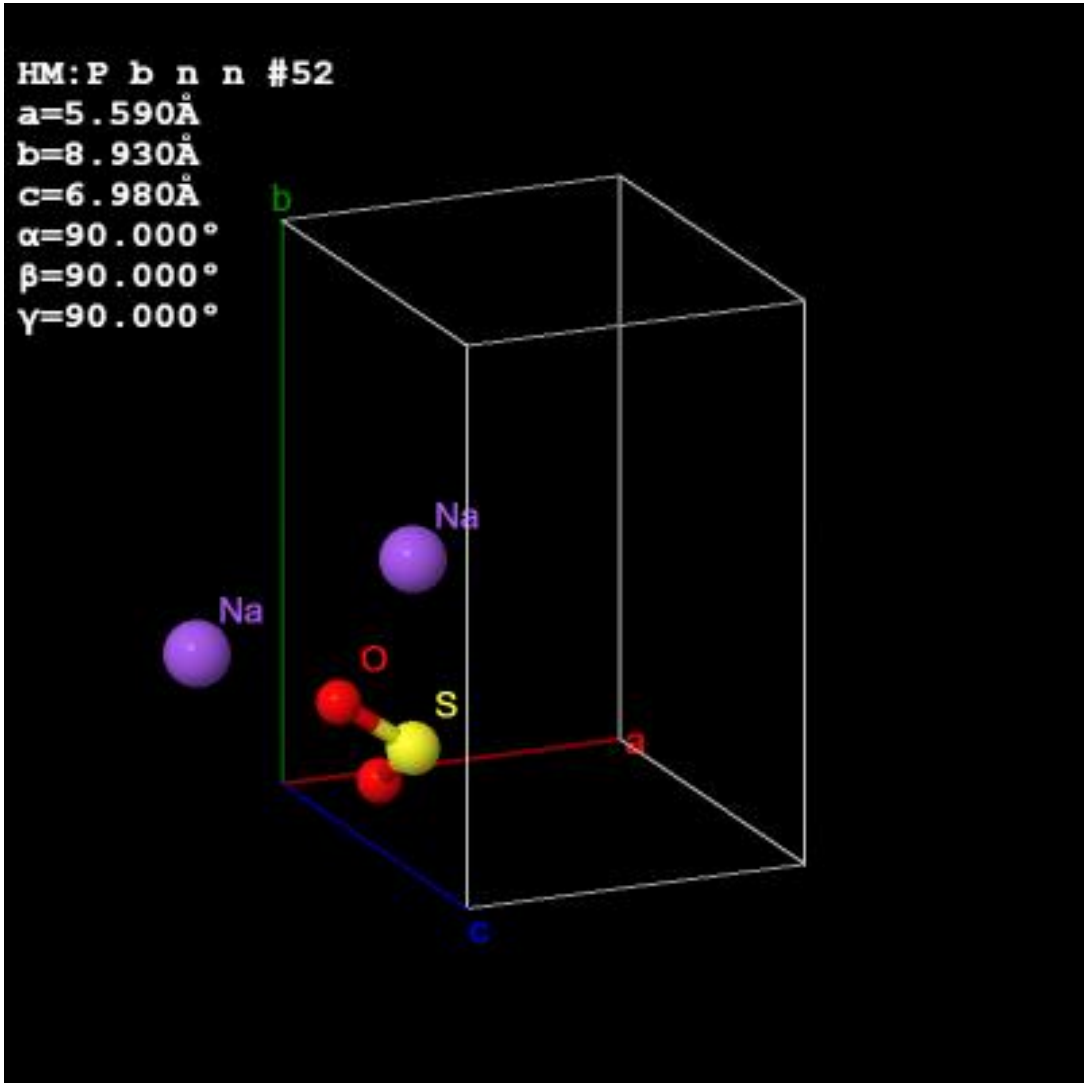

Figure 201: Crystallographic Information File (CIF) Sodium Sulfate *(Na_2 (SO_4))*. The images portray the crystal structure layout and the corresponding lattice mis-match.

Table 85: The Crystallographic information of Calcium Chloride. The table summarizes the lattice mismatch and Space Group.

Chemical Name	Sodium Sulfate
Formula	$Na2\ O_4\ S$
a	5.59 Å
b	8.93 Å
c	6.98 Å
α	90°
β	90 °
γ	90°
Cell Volume	348.4 $Å^3$
Number of Distinct Elements	3
Hermann - Mauguin Symmetry Space Group	P b n n
Hall symmetry Space Group	-P 2n 2b
Symmetry Class	Orthorhombic
Structure type	Thernadite

APPENDIX J

Specimen Tested	Thermal Cycling Data						Thermal Physical Properties							
	Initial Latent Heat (J/g)	% Δ(Latent Heat)	Trans Temp (°C)	% Δ (Trans Temp)	% Δ(Mass)	Sub Cooling (°C)	Lit Latent Heat (J/g)	Lit Trans Temp (°C)	Solid Density (g/ m^3)	Liquid Density (g/ m^3)	Solid Cp (J / g K)	Liquid Cp (J / g K)	k (Solid) (W / m K)	k (Liquid) (W / m K)
$Zn(NO_3)_2.6H_2O$ +3% Zinc Nitrate Hydroxyl [1000 Cycles]	145(σ ±3.2%) 265 MJ/m^3	-15	35 (MP) (σ ± 0.8%) 35.7 (FP) (σ ± 0.8%)	- 0.7(MP) -1.0 (FP)	1.8	2.4	136[1] 248 MJ/m^3	36.0[1]	1.937[1]	1.828[1]	-	-	0.86 @ 21°C (σ ± 3.3%) (Measured with Hot Disk)	0.47 @ 45°C (σ ± 8.5%) (Measured with Hot Disk)
$Zn(NO_3)_2.6H_2O$ +3% Zinc Oxide [1000 Cycles]	143(σ ±4.3%) 261 MJ/m^3	-15	35.3 (MP) (σ ± 0.7%) 36.1 (FP) (σ ± 0.7%)	- 0.5(MP) -0.8 (FP)	2.3	3								
$LiNO_3.3H_2O$ [150 Cycles]	273(σ ±7.8%) 382 MJ/m^3	-53	29.2 (MP) (σ ± 0.8%) 27.6 (FP) (σ ± 1.2%)	-2.6 (MP) -8.0 (FP)	1	12	287[2] 401 MJ/m^3	30.15[2]	1.58[2]	1.4[2]	1.63 (σ ± 2.1%) (Measured With DSC)	2.91 (σ ± 4.0%) (Measured with DSC)	0.84 @ 21°C (σ ± 4.0%) (Measured with Hot Disk)	0.41 @ 40°C (σ ± 8.5%) (Measured with Hot Disk)
$LiNO_3.3H_2O$ + 3% Zinc Hydroxyl Nitrate [1000 Cycles]	265(σ ±5.2%) 371MJ/m^3	-5	29.5 (MP) (σ ± 0.5%) 29.7 (FP) (σ ± 1.0%)	- 0.3(MP) -0.6 (FP)	2	3.8								
$CaCl_2.6H_2O$ +3% NaCl [300 Cycles]	199 (σ ±5.7%) 310 MJ/m^3	-10.6	29.5 (MP) (σ ± 0.7%) 28.7 (FP)	-1.6 (MP) -4.3 (FP)	+1.8	2.5	200[3] 312 MJ/m^3	30[3]	1.802[3]	1.562[3]	1.67 (σ ± 2.3%) (Measured With DSC)	2.32 (σ ± 4.0%) (Measured with DSC)	0.95 @ 20°C (σ ± 4.8%) (Measured with Hot Disk)	0.48 @ 40°C (σ ± 9.6%)

			(σ ± 0.5%)											(Measured with Hot Disk)
$CaCl_2.6H_2O$ +3% SrCl [1000 Cycles]	185 (σ ±9.0%) 288MJ/m^3	-4.5	29.7 (MP) (σ ± 0.5%) 29.5 (FP) (σ ± 1.0%)	-0.6 (MP) -0.2 (FP)	+0.8	2.5								
$Na_2SO_4.10H_2O$ [150 Cycles]	145 (σ ±6.2%) 215 MJ/m^3	-84.0	23.6(MP) (σ ± 0.5%) 21.1 (FP) (σ ± 1.0%)	-2.5(Mp) -.38(FP)	3.0	15.2								
$Na_2SO_4.10H_2O$ + 1% Borax [300 Cycles]	170 (σ ± 12%) 252 MJ/m^3	-13.7	32.4 (MP) (σ ±0.8%) 30.8 (FP) (σ ±1.8%)	-3.1 (MP) -3.8 (FP)	2.7	3.0	254[4] 377 MJ/m^3	32.4[4]	1.963[4]	1.485[4]	1.890 (σ ± 6.5%) (Measured With DSC)	2.7 (σ ± 3.0%) (Measured with DSC)	0.48[4] @23.3°C	0.61[4] @40.0°C
$Na_2SO_4.10H_2O$ + 1% Borax + 10% Gelatin [300 Cycles]	227 (σ ± 3.6%) 337MJ/m^3	-21.0	30.9 (MP) (σ ± 0.7%) 31.5(FP) (σ ± 1.2%)	-3.4(MP) -1.6(FP)	3.5	4.5								
PureTemp 29 [300 Cycles]	213 (σ ± 7.6%) 200 MJ/m^3	12.7	30.5 (MP) (σ ± 1.1%) 26.7 (FP) (σ ± 2.5%)	-	1.6	-	202[5] 171 MJ/m^3	29[5]	940[5]	850[5]	1.78 (σ ± 2.2%) (Measured With DSC)	2.0 (σ ± 0.5%) (Measured with DSC)	0.25 @ 21°C (σ ± 2.0%) (Measured with Hot Disk)	0.18 @ 35°C (σ ± 7.3%) (Measured with Hot Disk)

APPENDIX K

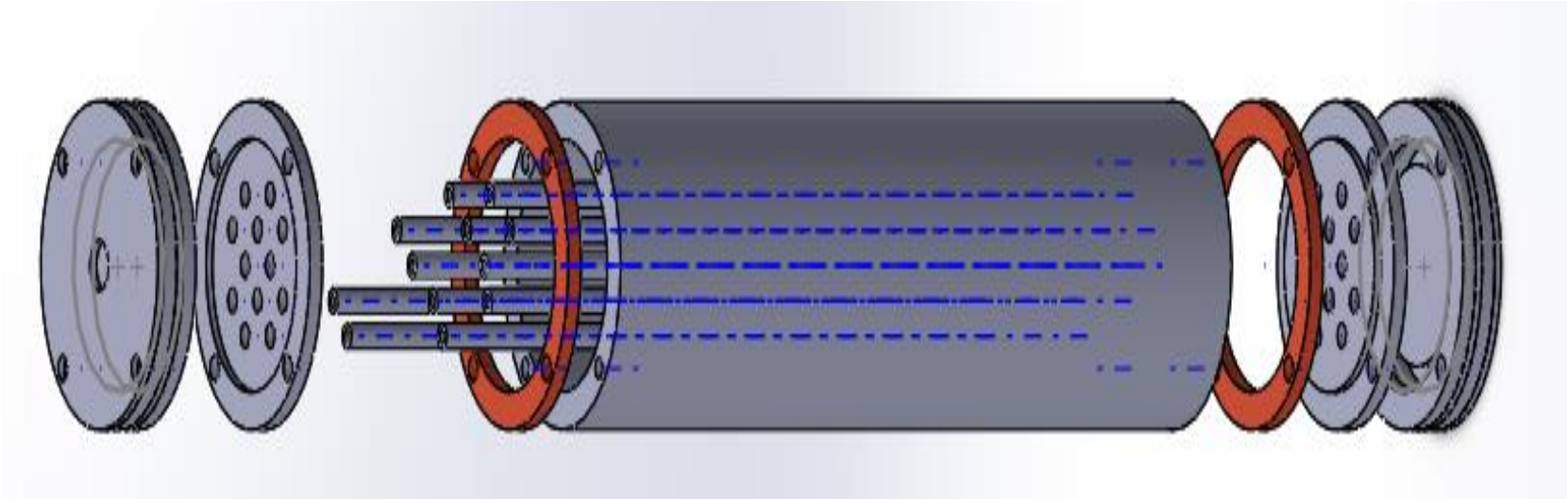

Figure 202: 3D Printed Shell and Tube Heat Exchanger. The shell contained PureTemp 29 PCM and HTF was flowed through the tubes. Total of 12 tubes. The outer diameter of the shell is 3.25" and the inner diameter of the shell is 2.51". The outer diameter of the tube is 0.25" and inner diameter is 0.17". Overall length is 10".

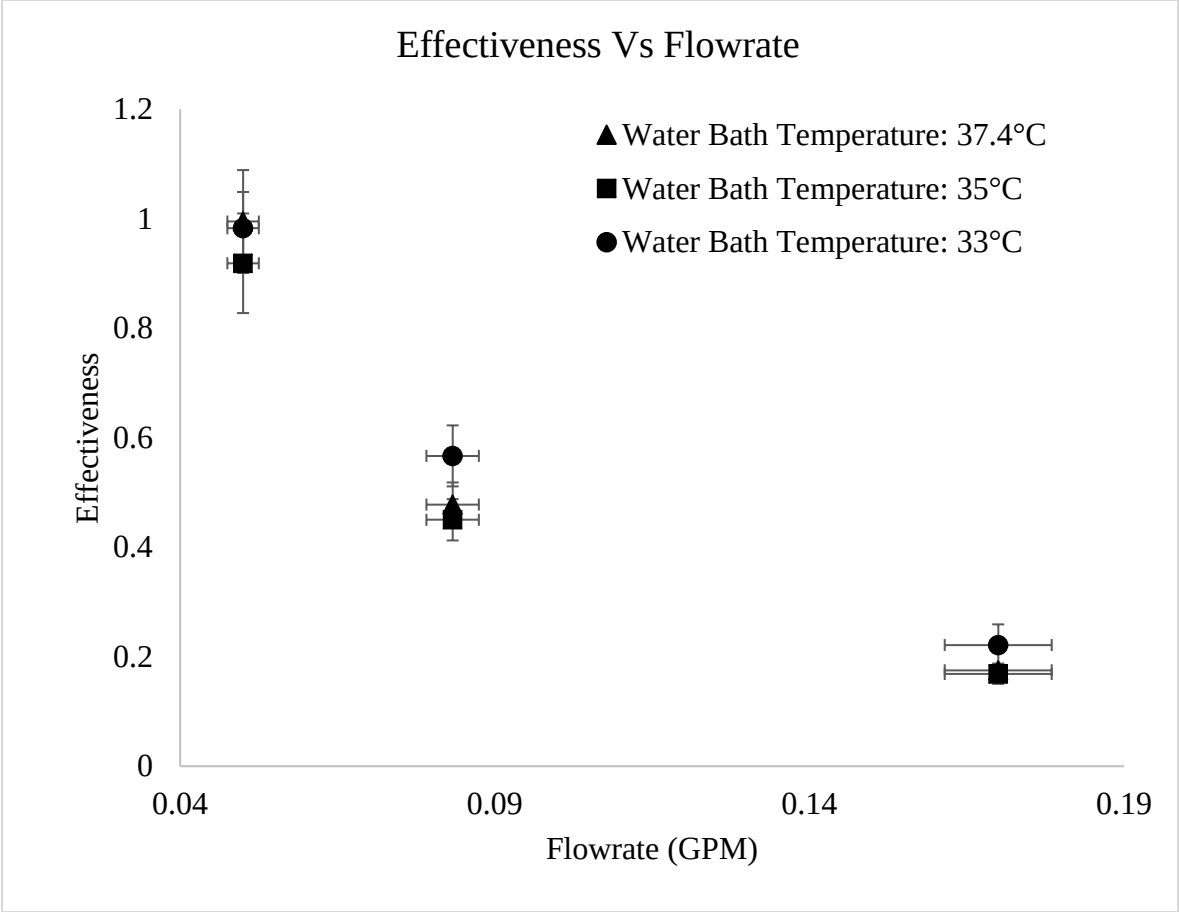

Figure 203: The effectiveness of 3D printed shell and tube heat exchanger with varying hot flow inlet temperature and flowrate during the melting process of PureTemp 29.

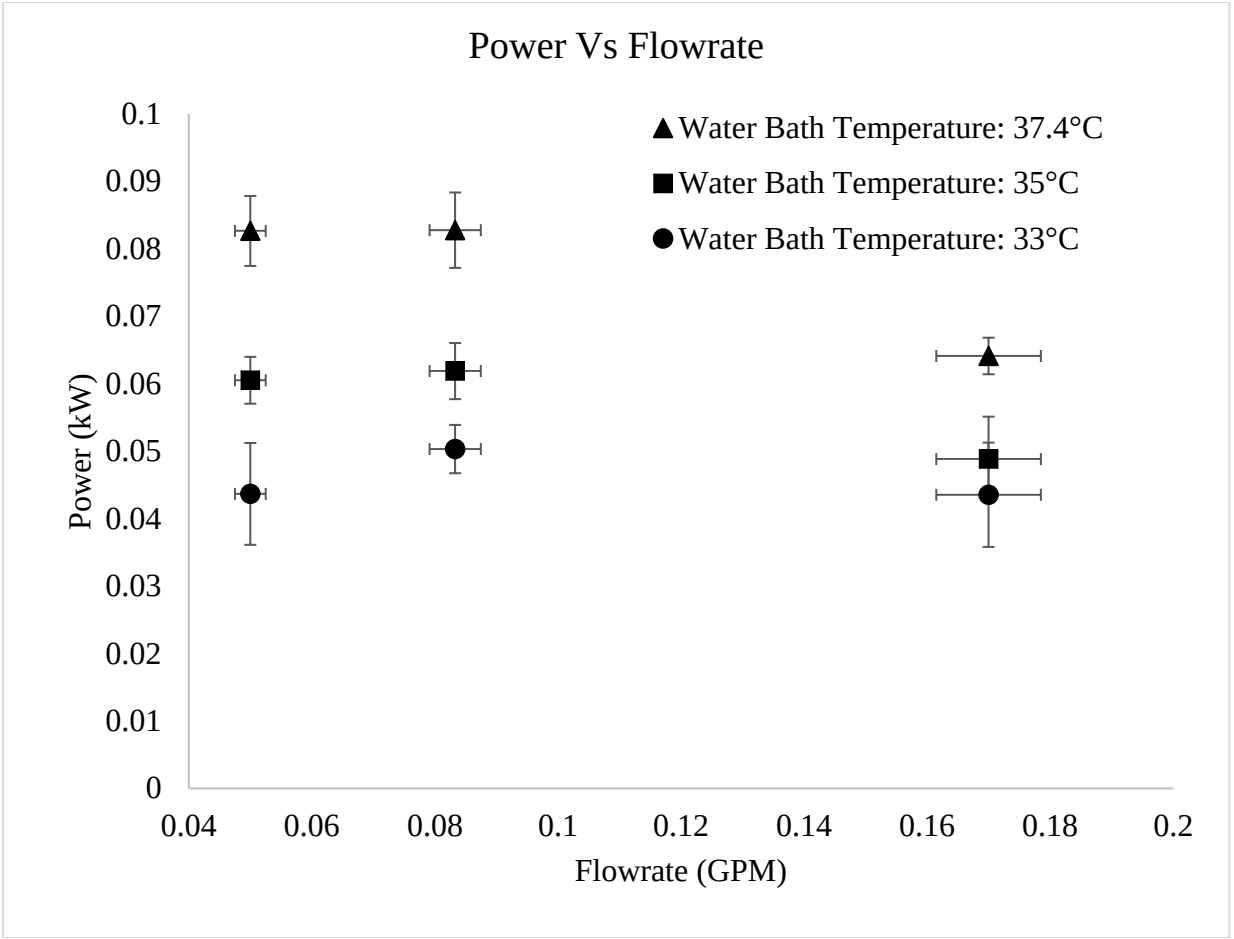

Figure 204: The power of 3D printed shell and tube heat exchanger with varying hot flow inlet temperature and flowrate during the melting process of PureTemp 29.

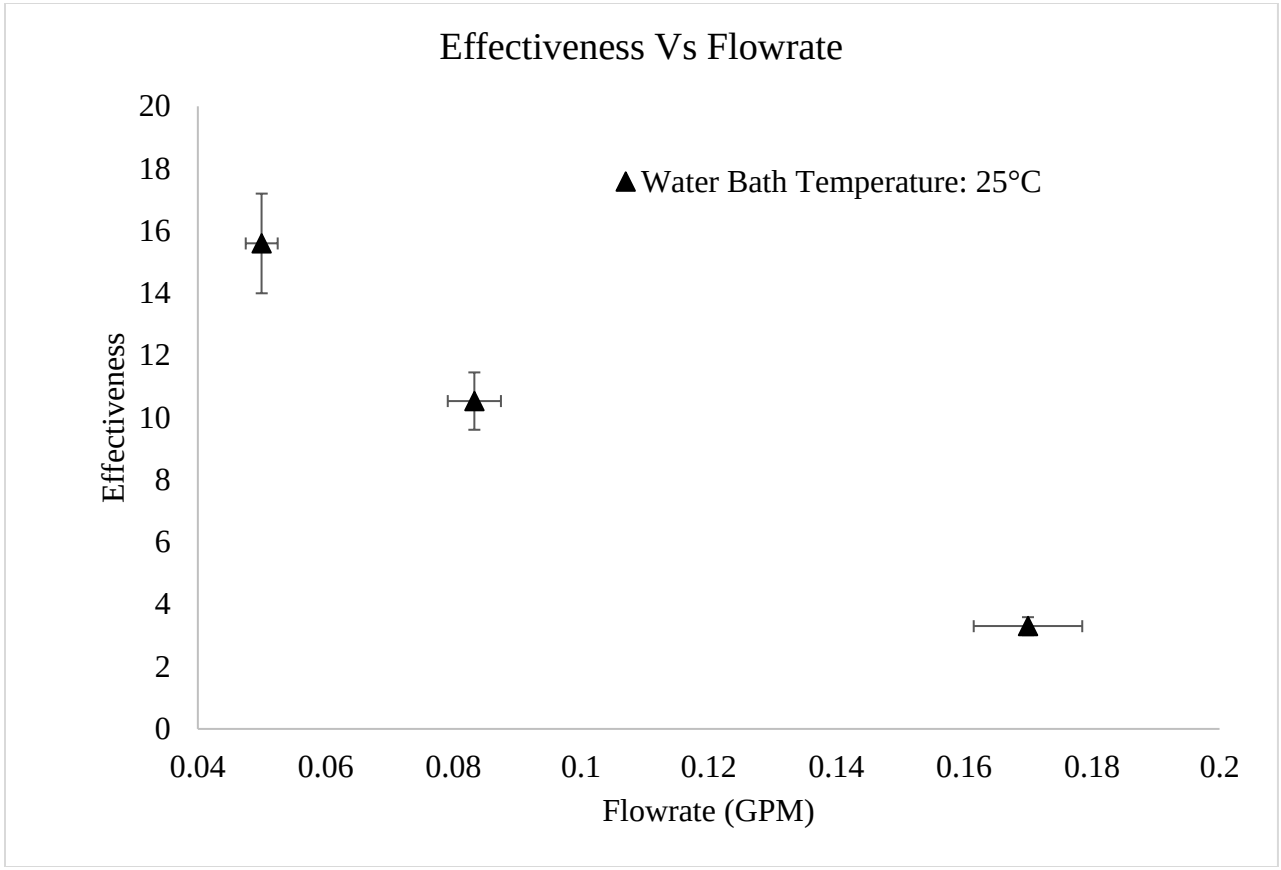

Figure 205: The effectiveness of 3D printed shell and tube heat exchanger with cold flow inlet temperature and flowrate at 25°C during solidification.

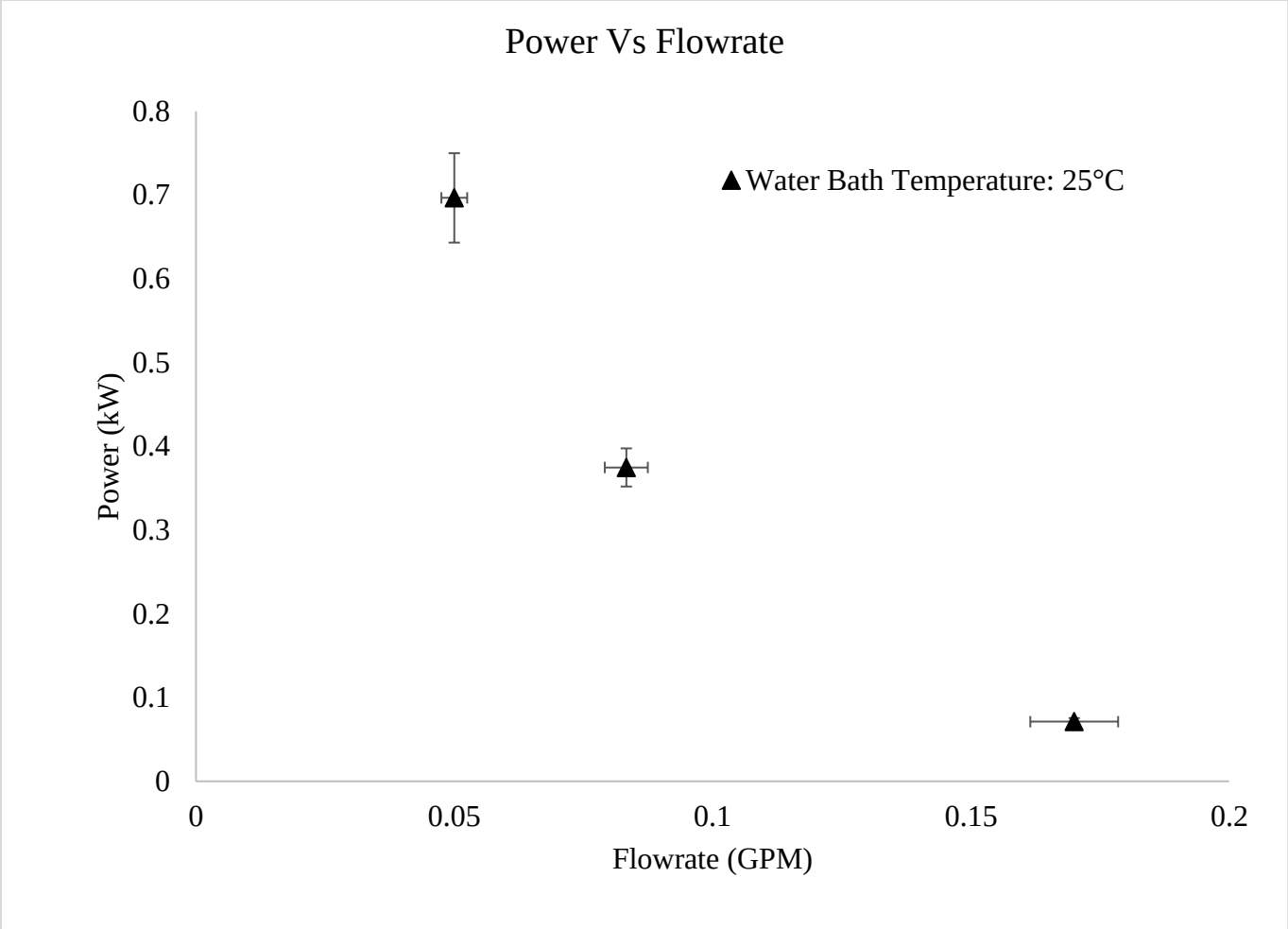

Figure 206: The power of 3D printed shell and tube heat exchanger with cold flow inlet temperature and flowrate at 25°C during solidification.

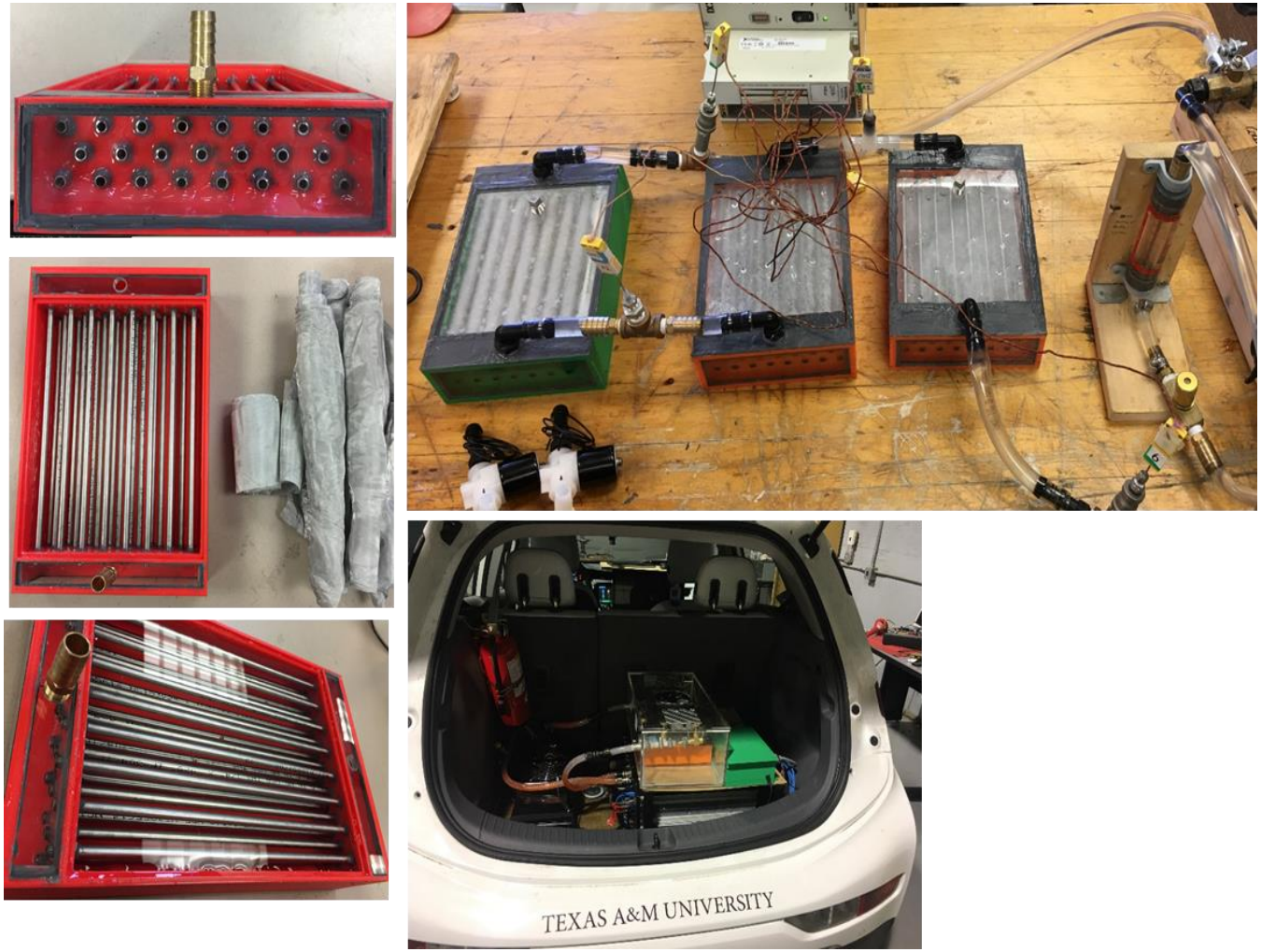

Figure 207: Future Direction for automotive industry.